



Universitat Autònoma de Barcelona

ADVERTIMENT. L'accés als continguts d'aquesta tesi queda condicionat a l'acceptació de les condicions d'ús establertes per la següent llicència Creative Commons:  http://cat.creativecommons.org/?page_id=184

ADVERTENCIA. El acceso a los contenidos de esta tesis queda condicionado a la aceptación de las condiciones de uso establecidas por la siguiente licencia Creative Commons:  <http://es.creativecommons.org/blog/licencias/>

WARNING. The access to the contents of this doctoral thesis it is limited to the acceptance of the use conditions set by the following Creative Commons license:  <https://creativecommons.org/licenses/?lang=en>



Autonomous University of Barcelona
Department of Electronic Engineering

Doctoral Thesis

Semiconducting metal oxide structures with surface nanoscale interfaces for gas sensing

Milena Tomić

Director

Stella Vallejos Vargas, PhD

Tutor

Prof. Montserrat Nafría Maqueda, PhD

Barcelona, 2021

Abstract

In this thesis, research on gas sensors based on non-modified and modified with second-phase materials structured metal oxides (MOXs) is presented. These types of sensors and materials are investigated due to the MOX sensors' relevance in current applications addressed to societal challenges, such as environment, security, and health, and impact of MOX materials on the functional properties of the sensor device. Compared with bulk and thin-film materials, structured MOX materials exhibit higher response due to their high surface-to-volume ratio and their particular morphology that is remarkably beneficial to the adsorption and desorption of gases. In addition, the modification of these structures with second-phase materials to form nanoscale interfaces (e.g., Schottky-barrier-like junctions or heterojunctions) at the structure's surface adds further improvements by sensitizing chemically and electronically the structured MOX. Hence, the focus of this thesis is on developing synthesis routes based on aerosol assisted chemical vapor deposition (AACVD) that allow tuning the surface morphology of MOXs (shape, size, and dimensional control) and modifying their surface with second-phase constituents, such as noble metals, another MOXs, or organo-functional molecules, that, altogether, promotes synergistic effects at the surface and enhances the sensor's sensitivity, selectivity, and/or operating temperature.

The 'host' structured MOXs include WO_3 , ZnO , and Fe_2O_3 deposited via AACVD, whereas the second-phase materials involve films or particles of another MOX (CeO_2 , Fe_2O_3 , and Cu_2O), noble metal (Au), or organo-functional molecule (APTES), incorporated via AACVD, impregnation method, or silanization process. Therefore, in total, seven types of modified MOX structures and sensors are developed ($\text{CeO}_2@ \text{WO}_3$, $\text{APTES}@ \text{WO}_3$, $\text{APTES}@ \text{CeO}_2@ \text{WO}_3$, $\text{Au}@ \text{ZnO}$, $\text{Fe}_2\text{O}_3@ \text{ZnO}$, $\text{Cu}_2\text{O}@ \text{ZnO}$, and $\text{Au}@ \text{Fe}_2\text{O}_3$) together with their corresponding non-modified versions (WO_3 , ZnO , and Fe_2O_3). The morphology, crystalline structure, and chemical composition of these structures are analyzed by different methods, among others, electron microscopy, diffraction, and X-ray photoelectron spectroscopy. Results demonstrate the formation of highly crystalline wires (WO_3), rods (ZnO), and pyramids (Fe_2O_3), with aspect ratios of 100, 7.5, and 1.5, respectively, and the incorporation of second-phase materials with characteristic loads between 1 and 12 at%. These structures integrated into sensor devices are evaluated in thermoactivated and photoactivated mode towards oxidizing and reducing gases recognized as the most relevant for further application in environmental monitoring, and/or medical application, amongst which are ethanol, acetone, toluene, hydrogen, ammonia, carbon monoxide, and/or nitrogen dioxide. Overall, the sensors demonstrate the best results in detecting acetone, ethanol, and NO_2 , with the highest sensitivity to acetone ($6.6 \% \text{ ppm}^{-1}$) and ethanol ($19.2 \% \text{ ppm}^{-1}$) recorded at room temperature for the photoactivated $\text{APTES}@ \text{CeO}_2@ \text{WO}_3$ and $\text{APTES}@ \text{WO}_3$ sensors, respectively, and to NO_2 ($39.96 \% \text{ ppm}^{-1}$) recorded at 310°C for the thermoactivated $\text{Au}@ \text{ZnO}$ sensors. Generally, gas sensors with surface modified materials prove enhanced gas sensing properties compared to pristine sensors, except in the case of $\text{Au}@ \text{Fe}_2\text{O}_3$, which is explained by the excessive Au loading compared to other modified systems, that locks the active sites on the surface of Fe_2O_3 , responsible for the gas adsorption, and thus lower the sensing capability of the sensor. The enhanced performance of the modified materials is mainly attributed to synergistic catalytic effects and the presence of nanoscale interfaces at the surface, which facilitate the electron transfer during the gas-solid interaction.

Key words

Gas sensors, metal oxides, surface modification, heterojunctions, AACVD, acetone, ethanol, nitrogen dioxide.

Bibliographic citation

Milena Tomić. Semiconducting metal oxide structures with surface nanoscale interfaces for gas sensing. Doctoral Thesis. Institute of Microelectronics of Barcelona (IMB-CNM, CSIC). Barcelona, 2021. Supervisor: Stella Vallejos Vargas, Tutor: Montserrat Nafria Maqueda.

Declaration

I hereby declare that this doctoral thesis is my own original research, which has been done under the tutoring of prof. Montserrat Nafria Maqueda, Ph.D. and supervision of Stella Vallejos Vargas, Ph.D. I have duly acknowledged all the sources of information, which have been used in the thesis.

Barcelona,

.....
(Author's signature)

Acknowledgment

The research presented in this thesis could not have been successfully finished without the assistance and encouragement of the people that were part of my life during this Ph.D. journey.

First of all I would like to thank my supervisors, Dr. Stella Vallejos Vargas from the *Gas Sensors* group of *IMB-CNM (CSIC)* and Prof. Montserrat Nafria Maqueda from the *Department of Electronic and Telecommunication Engineering* of *UAB*, for their continuous support, guidance, and advice throughout my Ph.D., as well as for their optimism, enthusiasm, and confidence in me.

I would also like to express my sincere gratitude to the other members of *Gas Sensors* group - Isabel Gràcia, Eduard Figueras, and Carles Cané for their warm welcome, encouragement, knowledge, and endless positivism that made my work on this thesis much easier.

I also own a huge thank to all colleagues that I collaborated with, Martha, Lukas, Ondrej, Zdenka, and Boutheina, which work contributed to the articles published during this thesis.

Many thanks to my former colleagues from the *IHS Research and Development Center*, Ljilja, Marijana, and Miloš, which advice and support were of great help.

I am grateful to the Spanish Ministry of Science and Innovation via Grant no. TEC2016-79898-C6-1-R, PID2019-107697RB-C42 (AEI/FEDER, EU) for supporting financially my doctoral studies.

Finally, I would like to thank all my friends, especially, Šetka, Jeka, Isi, Tića, Geri, Ale, Nole, Zeko, Milica, Ana, Sofija, Vuk, Marjana, Sunil, Joka, Mina, and Suza for their love and understanding.

Last but not the least, I would like to express my deepest gratitude to my parents, Ljuba and Mile, and my brother Milan for their unconditional love, support, and motivation.

List of Figures

Figure 1.1. Schematic representation of a thermoactivated gas sensor (cross-section).	5
Figure 1.2. Number of articles involving different types of the metal oxide based gas sensor reported in the literature (Scopus database from 1978 – 2021). The data were collected using the name of metal oxide (e.g. “ZnO”) + “gas sensor” as keywords.	7
Figure 1.3. Schematic representation of typical a) conventional and b) MEMS-based transducing platforms for gas sensors.	16
Figure 2.1. Scheme of AACVD system.....	18
Figure 2.2. a) Low and high (inset) magnification SEM, b) STEM, and c) HRTEM images of the Fe ₂ O ₃ structured film.....	22
Figure 2.3. Schematic diagram of the EDX working principle.....	23
Figure 2.4. Schematic diagram of the XPS working principle.	24
Figure 2.5. Schematic diagram of the XRD working principle.....	25
Figure 2.6. Schematic diagram of the DRS working principle.....	25
Figure 2.7. Schematic representation of the a) Si bulk sensor’s layers, b) micromachined sensor’s layers, and c) Si bulk sensor mounted on a standard TO8 package, and d) array of micromachined sensors mounted on a standard TO8 package. The image b) is adopted from [172].	27
Figure 2.8. Schematic view of the a) thermoactivated, b) photoactivated gas sensing measurement system. Not-to-scale.....	28

List of Tables

Table 1.1. Material characteristic and sensing properties of pristine ZnO, WO ₃ , and Fe ₂ O ₃	8
Table 1.2. Sensing properties of modified and non-modified gas-sensitive materials.	11
Table 1.3. Photoactivated gas sensing responses of MOX-based gas sensors.	13
Table 1.4. Summary of the most common synthesis and integration methods of MOX materials for gas sensing.....	14
Table 2.1. Conditions used for AACVD synthesized materials in this thesis.....	19
Table 2.2. Concentration of elements (Si, O, W, N, and C) at the APTES modified WO _{3-x} samples obtained under the different experimental conditions a) plasma treatment time (1 and 5 min), b) deposition time (10, 30 and 50 min), and c) amount of silane (15, 100 and 1000 µl).	20
Table 2.3. Sensor response calculation depending on the type of the target gas.	28
Table 4.1. Comparison of the synthesis conditions and material morphologies of the sensors fabricated in this thesis.	41
Table 4.2. Comparison of the sensing performances and working conditions of the sensors fabricated in this thesis.	42

List of abbreviations

Δc	Change in concentration
ΔR	Change in response
Å	Angstrom
<i>a.u.</i>	Arbitrary unit
AACVD	Aerosol assisted chemical vapor deposition
ACGIH	American Conference of Governmental Industrial Hygienists
<i>ads</i>	Adsorbed
Ag	Silver
ANN	Artificial neural network
ANOVA	Analysis of variance
APTES	(3-aminopropyl)triethoxysilane
AR	Aspect ratio
<i>at%</i>	Atomic percentage
Au	Gold
BC	Bacterial cellulose
BD	2,3-butanedione
BE	Electron binding energy
BE	Base edge
BN	Boron nitride
BP	Black phosphorus
<i>bsh</i>	Blue shift
<i>c</i>	Concentration
C_2H_5OH	Ethanol
CA	Cluster analysis
CB	Conduction band
<i>CbMs</i>	Carbon-based materials
CD	Cyclodextrin
<i>CdA</i>	Cadmium arachidate
$Ce(acac)_3 \cdot xH_2O$	Cerium(III)acetylacetonate hydrate
$Ce(dbm)_4$	Cerium(IV)dibenzoylmethane
<i>Ce/W</i>	Cerium oxide-tungsten oxide
CeO_2	Cerium oxide
CFL	Cauliflower-like
CH_3CH_2O	Etoxy group
CMOS	Complementary metal-oxide-semiconductor
<i>cNCs</i>	Concave nanocubes
CNTs	Carbon nanotubes
CO	Carbon monoxide
$c\emptyset$	Cavity diameter
COD	Crystallography open database
<i>com</i>	Commercial powder
CP	Conference paper
C_R	Concentration range
CREB	Concentration range in the exhaled breath
CS	Crystal size
<i>CSh</i>	Core shell
CTL	Cataluminescence
$Cu(NO_3)_2 \cdot 6H_2O$	Copper(II) nitrate hexahydrate
Cu_2O	Copper(I)oxide
CuO	Copper(II)oxide
CVD	Chemical vapor deposition
<i>d</i>	Spacing between the crystal lattice planes of atoms
DDDT	1,12-dodecanedithiol

<i>DFA</i>	Discriminant function analysis
<i>DMMP</i>	Dimethyl methylphosphonate
<i>DRS</i>	Diffuse reflectance spectroscopy
<i>DT</i>	Decanethiol
<i>E</i>	Energy
<i>e⁻</i>	Electrons
<i>e.g</i>	For example
<i>E_{cut-off}</i>	Binding energy cut-off
<i>EDS</i>	Energy-dispersive X-ray
<i>EDX</i>	Energy-dispersive X-ray
<i>E_F</i>	Fermi edge
<i>E_g</i>	Band gap energy
<i>e-nose</i>	Electronic nose
<i>EP</i>	Ethylphenol
<i>Er</i>	Erbium
<i>ESCA</i>	Electron spectroscopy for chemical analysis
<i>Eu</i>	Europium
<i>E_λ</i>	Irradiance
<i>f(R)</i>	Kubelka-Munk function
<i>Fe₂O₃</i>	Iron oxide
<i>FeCl₃·6H₂O</i>	Iron(III) chloride hexahydrate
<i>Fig.</i>	Figure
<i>fPys</i>	Flattened pyramids
<i>F_∅</i>	Fiber diameter
<i>FT</i>	Film thickness
<i>g</i>	Gaseous
<i>GC-MS</i>	Gas chromatography/Mass spectroscopy
<i>GLSR</i>	Generalized least squares regression
<i>GO</i>	Graphene oxide
<i>h</i>	Planck's constant
<i>h⁺</i>	Holes
<i>H₂S</i>	Hydrogen sulfide
<i>HAuCl₄·3H₂O</i>	Gold(III) chloride trihydrate
<i>HCA</i>	Hierarchical cluster analysis
<i>hMSp</i>	Hierarchical microsphere
<i>HOMO</i>	Highest occupied molecular orbital
<i>HPLC</i>	High-performance liquid chromatography
<i>HRTEM</i>	High-resolution transmission electron microscopy
<i>HSps</i>	Hollow spheres
<i>HTs</i>	Hemitubes
<i>hν</i>	Energy of the incident beam
<i>i.e.</i>	That is
<i>I_a</i>	Photocurrent in air
<i>IC</i>	Integrated circuits
<i>ICDD</i>	International Centre for Diffraction Data
<i>IDEs</i>	Interdigitated electrodes
<i>I_g</i>	Photocurrent in gas
<i>IMB-CNM (CSIC)</i>	Institute of Microelectronic of Barcelona
<i>I_∅</i>	Inner diameter
<i>IoT</i>	Internet of Things
<i>JA</i>	Journal article
<i>k</i>	Absorption coefficient
<i>KE</i>	Kinetic energy
<i>L</i>	Leaf-like
<i>L</i>	Length
<i>L-a ∅</i>	Long-axis diameter
<i>LBL-SA</i>	Layer-by-layer self-assembly

L_D	Debye length or depth of the depletion region from the surface
<i>LDA</i>	Linear discriminant analysis
LE	Lateral edge
<i>LED</i>	Light-emitting diode
<i>LOD</i>	Limit of detection
L_s	Layers
<i>LSPR</i>	Localized surface plasmon resonance
<i>LUMO</i>	Lowest unoccupied molecular orbital
<i>M</i>	Mesoporous
<i>m.r.</i>	Molar ratio
<i>MA</i>	Microwave assisted
<i>MEMS</i>	Micro-electro-mechanical system
<i>MF</i>	Mass flow
<i>MFI</i> s	Microflowers
<i>MHDA</i>	16-mercaptohexadecanoic acid
<i>ML</i>	Monolayer
<i>MLR</i>	Multiple linear regression
<i>MLShs</i>	Monolayer shells
<i>MNPs</i>	Magnetic nanoparticles
<i>MOF</i>	Metal-organic framework
MoO_3	Molybdenum oxide
<i>MOX</i>	Metal oxide
<i>MSp</i>	Microsphere
<i>MVLR</i>	Multivariate linear regression
<i>MWCNTs</i>	Multi-walled carbon nanotubes
<i>MXenes</i>	2D transition metal carbides/nitrides
n	Order of reflection
<i>N</i>	Noise
<i>N/A</i>	Data not available
N_2O	Nitrous oxide
<i>NCgs</i>	Nanocages
<i>NEs</i>	Nanoellipsoids
<i>NFI</i> s	Nanoflowers
<i>NFs</i>	Nanofibers
NH_3	Ammonia
<i>NNs</i>	Nanoneedles
NO_2	Nitrogen dioxide
<i>NPI</i> s	Nanoplates
<i>NPs</i>	Nanoparticles
<i>NRds</i>	Nanorods
<i>NRgs</i>	Nanorings
<i>NShs</i>	Nanosheets
<i>NTPs</i>	Nanotetrapods
<i>NWs</i>	Nanowires
\emptyset	Diameter
<i>OINCs</i>	Organic-inorganic nanocomposites
$o\emptyset$	Outer diameter
<i>Ov</i>	Oxygen vacancies
<i>P</i>	Porous
<i>PANI</i>	Polyaniline
<i>PCA</i>	Principal component analysis
<i>Pd</i>	Palladium
<i>PDMS</i>	Polydimethylsiloxane
<i>PEDOT</i>	Poly(3,4-ethylenedioxythiophene)
<i>PF</i>	Porous film
<i>PhA</i>	Photo-assisted
<i>PID</i>	Proportional integral derivative

<i>PIL</i>	Poly(ionic liquid)
<i>PIs</i>	Plates
<i>PLSR</i>	Partial least squares regression
<i>PMMA</i>	Poly(methyl methacrylate)
<i>pNTs</i>	Porous nanotubes
<i>POMs</i>	Polymers
<i>ppb</i>	Parts per billion
<i>ppm</i>	Parts per million
<i>PPy</i>	Polypyrrole
<i>pPys</i>	Porous pyramids
<i>PS</i>	Pore size
<i>Ps</i>	Particles
<i>PSS</i>	Poly(styrenesulfonate)
<i>PST</i>	Porous shell thickness
<i>Pt</i>	Platinum
<i>PTFE</i>	Polytetrafluoroethylene
<i>PTh</i>	Polythiophene
<i>PVD</i>	Physical vapor deposition
<i>Pys</i>	Pyramids
<i>QCM</i>	Quartz crystal microbalance
<i>QDs</i>	Quantum dots
<i>R</i>	Sensor response
<i>R_a</i>	Sensor resistance in ambient air
<i>RBF</i>	Radial basis function
<i>Rds</i>	Rods
<i>R_g</i>	Sensor resistance in target gas
<i>rGO</i>	Reduced graphene oxide
<i>RH</i>	Relative humidity
<i>rpm</i>	Revolutions per minute
<i>RT</i>	Room temperature
<i>s</i>	Size
<i>s</i>	Scattering coefficient
<i>S</i>	Sensitivity of the sensor
<i>S</i>	Signal peak
<i>s-a ∅</i>	Short-axis diameter
<i>SAE</i>	Smart anything everywhere
<i>SAM</i>	Self-assembled monolayer
<i>SAW</i>	Surface acoustic wave
<i>sccm</i>	Mass flow rate of one cubic centimeter per minute of a fluid
<i>SDA</i>	Stepwise discriminant analysis
<i>SEM</i>	Scanning electron microscopy
<i>Shs</i>	Sheets
<i>SnO₂</i>	Tin dioxide
<i>s-T</i>	Shell thickness
<i>STEM</i>	Scanning transmission electron microscopy
<i>SVM</i>	Support vector machine
<i>s-w T</i>	Side wall thickness
<i>SWCNTs</i>	Single-walled carbon nanotubes
<i>T</i>	Thickness
<i>T</i>	Temperature
<i>TCA</i>	2,4,6-trichloroanisole
<i>T_D</i>	Deposition temperature
<i>TEM</i>	Transmission electron microscopy
<i>TFB</i>	1,3,5-trifluorobenzene
<i>T_{GS}</i>	Working temperature of a gas sensor
<i>TiO₂</i>	Titanium dioxide
<i>TLV</i>	Threshold limit values

<i>TMDs</i>	Transition metal dichalcogenides
t_R	Response time
t_r	Recovery time
<i>Ts</i>	Tubes
$t-wT$	Top wall thickness
<i>TWA</i>	Time weighted averages
<i>UL</i>	Ultra large
<i>UPS</i>	Ultraviolet photoemission spectroscopy
<i>UV</i>	Ultraviolet
<i>v.</i>	Volume
<i>v.r.</i>	Volumetric ratio
<i>VB</i>	Valence band
<i>Vis</i>	Visible
<i>VOCs</i>	Volatile organic compounds
<i>vs.</i>	Versus
<i>w</i>	Width
<i>W(CO)₆</i>	Tungsten hexacarbonyl
<i>WCS</i>	Wet chemical synthesis
<i>WO₃</i>	Tungsten oxide
<i>Ws</i>	Wires
<i>wt%</i>	Weight percentage
<i>XPS</i>	X-ray photoelectron spectroscopy
<i>XRD</i>	X-ray diffraction analysis
<i>ZIF</i>	Zeolitic imidazolate framework
<i>ZnCl₂</i>	Zinc chloride
<i>ZnO</i>	Zinc oxide
ΔEN	Electronegativity difference
θ	Angle of incidence
λ	Wavelength
Φ	Work function

List of publications

Refereed Journal Articles

1. **Tomić, M.**, Claros, M., Gràcia, I., Figueras, E., Cané, C., Vallejos, S., ZnO structures with surface nanoscale interfaces formed by Au, Fe₂O₃, or Cu₂O modifier nanoparticles: characterization and gas sensing properties, *Sensors*, 2021, 21, 4509, doi: 10.3390/s21134509.
2. **Tomić, M.**, Šetka, M., Vojkúvka, L., Vallejos, S., VOCs sensing by metal oxides, conductive polymers, and carbon-based materials, *Nanomaterials*, 2021, 11(2), 552, doi: 10.3390/nano11020552.
3. **Tomić, M.**, Fohlerova, Z., Gràcia, I., Figueras, E., Cané, C., Vallejos, S., UV-light activated APTES modified WO_{3-x} nanowires sensitive to ethanol and nitrogen dioxide, *Sensors and Actuators, B: Chemical*, 2021, 328, 129046, doi: 10.1016/j.snb.2020.129046.
4. **Tomić, M.**, Šetka, M., Chmela, O., Gràcia, I., Figueras, E., Cané, C., Vallejos, S., Cerium oxide-tungsten oxide core-shell nanowire-based microsensors sensitive to acetone, *Biosensors*, 2018, 8(4), 116, doi: 10.3390/bios8040116.
5. Bendahmane B., **Tomić M.**, Toudjen N. H., Gràcia I., Vallejos S., Mansour F., Influence of Mg doping levels on the sensing properties of SnO₂ films, *Sensors*, 2020, 20, 2158, doi: 10.3390/s20072158.
6. Nikolić Bujanović, Lj., Čekerevac, M., Simičić, M., **Tomić, M.**, Encapsulation of micro-sized barium ferrate(VI) and its effectiveness in removing clomazone pesticide from water, *Journal of Materials Science*, 2020, 55(17), 7295, doi: 10.1007/s10853-020-04519-4.

Conference Proceedings

1. **Tomić, M.**, Gràcia, I., Figueras, E., Cané, C., Vallejos, S., ZnO nanorods and their modification with Au nanoparticles for UV-light activated gas sensing, *Spanish Conference on Electron Devices (CDE)*, Sevilla, Spain, 2021, doi: 0.1109/CDE52135.2021.9455726.
2. **Tomić M.**, Gràcia I., Salleras M., Figueras E., Cané C., Vallejos S., Gas microsensors based on cerium oxide modified tungsten oxide nanowires, *Spanish Conference on Electron Devices (CDE)*, Salamanca, Spain, 2018, doi: 10.1109/CDE.2018.8597067.
3. Vallejos S., **Tomić M.**, Gràcia I., Figueras E., Chmela O., Hubalek J., Domènech G., Prades D., Romano-Rodriguez A., Barth S., Cané C., Integration of one-dimensional gas-sensitive nanostructures grown via chemical vapour deposition into microdevices, *Smart Systems Integration 2018 - International Conference and Exhibition on Integration Issues of Miniaturized Systems*, Dresden, Germany, 2018, ISBN: 978-395735082-4.
4. Vallejos S., Fohlerová Z., **Tomić M.**, Gràcia I., Figueras E., Cané C., Room temperature ethanol microsensors based on silanized tungsten oxide nanowires, *International Conference Eurosensors*, Graz, Austria, 2018, doi: 10.3390/proceedings2130790.

Contents

<i>Abstract</i>	ii
Declaration	iv
Acknowledgment	v
List of Figures	vi
List of Tables	vii
List of abbreviations	viii
List of publications	xiii
Introduction	1
Motivation	1
Objectives	2
Thesis structure	3
Chapter 1	5
Literature review	5
1.1. Gas-sensitive materials	5
1.2. Photoactivated vs. thermoactivated gas sensors	12
1.3. Synthesis methods	13
1.4. Transducing platforms	15
Chapter 2	17
Methods	17
2.1 Synthesis methods	17
2.2 Material characterization	21
2.3 Gas sensors fabrication	26
2.4 Gas testing	27
Chapter 3	30
Results	30
3.1 Gas-sensitive materials	30
3.2 Modification of tungsten oxide by nanoscale interfaces	32
3.3 Modification of zinc oxide by nanoscale interfaces	34
3.4 Modification of iron oxide by nanoscale interfaces	36
Chapter 4	38
Conclusions and future work	38
References	43
Appendix A	57

Appendix B	58
Appendix C	59

Introduction

Motivation

Over the past few decades, industrial development and population growth have increased the global energy demand and, consequentially, air pollution. Air pollution is caused by toxic, flammable, and explosive gases, such as CO, H₂S, NH₃, CH₄, NO₂, and H₂, which represent critical factors that contribute to global warming, climate changes, and overall harm to human health. The human olfactory system can detect odorous gases, such as H₂S, NH₃. However, detection of some hazardous gases is impossible for humans, because some of them, like CO and H₂, are odorless, tasteless, and colorless [1]–[3]. Thus, early detection of these harmful gases has attracted a lot of interest among the researchers and this topic has been intensely investigated [4]–[11]. Additionally, in recent years, the interest has been extended to the detection of VOCs, not only because their presence is significant as markers for (indoor/outdoor) air quality [12], but also as markers for food quality [13], and early diagnosis of several diseases [14]. Therefore, the precise and reliable detection of these gases and their concentrations are of great significance to people's health and safety in everyday life, during industrial productions, or for medical applications. For this purpose, different instruments are available and they are mainly based on conventional analytical techniques such as high-performance liquid chromatography (HPLC) [15] and gas chromatography/mass spectroscopy (GC-MS) [16]. However, these techniques are bulky, time-consuming, expensive and most of the time incompatible with the new digital era. Hence, new simple, portable, low-cost, and reliable devices for detection of gases and vapors are in great demand.

Among a variety of sensors, systems, and technologies developed for gas sensing, the most used are pellistors, electrochemical, optical, and thick film metal oxides (MOXs). However, these cannot accomplish the conditions of size, cost, and performances at low concentration levels. As an alternative, this thesis is focused on the development of gas sensors, based on structured MOX materials and micro/nanotechnologies. Using micro/nanotechnologies ensures the miniaturization of the device, which reduces material consumption during the fabrication process and power consumption during the operation of the sensor. Compared with bulk and thin-film materials, structured MOX materials exhibit higher response due to their high surface-to-volume ratio as well as due to the presence of specific crystal facets that provide a particular electronic structure to the surface, which is remarkably beneficial to the adsorption and desorption of target gases [17] [18]. The functionality of structured materials can be enhanced additionally by tailoring their physical and chemical properties via the incorporation of second-phase modifiers. These modifications in the material increment not only the adsorption centers at the surface, but also modify its band energy structure due to the formation of nanoscale interfaces such as Schottky-barrier-like junctions (metal–MOX) or heterojunctions (MOX–MOX, organo-functional molecule–MOX) [19] [20]. Therefore, in this research, special attention is devoted to two possible ways of tailoring the gas sensing properties of the material. The first focuses on tuning the surface morphology (shape, size, and dimensional control), whereas the second involves the functionalization (or surface modification) of MOX crystalline structures with second-phase constituents such as noble metals, another MOXs, or organo-functional

molecules, that, altogether, promotes synergistic effects at the surface and enhances the sensor's sensitivity, selectivity, and/or operating temperature compared to traditional bulk gas-sensitive films. The synthetic routes for these structured and modified materials make use of aerosol assisted chemical vapor deposition (AACVD) method due to its industrially attractive characteristics that include, among others, scalability, compatibility with microelectronic fabrication processes, atmospheric pressure operation, and rates of deposition with a higher order of magnitude than low-pressure processes.

Objectives

The main objective of this thesis was directed to develop and evaluate the performance of micro gas sensor devices based on structured MOXs that incorporate surface modification in the form of nanoscale interfaces that consist of a 'host' MOX and a 'guest' material (i.e., another MOX, metal nanoparticles (NPs), or organo-functional molecules).

In this line, to achieve the main goal, the thesis pursued the following specific objectives and activities:

1. Synthesis and surface modification of structured MOXs and analysis of their physical and chemical properties.

The activities around this objective were focused on synthesizing gas-sensitive MOXs, e.g. WO_3 , ZnO , and Fe_2O_3 , with structured morphologies, e.g., wires, rods, sheets, etc. via a vapor synthesis method based on AACVD. This objective also included the surface modification of the MOX structures using particles of other gas-sensitive MOXs (e.g. CeO_2 , CuO , Fe_2O_3), noble metals (e.g. Au), or organo-functional species (e.g. APTES) introduced via vapor or liquid phase routes. Moreover, as a part of this objective, the synthesized structures were characterized using techniques such as SEM, TEM, XRD, XPS, etc.

2. Assembling of the gas microsensor devices.

This objective involved the integration of the structures synthesized in Objective 1 over the active area of appropriate transducing platforms. To this is end, different methods were explored, including direct deposition of structures using shielding masks and immersion of structures into colloidal solutions. The assembled structures were characterized by SEM, XRD, and/or XPS to confirm the correct integration of materials. In this research, micro platforms based on resistive transducing principle were used. These platforms were fabricated in the Clean Room facilities of the *IMB-CNM (CSIC)* by other researchers of the institute and with the support of the technical staff.

3. Test of the microsensor devices towards gases and VOCs

As a part of this objective, the performance of the assembled devices was verified by monitoring the oxidizing and reducing gases recognized as the most relevant for further application in environmental monitoring and/or medical applications, amongst which are ethanol, acetone, toluene, hydrogen, ammonia, carbon monoxide, and/or nitrogen dioxide. The purpose of these activities was to establish the optimal working temperature for each sensor and its functional properties including sensitivity, selectivity, response/recovery time, and stability, amongst others.

Thesis structure

The crucial topics of the thesis are described and discussed through the following structural sections:

Chapter 1 is devoted to the state of the art of the structured MOX materials utilized in gas sensing as well as modified MOX materials with formed nanoscale interfaces between materials (heterojunctions, Schottky barriers, and inorganic/organic interfaces). This chapter covers characteristics of the material, material activation, synthesis methods, transducing technologies in the gas sensor devices, and the MOX-based sensor performances towards a variety of gases.

Chapter 2 describes all the experimental techniques used during the research for the synthesis of MOX gas sensing materials, their complete characterization, and the techniques used for testing the developed gas sensor devices.

Chapter 3 is divided into four sections. *Section 3.1* further reviews state of the art in MOX gas-sensitive materials, with the focus on VOCs detection by non-modified and modified MOX-based sensors. *Sections 3.2, 3.3, and 3.4* present the novel results and contributions to the state of the art in the area of gas sensing, aerosol assisted chemical vapor deposited MOXs, and MOXs surface modified with second-phase materials. Achievements in the previously enumerated objectives are minutely described in these sections. The results are presented in the following journal articles:

3.1. Gas-sensitive materials

Journal Article 1 - VOCs sensing by metal oxides, conductive polymers, and carbon-based materials, Tomić, M., Šetka, M., Vojkúvka, L., Vallejos, S., *Nanomaterials*, 2021, 11(2), 552, doi: 10.3390/nano11020552.

3.2. Modification of tungsten oxide by nanoscale interfaces

Journal Article 2 - Cerium oxide-tungsten oxide core-shell nanowire-based microsensors sensitive to acetone, Tomić, M., Šetka, M., Chmela, O., Gràcia, I., Figueras, E., Cané, C., Vallejos, S., *Biosensors*, 2018, 8(4), 116, doi: 10.3390/bios8040116.

Journal Article 3 - UV-light activated APTES modified WO_{3-x} nanowires sensitive to ethanol and nitrogen dioxide, Tomić, M., Fohlerova, Z., Gràcia, I., Figueras, E., Cané, C., Vallejos, S., *Sensors and Actuators, B: Chemical*, 2021, 328, 129046, doi: 10.1016/j.snb.2020.129046.

Conference Paper 1 - Gas microsensors based on cerium oxide modified tungsten oxide nanowires, Tomić M., Gràcia I., Salleras M., Figueras E., Cané C., Vallejos S., *Spanish Conference on Electron Devices (CDE), Salamanca, Spain, 2018*, doi: 10.1109/CDE.2018.8597067.

3.3. Modification of zinc oxide by nanoscale interfaces

Journal Article 4 - ZnO structures with surface nanoscale interfaces formed by Au, Fe_2O_3 , or Cu_2O modifier nanoparticles: characterization and gas sensing properties, Tomić, M., Claros, M., Gràcia, I., Figueras, E., Cané, C., Vallejos, S., *Sensors*, 2021, 21, 4509, doi: 10.3390/s21134509.

Conference Paper 2 - ZnO nanorods and their modification with Au nanoparticles for UV-light activated gas sensing, Tomić, M., Gràcia, I., Figueras, E., Cané, C., Vallejos, S., *Spanish*

Conference on Electron Devices (CDE), Sevilla, Spain, 2021, doi: 0.1109/CDE52135.2021.9455726.

3.4. Modification of iron oxide by nanoscale interfaces

Journal Article 5 - Aerosol assisted chemical vapor deposition of gas sensitive Fe₂O₃ and Au-modified Fe₂O₃ structures, Tomić, M., Gràcia, I., Figueras, E., Cané, C., Vallejos, S. – To be submitted

Chapter 4 summarizes and compares the sensing properties of all the synthesized materials and sensors in this thesis. In this chapter are listed the general conclusions of this research.

Appendix A includes the gas sensing results of other modified MOX-based sensors obtained in collaboration with an internship student (B. Bendahmane) from the Electronic Department of Science and Technology Faculty, Frères Mentouri University, Constantine, Algeria. These results are published in the following article:

Journal Article 1 - Influence of Mg doping levels on the sensing properties of SnO₂ films, Bendahmane B., Tomić M., Toudjen N. H., Gràcia I., Vallejos S., Mansour F., Sensors, 2020, 20, 2158, doi: 10.3390/s20072158.

Appendix B includes results on the application of electrochemically synthesized ferrate(VI) salts in the treatment of pesticide-contaminated water. This article was published during the thesis, although the results were obtained in the Research and Development Center, IHIS Techno-Experts, Belgrade, Serbia before enrolling to the doctoral program at UAB:

Journal Article 2 - Encapsulation of micro-sized barium ferrate(VI) and its effectiveness in removing clomazone pesticide from water, Nikolić Bujanović, Lj., Čekerevac, M., Simičić, M., Tomić, M., Journal of Materials Science, 2020, 55(17), 7295, doi: 10.1007/s10853-020-04519-4.

Appendix C includes the contribution to the investigation of other researchers from the group on the development of MOX nanostructures and their application in gas sensing. These results are presented at the following conferences:

Conference Paper 1 - Integration of one-dimensional gas-sensitive nanostructures grown via chemical vapour deposition into microdevices, Vallejos S., Tomić M., Gràcia I., Figueras E., Chmela O., Hubalek J., Domènech G., Prades D., Romano-Rodriguez A., Barth S., Cané C., Smart Systems Integration 2018 - International Conference and Exhibition on Integration Issues of Miniaturized Systems, Dresden, Germany, 2018, ISBN: 978-395735082-4.

Conference Paper 2 - Room temperature ethanol microsensors based on silanized tungsten oxide nanowires, Vallejos S., Fohlerová Z., Tomić M., Gràcia I., Figueras E., Cané C., International conference Eurosensors, Graz, Austria, 2018, doi: 10.3390/proceedings2130790

Chapter 1

Literature review

Chemical gas sensors are devices that transform chemical information into an analytically useful signal (e.g., electrical, optical, piezoelectric. etc.), which can be measured and quantified directly or indirectly. They consist of two main components:

- Receptor - chemical recognition element (i.e., gas-sensitive material) that receive the information from the environment, and
- Transducer - recognition system that translates that chemical information (produced between the analyte and recognition element) into a physical output signal.

Additionally, a heater can be integrated into a gas sensor to activate the gas-sensitive layer. However, this component is not necessary if the receptor operates at room temperature or is photoactivated, which will be explained later in this chapter. A schematic illustration of the main gas sensor's components is presented in **Figure 1.1**.

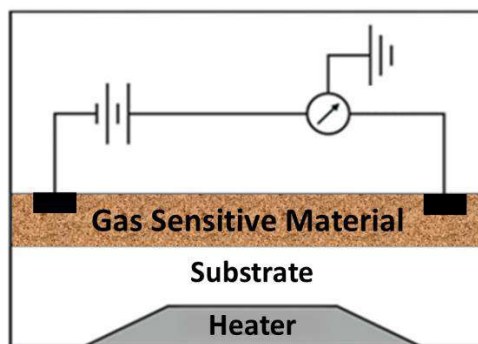


Figure 1.1. Schematic representation of a thermoactivated gas sensor (cross-section).

Therefore, this chapter reviews the advancements in the development of individual sensor's elements (gas-sensitive materials, their synthesis and possible activation, and transducing platforms) which improvement ensures overall amelioration of a gas sensor.

1.1. Gas-sensitive materials

The gas sensing material is one of the main components that directly influences the whole performance of the sensor device. Therefore, a gas-sensitive material should fulfill certain requirements related to its sensitivity, selectivity, stability, and speed of response; features known as the four "S"s of gas sensing. Moreover, the material is expected to interact reversibly and reproducibly with the specific analytes of interest showing strong stability in harsh conditions such as high temperature and/or high relative ambient humidity. From the economical point of view, the sensitive material should also be widely available, simply and inexpensively synthesized, compatible, and easily implemented with specific transducing platforms. These requirements could be accomplished by choosing materials with

semiconducting properties such as metal oxides (MOXs), polymers (POMs), and carbon-based materials (CbMs). Amongst them, MOXs are the primarily used materials in gas sensors since they have outstanding physical and chemical properties, use low cost and simple synthesis methods, and have the ability to detect different gases including flammable and toxic gases.

Nanoscale MOX materials and in particular nanostructures (with sizes within the Debye length of the surface, typically between 2–100 nm) are attractive in gas sensors. This is because nanostructures have proved to enhance the functionality of gas sensors, not only due to their higher surface-area-to-volume ratio, as opposed to bulk materials, but also due to the presence of specific crystal facets that provide a particular electronic structure to the surface.

Due to the electrostatic interactions between the positive metallic and negative oxygen ions, MOXs have firm and solid ionic bonds. Especially interesting are transition metal oxides, in which the s-shells are completely filled, ensuring good thermal and chemical stability of MOX while d-shells may not be completely filled, giving them a variety of unique properties that make them potentially of great use in electronic devices. These unique properties include wide band gaps, high dielectric constants, reactive electronic transitions, optical, and electrochromic characteristics, as well as gas sensing properties [21].

The statistics of the number of published articles available in the Scopus database (**Figure 1.1**) show that most studied MOXs are those with n-type conductivity (79.2 %), while p-type MOXs for gas sensors application are present in only 16.9 % of studies. A small percentage of articles (3.9 %) is devoted to MOXs that can have both, n- and p-type semiconducting behavior, for instance Fe_2O_3 , as the most representative case in the literature. From total number of n-type MOXs in the literature, the most investigated are ZnO (32.3 %), SnO_2 (32.3%), TiO_2 (12.5 %), WO_3 (10.6 %), and In_2O_3 (6.6 %). The studied n-type MOXs also include Mo_2O_3 (2.1 %), V_2O_5 (1.4 %), Ga_2O_3 (1.1 %), Nb_2O_5 (0.6 %), and Ta_2O_5 (0.4 %). On the other side, from the total number of p-type MOXs, researchers paid the most attention to CuO (30.0 %), NiO (24.8 %), Co_3O_4 (11.8 %), CeO_2 (9.5 %), Cu_2O (5.2 %), Cr_2O_3 (4.2 %), Y_2O_3 (3.6 %), Bi_2O_3 (3.0 %), La_2O_3 (2.9 %), TeO_2 (1.5 %), Ag_2O (1.3 %), Mn_3O_4 (1.2 %), and Sb_2O_3 (1.1 %). It is important to note that even the most investigated p-type MOX, i.e., CuO, represents only around 5 % of the total number of studied MOXs (both, n- and p-type).

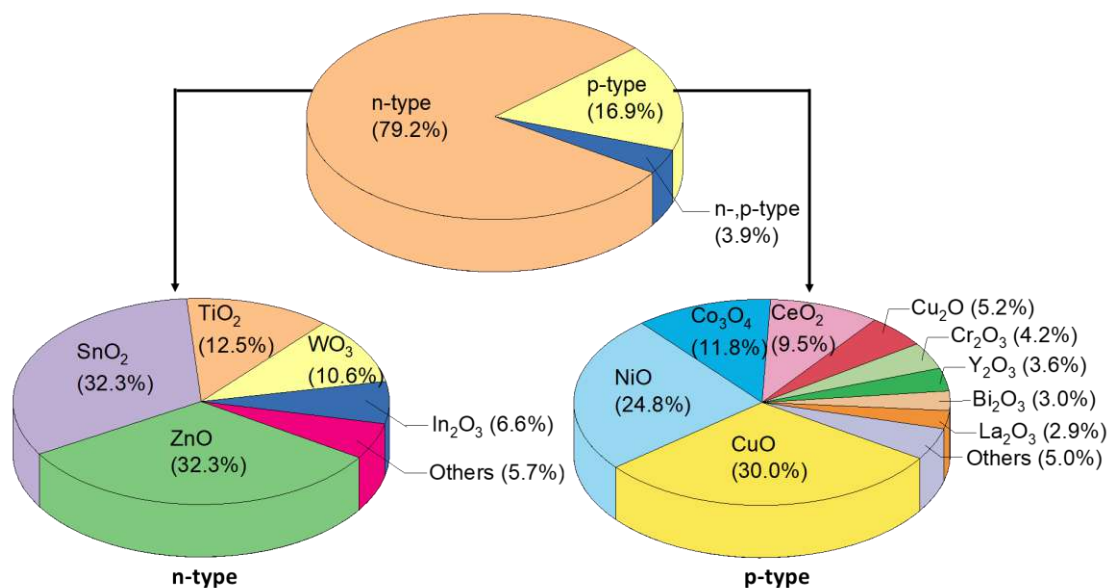


Figure 1.1. Number of articles involving different types of the metal oxide based gas sensor reported in the literature (Scopus database from 1978 – 2021). The data were collected using the name of metal oxide (e.g. “ZnO”) + “gas sensor” as keywords.

MOXs with wide band gaps (e.g., between 2 and 4 eV) and low activation energy of the centers are generally an optimal combination for chemoresistive sensors [22]. This combination is found for instance in ZnO, SnO₂, or WO₃; therefore their extended use in gas sensing and the interest in this thesis of using these MOXs as models for structuration via AACVD as well as for the evaluation of gas sensing performance after their surface modification with second-phase materials. The main physical, chemical, and gas sensing properties of the ‘host’ MOXs employed in this thesis are summarized below.

ZnO, for instance, is an n-type semiconductor with a direct band gap of 3.37 eV [23] which has shown large surface-to-volume ratio morphologies that improved sensitivity and response speed with respect to other morphologies with bulky characteristics. The wide use of ZnO in the literature is probably related to its relatively facile synthesis processes and high chemical stability [24]. It has shown outstanding results in the detection of methanol [25], ethanol [26], formaldehyde [27], acetaldehyde [28], nitrogen dioxide [29], hydrogen [30], and carbon monoxide [31]. WO₃ is also an n-type semiconductor with a band gap of 2.6 – 3.7 eV [32]. WO₃ is explored in the literature due to its sensitivity to gases such as acetone [33], methanol [33], toluene [34], hydrogen [35], carbon monoxide [36], and nitrogen dioxide [37]. The use of this material in the group of *Gas Sensors* at *IMB-CNM (CSIC)* has been exploited intensively in recent years due to its feasibility to form 1D structures via AACVD [34] [38]. So that the interest in exploring further the performance of WO₃ as ‘host’ MOX in this thesis. The thesis also devotes special attention to the development of Fe₂O₃ as a ‘host’ material, since it is low-cost, non-toxic, stable, resistive to corrosion, and earth-abundant transition metal oxide [39]. Previous research in the group of *Gas Sensors* at *IMB-CNM (CSIC)*, proved this material is a good modifier for WO₃ [34], and therefore, this thesis investigates its properties as a ‘host’ MOX, rather than only a modifier. The literature shows that Fe₂O₃ can be sensitive to gases such as methanol [40], ethanol [41] [42], butanol [43], acetone [44] [45], hydrogen sulphide [46] [47], hydrogen [42], nitrogen dioxide [48] [49], and carbon monoxide [21] [50].

Table 1.1 summarizes some of the literature reports on ZnO, WO₃, and Fe₂O₃ their characteristics, and gas sensing performances.

Table 1.1. Material characteristic and sensing properties of pristine ZnO, WO₃, and Fe₂O₃.

Material	Morphology	Size, nm	Gas	c, ppm	T, °C	R ^a	t _R , s	t _r , s	Ref.	
ZnO	NPIs	3.9 ^S	Methanol	50	360	4.8	N/A	N/A	[51]	
	NPs ^{com}	10–100 [∅]	Ethanol	100	N/A	2.6	16	100	[26]	
	NShs	1000 ^T		100	N/A	8.5	10	80	[26]	
	NTPs (NRds)	50 [∅] 1000 ^L		500	340	57	50	70	[52]	
	NPIs	19 ^T		100	380	8.9	32	17	[53]	
	HSps	300-350 [∅] 30-40 ^{s-T}	Acetone	320	270	7	79	108	[54]	
	NPs	N/A	Acetaldehyde	0.05	220	2	N/A	N/A	[28]	
	NRgs	N/A		0.05	220	1.1	N/A	N/A	[28]	
	NWs	50-80 [∅]	Benzene	50	80	1	N/A	N/A	[55]	
	NWs	50-80 [∅]	Toluene	50	80	1	N/A	N/A	[55]	
	NWs	50-60 [∅]	H ₂ S	20	150	1.15	180	60	[56]	
	pNTs	30 ^T	H ₂	5000	200	7.57	50	180	[57]	
	NPs	18-40 ^S	NO ₂	100	150	6.9	~20	~285	[58]	
	NRds	43.9 ^S		1	200	1.41	48	180	[59]	
	NPs	53 ^S	CO	80	250	3.8	21	70	[60]	
	NWs	50-80 [∅]		50	80	1.1	N/A	N/A	[55]	
	WO ₃	NPIs	50–80 ^T	Methanol	300	300	33	14	13	[61]
NShs		100 ^T	Ethanol	100	300	4.8	34	36	[62]	
NPIs		50–80 ^T		200	300	70	7	10	[61]	
NPs ^{com}		N/A		500	200	2.9	N/A	N/A	[63]	
NPIs		50–80 ^T	Butanol	2	300	31	16	9	[61]	
NPIs		100 ^L 40 ^T	Acetone	400	300	15.8	7	23	[64]	
NPIs		50 [∅] 5 ^T		500	200	38.7	3	6	[63]	
NPs ^{com}		N/A		500	200	5	N/A	N/A	[63]	
NNs		50-100 [∅] 10000 ^L	Toluene	100	220	2.5	400	170	[34]	
MFI (NPIs)		2000-3000 ^{∅-MFI} 50–300 ^{W-NPIs} 26 ^{T-NPIs}		100	320	16.7	2	21	[65]	
HTs		58.6 ^{t-w T} 32.2 ^{s-w T}	H ₂ S	2	300	6.7	120	300	[66]	
NPs ^{com}		N/A	H ₂	5000	RT	1.1	79	8	[67]	
PF		85 ^T	NO ₂	16 ppb	150	1.3	200	N/A	[68]	
NPIs		50.2 ^S		100	100	131.7	N/A	N/A	[69]	
CFL (NRds)		450-600 ^{∅-CFL} 30–95 ^{S-NRds}	CO	20	270	12.9	9-15	5-9	[70]	
Fe ₂ O ₃		ML (NPs)	58 ^{S-NPs}	Methanol	30	RT	11	20	50	[40]
		NPs	25 ^S	Ethanol	100	200	16.7	189	46	[41]
	Ts	60000 ^L	50		RT	27	N/A	N/A	[42]	
	NPs	200 ^S	50		RT	7	N/A	N/A	[42]	
	L	9-12 ^W 6000 ^L	Butanol	100	260	8.3	34	21	[43]	
	NPs	3 ^S	Acetone	100	340	9.1	N/A	N/A	[44]	
	NPs	8-20 ^S		1	250	1.9	N/A	N/A	[45]	
	NFs	50-100 [∅]	H ₂ S	1	250	6.1	40	300	[46]	
	NEs	275 ^{l-a ∅} 125 ^{s-a ∅}		50	260	8	0.8	2.2	[47]	
	Ts	60000 ^L	H ₂	50	RT	2.3	N/A	N/A	[42]	
	NPs	200 ^S		50	RT	0.7	N/A	N/A	[42]	
	NPs	50 ^S	NO ₂	5	200	3.4	10	180	[48]	
	NPs	50-60 ^S		200	200	1.2	12	188	[49]	
	NPs	40 ^S	CO	100	300	22.5	4	160	[21]	
	NPs	10-20 [∅]		100	350	2.3	N/A	N/A	[50]	

NPLs: nanoplates, NPs: nanoparticles, ^{com}: commercial powder, NShs: nanosheets, NTPs: nanotetrapods, NRds: nanorods, HSps: hollow spheres, MSps: microspheres, NRgs: nanorings, NWS: nanowires, pNTs: porous nanotubes, NFs: nanofibers, NEs: nanoellipsoids, L: leaf-like, MFIs: microflowers, PF: porous film, HTs: hemitubes, CFL: cauliflower-like, ML: monolayer, Ts: tubes, ^{CS}: crystal size, N/A: data not available, ϕ : diameter, T : thickness, l : length, ^{s-T}: shell thickness, ^{t-w} T : top wall thickness, ^{s-w} T : side wall thickness, ^S: size, ^{l-a} ϕ : long-axis diameter, ^{s-a} ϕ : short-axis diameter, ^W: width, RT: room temperature, c : concentration, T : operating temperature, R : response, t_R : response time, and t_r : recovery time.

^a Sensor responses are given (or recalculated, if needed) in accordance with the formula R_a/R_g (reducing gases) or R_g/R_a (oxidizing gases). Since some values are extracted from graphical data, some negligible inaccuracy is possible.

1.1.1. Tuning the surface morphology

Some examples of tuning the surface morphology approach are given in **Table 1.1**. In this context, various materials with morphological shapes in the nanometric scale with increased surface-to-volume ratio have proven to be more effective for gas detection [17] [18]. Generally, the surface properties of these peculiar morphologies, including crystalline and structural properties, have been shown to determine the sensing activity of these materials. More precisely, the density of states at the surface has been revealed to play an important role in the sensing mechanism of gases dominated by the space-charge-controlled grain-boundary conduction model, in which the grain sizes, surface chemical states, and gas adsorption amount determine the overall performance of the sensors [71]. For instance, comparative studies of sensors based on complex structures with flower-like hierarchical porous single-crystalline ZnO nanosheets and commercial ZnO powder demonstrated for the former three-times better responses to ethanol with nearly 40% faster response [26]. Another study, focused on controlling the features of various ZnO nanostructures [28], demonstrated enhanced sensitivity to acetaldehyde in the sub-ppm range (50 ppb) when tuning the ZnO morphology into nanorings instead of nanoparticles, nanorods, or nanotubes.

Most of the works involving pristine MOXs in the literature have found correlations between the sensor's performance and morphology, microstructure, and size of gas-sensitive materials [72]–[77]. Therefore, the sensor's performances have shown to improve by:

- Tuning the surface morphology: shape, size, and dimensional control to obtain 0D (e.g., nanoparticles and quantum dots), 1D (e.g., nanofibers, nanotubes, and nanowires), 2D (e.g., thin films, nanosheets, and nanoplates), and 3D (e.g., porous films and nanoflowers, which consist of 2D nanosheets) materials.

Additionally improvements in the sensor's performances could also be achieved by:

- Modifying or functionalizing the pristine material: control of type and level of intentional impurities (doping, formation of Schottky barriers, heterojunctions, and/or inorganic/organic hybrid structures).

1.1.2. Modification or functionalization of the pristine material

The effects of the second approach (i.e., modifying or functionalizing the pristine material) are demonstrated in **Table 1.2**, where the performances of the non-modified and modified sensors are compared. The modification or functionalization process, which consists of the incorporation of intentional "impurities" at/in the material surface/structure, includes:

- Decorated materials, when incorporating a low amount of noble metal, another MOX (with sizes less than 10 nm), or organic compound at the surface. These are represented by an "@" sign in between the 'guest' and 'host' material, e.g., Au@WO₃.
- Simple mixtures, when mixing two or more gas-sensitive materials randomly. These are represented by a hyphen "-" sign in between the constituents, e.g., ZnO-CuO.
- Bilayers and trilayers, when there is a well-defined partition or interface between the two or three gas-sensitive materials. These are represented by a slash "/" sign in between the constituents, e.g., CuO/SnO₂.
- Doped materials, when incorporating 'guest' atoms into the material structure, e.g., Ce-doped SnO₂.

The enhanced sensing performance of these functionalized materials has been attributed to electronic effects (band bending due to Fermi level equilibration, charge carrier separation, tuning of the depletion layer, and increased interfacial potential barrier energy) and/or chemical effects (decrease in activation energy, targeted catalytic activity, and synergistic surface reactions). Results in the literature [73] [78] show that functionalized materials improve further the sensitivity, response time, working temperature, and/or selectivity to some extent by reducing the cross-responses to different gaseous molecules.

Table 1.2 demonstrates that the decoration of popular gas-sensitive MOXs (SnO₂, ZnO, WO₃) with noble metals (e.g., Au, Ag, Pt, Pd), secondary oxides (ZnO, CeO₂, TiO₂, CuO, Fe₂O₃, PdO), or organo-functional molecule (APTES) is a generalized method for improving the sensing performance of MOX-based sensors. For instance, research on the load variations of Au at ZnO revealed the dependence of the response on Au concentration. Results showed that Au-loaded ZnO has better responses to various VOCs, including diethylether, acetone, chlorobenzene, trichloroethylene, isoprene, ethylacetate, butylacetate, formaldehyde, and hexaldehyde. The 3 at.% Au@ZnO systems improved the response to isoprene, while the 5 at.% Au@ZnO to methanol [51]. Similarly, investigations on Ce- and Mg-doped SnO₂ found better sensing performance to formaldehyde, methanol, ethanol, and acetone for 2% Ce-doped SnO₂ and ethanol, toluene, and acetone for 1 at.% Mg-doped SnO₂ as compared to non-modified SnO₂ [79]. Further, the decoration of TiO₂ nanorods with 12 at.% of Pd showed enhanced responses to isopropanol as well as a clear improvement to hydrogen, which registers 35 times better response for the Pd@TiO₂ systems than for the non-modified TiO₂ nanorods [80]. Besides improved responses, sensors usually have also shorter response and recovery times. This can be noticed for Au@SnO₂ sensors with the response time to NO₂ of 35 s, compared to 470 s recorded for non-modified sensors [81]. Also, for Pt@WO₃ sensors to toluene, which have 4 and 5.7 times faster response and recovery times, respectively, than WO₃ sensors [34].

The functionalization of MOXs with secondary MOXs, instead of noble metals, also revealed further advantages. For instance, the sensing properties of WO₃ nanowires decorated with Fe₂O₃ nanoparticles to toluene proved to be comparable to Pt@WO₃ nanowires, indicating that the use of expensive precious metals for MOXs functionalization could be circumvented [33] [34]. Other examples of secondary MOXs include CuO, which was employed to improve the sensing properties of ZnO to acetone [82] and SnO₂ to xylene [83]. This type of modified system (i.e., MOX/MOX) also showed advantages in cataluminescence (CTL) gas/vapor sensors. Thus, TiO₂/SnO₂ exhibited better CTL properties including stable intensity, high signal/noise values, short response, and better sensitivity to benzene and toluene compared to intrinsic SnO₂ [84].

Remarkable results were reported for 2.25 at% CuO addition to pure WO₃ sensor, which achieved more than 25 times higher response to H₂S compared to non-modified WO₃ sensor [85]. The importance of molar ratio between two MOXs was also studied. Thus, ZnO/WO₃ sensor response to CO was 38 for ZnO:WO₃ molar ratio 6:4, and only 2 for molar ratios 2:8 and 8:2 [86].

Functionalization of MOXs with organo-functional molecules, more precisely with APTES, is another alternative already shown in the literature [20] [87], although is less extended compared to noble metal or MOX decoration. Despite less investigated, it has shown the potential to activate the MOX gas sensitivity and selectivity, as the organo-functional modifier can interact with the gaseous species and influence the electrical properties of the MOX 'support'. Thus, for instance, APTES@P-WO₃ operating at 340 °C [20] demonstrates its competitiveness with metal or MOX modified materials, showing the sensor's performances in the same order of magnitude as M@MOX or MOX@MOX sensors as well as more than 5 times higher response to NO₂ compared to the pure P-WO₃.

Table 1.2. Sensing properties of modified and non-modified gas-sensitive materials.

Material	Loading	Gas	c, ppm	T, °C	R ^a	t _r , s	t _s	Ref.
Au@ZnO	Au 3 at.%	Isoprene	50	360	31	N/A	N/A	[51]
ZnO	Au 0 at.%				25	N/A	N/A	
Au@ZnO	Au 5 at.%	Methanol	50	360	21	4	3	[51]
ZnO	Au 0 at.%				4.8	N/A	N/A	
Ag@ZnO	Ag 1 at.%	Formaldehyde	100	240	170.4	12	90	[88]
ZnO	Ag 0 at.%				6	46	102	
Pd@ZnO	N/A	CO	100	220	15	100	255	[89]
ZnO	N/A				1.4	350	425	
Pd@ZnO	N/A	Benzene	50	80	2.2	N/A	N/A	[55]
Pt@ZnO	N/A				1.0	N/A	N/A	
ZnO	N/A	1.0	N/A	N/A				
Pd@ZnO	N/A	Toluene	50	80	1.0	N/A	N/A	[55]
Pt@ZnO	N/A				2.7	N/A	N/A	
ZnO	N/A	1.1	N/A	N/A				
SnO ₂ -ZnO	ZnO m.r. 0.1	H ₂	10	300	168.6	187	592	[90]
SnO ₂	ZnO m.r. 0				4.2	N/A	N/A	
ZnO	SnO ₂ m.r. 0				63.8	N/A	N/A	
Ce-doped SnO ₂	Ce 2 at.%	Formaldehyde	500	320	10	8	4	[79]
SnO ₂	Ce 0 at.%				28	10	5	
Mg-doped SnO ₂	Mg 1 at.%	Ethanol	80	160	14	143	N/A	[91]
SnO ₂	Mg 0 at.%				1	N/A	N/A	
Pd@TiO ₂	Pd 12 at.%	Isopropanol	5000	200	4.4	N/A	N/A	[80]
TiO ₂	Pd 0 at.%				1.6	N/A	N/A	
Pd/M-WO ₃	Pd 1 wt.%	H ₂	5000	RT	11.8	80	10	[67]
M-WO ₃	Pd 0 wt.%				2.9	64	15	
Fe ₂ O ₃ @WO ₃	Fe 3.9 at.%	Toluene	100	220	8	150	15	[34]
Pt@WO ₃	Pt 3.7 at.%				7.8	100	30	
WO ₃	Fe & Pt 0 at.%				2.5	400	170	
Au@WO ₃	Au 0.01 wt.%	H ₂ S	2	300	7.5	45	25	[92]
WO ₃	Au 0 wt.%				4.8	48	28	
Pt@WO ₃	N/A	Acetone	2	300	3.4	N/A	N/A	[92]
WO ₃	N/A				1.2	N/A	N/A	
Pt@WO ₃	N/A	Toluene	2	300	1.7	N/A	N/A	[92]
WO ₃	N/A				1.0	N/A	N/A	
Pt/Fe ₂ O ₃	Pt 1 wt.%	Acetone	1	250	2.9	N/A	N/A	[45]
Fe ₂ O ₃	Pt 0 at.%				1.9	N/A	N/A	
Au/Fe ₂ O ₃	N/A	NO ₂	5	100	8.5	60	450	[93]
Fe ₂ O ₃	N/A				1.3	N/A	N/A	
Au@SnO ₂	N/A	NO ₂	30	300	4	35	N/A	[81]
SnO ₂	N/A				1.4	470	N/A	
CuO/SnO ₂	Cu 3 mol%	Xylene	50	280	10	N/A	N/A	[83]

SnO ₂	Cu 0 mol%				2.5	N/A	N/A	
PdO-SnO ₂	Pd 0.1 mol%		200	300	320	N/A	N/A	[94]
SnO ₂	Pd 0 mol%	CO			40			
ZnO-CuO	Cu 65 at.% Zn 35 at.%	Acetone	10	300	1.2	22	26	[82]
ZnO/WO ₃	m.r. 6:4				38	48	62	
ZnO/WO ₃	m.r. 2:8	CO	200	RT	2	63	71	[86]
ZnO/WO ₃	m.r. 8:2				2	67	72	
CuO/WO ₃	Cu 2.25 at.%				534	5	1440	
WO ₃	Cu 0 at.%	H ₂ S	10	300	21	7	1860	[85]
TiO ₂ /SnO ₂	N/A				13,000 *	N/A	N/A	
SnO ₂	N/A	Benzene	100	220	5000 *	N/A	N/A	[84]
APTES@P-WO ₃	APTES 2 mol%				45	30	31	
P-WO ₃	APTES 0 mol%	NO ₂	1	340	8.8	37	35	[20]

M: mesoporous, P: porous, m.r.: molar ratio, N/A: data not available, v.: volume, * CTL sensors: the response represents the relative CTL intensity, RT: room temperature, c: concentration, T: operating temperature, R: response, t_R: response time, and t_r: recovery time.

* Sensor responses are given (or recalculated, if needed) in accordance with the formula R_a/R_g (reducing gases) or R_g/R_a (oxidizing gases). Since some values are extracted from graphical data, some negligible inaccuracy is possible.

The literature survey demonstrates the significance of formation of surface nanoscale interfaces through the modification of MOXs with noble metals or other MOXs. However, it does not discuss in detail the influence of certain parameters such as the type of conductivity of the modifier MOXs or the utility of these modified structures in photoactivation mode. The vast number of studies on functionalized MOXs use synthesis methods that are not scalable or fully compatible with micro- and nano-fabrication processes. In that context, this research has a complete strategy that aims at fulfilling part of the missing information in the field of functionalized structured MOX gas-sensitive materials, their synthesis, integration, and performance both in thermoactivated and photoactivated mode.

1.2. Photoactivated vs. thermoactivated gas sensors

Typically, MOXs are chemically poorly responsive to gaseous species at room temperature (RT) since they are passivated by the adsorption of oxygen molecules from the atmosphere. Therefore, two strategies are generally employed to activate MOXs – thermoactivation using temperatures in the range of 200–500 °C [95] or photoactivation using light irradiation usually in the ultraviolet (UV) range. In general, the major drawback of using thermoactivation lies in the heaters' power consumption and its loss of reliability with the time [96]. The high temperatures needed for MOX activation may also limit its applicability in explosive and flammable environments, and bring poisoning issues [97] [98]. Traditional gas sensors use thermoactivation, therefore the reports in the literature make usually reference to results obtained in thermoactivated mode, as can be noticed in **Table 1.1** and **Table 1.2**. However, in recent years, photoactivation of gas-sensitive materials for RT operation [99] has been used as an alternative to thermoactivation to circumvent these drawbacks, particularly the high power consuming resistive heaters, considering that the on-chip integration of light emitter components with low power consumption (tens of μ W or less) in gas sensing microsystems is progressively being implemented [97]. Hence, there is an increasing number of articles in the literature (some of them are given in **Table 1.3**) that demonstrate the possibility of detecting various gases using photoactivated gas sensors. Moreover, it can be noticed that the responses of the sensors to the similar concentrations of the gases are comparable with the responses of

thermoactivated sensors presented in **Table 1.1** and **Table 1.2**. Therefore, in this research, both approaches are used, thermoactivation and photoactivation.

As a way of photoactivation, light sources, such as LEDs (light-emitting diodes), xenon, or mercury lamps were used to provide sufficient energy for charge carrier promotion and by increasing their irradiance, the sensor performance to target gases can be improved to some extent [100]. UV-light is preferred for photoactivated gas-sensitive MOXs due to their wide band gaps. However, the intrinsic drawbacks of energy consumption and high cost hinder currently the wide application of typical UV-light sources in gas sensors. In that context, visible light can be a good substitution, although not always applicable for wide band gap MOXs. Modifying MOXs with nanoscale interfaces, particularly heterojunctions, may also bring a solution to this issue by introducing localized band gap changes in the MOX that potentially shift its operation into the visible region of the light.

Table 1.3. Photoactivated gas sensing responses of MOX-based gas sensors.

Material	Gas	c, ppm	T, °C	Irradiation Parameters			R [‡]	Ref.
				Light	λ , nm	E_{λ} , mW·cm ⁻²		
ZnO	Formaldehyde	100	RT	LED	365	N/A	12.6	[101]
ZnO	H ₂ S	25	RT	LED	354	1.22	3.5	[102]
ZnO	Ethanol	60	RT	Mercury lamp	365	N/A	1.7	[103]
ZnO	Ethanol	100	RT	LED array	365	3.6	1.1	[104]
SnO ₂	Acetone	54	RT	Mercury lamp	>200	20	1.8	[105]
TiO ₂	NO ₂	100	RT	LED	365	N/A	2.3	[106]
In ₂ O ₃	NO ₂	1	RT	LED	400	N/A	60	[107]
In ₂ O ₃	NO ₂	8	RT	LED	380	5	180	[108]
In ₂ O ₃	NO ₂	0.5	RT	LED	325	400 μ W	1.8	[109]
In ₂ O ₃	NO ₂	2	RT	LED	365	1.2	3.6	[110]
Au@ZnO	Ethanol	100	RT	Xe	365	1.2	2.0	[111]
Au@ZnO	NO ₂	5	RT	Xe	365	1.2	4.5	[111]
Pt@ZnO	NO ₂	5	RT	LED	365	25	5.4	[98]
Pd@SnO ₂	Ethanol	100	RT	N/A	365	480	10.2	[112]
ZnO/Pd	NO ₂	100 ppb	RT	Xe	475	0.8	2.6	[113]
Au/WO ₃	NO ₂	10	RT	LED	400	15	2.2	[114]
C-doped ZnO	Ethanol	400	RT	N/A	370	0.5	~6	[115]
ZnO/In ₂ O ₃	NO ₂	5	RT	LED	365	25	3.2	[116]
ZnO/SnO ₂	Formaldehyde	100	RT	LED	365	N/A	~8	[117]
SnO ₂ /ZnO	NO ₂	5	RT	N/A	365	1.2	6.2	[118]
Bi ₂ O ₃ /ZnO	NO ₂	5	RT	N/A	254	1.2	6.7	[119]
TiO ₂ /SnO ₂	Formaldehyde	0.6	RT	LED	365	10	~5	[120]

T – Temperature; λ – wavelength; N/A – not available; E_{λ} – irradiance; c – concentration; R – response.

[‡] Sensor responses are given (or recalculated, if needed) in accordance with the formula R_a/R_g (reducing gases) or R_g/R_a (oxidizing gases). Since some values are extracted from graphical data, some negligible inaccuracy is possible.

1.3. Synthesis methods

The integration of MOX material over the transducing platforms and material synthesis methods is an essential phase for sensors' scalability and large production. This integration can mostly be achieved by direct or transfer methods [121] [122] as demonstrated in **Table 1.4**. The first (direct methods) involve the selective deposition of the material over the transducing

platform. Direct methods can reduce the processing time and steps of the whole sensor assembling process, particularly when using bottom-up approaches (i.e., synthesis of materials through assembling of atoms derived from chemical precursors) rather than top-down approaches (i.e., based on carving, slicing, or etching a macroscale material source). The second (transfer method) relies on the use of pre-synthesized materials and their dry or wet transfer (re-deposition) over the transducing platform. Transfer methods can facilitate a broad choice of materials and modifications and can be especially useful when integrating aligned single 1D structures into a transducing platform, although one must be aware of the surface contamination issues which entail most of the transfer procedures [122].

Table 1.4. Summary of the most common synthesis and integration methods of MOX materials for gas sensing

	Synthesis Method	Typical Integration Method	Reference
Wet Chemical Synthesis (WCS)	Hydrothermal Process	Transfer Direct	[17] [18] [25] [67] [79] [80] [84] [123]–[128]
	Precipitation	Transfer	[45] [67] [94] [129] [130]
	Sol-Gel Method	Transfer	[131]–[134]
	Sonochemical Process	Transfer	[27] [28]
	Microwave-Assisted Approach	Transfer	[83] [135]
	One-Pot Wet-Chemical Method	Transfer	[26]
	Photodeposition	Transfer	[51]
	Calcination of Precursors	Transfer	[136]
Chemical Vapor Deposition (CVD)		Direct Transfer	[33] [34] [55] [81] [93]
Sputtering		Direct	[85] [137]
Electrochemical Deposition		Direct	[138]

Table 1.4 summarizes the most commonly used MOX synthesis methods reported in the literature and the typical integration of MOX material into the transducing platform. Most of the synthesis methods belong to wet chemical synthesis (WCS) methods which include hydrothermal process [17] [18] [25] [67] [79] [80] [84] [123]–[128], precipitation method [45] [67] [94] [129] [130], and sol-gel method [131]–[134] as most frequently used as well as sonochemical process [27] [28], microwave-assisted approach [83] [135], one-pot wet-chemical method [26], photodeposition [51], and calcination of precursors [136]. As it can be noticed from the table, transfer methods are by far the most used approaches in the literature for integrating the materials synthesized by WCS into the transducing platforms. Transfer methods are generally based on the formation of pastes or suspended solutions using common solvents (e.g., ethanol, terpineol) for their subsequent printing or drop coating.

Besides WCS, other popular synthesis methods are chemical vapor deposition (CVD) [33] [34] [55] [81] [93], sputtering [85] [137], and electrochemical deposition [138]. The preferable integration methods for these techniques are either direct methods (sputtering and electrochemical deposition) or both, transfer and direct (CVD). Direct methods allow for the selective integration of films and structures by implementing masks or patterns on desired locations. Even though these techniques are not exempt from introducing residual impurities during material processing, the in-situ integration approach with no further manipulation or extra steps diminishes considerably the contamination of the material surface.

Although traditional CVD methods are the most commonly used methods for direct integration of the sensing material they have several disadvantages such as high deposition

temperature (above 800 °C), need of catalyst seeds for material growth, need of volatile precursors which results in a narrowed choice of precursors, and often pressure below the atmospheric [139] [140]. To overcome these obstacles in this research is used a CVD variation – aerosol assisted chemical vapor deposition (AACVD), which operates at lower temperatures and atmospheric pressure. In AACVD, precursors need to be only soluble but not necessarily volatile, and the material can grow without catalyst seeds. The last is especially important for structured materials since previously, the growth of the structures was possible only with the support of catalyst seeds and at higher temperatures. For example, the AACVD of ZnO structures in the form of rods was achieved only at temperatures exceeding 550 °C by using pregrown TiO₂ catalyst seeds [141]. However, recently, the researchers from the *Gas Sensors* group at *IMB-CNM (CSIC)* demonstrated the AACVD of ZnO rods at 400 °C without using catalyst seeds by adjusting the solvents and concentrations of the precursor solution [142]. These findings were used as a base in this thesis for tuning the deposition of other MOXs, particularly CeO₂, Cu₂O, and Fe₂O₃.

1.4. Transducing platforms

Enabling the usage of gas-sensitive materials in advanced applications demands their coupling with appropriate transducing platforms, which allow measuring the electrical or optical changes induced by the physicochemical phenomena experienced in the material during the target gas-sensitive material interactions. These platforms can be based on different working principles: mass-sensitive (e.g., resonating cantilevers), thermal (e.g., pellistors, thermoelectric, or Seebeck-effect-based sensors), optical (e.g., phosphorescence/fluorescence or chemiluminescence sensors), or electrochemical (e.g., conductometric, amperometric, and potentiometric sensors) [143]. Among these different transducing approaches, resistive-based gas sensors (chemosensors), used in this thesis, are the most popular due to their simple operation principle, small size, and low cost [144].

Back in the past, most of the technologies for gas sensing transducing platforms relied on thick film technology, particularly using silica or alumina substrates. Currently, however, the transducing platforms exploit micro/nano fabrication technologies (usually based on silicon as substrate), which makes it possible for their incorporation into integrated circuits (IC) at micro/nano scale in a single chip [97] [145]. During the past decades, various types of gas sensors (resistive, thermal, mass-sensitive, optical) have been studied using standard micro-electro-mechanical systems (MEMS) technology. MEMS are three-dimensional, electro-mechanical devices, which are made by micromachining silicon wafers using standard microelectronic fabrication and post-process techniques [146]. MOX materials integrated with MEMS technology are widely employed in gas sensing applications due to the drastically reduced size, low cost, and significantly lower power consumption of such devices, while improving overall performance [147]–[149]. A comparison of conventional (bulk) and MEMS-based transducing platforms for gas sensors is displayed in **Figure 1.2**. The main difference is that in MEMS, silicon is etched from the back side avoiding thermal conduction through the bulk and thus, improving heat dissipation and unnecessary power consumption.

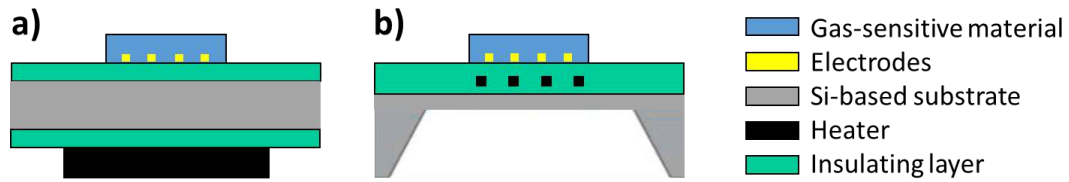


Figure 1.2. Schematic representation of typical **a)** conventional and **b)** MEMS-based transducing platforms for gas sensors.

Another significant advantage of using micro/nano fabrication technologies is the possibility to integrate several different transducers on a single chip along with the driving and signal conditioning circuitry or other smart features (e.g., wireless communication) to build electronic noses with potentially low cost via mass production [143]. A good approximation of this concept, in which various transducing principles were implemented monolithically in a microsystem to operate simultaneously, was developed previously using micro/nano fabrication technology [150].

Recently, miniaturized light platforms (micro light plates) for the photoactivation instead of thermoactivation of gas-sensitive material have also been developed. It was demonstrated that MEMS technology can also be appropriate technology for photoactive materials since LEDs can be integrated in the transducing platforms of resistive gas sensors [97].

Chapter 2

Methods

2.1 Synthesis methods

The synthesis of pure MOX materials and most of their modifications in this thesis was performed using aerosol assisted chemical vapor deposition (AACVD) method. Exceptionally, other methods were used for WO_3 functionalization with APTES (*Journal article 3*) and ZnO modification with Au (*Journal article 4*), when AACVD showed no effectiveness. All synthesis methods are described below:

2.1.1 AACVD

AACVD method is based on atomization (using ultrasonic atomizer) of the precursor solution, composed of a metal precursor dissolved in an organic solvent into fine droplets of aerosol [139]. These droplets are further transported using carrier gas, usually nitrogen, to a heated reactor controlled by a PID (Proportional Integral Derivative) system. There, the aerosol droplets of precursor solution undergo evaporation, forming precursor vapor, which undergoes homogeneous and/or heterogeneous chemical reactions [151]. In the heterogeneous reaction, preliminary decomposition of the vaporized precursor may occur in the gas phase. The vaporized precursors and their gaseous intermediate species can be adsorbed onto the surface of the heated substrates, where they undergo substantial decomposition and chemical reactions, and yield the desired materials. If the deposition temperature is too high, the major decomposition and/or chemical reactions may occur much earlier in the vapor phase, leading to homogeneous nucleation and the formation of fine particles (homogenous reaction).

The reactor used in this thesis has a volume of approximately 8 cm^3 , and a height of 0.8 cm. The schematic illustration of a typical synthesis process is shown in **Figure 2.1**.

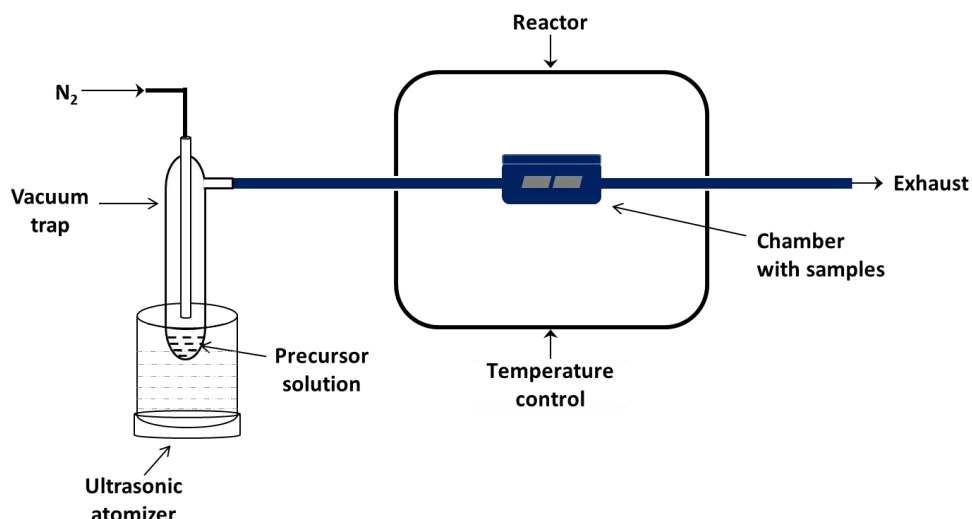


Figure 2.1. Scheme of AACVD system

The material deposition is initially performed on Si or SiO₂ tiles, and after the optimal synthesis conditions are defined, MOX structures are grown over Si-based transducing platforms. During the material deposition over the platforms, a shadow mask was used to protect the contacts and limit the growth of the structures exclusively over the electrode area [139].

The features of the synthesized material, for instance, the morphology of the structures or the density of the decorating NPs, are highly dependent on the applied conditions such as:

- Precursor – Metal salt soluble in an organic solvent,
- Solvent – Organic solvent (e.g. methanol, ethanol, acetone, etc.),
- Aerosol capacity – The volume of aerosol mist per time produced using ultrasonic liquids atomizer,
- Deposition temperature – The optimal temperature at which the desired morphology of the structures is obtained,
- Carrier gas and flow – N₂ was used as a carrier gas in this work. The optimal flow for all depositions was 200 sccm [139], and
- Position of the substrate in the chamber – Most of the materials had the center of the deposition in the area between the middle and the outlet of the chamber; however, Fe₂O₃ deposition was possible throughout the whole chamber, resulting in different morphologies at the inlet and at the outlet of the chamber.

Therefore, all the materials synthesized during this thesis passed through the process of adjustment of the above conditions to find the optimal ones for the specific material and morphology. These optimized conditions are summarized in **Table 2.1**. For each material in the table, it is indicated whether it is synthesized as a non-modified (intrinsic) MOX or as a modifier material (noble metal or MOXs).

Table 2.1. Conditions used for AACVD synthesized materials in this thesis

Material	Morphology	Precursor	Solvent	Aerosol capacity, l/h	Deposition T, °C	Carrier gas (N ₂), sccm	Substrate position in the chamber	Deposition time, min	Annealing T, °C	Reference
WO_{3-x} (pure MOX)	Ws	W(CO) ₆ , 30 mg	M, 5 ml	0.25	390	200	Middle-Outlet	60	500	JA 2 [152]
CeO₂ (modification)	Ps	Ce(acac) ₃ *xH ₂ O, 28 mg	M, 2 ml	0.25	500	200	Middle-Outlet	15	500	
WO_{3-x} (pure MOX)	Ws	W(CO) ₆ , 20 mg	M, 5 ml	0.25	390	200	Middle-Outlet	60	500	JA 3 [153]
ZnO (pure MOX)	Rds	ZnCl ₂ , 50 mg	E, 5 ml	0.25	400	200	Middle-Outlet	45	450	JA 4 [154]
Fe₂O₃ (modification)	Ps	FeCl ₃ *6H ₂ O, 3mg	A, 3 ml	0.5	430	200	All positions	5	450	
CuO (modification)	Ps	Cu(NO ₃) ₂ *6H ₂ O, 3 mg	E, 3 ml	0.5	450	200	Middle-Outlet	5	450	
Fe₂O₃ (pure MOX)	fPys	FeCl ₃ *6H ₂ O, 100 mg	A, 5 ml	0.3	370	200	Outlet	20	400	JA 5
Fe₂O₃ (pure MOX)	pPys	FeCl ₃ *6H ₂ O, 80 mg	A, 5 ml	0.3	370	200	Inlet	25	400	
Fe₂O₃ (pure MOX)	Pys	FeCl ₃ *6H ₂ O, 100 mg	A, 5 ml	0.3	370	200	Inlet	20	400	
Fe₂O₃ (pure MOX)	Shs	FeCl ₃ *6H ₂ O, 100 mg	A, 4 ml E, 1 ml	0.3	340	200	Outlet	30	400	
Au (modification)	Ps	HAuCl ₄ · 3H ₂ O, 50 µg	M, 2 ml	0.5	370	200	All positions	10	400	

Ws – wires, Rds – rods, Ps – particles, fPys – flattened pyramids, pPys – porous pyramids, Pys – pyramids, Shs – sheets, M – methanol, E – ethanol, A – acetone, T – temperature, sccm – mass flow rate of one cubic centimeter per minute of a fluid, JA – journal article.

2.1.2 Silanization method

The silanization process, used during the experiments from the *Journal Article 3*, consists of surface modification of MOX (i.e., WO_{3-x}) with organo-functional alkoxy silane molecules (i.e., APTES). In this process, the sample with previously deposited MOX structures was placed inside a custom-made self-assembled monolayer (SAM) chamber (with a volume of 77 cm³) in close proximity (next to each other) to a drop of 15 µl of silane (APTES 99% liquid) on a glass slide. The chamber was closed and dried three times under the N₂ stream. The silanization was carried out by heating the chamber to achieve 5 torr vapor pressure. The temperature for silane evaporation was maintained at 120 °C for 10 min.

Oxygen plasma treatment was used as an initial driving force for APTES adsorption on MOX. This technique, that has been already reported in the literature, has a role to activate MOX surface for the APTES adsorption by creating hydroxyl groups [155].

The conditions for the silanization process were set by adjusting three parameters, including the duration of plasma treatment, APTES deposition time, and the amount of silane. The concentrations of Si, O, W, N, and C elements at the surface were determined from the XPS

spectra recorded for each applied condition using CasaXPS software. A summary of these results is displayed in **Table 2.2**, in which the control refers to the reference sample prior plasma treatment and APTES functionalization.

Table 2.2. Concentration of elements (Si, O, W, N, and C) at the APTES modified WO_{3-x} samples obtained under the different experimental conditions **a)** plasma treatment time (1 and 5 min), **b)** deposition time (10, 30 and 50 min), and **c)** amount of silane (15, 100 and 1000 μ l).

a)				b)				c)			
wt.%	Control	1 min	5 min	wt.%	10 min	30 min	50 min	wt.%	15 μ l	100 μ l	1000 μ l
Si 2p	-	8.8	5.7	Si 2p	8.8	6.9	7.1	Si 2p	8.8	6.9	11.5
O 1s	61.2	40.1	44.9	O 1s	40.1	45.2	39.2	O 1s	40.1	46.1	33.7
W 4f	22.8	11.9	15.2	W 4f	11.9	14.9	13.1	W 4f	11.9	16.1	8.3
N 1s	1.5	5.5	3.7	N 1s	5.5	4.6	4.9	N 1s	5.5	4.9	7.9
C 1s	14.5	33.8	30.4	C 1s	33.8	28.3	35.8	C 1s	33.8	26.1	38.6

The obtained results indicate that the best conditions for APTES adsorption (the highest amount of Si and N) occurs for the plasma treatment time of 1 minute, deposition time of 10 minutes, and 1000 μ l of silane. Therefore, these conditions were used for the APTES modified WO_{3-x} samples synthesized in this thesis.

2.1.3 Impregnation method

Despite the previous evidence of Au deposition by AACVD on Si and glass tiles and other surfaces including WO_3 structures [156][157], this method did not show appropriate for the incorporation of Au NPs at the ZnO rods, reported in the *Journal Article 4* [154]. Hence, the ZnO structures were modified with Au by impregnation using preformed nanoparticles synthesized by chemical reduction of $H AuCl_4 \cdot 3H_2O$ with $Na_3C_6H_5O_7 \cdot 2H_2O$ [158]. Prior to the impregnation process, the as-synthesized nanoparticles were washed with distilled water by centrifugation (15000 rpm, 30 min) to eliminate the unreacted chemicals. The impregnation process consisted of immersing the ZnO samples during 60 s into the solution with the preformed Au nanoparticles suspended in methanol and heated at 60 °C. Methanol was the chosen organic solvent since it has previously used for the AACVD decoration of MOX with Au NPs [33]. The temperature and the impregnation time adjustment included the series of probes in which these parameters were varied and the obtained samples were characterized using SEM. These tests showed the best distribution and morphology of Au NPs for the impregnation time of 60 seconds and the temperature of Au NPs solution of 60 °C.

2.1.4 Annealing process

After each deposition, the samples were annealed prior to further characterization. Annealing is performed in a heated chamber controlled by a PID system, with the presence of synthetic air and using the high temperatures as shown in **Table 2.1**. The heating of the reactor and the samples has to be conducted gradually (approximately 15 °C/min), from room temperature to the desired annealing temperature. From the moment of reaching this temperature, the time of annealing was set to one hour; this procedure was determined in previous studies [34]. After that, the heating system is switched off, letting the samples in the chamber to cool down slowly for several hours, with the presence of airflow, until it reaches room temperature.

2.2 Material characterization

The properties of materials (i.e. morphology, optical properties, and chemical composition) greatly influence the performances of a sensor. As stated in the previous chapter, they are highly dependent on the synthesis conditions and therefore can be tuned to some extent. Because of that, the characterization of the material is an important step that can confirm if the material with the desired properties is synthesized.

In the following sub-chapters, the application and working principles of *Microscopy Techniques* and *Spectroscopy Techniques* are described. These methods were used to investigate MOX gas sensing materials' structural and morphological characteristics listed in **Table 2.1**. The specific experimental conditions and equipment features of each characterization technique are included in the published articles in *Chapter 3*.

2.2.1 Microscopy techniques

The most commonly used microscope today is a light microscope because it is inexpensive, robust, and noninvasive. However, this microscope is not capable to distinguish objects and features smaller than about 100 nm [159]. Therefore, in this thesis, instead of light microscopy, electron microscopy techniques such as **scanning electron microscopy (SEM)** and **transmission electron microscopy (TEM)** are used due to their possibility to achieve high image resolution. Electron microscopes offer a very high magnification range, typically in the range 10 - 500000 times for SEM, and 2000 - 1 million times for TEM [160]. This enables the characterization of microstructures from micro- to nanoscale or even smaller.

SEM microscopes are designed primarily to examine surfaces features of the material, such as topography (texture), morphology (shape and size), structures orientation, and other physical and chemical properties of a specimen, whereas TEM microscopes are primarily designed to examine the internal structure of specimens, down to the atomic level.

Contrary to optical light microscopes, which use light energy as a source to form images, SEM and TEM use electron beam sources. These microscopes generate a highly focused beam of electrons, which influence the sample inside a vacuum chamber. The interaction of these electrons with the examined material is a function of the kinetic energy of the incident electrons. Typical electron microscopes operate with electron energies of 1 - 300 keV [160], depending on the microscope used and the examined material. In this thesis, for instance, the energy of 3 keV is used for SEM, and 200 keV for TEM analysis. In comparison with SEM, which detects the scattered electrons emitted from the surface of the sample [161] after the electron beam-sample interaction, TEM detects the transmitted electrons from the sample [162]. The images in electron microscopy are formed by collecting a signal generated by electron-sample interactions at different points across the sample. In SEM analysis the images are obtained by scanning an electron beam of high energy on the sample surface, hence the name scanning electron microscope. Electrons from the source travel in a vacuum within a column lined with electromagnetic lenses, which focus these electrons to a spot on the surface of the sample. At each location of the sample, information from the electron-sample interactions is collected by detectors and the image on a display is created [160]. In TEM, the electrons, with the electron energies much higher than SEM (80 - 300 kV) [162] which enable them to penetrate through a material, are transmitted through the sample focused by lenses and collected by a parallel

detector to form an image. At the highest resolution, the arrangement of atoms into different types of crystal structures can be determined.

Scanning transmission electron microscopy (STEM) combines the principles of transmission electron microscopy and scanning electron microscopy and can be performed on either type of instrument [160]. A TEM can be modified into a STEM by the addition of a system that scans a focused beam across the specimen to form the image. Further, by fitting a transmission stage and a detector, SEM can also be operated in the STEM mode. Thus, STEM combines some of the advantages of SEM and TEM. Like TEM, STEM requires very thin samples and looks primarily at beam electrons transmitted by the sample. Like SEM, the STEM technique scans a very finely focused beam of electrons across the sample in a raster pattern.

High-resolution transmission electron microscopy (HRTEM) provides direct images of the atomic structure of the samples, hence, it is possible to have direct information about the crystallographic structure of materials from images [160]. High phase contrast images as small as a crystal cell can be acquired. Additionally, HRTEM coupled with energy-dispersive X-ray spectroscopy (EDX), explained further in this section, are essential tools for the structural characterization of the material providing lattice parameters, crystal structure, morphology, and size of the MOX structures.

Examples of the typical SEM and TEM images recorded in the thesis are shown in **Figure 2.2**.

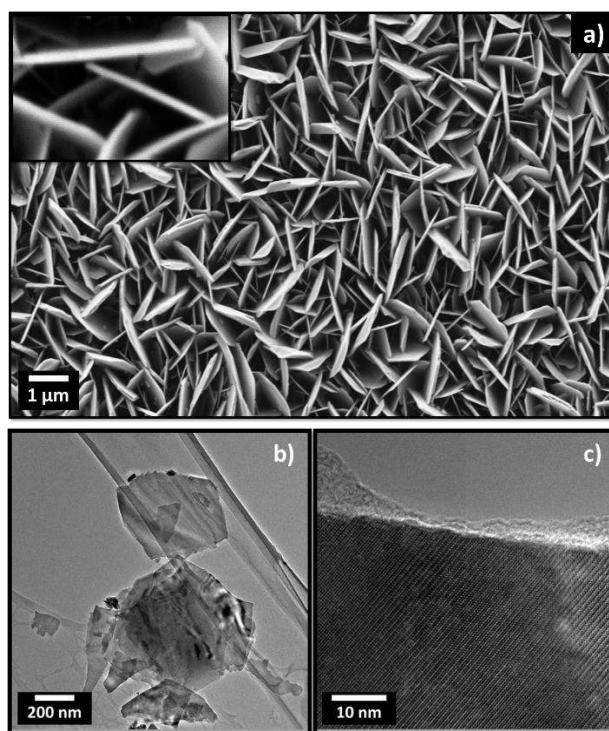


Figure 2.2. a) Low and high (inset) magnification SEM, b) STEM, and c) HRTEM images of the Fe_2O_3 structured film.

2.2.2. Spectroscopy Techniques

Spectroscopy techniques are methods that are widely used for material characterization since they provide information about the atomic and molecular structures of materials. The working principle consists of analyzing the interaction between matter and electromagnetic radiation.

In this thesis, the characterization of the gas-sensitive materials was performed using several spectroscopy techniques, such as EDX, XPS, XRD, and DRS.

Energy-dispersive X-ray spectroscopy (EDX or EDS) is an analytical technique used to analyze the composition of solid materials and thus, it was useful for the examination of MOX materials. The working principle relies on the excitation of electrons situated near the nucleus with a beam of electrons, causing more distant electrons to drop energy levels to fill the created vacancies in the electronic structure of the atom (**Figure 2.3**). This leads to a cascade of electrons from higher energy levels until the atom regains a minimum-energy state. Due to conservation of energy, each element emits a different set of X-ray frequencies as their vacated lower energy states are refilled, and measuring of these emissions provides qualitative and quantitative information about the near surface of the sample. To determine the sample's composition, the peaks in the spectrum are matched with peaks from the literature or standards [163].

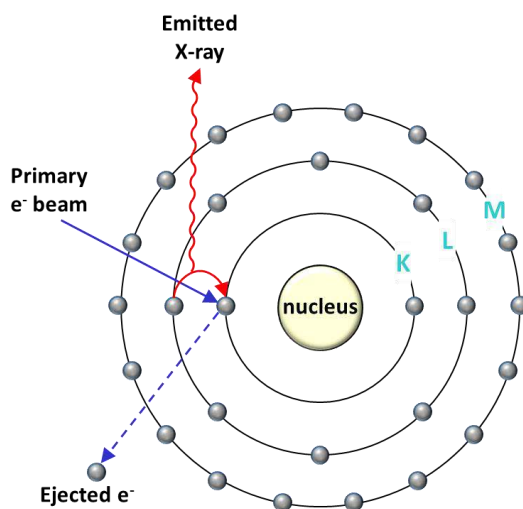


Figure 2.3. Schematic diagram of the EDX working principle.

X-ray photoelectron spectroscopy (XPS), also known as electron spectroscopy for chemical analysis (ESCA), is one of the most widely used surface techniques in materials science. It is a semiquantitative method for determination of the atomic composition of the sample. Additionally, it provides us with other chemical information, such as oxidation states of the components and speciation (the way in which the atoms are bound). The working principle is based on irradiation of the sample by a high-energy X-ray source. The X-rays penetrate only 5 - 20 Å into the sample, allowing for surface, rather than bulk, chemical analysis [164]. As an atom absorbs the X-rays, the energy of the X-ray will cause an electron from the lowest energy shell of the atom (K-shell) to be ejected, as illustrated in **Figure 2.4**.

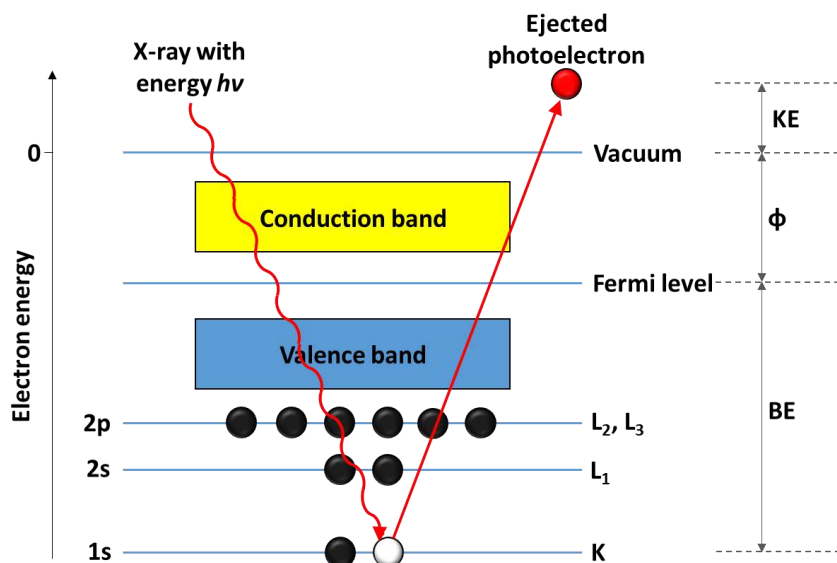


Figure 2.4. Schematic diagram of the XPS working principle.

The ejected electron has kinetic energy (KE) that is related to the energy of the incident beam ($h\nu$), the electron binding energy (BE), and the work function of the spectrometer (Φ). Thus, the binding energy of the electron can be calculated [164].

$$BE = h\nu - KE - \Phi_s \quad (2.1)$$

Ultraviolet photoemission spectroscopy (UPS) is similar to XPS with the difference that XPS uses X-rays (with a photon energy of 200-2000 eV) to examine electrons at the core level, while UPS uses vacuum UV radiation (with a photon energy of 10-45 eV) to examine electrons in valence level [165]. In UPS the excitation source is a helium discharge source and depending on the operating conditions of the source, the photon energy can be optimized for He-I (21.22 eV) or He-II (40.8 eV) [166]. Due to this lower photon energy, only the low binding energy valence electrons may be excited using the He source. The working principle is based on photon interaction with valence levels of the molecule or solid, leading to ionization by the removal of one of these valence electrons. The kinetic energy distribution of the emitted photoelectrons (i.e. the number of emitted photoelectrons as a function of their kinetic energy) is measured using an electron energy analyzer and a photoelectron spectrum is recorded, providing information about the composition and electronic state of the surface region of a sample.

The obtained data from the UPS spectra allow the determination of the sample's work function (Φ) from the difference in the photon energy of He-I and the energy difference (ΔE) between the binding energy cut-off ($E_{\text{cut-off}}$) and the Fermi edge ($E_F = 0$ eV), following the equation [21]:

$$\phi = 20 \text{ eV} - \Delta E \quad (2.2)$$

X-ray diffraction analysis (XRD) is a technique used in materials science to determine the crystallographic structure of a material. XRD is based on the ability of crystals to diffract X-rays in a characteristic manner allowing a precise identification of materials based on their diffraction pattern. The working principle is based on irradiation of crystals (regular arrays of atoms) with incident X-rays (waves of electromagnetic radiation with a wavelength between 10^{-3} and 10^1 nm [167]) and then measuring the intensities and scattering angles of the X-rays that leave the

material (**Figure 2.5**). Each rational plane of atoms in a crystal will undergo refraction at a single, unique angle (for X-rays of a fixed wavelength).

The general relationship between the wavelength of the incident X-rays (λ), angle of incidence (θ) and spacing between the crystal lattice planes of atoms (d) is known as Bragg's Law, expressed as:

$$n\lambda = 2d\sin\theta \quad (2.3)$$

Where n (an integer) is the "order" of reflection [168].

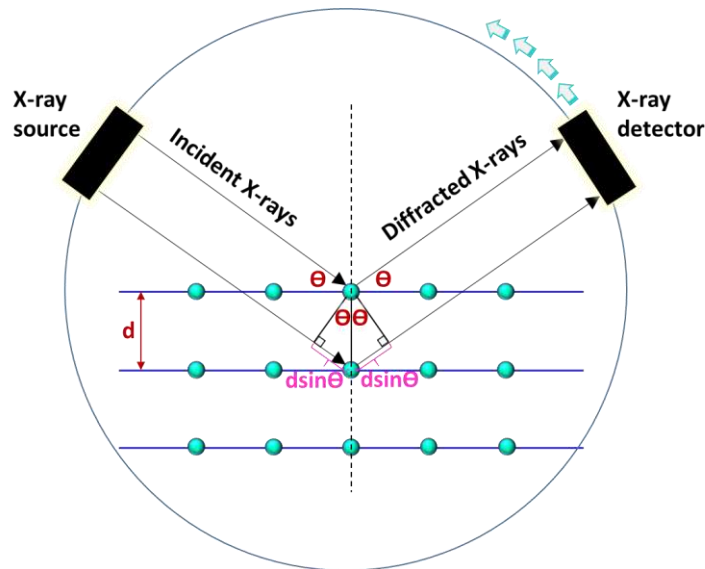


Figure 2.5. Schematic diagram of the XRD working principle.

Diffuse Reflectance Spectroscopy (DRS), sometimes known as Elastic Scattering Spectroscopy, is a technique that measures the characteristic reflectance spectrum produced when UV-Vis light interacts with a sample. DRS not only detects the light reflected from the surface (specular reflected light), but also the light reflected internally which leaves the sample in all directions (diffuse reflected light) as demonstrated in **Figure 2.6**.

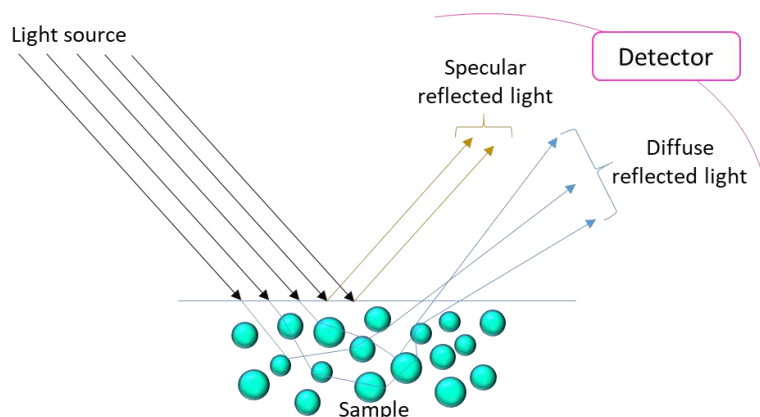


Figure 2.6. Schematic diagram of the DRS working principle.

The spectrum obtained from this technique contains information about the optical properties and structure of the examined material. This allows the estimation of the band gap energy of the material by applying the Kubelka-Munk function, $f(R)$, on the measured reflectance:

$$f(R) = \frac{(1 - R)^2}{2R} = \frac{k}{s} \quad (2.4)$$

Where R is the diffuse reflectance, k is the absorption coefficient, and s is the scattering coefficient [169].

Further, the band gap energy (E_g) is calculated using the wavelength obtained from the diffuse reflectance spectrum according to the equation:

$$E_g = \frac{hc}{\lambda} \quad (2.5)$$

Where h is Planck's constant, c is the speed of light, and λ is wavelength cut off [164].

2.3 Gas sensors fabrication

In this thesis, two types of transducing platforms were employed - the first, based on an array of 4 silicon micromachined platforms (400 x 400 μm each), and the second, based on bulk silicon substrates (5000 x 4000 μm). Structures of both types of the platforms are demonstrated in **Figure 2.7** and they consist of (from the top to the bottom):

- Interdigitated electrodes (IDEs): The micromachined substrates contain IDEs of Ti/Pt (25 nm/250 nm thick), with different electrode gaps of 5, 10, or 15 μm , whereas the bulk silicon substrates contain IDEs of Cr/Au (25 nm/250 nm thick), with electrode gap of 5 μm .
- Insulating layer - 500 nm thick silicon oxide layer to isolate the IDEs from the microheaters (for the micromachined structure) or the Si (for the silicon bulk structure).
- Resistive heater – 25 nm/250 nm thick Ti/Pt heater, only in the micromachined structure.
- Suspended membrane – $\text{Si}_3\text{N}_4/\text{SiO}_2$ (300 nm/500 nm thick) membrane processed by wet-etching of the silicon bulk, only in the micromachined structure.

The micromachined and silicon bulk platforms were produced at the wafer level employing various microfabrication steps such as oxidation, metallization, implantation, lithography, and etching of the substrate to define the membranes (in the case of micromachines). The platforms used in this thesis were designed and processed by other researchers and the technical staff of the Clean Room at *IMB-CNM (CSIC)*, Barcelona, Spain. The design and development of the platforms have been discussed previously elsewhere [170]–[172].

Finally, the MOX sensitive layer is deposited over the transducing platform using the shielding mask, as described previously, in *Section 2.1.1* and the fabricated gas sensors are mounted on a standard TO-8 package as shown in **Figure 2.7c**.

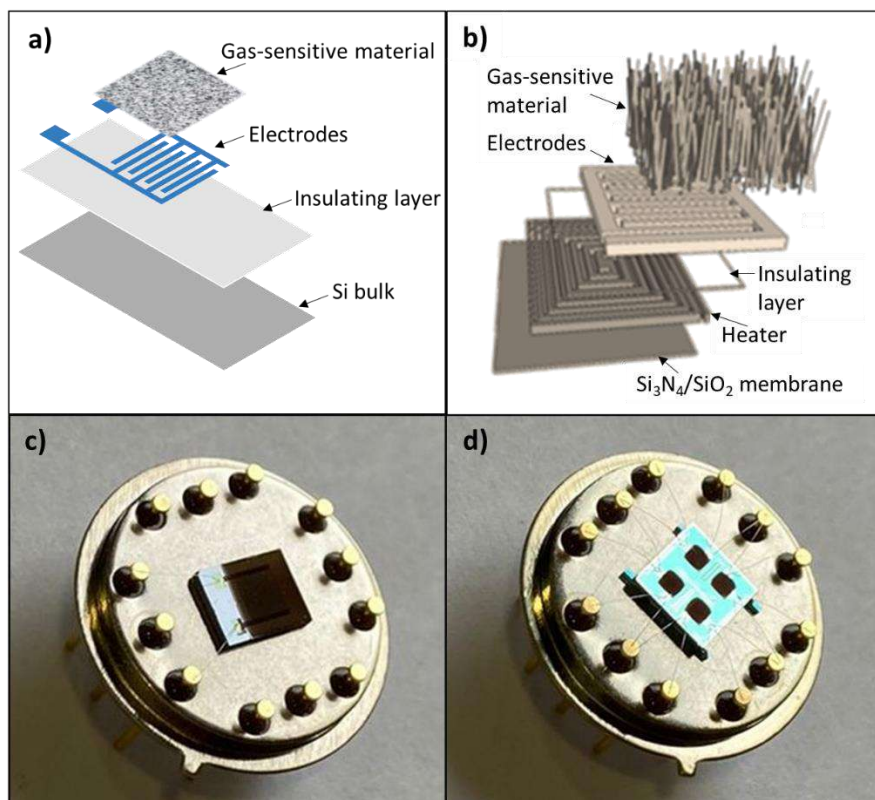


Figure 2.7. Schematic representation of the **a)** Si bulk sensor's layers, **b)** micromachined sensor's layers, and **c)** Si bulk sensor mounted on a standard TO8 package, and **d)** array of micromachined sensors mounted on a standard TO8 package. The image **b)** is adopted from [172].

2.4 Gas testing

The assembled MOX based microsensors were tested in a continuous flow test chamber provided with mass flow (MF) controllers that allow the mixture of dry/humid air and calibrated gaseous analytes (ethanol, acetone, toluene, carbon monoxide, nitrogen dioxide, and hydrogen) to obtain the desired concentration. Subsequently the gaseous analytes were purged with synthetic air until the initial baseline resistance was recovered. The electrical resistance measurements of the microsensors were achieved in a system provided with an electrometer and a multimeter with a 20-channel relay multiplexer to monitor various sensors simultaneously. To have proper control of the relative humidity (RH) inside the gas test chamber, an evaluation kit with a humidity sensor was also used. For the sensors that operate using photoactivation, continuous illumination from a light-emitting diode (LED) with a wavelength of 365 nm was coupled to the system. The schemes of the thermoactivated and photoactivated gas testing systems are depicted in **Figure 2.8**. Further information about the specific conditions and equipment used for each of the tested sensors can be found in the journal articles published during the thesis (*Chapter 3*).

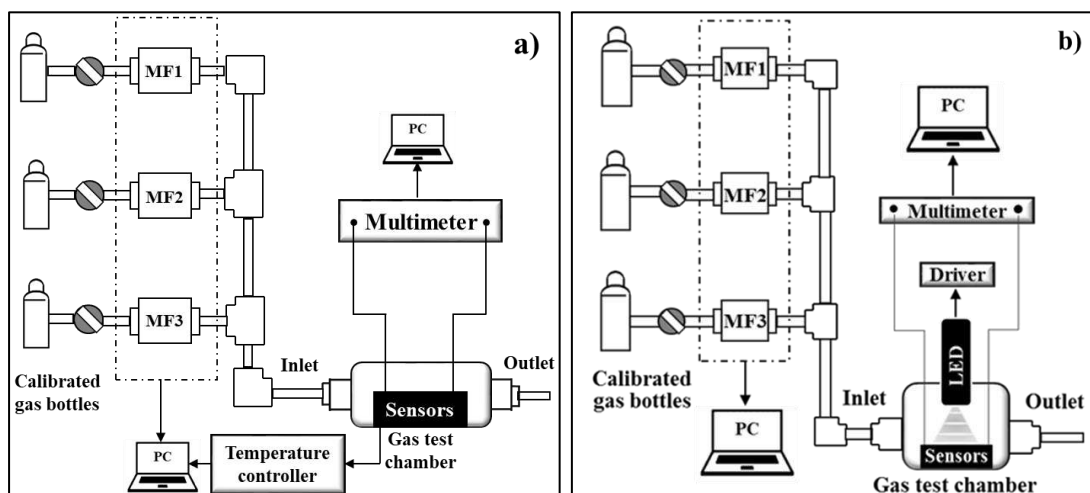


Figure 2.8. Schematic view of the a) thermoactivated, b) photoactivated gas sensing measurement system. Not-to-scale.

2.4.1. Gas sensor parameters

The main parameters considered during the validation of a sensor include its response, sensitivity, selectivity, response and recovery time, stability, limit of detection, and working temperature. The meaning of each parameter is described below:

- **Sensor response**

The response (R) of a chemoresistive sensor is proportional to the change in the resistance of the material when exposed to the gas. In this thesis, two different forms were used to mathematically express the response, as shown in **Table 2.3**:

Table 2.3. Sensor response calculation depending on the type of the target gas.

Reducing gases	Oxidizing gases
R_a/R_g or $(R_a-R_g)/R_a$	R_g/R_a or $(R_g-R_a)/R_a$

R_a – sensor resistance in ambient air, R_g – sensor resistance in target gas.

The expression used for a specific sensor can be found in the *Experimental part* of each *Journal Article*, in *Chapter 3*.

- **Sensitivity**

The sensitivity of the sensor (S) is defined as the ratio between the change in response (ΔR) and a fixed change in analyte concentration (Δc) [152].

- **Selectivity**

Generally, the selectivity of a gas sensor means the preferential detection of a particular gas in the presence of another gas under the same operating conditions. Hence, it can be expressed as the ratio between the sensitivity of the sensor towards the interference gas and the sensitivity of the sensor toward the target gas [173]. In some cases, statistical method, analysis of variance (ANOVA), was also used to compare the responses of the sensors towards the tested gases. Similarly, to have an appraisal of the selectivity among different gases, a mathematical algorithm based on principal component analysis (PCA) was employed sometimes. PCA serves as a dimensionality-reduction method that reduces the dimensionality of large data sets, by transforming a large set of variables into a smaller one that still contains most of the information as the large set [174].

- **Response/Recovery time**

Response time is defined as the time required for a sensor to reach 90 % of the total response upon exposure to the target gas [175].

Recovery time is defined as the time required for a sensor to return to 90 % of the original baseline signal after the target gas is removed and the sensor is subsequently cleaned with dry air [175].

- **Stability**

The stability of the sensor refers to its ability to maintain the sensing properties repeatedly for a determined period. The sensors fabricated in this thesis were tested for at least four weeks accumulating a minimum of 120 h of operation.

- **Limit of detection**

For high-performance sensor applications, sensors should be capable to detect even very low concentrations of the gases. The minimum concentration of analyte gas, which can be detected by a sensor, is called its limit of detection (LOD) [176]. It is defined as concentration for which the signal peak (S) should have height at least three times the noise (N) [177]:

$$LOD = \frac{S}{N} = 3 \quad (2.6)$$

- **Working temperature/Light wavelength**

Working temperature is a key property that influences the performance of a thermoactivated sensor. It is the temperature at which the sensor material must be heated to obtain the most optimal response.

Analogously, for the photoactivated sensors, the crucial property is the light wavelength. The wavelength (λ) of the applied light used for the activation has to meet the following requirement:

$$\lambda \leq \frac{hc}{E_g} \quad (2.7)$$

Where h is Planck's constant, c is the velocity of light, and E_g is the band gap of MOX [178].

Due to the wide band gaps of most gas-sensitive MOXs, it was found that the most appropriate wavelengths for their activation are those in the UV range. Therefore, the photoactivated tests in this thesis were run under UV light.

Additionally, the optimal irradiance of the lamp was examined on the APTES modified WO_{3-x} sensor and it was found to be $1800 \text{ mW}\cdot\text{cm}^{-2}$ (more details can be found in the *Journal Article 3, Section 3.2*). This irradiance was used for all further photoactivated measurements.

Chapter 3

Results

3.1 Gas-sensitive materials

Most studies on gas-sensitive materials are focused on the detection of chemicals such as CO, NO₂, O₃, H₂, NH₃, or H₂S due to their toxicity, their relation with atmospheric composition, and their presence in the environment [4]–[11]. However, in recent years, the application of gas-sensitive materials has been extended to the detection of volatile organic compounds (VOCs), not only because they are common industrial contaminants, but also because they are key markers for (indoor/outdoor) air quality assessment [12] and early diagnosis of several diseases [14]. In this context, the development of new and optimized gas-sensitive materials is suitable and of interest to the state-of-the-art and the sensor's industry. This section presents the results of a review article on materials for VOCs sensing realized during the thesis and published in Nanomaterials MDPI journal with the title "**VOCs sensing by metal oxides, conductive polymers, and carbon-based materials**" [179]. The review focuses on non-modified or modified metal oxides (MOXs), polymers (POMs), and carbon-based materials (CbMs), paying special attention to their functional properties such as sensitivity, response time, and particularly selectivity (from a cross-sensitivity point of view), as this information is generally not found in other reviews. The work also identifies the most common technological solutions reported in the literature, including material features, synthesis methods, sensing principles, and the key enabling systems for their practical use. The objective of this work was directed to define the knowledge gap in the field of gas and VOCs sensitive materials and sensors.

3.1.1. Results

The review article compiles the literature data which refers to the use of metal oxides (e.g., ZnO, SnO₂, TiO₂, WO₃), conductive polymers (e.g., polypyrrole, polythiophene, poly(3,4-ethylenedioxythiophene)), and carbon-based materials (e.g., graphene, graphene oxide, carbon nanotubes), and their mutual combination for VOCs sensing. Among these materials, special attention is devoted to MOXs, due to their versatile properties and large presence in the literature. According to this literature survey, gas-sensitive materials with different morphologies (e.g., particles, rods, sheets, flowers, etc.) and with incorporated intentional impurities to form extra interfaces (e.g., Schottky junctions, heterojunctions) were synthesized using various synthesis methods (e.g., wet chemical synthesis, chemical vapor deposition) and employed to detect VOCs. The collected literature shows the correlation between the sensor performances on one side, and morphology, microstructure, size, and composition of the gas-sensitive materials on the other, to show the reader at one glance the attributes of most common systems for VOCs sensing. The review provides tables and data that compare the response of sensitive materials to an extensive list of VOCs, as well as other sensor characteristics, such as operating temperatures, transducing principles, and response and recovery times.

3.1.2. Conclusions

The literature review of MOXs, POMs, and CbMs showed the suitability of these materials to sense a wide range of VOCs, particularly those from the group of oxygenated hydrocarbons (e.g., methanol, ethanol). Lot of attention was directed to the optimization of these materials, which mainly involves tuning morphology, size, and composition, with aim of improving the properties of the sensor in terms of sensitivity, speed of response, and selectivity to certain degree. Structured materials with intentionally introduced “decorative impurities” to form extra interfaces showed the best characteristics for VOCs detection. These decorated structures mainly include MOXs, either as a ‘host’ or as a ‘guest’ element in POMs or CbMs, due to their better stability as gas-sensitive materials compared to POMs and CbMs. In that sense, the thesis was further developed in the direction of investigating sensors based on structured MOXs with nanoscale interfaces at the surface. The literature survey also showed a lack of synthesis methods that allow for direct integration of structured materials into transducing platforms, reinforcing the need to continue developing methods, such as AACCD, which allows the direct integration, structuration, and modification of MOXs. Hence, WO_3 , ZnO , Fe_2O_3 , CeO_2 , and CuO_2 were chosen as ‘host’ or ‘guest’ materials due to their proven gas sensing properties and the gap in the AACVD literature for obtaining modified structured versions of these materials. This list of materials was also found interesting due to the abundance of their elements, as is the case for iron, or their different conduction types (for WO_3 and ZnO : n-type conductivity, for CeO_2 , and Cu_2O : p-type conductivity, and for Fe_2O_3 : n- or p-type conductivity).

3.1.3. Journal Article 1

VOCs sensing by metal oxides, conductive polymers, and carbon-based materials, Tomić, M., Šetka, M., Vojkůvka, L., Vallejos, S., Nanomaterials, 2021, 11(2), 552, doi: 10.3390/nano11020552.

Review

VOCs Sensing by Metal Oxides, Conductive Polymers, and Carbon-Based Materials

Milena Tomić^{1,2}, Milena Šetka³, Lukaš Vojkúvka⁴ and Stella Vallejos^{1,3,*}

¹ Institute of Microelectronics of Barcelona (IMB-CNM, CSIC), Campus UAB, 08193 Cerdanyola del Vallès, Barcelona, Spain; milena.tomic@imb-cnm.csic.es

² Department of Electronic Engineering, Autonomous University of Barcelona (UAB), Campus UAB, 08193 Cerdanyola del Vallès, Barcelona, Spain

³ CEITEC—Central European Institute of Technology, Brno University of Technology, 61200 Brno, Czech Republic; milena.setka@ceitec.vutbr.cz

⁴ Silicon Austria Labs, Microsystem Technologies, High Tech Campus Villach, Europastraße 12, A-9524 Villach, Austria; Lukas.Vojkuvka@silicon-austria.com

* Correspondence: stella.vallejos@imb-cnm.csic.es or vargas@vutbr.cz; Tel.: +34-935947700; Fax: +34-935800267

Abstract: This review summarizes the recent research efforts and developments in nanomaterials for sensing volatile organic compounds (VOCs). The discussion focuses on key materials such as metal oxides (e.g., ZnO, SnO₂, TiO₂, WO₃), conductive polymers (e.g., polypyrrole, polythiophene, poly(3,4-ethylenedioxythiophene)), and carbon-based materials (e.g., graphene, graphene oxide, carbon nanotubes), and their mutual combination due to their representativeness in VOCs sensing. Moreover, it delves into the main characteristics and tuning of these materials to achieve enhanced functionality (sensitivity, selectivity, speed of response, and stability). The usual synthesis methods and their advantages towards their integration with microsystems for practical applications are also remarked on. The literature survey shows the most successful systems include structured morphologies, particularly hierarchical structures at the nanometric scale, with intentionally introduced tunable “decorative impurities” or well-defined interfaces forming bilayer structures. These groups of modified or functionalized structures, in which metal oxides are still the main protagonists either as host or guest elements, have proved improvements in VOCs sensing. The work also identifies the need to explore new hybrid material combinations, as well as the convenience of incorporating other transducing principles further than resistive that allow the exploitation of mixed output concepts (e.g., electric, optic, mechanic).

Keywords: volatile organic compounds; gas sensors; nanomaterials



Citation: Tomić, M.; Šetka, M.; Vojkúvka, L.; Vallejos, S. VOCs Sensing by Metal Oxides, Conductive Polymers, and Carbon-Based Materials. *Nanomaterials* **2021**, *11*, 552. <https://doi.org/10.3390/nano11020552>

Academic Editor:
Giuseppe Cappelletti

Received: 23 December 2020

Accepted: 7 February 2021

Published: 22 February 2021

Publisher's Note: MDPI stays neutral with regard to jurisdictional claims in published maps and institutional affiliations.



Copyright: © 2021 by the authors. Licensee MDPI, Basel, Switzerland. This article is an open access article distributed under the terms and conditions of the Creative Commons Attribution (CC BY) license (<https://creativecommons.org/licenses/by/4.0/>).

1. Introduction

Nanoscaled materials, with sizes within the Debye length of the surface (typically on the order of 2–100 nm), are used as highly sensitive (receptor) elements in gas/vapor sensors due to their large surface-to-volume-ratio and their proven better chemical, optical, and electrical properties as compared to non-nanoscaled materials. These gas/vapor sensitive materials include usually unmodified or modified metal oxides (MOXs), polymers (POMs), and/or carbon-based materials (CbMs) with varied morphological shapes, integrated into conventional transducers (e.g., resistive, capacitive, gravimetric, or optical). The sensing properties of these materials generally depend on the chemisorption of negatively charged oxygen adsorbates (O²⁻, O⁻, and O²⁻) in air, which, due to charge transfer between the material and the analytes, change the electron density on the material surface. They may also depend on the chemical reaction between the sensitive material and the analyte, or the diffusion of species into the bulk of the material [1–10].

Most studies of gas/vapor sensitive materials are focused on the detection of low concentrations of CO, NO₂, O₃, H₂, NH₃, or H₂S due to their toxicity, their relation with

atmospheric composition, or the fact that these gases can be found at high levels in certain environments [11–18]. However, in recent years, the application of gas/vapor sensitive materials has been extended to the detection of volatile organic compounds (VOCs), not only because their presence is significant in the industry and domestic sector, but also because of their relevance as markers for (indoor/outdoor) air [19] and food quality [20], and early diagnosis of several diseases [21].

VOCs are organic chemicals that possess a high vapor pressure at room temperature [22]. These compounds are numerous and varied, commonly classified according to their functional group into aliphatic hydrocarbons, simple oxygenated hydrocarbons, halogenated hydrocarbons, carbonyl compounds, aromatic hydrocarbons, etc. [23]. Most applications, in which one or more of these compounds need to be monitored, typically involve a broad background of other vapors and/or gases. For instance, thousands of VOCs have been found in the environment, food products, and/or exhaled breath. Therefore, the selectivity of sensitive materials, or its approximation by means of reducing the cross-sensitivity, is imperative. Table 1 exemplifies the VOCs profile in the field of air quality and breath analysis (note that these profiles contain only the most representative VOCs usually reported in the literature).

Table 1. Summary of the volatile organic compounds (VOCs) profiles in air-quality due to anthropogenic emissions in the atmosphere [24] and exhaled breath due to cancer (e.g., lung, breast, gastroesophageal, colorectal, oral cavity, head and neck, etc.) [21]. The presented threshold limit values (TLV) are based on the documentation of the American Conference of Governmental Industrial Hygienists (ACGIH) from 2019 [25]. The concentration range in the exhaled breath (CREB) for the selected gases/vapors, which include the minimum and maximum levels found within healthy and unhealthy subjects, were adopted from the references [26–30]; these references are also summarized in reference [21].

VOCs Monitoring												
	Air Quality				Breath Analysis							
	VOCs Profile	Representative Vapor Analytes	TLV (ppm)		VOCs Profile	Representative Vapor Analytes	CREB (ppb)					
Anthropogenic VOCs emission	Alcohols	Methanol	200 TWA	Cancer	Alcohols	Methanol	157–344					
		Ethanol	1000 TWA			Ethanol	96–2848					
	Ethers	1-Propanol	200 TWA		Aldehydes	1-Propanol	4–13					
		Furan	N/A			Pentanal	2–7					
	Aldehydes	Formaldehyde	0.1 TWA		Heptanal	2–7						
		Acetaldehyde	25 C		Nonanal	2–107						
		Propenal	0.1 C		Ketones	Acetone	35–1000					
	Ketones	Acetone	250 TWA			2-Butanone	0.002–3					
		2-Butanone	200 TWA			3-Hydroxy-2-Butanone	0.002–0.05					
	Esters	Ethylacetate	400 TWA		Alkanes	Alkanes	Pentane 4-Methyloctane	2–18 16–19				
		Carboxylic acid	Acetic acid						10 TWA			
	Alkanes	Ethane	N/A						Alkenes	Alkenes	Isoprene	41–109
		Propane	N/A									
		Butane	1000 TWA									
		Pentane	1000 TWA									
		Hexane	50 TWA									
		Heptane	400 TWA									
		Octane	300 TWA									
		Nonane	200 TWA									
		Decane	N/A									
Undecane		N/A										
Dodecane	N/A											
Alkenes	Ethylene	200 TWA	Alkynes	Aromatics	Ethylbenzene Toluene	1–18 1–37						
	Propylene	500 TWA										
	Butylene	250 TWA										
Aromatics	1,3-Butadiene	2 TWA	Halohydrocarbons	Other	Acetonitrile Dimethyl disulfide Limonene	20 TWA 0.5 TWA N/A						
	Acetylene	N/A										
	Benzene	0.5 TWA										
	Ethylbenzene	20 TWA										
	Styrene	10 TWA										
Halohydrocarbons	Toluene	20 TWA	Other	Acetonitrile	20 TWA							
	Xylene	100 TWA										
	Chloroform	10 TWA										
	Dichloromethane	50 TWA										
Other	Dichloroethane	100 TWA	Dimethyl disulfide	0.5 TWA	N/A							
	Chlorobenzene	10 TWA										
	Acetonitrile	20 TWA										

8-h time weighted averages (TWA)—the average values of exposure over the course of an 8-h work shift; ceiling values (C)—the exposure limits that should not be exceeded at any time; N/A—data not available.

The present review focuses on the materials utilized to improve VOCs sensing, paying special attention to properties such as the sensitivity, the response time, and particularly selectivity from a cross-sensitivity point of view. The key materials taken into account in this review are MOXs, POMs, and CbMs and their modifications, with a special effort dedicated to MOXs due to their large presence in the literature, even after several years of research in this field. This can be noticed in Figure 1a, which displays an example of the weight of reports for these materials in the recent five years, as well as the most common unmodified and modified MOXs (Figure 1b). In considering the literature, we have compiled extensive tables with selected sensing data. A schematic view of the criteria used for such selection is depicted in Figure 2. The filtering stages have focused on finding reports in which the targeted materials were tested to various VOCs at the same concentrations and operating temperatures to compare their crossed response. This search sorting has significantly reduced the number of reports as compared to the comprehensive list of available literature, which certainly provides extraordinary examples of materials and their analysis, but often these publications do not cover in depth the test of analytes or in many cases, they present responses to incomparable analytes concentrations or operating temperatures.

In summary, the tables provide to the reader a quick visualization of the best responses for a given material and the degree of cross-response recorded at the same operating temperature for similar concentrations of various VOCs. The tables showing functional parameters, although providing quantitative data, are recommended to be used only for qualitative comparison, as the reports do not share generalized protocols for the tests. Thus, the functional outputs are prone to not depend only on the material properties, but also on the conditions used to test the analytes. The review, in addition, provides the most common technological solutions reported in the literature, including material features, synthetic methods, sensing principles, and the key enabling systems for their practical use. We believe this work will allow for identifying at one glance the attributes of most common systems for VOCs sensing, among MOXs, POMs, and CbMs in terms of cross-response amongst selected VOCs; information generally not found in other reviews. Hence, here we present the recent research efforts and developments in materials for VOCs sensing.

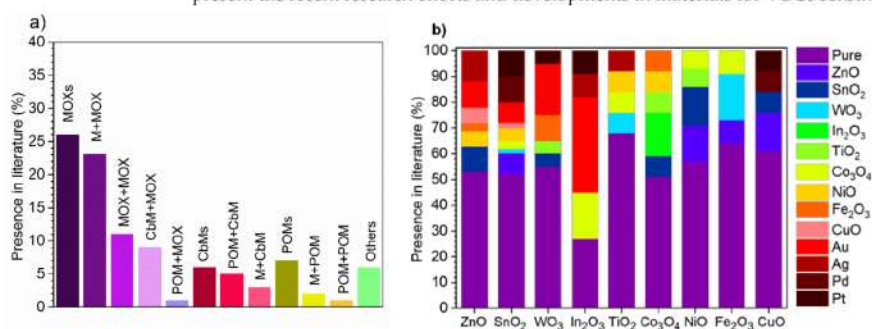


Figure 1. Materials for VOCs sensing summed up from the Web of Science (WOS) database. The data were collected using “gas sensors + VOCs” as keywords and only journal articles between 2015 and 2020 were taken into account. The materials were generalized as modified metal oxides (MOXs) (e.g., ZnO, SnO₂, WO₃), carbon-based materials (CbMs) (e.g., graphene, graphene oxide, carbon nanotubes), and polymers (POMs) (e.g., conductive polymers and others such as Poly(methyl methacrylate)—PMMA). (a) Summary of MOXs, POMs, and CbMs, plus their mutual modifications (MOX + MOX, CbM + MOX, POM + MOX, POM + CbM, POM + POM) or metal modifications (M + MOX, M + POM, M + CbM), and other minority materials (e.g., zeolitic imidazolite framework (ZIF) materials, metal dichalcogenides, and perovskites) used for VOCs sensing. (b) List and presence in the literature of the most common VOC sensitive MOXs (pure) and their modifications with metals or another MOX. Notice that the literature provides further examples of single and complex MOXs (based on elements from the transition, post-transition, lanthanide, and alkaline earth groups from the periodic table) than those presented here, but these examples are comparatively less recurrent in VOC sensing.

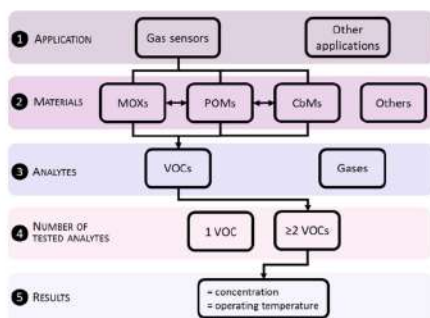


Figure 2. Schematic representation of the filtering stages used as criteria to search the literature reports for this review, in particular those displayed in the tables (4 to 9). The stages include a selection by application, materials, analytes, and number of analytes tested, with the results limiting the data to those reports in which two or more VOCs are evaluated using the same operating temperature and concentration for each analyte.

2. Gas/Vapor Sensitive Materials

The gas/vapor sensitive receptors usually include materials with semiconducting properties such as MOXs, POMs, and CbMs, although, amongst them, MOXs are the primary materials used for gas/vapor sensing. MOXs work as sensitive materials due to their properties to adsorb gas/vapor chemicals and transduce them into conductivity changes. These properties were exploited for the first time in the 60s by Seiyama et al. to fabricate ZnO based chemoresistive gas sensors [31]. Since then, a vast number of MOXs have been studied and addressed to enhance their sensing features, taking into account their electro-physical (band gap, electroconductivity, type of conductivity, oxygen diffusion), thermodynamic, surface, electronic, structural, and catalytic properties [3,32]. Thus, the literature [33] demonstrated that MOXs with large band gaps (e.g., between 2 and 4 eV) and low activation energy of the centers are generally an optimal combination for chemoresistive sensors. In addition, the studies on various n- and p-type MOXs pointed out that the most effective and widely used MOXs are those with n-type conductivity, such as ZnO, SnO₂, and WO₃ [33,34]. Certainly, this is consistent with Figure 1b, which suggests that these three materials are amongst the dominant gas/vapor receptors in the literature. ZnO, for instance, is an n-type semiconductor with a direct band gap of 3.37 eV [35] which has shown large surface-to-volume ratio morphologies that improved sensitivity and response speed with respect to other morphologies with bulky characteristics. This material showed especially good sensitivity to methanol [36], ethanol [37,38], chlorophenol [36], formaldehyde [39], and acetaldehyde [39,40]. The wide use of ZnO in the literature is probably related to its relatively facile synthesis processes and high chemical stability [41]. SnO₂ is another n-type gas/vapor sensitive MOX with wide band gap of 3.6 eV [42]. This material has been used intensively for studying the influence of grain size on sensor response [2,43], the conductivity of MOX gas sensors [1], or the key surface properties for gas sensing [3], amongst others. SnO₂ has shown good mechanical stability, high conductivity, wide operating temperature range (200–600 °C) [44] and excellent performance in the detection of ethanol [45], butanol [46], acetone [45], and toluene [47]. Other important gas/vapor sensitive MOXs include WO₃, In₂O₃, TiO₂, and Fe₂O₃. Specifically, WO₃ showed high sensitivity to VOCs such as acetone [48], methanol [48], and toluene [49]. Moreover, In₂O₃ exhibited very high responses to acetone and toluene with a detection limit of 500 ppb [50] and TiO₂ demonstrated very promising results in acetone [51] and hydrogen [52] detection, while Fe₂O₃ nanoparticles were used for the decoration of common MOXs (e.g., WO₃ or SiO₂) showing high sensitivity to toluene [49] and ethylacetate [53].

POMs are organic materials usually belonging to the category of insulators, as they possess covalent bonds without free movable charge carriers (electrons or ions), although within POMs there is a group of conductive polymers, which behave similarly to semiconductor MOXs. Their conductivity originates from highly delocalized electrons between the conjugated polymer backbone (alternating single bonds (σ) and double bonds (π)) and the dopant (negatively charged species). When conductive polymers are exposed to the gas/vapor, these materials undergo oxidation and reduction processes as a function of the dopants (p- or n-type) [4]. During the oxidation, electrons are extracted from the highest occupied molecular orbital (HOMO) of the valence band, whereas during the reduction, electrons are transferred to the lowest unoccupied molecular orbital (LUMO) of the conduction band. The charge carriers in the form of polarons, bipolarons, or an equilibrium between both are created during the redox processes [5,6]. This charge transfer is generally transduced in conductivity changes that enable the gas/vapor detection even at room temperature, circumventing the need for thermal activation as in MOXs. Conductive polymers such as polypyrrole (PPy), polyaniline (PANI), polythiophene (PTh), and poly(3,4-ethylenedioxythiophene) (PEDOT), and their modifications with metals have been the most studied candidates for sensing VOCs [4,7] (Figure 1a). These materials demonstrated mostly resistive responses to vapors such as ethanol, methanol, and acetone, and gases such as NH_3 , NO_2 , and CO [5]. Macrocyclic compounds such as cyclodextrins (CDs), calixarenes, and cavitands have also been investigated due to the presence of cavities with molecular dimensions, which can act as molecular receptors [8].

CbMs include mainly carbon nanotubes (CNTs), graphene oxide (GO), or reduced graphene oxide (rGO). Like other gas-sensitive materials, it is widely accepted that the charge transfer between gas/vapor species and CbMs is responsible for the conductivity changes of these materials and thus gas/vapor detection. Due to the typical two-dimensional (2D) single-atom-thick structure of graphene, GO and rGO, these materials are prone to change the local carrier concentration electron by electron providing these structures advantages over CNTs and other MOXs and POMs [9,10]. Overall, the gas sensing properties of CbMs are strongly connected with the presence of defects and residual contaminants at the surface. Hence, for practical applications, the sensitivity of CbMs is usually enhanced by modifying or functionalizing them with metals [54,55], MOXs [56], or POMs [57,58], as can be seen in Figure 1a.

Overall, the key sensing features pursued in gas/vapor sensitive materials include sensitivity, selectivity, stability, and speed of response; features known as the four “S”s of gas sensing. Moreover, these materials are expected to interact reversibly and reproducibly with the specific analyte of interest showing strong stability in harsh conditions such as high temperature and/or high relative ambient humidity. From the economical point of view, the sensitive material should be widely available, simply and inexpensively synthesized, compatible, and easily implemented with specific transducing platforms. Table 2 presents a summary of the possible advantages and limits of these materials in their unmodified form. This table is intended to provide only a qualitative view, the quantitative evaluation for these materials is provided in the next sections.

Despite the great efforts invested in solving the mentioned limitations for each material type, and the large amount of literature showing important improvements, there is still a continuous demand in the gas sensor field for enhanced materials properties. The pursued improvements are especially focused on finding materials with more sensitivity and selectivity to VOCs from the aliphatic and aromatic hydrocarbons, and carbonyl groups, rather than just those from the simple oxygenated hydrocarbons group, as well as lower detection limits that reach ppb-ppt levels. The demands also emphasize the search for scalable synthetic methods for on-chip integration and low operational power consumption. Currently, the most common strategies to pursue these improvements at the material level generally involve tailoring of the material by:

- Tuning the surface morphology: shape, size, and dimensional control to obtain 0D (e.g., nanoparticles and quantum dots), 1D (e.g., nanofibers, nanotubes, and nanowires),

- 2D (e.g., thin films, nanosheets, and nanoplates), and 3D (e.g., porous films and nanoflowers, which consist of 2D nanosheets) materials.
- Modifying or functionalizing the material: control of type and level of intentional impurities (doping, formation of Schottky barriers, heterojunctions, and/or inorganic/organic hybrid structures).

Table 2. Comparative table showing the main properties of MOXs, POMs, and CbMs. The symbols attached to each qualitative estimation remark the degree, major (↑) or minor (↓), of each characteristic with respect to the other groups of materials.

Properties	MOXs	POMs	CbMs	Notes
Sensitivity	High↑↑	High↑	High	Advantageous for all materials to specific gases/vapors, although in major degree for MOXs with respect to POMs and CbMs.
Selectivity	Poor↓	Poor	Poor	Poor for all materials within a large number of gases/vapors. POMs and CbMs have shown advantages for specific gases such as NH ₃ and NO ₂ .
Stability	High	Medium↓	Medium	More advantageous for MOXs due to operation at high temperatures. The stability of POMs is highly dependent on humidity.
Speed of response	High	Low	Low	More advantageous for MOXs due to operation at high temperatures.
Long-lasting lifetime	High	Low↓	Low	More advantageous for MOXs due to low probability of poisoning and degradation. POMs have more probability of degradations in humid ambient with respect to CbMs.
Operating temperature	High	Low	Low	More advantageous for POMs and CbMs due to the capacity of adsorption at room temperature.
Energy consumption	High	Low	Low	More advantageous for POMs and CbMs as they do not require thermal activation.
Cost	Low↓	Low	High	More advantageous for MOXs and POMs due to the wider choice of synthesis methods.
Miniaturization potential	High↑	High	High	Advantageous for all materials according to the transducing principle. MOXs are more advantageous in this area due to their proved compatibility with micro/nano fabrication processes, although the recent scalable integration methods based on roll-to-roll and printed electronics are facilitating more the scalable integration of POMs and CbMs into miniaturized systems.

3. Tailoring Materials for Enhanced Sensing Properties to VOCs

3.1. Surface Area—The Larger, the Better

Several works in the literature have stated the correlation between the sensing performances, morphology, microstructure, and size of gas/vapor sensitive materials [59–64]. In this context, various materials with morphological shapes in the nanometric scale with increased surface-to-volume ratio have proven to be more effective for gas detection [46,47]. Generally, the surface properties of these peculiar morphologies, including crystalline and structural properties, have been shown to determine the sensing activity of these materials. More precisely, the density of states at the surface has been revealed to play an important role in the sensing mechanism of gases and vapors dominated by the space-charge-controlled grain-boundary conduction model, in which the grain sizes, surface chemical states, and gas/vapor adsorption amount determine the overall response of the sensors [1].

Table 3 displays a collection of low dimensional and 3D nanomaterials that have proved greatly improved functionality compared to bulk materials for VOCs sensing.

Examples of the appearance of selected morphologies are also displayed in Figure 3. Certainly, MOXs, and in particular SnO₂, have been the primary reference materials for determining the influence of surface area (particle size) on gas sensing properties in the past [2,43]. The literature related to VOCs, for instance, shows that SnO₂ nanoparticles with reduced crystalline size (from 9.1 to 6.1 nm) show higher and faster response to butanol [46] and that non-commercial nanoparticles can be improved for obtaining better responses to toluene [47] (Table 4). Similarly, other comparative studies of sensors based on complex structures with flower-like hierarchical porous single-crystalline ZnO nanosheets and commercial ZnO powder demonstrated for the former three-times better responses to ethanol with nearly 40% faster response [37]. This fact brought attention to further studies, which focused on controlling the features of various ZnO nanostructures [40]. The results demonstrated enhanced sensitivity to acetaldehyde in the sub-ppm range (50 ppb) when tuning the morphology into nanorings shape instead of nanoparticles, nanorods, or nanotubes.

Table 3. Summary of VOCs sensitive materials reported in the literature according to their dimensionality and/or morphology.

Materials	Morphology	Features	Ref.
0D	Particles	Diameters of 1–100 nm	[45,48,49,52,65–68]
	Cubes	Average size of 200 nm	[69]
	Hollow spheres	Diameter of 72 nm	[70]
1D	Rods and needles	Diameters of 100–200 nm and lengths up to 10,000 nm	[48,49,52,71]
	Rings	Diameters of 120 nm (inner) and 180 nm (outer) and lengths of 1000–1500 nm	[40]
2D	Sheets and monolayers	Size of 100–400 nm or as large as 30–70 μm and thickness of 10–60 nm	[57,72]
3D	Porous films	Pore size of 6–150 nm	[36,38,45,46,73]
	Flowers	Sheet size of 120–2000 nm and thickness of 12–50 nm	[37,39,47,50,51,74,75]
	Tetrapods	Rod diameters of 50 nm and lengths of 1000 nm	[76]

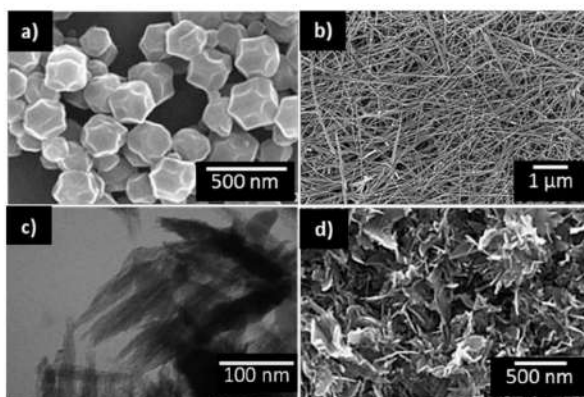


Figure 3. SEM images of MOX nanostructures with different morphologies and dimensionalities (a) 0D—cubes, (b) 1D—needles, (c) 2D—sheets, and (d) 3D—flowers. Adapted from references [39,69,75], with permission from the American Chemical Society, 2014, and Elsevier B.V., 2013 and 2016, respectively.

Other studies discussed the impact of the dimensionality of TiO₂ nanostructures on the gas sensing performance. For instance, hierarchical 3D TiO₂ nanoflowers [51] showed enhanced properties towards acetone at room temperature with respect to TiO₂

nanoparticles [77]. The use of hierarchical flower-like CuO nanostructures is another example of complex 3D-shaped MOX [74], which has reported excellent results towards ethanol, formaldehyde, acetone, and xylene for concentrations as low as 20 ppb and yet with fast response (11.2 s) and short recovery time (8.4 s). Novel MOXs based on highly porous Co₃O₄ concave nanocubes with high surface area (120.9 m²g⁻¹) have also proven fast response and recovery time below 10 s to 10 ppm of ethanol [69]. Similarly, Co₃O₄ in the form of monolayer has shown high responses to ethanol and xylene [72]. Other complex structures, for instance, nanosheet-based 3D hierarchical rosette-like In₂O₃ microspheres in their hollow and full form, also showed promising properties to low (500 ppb) acetone and toluene concentrations [50]. Recently, a new study [76] reported the use of ZnO nanotetrapods, consisting of four cylindrical nanorod legs, which showed good results in the detection of VOCs, especially ethanol. Although there is no general rule to state a better sensing functionality for one or another morphological dimension [78], the literature compiled for this review suggests the 3D morphology to be superior in gas/vapor sensing compared to 0D, 1D, and 2D. It is worth bearing in mind that 3D structures are assembled from low dimensional (0D, 1D, or 2D) nano-building blocks and therefore further improvements might be related to synergistic effects [79]. The apparent improved behavior in 3D structures could also relate to their particular surface defects due to their porous and irregular arrangement. In addition, the interconnected structure, usually present in 3D-based films, seems to provide further advantages, especially in resistive-based sensors (the most representative in the literature of nanomaterial-based sensors) as it favors the electrical current percolation [80,81]. This is the opposite for other types of structures, for instance, those based on vertically aligned 1D structures. Thus, the selection of the materials by their dimension should not be associated exclusively with the surface-to-volume-ratio feature, but rather with the employed working principle and the targeted transducing platform.

The reports in the literature are not limited only to single oxides; the morphology control of multicomponent oxides as well as the chemical composition for sensing VOCs have also shown to improve the sensing performance. For example, large surface nonstoichiometric Co-rich ZnCo₂O₄ in the form of hollow nanospheres reported high sensitivity to formaldehyde with superior experimental and estimated detection limits of 13 ppb and 2 ppb, respectively, as compared to other reports in the literature [70].

POMs and CbMs with large surface areas are also pursued to enhance VOCs detection. However, in the gas/vapor sensing literature, there is a lack of information about the size influence on POMs and CbMs as frequently the reports regard the functionalization effect on these materials, which indeed have proven essential to promoting VOCs sensitivity; this is further discussed in the next section. Most of the reports on pristine POMs and CbMs state high sensitivity to gases such as NO_x and NH₃, and nearly insensitivity to VOCs especially from the aromatic family [4,57,82–84]. Among the few examples of VOCs sensing with pristine CbMs materials (Table 4), we found that using pristine single-walled carbon nanotubes (SWCNTs) instead of multi-walled carbon nanotubes (MWCNTs) might be favorable to detect toluene at room temperature [85].

Besides MOX- and GO-based 2D materials, it is important to mention other emerging materials with the same dimensionality that have a significant role in VOCs detection, although not the scope of this review. Among them are 2D transition metal dichalcogenides (TMDs) with their unique physical and chemical properties, such as a high surface-to-volume ratio, large number of active sites for redox reactions, high surface reactivity, and high absorption coefficient [86]. These materials have the formula MX₂, where M stands for transition metal element (e.g., Ti, Zr, Hf, V, Nb, Ta, Mo, W, Re, etc.) and X represents a chalcogen (Se, S, or Te) [87]. Some of the most common TMDs for VOCs detection are MoS₂, WS₂, MoSe₂, WSe₂, and SnS₂ [86,88–91].

Table 4. Sensing properties of pristine gas sensitive materials to VOCs.

Material	Morphology	Size, nm	VOCs	c, ppm	T, °C	R	t _R , s	t _r , s	Ref.
SnO ₂	NPs	9.1 ^{CS}	Butanol	10	150	190	9	N/A	[46]
		6.1 ^{CS}			150	630	11	N/A	
SnO ₂	NPs NPs ^{com}	6.3 ^{CS}	Toluene	100	260	9.7	3	10	[47]
		N/A			240	6.2	N/A	N/A	
ZnO	NPs ^{com} NShs	10–100 ^Ø	Ethanol	100	N/A	2.6	16	100	[37]
		1000 ^T			N/A	8.5	10	80	
ZnO	NTPs (NRds)	50 ^Ø 1000 ^L	Ethanol	500	340	57	50	70	[76]
ZnO	NPs NRgs	N/A	Acetaldehyde	0.05	220	2	N/A	N/A	[40]
		N/A			220	1.1	N/A	N/A	
TiO ₂	NPs NShs	10 ^Ø	Acetone	200	400	7.8	240	N/A	[77]
		120 ^L			700	60	1.7	10	
		12–23 ^T							[51]
CuO	NShs	50 ^T	Ethanol	0.2	250	2.1	11.2	8.4	[74]
Co ₃ O ₄	cNCs ML	2000 ^S 50 ^T	Ethanol	10	300	1.7	<10	<10	[69]
		17.6 ^{CS}			200	114	N/A	N/A	
In ₂ O ₃	NShs-hMSP NShs-MSP	20 ^T	Acetone	5	350	1.8	4	10	[50]
		20 ^T			350	1.7	4	10	
Co ₃ O ₄ ZnCo ₂ O ₄	HSps HSps	72 ^Ø	Formaldehyde	1	225	1.3	N/A	N/A	[70]
					225	7.3	149	497	
SWCNTs	SWCNTs	6 ^Ø 2000 ^L	Toluene	N/A	RT	7.5*	N/A	N/A	[85]
MWCNTs	MWCNTs	20 ^Ø 4000 ^L			RT	2.0*	N/A	N/A	

NPs: nanoparticles, ^{com}: commercial powder, NShs: nanosheets, NTP: nanotetrapods, NRds: nanorods, NRgs: nanorings, cNCs: concave nanocubes, ML: monolayer, hMSP: hierarchical microsphere, MSP: microsphere, HSps: hollow spheres, SWCNTs: single-walled carbon nanotubes, MWCNTs: multi-walled carbon nanotubes, ^{CS}: crystal size, N/A: data not available, ^Ø: diameter, ^T: thickness, ^L: length, ^S: size, RT: room temperature, c: concentration, T: operating temperature, R: response defined as R_s/R_g, t_R: response time, t_r: recovery time, and * sensitivity (kHz/ppm).

Within the novel 2D materials, transition metal carbides/nitrides (MXenes) represent another important group. These materials have stable and easily tunable microstructure, high electrical conductivity, large chemically active surface, and adjustable hydrophilicity, which makes them good candidates for VOCs monitoring [86]. The most studied MXenes for VOCs detection are Ti₃C₂T_x, V₂CT_x, Mo₂C, and Ti₂CO₂ [92,93]. Another noteworthy 2D material is boron nitride (BN). The high sensitivity reported for BN toward VOCs is related to localized charges induced by the presence of B and N atoms [94]. Amongst 2D materials, there are also those that are constituted of just one atomic species such as one layer thick black phosphorus (phosphorene), silicon (silicene), or germanium (germanene) [95]. Black phosphorus (BP) is considered to be a promising alternative [96,97], since compared to graphene and TMDs, BP possesses a higher surface-to-volume ratio due to its puckered honeycomb lattice structure [98,99].

3.2. Modification or Functionalization—Pushing the Performance Further

Another strategy commonly used to improve further the sensing properties of materials towards VOCs consists in the incorporation of intentional “impurities” at/in the material surface/structure. This modification or functionalization process includes the so-called:

- Decorated materials, when incorporating low amounts of noble metals or secondary materials (e.g., MOXs, POMs, CbMs) at the surface. These are represented by an “@” sign in between the guest and host material, e.g., Au@WO₃. Figure 4 displays examples of the decoration of WO₃ nanowires with gold, platinum, or iron oxide.

- Simple mixtures, when mixing two or more gas sensitive materials randomly. These are represented by a hyphen “-” sign in between the constituents, e.g., ZnO-CuO.
- Bilayers and trilayers, when there is a well-defined partition or interface between the two or three gas sensitive materials. These are represented by a slash “/” sign in between the constituents, e.g., CuO/SnO₂ and GO/ZnO/GO.
- Doped materials, when incorporating “guest” atoms into the material structure, e.g., Ce-doped SnO₂.

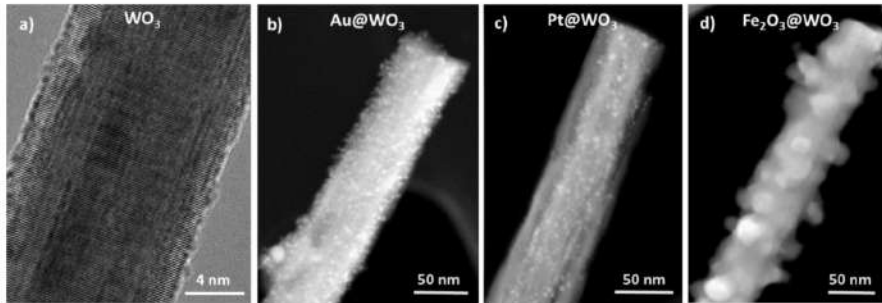


Figure 4. TEM images of (a) unmodified (high-resolution TEM) WO₃ nanowire and modified (scanning TEM) with (b) Au, (c) Pt, and (d) Fe₂O₃ nanoparticles.

Hereafter, the review differentiates the functionalized materials by the nomenclatures exposed above. The enhanced sensing performance of these functionalized materials has been attributed to electronic effects (band bending due to Fermi level equilibration, charge carrier separation, tuning of the depletion layer, and increased interfacial potential barrier energy) and/or chemical effects (decrease in activation energy, targeted catalytic activity, and synergistic surface reactions). The functionalization in terms of doping and decoration by forming nano-Schottky barriers or heterojunctions has been discussed broadly in previous studies [32,100]. Results in the literature [60,101] show that functionalized materials improve further the sensitivity, response time, working temperature, and/or selectivity to some extent by reducing the cross-responses to different gas or vapor molecules. In this work, we bring attention to the “decorative” and doping materials that have improved MOXs, POMs, and CbMs based sensors towards VOCs detection (Table 5).

The number of entries in Table 5 demonstrates that the decoration of popular gas-sensitive MOXs (SnO₂, ZnO, WO₃) with noble metals (e.g., Au, Pt, Pd) or secondary oxides (ZnO, TiO₂, CuO, Fe₂O₃) is a generalized method for improving the sensing performance of MOXs towards VOCs. For instance, research on the load variations of Au at ZnO revealed the dependence of the response on Au concentration. Results showed that Au-loaded ZnO has better responses to various VOCs, including diethylether, acetone, chlorobenzene, trichloroethylene, isoprene, ethylacetate, butylacetate, formaldehyde, and hexaldehyde. The 3 at.% Au@ZnO systems improved the response to isoprene, while the 5 at.% Au@ZnO to methanol [65]. Similarly, investigations on Ce- and Mg-doped SnO₂ found better sensing performance to formaldehyde, methanol, ethanol, and acetone for 2% Ce-doped SnO₂ and ethanol, toluene, and acetone for 1 at.% Mg-doped SnO₂ as compared to unmodified SnO₂ [73]. Further, the decoration of TiO₂ nanorods with 12 at.% of Pd showed enhanced responses to isopropanol as well as a clear improvement to hydrogen, which registers 35 times better response for the Pd@TiO₂ systems than for the unmodified TiO₂ nanorods [52].

Table 5. Sensing properties of modified and unmodified gas sensitive materials to VOCs.

Material	Loading	VOCs	c, ppm	T, °C	R	t _R , s	t _r , s	Ref.
Au@ZnO ZnO	Au 3 at.% Au 0 at.%	Isoprene	50	360	31 25	N/A N/A	N/A N/A	[65]
Au@ZnO ZnO	Au 5 at.% Au 0 at.%	Methanol	50	360	21 4.8	4 N/A	3 N/A	[65]
Ce-doped SnO ₂ SnO ₂	Ce 2 at.% Ce 0 at.%	Formaldehyde	500	320	10 28	8 10	4 5	[73]
Mg-doped SnO ₂ SnO ₂	Mg 1 at.% Mg 0 at.%	Ethanol	80	160	14 1	143 N/A	N/A N/A	[103]
Pd@TiO ₂ TiO ₂	Pd 12 at.% Pd 0 at.%	Isopropanol	5000	200	4.4 1.6	N/A N/A	N/A N/A	[52]
Fe ₂ O ₃ @WO ₃ Pt@WO ₃ WO ₃	Fe 3.9 at.% Pt 3.7 at.% Fe & Pt 0 at.%	Toluene	100	220	8 7.8 2.5	150 100 400	15 30 170	[49]
CuO/SnO ₂ SnO ₂	CuO 3 mol% CuO 0 mol%	Xylene	50	280	10 2.5	N/A N/A	N/A N/A	[45]
ZnO-CuO	Cu 65 at.% Zn 35 at.%	Acetone	10	300	1.2	22	26	[75]
TiO ₂ /SnO ₂ SnO ₂	N/A N/A	Benzene	100	220	13,000* 5000*	N/A N/A	N/A N/A	[102]
Pt@MWCNTs Pd@MWCNTs MWCNTs	Pt 1.8 at.% Pd 2.1 at.% O plasma treat.	Methanol	11	RT	1.01 1.01 1.01	N/A N/A N/A	N/A N/A N/A	[54]
FeO-MWCNTs MWCNTs	Fe 2 at.% O plasma treat.	Toluene	5.8	RT	1.02 1.07	489 457	N/A N/A	[104]
NiO/MWCNTs NiO	N/A N/A	Ethanol	500	180	3 1.5	27 ¹⁰⁰ N/A	87 ¹⁰⁰ N/A	[105]
ZnO/MWCNTs ZnO	0.1 wt.% CNTs 0 wt.% CNTs	Acetone	320	270	62 7	41 79	90 108	[106]
Ag/PPy PPy	1:10 v.v. N/A	Acetone	5	RT	5 kHz 3 kHz	150 160	230 240	[107]
CdTe/PPy PPy	0.03 at.% Cd N/A	Acetone	5	RT	4 kHz 3.5 kHz	155 165	270 290	[108]
Ti-PTFE	N/A	Acetone	2000	RT	1.03	N/A	N/A	[109]
PEDOT-PSS/GO PEDOT-PSS	GO 0.04 wt.% GO 0 wt.%	Methanol	35	RT	11 1	3.2 N/A	16 N/A	[57]
PANI PANI-CD	N/A N/A	Benzene	150	RT	45.65 NCC% 57.66 NCC%	N/A	N/A	[68]
PANI PANI-CD	N/A N/A	Toluene	46	RT	39.36 NCC% 40.68 NCC%	N/A	N/A	[68]
Ag/SnO ₂ /GO SnO ₂ /GO	N/A N/A	Acetone	150	300	1.26 1.05	2 3	8 50	[110]
GO/ZnO GO/ZnO/GO ZnO	N/A N/A N/A	Acetone	200	450	7 7 12	<14 <12 <13	N/A N/A N/A	[111]
rGO-SnO ₂ SnO ₂	23.7 at.% C, 38.4 at.% Sn, 37.9 at.% O 14.6 at.% C, 45.2 at.% Sn, 40.2 at.% O	Ethanol	100 100	300 300	70 62	11 9	N/A N/A	[112]

MWCNTs: multi-walled carbon nanotubes, PPy: polypyrrole, PTFE: polytetrafluoroethylene, PEDOT: poly(3,4-ethylenedioxythiophene), PSS: poly(styrenesulfonate), PANI: polyaniline, CD: cyclodextrin, GO: graphene oxide, rGO: reduced graphene oxide, v.v.: volumetric ratio, N/A: data not available, * CTL sensors: the response represents the relative CTL intensity, ¹⁰⁰: response and recovery time for 100 ppm, kHz: SAW sensors: frequency shift, NCC%: sensor efficiencies in%, RT: room temperature, c: concentration, T: operating temperature, R: response defined as R_s/R_g, t_R: response time, and t_r: recovery time.

The functionalization of MOXs with secondary MOXs, instead of noble metals, also revealed further advantages. For instance, the sensing properties of WO₃ nanowires decorated with Fe₂O₃ nanoparticles to toluene proved to be comparable to Pt@WO₃ nanowires, indicating that the use of expensive precious metals for MOXs functionalization could be circumvented [48,49]. Other examples of secondary MOXs include CuO, which was employed to improve the sensing properties of ZnO to acetone [75] and SnO₂ to xylene [45]. This type of modified system (i.e., MOX/MOX) also showed advantages in cataluminescence (CTL) gas/vapor sensors. Thus, TiO₂/SnO₂ exhibited better CTL

properties including stable intensity, high signal/noise values, short response, and better sensitivity to benzene and toluene compared to intrinsic SnO₂ [102].

The modification of CbMs and POMs with inorganic materials, mainly MOXs and noble metals for improving their VOCs sensing properties is also frequent in the literature (Table 5). In this context, results on the use of Pt and Pd to decorate MWCNTs are of great interest since these modified materials enabled response to non-aromatic VOCs, in particular methanol [54]. Further studies in the same context showed that the array of oxygen treated MWCNTs and FeO decorated MWCNTs allows for distinguishing the presence of aromatic VOCs such as toluene and benzene in a background of non-aromatic VOCs [104]. Another example of CbMs modification involves NiO/MWCNTs [55]. This composite material exhibited higher response than unmodified NiO nanoparticles to VOCs, especially ethanol. Authors attributed these improvements to the increased surface area and extra interfaces in NiO/MWCNTs, which offer more active sites for the adsorption of VOC molecules and facilitate to get over the energy barriers as well as reducing the operating temperature. CbMs have also been used as modifiers, for instance, low amounts (0.1 wt.%) of MWCNTs on ZnO hollow spheres matrix enhanced dramatically the response of ZnO to VOCs, mainly acetone [106]. These experiments also determine that the content of MWCNTs defines the optimum operating temperature and degree of response enhancement to VOCs, allowing for a modulation of the cross-response among the targeted VOCs.

The reports related to POMs modification also point out improved functionality by their combination with other materials. In this line, a study of nanocomposites in which small amounts of Au [113] or Ag [107] were embedded into PPy showed improvement in the sensing properties of PPy to low ethylene and acetone concentrations, respectively. A similar approach also indicated potential advantages on acetone detection for PPy modified with CdTe quantum dots [108] and polytetrafluoroethylene (PTFE) modified with Ti [109]. The modification of PEDOT with a low amount of GO also proved a higher response for PEDOT to methanol at room temperature. Similarly, CD incorporation in PANI enhances the sensor efficiency of pristine PANI to benzene and toluene detection [68].

Further modifications on gas/vapor sensitive materials include the use of multi-component such as Ag/SnO₂/GO [110] or multilayers of GO/ZnO/GO [111], although their performances were not proven to represent additional advantages with respect to traditional modified materials with two components.

4. Selectivity—In Search of Specificity

Another important consideration in gas/vapor sensitive materials relates to their selectivity. In gas/vapor sensors, the selectivity refers to the ability of the system to identify (discriminate) a particular gas/vapor analyte in a complex mixture, avoiding interfering responses from other analytes, with the ultimate achievement of specificity [114]. However, in practice, a specific response is unrealistic, and thus most of the analysis of gas/vapor sensitive materials deal with selectivity, and usually, straightforward comparative studies of responses to various analytes. Tables 6 and 7 summarize these findings so that the reader can distinguish the degree of cross-response recorded for a given material and group of VOCs in selected reports.

VOCs are numerous, varied, and ubiquitous. The list of these compounds amounts to more than 1000 species [115]. However, only a few of these are recurrent in gas sensing studies (e.g., ethanol, methanol, acetone, benzene, toluene, formaldehyde, or acetaldehyde) probably because of their abundance in the industry and the indoor/outdoor environment, and their significance as biomarkers in disease diagnosis, as summarized in Table 1. Therefore, Tables 6 and 7 display a list of over 30 VOCs, which correspond to the usual compounds analyzed by the gas sensors community. The higher data density for ethanol, methanol, and acetone compared to the other compounds evidences the special attention on such vapors. The tables also include other gases of interest (e.g., ammonia, hydrogen, nitrogen dioxide, carbon monoxide, and hydrogen sulfide) commonly used in the cross-response tests performed in the literature. The bottom and top of the table display the

gas-sensitive materials and the “optimum” operating temperatures for the concentration annotated in each referenced material, respectively. The color codes from blue to red and numbers from 1 to 10 along each column show the tested VOCs and their increasing load of response with an increasing number for each referenced material; note the responses are compared for the same VOCs concentration in each case. The numbers from 1 to 10 are calculated so that the highest gas response (for one specific material) is marked with the number 10, while the responses from other gases are compared to that one. This calculation was repeated for each reference (each column) separately. Thus, for instance, in the first column of Table 6, one can notice that porous ZnO film synthesized by hydrothermal reactions showed the highest responses to methanol (red 10) with a high probability of interference from other VOCs such as 2-chlorophenol (brown 9), acetone (orange 8), and 2-chloroethanol (green 6) and moderate interference from VOCs such as formaldehyde (turquoise 3), and chlorobenzene (blue 1) [36].

It is worth noting that most of the gas-sensitive materials in Tables 6 and 7 rely on the resistive transducing principle (Tables 8 and 9 highlight this in more detail). For those reports using other approaches (e.g., cataluminescence or surface acoustic waves), the discussion includes a specific remark on this aspect. A couple of examples on the cross-response of Au and Ag nanoparticles using localized surface plasmon resonance is also included, due to the potential use of this transducing principle on MOXs, POMs, and CbMs modified with plasmonic nanoparticles. Hereafter, we sum up the VOCs interfering patterns by their functional group classification.

- Simple oxygenated hydrocarbons

Simple oxygenated hydrocarbons are hydrocarbons that contain oxygen as a part of their chemical structure. These compounds involve species such as alcohols (e.g., ethanol, methanol, butanol, to cite a few), and ethers (e.g., diethylether and tetrahydrofuran).

The selectivity to **methanol** is apparently favored by using Pt-decorated WO₃ nanoneedles [48] and localized surface plasmon resonance (LSPR) Au nanoparticles-based sensors [66], which have shown moderate interference to ethanol with promising low cross-responses to acetone, toluene, and isopropanol. Another possible option for high sensitive methanol materials includes ZnO porous films [36], although acetone and 2-chlorophenol may interfere with methanol response. Among organic materials, poly(3,4-ethylenedioxythiophene)-poly(styrenesulfonate) modified with ultralarge graphene oxide (PEDOT-PSS/UL-GO) showed excellent selectivity to methanol in front of vapors such as ethanol, acetone, propanol, toluene, formaldehyde, and water [57]. MWCNTs decorated with Pt or Pd worked successfully for methanol detection too proving low cross-sensitivity to acetone, although with high interference to ethanol [54]. The combination of ZnO hollow spheres with 0.05 wt.% MWCNTs [106] also showed improved selectivity to methanol with moderate interference from ethanol and much lower interference from acetone and ether. Additionally, core-shell hybridized Fe₃O₄ magnetic nanoparticles synthesized in the presence of polymerized ionic liquids and modified with poly(3,4-ethylenedioxythiophene) derived from poly(ionic liquid) (PEDOT-PIL@Fe₃O₄) [116] suggested advantages to discriminate methanol from benzene and toluene, but with high interference from ethanol and acetone.

Generally, the interference patterns in Tables 6 and 7 for oxygenated hydrocarbons such as **ethanol** indicate the best selectivity to this compound with only minor interferences from acetone and toluene by using flower-like hierarchical structures consisting of porous single-crystalline ZnO nanosheets [37], porous Co₃O₄ concave nanocubes [69], or ZnO nanotetrapods [76]. Another alternative for ethanol detection, although with moderate interferences from acetone and low interference from isopropanol and toluene, was achieved by electrochemically synthesized ZnO porous films [38]. SnO₂ obtained by microwave-assisted approach [45] has shown to be a less discriminating material for ethanol in the presence of acetone. However, this material shows the potential to discriminate either ethanol or acetone in the presence of various aromatic compounds (e.g., benzene, toluene, and xylene) and formaldehyde. In contrast, hierarchical flower-like CuO nanostructures [74] have shown high ethanol responses, though with high interferences

to acetone, xylene, and formaldehyde. CbMs such as MWCNTs decorated with Au also showed a good response to ethanol with possible interference from benzene [55]. The addition of MHDA to this composite (i.e., MWCNTs/Au) improved further the selectivity to ethanol, reducing the interference to benzene. This implies that the functionalization with MHDA improves discrimination by boosting sensitivity to non-aromatic VOCs and suppressing the response to aromatic VOCs [55]. The use of composites formed by rGO and SnO₂ also proved to be appropriate to distinguish ethanol among aromatic VOCs, such as benzene, toluene, and xylene with moderate interferences from methanol [112].

The reports in Tables 6 and 7 also show that the detection of **propanol** has been favored by the use of modified materials such as Ag-BC-bsh [117] and Ni/MWCNTs [105]. However, these materials present high cross-responses with other oxygenated hydrocarbons and eventually with ammonia. Further studies suggest the selectivity to **butanol** among ethanol, methanol, acetone, benzene, toluene, and formaldehyde by using mesoporous worm-like SnO₂ films [46]. Similarly, an improved selectivity to **pentanol** with respect to octane and toluene could be achieved by Ag nanoparticles with LSPR, bearing in mind possible high cross-sensitivity to xylene [67].

Improved properties to **ether** were achieved using La₂O₃ and SiO₂/Fe₃O₄ nanoparticles, both indicating very low interferences with tetrahydrofuran, alcohols, acetone, benzene, aldehydes, and halogenated hydrocarbons [53]. Results for **diethylether** also suggested good selective detection of this VOC among acetone, heptane, decane, benzene, toluene, and xylene, with partial selectivity to methanol, hexaldehyde, chlorobenzene, and high interferences to isoprene and ethylacetate.

- Aliphatic hydrocarbons

Aliphatic hydrocarbons are present in several environmental and industrial sectors, with methane as the most representative compound among them. The track of results on aliphatic hydrocarbons using MOXs, POMs, or CbMs is not extensive, most likely influenced by the low sensitivity often reported for semiconducting materials to these compounds. This fact is visible in Tables 6 and 7 that display a low amount of reports, in which aliphatic compounds registered higher responses in respect to other VOCs or toxic gases. Among the few reports, one can see a relatively good selectivity to **isoprene** by using porous single-crystalline ZnO nanoplates decorated with Au NPs [65]. These records suggest low interferences of isoprene with heptane, decane, acetone, formaldehyde, trichloroethylene, and aromatic compounds including benzene, toluene, and xylene, as well as high interferences, particularly to ethylacetate and diethylether. Recently, hierarchical hollow SnO₂ spheres modified with Pt have also shown potential to detect **methane**, although their performances in terms of selectivity to compounds such as ethanol, benzene, formaldehyde, and ammonia appear to be unviable as their cross-responses are reduced only when the methane concentrations are hundreds of ppm (>250) higher than the concentration of the other compounds [118].

Table 8. Summary of MOXs for VOCs sensing, their features and corresponding synthesis method and integration.

Material	Morphology	Features, nm	Method	Integration	Principle	Ref.
ZnO	PF	27 ^{PS}	WCS	Transfer	Resistive	[36]
ZnO	NShs	200–400 ^S 10–60 ^T	WCS	Transfer	Resistive	[39]
ZnO	NRgs	180 ^{OO} 120 ^{IO} 1000–1500 ^L	WCS	Transfer	Resistive	[40]
ZnO	NShs (NFIs)	1000 ^S	WCS	Transfer	Resistive	[37]
ZnO	PF	33.8 ^{CS}	Sputtering	Direct	Resistive	[38]
ZnO	NTPs (NRds)	1000 ^{L-NRds} 9 ^{O-NRds}	PVD	Transfer	Resistive	[76]
Au@ZnO	NPs@NShs	9 ^{O-NPs}	WCS ^{PhA}	Transfer	Resistive	[65]
Pd@ZnO	NPs@NRds	200 ^{O-NRds}	WCS	Direct	QCM	[71]
SnO ₂	PF	6–15 ^{O-Pores}	WCS	Transfer	Resistive	[46]
SnO ₂	PF	150 ^{O-Pores} 20 ^{O-NPs}	WCS ^{MA}	Transfer	Resistive	[45]
SnO ₂	NShs	6.3 ^{CS}	WCS	Transfer	Resistive	[47]
Ce-doped SnO ₂	PF	10.3 ^{CS-SnO2}	WCS	Transfer	Resistive	[73]
WO ₃	NNs	100 ^T 10,000 ^L	CVD	Direct	Resistive	[48]
Au@WO ₃	NPs@NNs	100 ^T 10,000 ^L 3–10 ^{S-NPs}	CVD	Direct	Resistive	[48]
Pt@WO ₃	NPs@NNs	100 ^T 10,000 ^L 1–5 ^{S-NPs}	CVD	Direct	Resistive	[48]
Fe ₂ O ₃ @WO ₃	NPs@NNs	5–100 ^{O-NNs} 10,000 ^{L-NNs} 4–15 ^{O-NPs}	CVD	Direct	Resistive	[49]
TiO ₂	NShs (NFIs)	120 ^L 12–23 ^T	WCS	Direct	Resistive	[51]
Pd@TiO ₂	NPs@NRds	20 ^{O-NPs} 100 ^{O-NRs} 4500 ^{L-NRs}	CVD + WCS	Direct	Resistive	[52]
In ₂ O ₃	NShs-hMSP (NFIs)	20 ^T	WCS	Transfer	Resistive	[50]
CuO	NShs (NFIs)	2000 ^S 50 ^T	WCS	Transfer	Resistive	[74]
Co ₃ O ₄	cNCs	200 ^S	WCS	Transfer	Resistive	[69]
Co ₃ O ₄	ML	17.6 ^{CS}	WCS	Transfer	Resistive	[72]
SiO ₂	NPs	-	-	Transfer	CTL	[53]
CeO ₂	NPs	-	-	Transfer	CTL	[53]
Y ₂ O ₃	NPs	-	-	Transfer	CTL	[53]
La ₂ O ₃	NPs	-	-	Transfer	CTL	[53]
Au@La ₂ O ₃	NPs@NRds	-	WCS	Transfer	CTL	[119]
TiO ₂ -SnO ₂	PF	-	WCS	Transfer	CTL	[102]
CuO/SnO ₂	PF	150 ^{O-Pores} 20 ^{O-NPs}	WCS ^{MA}	Transfer	Resistive	[45]
ZnO-CuO	NShs	20–25 ^T	PVD	Direct	Resistive	[75]
SiO ₂ /Fe ₃ O ₄	NPs	-	-	Transfer	CTL	[53]
ZnCo ₂ O ₄	HSP	72 ^O	WCS	Transfer	Resistive	[70]
Au	NPs	36 ^O	WCS	Transfer	LSPR	[66]
Ag	NPs	51 ^O	WCS	Transfer	LSPR	[67]

PF: porous film, NShs: nanosheets, NRgs: nanorings, NTPs: nanotetrapods, NFIs: nanoflowers, NPs: nanoparticles, NRds: nanorods, NNs: nanoneedles, hMSP: hierarchical microsphere, cNCs: concave nanocubes, ML: monolayer, HSPs: hollow spheres, PS: pore size, ^S: size, ^T: thickness, ^O: diameter, ^{OO}: outer diameter, ^{IO}: inner diameter, ^L: length, ^{CS}: crystal size, WCS: wet chemical synthesis, PhA: photo-assisted, MA: microwave assisted, CVD: chemical vapor deposition, PVD: physical vapor deposition, QCM: quartz crystal microbalance, CTL: cataluminescence, LSPR: localized surface plasmon resonance.

Table 9. Summary of POMs and CbMs for VOCs sensing, their features and corresponding synthesis method and integration.

Material	Morphology	Features, nm	Method	Integration	Principle	Ref
Pt@MWCNTs	NPs/MWCNTs	2 \emptyset /Up to 50,000 ^L	CVD	Transfer	Resistive	[54]
Pd@MWCNTs	NPs/MWCNTs	3 \emptyset /Up to 50,000 ^L	CVD	Transfer	Resistive	[54]
PEDOT-PIL@Fe ₃ O ₄	CSh (Ls ^{PEDOT} -MNP _s ^{PIL@Fe₃O₄})	15 S-NPs	WCS	Transfer	Resistive	[116]
ZnO/MWCNTs	HSps ^{ZnO} -MWCNTs	300–350 \emptyset -HSps 30–40 ^L HSps	WCS	Transfer	Resistive	[106]
DT-capped Au	MLShs ^{DT} _{NPs} ^{Au}	100–300 ^{FT} 2–5 \emptyset -NPs	WCS	Transfer	Resistive	[122]
MOF-ZnO	NCgs	100 S-NPs 60 CO ²⁵ PST	WCS	Transfer	Resistive	[121]
SWCNTs/CdA	SWCNTs	1–5 \emptyset 1000–10,000 ^L	WCS	Transfer	QCM	[123]
SWCNTs-calixarene	SWCNTs	-	WCS	Transfer	Resistive	[120]
PANI-CD	NPs	100	WCS	Transfer	Resistive	[68]
Ti-PTFE	Cls	10–30 ^{NPs}	PVD	Transfer	Resistive	[109]
Ag-BC-bsh	NPs ^{Ag} NPP	10 \pm 7 \emptyset -NPs 45 \pm 10 ^{FO} >10,000 ^{L-NPP}	WCS	Transfer	LSPR	[117]
Au-DDDT	NPs ^{Au} Ls	4 \emptyset -NPs/Up to 60 ^{T-Ls}	LBL-SA	Transfer	Resistive	[124]
PEDOT-PSS/UL-GO	NShs ^{UL-GO} PF	10,000–300,000 ^{S-UL-GO}	PVD	Transfer	Resistive	[57]
Ag/SnO ₂ /GO	NPs ^{Ag}	-	WCS	Transfer	Resistive	[110]
GO/ZnO	NRds ^{ZnO} NShs ^{GO}	640 ^{L-ZnO}	WCS	Transfer	Resistive	[111]
GO/ZnO/GO	NRds ^{ZnO} NShs ^{GO}	640 ^{L-ZnO}	WCS	Transfer	Resistive	[111]
MWCNTs/Au	MCWNTs- NPs ^{Au}	Up to 50,000 ^{L-MWCNTs} 3–15 ^{OO-MWCNTs} 3–7 ^{IO-MWCNTs} 2 \emptyset -Au	CVD/WCS	Transfer	Resistive	[55]
MWCNTs/Au/ MHDA	MCWNTs- NPs ^{Au} -ML ^{MHDA}	Up to 50,000 ^{L-MWCNTs} 3–15 ^{OO-MWCNTs} 3–7 ^{IO-MWCNTs} 2 \emptyset -Au	CVD/WCS	Transfer	Resistive	[55]
NiO/MWCNTs	NPs/MWCNTs	25 \emptyset -NPs 20–35 \emptyset -MWCNT	WCS	Transfer	Resistive	[105]
O ₂ /MWCNTs	MWCNTs	50,000 ^{L-MWCNTs} 3–15 ^{OO-MWCNTs} 3–7 ^{IO-MWCNTs}	CVD	Transfer	Resistive	[104]
FeO/MWCNTs	MWCNTs	50,000 ^{L-MWCNTs} 3–15 ^{OO-MWCNTs} 3–7 ^{IO-MWCNTs}	CVD	Transfer	Resistive	[104]
PPy/rGO	NPs ^{PPy} /NShs ^{rGO}	80 \emptyset -NPs	WCS	Transfer	Resistive	[58]
rGO/SnO ₂	NShs ^{rGO} /NPs ^{SnO2}	6–10 \emptyset -NPs	WCS	Transfer	Resistive	[112]
Ag/PPy	NPs	17 \pm 3 ^{S-Au-NPs} 44 \pm 10 ^{S-PPy-NPs}	WCS	Transfer	SAW	[107]
CdTe/PPy	QDs ^{CdTe} /NPs ^{PPy}	3.1 \pm 0.7 ^{S-QDs} 35–55 ^{S-NPs}	WCS	Transfer	SAW	[108]

MWCNTs: multi-walled carbon nanotubes, PEDOT: Poly(3,4-ethylenedioxythiophene), PIL: polymerized ionic liquid, DT: decanethiol, MOF: metal-organic frameworks, SWCNTs: single-walled carbon nanotubes, CdA: cadmium arachidate, PANI: polyaniline, CD: cyclodextrin, PTFE: polytetrafluoroethylene, Ag-BC: Ag nanoparticles embedded in bacterial cellulose nanopaper, bsh: blue shift, DDDT: 1,12-dodecanedithiol, PSS: poly(styrenesulfonate), UL-GO: ultra-large graphene oxide, GO: graphene oxide, MHDA: 16-mercaptohexadecanoic acid, PPy: polypyrrole, rGO: reduced graphene oxide, NPs: nanoparticles, CSh: core shell, Ls: layers MNPs: magnetic nanoparticles, HSps: hollow spheres, MLShs: monolayer shells, NCgs: hierarchical hollow nanocages, Cls: clusters, NPP: nanopaper, NShs: nanosheets, PF: porous film, NRds: nanorods, ML: monolayer, \emptyset : diameter, ^L: length, ^S: size, ^T: thickness, ^{FT}: film thickness, ^{CO}: cavity diameter, ^{PST}: porous shell thickness, ^{FO}: fiber diameter, ^{OO}: outer diameter, ^{IO}: inner diameter, QDs: quantum dots, CVD: chemical vapor deposition, WCS: wet chemical synthesis, LBL-SA: layer-by-layer self-assembly, PVD: physical vapor deposition, QCM: quartz crystal microbalance, SAW: surface acoustic wave.

- Aromatic hydrocarbons

Aromatic hydrocarbons are generally associated with compounds containing the benzene ring. These compounds exhibit aromaticity, most of them characterized by sweet or pleasant odor. The reports on sensitive materials for aromatic hydrocarbons are not as extensive as those for oxygenated hydrocarbons. In fact, a search of the literature in terms of their selectivity indicates frequently poor load of response for these compounds among oxygenated hydrocarbons, as well as esters, ethers, and aldehydes.

According to Tables 6 and 7, the strongest selectivity to **benzene**, in front of various alcohols, and other aromatic compounds such as toluene and xylene, were recorded for modified La_2O_3 nanorods with Au nanoparticles [119] and coral-like $\text{TiO}_2/\text{SnO}_2$ porous film [102] implemented using CTL concept. Partial selectivity to benzene was also noticed for MWCNTs decorated with Au nanoparticles [55], especially in comparison to acetone. Materials based on modified $\text{Fe}_2\text{O}_3/\text{WO}_{3-x}$ nanoneedles [49] and porous flower-like SnO_2 nanosheets [47] also appear to be a good option to attain partial selectivity to **toluene** among ethanol, methanol, and acetone. However, the cross-response to benzene and formaldehyde could still be an issue. As for **xylene**, the selectivity to this compound among acetone, methanol, isopropanol, and chloroform seems to be greatly improved for Pd-functionalized ZnO nanorods [71] integrated into quartz crystal microbalance (QCM). Results for CuO/SnO_2 , in contrast, show higher interferences for xylene in front of alcohols and other aromatic compounds, though the interferences could be reduced towards formaldehyde and ammonia. In the same gas family, a strong selectivity to xylene among ethanol, benzene, formaldehyde, and carbon monoxide has been reported using monolayers of periodic porous Co_3O_4 inverse opal thin films [72]. Although calixarene functionalized SWCNTs has shown good potential for xylene detection, high interferences from toluene and ethylbenzene are noticed [120].

- Carbonyl compounds

Carbonyl compounds can be also classified as oxygenated hydrocarbons, since they contain oxygen atoms in their structure, but unlike simple oxygenated hydrocarbons, carbonyl compounds come from carboxylic acids. This group includes ketones, aldehydes, carboxylic acids, acid anhydrides, esters, amides, and acid halides.

As far as **acetone** detection is concerned, the reports indicate a strong selectivity to this compound among methanol, butanone, isopropanol, and toluene for hierarchical 3D TiO_2 nanoflowers operating at low temperature (60 °C) [51]. Other materials, based on unmodified or Au-modified WO_3 nanoneedles [48], also point toward good selectivity to acetone among ethanol, methanol, and toluene, contrary to Ce-doped SnO_2 , which revealed higher interferences for acetone among methanol, ethanol, and formaldehyde [73]. The use of a mixture based on ZnO-CuO has also shown the potential to discriminate acetone among ethanol and typical toxic gases including ammonia, nitrogen dioxide, and hydrogen sulfide [75]. In_2O_3 [50] and Y_2O_3 (with CTL-based signal) [53] present themselves as other unmodified MOXs with prospective partial selectivity to acetone, the first suggesting good or moderate discrimination from methane, formaldehyde, and chloroform, whereas the second showing good discrimination from various alcohols, aldehydes, and aromatic compounds. ZnO/MWCNTs hybrid material with MWCNTs content of 0.1 wt.% also showed to be selective to acetone among ethanol, methanol, and ether [106]. Other materials such as metal-organic frameworks derived hierarchical hollow ZnO nanocages (MOF-ZnO) displayed good acetone discrimination among ethanol, benzene, toluene, and ethylacetate [121]. In the same line, $\text{Ag}/\text{SnO}_2/\text{GO}$ ternary nanocomposites proved relevant for acetone detection among furan, formaldehyde, chlorobenzene, and ammonia [110], while other graphene-based materials such as $\text{GO}/\text{ZnO}/\text{GO}$ showed moderate interferences to ethanol but good selectivity among methanol and benzene [111].

One of the best selectivities to **formaldehyde** among several gases (ammonia, nitrogen dioxide, and carbon monoxide) and vapors (benzene, acetone, and methanol) all at ppb level has been identified for nonstoichiometric Co-rich ZnCo_2O_4 hollow nanospheres [70]. Other candidates to achieve partial selectivity to formaldehyde suggesting potential low

interferences to butanol, methanol, acetone, and ammonia involve nanosheets of SnO₂ prepared by heat treating Cu₃SnS₄ nanostructures [47]. NiO/MWCNTs [105] have also shown good sensitivity to formaldehyde, although the selectivity among other tested gasses, including methanol, ethanol, propanol, and acetone, was poor.

The literature also shows good responses at sub-ppm concentrations for **acetaldehyde** by employing ZnO nanostructures [39,40], however, their performance in terms of selectivity in respect to formaldehyde have proved to be poor. The information in Table 6 for ethylacetate shows excellent results for CTL sensors based on SiO₂ and CeO₂ nanoparticles [53] with moderate interference to acetone in the case of CeO₂ and low interference to ether, tetrahydrofuran, ethanol, methanol, aldehydes (e.g., formaldehyde and acetaldehyde), and halogenated hydrocarbons (e.g., chlorobenzene and chloroform).

Humidity Effects—The Uninvited Guest

The relative humidity (RH) in the atmosphere is one of the most common interfering species that has a great impact on the sensing properties of the material and its operation in a “real” environment. This is due to water molecules being sorbed at the surface (e.g., in MOXs) or in the bulk (e.g., in POMs) and abruptly changing the properties (e.g., electrical or mechanical) of the gas sensitive material. In MOXs, for instance, the adsorption of water at temperatures below 150 °C is attributed to physisorption or hydrogen bonding. However, at high temperatures (150–500 °C) the literature proposes various possible mechanisms behind the surface conductivity changes in the presence of water vapor [1]. One of these mechanisms, for instance, suggests that the OH[−] side of water molecule can react with the Lewis acid sites (metal cation (M_{metal}^+)) forming $M_{metal}^+ - OH^-$, while the dissociated hydrogen from water can react with the lattice oxygen from the Lewis base or with oxygen adsorbed on surface. This mechanism involves the release of electrons (e^-). As a result, the changes of conductivity (e.g., in resistive type sensors) or mass (e.g., in QCM type sensors) produced by the target analytes are hindered and the whole performance of the sensor is affected [71]. The possibility for hydrogen bonding interactions with water molecules at room temperature is also presented in the case of POMs, due to the polar groups on their backbone (e.g., $N^{\delta-} - H^{\delta+}$ in PPy and PANI). This can further result in sorption of the water molecules within the POM, which fill the free volume fraction in the polymer (e.g., swelling) and reduce the gas permeability [108]. The adsorption and permeation of water molecules within the CbMs such as graphene oxide also respond to the hydrogen bonding between water and hydrophilic groups on graphene oxide (e.g., hydroxyl groups), which can cause direct interference with gas sensing [125].

Usually, not all the reports in the literature related to VOCs sensitive materials analyze the effects of humidity ambient on the sensing performance. In fact, only a few reports of those summarized in Tables 5 and 6 show humidity interference tests. From these results, specifically, the analysis of Co-rich ZnCo₂O₄ hollow spheres in 80% RH ambient shows that the response of this material to 100 ppb of formaldehyde is relatively stable with a loss of response of only 28% compared to the response registered in dry ambient [70]. Similar studies for ZnO modified with low (5%) amounts of Au to various VOCs (isoprene, ethylacetate, heptane, chlorobenzene, benzene, and formaldehyde) reported minor fluctuations of the response for RH below 35% [65]. The effect of humidity on the sensing performance of hierarchical 3D TiO₂ nanoflowers to acetone was also tested. These studies showed that the response to acetone in 75% RH deviates only $\pm 4.5\%$ from that in dry air [51].

Tests of unmodified SnO₂ and rGO modified SnO₂ to ethanol in a humid atmosphere (from 24 to 98% RH) registered a loss of response for both materials, although the losses were superior for SnO₂ than for rGO-SnO₂ [112]. Evaluation of FeO-MWCNTs and oxygen-treated MWCNTs in moisture also revealed a decrement of the response for both materials. This drop of response turned out to be larger when the humidity changed from 0 to 20% RH than when the humidity increased further from 20 to 50 or 80% RH. Moreover, the loss of response to the step changes of moisture proved to be greater for the oxygen treated MWCNTs than for the FeO-MWCNTs based sensors [104].

In the literature, one can also find different strategies to avoid the high impact of humidity in VOCs sensitive materials. The most common solutions encompass the use of external components in the sensor device as filters or dehydration elements [126]. Other strategies to reduce the impact of humidity typically include the incorporation of intentional humidity-insensitive additives (surface decoration), such as NiO [127,128], CuO [129,130], or SiO₂ [131]. Previously, it has also been proven that the application of high-humidity (90% RH) aging treatment in MOXs such as WO₃ [132] and SnO₂ (the last loaded with Pd and Au) [133] significantly reduces the humidity effects at the surface while sensing toluene or a specific group of total VOCs in a range of 25 and 75% RH. Similar treatment was performed for Pt-loaded SnO₂ films, although the humidity interference towards total VOCs for this system was found ineffective [133].

Recent studies also indicate the possibility to attenuate the humidity interference in MOXs, such as ZnO, by tuning their morphology, structural, and surface properties to increase the hydrophobicity of the surface not only at the structural level but also at the chemical level [134]. These findings are linked with those reported on oxygen treated MWCNTs, as the hydrophilic MWCNTs surface stimulated by oxygen plasma treatment made the MWCNT more sensitive to humidity compared to non-oxygen treated FeO-MWCNTs [104]. Similarly, the tests of MWCNTs/Au and MWCNTs/Au/MHDA in a humid ambient suggested that the hydrophilic nature of the carboxyl terminal from the MHDA molecules grafted to the MWCNTs/Au binds the water molecule keeping it far away from the MWCNTs, thus, providing more resilience to the MWCNTs to humidity as compared to the unmodified MWCNT [55].

5. Enabling the Material Properties for Their Practical Use

5.1. Transducing Platforms—On the Capture of the Sensor Response

The sections above focused on the materials with the ability to sense VOCs and their main sensing properties. In practice, however, the enabling of these materials for their use in advanced applications demands their coupling with appropriate transducing platforms, which allow measuring the electrical or optical changes induced by the physicochemical phenomena experienced in the material during the gas-solid interactions. These platforms can be based on different working principles: mass-sensitive (e.g., resonating cantilevers), thermal (e.g., pellistors, thermoelectric, or Seebeck-effect-based sensors), optical (e.g., phosphorescence/fluorescence or chemiluminescence sensors), or electrochemical (e.g., conductometric and potentiometric sensors) [135]. Figure 5 displays examples of transducing platforms for measuring resistive and mass-load changes. Electrochemical-based transducing platforms are the most common approach in the literature and commercial field, probably due to their relatively simple fabrication process and characterization. Within this group, chemoresistive sensors are generally the most representative and this fact is reflected in Tables 8 and 9, in which most of the accounted materials for VOCs report the operation under the resistive principle. One can see in these tables that VOCs sensitive materials are also enabled by monitoring optical parameters such as CTL [53,102,119] or LSPR [66,67], and mass-load changes mainly using QCM [71], although with less frequency. From this, it is concluded that the properties of VOCs sensitive materials can be exploited using various physical changes so the systems are not limited to only resistive changes. Enabling the signal capture of the different physical changes, separately or in conjunction, would allow for VOCs sensing systems with better selectivity.

Back in the past, most of the technology for gas sensing transducing platforms relied on thick film technology, particularly using silica or alumina substrates. Currently, however, the transducing platforms exploit micro/nano fabrication technologies (usually based on silicon as substrate), which makes it possible for their incorporation into integrated circuits (IC) at micro/nano scale in a single chip [135,136]. During the past decades, various types of gas/vapor sensors (resistive, thermal, mass-sensitive, optical) have been reported in the literature using standard micro-electro-mechanical systems (MEMS) technology. This technology for instance has been shown to facilitate the formation of thermally well-

isolated structures for more efficient conductometric and Seebeck-effect based sensors or the formation of miniaturized cantilevers for mass-sensitive based sensing. Recently, miniaturized light platforms for the photoactivation instead of thermoactivation of gas sensitive material have also been developed [137].

Another significant advantage of using micro/nano fabrication technologies is the possibility to integrate several different transducers on a single chip along with the driving and signal conditioning circuitry or other smart features (e.g., wireless communication) to build electronic noses with potentially low cost via mass production [135]. A good approximation of this concept, in which various transducing principles were implemented monolithically in a microsystem to operate simultaneously, was developed previously using micro/nano fabrication technology [138]. Recently, other emerging technologies based on flexible substrate materials such as polymers, textiles, and paper are positioning well in electronics and thus in sensing systems (including VOCs sensors) [139,140]. These novel technologies can introduce biocompatibility, reusability, and/or biodegradability to consumer electronics, alleviating environmental issues and reducing significantly the costs associated with recycling operations.

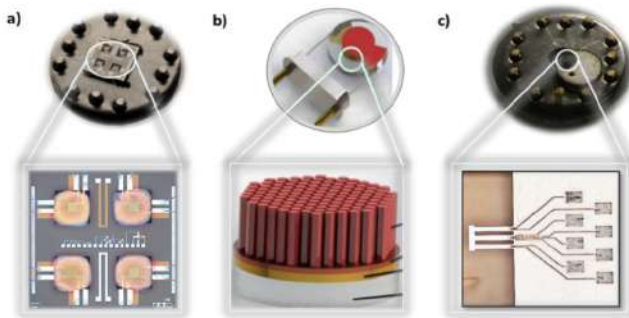


Figure 5. Schematic illustration of transducing platforms: (a) micromachined resistive, (b) quartz crystal microbalance, and (c) micromachined cantilever. Adapted from [71,141], with permission from Elsevier B.V., 2018 and 2015, respectively.

Therefore, micro/nano technologies have the potential to contribute and enable improving further the properties of materials for different applications. VOCs monitoring systems built by micro/nano technologies may have an impact in various fields and cover the current demands of traditional markets focused on the industry and environmental control, as well as emerging niches dedicated to the food industry, agriculture, and medicine. Most of these fields are keen to implement solutions in line with the digital future and the smart anything everywhere (SAE) concept, in which VOCs sensors could be the next family of sensors for smart portable devices. Hence, there is a need to go further in the effective integration and synthesis of sensitive materials into miniaturized systems with low power consumption and reduced fabrication costs at a large-scale.

5.2. Synthesis of Materials—Path to the On-Chip Integration

The integration of transducing platforms and material synthesis methods is an essential phase for VOC sensors' scalability and large production. Such integration can mostly be achieved by direct or transfer methods [140,142]. The first (direct method) involves the selective deposition of the material over the transducing platform. Direct methods can reduce the processing time and steps of the whole sensor assembling process, particularly when using bottom-up approaches (i.e., synthesis of materials through assembling of atoms derived from chemical precursors) rather than top-down approaches (i.e., based on carving, slicing, or etching a macroscale material source). The second (transfer method) relies on

the use of pre-synthesized materials and their dry or wet transfer (re-deposition) over the transducing platform. Transfer methods can facilitate a broad choice of materials and modifications and can be especially useful when integrating aligned single 1D structures into a transducing platform, although one must be aware of the surface contamination issues which entail most of the transfer procedures [142]. Dielectrophoresis [143] and contact printing using polydimethylsiloxane (PDMS) [144] are two examples of the wet and dry transfer approach, respectively.

Transfer methods are by far the most used approaches in the literature for integrating the materials into the transducing platforms. Tables 8 and 9 evidence this fact, indicating a preference for developing VOCs sensitive materials by wet chemical synthesis (WCS) and their subsequent transfer (or re-deposit) over the transducing platforms. The preferred WCS methods for VOCs sensitive MOXs, POMs, or CbMS include sonochemical process [39,40], hydrothermal process [36,46,47,50–52,73,102], one-pot wet-chemical method [37], photodeposition [63], sol-gel method [74], microwave-assisted approach [45,112,116], precipitation [69,70,105,122], calcination of precursors [119], seed mediated growth method [66], pyrolysis [121], spray deposition [116], Langmuir–Blodgett method [123], chemical bath deposition [111], electrochemical methods, and chemical oxidation polymerization [58]. The transfer methods are generally based on the formation of pastes or suspended solutions using common solvents (e.g., ethanol, terpineol) for their subsequent printing or drop coating. Previously, it was found that the synthesis and the post-treatment process of materials (e.g., MWCNTs) can also facilitate the transfer procedures by improving the solubility or dispersion of materials [104].

The reports centered on WCS synthesis concentrate regularly on tuning conditions and finding their correlation with the material functionality towards common VOCs. An example of the synthesis of ZnO shows that different salts (e.g., zinc acetate, zinc chloride, or zinc sulfate) in hydrothermal synthesis influence the morphologies and microstructural features of the porous ZnO products. Measurements on the gas sensing properties of the porous products to VOCs (e.g., acetone, chlorophenol, and formaldehyde) revealed improved sensing characteristics for porous ZnO synthesized using zinc sulfate compared to those obtained using zinc chloride and zinc acetate. A similar example on the synthesis of SnO₂ shows that the use of a starch template for the hydrothermal synthesis of worm-like nanostructured SnO₂ and the variation of starch content has a great impact on the microstructure of the final product. The gas-sensing tests of this study exhibited better sensing properties towards butanol for the material processed with higher content (2 g) of starch [46]. In the same way, the sensor fabricated with 0.05 wt.% of MWCNTs showed to be selective to ethanol and methanol while the sensor with 0.1 wt.% of MWCNTs demonstrated selectivity to acetone and ether among the other tested VOCs [106]. These examples and other similar ones in the literature often attribute the improvements to the differences in morphology and/or surface area [36]. The effect of the impurity levels derived from the synthesis and transfer-processing steps are generally less discussed, despite there being evidence that residual ions (e.g., chlorine, sulfur, alkali and alkaline earth metals) account for the widespread of physical and chemical properties of similar oxide materials [145].

Direct methods for integrating VOCs sensitive materials into transducing platforms are a minority in Tables 8 and 9. Among the representative techniques for direct integration are sputtering [38], chemical vapor deposition (CVD) [48,49], and hydrothermal [51] and electrochemical deposition [71]. These techniques allow for the selective integration of films and structures by implementing masks or patterns on desired locations. Even though these techniques are not exempt from introducing residual impurities during material processing, the in-situ integration approach with no further manipulation or extra steps diminishes considerably the contamination of the material surface. An example of a direct method using CVD shows that the integration of one-dimensional WO₃ structures modified with Au or Pt either over MEMS- or polymer-based transducing platforms is feasible in a single step. These structures reported enhanced sensing properties to acetone or methanol as a function of the surface modification with Au or Pt, respectively. Another example of the

use of the direct method shows the integration by electrodeposition of ZnO rods modified with Pd over QCM-based transducing platforms [71]. As for the previous example, this report also emphasized the improvement of sensing properties to ethanol and xylene by modifying the ZnO structures with Pd. Overall, the literature search suggests that there is still a lot of room for investigating synthesis methods for direct integrations of tuned VOCs sensitive materials.

5.3. Machine-Learning—Mimicking the Human Olfactory Systems

Another essential phase in the practical use of gas/vapor sensitive nanomaterials and systems is their coupling with appropriate machine learning algorithms. The ensemble of these elements, i.e., hardware and software, is usually known as electronic nose (e-nose) technology, in reference to their approximation to reproduce the human olfactory system [146,147]. In e-noses, the selection of suitable materials and transducers for the sensor array is accompanied by the selection of proper machine-learning algorithms to comprehend the large amount of data delivered by the sensor array and identify/classify the information with the aim to make the system more selective and precise for practical implementations. Figure 6 displays a summarized representation of the main constituents of an e-nose system. The figure shows the hardware stage (i.e., materials, transducers, and sensor arrays) and the machine-learning stage, which involves the data collection, modeling, training, and evaluation steps. So far, this review has focused on the hardware stage, and in particular on VOC sensitive materials, whereas this section aims to provide the reader with a complementary overview of the basic attributes of e-noses and their application. As the scope of this topic is vast, the section is not intended to be exhaustive and for deeper insight into e-noses, their principles, and application, we invite the reader to revise recent reviews, for instance, [148–152].

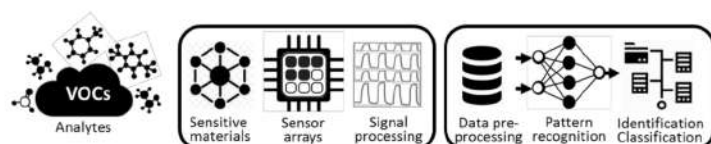


Figure 6. Block representation of the main constituents of an e-nose system. The hardware block includes the sensitive materials, transducers, integrated sensor arrays, and signal processing elements. The software or machine learning block includes the data collection and preprocessing, featuring extraction, pattern recognition, and classification algorithms.

Amongst a host of machine-learning algorithms, those based generically on pattern recognition methods, i.e., algorithms that recognize (ir)regularities or specific patterns in the data to subsequently classify them by means of training models, are frequent in e-nose applications. In this context, methods such as principal component analysis (PCA), discriminant analysis (linear—LDA, function—DFA, stepwise—SDA), regressions (partial least squares—PLSR, generalized least squares—GLSR, multiple linear—MLR), support vector machines (SVMs), and artificial neural networks (ANN) are the most sounded data analysis methods [148].

Typical e-nose applications, in which VOC analytes are potentially involved, include the discrimination of samples (not necessarily specific analytes) by finding differences in the patterns to identify, for instance, the meat origin [153], rice aging [154], beverage brands [155], coffee beans [156], or controlled populations of healthy and unhealthy subjects [157–159]. However, there are also other studies, which target the discrimination of more specific analytes and their concentrations. Table 10 summarizes a few examples in this context with focus on e-noses with (nano)materials-based sensor arrays. In terms of algorithmic tools, the works make references especially to PCA, LDA, and ANN methods [160–164]. Whilst PCA and LDA methods are useful tools for reducing the dimensionality of measurement space and extracting the information for pattern recognition,

ANN methods are usually employed for classification tasks, although ANN can also be trained to learn sample patterns and predict responses for unidentified samples. The use of deep learning tools with basis on ANN methods to automatically detect and classify information in raw datasets (without pre-processing) are also relatively new alternatives in e-noses [148,155]. As noticed in Table 10, the sensor elements used in e-noses seems to be characterized specially for the use of resistive sensors based on MOXs. The justification for this is frequently supported by the broad gas/vapor sensitivity of these components, their low cost, and the need of simple drive circuits, amongst other characteristics such as fast and stable responses and long life [146,157,161,165,166].

Table 10. A few literature examples of the application of e-noses in the area of air, water, and food quality, health care, and medicine. The table shows the number of sensors in the array, the targeted analytes, and data processing algorithms employed in each report.

Area	Objective	Sensor Elements	Number	Analytes	Algorithms	Ref.
Air quality and security	Indoor identification of low formaldehyde concentrations	Commercial MOX-Resistive	5	Formaldehyde	BP-ANN	[167]
	Identification of binary mixture: DMMP (ppb level) and methanol (sub ppm level)	Experimental MOX-Resistive MOX-SAW	4	DMMP, Methanol	PCA, ANN	[160]
	Detection of mixed indoor hazardous gases	Commercial MOX-Resistive	6	Methane, Formaldehyde, CO, Hydrogen	PCA, LDA, BP-ANN	[161]
Water quality	Discrimination polluted from clean water	Commercial MOX-Resistive	6	Propanol, Phenol, TFB, Benzene	PCA, HCA, SVM	[165]
	Identification of pollutants in water	Commercial MOX-Resistive	8	Ethanol, Acetone, Toluene, Ammonia, Ethylacetate	PCA, ANN, RBF-ANN, BP-ANN	[162]
	Identification of pollutants in water	Commercial MOX-Resistive	N/A	Chloroform Ammonia	PCA, LDA	[166]
Food quality	Off-flavors detection in alcoholic beverage (wine, beer)	N/A MOX-Resistive	18	Ethylacetate, TCA, 4-EP, Hexanol, Octenol, Diacetyl, BD	PCA, DFA	[168]
	Rice quality assessment—early detection of fungal infection	Commercial MOX-Resistive	12	Cotane, 2-pentylfuran, Dodecane, Toluene, Decane, Ethanol	PCA, LDA, SVM, PLS	[169]
	Fruit ripeness classification	Commercial MOX-Resistive *	7	Alkanes, Alcohols, Esters	PCA, LDA	[163]
Healthcare/medicine	Discrimination of pathogenic bacterial VOCs	Commercial MOX-Resistive Experimental OINCs-Resistive	6	Acetone, Formaldehyde, Ammonia, Ethanol, Ethylacetate, Acetic acid	PCA, CA	[170]
	Lung cancer and renal failure diagnosis	Experimental CbMs-Resistive	8	Acetone, Isoprene, Ammonia, Hydrothion	PCA, LDA	[164]
	Lung cancer diagnosis	Experimental MOX-Resistive	4	Formaldehyde	MVLR	[171]

* The classification of fruit ripeness is assisted by a digital camera system, OINCs: organic-inorganic nanocomposites, N/A: data not available, DMMP: dimethyl methylphosphonate, TFB: 1,3,5-trifluorobenzene, TCA: 2,4,6-trichloroanisole, EP: ethylphenol, BD: 2,3-butanedione, BP: back-propagation, ANN: artificial neural network, PCA: principal component analysis, LDA: linear discriminant analysis, HCA: hierarchical cluster analysis, SVM: support vector machine, RBF: radial basis function, DFA: discriminant factor analysis, PLS: partial least squares, CA: cluster analysis, MVLR: multivariate linear regression.

Certainly, the application of machine learning for artificial olfactory systems has demonstrated further solving the selectivity issues of (nano)material-based gas/vapor sensors. In fact, the reports on e-noses show that partial selective commercial sensors can provide sufficient data to discriminate and classify samples [161–163,165–167,169]. However, despite e-noses technology apparently being resolved by the existing sensors, there is still a continuous demand in the field for more miniaturized sensor components with broader gas/vapor sensitivity, lower detection limits (at ppb-ppt level), low power consumption, low cost, and operation without consumables; features which are still not fully available in current commercial sensors [172]. These new characteristics would allow for even more generalized use of e-noses in the fields in which they have already shown their potential. Hence, new developments in materials and system integration as the primary components of the value chain are still timely to pave the way towards advanced artificial olfactory systems.

6. Outlook and Conclusions

Nanomaterials based on metal oxides, conductive polymers, and carbon-based materials are representative in VOCs sensing. Their optimization and enhanced properties generally involve the control of morphology, size, and composition. The most successful systems include structured morphologies, particularly hierarchical structures at the nanometric scale with intentionally introduced tunable “decorative impurities” or well-defined interfaces forming bilayer structures. These groups of modified or functionalized structures, in which metal oxides are still the main protagonists either as host or guest elements, have proved improvements in VOCs sensing. Whilst the main improvements usually include better and faster responses, lower operating temperatures, or better stability, the advances in terms of selectivity are still blurred. First, because most reports in the literature concentrate on studying a reduced number of VOCs, among them especially simple oxygenated hydrocarbons, and second because the selectivity is evaluated by the response comparison of single analytes often with incomparable concentrations among them. Overall, the literature survey points out the need for investigating more in depth the material functionality to larger groups of VOCs as well as the convenience of probing other transducing principles rather than resistive for nanomaterial-based sensors. In terms of materials, the needs are directed overall to explore new hybrid material combinations that involve the formation of nanoscale interfaces between (i) inorganic and organic semiconductors (e.g., MOXs and POMs), (ii) inorganic and carbon-based materials (MOXs and graphene), and (iii) organic and carbon-based materials (e.g., POMs and graphene) to exploit the synergistic effects of these combinations. It is worth mentioning the availability of a broad group of emerging materials with less tradition in gas sensing, but with promising results to operate alone or in combination with traditional gas-sensitive materials. Within this group, the exploration of (i) perovskite and spinel oxides with multication variations; (ii) transition metal dichalcogenides (TMDs) and transition metal carbides/nitrides (MXenes); and (iii) nitrides, and phosphorene, silicene, or germanene are attractive. For both groups (i.e., traditional and emerging gas-sensitive materials), the new research efforts need to be invested in (i) controlling the load of constituents and their correlation with the VOC sensing patterns (information rarely found in the reports), (ii) finding dedicated materials for detecting compounds from the group of aliphatic hydrocarbons and carbonyl compounds, (iii) exploring the possible multifunctional properties in the material for exploiting mixed output concepts (e.g., electric, optic, mechanic), and (iv) developing synthetic methods for a more realistic use of the materials in miniaturized integrated systems and their projection into the application market. The solution to those needs will pave the way to the selective detection of specific VOCs in the future and the generalized use of artificial olfactory systems adapted to the society demands.

Author Contributions: Writing—original draft preparation, M.T. and S.V.; writing—review and editing, M.T., M.Š., L.V., and S.V.; funding acquisition, S.V. All authors have read and agreed to the published version of the manuscript.

Funding: This work has been funded by the Czech Science Foundation (GAČR), via Grant N° 20-20123S, and the Spanish Ministry of Science and Innovation, via Grant PID2019-107697RB-C42 (AEI/FEDER, EU) and the Ramón y Cajal programme.

Institutional Review Board Statement: Not applicable.

Informed Consent Statement: Not applicable.

Data Availability Statement: Not applicable.

Acknowledgments: We acknowledge the support of the Czech Science Foundation (GAČR), via Grant N° 20-20123S, and the Spanish Ministry of Science and Innovation, via Grant PID2019-107697RB-C42 (AEI/FEDER, EU) and the Ramón y Cajal programme.

Conflicts of Interest: The authors declare no conflict of interest.

References

1. Barsan, N.; Weimar, U. Conduction Model of Metal Oxide Gas Sensors. *J. Electroceram.* **2001**, *7*, 143–167. [\[CrossRef\]](#)
2. Yamazoe, N.; Shimano, K. Receptor Function and Response of Semiconductor Gas Sensor. *J. Sens.* **2009**, *2009*. [\[CrossRef\]](#)
3. Korotcenkov, G. Metal oxides for solid-state gas sensors: What determines our choice? *Mater. Sci. Eng. B* **2007**, *139*, 1–23. [\[CrossRef\]](#)
4. Wong, Y.C.Y.H.; Ang, B.C.; Haseeb, A.S.M.A.; Baharuddin, A.A.; Wong, Y.C.Y.H. Review—Conducting Polymers as Chemiresistive Gas Sensing Materials: A Review. *J. Electrochem. Soc.* **2020**, *167*, 037503. [\[CrossRef\]](#)
5. Bai, H.; Shi, G. Gas sensors based on conducting polymers. *Sensors* **2007**, *7*, 267–307. [\[CrossRef\]](#)
6. Li, C.; Bai, H.; Shi, G. Conducting polymer nanomaterials: Electrosynthesis and applications. *Chem. Soc. Rev.* **2009**, *38*, 2397–2409. [\[CrossRef\]](#)
7. Yan, Y.; Yang, G.; Xu, J.L.; Zhang, M.; Kuo, C.C.; Wang, S.D. Conducting polymer-inorganic nanocomposite-based gas sensors: A review. *Sci. Technol. Adv. Mater.* **2020**, *21*, 768–786. [\[CrossRef\]](#)
8. Clément, P.; Llobet, E. Carbon nanomaterials functionalized with macrocyclic compounds for sensing vapors of aromatic VOCs. In *Semiconductor Gas Sensors*; Woodhead Publishing: Cambridge, UK, 2019; pp. 223–237, ISBN 9780081025598.
9. Lee, S.W.; Lee, W.; Hong, Y.; Lee, G.; Yoon, D.S. Recent advances in carbon material-based NO₂ gas sensors. *Sens. Actuators B Chem.* **2018**, *255*, 1788–1804. [\[CrossRef\]](#)
10. Llobet, E. Gas sensors using carbon nanomaterials: A review. *Sens. Actuators B Chem.* **2013**, *179*, 32–45. [\[CrossRef\]](#)
11. Mahajan, S.; Jagtap, S. Metal-oxide semiconductors for carbon monoxide (CO) gas sensing: A review. *Appl. Mater. Today* **2020**, *18*, 100483–100513. [\[CrossRef\]](#)
12. Li, T.; Shen, Y.; Zhao, S.; Zhong, X.; Zhang, W.; Han, C.; Wei, D.; Meng, D.; Ao, Y. Sub-ppm level NO₂ sensing properties of polyethyleneimine-mediated WO₃ nanoparticles synthesized by a one-pot hydrothermal method. *J. Alloys Compd.* **2019**, *783*, 103–112. [\[CrossRef\]](#)
13. Peterson, P.J.D.; Aujla, A.; Grant, K.H.; Brundle, A.G.; Thompson, M.R.; Hey, J.V.; Leigh, R.J. Practical use of metal oxide semiconductor gas sensors for measuring nitrogen dioxide and ozone in urban environments. *Sensors* **2017**, *17*, 1653. [\[CrossRef\]](#) [\[PubMed\]](#)
14. Punetha, D.; Kar, M.; Pandey, S.K. A new type low-cost, flexible and wearable tertiary nanocomposite sensor for room temperature hydrogen gas sensing. *Sci. Rep.* **2020**, *10*, 2151–2162. [\[CrossRef\]](#)
15. Shen, W.C.; Shih, P.J.; Tsai, Y.C.; Hsu, C.C.; Dai, C.L. Low-concentration ammonia gas sensors manufactured using the CMOS-MEMS technique. *Micromachines* **2020**, *11*, 92. [\[CrossRef\]](#) [\[PubMed\]](#)
16. Peng, F.; Wang, S.; Yu, W.; Huang, T.; Sun, Y.; Cheng, C.; Chen, X.; Hao, J.; Dai, N. Ultrasensitive ppb-level H₂S gas sensor at room temperature based on WO₃/rGO hybrids. *J. Mater. Sci. Mater. Electron.* **2020**, *31*, 5008–5016. [\[CrossRef\]](#)
17. Binions, R.; Naik, A.J.T. Metal oxide semiconductor gas sensors in environmental monitoring. In *Semiconductor Gas Sensors*; Woodhead Publishing: Cambridge, UK, 2013; pp. 433–466, ISBN 9780857092366.
18. Llobet, E.; Brunet, J.; Pauly, A.; Ndiaye, A.; Varenne, C. Nanomaterials for the selective detection of hydrogen sulfide in air. *Sensors* **2017**, *17*, 391. [\[CrossRef\]](#) [\[PubMed\]](#)
19. Sun, J.; Shen, Z.X.; Zhang, L.M.; Zhang, Y.; Zhang, T.; Lei, Y.L.; Niu, X.Y.; Zhang, Q.; Dang, W.; Han, W.P.; et al. Volatile organic compounds emissions from traditional and clean domestic heating appliances in Guanzhong Plain, China: Emission factors, source profiles, and effects on regional air quality. *Environ. Int.* **2019**, *133*, 1052522–1052534. [\[CrossRef\]](#)
20. Mohd Ali, M.; Hashim, N.; Abd Aziz, S.; Lasekan, O. Principles and recent advances in electronic nose for quality inspection of agricultural and food products. *Trends Food Sci. Technol.* **2020**, *99*, 1–10. [\[CrossRef\]](#)
21. Hanna, G.B.; Boshier, P.R.; Markar, S.R.; Romano, A. Accuracy and Methodologic Challenges of Volatile Organic Compound-Based Exhaled Breath Tests for Cancer Diagnosis A Systematic Review and Meta-analysis. *JAMA Oncol.* **2019**, *5*, e182815. [\[CrossRef\]](#)
22. Berenjian, A.; Chan, N.; Malmiri, H.J. Volatile Organic Compounds removal methods: A review. *Am. J. Biochem. Biotechnol.* **2012**, *8*, 220–229. [\[CrossRef\]](#)
23. Wille, S.M.R.; Lambert, W.E.E. Volatile substance abuse—Post-mortem diagnosis. *Forensic Sci. Int.* **2004**, *142*, 135–156. [\[CrossRef\]](#)

24. Koppmann, R. *Volatile Organic Compounds in the Atmosphere*; Blackwell Publishing Ltd.: Oxford, UK, 2008; ISBN 9780470994153.
25. ACGIH 2019 TLVs and BEIs; American Conference of Governmental Industrial Hygienists: Cincinnati, OH, USA, 2019; ISBN 9781607261056.
26. Tomer, V.K.; Singh, K.; Kaur, H.; Shorie, M.; Sabherwal, P. Rapid acetone detection using indium loaded WO_3/SnO_2 nano hybrid sensor. *Sens. Actuators B Chem.* **2017**, *253*, 703–713. [[CrossRef](#)]
27. Buszewski, B.; Ligor, T.; Jezewski, T.; Wenda-Piesik, A.; Walczak, M.; Rudnicka, J. Identification of volatile lung cancer markers by gas chromatography-mass spectrometry: Comparison with discrimination by canines. *Anal. Bioanal. Chem.* **2012**, *404*, 141–146. [[CrossRef](#)]
28. Kumar, S.; Huang, J.Z.; Abbassi-Ghadi, N.; Mackenzie, H.A.; Veselkov, K.A.; Hoare, J.M.; Lovat, L.B.; Spanel, P.; Smith, D.; Hanna, G.B. Mass Spectrometric Analysis of Exhaled Breath for the Identification of Volatile Organic Compound Biomarkers in Esophageal and Gastric Adenocarcinoma. *Ann. Surg.* **2015**, *262*, 981–990. [[CrossRef](#)]
29. Kumar, S.; Huang, J.Z.; Abbassi-Ghadi, N.; Spanel, P.; Smith, D.; Hanna, G.B. Selected Ion Flow Tube Mass Spectrometry Analysis of Exhaled Breath for Volatile Organic Compound Profiling of Esophago-Gastric Cancer. *Anal. Chem.* **2013**, *85*, 6121–6128. [[CrossRef](#)] [[PubMed](#)]
30. Amal, H.; Leja, M.; Funka, K.; Lasina, I.; Skapars, R.; Sivins, A.; Ancans, G.; Kikuste, I.; Vanags, A.; Tolmanis, I.; et al. Breath testing as potential colorectal cancer screening tool. *Int. J. Cancer* **2016**, *138*, 229–236. [[CrossRef](#)] [[PubMed](#)]
31. Seiyama, T.; Kato, A.; Fujiishi, K.; Nagatani, M. A New Detector for Gaseous Components Using Semiconductive Thin Films. *Anal. Chem.* **1962**, *34*, 1502–1503. [[CrossRef](#)]
32. Miller, D.R.; Akbar, S.A.; Morris, P.A. Nanoscale metal oxide-based heterojunctions for gas sensing: A review. *Sens. Actuators B Chem.* **2014**, *204*, 250–272. [[CrossRef](#)]
33. Malik, R.; Tomer, V.K.; Mishra, Y.K.; Lin, L. Functional gas sensing nanomaterials: A panoramic view. *Appl. Phys. Rev.* **2020**, *7*, 21301. [[CrossRef](#)]
34. Joshi, N.; Hayasaka, T.; Liu, Y.; Liu, H.; Oliveira, O.N.; Lin, L. A review on chemiresistive room temperature gas sensors based on metal oxide nanostructures, graphene and 2D transition metal dichalcogenides. *Microchim. Acta* **2018**, *185*. [[CrossRef](#)]
35. Kamarulzaman, N.; Kasim, M.F.; Chayed, N.F. Elucidation of the highest valence band and lowest conduction band shifts using XPS for ZnO and Zn_{0.99}Cu_{0.01}O band gap changes. *Results Phys.* **2016**, *6*, 217–230. [[CrossRef](#)]
36. Song, H.; Yang, H.; Ma, X. A comparative study of porous ZnO nanostructures synthesized from different zinc salts as gas sensor materials. *J. Alloys Compd.* **2013**, *578*, 272–278. [[CrossRef](#)]
37. Meng, F.; Hou, N.; Ge, S.; Sun, B.; Jin, Z.; Shen, W.; Kong, L.; Guo, Z.; Sun, Y.; Wu, H.; et al. Flower-like hierarchical structures consisting of porous single-crystalline ZnO nanosheets and their gas sensing properties to volatile organic compounds (VOCs). *J. Alloys Compd.* **2015**, *626*, 124–130. [[CrossRef](#)]
38. Al-Salman, H.; Abdullah, M.J. Preparation of ZnO nanostructures by RF-magnetron sputtering on thermally oxidized porous silicon substrate for VOC sensing application. *Measurement* **2015**, *59*, 248–257. [[CrossRef](#)]
39. Zhang, S.-L.; Lim, J.-O.; Huh, J.-S.; Noh, J.-S.; Lee, W. Two-step fabrication of ZnO nanosheets for high-performance VOCs gas sensor. *Curr. Appl. Phys.* **2013**, *13*, S156–S161. [[CrossRef](#)]
40. Zhang, S.; Byun, H.; Lim, J.; Huh, J.; Lee, W. Controlled Synthesis of ZnO Nanostructures for Sub-ppm-Level VOC Detection. *IEEE Sens. J.* **2012**, *12*, 3149–3155. [[CrossRef](#)]
41. Kang, Y.; Yu, F.; Zhang, L.; Wang, W.; Chen, L.; Li, Y. Review of ZnO-based nanomaterials in gas sensors. *Solid State Ionics* **2021**, *360*, 115544–115566. [[CrossRef](#)]
42. Zhou, W.; Liu, Y.; Yang, Y.; Wu, P. Band gap engineering of SnO_2 by epitaxial strain: Experimental and theoretical investigations. *J. Phys. Chem. C* **2014**, *118*, 6448–6453. [[CrossRef](#)]
43. Rothschild, A.; Komem, Y. The effect of grain size on the sensitivity of nanocrystalline metal-oxide gas sensors. *J. Appl. Phys.* **2004**, *95*, 6374–6380. [[CrossRef](#)]
44. Shimizu, Y.; Kai, S.; Takao, Y.; Hyodo, T.; Egashira, M. Correlation between methylmercaptan gas-sensing properties and its surface chemistry of SnO_2 -based sensor materials. *Sens. Actuator B Chem.* **2000**, *65*, 349–357. [[CrossRef](#)]
45. Ren, F.; Gao, L.; Yuan, Y.; Zhang, Y.; Alqmi, A.; Aldossary, O. Enhanced BTEX gas-sensing performance of CuO/ SnO_2 composite. *Sens. Actuators B Chem.* **2015**, *223*, 914–920. [[CrossRef](#)]
46. Wang, H.; Qu, Y.; Chen, H.; Lin, Z.; Dai, K. Highly selective n-butanol gas sensor based on mesoporous SnO_2 prepared with hydrothermal treatment. *Sens. Actuators B Chem.* **2014**, *201*, 153–159. [[CrossRef](#)]
47. Gu, C.; Xu, X.; Huang, J.; Wang, W.; Sun, Y.; Liu, J. Porous flower-like SnO_2 nanostructures as sensitive gas sensors for volatile organic compounds detection. *Sens. Actuators B Chem.* **2012**, *174*, 31–38. [[CrossRef](#)]
48. Vallejos, S.; Gràcia, I.; Bravo, J.; Figueras, E.; Hubálek, J.; Cané, C. Detection of volatile organic compounds using flexible gas sensing devices based on tungsten oxide nanostructures functionalized with Au and Pt nanoparticles. *Talanta* **2015**, *139*, 27–34. [[CrossRef](#)]
49. Vallejos, S.; Gràcia, I.; Figueras, E.; Cané, C. Nanoscale Heterostructures Based on $\text{Fe}_2\text{O}_3@/\text{WO}_{3-x}$ Nanoneedles and Their Direct Integration into Flexible Transducing Platforms for Toluene Sensing. *ACS Appl. Mater. Interfaces* **2015**, *7*, 18638–18649. [[CrossRef](#)] [[PubMed](#)]
50. Dong, H.; Liu, Y.; Li, G.; Wang, X.; Xu, D.; Chen, Z.; Zhang, T.; Wang, J.; Zhang, L. Hierarchically rosette-like In_2O_3 microspheres for volatile organic compounds gas sensors. *Sens. Actuators B Chem.* **2013**, *178*, 302–309. [[CrossRef](#)]

51. Bhowmik, B.; Manjuladevi, V.; Gupta, R.; Bhattacharyya, P. Highly Selective Low-Temperature Acetone Sensor Based on Hierarchical 3-D TiO₂ Nanoflowers. *IEEE Sens. J.* **2016**, *16*, 3488–3495. [\[CrossRef\]](#)
52. Şennik, E.; Alev, O.; Öztürk, Z. The effect of Pd on H₂ and VOCs sensing properties of TiO₂ nanorods. *Sens. Actuators B Chem.* **2016**, *229*, 692–700. [\[CrossRef\]](#)
53. Li, B.; Liu, J.; Shi, G.; Liu, J. A research on detection and identification of volatile organic compounds utilizing cataluminescence-based sensor array. *Sens. Actuators B Chem.* **2013**, *177*, 1167–1172. [\[CrossRef\]](#)
54. Baccar, H.; Thamri, A.; Clément, P.; Lobet, E.; Abdelghani, A. Pt- and Pd-decorated MWCNTs for vapour and gas detection at room temperature. *Beilstein J. Nanotechnol.* **2015**, *6*, 919–927. [\[CrossRef\]](#)
55. Thamri, A.; Baccar, H.; Struzzi, C.; Bittencourt, C.; Abdelghani, A.; Lobet, E. MHDA-functionalized multiwall carbon nanotubes for detecting non-aromatic VOCs. *Sci. Rep.* **2016**, *6*, 35130–35142. [\[CrossRef\]](#) [\[PubMed\]](#)
56. Pargoletti, E.; Cappelletti, G. Breakthroughs in the design of novel carbon-based metal oxides nanocomposites for vocs gas sensing. *Nanomaterials* **2020**, *10*, 1485. [\[CrossRef\]](#)
57. Hasani, A.; Dehsari, H.S.; Gavgani, J.N.; Shalamzari, E.K.; Salehi, A.; Afshar Taromi, E.; Mahyari, M. Sensor for volatile organic compounds using an interdigitated gold electrode modified with a nanocomposite made from poly(3,4-ethylenedioxythiophene)-poly(styrenesulfonate) and ultra-large graphene oxide. *Microchim. Acta* **2015**, *182*, 1551–1559. [\[CrossRef\]](#)
58. Sun, J.; Shu, X.; Tian, Y.; Tong, Z.; Bai, S.; Luo, R.; Li, D.; Liu, C.C. Facile preparation of polypyrrole-reduced graphene oxide hybrid for enhancing NH₃ sensing at room temperature. *Sens. Actuators B Chem.* **2017**, *241*, 658–664. [\[CrossRef\]](#)
59. Gurlo, A. Nanosensors: Towards morphological control of gas sensing activity. SnO₂, In₂O₃, ZnO and WO₃ case studies. *Nanoscale* **2011**, *3*, 154–165. [\[CrossRef\]](#)
60. Sabu Joshi, T.; Nirav Tomer, V.K. (Eds.) *Functional Nanomaterials*; Springer: Singapore, 2020; ISBN 978-981-15-4809-3.
61. Lingmin, Y.; Xinhui, F.; Lijun, Q.; Lihe, M.; Wen, Y. Dependence of morphologies for SnO₂ nanostructures on their sensing property. *Appl. Surf. Sci.* **2011**, *257*, 3140–3144. [\[CrossRef\]](#)
62. Batzill, M.; Diebold, U. The surface and materials science of tin oxide. *Prog. Surf. Sci.* **2005**, *79*, 47–154. [\[CrossRef\]](#)
63. Hassan, H.S.; Elkady, M.F. Semiconductor Nanomaterials for Gas Sensor Applications. In *Environmental Nanotechnology Volume 3. Environmental Chemistry for a Sustainable World*; Springer: Cham, Switzerland, 2020; pp. 305–355.
64. Nunes, D.; Pimentel, A.; Goncalves, A.; Pereira, S.; Branquinho, R.; Barquinha, P.; Fortunato, E.; Martins, R. Metal oxide nanostructures for sensor applications. *Semicond. Sci. Technol.* **2019**. [\[CrossRef\]](#)
65. Han, X.; Sun, Y.; Feng, Z.; Zhang, G.; Chen, Z.; Zhan, J. Au-deposited porous single-crystalline ZnO nanoplates for gas sensing detection of total volatile organic compounds. *RSC Adv.* **2016**, *6*, 37750–37756. [\[CrossRef\]](#)
66. Nengsih, S.; Ali Umar, A.; Mat Salleh, M.; Yahaya, M. Detection of Volatile Organic Compound Gas Using Localized Surface Plasmon Resonance of Gold Nanoparticles. *Sains Malays.* **2011**, *40*, 231–235.
67. Cheng, C.-S.; Chen, Y.-Q.; Lu, C.-J. Organic vapour sensing using localized surface plasmon resonance spectrum of metallic nanoparticles self assemble monolayer. *Talanta* **2007**, *73*, 358–365. [\[CrossRef\]](#)
68. Subramanian, E.; Jeyarani, B.M.L.; Murugan, C.P.D. Crucial role of undoped/doped state of polyaniline-b-cyclodextrin composite materials in determining sensor functionality toward benzene/toluene toxic vapor. *J. Chem. Mater. Res.* **2016**, *5*, 129–134.
69. Lü, Y.; Zhan, W.; He, Y.; Wang, Y.; Kong, X.; Kuang, Q.; Xie, Z.; Zheng, L. MOF-Templated Synthesis of Porous Co₃O₄ Concave Nanocubes with High Specific Surface Area and Their Gas Sensing Properties. *ACS Appl. Mater. Interfaces* **2014**, *6*, 4186–4195. [\[CrossRef\]](#) [\[PubMed\]](#)
70. Park, H.J.; Kim, J.; Choi, N.-J.; Song, H.; Lee, D.-S. Nonstoichiometric Co-rich ZnCo₂O₄ Hollow Nanospheres for High Performance Formaldehyde Detection at ppb Levels. *ACS Appl. Mater. Interfaces* **2016**, *8*, 3233–3240. [\[CrossRef\]](#)
71. Öztürk, S.; Kösemen, A.; Kösemen, Z.A.; Kiliç, N.; Öztürk, Z.Z.; Penza, M. Electrochemically growth of Pd doped ZnO nanorods on QCM for room temperature VOC sensors. *Sens. Actuators B Chem.* **2016**, *222*, 280–289. [\[CrossRef\]](#)
72. Lee, C.-S.; Dai, Z.; Jeong, S.-Y.; Kwak, C.-H.; Kim, B.-Y.; Kim, D.H.; Jang, H.W.; Park, J.-S.; Lee, J.-H. Monolayer Co₃O₄ Inverse Opals as Multifunctional Sensors for Volatile Organic Compounds. *Chem. A Eur. J.* **2016**, *22*, 7102–7107. [\[CrossRef\]](#)
73. Liu, D.; Liu, T.; Zhang, H.; Lv, C.; Zeng, W.; Zhang, J. Gas sensing mechanism and properties of Ce-doped SnO₂ sensors for volatile organic compounds. *Mater. Sci. Semicond. Process.* **2012**, *15*, 438–444. [\[CrossRef\]](#)
74. Deng, H.; Li, H.; Wang, F.; Yuan, C.; Liu, S.; Wang, P.; Xie, L.; Sun, Y.; Chang, F. A high sensitive and low detection limit of formaldehyde gas sensor based on hierarchical flower-like CuO nanostructure fabricated by sol-gel method. *J. Mater. Sci. Mater. Electron.* **2016**, *27*, 6766–6772. [\[CrossRef\]](#)
75. Behera, B.; Chandra, S. An innovative gas sensor incorporating ZnO-CuO nanoflakes in planar MEMS technology. *Sens. Actuators B Chem.* **2016**, *229*, 414–424. [\[CrossRef\]](#)
76. Xu, F.; Zhou, C.; Ho, H.P. A rule for operation temperature selection of a conductometric VOC gas sensor based on ZnO nanoletrapods. *J. Alloys Compd.* **2021**, *858*, 158294–158303. [\[CrossRef\]](#)
77. Rella, R.; Spadavecchia, J.; Manera, M.G.; Capone, S.; Taurino, A.; Martino, M.; Caricato, A.P.; Tunno, T. Acetone and ethanol solid-state gas sensors based on TiO₂ nanoparticles thin film deposited by matrix assisted pulsed laser evaporation. *Sens. Actuators B Chem.* **2007**, *127*, 426–431. [\[CrossRef\]](#)
78. Tiwari, J.N.; Tiwari, R.N.; Kim, K.S. Zero-dimensional, one-dimensional, two-dimensional and three-dimensional nanostructured materials for advanced electrochemical energy devices. *Prog. Mater. Sci.* **2012**, *57*, 724–803. [\[CrossRef\]](#)

79. Lee, J.H. Gas sensors using hierarchical and hollow oxide nanostructures: Overview. *Sens. Actuators B Chem.* **2009**, *140*, 319–336. [CrossRef]
80. Park, J.Y.; Choi, S.W.; Kim, S.S. Junction-tuned SnO₂ nanowires and their sensing properties. *J. Phys. Chem. C* **2011**, *115*, 12774–12781. [CrossRef]
81. Vallejos, S.; Gràcia, I.; Chmela, O.; Figueras, E.; Hubálek, J.; Cané, C. Chemoresistive micromachined gas sensors based on functionalized metal oxide nanowires: Performance and reliability. *Sens. Actuators B Chem.* **2016**, *235*, 525–534. [CrossRef]
82. Battie, Y.; Ducloux, O.; Thobois, P.; Dorval, N.; Lauret, J.S.; Attal-Trétout, B.; Loiseau, A. Gas sensors based on thick films of semi-conducting single walled carbon nanotubes. *Carbon N. Y.* **2011**, *49*, 3544–3552. [CrossRef]
83. Tasaltin, C.; Basarir, F. Preparation of flexible VOC sensor based on carbon nanotubes and gold nanoparticles. *Sens. Actuators B Chem.* **2014**, *194*, 173–179. [CrossRef]
84. Šetka, M.; Drbohlavová, J.; Hubálek, J. Nanostructured polypyrrole-based ammonia and volatile organic compound sensors. *Sensors* **2017**, *17*, 562. [CrossRef]
85. Penza, M.; Antolini, F.; Antisari Vittori, M. Carbon nanotubes as SAW chemical sensors materials. *Sens. Actuators B Chem.* **2004**, *100*, 47–59. [CrossRef]
86. Chen, W.Y.; Jiang, X.; Lai, S.N.; Peroulis, D.; Stanciu, L. Nanohybrids of a MXene and transition metal dichalcogenide for selective detection of volatile organic compounds. *Nat. Commun.* **2020**, *11*, 1302–1312. [CrossRef] [PubMed]
87. Rajkumar, K.; Kumar, R.T.R. Gas sensors based on two-dimensional materials and its mechanisms. In *Fundamentals and Sensing Applications of 2D Materials*; Woodhead Publishing: Cambridge, UK, 2019; pp. 205–258, ISBN 9780081025772.
88. Cho, S.Y.; Koh, H.J.; Yoo, H.W.; Kim, J.S.; Jung, H.T. Tunable Volatile-Organic-Compound Sensor by Using Au Nanoparticle Incorporation on MoS₂. *ACS Sens.* **2017**, *2*, 183–189. [CrossRef] [PubMed]
89. Gu, D.; Li, X.; Wang, H.; Li, M.; Xi, Y.; Chen, Y.; Wang, J.; Rumyantseva, M.N.; Gaskov, A.M. Light enhanced VOCs sensing of WS₂ microflakes based chemiresistive sensors powered by triboelectric nengenerators. *Sens. Actuators B Chem.* **2018**, *256*, 992–1000. [CrossRef]
90. Liu, T.; Cui, Z.; Li, X.; Cui, H.; Liu, Y. Al-Doped MoSe₂ Monolayer as a Promising Biosensor for Exhaled Breath Analysis: A DFT Study. *ACS Omega* **2021**, *6*, 988–995. [CrossRef]
91. Wan, Q.; Chen, X.; Gui, Y. First-Principles Insight into a Ru-Doped SnS₂ Monolayer as a Promising Biosensor for Exhale Gas Analysis. *ACS Omega* **2020**, *5*, 8919–8926. [CrossRef] [PubMed]
92. Anasori, B.; Gogotsi, Y. *2D Metal Carbides and Nitrides (MXenes): Structure, Properties and Applications*; Springer International Publishing: New York, NY, USA, 2019; ISBN 9783030190262.
93. Lee, E.; Kim, D.-J. Review—Recent Exploration of Two-Dimensional MXenes for Gas Sensing: From a Theoretical to an Experimental View. *J. Electrochem. Soc.* **2020**, *167*, 37515. [CrossRef]
94. Aghaei, S.M.; Aasi, A.; Farhangdoust, S.; Panchapakesan, B. Graphene-like BC₆N nanosheets are potential candidates for detection of volatile organic compounds (VOCs) in human breath: A DFT study. *Appl. Surf. Sci.* **2021**, *536*, 147756–147769. [CrossRef]
95. Donarelli, M.; Ottaviano, L. 2d materials for gas sensing applications: A review on graphene oxide, MoS₂, WS₂ and phosphorene. *Sensors* **2018**, *18*, 3638. [CrossRef]
96. Ou, P.; Song, P.; Liu, X.; Song, J. Superior Sensing Properties of Black Phosphorus as Gas Sensors: A Case Study on the Volatile Organic Compounds. *Adv. Theory Simul.* **2019**, *2*, 1800103. [CrossRef]
97. Choi, J.R.; Yong, K.W.; Choi, J.Y.; Nilghaz, A.; Lin, Y.; Xu, J.; Lu, X. Black phosphorus and its biomedical applications. *Theranostics* **2018**, *8*, 1005–1026. [CrossRef]
98. Fukuoka, S.; Taen, T.; Osada, T. Electronic structure and the properties of phosphorene and few-layer black phosphorus. *J. Phys. Soc. Japan* **2015**, *84*, 121004–121016. [CrossRef]
99. Yang, A.; Wang, D.; Wang, X.; Zhang, D.; Koratkar, N.; Rong, M. Recent advances in phosphorene as a sensing material. *Nano Today* **2018**, *20*, 13–32. [CrossRef]
100. Yamazoe, N.; Sakai, G.; Shimano, K. Oxide semiconductor gas sensors. *Catal. Surv. Asia* **2003**, *7*, 63–75. [CrossRef]
101. Nikolic, M.V.; Milovanovic, V.; Vasiljevic, Z.Z.; Stamenkovic, Z. Semiconductor gas sensors: Materials, technology, design, and application. *Sensors* **2020**, *20*, 6694. [CrossRef] [PubMed]
102. Sha, W.; Ni, S.; Zheng, C. Development of cataluminescence sensor system for benzene and toluene determination. *Sens. Actuators B Chem.* **2015**, *209*, 297–305. [CrossRef]
103. Bendahmane, B.; Tomić, M.; Toudjén, N.E.H.; Gràcia, I.; Vallejos, S.; Mansour, F. Influence of Mg doping levels on the sensing properties of SnO₂ films. *Sensors* **2020**, *20*, 2158. [CrossRef]
104. Clément, P.; Hafaiedh, I.; Parra, E.; Thamri, A.; Guillot, J.; Abdelghani, A.; Llobet, E. Iron oxide and oxygen plasma functionalized multi-walled carbon nanotubes for the discrimination of volatile organic compounds. *Carbon N. Y.* **2014**, *78*, 510–520. [CrossRef]
105. Chen, N.; Li, Q.; Li, Y.; Deng, D.; Xiao, X.; Wang, Y. Facile synthesis and gas sensing performances based on nickel oxide nanoparticles/multi-wall carbon nanotube composite. *J. Mater. Sci. Mater. Electron.* **2015**, *26*, 8240–8248. [CrossRef]
106. Farbod, M.; Joula, M.H.; Vaezi, M. Promoting effect of adding carbon nanotubes on sensing characteristics of ZnO hollow sphere-based gas sensors to detect volatile organic compounds. *Mater. Chem. Phys.* **2016**, *176*, 12–23. [CrossRef]
107. Šetka, M.; Bahos, F.A.; Matatagui, D.; Gràcia, I.; Figueras, E.; Drbohlavová, J.; Vallejos, S. Love Wave Sensors with Silver Modified Polypyrrole Nanoparticles for VOCs Monitoring. *Sensors* **2020**, *20*, 1432. [CrossRef]

108. Šetka, M.; Bahos, F.A.; Chmela, O.; Matatagui, D.; Grácia, I.; Drbohlavová, J.; Vallejos, S. Cadmium telluride/polypyrrole nanocomposite based Love wave sensors highly sensitive to acetone at room temperature. *Sens. Actuators B Chem.* **2020**, *321*, 128573–128582. [CrossRef]
109. Rujisamphan, N.; Murray, R.E.; Deng, F.; Supasai, T. Co-sputtered metal and polymer nanocomposite films and their electrical responses for gas sensing application. *Appl. Surf. Sci.* **2016**, *368*, 114–121. [CrossRef]
110. Ge, S.; Zheng, H.; Sun, Y.; Jin, Z.; Shan, J.; Wang, C.; Wu, H.; Li, M.; Meng, F. Ag/SnO₂/graphene ternary nanocomposites and their sensing properties to volatile organic compounds. *J. Alloys Compd.* **2016**, *659*, 127–131. [CrossRef]
111. Vessalli, B.A.; Zito, C.A.; Perfecto, T.M.; Volanti, D.P.; Mazon, T. ZnO nanorods/graphene oxide sheets prepared by chemical bath deposition for volatile organic compounds detection. *J. Alloys Compd.* **2017**, *696*, 996–1003. [CrossRef]
112. Zito, C.A.; Perfecto, T.M.; Volanti, D.P. Impact of reduced graphene oxide on the ethanol sensing performance of hollow SnO₂ nanoparticles under humid atmosphere. *Sens. Actuators B Chem.* **2017**, *244*, 466–474. [CrossRef]
113. Šetka, M.; Bahos, F.A.; Matatagui, D.; Potoček, M.; Kral, Z.; Drbohlavová, J.; Grácia, I.; Vallejos, S. Love wave sensors based on gold nanoparticle-modified polypyrrole and their properties to ammonia and ethylene. *Sens. Actuators B Chem.* **2020**, *304*, 127337–127346. [CrossRef]
114. Vessman, J.; Stefan, R.I.; Van Staden, J.F.; Danzer, K.; Lindner, W.; Burns, D.T.; Fajgelj, A.; Müller, H. Selectivity in analytical chemistry: (IUPAC Recommendations 2001). *Pure Appl. Chem.* **2001**. [CrossRef]
115. Bedia, C.; Cardoso, P.; Dalmáu, N.; Garreta-Lara, E.; Gómez-Canela, C.; Gorrochategui, E.; Navarro-Reig, M.; Ortiz-Villanueva, E.; Puig-Castellví, F.; Tauler, R. Chapter Nineteen—Applications of Metabolomics Analysis in Environmental Research. In *Comprehensive Analytical Chemistry*; Jaumot, J., Bedia, C., Tauler, R., Eds.; Elsevier: Amsterdam, The Netherlands, 2018; Volume 82, pp. 533–582, ISBN 0166-526X.
116. Tung, T.T.; Losic, D.; Park, S.J.; Feller, J.F.; Kim, T. Core-shell nanostructured hybrid composites for volatile organic compound detection. *Int. J. Nanomed.* **2015**, *10*, 203–214. [CrossRef]
117. Heli, B.; Morales-Narváez, E.; Golmohammadi, H.; Aji, A.; Merkoçi, A. Modulation of population density and size of silver nanoparticles embedded in bacterial cellulose: Via ammonia exposure: Visual detection of volatile compounds in a piece of plasmonic nanopaper. *Nanoscale* **2016**, *8*, 7984–7991. [CrossRef] [PubMed]
118. Yang, L.; Zhou, X.; Song, L.; Wang, Y.; Wu, X.; Han, N.; Chen, Y. Noble Metal/Tin Dioxide Hierarchical Hollow Spheres for Low-Concentration Breath Methane Sensing. *ACS Appl. Nano Mater.* **2018**, *1*, 6327–6336. [CrossRef]
119. Li, B.; Zhang, Y.; Liu, J.; Xie, X.; Zou, D.; Li, M.; Liu, J. Sensitive and selective system of benzene detection based on a cataluminescence sensor. *Luminescence* **2014**, *29*, 332–337. [CrossRef] [PubMed]
120. Sarkar, T.; Srinives, S.; Rodriguez, A.; Mulchandani, A. Single-walled Carbon Nanotube-Calixarene Based Chemiresistor for Volatile Organic Compounds. *Electroanalysis* **2018**, *30*, 2077–2084. [CrossRef]
121. Li, W.; Wu, X.; Han, N.; Chen, J.; Qian, X.; Deng, Y.; Tang, W.; Chen, Y. MOF-derived hierarchical hollow ZnO nanocages with enhanced low-concentration VOCs gas-sensing performance. *Sens. Actuators B Chem.* **2016**, *225*, 158–166. [CrossRef]
122. Zhao, W.; Al-Nasser, L.F.; Shan, S.; Li, J.; Skeete, Z.; Kang, N.; Luo, J.; Lu, S.; Zhong, C.J.; Grausgruber, C.J.; et al. Detection of mixed volatile organic compounds and lung cancer breaths using chemiresistor arrays with crosslinked nanoparticle thin films. *Sens. Actuators B Chem.* **2016**, *232*, 292–299. [CrossRef]
123. Penza, M.; Cassano, G.; Aversa, P.; Antolini, F.; Cusano, A.; Consales, M.; Giordano, M.; Nicolais, L. Carbon nanotubes-coated multi-transducing sensors for VOCs detection. *Sens. Actuators B Chem.* **2005**, *111–112*, 171–180. [CrossRef]
124. Joseph, Y.; Guse, B.; Vossmeier, T.; Yasuda, A. Gold nanoparticle/organic networks as chemiresistor coatings: The effect of film morphology on vapor sensitivity. *J. Phys. Chem. C* **2008**, *112*, 12507–12514. [CrossRef]
125. Fatima, Q.; Haidry, A.A.; Yao, Z.; He, Y.; Li, Z.; Sun, L.; Xie, L. The critical role of hydroxyl groups in water vapor sensing of graphene oxide. *Nanoscale Adv.* **2019**, *1*, 1319–1330. [CrossRef]
126. Ahmadi, M.T.; Ismail, R.; Anwar, S. *Handbook of Research on Nanoelectronic Sensor Modeling and Applications*; IGI Global: Hershey, PA, USA, 2016.
127. Wang, J.; Yang, P.; Wei, X. High-Performance, Room-Temperature, and No-Humidity-Impact Ammonia Sensor Based on Heterogeneous Nickel Oxide and Zinc Oxide Nanocrystals. *ACS Appl. Mater. Interfaces* **2015**, *7*, 3816–3824. [CrossRef]
128. Kim, H.-R.; Haensch, A.; Kim, I.-D.; Barsan, N.; Weimar, U.; Lee, J.-H. The Role of NiO Doping in Reducing the Impact of Humidity on the Performance of SnO₂-Based Gas Sensors: Synthesis Strategies, and Phenomenological and Spectroscopic Studies. *Adv. Funct. Mater.* **2011**, *21*, 4456–4463. [CrossRef]
129. Choi, K.-I.; Kim, H.-J.; Kang, Y.C.; Lee, J.-H. Ultrasensitive and ultrasensitive detection of H₂S in highly humid atmosphere using CuO-loaded SnO₂ hollow spheres for real-time diagnosis of halitosis. *Sens. Actuators B Chem.* **2014**, *194*, 371–376. [CrossRef]
130. Annanouch, F.E.; Haddi, Z.; Vallejos, S.; Umek, P.; Guttmann, P.; Bittencourt, C.; Llobet, E. Aerosol-Assisted CVD-Grown WO₃ Nanoneedles Decorated with Copper Oxide Nanoparticles for the Selective and Humidity-Resilient Detection of H₂S. *ACS Appl. Mater. Interfaces* **2015**, *7*, 6842–6851. [CrossRef]
131. Niarchos, G.; Dubourg, G.; Afroudakis, G.; Georgopoulos, M.; Tsouti, V.; Makarona, E.; Crnojevic-Bengin, V.; Tsamis, C. Humidity Sensing Properties of Paper Substrates and Their Passivation with ZnO Nanoparticles for Sensor Applications. *Sensors* **2017**, *17*, 516. [CrossRef]
132. Itoh, T.; Matsubara, I.; Tamaki, J.; Kanematsu, K.; Shin, W.; Izu, N.; Nishibori, M. Effect of High-Humidity Aging on Performance of Tungsten Oxide-Type Aromatic Compound Sensors. *Sens. Mater.* **2012**, *24*, 13–19.

133. Itoh, T.; Matsubara, I.; Kadosaki, M.; Sakai, Y.; Shin, W.; Izu, N.; Nishibori, M. Effects of high-humidity aging on platinum, palladium, and gold loaded tin oxide-volatile organic compound sensors. *Sensors* **2010**, *10*, 6513–6521. [CrossRef]
134. Vallejos, S.; Gracia, I.; Pizúrová, N.; Figueras, E.; Čechal, J.; Hubálek, J.; Cané, C. Gas sensitive ZnO structures with reduced humidity-interference. *Sens. Actuators B Chem.* **2019**, *301*, 127054–127063. [CrossRef]
135. Hierlemann, A.; Baltes, H. CMOS-based chemical microsensors. *Analyst* **2003**, *128*, 15–28. [CrossRef] [PubMed]
136. Janata, J. *Principles of Chemical Sensors*; Springer: New York, NY, USA, 2009; ISBN 978-0-387-69931-8.
137. Markiewicz, N.; Casals, O.; Fabrega, C.; Gracia, I.; Cané, C.; Wasisto, H.S.; Waag, A.; Prades, J.D. Micro light plates for low-power photoactivated (gas) sensors. *Appl. Phys. Lett.* **2019**, *114*, 53508–53514. [CrossRef]
138. Hagleitner, C.; Hierlemann, A.; Lange, D.; Kummer, A.; Kerness, N.; Brand, O.; Baltes, H. Smart single-chip gas sensor microsystem. *Nature* **2001**, *414*, 293–296. [CrossRef] [PubMed]
139. Gao, W.; Ota, H.; Kiriya, D.; Takei, K.; Javey, A. Flexible Electronics toward Wearable Sensing. *Acc. Chem. Res.* **2019**, *52*, 523–533. [CrossRef] [PubMed]
140. Comini, E. Integration of Metal Oxide Nanowires in Flexible Gas Sensing Devices. *Sensors* **2013**, *13*, 10659–10673. [CrossRef]
141. Vallejos, S.; Gracia, I.; Lednický, T.; Vojkuvka, L.; Figueras, E.; Hubálek, J.; Cané, C. Highly hydrogen sensitive micromachined sensors based on aerosol-assisted chemical vapor deposited ZnO rods. *Sens. Actuators B Chem.* **2018**, *268*, 15–21. [CrossRef]
142. Li, Y.; Delaunay, J.-J. Progress Toward Nanowire Device Assembly Technology. In *Nanowires*; InTech: London, UK, 2010; ISBN 978-953-7619-79-4.
143. Chmela, O.; Sadílek, J.; Domènech-Gil, G.; Samá, J.; Somer, J.; Mohan, R.; Romano-Rodríguez, A.; Hubálek, J.; Vallejos, S. Selectively arranged single-wire based nanosensor array systems for gas monitoring. *Nanoscale* **2018**, *10*, 9087–9096. [CrossRef] [PubMed]
144. Fan, Z.; Ho, J.C.; Takahashi, T.; Yerushalmi, R.; Takei, K.; Ford, A.C.; Chueh, Y.-L.; Javey, A. Toward the Development of Printable Nanowire Electronics and Sensors. *Adv. Mater.* **2009**, *21*, 3730–3743. [CrossRef]
145. Pavelko, R.G.; Yuasa, M.; Kida, T.; Shimano, K.; Yamazoe, N. Impurity level in SnO₂ materials and its impact on gas sensing properties. *Sens. Actuators B Chem.* **2015**, *210*, 719–725. [CrossRef]
146. Mottram, D.S.; Elmore, J.S. SENSORY EVALUATION | Aroma. In *Encyclopedia of Food Sciences and Nutrition*; Academic Press: Cambridge, UK, 2003; pp. 5174–5180.
147. Turner, A.P.F.; Magan, N. Electronic noses and disease diagnostics. *Nat. Rev. Microbiol.* **2004**, *2*, 160–166. [CrossRef]
148. Karakaya, D.; Ulucan, O.; Turkan, M. Electronic Nose and Its Applications: A Survey. *Int. J. Autom. Comput.* **2020**, *17*, 179–209. [CrossRef]
149. Cipriano, D.; Capelli, L. Evolution of electronic noses from research objects to engineered environmental odour monitoring systems: A review of standardization approaches. *Biosensors* **2019**, *9*, 75. [CrossRef] [PubMed]
150. Bonah, E.; Huang, X.; Aheto, J.H.; Osae, R. Application of electronic nose as a non-invasive technique for odor fingerprinting and detection of bacterial foodborne pathogens: A review. *J. Food Sci. Technol.* **2020**, *57*, 1977–1990. [CrossRef]
151. Loutfi, A.; Coradeschi, S.; Mani, G.K.; Shankar, P.; Rayappan, J.B.B. Electronic noses for food quality: A review. *J. Food Eng.* **2015**, *144*, 103–111. [CrossRef]
152. Licht, J.C.; Grasemann, H. Potential of the electronic nose for the detection of respiratory diseases with and without infection. *Int. J. Mol. Sci.* **2020**, *21*, 9416. [CrossRef]
153. Haddi, Z.; El Barbri, N.; Tahri, K.; Bougrini, M.; El Bari, N.; Llobet, E.; Bouchikhi, B. Instrumental assessment of red meat origins and their storage time using electronic sensing systems. *Anal. Methods* **2015**, *7*, 5193–5203. [CrossRef]
154. Rahimzadeh, H.; Sadeghi, M.; Ghasemi-Varnamkhandi, M.; Mireei, S.A.; Tohidi, M. On the feasibility of metal oxide gas sensor based electronic nose software modification to characterize rice ageing during storage. *J. Food Eng.* **2019**, *245*, 1–10. [CrossRef]
155. Santos, J.P.; Lozano, J.; Alexandre, M. Electronic Noses Applications in Beer Technology. In *Brewing Technology*; InTech: London, UK, 2017; pp. 177–203.
156. Giungato, P.; Laiola, E.; Nicolardi, V. Evaluation of Industrial Roasting Degree of Coffee Beans by Using an Electronic Nose and a Stepwise Backward Selection of Predictors. *Food Anal. Methods* **2017**, *10*, 3424–3433. [CrossRef]
157. Liao, Y.H.; Shih, C.H.; Abbod, M.F.; Shieh, J.S.; Hsiao, Y.J. Development of an E-nose system using machine learning methods to predict ventilator-associated pneumonia. *Microsyst. Technol.* **2020**. [CrossRef]
158. Yang, H.Y.; Wang, Y.C.; Peng, H.Y.; Huang, C.H. Breath biopsy of breast cancer using sensor array signals and machine learning analysis. *Sci. Rep.* **2021**, *11*, 103–112. [CrossRef] [PubMed]
159. Tozlu, B.H.; Şimşek, C.; Aydemir, O.; Karavelioglu, Y. A High performance electronic nose system for the recognition of myocardial infarction and coronary artery diseases. *Biomed. Signal Process. Control* **2021**, *64*, 102247–102255. [CrossRef]
160. Singh, H.; Raj, V.B.; Kumar, J.; Mittal, U.; Mishra, M.; Nimal, A.T.; Sharma, M.U.; Gupta, V. Metal oxide SAW E-nose employing PCA and ANN for the identification of binary mixture of DMMP and methanol. *Sens. Actuators B Chem.* **2014**, *200*, 147–156. [CrossRef]
161. Zhang, J.; Xue, Y.; Sun, Q.; Zhang, T.; Chen, Y.; Yu, W.; Xiong, Y.; Wei, X.; Yu, G.; Wan, H.; et al. A miniaturized electronic nose with artificial neural network for anti-interference detection of mixed indoor hazardous gases. *Sens. Actuators B Chem.* **2021**, *326*, 128822–128831. [CrossRef]
162. Lozano, J.; Santos, J.P.; Suárez, J.I.; Herrero, J.L.; Alexandre, M. Detection of pollutants in water using a wireless network of electronic noses. *Chem. Eng. Trans.* **2016**, *54*, 157–162. [CrossRef]

163. Chen, L.Y.; Wu, C.C.; Chou, T.I.; Chiu, S.W.; Tang, K.T. Development of a dual MOS electronic nose/camera system for improving fruit ripeness classification. *Sensors* **2018**, *18*, 3256. [[CrossRef](#)]
164. Chen, Q.; Chen, Z.; Liu, D.; He, Z.; Wu, J. Constructing an E-Nose Using Metal-Ion-Induced Assembly of Graphene Oxide for Diagnosis of Lung Cancer via Exhaled Breath. *ACS Appl. Mater. Interfaces* **2020**, *12*, 17713–17724. [[CrossRef](#)] [[PubMed](#)]
165. Moufid, M.; Hofmann, M.; El Bari, N.; Tiebe, C.; Bartholmai, M.; Bouchikhi, B. Wastewater monitoring by means of e-nose, VE-tongue, TD-GC-MS, and SPME-GC-MS. *Talanta* **2021**, *221*, 121450–121461. [[CrossRef](#)]
166. Goschnick, J.; Koroncz, I.; Frietsch, M.; Kiselev, I. Water pollution recognition with the electronic nose KAMINA. *Sens. Actuators B Chem.* **2005**, *106*, 182–186. [[CrossRef](#)]
167. He, J.; Xu, L.; Wang, P.; Wang, Q. A high precise E-nose for daily indoor air quality monitoring in living environment. *Integr. VLSI J.* **2017**, *58*, 286–294. [[CrossRef](#)]
168. Ragazzo-Sanchez, J.A.; Chalier, P.; Chevalier-Lucia, D.; Calderon-Santoyo, M.; Ghommidh, C. Off-flavours detection in alcoholic beverages by electronic nose coupled to GC. *Sens. Actuators B Chem.* **2009**, *140*, 29–34. [[CrossRef](#)]
169. Jiarpinijnun, A.; Osako, K.; Siripatrawan, U. Visualization of volatome profiles for early detection of fungal infection on storage Jasmine brown rice using electronic nose coupled with chemometrics. *Meas. J. Int. Meas. Confed.* **2020**, *157*, 107561–107571. [[CrossRef](#)]
170. Seesaard, T.; Thippakorn, C.; Kerdcharoen, T.; Kladsomboon, S. A hybrid electronic nose system for discrimination of pathogenic bacterial volatile compounds. *Anal. Methods* **2020**, *12*, 5671–5683. [[CrossRef](#)]
171. Güntner, A.T.; Koren, V.; Chikkadi, K.; Righettoni, M.; Pratsinis, S.E. E-Nose Sensing of Low-ppb Formaldehyde in Gas Mixtures at High Relative Humidity for Breath Screening of Lung Cancer? *ACS Sens.* **2016**, *1*, 528–535. [[CrossRef](#)]
172. Potyrailo, R.A. Multivariable Sensors for Ubiquitous Monitoring of Gases in the Era of Internet of Things and Industrial Internet. *Chem. Rev.* **2016**, *116*, 11877–11923. [[CrossRef](#)]

3.2 Modification of tungsten oxide by nanoscale interfaces

Tungsten oxide as an n-type semiconductor with wide band gap of 2.6 – 3.6 eV [32] is one of the most interesting MOXs for gas sensors. Previous investigations at *IMB-CNM (CSIC)* were devoted to the investigation of this material in its structured form and with Au, Pt, or Fe₂O₃ nanoparticles as surface modifiers [33] [34] [156] [38]. These modified tungsten oxide structures showed excellent results in the detection of various gases, such H₂, CO and NO₂, and VOCs, such as ethanol and toluene. Therefore, my research on this material was intended to fill the knowledge gap related to the influence of other surface modifier materials (inorganic and organic) on its gas sensing properties. In that line, this part of the thesis was focused on studying the properties of tungsten oxide-based sensors modified with another MOX (cerium oxide) and organo-functional molecule (APTES). Part of the experiments also explored the possibility of using photoactivation instead of thermoactivation for the operation of the sensors; a topic that was not investigated in the earlier studies at *IMB-CNM (CSIC)*. In this context, this section presents the results of two research articles. The first was published in the journal *Biosensors, MDPI* with the title **“Cerium oxide-tungsten oxide cores-shell nanowire-based microsensors sensitive to acetone”** [152], in which the sensors were operated using thermoactivated principles. The second article was published in the journal *Sensors and Actuators - B: Chemical* with the title **“UV-light activated APTES modified WO_{3-x} nanowires sensitive to ethanol and nitrogen dioxide”** [153], in which the sensors were operated using photoactivation principles. Additionally, the section also show the results of the *CDE 2018* conference proceedings article entitled **“Gas microsensors based on cerium oxide modified tungsten oxide nanowires”** [180], which contains the preliminary studies that paved the way for the findings of the two articles mentioned above.

3.2.1. Results

The first scientific contribution related to the cerium oxide-tungsten oxide core-shell nanowires describes the synthesis steps and the optimal deposition temperatures, solvents and precursors for the formation of this modified structured material using AACVD method. Characterization techniques (SEM, DRS, XRD, and XPS) confirmed the presence of both components, tungsten oxide and cerium oxide, in the synthesized structures. Gas tests demonstrated enhanced sensitivity to acetone for the core-shell structures compared to the non-modified materials (i.e., only tungsten oxide or cerium oxide). The sensors were also tested to acetone in humid ambient and it was demonstrated that the responses were declined as a consequence of the lowering of the baseline resistance due to humidity.

The second scientific contribution includes the set-up of conditions to modify the surface of tungsten oxide nanowires with (3-aminopropyl)triethoxysilane molecule (APTES@WO_{3-x}) and their performance upon reducing (acetone, ethanol, toluene, hydrogen, and carbon monoxide) and oxidizing (nitrogen dioxide) gases. These sensors were tested at room temperature, using UV-light activation. Characterization results (SEM and XRD) confirmed the deposition of crystalline nanostructured WO_{3-x} in the form of nanowires while analysis of the surface by XPS corroborated the silanization process, showing additional Si 2p, Si 2s, and N 1s core-level peaks in the spectra of the APTES modified samples. Gas sensing results revealed enhanced sensing properties including better reproducibility, stability, and sensitivity of the APTES@WO_{3-x} sensors

compared to the non-modified WO_{3-x} sensors, especially to ethanol and nitrogen dioxide as well as strong selectivity to ethanol among other reducing gases (acetone, toluene, hydrogen, and carbon monoxide). Further analysis of the role of APTES in the gas sensing properties of cerium oxide-tungsten oxide core-shell nanowires corroborated the enhancement of the response for the APTES modified structures, with respect to those without modification. Interestingly, cerium oxide-tungsten oxide core-shell nanowires showed further enhancement of the sensitivity (approximately four times) to nitrogen dioxide with respect to the APTES@ WO_{3-x} sensors. Additionally, the journal article describes in detail the gas sensing mechanism of UV-LED-activated APTES modified WO_{3-x} sensor.

3.2.2. Conclusions

In summary, the development of tungsten oxide sensors modified with inorganic (cerium oxide) and organic (APTES) modifiers was achieved. The results confirmed the positive influence of the material modification in the overall sensing properties of tungsten oxide by demonstrating an improved performance including better sensitivity, stability, and selectivity of the sensors with modified materials compared to those without modification. Cerium oxide-tungsten oxide core-shell nanowires without and with APTES modification showed the best response to acetone whereas APTES modified tungsten oxide nanowires showed the highest response to NO_2 and ethanol. Certainly, the modification of the structures with APTES demonstrated the possibility to achieve good performances of the sensors at room temperature using photoactivation principles. These results were discussed and attributed to the presence of the reactive amino group at the APTES@ WO_{3-x} sensors, which facilitated the reaction with the tested gases and the electron transfer to/from the MOX under UV-light excitation.

3.2.3. Journal Article 2

Cerium oxide-tungsten oxide core-shell nanowire-based microsensors sensitive to acetone, Tomić, M., Šetka, M., Chmela, O., Gràcia, I., Figueras, E., Cané, C., Vallejos, S., Biosensors, 2018, 8(4), 116, doi: 10.3390/bios8040116.

3.2.4. Journal Article 3




UV-light activated APTES modified WO_{3-x} nanowires sensitive to ethanol and nitrogen dioxide, Tomić, M., Fohlerova, Z., Gràcia, I., Figueras, E., Cané, C., Vallejos, S., Sensors and Actuators, B: Chemical, 2021, 328, 129046, doi: 10.1016/j.snb.2020.129046.

3.2.5. Conference Paper 1

Gas microsensors based on cerium oxide modified tungsten oxide nanowires, Tomić M., Gràcia I., Salleras M., Figueras E., Cané C., Vallejos S., Spanish Conference on Electron Devices (CDE), Salamanca, Spain, 2018, doi: 10.1109/CDE.2018.8597067.

Article

Cerium Oxide-Tungsten Oxide Core-Shell Nanowire-Based Microsensors Sensitive to Acetone

Milena Tomić ¹, Milena Šetka ², Ondřej Chmela ² , Isabel Gràcia ¹ , Eduard Figueras ¹, Carles Cané ¹ and Stella Vallejos ^{1,2,*} 

¹ Instituto de Microelectrónica de Barcelona (IMB-CNM, CSIC), Campus UAB, 08193 Bellaterra, Spain; milena.tomic@imb-cnm.csic.es (M.T.); isabel.gracia@imb-cnm.csic.es (I.G.); Eduard.Figueras@imb-cnm.csic.es (E.F.); carles.cane@imb-cnm.csic.es (C.C.)

² CEITEC-Central European Institute of Technology, Brno University of Technology, 61200 Brno, Czech Republic; milena.setka@ceitec.vutbr.cz (M.Š.); Ondrej.Chmela@ceitec.vutbr.cz (O.C.)

* Correspondence: stella.vallejos@imb-cnm.csic.es; Tel.: +34-935-947700

Received: 31 October 2018; Accepted: 19 November 2018; Published: 23 November 2018



Abstract: Gas sensitive cerium oxide-tungsten oxide core-shell nanowires are synthesized and integrated directly into micromachined platforms via aerosol assisted chemical vapor deposition. Tests to various volatile organic compounds (acetone, ethanol, and toluene) involved in early disease diagnosis demonstrate enhanced sensitivity to acetone for the core-shell structures in contrast to the non-modified materials (i.e., only tungsten oxide or cerium oxide). This is attributed to the high density of oxygen vacancy defects at the shell, as well as the formation of heterojunctions at the core-shell interface, which provide the modified nanowires with ‘extra’ chemical and electronic sensitization as compared to the non-modified materials.

Keywords: gas sensors; volatile organic compounds (VOCs); acetone; metal oxides; heterojunctions

1. Introduction

Odor (gas, vapor, aroma) detection systems are of high interest as they are non-invasive key-enabling technologies, which are relevant in both traditional (e.g., environment, industry) and innovative applications such as the early detection of diseases from exhaled breath [1,2]. The literature related to exhaled breath as bio information for disease diagnosis has shown previously that human breath contains more than two hundred different gases and volatile organic compounds (VOCs) species that vary from person to person [3]. In the midst of a wide range of analytes, acetone, toluene, and ethanol are within the most relevant VOCs that are typically involved in various diseases, including diabetes and cancer. Thus, for instance, high acetone concentrations (~21 ppm) have been identified in the exhaled breath of diabetic patients, as compared to healthy patients (~2.7 ppm) and oppositely to patients with lung cancer, who showed lower acetone concentrations (~0.9 ppm). Similarly, the ethanol concentration in breath has shown an increase (~2.1 ppm) in patients with lung/breast cancer and diabetes with respect to healthy patients (~0.2 ppm) [4–6].

Currently, the analysis of breath is still an emerging diagnosis technology that uses large and expensive laboratory equipment such as gas-chromatograph, ion-mobility and/or mass spectrometers [7]. In the future, however, miniaturized, portable, and wearable systems with enhanced functionality (sensitivity, selectivity, and stability) and high autonomy at a low cost could substitute this equipment; a fact that demands the innovation of current odor detection systems. In this context, metal oxide (MOX) gas sensors based on the chemoresistive principle represent an alternative to bulky equipment providing simpler architecture and fabrication processes compatible with ‘standard’ MEMS and CMOS technologies [2]. Chemoresistive gas sensors devices generally consist of a transducing

platform (microscale) and a gas sensitive MOX optimized to interact with specific groups of gaseous or vapor analytes. However, among the diverse issues that may potentially be addressed to improve the functionality of these monitoring systems (e.g., optimization of sensing modes and control electronics or the integration of smart systems with new micro/nano fabrication concepts), the focus on nanoscaled sensitive materials is still essential to radically improve their performance. Thus, several studies have demonstrated that MOXs modified with second-phase constituents, either nanosized noble metals or other MOXs, have a positive effect on the sensing properties of both the host MOX and the second-phase constituent, particularly when the size of both materials is within the Debye length of the surface (typically on the order of 2–100 nm) [8]. Moreover, recently, it has been pointed out that the modification of a MOX with noble metals or other MOXs allows for the formation of nanoscale heterojunctions and, in turn, sensing mechanisms dominated not only by the surface, but also the interface, which has proved to improve the sensing properties of these materials [9].

In recent years, tungsten oxide has demonstrated high potential in gas sensing among traditional gas sensitive MOXs such as SnO₂ and ZnO (Figure 1), showing a strong sensitivity to oxidizing gases including nitrogen dioxide and ozone [10]. Moreover, the modification of tungsten oxide with second-phase constituents such as platinum, copper oxide, or iron oxide has shown an improved sensitivity and selectivity to reducing species including hydrogen [11], hydrogen sulfide [12] or toluene [13], respectively. As far as cerium oxide is concerned, the peculiarity that makes this oxide also attractive in gas sensors reside overall in the defect sites caused by the valence state changes between Ce⁴⁺ and Ce³⁺, which considerably alter the concentration of oxygen vacancies, and provides a good redox behavior and catalytic activity [14–16]. However, and despite these favorable surface properties the use of cerium oxide in gas sensing is still infrequent (Figure 1) and its sensing properties upon VOCs have not been fully explored in the literature related to gas sensors.

Optimized gas sensitive MOXs need synthetic methods able to produce well defined and even structures. Additive (bottom-up) synthetic methods, as opposed to subtractive (top-down) methods, are ideal for this task and industrially attractive as they provide the ability to generate films in a continuous mode with high purities and high throughput. Aerosol assisted (AA) chemical vapor deposition (CVD) is a versatile additive synthetic method used previously to obtain non-modified (e.g., WO₃) or metal/MOX modified MOXs (e.g., Pt/WO₃, Fe₂O₃/WO₃) [11,13]. Additionally, recently, the AACVD of cerium oxide from Ce (dbm)₄ has been proved as a strategy to overcome the low volatility of traditional cerium CVD precursors [17]. In this work, however, we achieve the AACVD of cerium oxide from Ce (acac)₃ precursor and use this route to synthesize cerium oxide-tungsten oxide core-shell nanowires in a two-step process performed directly on silicon-based micromachined platforms. In addition, we validate the sensing properties of these systems to acetone, and other relevant VOCs monitored in early disease diagnosis.

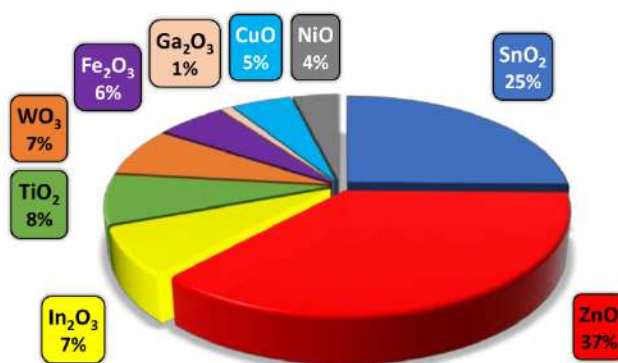


Figure 1. A survey of the most applicable gas sensitive MOXs reported in the literature (Web of Science database from 1998 to 2018).

2. Materials and Methods

Tungsten oxide (non-modified nanowires), cerium oxide (non-modified porous films), and cerium oxide-tungsten oxide core-shell nanowires were grown directly onto micromachined transducing platforms (Figure 2a) [18] using the AACVD system described previously [19]. AACVD is a variant of the conventional CVD technique, which uses aerosol to transport dissolved precursors to a heated reaction zone. Here, the non-modified tungsten oxide nanowires films were deposited at 350 °C from a solution of tungsten hexacarbonyl (30 mg, $W(CO)_6$, Sigma-Aldrich, St. Louis, MO, USA, $\geq 97\%$) and methanol (5 mL Sigma-Aldrich, $\geq 99.6\%$), whereas the non-modified cerium oxide films were deposited at 500 °C from cerium (III) acetylacetonate hydrate (28 mg, $Ce(acac)_3 \cdot xH_2O$, Sigma-Aldrich) dissolved in methanol (2 ml, Sigma-Aldrich). On the other hand, the cerium oxide-tungsten oxide core-shell nanowires were achieved using a two-step AACVD process [20], in which the tungsten oxide nanowire cores were deposited at 350 °C in the first step and the cerium oxide shell film at 500 °C in the second step employing the same protocols described above for the non-modified films. Finally, the non-modified and modified films were annealed at 500 °C in air.

The morphology of the films was examined using scanning electron microscopy (SEM— Auriga Series, 3 KV, Carl Zeiss, Jena, Germany) and the phase using X-ray Diffraction (XRD—Bruker-AXS, model A25 D8 Discover, Cu $K\alpha$ radiation, Billerica, MA, USA). Further analysis of the material was carried out using X-ray photoelectron spectroscopy (XPS—Kratos Axis Supra with monochromatic Al $K\alpha$ X-ray radiation, an emission current of 15 mA and hybrid lens mode, Manchester, UK). The survey and detailed spectra were measured using pass energy of 80 eV and 20 eV, respectively. The band gap of the films was estimated by measuring the diffuse reflectance (AvaSpec-UV/VIS/NIR, Avantes, Apeldoorn, the Netherlands) of the films and performing Kubelka–Munk transformation.

The microsensors were tested in a continuous flow test chamber provided with mass flow controllers that allow the mixture of dry/humid air and calibrated gaseous analytes (ethanol, acetone, toluene, carbon monoxide and hydrogen purchased from Praxair, Danbury, CT, USA) to obtain the desired concentration. To have a proper control of the relative humidity (RH) inside the gas test chamber, an evaluation kit (EK-H4, Sensirion AG, Stäfa, Switzerland) with a humidity sensor was also used. The dc resistance measurements of the microsensor were achieved in a system provided with an electrometer (Keithley 6517A, Cleveland, OH, USA) and a multimeter (Keithley 2700, Cleveland, OH, USA) with switch system to monitor various sensors simultaneously. More details of the characterization systems were reported elsewhere [18]. The sensor response was defined as R_a/R_g , where R_a and R_g are the resistance in dry/humid air and the resistance after 600 s of analyte exposure, respectively. The sensors were tested for a period of one month during which each sensor accumulated 180 h of operation under the different conditions (analytes, temperatures, humidity) employed.

3. Results

3.1. Gas Sensitive Films

SEM imaging of the microsensors after AACVD of the gas sensitive structures showed uniform deposited films that covered the electrodes integrated into the micromachined membrane (Figure 2a). A close view of the non-modified tungsten oxide wires (W) showed bare and even surfaces as noticed previously for other AACVD tungsten oxide structures [21]. In contrast, a close view of the cerium oxide-tungsten oxide core-shell wires (Ce/W) displayed the presence of a rugged thin film covering the wire surface (Figure 2b,c), similarly to that observed when depositing non-modified cerium-based films (Ce) from a $Ce(acac)_3$ methanolic solution via AACVD (Figure 2d).

Generally, AACVD of the non-modified (W and Ce) and modified (Ce/W) films showed a good adherence to the substrate, with the wire-like morphology films (i.e., W and Ce/W) forming a mat-like network of non-aligned nanowires with diameters below 100 nm, and the particle-like morphology films (i.e., Ce) displaying a porous surface composed of grains with diameters below 40 nm. The as-deposited non-modified W films displayed a bluish color, whereas the Ce/W films

displayed a dark yellowish to dark green color, similarly to the color observed on the *Ce* films. However, after annealing the non-modified *W* and modified *Ce/W* films became whitish and pale yellowish, respectively. Figure 3 displays the diffuse reflectance spectra of the films deposited without modification (i.e., only tungsten oxide or only cerium oxide) via AACVD. These measurements and their corresponding Kubelka–Munk transformation indicated optical band gaps at ~ 3.2 eV for the tungsten oxide films and ~ 3.1 eV for the cerium oxide films, in agreement with the literature band gap values of tungsten oxide (2.6–3.7 eV) [22] and cerium oxide (2.7–3.4 eV) [15].

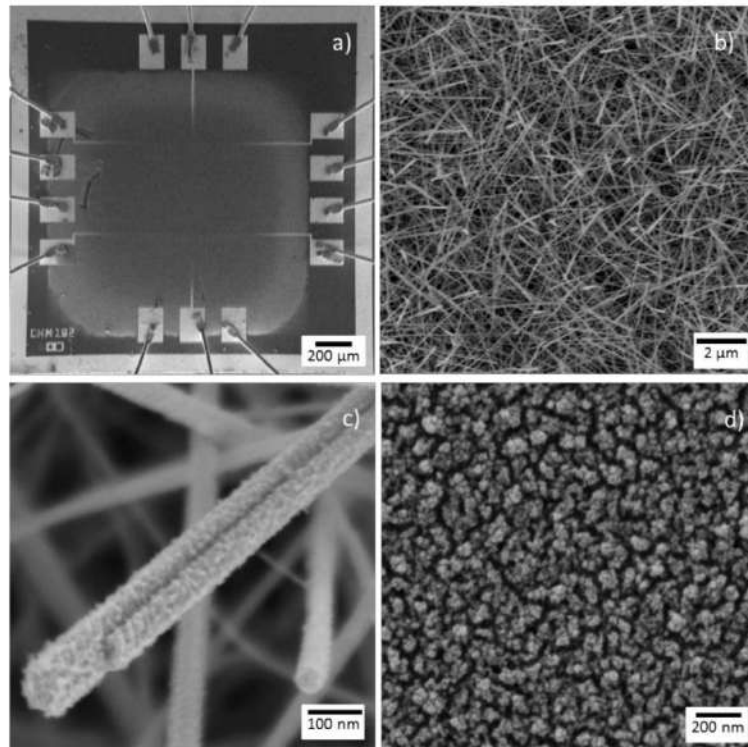


Figure 2. The SEM imaging of a (a) gas sensor device, the *Ce/W* nanowires at (b) low and (c) high magnification, and (d) the non-modified *Ce* films integrated on the micromachined membrane.

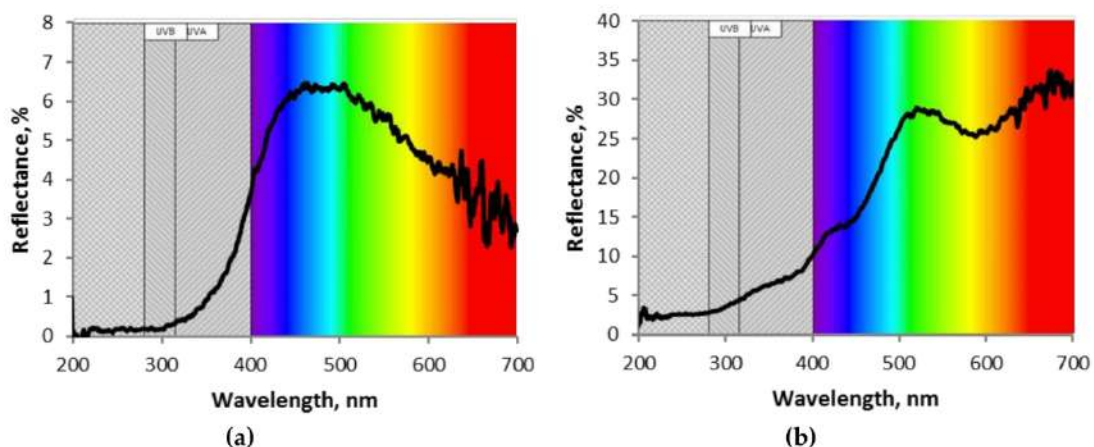


Figure 3. The diffuse reflectance spectra of the aerosol assisted chemical vapor deposited (a) tungsten oxide and (b) cerium oxide films without modification.

XRD analysis of the films revealed the presence of a monoclinic-phase (International Centre of Diffraction Data–ICDD card no. 72-0677) in the *W* and *Ce/W* films with greatly enhanced intensity (preferred orientation) in the [001] direction, consistent with our previous results for AACVD of tungsten oxide [13]. A weak diffraction peak was also noticed at 47.8° 2θ for the *Ce/W* films

(Figure 4). This diffraction peak is in line with the pattern identified on the non-modified Ce based films corresponding to cerium dioxide (Crystallography Open Database–COD ID card no. 7217887).

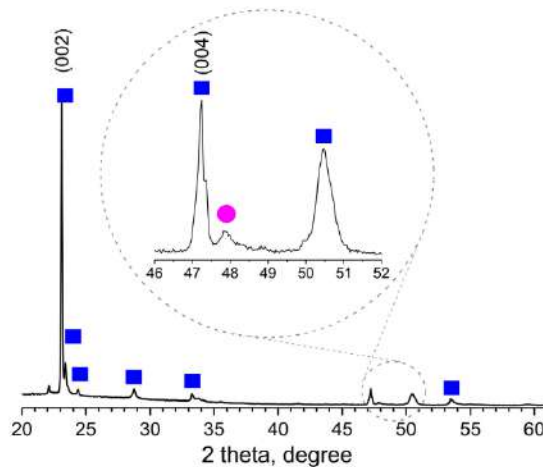


Figure 4. The XRD pattern of the Ce/W films. The diffraction peak at 47.8° 2θ (full pink circle) corresponds to cerium dioxide cubic phase (P1), COD ID card no. 7217887, the rest of the diffraction peaks (full blue squares) in the data can be indexed to a monoclinic phase (P21/n), ICDD card no. 72-0677, with only peaks of greatly enhanced intensity (preferred orientation), specifically indexed.

The XPS of both W and Ce/W films exhibited typical W 4f_{7/2}, W 4f_{5/2} and W 5p_{3/2} XPS core level peaks (Figure 5a), consistent with the literature and previous tungsten oxide nanowires synthesized via AACVD [13]. XPS narrow scan spectra of the Ce 3d core level peaks at the Ce and Ce/W wires displayed multiplet splitting between 875 and 920 eV in agreement with the standard binding energies for Ce 3d peaks and partially reduced cerium oxide [23,24]. Figure 5b displays the experimental data and the corresponding deconvolution of the Ce 3d spectrum recorded on the Ce/W wires. The peaks v , v'' and v''' are attributed to the main and satellite peaks of the Ce⁴⁺ state, whereas the peaks v_0 , v' correspond to the peaks of Ce³⁺ state. The relative contribution of Ce⁴⁺ and Ce³⁺ species at the Ce/W films was estimated from the ratio of integrated Ce⁴⁺ peaks to the total Ce⁴⁺ and Ce³⁺ peaks, finding a value of ~42% for Ce⁴⁺ and 58% Ce³⁺ species. The relatively high amount of Ce³⁺ species indicate a charge imbalance with oxygen vacancy defects and an unsaturated chemical bond at the Ce/W film suggesting a high redox nature of the film.

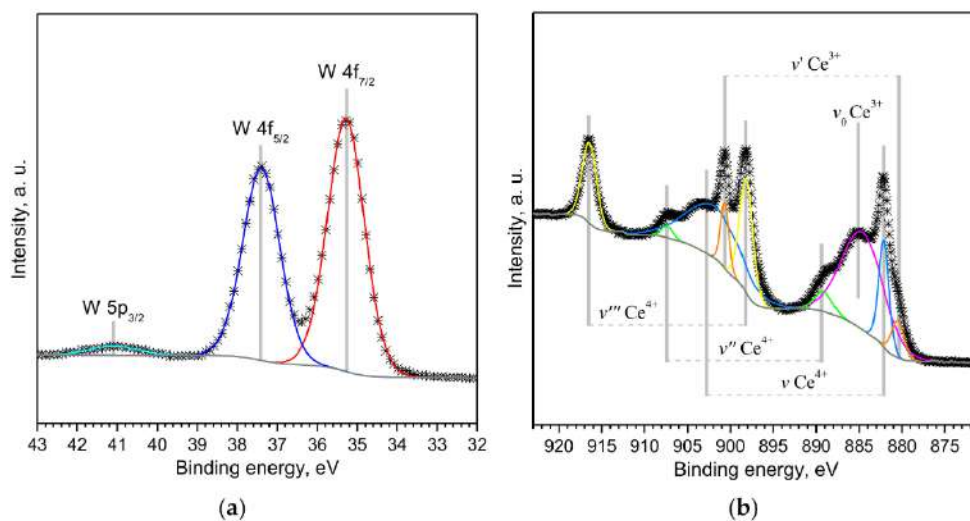


Figure 5. (a) The W 4f and (b) Ce 3d spectra recorded on the cerium-modified wires. The W 4f spectrum recorded on the non-modified tungsten oxide wires showed similar characteristics.

Linear extrapolation of the valence band (VB) leading edge on the XPS spectra recorded on the *Ce/W* film near the Fermi level ($E_B = 0$) indicates the simultaneous presence of both cerium oxide and tungsten oxide induced VB (Figure 6a). One can notice that the VB onset for cerium oxide occurs ~ 0.5 eV (ΔE_V) above the VB onset for tungsten oxide. Therefore, according to the band gap estimated by diffuse reflectance for each non-modified material in the position of the conduction band (CB) of cerium oxide is ~ 0.4 eV (ΔE_C) above the CB of tungsten oxide, consequently suggesting a staggered type of heterojunction at the interface of the *Ce/W* core-shell structures (Figure 6b). In contrast, the linear extrapolation of VB leading edge on the XPS spectra of the *W* and *Ce* films showed only the presence of tungsten oxide induced VB at 2.9 eV in agreement with previous reports [13].

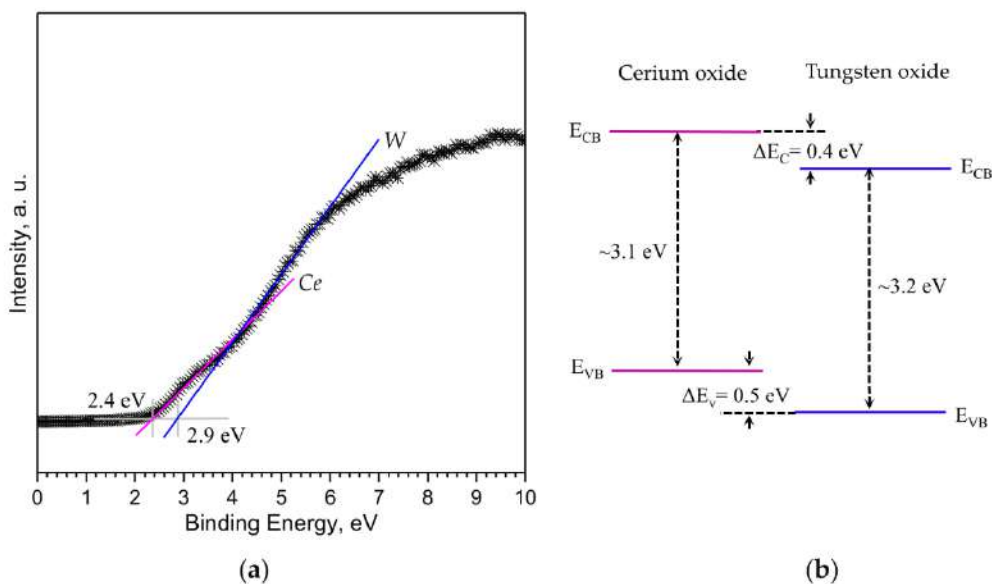


Figure 6. (a) The XPS valence band spectra of the cerium-modified tungsten oxide nanowires, and (b) schematic of the estimated energy level diagram at the interface. E_{CB} and E_{VB} represent the conduction band minimum and the valence band maximum (not to scale).

In brief, the characterization of the films deposited via AACVD demonstrates the formation of crystalline cerium oxide-tungsten oxide core-shell wires with a relatively high amount of Ce^{3+} species at the surface and the presence of the characteristic valence band onsets for cerium oxide and tungsten oxide.

3.2. Gas Sensing Tests

Overall, the sensors displayed an n-type response with a good reproducibility to the target gaseous analytes (acetone, ethanol, toluene, carbon monoxide, and hydrogen) and relatively low variations of the baseline resistance along the testing period. Gas sensing tests of the microsensors were carried out at various operating temperatures from 150 °C to 400 °C by DC resistance measurements of the films integrated via AACVD. These tests proved a better sensor functionality to 80 ppm of acetone at 300 °C for the sensors based on *W* and *Ce/W* films and 400 °C for the sensors based on *Ce* films. As the *Ce* based sensors registered comparatively higher baseline resistances (~ 40 G Ω at 400 °C) than *W* (13 k Ω at 300 °C) and *Ce/W* (65 k Ω at 300 °C) sensors, additionally requiring higher temperatures to achieve the maximum responses (e.g., response to acetone 4.9 at 400 °C for the *Ce* sensors and 5.6 at 300 °C for the *Ce/W* sensors), further analyses related to the analyte concentration and humidity dependence of the sensor response were performed only for the *W* and *Ce/W* based sensors at 300 °C.

Figure 7a displays the sensor response to 80 ppm of each analyte and type of sensor at 300 °C. These results show the improved responses registered for the *Ce/W* sensors, as opposed to the *W* sensors, as well as the higher responses to acetone compared to the rest of the analytes. Results in

Figure 7a also suggests an improved selectivity for the *Ce/W* films with lower cross-responses among the analytes; for instance, the difference of the response to acetone in relation to ethanol is 1.6 for the *Ce/W* films and 1 for the *W* films. The low cross response registered on the *Ce/W* sensor is noticed in more detail in Figure 7b, in which is displayed the analysis of variance (ANOVA) realized for a data set comprising four replicates for each type of sensor and analyte. Additionally, the principal component (PC) analysis performed using replicated responses of both sensors (i.e., *W* and *Ce/W*) to each analyte is represented in Figure 8. These results, specifically the scores, which correspond to the projections of the measurements in an orthogonal base of PCs, indicate the possibility to improve the discrimination of the analytes by using an array of *W* and *Ce/W* based sensors.

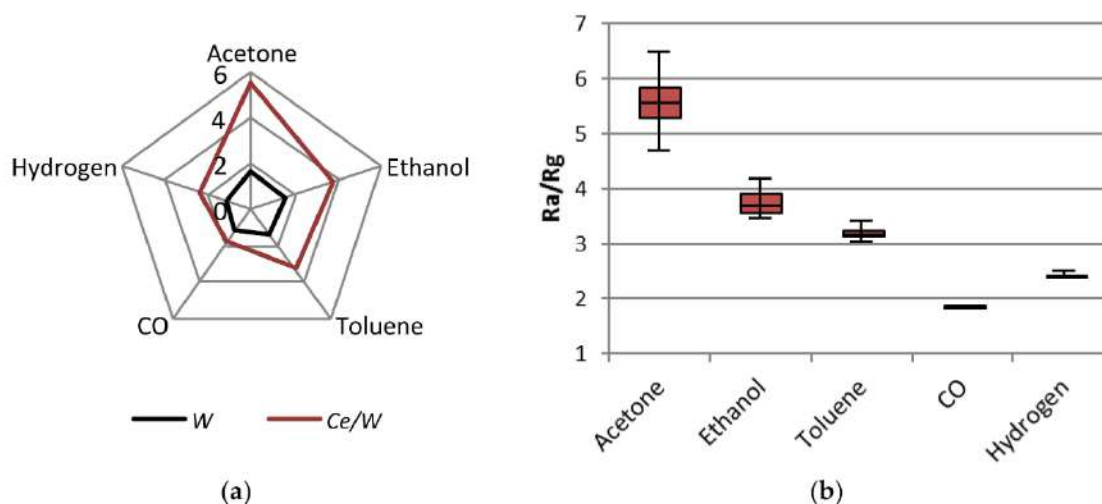


Figure 7. (a) The radial plot of the sensor response to 80 ppm of acetone, ethanol, toluene, carbon monoxide, and hydrogen using the *W* and *Ce/W* based sensors. (b) Box plots of the sensor response to each analyte recorded by the *Ce/W* based sensors. Each box displays the median and upper and lower quartiles (first and third) of the respective distribution. Box whiskers indicate the dispersion of the measurements.

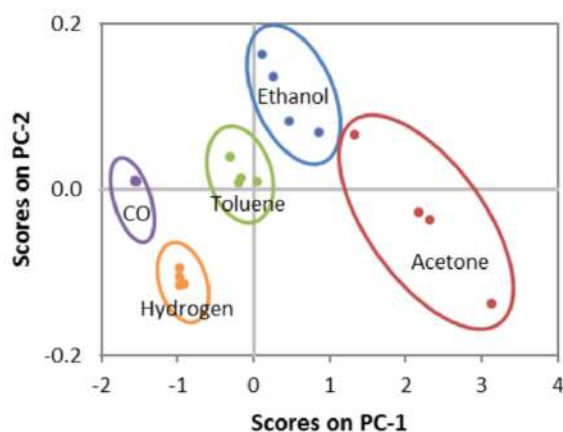


Figure 8. Principal component analysis applied to discriminate the tested VOCs by using an array of non-modified tungsten oxide wires and the cerium oxide-tungsten oxide core-shell wire-based sensors.

Further tests of the sensors to various concentrations of each analyte showed direct proportional changes in the response to concentration. An example of the response registered with both types of sensors to acetone is shown in Figure 9. For these conditions, the limit of detection corresponding to three times the noise level [25] was estimated at 1 ppm for *W* and 0.2 ppm for *Ce/W* sensors. Overall, the changes respect to concentration for the *W* sensors proved a lower sensitivity compared to the *W/Ce* sensors, which demonstrates a better sensitivity to the analytes. The sensitivity (*S*), defined as the

ratio between the change in response (ΔR) and a fixed change in analyte concentration (ΔC) for each sensor and analyte, was registered to be nearly five times higher for acetone and three times higher for ethanol when using the cerium-modified sensors (found $\Delta R/\Delta C_{\text{acetone}}$ for *W* sensors 0.8%, *Ce/W* sensors 4.7%; $\Delta R/\Delta C_{\text{ethanol}}$ for *W* sensors 0.8%, *Ce/W* sensors 2.2%).

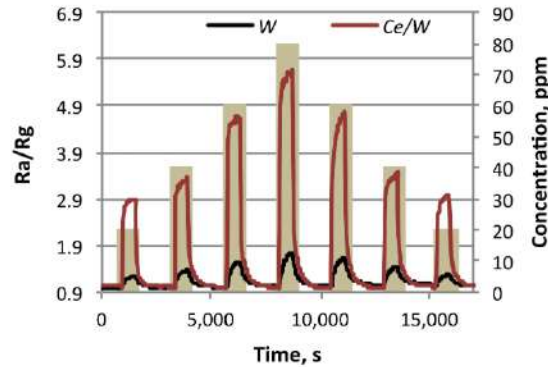


Figure 9. The sensor response to various concentrations (from 20 to 80 ppm) of acetone recorded with the *W* and *Ce/W* based sensors.

Additional tests of the sensors in a controlled humid ambient (10 and 20% RH), consistent with those reported after preconditioning the relative humidity in breath samples [26], registered lower sensor response to the analytes. The loss of response in humid ambient is a consequence of the proportional drop of the baseline resistance to relative humidity. This proportional change is usually present in metal oxides exposed to humidity due to the formation of hydroxyl groups at temperatures above 100 °C [18]. Currently, most of the strategies to attenuate further the humidity interference from the material point of view are connected with the fine tune of the MOX morphology [27] and/or the incorporation of humidity-insensitive additives (e.g., NiO [28], CuO [12], or SiO₂ [29]). Figure 10 displays the typical resistance changes for the *W* and *Ce/W* sensors to each mixture of RH and acetone tested and their replicates.

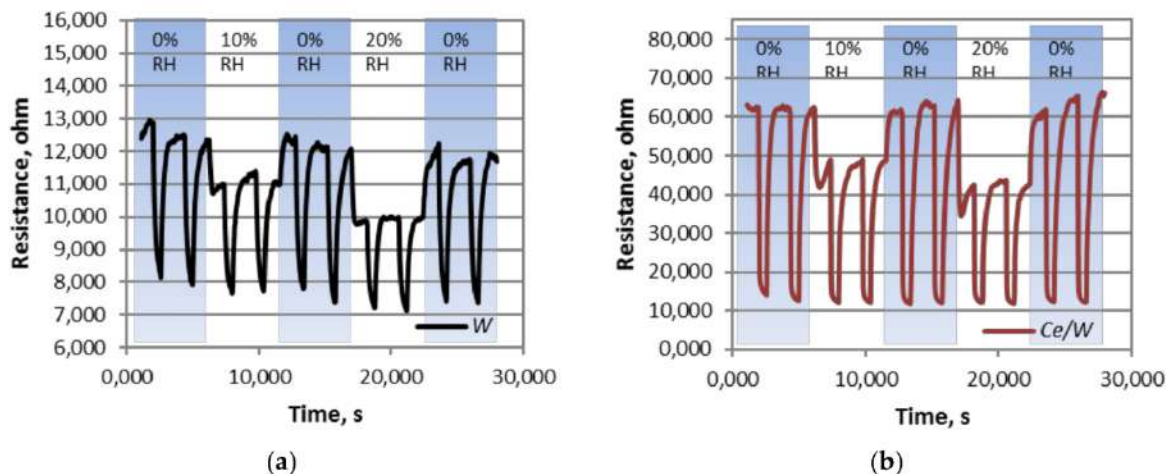


Figure 10. The resistance changes registered for (a) *W* and (b) *Ce/W* to acetone in dry and humid ambient (RH: relative humidity).

Previous reports in the literature related to acetone sensing using modified tungsten oxide films (with Au, Pd, AuPd) suggest the functionality of tungsten oxide at 300 °C for relatively high acetone concentrations (200–1000 ppm) [30]. Further tests, also performed on tungsten oxide, modified with TiO₂ [31] or Si [32] show the functionality of the sensors at similar (30 ppm) or lower (100–600 ppb) acetone concentrations, respectively, although requiring higher operating temperatures (400–500 °C),

than those needed in this work. On the other hand, the use of cerium oxide as the gas sensitive element has been rarely reported in the literature, with the performance of this material having indicated the potential for sensing VOCs including acetone [33,34]. In general, the responses of the above mentioned non-miniaturized acetone sensors in the literature [30–34] are in the same order of magnitude than our micromachined sensors based on the cerium oxide-tungsten oxide core-shell wires, which suggests the viability of sensor miniaturization without losing the sensitivity of the system when optimizing the sensitive material. In addition, the good reproducibility of the responses during the testing period and the analysis (SEM, XRD) of the samples after the gas sensing experiments (which showed unchanged properties of the material with respect to the properties recorded initially) indicated a good stability of the sensors.

The enhanced functionality recorded on the *Ce/W* sensors is connected with the formation of heterojunctions at the interface of the tungsten oxide wires and the cerium oxide porous films. These heterojunctions are present due to the different band energies in both MOXs (Figure 6b), which facilitate electron migration from the cerium oxide film to the tungsten oxide wire. Generally, as oxygen is preadsorbed at the sensitive film during air exposure, the surface depletion region (L_D) and, in turn, the conduction channel along the wires are narrowed, which leads to lower conductivity along the film (Figure 11a). Alternatively, when a reducing analyte (i.e., VOCs) reacts with the preadsorbed oxygen, electrons are released back to the conduction band, and the depth of the surface depletion is narrowed, increasing the conduction channel along the wire and, in turn, its conductivity (Figure 11b). This mechanism controlled by the pre-adsorbed oxygen is similar for the non-modified and modified films, with the peculiarity that the charge transfer process (electron migration) occurring at the junction of the cerium oxide film and tungsten oxide wire provides larger electron density to the wires (accumulation layer) in the pre-adsorption cycle (as opposed to the non-modified *W* or *Ce* films). This allows for larger changes of the depletion layer and an enhanced modulation of the wire conduction channel, which is reflected finally on the sensor response.

In the same line, the lowering of the baseline resistance upon humidity implies a diminution of the chemically active oxygen species at the surface and, in turn, a narrow surface depletion in the air (pre-adsorption). Thus, as the conduction channel in humid ambient is wider than in dry ambient (Figure 11), the conduction changes induced by the reducing gas are less significant, and thus the sensor response is as well.

Summarizing, the gas sensing tests showed improved acetone sensing properties for *Ce/W* based microsensors showing a higher response, and better sensitivity and selectivity to the analytes tested in relation to the *W* or *Ce* based microsensors.



Figure 11. The schematic view of the heterojunction formed at the surface of the cerium oxide (*Ce*) core-shell tungsten oxide (*W*) wires and the possible mechanism (a) after exposure to air and (b) reducing gases such as acetone. L_D is the Debye length or depth of the depletion region from the surface (not at scale).

4. Conclusions

These results demonstrate the formation of cerium oxide-tungsten oxide core-shell nanowires with improved response and sensitivity to acetone as compared to non-modified tungsten oxide wires or cerium oxide porous films. Tests of these sensors to acetone in humid ambient showed a drop of the responses as a consequence of the lowering of the baseline resistance due to humidity. Principal

component analysis of the responses obtained for each analytes using an array the non-modified and modified sensitive films indicated the possibility to enhance the selectivity of the microsensors by improving the discrimination of analytes. The improved sensitivity is attributed to the formation of heterojunctions at the interface of both oxides (i.e., tungsten oxide and cerium oxide) which leads to an 'extra' chemical and electronic sensitization to the modified films as compared to the non-modified films.

Author Contributions: M.T.; synthesis and integration of gas sensitive films, M.S. and S.V.; XPS analysis, M.T. and I.G. diffuse reflectance tests, I.G., E.F. and C.C.; Si-based micromachined platforms; I.G., E.F. and O.C. gas sensing characterization, M.T., M.S. and O.C., literature search, M.T., I.G. and S.V.; writing review and editing, S.V. and C.C.; funding acquisition.

Funding: This work has been supported by the Czech Science Foundation (GAČR) via Grant no. 17-16531S, and the Spanish Ministry of Science and Innovation via the Ramón y Cajal Programme and Grants TEC2015-74329-JIN-(AEI/FEDER,EU) and TEC2016-79898-C6-(AEI/FEDER,EU). This research has used the Spanish ICTS Network MICRONANOFABS (partially funded by MINECO). CEITEC Nano Research Infrastructure (IDL2015041, MEYS CR, 2016–2019) is also acknowledged.

Conflicts of Interest: The authors declare no conflict of interest.

References

1. Brattoli, M.; de Gennaro, G.; de Pinto, V.; Loiotile, A.D.; Lovascio, S.; Penza, M. Odour detection methods: Olfactometry and chemical sensors. *Sensors* **2011**, *11*, 5290–5322. [[CrossRef](#)] [[PubMed](#)]
2. Di Natale, C.; Paolesse, R.; Martinelli, E.; Capuano, R. Solid-state gas sensors for breath analysis: A review. *Anal. Chim. Acta* **2014**, *824*, 1–17. [[CrossRef](#)] [[PubMed](#)]
3. Phillips, M.; Herrera, J.; Krishnan, S.; Zain, M.; Greenberg, J.; Cataneo, R.N. Variation in volatile organic compounds in the breath of normal humans. *J. Chromatogr. B Biomed. Sci. Appl.* **1999**, *729*, 75–88. [[CrossRef](#)]
4. Das, S.; Pal, S.; Mitra, M. Significance of Exhaled Breath Test in Clinical Diagnosis: A Special Focus on the Detection of Diabetes Mellitus. *J. Med. Biol. Eng.* **2016**, *36*, 605–624. [[CrossRef](#)] [[PubMed](#)]
5. Dent, A.G.; Sutedja, T.G.; Zimmerman, P.V. Exhaled breath analysis for lung cancer. *J. Thorac. Dis.* **2013**, *5*, S540–S550. [[CrossRef](#)] [[PubMed](#)]
6. Li, J.; Peng, Y.; Liu, Y.; Li, W.; Jin, Y.; Tang, Z.; Duan, Y. Investigation of potential breath biomarkers for the early diagnosis of breast cancer using gas chromatography–mass spectrometry. *Clin. Chim. Acta* **2014**, *436*, 59–67. [[CrossRef](#)] [[PubMed](#)]
7. Van de Kant, K.D.; van der Sande, L.J.; Jöbsis, Q.; van Schayck, O.C.; Dompeling, E. Clinical use of exhaled volatile organic compounds in pulmonary diseases: A systematic review. *Respir. Res.* **2012**, *13*. [[CrossRef](#)] [[PubMed](#)]
8. Yamazoe, N. New approaches for improving semiconductor gas sensors. *Sens. Actuator B Chem.* **1991**, *5*, 7–19. [[CrossRef](#)]
9. Miller, D.R.; Akbar, S.A.; Morris, P.A. Nanoscale metal oxide-based heterojunctions for gas sensing: A review. *Sens. Actuator B Chem.* **2014**, *204*, 250–272. [[CrossRef](#)]
10. Vallejos, S.; Khatko, V.; Calderer, J.; Gracia, I.; Canè, C.; Llobet, E.; Correig, X. Micro-machined WO₃-based sensors selective to oxidizing gases. *Sens. Actuator B Chem.* **2008**, *132*, 209–215. [[CrossRef](#)]
11. Vallejos, S.; Umek, P.; Stoycheva, T.; Annanouch, F.; Llobet, E.; Correig, X.; De Marco, P.; Bittencourt, C.; Blackman, C. Single-step deposition of Au- and Pt-nanoparticle-functionalized tungsten oxide nanoneedles synthesized via aerosol-assisted CVD, and used for fabrication of selective gas microsensor arrays. *Adv. Funct. Mater.* **2013**, *23*, 1313–1322. [[CrossRef](#)]
12. Annanouch, F.E.; Haddi, Z.; Vallejos, S.; Umek, P.; Guttman, P.; Bittencourt, C.; Llobet, E. Aerosol-assisted CVD-grown WO₃ nanoneedles decorated with copper oxide nanoparticles for the selective and humidity-resilient detection of H₂S. *ACS Appl. Mater. Interfaces* **2015**, *7*, 6842–6851. [[CrossRef](#)] [[PubMed](#)]
13. Vallejos, S.; Gràcia, I.; Figueras, E.; Canè, C. Nanoscale heterostructures based on Fe₂O₃@WO_{3-x} nanoneedles and their direct integration into flexible transducing platforms for toluene sensing. *ACS Appl. Mater. Interfaces* **2015**, *7*, 18638–18649. [[CrossRef](#)] [[PubMed](#)]

14. Ma, R.; Jahurul Islam, M.; Amaranatha Reddy, D.; Kim, T.K. Transformation of CeO₂ into a mixed phase CeO₂/Ce₂O₃ nanohybrid by liquid phase pulsed laser ablation for enhanced photocatalytic activity through Z-scheme pattern. *Ceram. Int.* **2016**, *42*, 18495–18502. [[CrossRef](#)]
15. Montini, T.; Melchionna, M.; Monai, M.; Fornasiero, P. Fundamentals and Catalytic Applications of CeO₂-Based Materials. *Chem. Rev.* **2016**, *116*, 5987–6041. [[CrossRef](#)] [[PubMed](#)]
16. Magesh, G.; Viswanathan, B.; Viswanath, R.P.; Varadarajan, T.K. Photocatalytic behavior of CeO₂-TiO₂ system for the degradation of methylene blue. *Indian J. Chem. Sect. A* **2009**, *48A*, 480–488.
17. Evans, M.; Di Maggio, F.; Blackman, C.; Sankar, G. AACVD synthesis of catalytic gold nanoparticle-modified cerium(IV) oxide thin films. *Phys. Status Solidi C* **2015**, *12*, 996–1000. [[CrossRef](#)]
18. Vallejos, S.; Gràcia, I.; Chmela, O.; Figueras, E.; Hubálek, J.; Cané, C. Chemoresistive micromachined gas sensors based on functionalized metal oxide nanowires: Performance and reliability. *Sens. Actuator B Chem.* **2016**, *235*, 525–534. [[CrossRef](#)]
19. Vallejos, S.; Pizúrová, N.; Čechal, J.; Gràcia, I.; Cané, C. Aerosol-assisted chemical vapor deposition of metal oxide structures: Zinc oxide rods. *J. Vis. Exp.* **2017**, *127*, 56127. [[CrossRef](#)] [[PubMed](#)]
20. Annanouch, F.E.; Haddi, Z.; Ling, M.; Di Maggio, F.; Vallejos, S.; Vilic, T.; Zhu, Y.; Shujah, T.; Umek, P.; Bittencourt, C.; et al. Aerosol-Assisted CVD-Grown PdO Nanoparticle-Decorated Tungsten Oxide Nanoneedles Extremely Sensitive and Selective to Hydrogen. *ACS Appl. Mater. Interfaces* **2016**, *8*, 10413–10421. [[CrossRef](#)] [[PubMed](#)]
21. Vallejos, S.; Gràcia, I.; Figueras, E.; Cané, C. Catalyst-free vapor-phase method for direct integration of gas sensing nanostructures with polymeric transducing platforms. *J. Nanomaterials* **2014**, *2014*. [[CrossRef](#)]
22. Watanabe, H.; Fujikata, K.; Oaki, Y.; Imai, H. Band-gap expansion of tungsten oxide quantum dots synthesized in sub-nano porous silica. *Chem. Comm.* **2013**, *49*, 8477–8479. [[CrossRef](#)] [[PubMed](#)]
23. Mysliveček, J.; Matolín, V.; Matolínová, I. Heteroepitaxy of Cerium Oxide Thin Films on Cu(111). *Materials* **2015**, *8*, 6346–6359. [[CrossRef](#)] [[PubMed](#)]
24. Naganuma, T.; Traversa, E. Stability of the Ce³⁺ valence state in cerium oxide nanoparticle layers. *Nanoscale* **2012**, *4*, 4950–4953. [[CrossRef](#)] [[PubMed](#)]
25. Nicolas, J.; Romain, A.-C. Establishing the limit of detection and the resolution limits of odorous sources in the environment for an array of metal oxide gas sensors. *Sens. Actuator B Chem.* **2004**, *99*, 384–392. [[CrossRef](#)]
26. Prabhakar, A.; Iglesias, R.A.; Shan, X.; Xian, X.; Zhang, L.; Tsow, F.; Forzani, E.S.; Tao, N. Online Sample Conditioning for Portable Breath Analyzers. *Anal. Chem.* **2012**, *84*, 7172–7178. [[CrossRef](#)] [[PubMed](#)]
27. Vallejos, S.; Gràcia, I.; Pizúrová, N.; Figueras, E.; Hubálek, J.; Cané, C. Tuning of the Humidity-Interference in Gas Sensitive Columnar ZnO Structures. *Proceedings* **2017**, *1*. [[CrossRef](#)]
28. Wang, J.; Yang, P.; Wei, X. High-Performance, Room-Temperature, and No-Humidity-Impact Ammonia Sensor Based on Heterogeneous Nickel Oxide and Zinc Oxide Nanocrystals. *ACS Appl. Mater. Interfaces* **2015**, *7*, 3816–3824. [[CrossRef](#)] [[PubMed](#)]
29. Niarchos, G.; Dubourg, G.; Afroudakis, G.; Georgopoulos, M.; Tsouti, V.; Makarona, E.; Crnojevic-Bengin, V.; Tsamis, C. Humidity Sensing Properties of Paper Substrates and Their Passivation with ZnO Nanoparticles for Sensor Applications. *Sensors* **2017**, *17*. [[CrossRef](#)] [[PubMed](#)]
30. Kim, S.; Park, S.; Park, S.; Lee, C. Acetone sensing of Au and Pd-decorated WO₃ nanorod sensors. *Sens. Actuator B Chem.* **2015**, *209*, 180–185. [[CrossRef](#)]
31. Bertuna, A.; Comini, E.; Poli, N.; Zappa, D.; Sberveglieri, G. Acetone Detection by Chemical Sensors Based on Tungsten and Titanium Oxide Nanowires. *Proceedings* **2017**, *1*. [[CrossRef](#)]
32. Righettoni, M.; Tricoli, A.; Pratsinis, S.E. Si:WO₃ Sensors for Highly Selective Detection of Acetone for Easy Diagnosis of Diabetes by Breath Analysis. *Anal. Chem.* **2010**, *82*, 3581–3587. [[CrossRef](#)] [[PubMed](#)]
33. Pandeewari, R.; Jeyaprakash, B.G. CeO₂ thin film as a low-temperature formaldehyde sensor in mixed vapour environment. *Bull. Mater. Sci.* **2014**, *37*, 1293–1299. [[CrossRef](#)]
34. Nagaraju, P.; Vijayakumar, Y.; Choudhary, R.J.; Ramana Reddy, M.V. Preparation and characterization of nanostructured Gd doped cerium oxide thin films by pulsed laser deposition for acetone sensor application. *Mater. Sci. Eng., B* **2017**, *226*, 99–106. [[CrossRef](#)]





UV-light activated APTES modified WO_{3-x} nanowires sensitive to ethanol and nitrogen dioxide

M. Tomić^{a,b}, Z. Fohlerova^{c,d}, I. Gràcia^a, E. Figueras^a, C. Cané^a, S. Vallejos^{a,c,*}

^a Institute of Microelectronics of Barcelona (IMB-CNM, CSIC), Campus UAB, 08193 Cerdanyola del Vallès, Barcelona, Spain

^b Autonomous University of Barcelona (UAB), Campus UAB, 08193 Cerdanyola del Vallès, Barcelona, Spain

^c CEITEC - Central European Institute of Technology, Brno University of Technology, 61200, Brno, Czech Republic

^d Department of Microelectronics, Faculty of Electrical Engineering and Communication, Brno University of Technology, Technická 3058/10, 61600, Brno, Czech Republic

ARTICLE INFO

Keywords:

Tungsten oxide
APTES
Nanowires
Gas sensor
UV-light activation

ABSTRACT

The sensing properties of (3-aminopropyl)triethoxysilane modified tungsten oxide nanowires (APTES@WO_{3-x}) based sensors towards several gases and vapors are reported in this work. The developed sensors show high sensitivity to ethanol and nitrogen dioxide under UV-irradiation at room temperature (24 °C). Gas sensing results demonstrate enhanced sensing properties for the APTES@WO_{3-x} compared to non-modified WO_{3-x} sensors, with the APTES@WO_{3-x} sensors showing approximately 17 and 20 times more sensitivity to ethanol and nitrogen dioxide, respectively, compared to the non-modified WO_{3-x} sensors. The APTES@WO_{3-x} sensors also display improved selectivity to nitrogen dioxide (oxidizing gas) and ethanol (among other reducing gases including acetone, toluene, hydrogen, and carbon monoxide). These results are attributed to the presence of the reactive amino group at the APTES@WO_{3-x} sensors, which facilitates the chemical interaction with nitrogen dioxide and ethanol and the electron transfer towards/from WO_{3-x} under UV-light excitation.

1. Introduction

Semiconducting metal oxides (MOXs) based gas sensors are able to operate with high sensitivity, stability, and relatively good selectivity compared to other materials such as polymers. Also, MOXs are compatible with state-of-the-art micro/nano fabrication processes and suitable for being integrated into miniaturized systems with low production costs. Specifically, nanostructured MOXs, e.g., nanowires, are attractive in gas sensors because they have proved repeatedly in the literature to enhance the functionality of these devices, particularly in terms of sensitivity, due to their higher surface-area-to-volume ratio compared to bulk MOXs [1–3]. Nanostructured MOXs can be synthesized via scalable and industrially relevant top-down or bottom-up techniques. Previously, for instance, we have demonstrated the bottom-up synthesis of various MOXs (e.g., WO_{3-x}, [4,5] ZnO [6], and SnO₂ [7]) via aerosol-assisted (AA) chemical vapor deposition (CVD), and their gas sensing functionality [8].

Typically, MOXs are chemically poorly responsive to gaseous species at room temperature (RT) since they are passivated by the adsorption of oxygen molecules from the atmosphere. Therefore, two strategies are

generally employed to activate MOXs – thermoactivation using temperatures in the range of 200–500 °C or photoactivation using light irradiation usually in the ultraviolet (UV) range. In general, the major drawback of using thermoactivation lies in the heaters' power consumption. The high temperatures needed for MOX activation may also limit its applicability in explosive and flammable environments, and bring stability and poisoning issues [9,10]. In recent years, photoactivation of gas sensitive materials for RT operation [11] has been used as an alternative to thermoactivation to circumvent these drawbacks, particularly the high power consuming resistive heaters, considering that the on-chip integration of light emitter components with low power consumption (tens of μW or less) in gas sensing microsystems is progressively being implemented [9]. As a way of photoactivation, UV sources, such as UV-LEDs (light-emitting diodes) can provide sufficient energy for charge carrier promotion and by increasing the irradiance, the sensor performance to target gases can be improved to some extent [12].

Nanostructured MOXs are generally oxygen deficient surfaces, which deviate from the stoichiometric composition and contain defects and impurities that form intra-bandgap states and produce changes in the

* Corresponding author at: Institute of Microelectronics of Barcelona (IMB-CNM, CSIC), Campus UAB, 08193 Cerdanyola del Vallès, Barcelona, Spain.
E-mail addresses: stella.vallejos@imb-cnm.csic.es, vargas@vutbr.cz (S. Vallejos).

electronic structure of the MOX, thus, allowing to adjust the electronic and gas sensing properties towards specific needs [13]. The formation of oxygen vacancies in MOXs is another characteristic that plays a crucial role in gas sensing mechanism, facilitating the low-temperature oxygen chemisorption process and enhancing the performance of gas sensors [14]. Further improvements in gas sensitive MOXs include the modification of its surface chemistry with inorganic materials, such as metals or second-phase MOXs [1], or organo functional molecules [15]. The last is a less extended strategy, but has shown potential to activate the MOX gas sensitivity and selectivity, as the organo functional modifier can interact with the gaseous species and influence the electrical properties of the MOX 'support'.

Silanization method is an example of this modification, where MOX surface is being modified by organofunctional alkoxy silane molecules, such as (3-aminopropyl)triethoxysilane (APTES) [15]. APTES molecule used in the silanization process consists of hydrolysable ethoxy groups bonded to Si via oxygens, an alkyl chain as a linker, and an amino-functional group, as shown in Fig. 1. Ethoxy groups in APTES enable surface reactions with other molecules (e.g., MOXs), whereas a reactive terminal amino group can easily bond other gas/vapor active molecules to the APTES structure. With three ethoxy groups, APTES is very prone to react with MOX surface. Previously, APTES was used for SnO₂ surface modification as an intermediate step, followed by functionalization with alkyl, acid, and ester functional groups for sensing ammonia, ethanol and carbon monoxide [16]. The modification of thin-walled porous tungsten oxide nanotubes with APTES was also stated to favor the thermoactivated response of tungsten oxide to low nitrogen dioxide concentrations [15]. Our recent study [17] on the gas sensing properties of silanized WO_{3-x} using UV photoactivation also suggested the positive influence of APTES on the sensing properties of this MOX.

Therefore, here, we explore further the influence of APTES on the gas sensing properties of sub-stoichiometric WO_{3-x} nanowires. The work provides a complete strategy to fabricate gas microsensors based on silanized MOXs and evaluates the sensing properties of these microsystems under UV photoactivation at RT towards various vapors and gases, which are relevant in different areas, including biomedicine, biochemistry, environment control, security, and industry [4,18,19].

2. Materials and methods

2.1. Microsensors based on silanized WO_{3-x} nanowires

The microsensors consist of four membranes (1100 × 1100 μm) of Si₃N₄/SiO₂ (300 nm/500 nm thick), each containing four Ti/Pt interdigitated electrodes (25 nm/250 nm thick, 95 μm long, with electrode gap of 10 μm) on the top processed using various Clean Room micro-fabrication steps (oxidation, metallization, implantation, lithography, and etching) as reported previously [20]. WO_{3-x} nanowires were grown at 390 °C directly onto the interdigitated electrodes using the AACVD method described elsewhere [6]. Briefly, tungsten hexacarbonyl (20 mg, W(CO)₆, Sigma-Aldrich, ≥97 %) and methanol (5 mL, Sigma-Aldrich,

≥99.9 %) were mixed to form the precursor solution. The aerosol droplets of the solution were transported to the heated substrate using nitrogen gas flow (200 sscm) and after this process the samples were annealed for 1 h at 500 °C in air. Subsequently, the gas sensitive nanowires underwent a cleaning process, which included rinsing in deionized water, drying in desiccator to remove the adsorbed species, and generating active hydroxyl groups on the surface by plasma treatment (1 min, 600 W, 0.5 mbar). Prior to the silanization, the samples were placed inside the vacuum chamber and purged three-times under N₂ stream.

The silanization of the nanowires surface was carried out at 120 °C via CVD using an aminosilane (APTES; (3-aminopropyl)triethoxysilane, Sigma-Aldrich, 97 %) solution. After silanization the CVD chamber was purged three-times with N₂ gas to remove residuals and unreacted silane from the chamber and surface, respectively. Generally, the silanization conditions were set by adjusting three parameters, including the duration of plasma treatment (times tested: 1 and 5 min), the APTES deposition time (times tested: 10, 30, and 50 min), and the amount of silane (volumes tested: 15, 100, and 1000 μL). The samples were analyzed at each step by X-ray photoelectron spectroscopy (XPS), finding the best condition for the silanization (i.e. major concentration of Si 2p at the nanowires surface) when using a plasma treatment of 1 min, APTES deposition time of 10 min, and a volume of 1000 μL (Table S1, Supporting Information). Therefore, these conditions were used for the APTES modified samples characterized in this work.

2.2. Characterization techniques

The morphology of the films was examined using Scanning Electron Microscopy (SEM - Carl Zeiss, Auriga Series) and the chemical composition using X-ray photoelectron spectroscopy (Kratos Axis Supra spectrometer, with Al/Ag monochromatic X-ray source). The XPS spectra was analyzed by a peak fitting software (CasaXPS version 2.3.18PR1.0). Raw data were processed by the subtraction of a Shirley background for secondary electrons and element peak fitting was used to estimate the relative element molar fraction. Ultraviolet photoelectron spectroscopy (UPS) analysis of the samples was also performed using Kratos Axis Supra spectrometer, with Al/Ag monochromatic X-ray source. The UPS spectra were recorded using a He lamp (He-I) with excitation energy $h\nu = 20.0$ eV. The obtained data from the UPS spectra allow the determination of the sample's work function (Φ) from the difference in the photon energy of He-I and the energy difference (ΔE) between the binding energy cut-off ($E_{\text{cut-off}}$) and the Fermi edge ($E_{\text{F}} = 0$ eV), following the equation [21]:

$$\Phi = 20 \text{ eV} - \Delta E.$$

Further analysis of the films was carried out using X-ray Diffraction (XRD - Bruker, AXS D8 Advance operated at 40 kV and 40 mA, Cu K α radiation) and high-resolution Transmission Electron Microscopy (TEM - FEI Tecnai F20, 200 kV). The band gap of the films was estimated using UV-Vis diffuse reflectance spectrum (AvaSpec-UV/VIS/NIR, Avantes, Apeldoorn) and applying Kubelka-Munk transformation.

2.3. Gas sensing measurements

The microsensors were tested at RT (24 °C) in a continuous flow (200 sscm) test chamber [5] provided with mass flow controllers and continuous illumination from a LED (light-emitting diode, LC-L1V3 Hamamatsu) with wavelength of 365 nm. The wavelength of 365 nm is selected based on the bandgap of the sensing material, since the UV-activated sensors have maximum response when striking photons have energy close to this bandgap. The tests were performed using various irradiance, equal or below 1800 mW·cm⁻². The sensors were exposed to various gas concentrations obtained by diluting calibrated cylinders of ethanol (Praxair, 100 ppm), acetone (Praxair, 100 ppm), toluene (Praxair 200 ppm), carbon monoxide (Praxair 100 ppm), hydrogen (Praxair 100 ppm) or nitrogen dioxide (Praxair 100 ppm) with

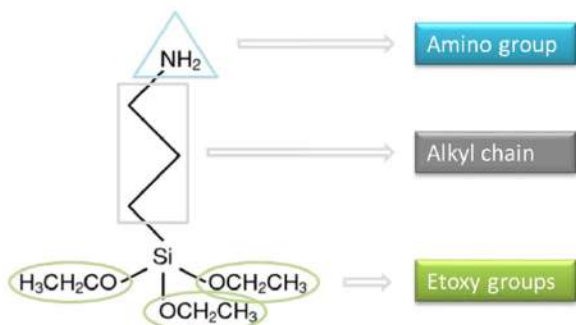


Fig. 1. Schematic view of APTES molecule.

synthetic air (3X, Praxair). Subsequently the gaseous analytes were purged with synthetic air until the initial baseline resistance was recovered. The electrical resistance measurements were performed using a multimeter Keithley 2700. Humidity was introduced to the system by bubbling through water under controlled conditions at 24 °C. The relative humidity (RH) and the temperature inside the test chamber was monitored throughout the whole test using a humidity/temperature sensor (SHT71, operating ranges from 0 to 100 % RH, accuracy of ± 3 % RH and ± 0.4 °C). Note that the sensors and the test chamber were kept at RT for all the tests performed in the present work. A scheme of the gas testing system is depicted in Fig. 2.

The sensor response (R) was defined as Ra/Rg for reducing and Rg/Ra for oxidizing gases, where Ra and Rg represent the electrical resistance of the sensitive film in air and the target gas, respectively, while the sensitivity of the sensor (S) expresses the variation of the sensor response as a function of the change in the tested gas concentration (from 10 to 80 ppm). The response time was defined as the time required for the sensor to reach 90 % of the response, and the recovery time as the time required to return to 10 % of the initial baseline resistance after the analyte was purged. The gas sensing measurements included various non-modified (WO_{3-x}) and APTES modified ($APTES@WO_{3-x}$) based microsensors and replicated measures to each gas and condition. The whole testing period spanned for the sensors was 70 days with the sensors accumulating a total of 560 h of operation.

3. Results and discussion

3.1. WO_{3-x} films

The morphology of the synthesized WO_{3-x} was examined using SEM as shown in Fig. 3. The imaging of the sensing film displayed a high density of non-aligned nanowires deposited uniformly over the electrodes (Fig. 3a). The estimated diameters and lengths of the nanowires (Fig. 3b and c) are ~ 100 nm and ~ 8 μ m, respectively, corresponding to an aspect ratio of 80.

Fig. 4a shows the XRD pattern of the WO_{3-x} films. Similarly to our previous work [5] the films showed crystalline structures with intense diffraction peaks at $23.1^\circ 2\theta$ ($d = 3.85$ Å) and $47.2^\circ 2\theta$ ($d = 1.92$ Å) that correspond to the (002) and (004) reflections of the monoclinic phase WO_{3-x} (P21/n space group; ICDD card no. 72-0677), respectively, as well as other characteristic diffractions assigned to the same phase. The pattern in Fig. 4a also displays an intense diffraction assigned to the

face-centered cubic phase Pt (Fm3m space group; ICDD card no. 04–0802) that corresponds to the interdigitated electrodes. High-resolution TEM of the nanowires (Fig. 4a) corroborated the crystalline structure of the wires, with highly ordered lattice separated by 3.85 Å, consistent with the (002) diffraction observed by XRD. The low magnification TEM image in Fig. 4b displays the top of a wire (diameter < 100 nm).

The XPS spectra of the WO_{3-x} films (Figure S1, Supporting Information) confirmed the presence of typical W $4f_{7/2}$, W $4f_{5/2}$, W $5p_{3/2}$ core level peaks centered at binding energies of 35.3 eV, 37.4 eV and 41.1 eV, respectively. These results indicate the films are oxygen deficient showing an oxygen to tungsten ratio of 2.7 (anal. calcd. for WO_3 : W 24.98, O 74.99 at. %; found: W 26.8, O 73.2 at. %), which is in agreement with our previous works on the AACVD of tungsten oxide nanowires [4,5]. Additionally, the diffuse reflectance spectra of the WO_{3-x} films (Figure S2, Supporting Information) and its corresponding Kubelka-Munk transformation indicated optical band gap at ~ 3.1 eV. This is in agreement with the literature values for tungsten oxide (2.6–3.7 eV) [22].

3.2. APTES@ WO_{3-x} films

Analysis of the morphology, crystalline structure, and diffuse reflectance of the APTES@ WO_{3-x} films after the silanization of the surface showed similar characteristics to those recorded on the non-modified WO_{3-x} films with no apparent changes (see Fig. 1, 2 and S2). The silanized sample also displayed similar W $4f$ and W $5p$ core level peaks centered at approximately the same binding energies than those recorded in the non-modified sample. The XPS spectra also corroborated the silanization of the surface showing characteristic Si 2p, Si 2s and N 1s core-level peaks. Figure S1 (Supporting Information) compares the wide XPS spectra for the WO_{3-x} and APTES@ WO_{3-x} films. Fig. 5a shows the high-resolution XPS spectrum of APTES modified WO_{3-x} sample in the Si 2p region. The deconvoluted XPS spectrum shows only one component at 102.1 eV, which is attributed to O-Si-O bond. The N 1s high-resolution spectrum is shown in Fig. 5b and it consists of two components. The first, located at 399.2 eV, corresponds to NH_2 group and the second, located at 401.1 eV, corresponds to NH_3^+ group. The results from the deconvoluted XPS spectra showed good agreement with the literature data [23] and proved the modification of the WO_{3-x} surface with APTES.

The surface modification process can be explained through a simplified mechanism of APTES reaction with the WO_{3-x} nanowire surface (Fig. 6), in which four possible types of interaction can occur [24]. The first two (I and II) may include the APTES adsorption to the hydroxyl-terminated nanowires surface via oxygen bonding from one (Fig. 6a) or two (Fig. 6b) ethoxy groups. Similarly, the third (III), may include the bonding of oxygen from all three ethoxy groups to the WO_{3-x} surface (Fig. 6c). This could also lead to the polymerization of the adsorbed APTES by forming siloxane bonds (Si-O-Si) (Fig. 6d). Finally, ethanol is produced as by-product of the process in all three scenarios. The presence of the activated hydroxyl groups on the surface after the exposure of WO_{3-x} film to the plasma treatment was confirmed by XPS measurements (Figure S3, Supporting Information). Another possible reaction route (IV) during the modification of WO_{3-x} with APTES may include adsorption via amino group as shown in the Fig. 6e. The mechanism of silanization is rather complex and still not understood in detail. Our results from XPS spectra suggest the APTES binding could be attained via the model depicted in Fig. 6d.

Further analysis of the APTES@ WO_{3-x} films by UPS (Fig. 7a) displayed an $E_{cut-off}$ of ~ 16.68 eV, slightly higher than that reported for only tungsten oxide (~ 16.50 eV) [25] and APTES (~ 16.55 eV) [26]. This indicates a lower work function (ϕ) of -3.32 eV for the APTES@ WO_{3-x} films compared to literature tungsten oxide (-3.50 eV) [25] and APTES (-3.45 eV) [26] work functions. The spectrum also suggests the presence of two slopes in the valence band (VB) leading edge (Fig. 7b),

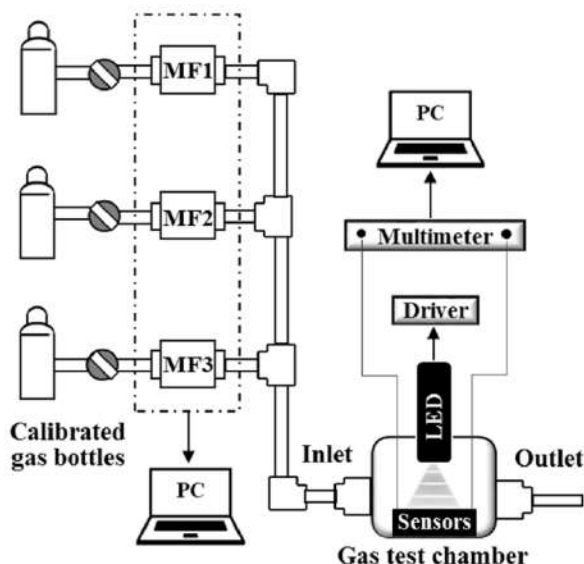


Fig. 2. Gas testing system. MF: Mass Flow, LED: Light Emitting Diode. Not-to-scale.

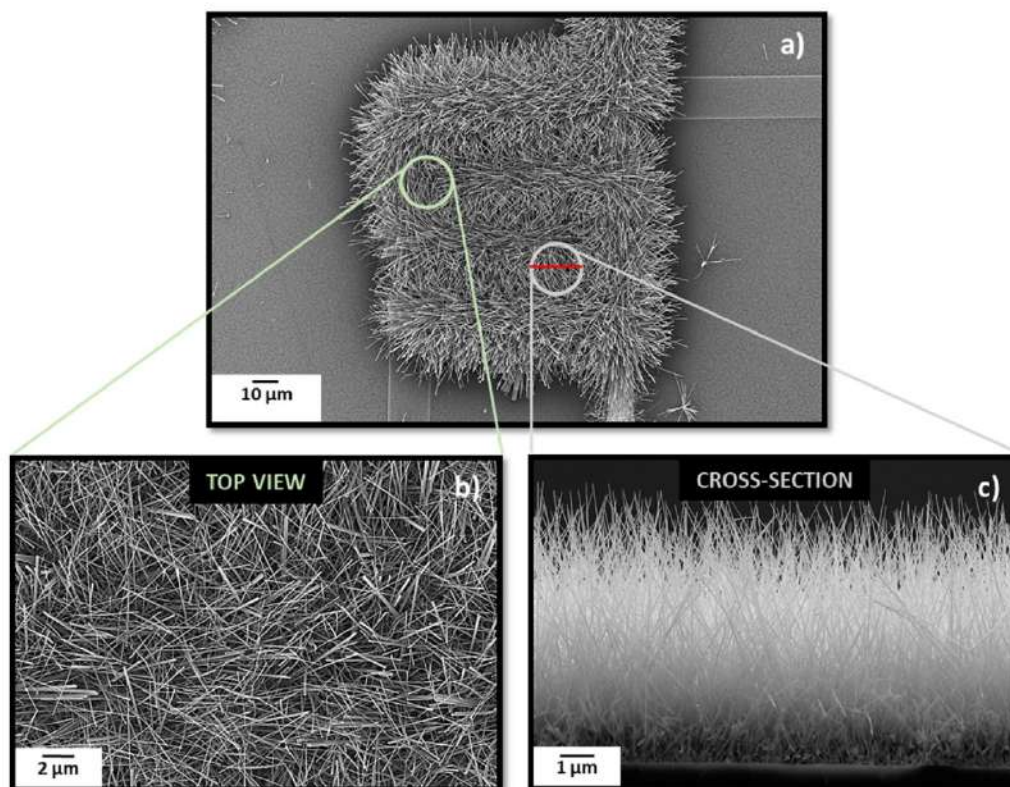


Fig. 3. SEM imaging of **a)** the WO_{3-x} nanowires grown on the interdigitated electrode area, and **b)** top-view and **c)** cross-section of the structured film. These structures displayed similar characteristics after their modification with APTES.

the first, at binding energies between 10 and 12 eV (connected with propyl chains from APTES molecule [23]) and the second, at binding energies between 5 and 7 eV (connected with the O 2p orbitals for tungsten oxide [27]).

Therefore, the UPS spectrum points out the presence of WO_{3-x} and APTES induced VB at the APTES@ WO_{3-x} films, with the VB onset for WO_{3-x} and APTES occurring at -3.7 eV and -3.9 eV, respectively. This suggests that the VB of WO_{3-x} lies -0.2 eV above the highest occupied molecular orbital (HOMO) of the APTES molecule. Moreover, considering the estimated band gap (~ 3.1 eV) from diffuse reflectance spectra (Figure S2, Supporting Information) and the APTES band gap (~ 3.8 eV) reported in the literature [28], the results suggest that the position of the lowest unoccupied molecular orbital (LUMO) of APTES lies -0.7 eV above the conduction band (CB) of WO_{3-x} (Fig. 7), thus, producing straddling type of heterojunction. Also, the lower work function of APTES compared to WO_{3-x} poses a higher Fermi level for the APTES than for WO_{3-x} , so that electrons are transferred from the LUMO of APTES to the CB of WO_{3-x} . Simultaneously, the holes are transferred from the VB of WO_{3-x} to the HOMO of APTES. The possible energy level diagram at the interface of WO_{3-x} and APTES is depicted in Fig. 8.

3.3. Gas sensing tests

Four different microsensors of each type (i.e., WO_{3-x} or APTES@ WO_{3-x}) were tested repeatedly at RT employing various UV irradiances and performing at least three replicates for each condition. Generally, the tested sensors displayed typical n-type semiconducting behavior with increasing or decreasing electrical resistance changes when exposed to the reducing (acetone, ethanol, toluene, hydrogen, carbon monoxide) or oxidizing (nitrogen dioxide) analytes, respectively. Fig. 9 summarizes the results obtained towards various concentrations of these analytes for an irradiance of $1800 \text{ mW}\cdot\text{cm}^{-2}$. These results demonstrate noticeable higher responses for the APTES@ WO_{3-x} sensors,

particularly towards ethanol and nitrogen dioxide, as opposed to the WO_{3-x} sensors, which showed negligible response to all gases. Results show, for instance, that for a concentration of 80 ppm of ethanol and nitrogen dioxide the response of the APTES@ WO_{3-x} sensors reaches in average approximately eight-fold the response of the non-modified WO_{3-x} sensors. The standard errors for 80 ppm of ethanol and nitrogen dioxide are ± 1.2 and ± 1.9 for APTES@ WO_{3-x} sensors and ± 0.1 and ± 0.2 for WO_{3-x} sensors, respectively. These results also display an apparent response-interception (above 1) for the NO_2 calibration curve, which suggests the presence of a larger slope calibration curve for low (< 10 ppm) NO_2 concentrations, as observed previously for other gas sensors [29].

A comparative image of the dynamic of the response to ethanol and nitrogen dioxide registered by the WO_{3-x} and APTES@ WO_{3-x} sensors is displayed in Fig. 10. These results indicate that the response to both analytes reaches a stationary state for all the concentrations tested and a complete recovery after 25 min of purging the analytes with air. The response time recorded for 10 ppm of ethanol and nitrogen dioxide with the APTES@ WO_{3-x} sensors was 2.8 min and 9 min, respectively.

Generally, electrical measurements of various sensors (i.e., based on WO_{3-x} and APTES@ WO_{3-x} nanowires) at room temperature and without irradiation revealed resistances between 3 and $5 \text{ M}\Omega$. However, after irradiating the sensor active area (interdigitated electrode area), we noticed a decline of the baseline resistance with a different decrease factor for each type of sensor. For instance, the resistance for the WO_{3-x} sensors decreased to hundreds of ohms, whereas that for the APTES@ WO_{3-x} sensors decreased to thousands of ohms, as can be noticed in Fig. 11. These results also show that the baseline resistance of the APTES@ WO_{3-x} sensors has a proportional change with the irradiance, as opposed to the WO_{3-x} sensors, which registered almost no changes in the baseline resistance.

Generally, the response to the target analytes for irradiance below $1000 \text{ mW}\cdot\text{cm}^{-2}$ registered negligible changes and long recovery times

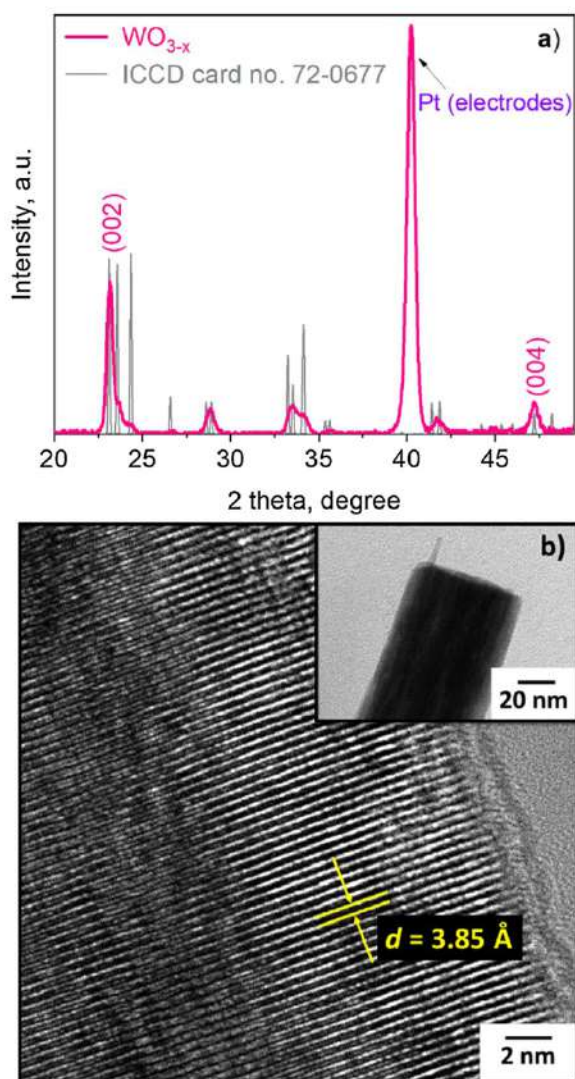


Fig. 4. a) Typical XRD pattern and b) high-resolution TEM image of the WO_{3-x} nanowires (the inset low magnification TEM displays the top of a wire). All of the diffraction peaks in the data can be indexed either to platinum (Fm3m space group; ICCD card no. 04 – 0802) from the electrodes or WO_{3-x} (P21/n, ICCD card no. 72-0677) from the nanowires, with only peaks of greatly enhanced intensity specifically indexed. Examination of the structures after APTES modification showed similar characteristics.

after the purging. In contrast, results for irradiance above $1000 \text{ mW}\cdot\text{cm}^{-2}$ displayed a better dynamic of the response to ethanol and nitrogen dioxide, with higher and/or faster responses as the irradiance increased. This is remarked particularly for the APTES@ WO_{3-x} sensors, which show noticeable improvements in the response towards ethanol (Fig. 11a) and nitrogen dioxide (Fig. 11b) at $1800 \text{ mW}\cdot\text{cm}^{-2}$ compared to the WO_{3-x} sensors. A similar trend was noticed for the response and recovery times, which are better for the high irradiance ($1800 \text{ mW}\cdot\text{cm}^{-2}$) than for the low irradiance ($1000 \text{ mW}\cdot\text{cm}^{-2}$).

Results in Fig. 11 also indicate good reproducibility and stability of the sensors. An analysis of the baseline resistance along the testing period (i.e., 560 h) revealed better stability for the APTES@ WO_{3-x} sensors with an oscillation of the baseline resistance of 8 % as compared to the non-modified WO_{3-x} sensors, which show an oscillation of the baseline resistance of 20 %. The high dispersion for the WO_{3-x} sensors is connected with a drastic change of their baseline resistance after 300 h of operation. Analysis of the morphology and structural properties of the APTES@ WO_{3-x} and WO_{3-x} sensors after the tests, showed no evident

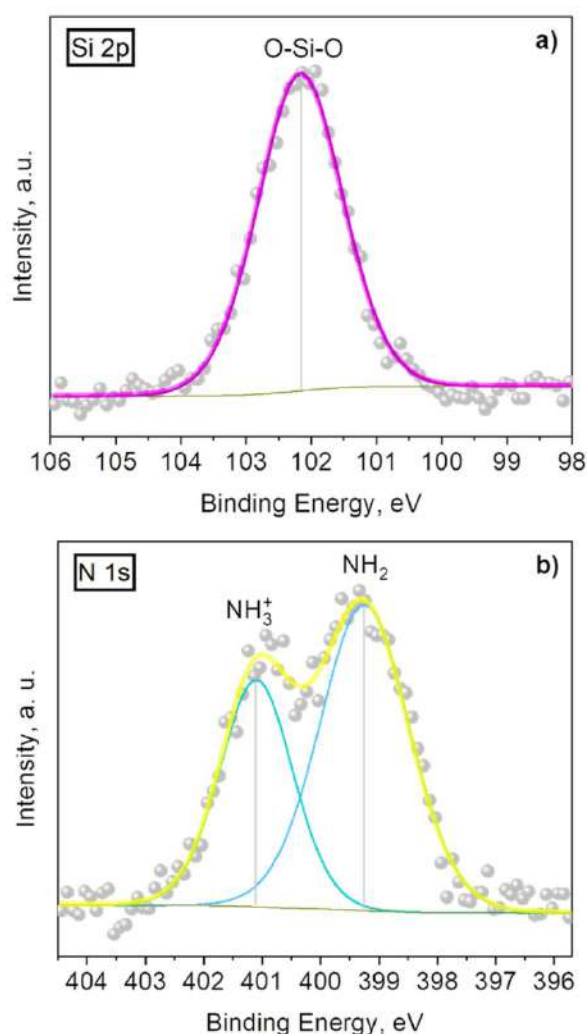


Fig. 5. Core level XPS spectra of a) Si 2p, and b) N 1s recorded on the APTES@ WO_{3-x} films. The gray dots show the XPS raw data, colored solid lines correspond to the envelope-fitting curve and the components.

changes with respect to the characteristics recorded before the tests. Hence, the sensors, particularly the APTES@ WO_{3-x} sensors, indicated relatively good middle-term stability.

The sensor's sensitivity is displayed in Fig. 12. As noticed also above, in Fig. 9, the APTES@ WO_{3-x} sensors show good sensitivity to ethanol and nitrogen dioxide with a strong selectivity to ethanol among the other reducing gases (acetone, toluene, hydrogen, and carbon monoxide). The enhanced sensitivity of the APTES@ WO_{3-x} sensors ($S = 19.1 \%$ for ethanol and $S = 7.9 \%$ for NO_2) compared to their WO_{3-x} counterpart ($S = 1.1 \%$ for ethanol and $S = 0.4 \%$ for NO_2) are attributed to the presence of a reactive polar amino group at the nanowire surface, which has proved to be chemically more active with polar (ethanol, acetone, carbon monoxide, and nitrogen dioxide) than nonpolar (toluene and hydrogen) molecules since the polar molecules are attracted to each other by dipole-dipole interactions between the partial negative charge of one polar molecule and the partial positive charge of another polar molecule. Thus, the higher sensitivity of the APTES@ WO_{3-x} sensors to ethanol may be influenced by the higher polarity of this analyte given its larger electronegative difference ($\Delta EN = 1.4$ for ethanol) in the polar region compared to acetone ($\Delta EN = 1$) and carbon monoxide ($\Delta EN = 1$) [30]. The correlation of the sensitivity and the polarity of various reducing analytes has also been noticed in recent literature reports [31]. Similarly, the sensitivity to nitrogen dioxide could be connected with the polar nature of this analyte and the high sensitivity of tungsten oxide to

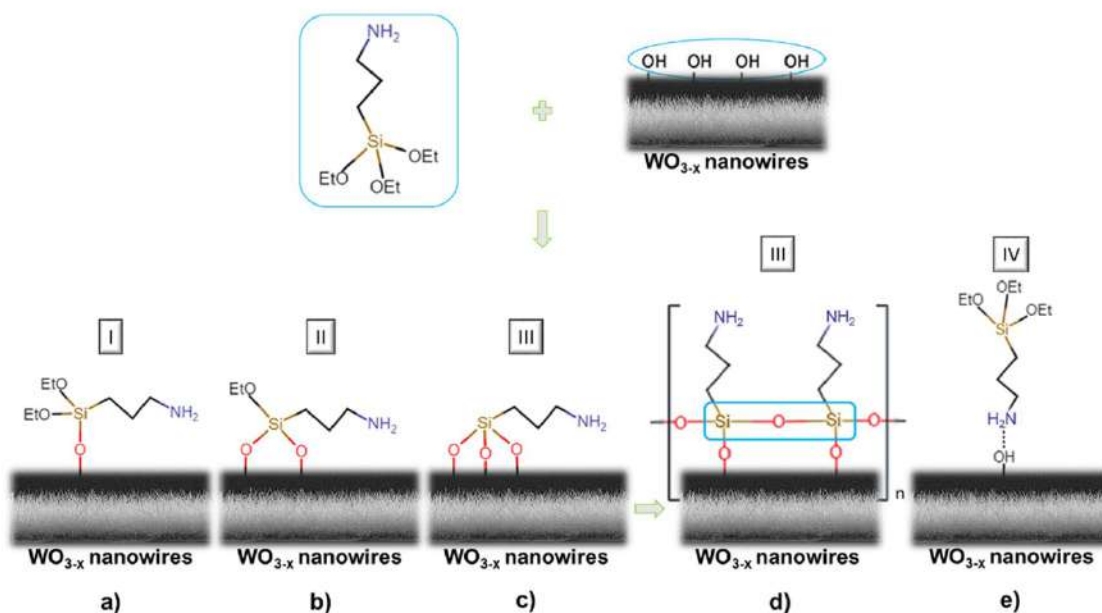


Fig. 6. Schematic representation of the silanization process – adsorption of APTES molecule via oxygen bonding from the a) one, b) two, and c) three ethoxy groups; d) the polymerization of the APTES adsorbed through all three ethoxy groups; e) adsorption of APTES molecule via amino group.

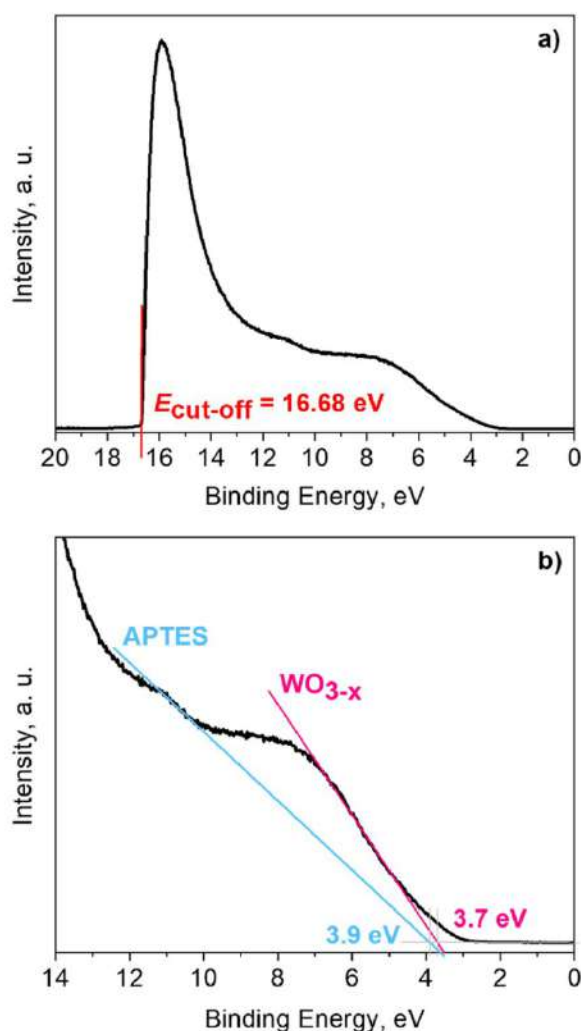


Fig. 7. a) UPS spectra and b) valence band maximum obtained by linear extrapolation for the APTES@WO_{3-x} sample.

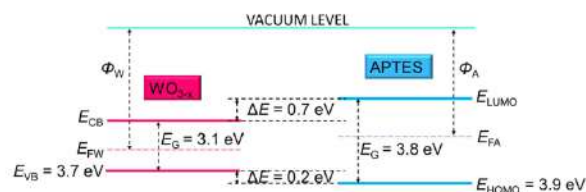


Fig. 8. Schematic representation of the possible energy level diagram at the interface of APTES molecule and WO_{3-x} nanowires. E_{CB} represents the conduction band minimum, E_{VB} is the valence band maximum, E_{HOMO} is the highest occupied molecular orbital, E_{LUMO} is the lowest unoccupied molecular orbital, E_{FW} and E_{FA} are Fermi level energies of WO_{3-x} and APTES, respectively, and Φ_W and Φ_A are work function of WO_{3-x} and APTES, respectively (not to scale).

electron acceptor (oxidizing) than electron donor (reducing) analytes [32]. The UV-activated sensing mechanism of ethanol and nitrogen dioxide is discussed further in section 3.4.

Additional tests of the sensors towards relative humidity (RH) from 10 % to 80 % are presented in Figure S4 (Supporting Information). Results for both sensors show the saturation of the response at approximately 60 % RH with nearly no change in the electrical resistance after further increase of RH. The saturation point to RH has also been observed before for other MOX systems, e.g., for ZnO rods at 20 % RH [20] and SnO₂/WO₃ heterojunctions at 50 % RH [33] and is linked to the properties of the material, generally, the morphology and chemistry of the surface. Similarly to the target analytes (Fig. 9), the response of the APTES@WO_{3-x} sensors to humidity was higher compared to the WO_{3-x} sensors. Tests of the sensors to ethanol in humid ambient revealed a loss of response to this analyte with the increasing of the RH in the ambient. Results in Figure S5 (Supporting Information) show, for instance, that the loss of response for the APTES@WO_{3-x} sensors to 40 ppm of ethanol exceeds 50 % at 60 % RH. Due to the low sensitivity of the non-modified WO_{3-x} sensors to ethanol, the response for these sensors in humid ambient is completely lost even at low RH.

Further analysis of the role of APTES in the gas sensing properties of other modified metal oxide system such as CeO₂@WO_{3-x} nanowires corroborated the enhancement of the response for the APTES modified structures with respect to those without modification (Figure S6, Supporting Information). The details of the synthesis and properties of the

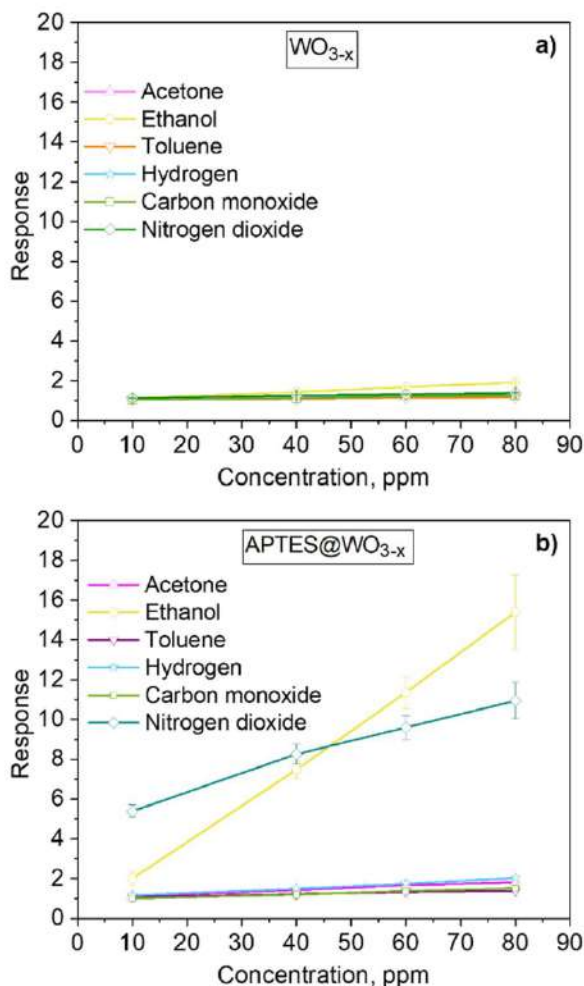


Fig. 9. Dependence of the response on gas concentration for the sensors based on a) WO_{3-x} and b) APTES@WO_{3-x} . The calibration curves display the mean of the response and the standard error of the mean obtained by using four different sensors of each type and at least three replicates for each tested condition.

non-modified $\text{CeO}_2@\text{WO}_{3-x}$ nanowires was reported elsewhere [4] and the APTES modification of these structures was achieved using the same conditions described for the APTES@WO_{3-x} . Interestingly, the $\text{CeO}_2@\text{WO}_{3-x}$ modified with APTES showed further enhancement of the sensitivity to NO_2 ($S = 29\%$), i.e., approximately four-fold the sensitivity registered for the APTES@WO_{3-x} sensors (Fig. 12). Note that the gas sensing test for the non-modified and APTES modified WO_{3-x} and $\text{CeO}_2@\text{WO}_{3-x}$ sensors were performed simultaneously using the same conditions as reported above in the experimental section.

A summary of the performance of different MOX based sensors activated by UV-light towards ethanol and nitrogen dioxide is presented in Table 1. The comparison of our results with those of the literature reveals significantly higher response for the APTES@WO_{3-x} sensors compared to other reports, in which non-modified or modified MOX were tested to similar or higher ethanol concentrations. However, it is worth noting that a direct comparison of the sensor outputs is complex, as the conditions from reference to reference varied, not only on the sensor fabrication method, but also on the gas test conditions which use different gas exposure times and static or continuous gas flow systems. Also, the tests use different type of lights (LED or Xe lamp) or frequently the light type is not reported. Despite this, we believe that Table 1 is still meaningful to offer a general idea of the systems studied previously and their comparison with respect to our system. As for nitrogen dioxide, our results suggest responses in the same order of magnitude as those

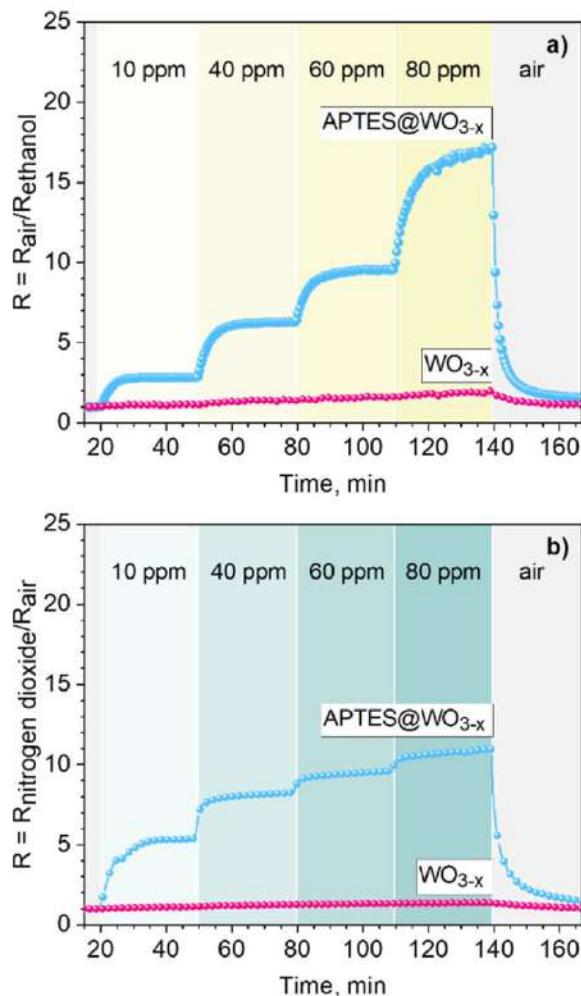


Fig. 10. Typical response to various concentrations of a) ethanol and b) nitrogen dioxide registered by the sensors based on WO_{3-x} and APTES@WO_{3-x} sensors. The yellow and green bars represent the on-off for the different concentrations of ethanol and nitrogen dioxide, respectively (For interpretation of the references in colour in this figure legend, the reader is referred to the web version of this article.).

extracted from the literature, although for different concentration as most of the reports in Table 1 were conducted to gas concentrations of 5 ppm or less, in contrast to our tests.

3.4. Gas sensing mechanism

Overall, the APTES modified WO_{3-x} films demonstrated UV-light-activated gas sensing properties to ethanol and nitrogen dioxide. UV-light-activated gas sensing mechanism could be divided into two stages after the dark stage (Fig. 13a). The first includes the photo-activation of MOX surface during the pre-adsorption cycle (i.e., before introducing the target gases, Fig. 13b and 13c), whereas the second includes the photocatalytic reactions occurring during the target gas exposure (Fig. 13d).

When APTES modified n-type MOX semiconductor such as WO_{3-x} is in contact with air (under dark conditions, Fig. 13a), its free electrons are extracted and trapped by oxygen molecules ($\text{O}_2(\text{g})$) forming oxygen ions adsorbed on the surface, mainly molecularly ($\text{O}_2^-(\text{ads})$). The oxygen adsorption results in the formation of depletion region with built-in electric field [41].

Under UV-light exposure (Fig. 13b), with a photon energy above the band gap energy, electrons and holes are generated in the

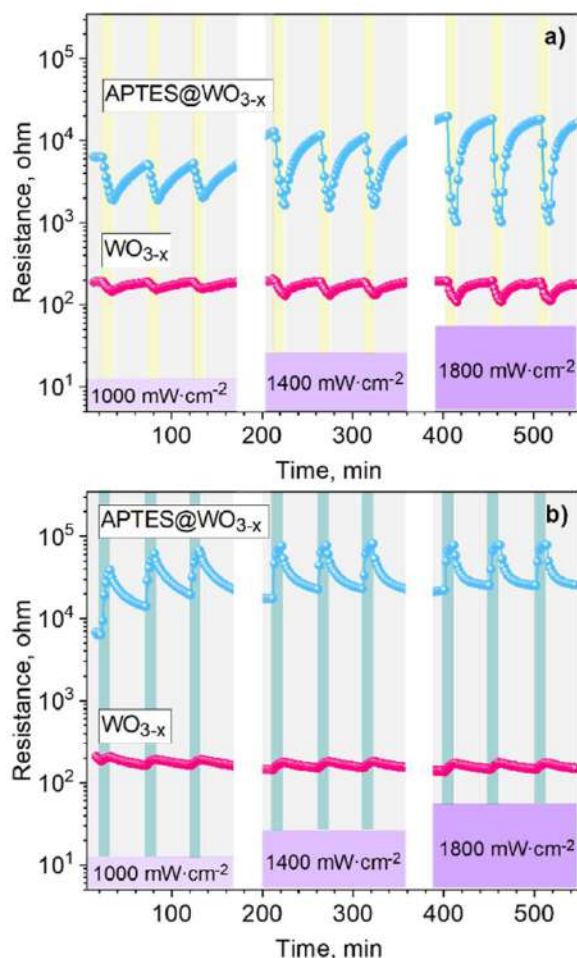


Fig. 11. Typical resistance changes for the sensors based on WO_{3-x} and APTES@WO_{3-x} sensors to 80 ppm of a) ethanol and b) nitrogen dioxide and various radiant flux. The yellow and green bars represent the on-off for ethanol and nitrogen dioxide, respectively (For interpretation of the references to colour in this figure legend, the reader is referred to the web version of this article.).

semiconductor (photo-generated electrons/holes) and separated due to the effect of the built-in electric field. Photo-generated holes release the adsorbed oxygen ions (O₂⁻(ads)) by leaving behind electrons which migrate inside of the particle. Simultaneously, however, the ambient oxygen reacts with the photo-generated electrons and forms photo-

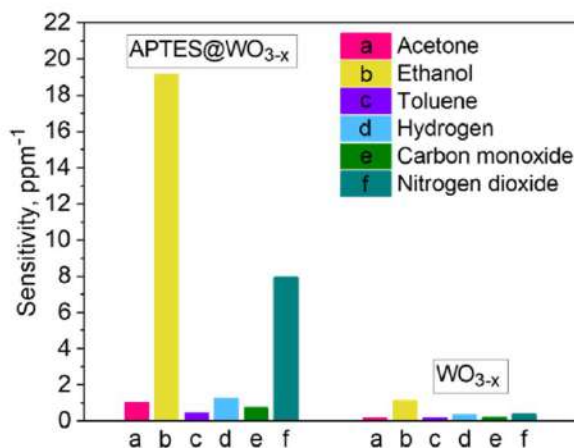


Fig. 12. Sensitivity (ppm⁻¹) of a) WO_{3-x} and b) APTES@WO_{3-x} sensors.

induced oxygen ions (O₂⁻(hν)). Finally, when the balance between the reactions of desorption of O₂⁻(ads) ions and adsorption of O₂⁻(hν) ions is achieved (Fig. 13c), the depletion layer and the conductivity are in stable stage and WO_{3-x} surface is prepared for the reaction with the target gas analytes (e.g., ethanol or nitrogen dioxide).

Generally, the adsorption of photo-induced oxygen ions (O₂⁻(hν)) is weaker compared to the chemically adsorbed oxygen ions (O₂⁻(ads)), but similarly to the O₂⁻(ads), the O₂⁻(hν) increase the depletion layer width at the surface. This, in turn, raises the baseline resistance after the UV-light exposure, as observed in our results. The formation of O₂⁻(hν) ions is quite important since these ions are the key reactants in the next stage reaction with the tested gas.

In the second stage, after the sensor exposure to reducing gas, such as ethanol, the reaction between photo-generated oxygen ions (O₂⁻(hν)) and ethanol occurs (Fig. 13d). As consequence of this reaction, electrons are released and, thus, the conductance is increased.

The presented UV-light driven mechanism illustrates the sensing principle of modified n-type MOX towards reducing gases, such as ethanol. In contrast to the reducing gases, in which the electrons are released and thus the resistance decreases, oxidizing gases consume electrons and therefore lead to the increasing of the MOX resistance, as can be noticed in the electrical resistance changes recorded to both analytes in Fig. 11.

Even though APTES molecule as an organic compound is not conductive by itself, it can affect the conductivity of the WO_{3-x} semiconductor. The energy level diagram at the interface of APTES and WO_{3-x} estimated in Fig. 8 indicates that in dark conditions (in air) the HOMO

Table 1

Comparison of the APTES modified WO_{3-x} nanowires sensor responses to ethanol and nitrogen dioxide with other MOX based sensors reported in the literature.

Material	T °C	λ nm	Light	E _λ mW·cm ⁻²	Gas	ppm	R	Refs.
APTES@WO _{3-x}	RT	365	LED	1800	Ethanol	80	15	This work
Pd@SnO ₂	RT	365	N/A	480	Ethanol	100	10.2*	[34]
ZnO	RT	365	LED array	3.6	Ethanol	100	1.1*	[35]
Au@ZnO	RT	365	Xe	1.2	Ethanol	100	2	[36]
C-doped ZnO	RT	370	N/A	0.5	Ethanol	400	6*	[37]
APTES@WO _{3-x}	RT	365	LED	1800	NO ₂	10	5.5	This work
Bi ₂ O ₃ /ZnO	RT	254	N/A	1.2	NO ₂	5	6.7	[38]
Pt@ZnO	RT	365	LED	25	NO ₂	5	5.4 [†]	[10]
ZnO/In ₂ O ₃	RT	365	LED	25	NO ₂	5	3.2 [†]	[39]
Au@ZnO	RT	365	Xe	1.2	NO ₂	5	4.5	[36]
SnO ₂ /ZnO	RT	365	N/A	1.2	NO ₂	5	6.2	[40]

T – Temperature; λ – wavelength; N/A – not available; E_λ – irradiance; c – concentration; R – response.

* The response, as defined in this work, is estimated from the data reported in each reference, which defined the response as (I_g – I_a) / I_a, where I_g and I_a are the photocurrent in ethanol and in air, respectively.

† The response, as defined in this work, is estimated from the data reported in each reference, which defined the response as (R_g – R_a) / R_a, where R_g and R_a are the electrical resistances of the sensors in NO₂ and in air, respectively.

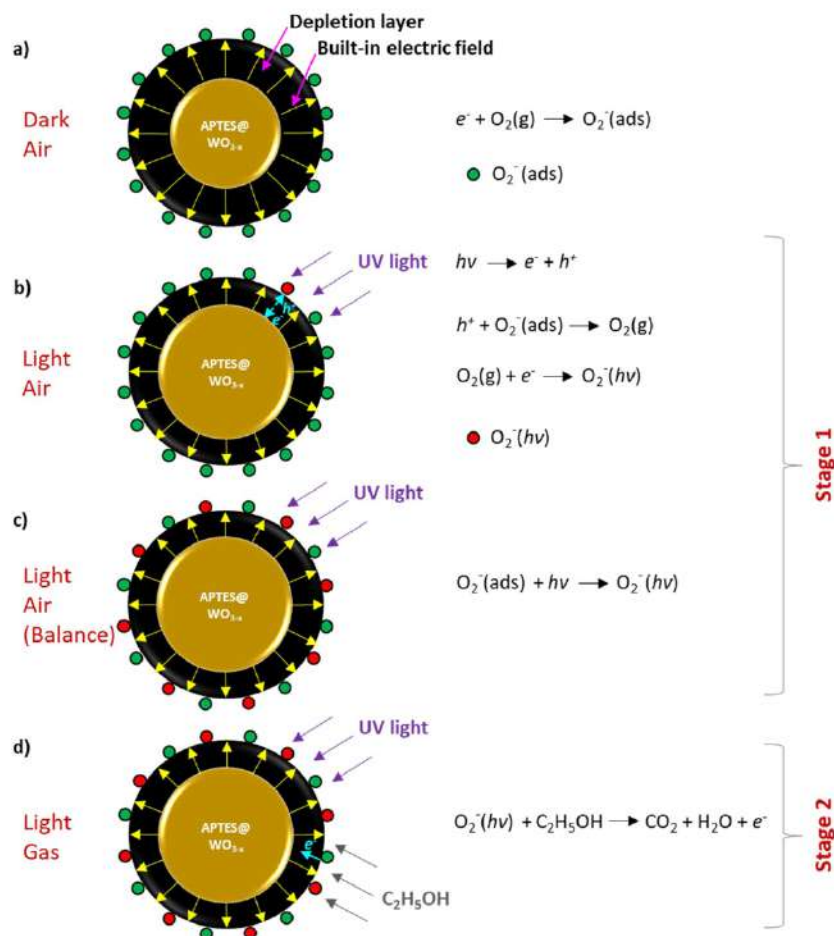


Fig. 13. Schematic illustration of the gas sensing mechanism of UV-LED-activated APTES modified WO_{3-x} sensor under different conditions: **a)** exposed to dry air in the dark, **b)** exposed to dry air under UV light, **c)** exposed to dry air under UV light after achieving oxygen adsorption/desorption balance, **d)** exposed to ethanol under UV light.

level of APTES molecule lies below the Fermi level of WO_{3-x} semiconductor. Under UV-light, APTES electrons are excited from the HOMO to the LUMO level, which is above the MOX Fermi level, so they are easily transferred to the WO_{3-x} conduction band, thus, increasing its conductivity. Therefore, the adsorption of reducing gases (electron donors), such as ethanol, toluene or acetone, also affects the MOX conductivity. In dark conditions (with a reducing gas) electrons from the gas are transferred to the LUMO level of APTES and then to the WO_{3-x} conduction band. In contrast, under UV-light, electrons from HOMO level are already excited to the higher LUMO level. Then, electrons from the adsorbed molecule are more easily transferred to the depleted HOMO level and transferred to the LUMO level and then to the MOX conduction band. This process increases electrons in the MOX conduction band leading to a decrease of the surface band bending and the surface potential of the material, which increases the conductivity along the MOX [42]. In summary, the modification of WO_{3-x} with APTES facilitates the reaction with the tested gases and the transfer of active species to/from the MOX under UV-light excitation.

4. Conclusions

Non-modified WO_{3-x} and APTES modified WO_{3-x} gas sensors were fabricated and tested under UV-light towards different gases at room temperature. Results (SEM and XRD) confirmed the deposition of crystalline nanostructured WO_{3-x} in the form of nanowires. Analysis of the surface by XPS corroborated the silinization process, showing additional Si 2p, Si 2s and N 1s core-level peaks in the spectra of the APTES

modified samples. Moreover, the results obtained employing UPS and diffuse reflectance analysis allowed to infer the energy level diagram and the possible role of APTES in the sensing mechanism under UV-light exposure. Gas sensing results revealed enhanced sensing properties including better reproducibility and stability for the APTES@WO_{3-x} sensors compared to the non-modified WO_{3-x} sensors. For instance, tests of the APTES@WO_{3-x} sensors to 80 ppm of ethanol and nitrogen dioxide displayed approximately eight-fold the response of the non-modified WO_{3-x} sensors. Further, results also indicated good sensitivity for the APTES@WO_{3-x} sensors to ethanol (19.1 %) and nitrogen dioxide (7.9 %) compared to the WO_{3-x} sensors (1.1 % and 0.4 % to ethanol and nitrogen dioxide, respectively) with a strong selectivity to ethanol among other reducing gases (acetone, toluene, hydrogen, and carbon monoxide). These results are attributed to the presence of the reactive amino group at the APTES@WO_{3-x} sensors, which facilitates the reaction with the tested gases and the electron transfer to/from the MOX under UV-light excitation.

CRedit authorship contribution statement

M. Tomić: Validation, Formal analysis, Writing - original draft. **Z. Fohlerova:** Conceptualization, Methodology, Formal analysis, Writing - review & editing. **I. Gràcia:** Methodology, Validation. **E. Figueras:** Methodology, Validation. **C. Cané:** Funding acquisition. **S. Vallejos:** Conceptualization, Methodology, Formal analysis, Writing - review & editing, Funding acquisition.

Declaration of Competing Interest

The authors report no declarations of interest.

Acknowledgments

This work has been supported by the Spanish Ministry of Science and Innovation via Grant TEC2016-79898-C6-1-R, PID2019-107697RB-C42 (AEI/FEDER, EU) and the Ramón y Cajal programme, and the Czech Science Foundation (GAČR) via Grant No 20-20123S. This research has made use of the infrastructures of the Spanish ICTS Network MICRO-NANOFABS, partially supported by MINECO, and Czech CEITEC Nano Research Infrastructure, supported by MEYS CR (LM2018110). We are grateful to Tomáš Lednický and Milena Šerka for acquiring the XPS spectra.

Appendix A. Supplementary data

Supplementary material related to this article can be found, in the online version, at doi:<https://doi.org/10.1016/j.snb.2020.129046>.

References

- [1] D.R. Miller, S.A. Akbar, P.A. Morris, Nanoscale metal oxide-based heterojunctions for gas sensing: a review, *Sensors Actuators B Chem.* 204 (2014) 250–272, <https://doi.org/10.1016/j.snb.2014.07.074>.
- [2] X. Chen, C.K.Y. Wong, C.A. Yuan, G. Zhang, Nanowire-based gas sensors, *Sensors Actuators, B Chem.* (2013), <https://doi.org/10.1016/j.snb.2012.10.134>.
- [3] E. Brunet, T. Maier, G.C. Mutinati, S. Steinhauer, A. Köck, C. Gspan, W. Grogger, Comparison of the gas sensing performance of SnO₂ thin film and SnO₂ nanowire sensors, *Sensors Actuators, B Chem.* 165 (2012) 110–118, <https://doi.org/10.1016/j.snb.2012.02.025>.
- [4] M. Tomić, M. Šerka, O. Chmela, I. Gràcia, E. Figueras, C. Cané, S. Vallejos, Certium oxide-tungsten oxide core-shell nanowire-based microsensors sensitive to acetone, *Biosensors* 8 (2018) 116–127, <https://doi.org/10.3390/bios8040116>.
- [5] S. Vallejos, I. Gràcia, O. Chmela, E. Figueras, J. Hubálek, C. Cané, Chemoresistive micromachined gas sensors based on functionalized metal oxide nanowires: performance and reliability, *Sensors Actuators, B Chem.* 235 (2016) 525–534, <https://doi.org/10.1016/j.snb.2016.05.102>.
- [6] S. Vallejos, N. Pizúrová, J. Čechal, I. Gràcia, C. Cané, Aerosol-assisted chemical vapor deposition of metal oxide structures: zinc oxide rods, *JoVE* (2017) e56127, <https://www.jove.com/video/56127>.
- [7] S. Vallejos, S. Selina, F.E. Annanouch, I. Gràcia, E. Llobet, C. Blackman, Aerosol assisted chemical vapour deposition of gas sensitive SnO₂ and Au-functionalised SnO₂ nanorods via a non-catalysed vapour solid (VS) mechanism, *Sci. Rep.* 6 (2016) 28464, <https://doi.org/10.1038/srep28464>.
- [8] S. Vallejos, P. Umek, C. Blackman, Aerosol assisted chemical vapour deposition control parameters for selective deposition of tungsten oxide nanostructures, *J. Nanosci. Nanotechnol.* 11 (2011) 8214–8220, <https://doi.org/10.1166/jnm.2011.5027>.
- [9] N. Markiewicz, O. Casals, C. Fabrega, I. Gràcia, C. Cané, H.S. Wasisto, A. Waag, J. D. Prades, Micro light plates for low-power photoactivated (gas) sensors, *Appl. Phys. Lett.* 114 (2019) 53508, <https://doi.org/10.1063/1.5078497>.
- [10] E. Espid, B. Adeli, F. Taghipour, Enhanced gas sensing performance of photo-activated, Pt-Decorated, single-crystal ZnO nanowires, *J. Electrochem. Soc.* 166 (2019) H3223–H3230, <https://doi.org/10.1149/2.0301905jes>.
- [11] J.D. Prades, R. Jimenez-Diaz, F. Hernandez-Ramirez, S. Barth, A. Cirera, A. Romano-Rodriguez, S. Mathur, J.R. Morante, Equivalence between thermal and room temperature UV light-modulated responses of gas sensors based on individual SnO₂ nanowires, *Sensors Actuators B Chem.* 140 (2009) 337–341, <https://doi.org/10.1016/j.snb.2009.04.070>.
- [12] L. Deng, X. Ding, D. Zeng, S. Tian, H. Li, C. Xie, Visible-light activate mesoporous WO₃ sensors with enhanced formaldehyde-sensing property at room temperature, *Sensors Actuators B Chem.* 163 (2012) 260–266, <https://doi.org/10.1016/j.snb.2012.01.049>.
- [13] N. Tsuda, K. Nasu, A. Yanase, K. Siratori, *Electronic conduction in oxides*, Springer Sci. Bus. Media. (2000). <https://www.springer.com/gp/book/9783540669562>.
- [14] W. Yu, Z. Shen, F. Peng, Y. Lu, M. Ge, X. Fu, Y. Sun, X. Chen, N. Dai, Improving gas sensing performance by oxygen vacancies in sub-stoichiometric WO_{3-x}, *RSC Adv.* 9 (2019) 7723–7728, <https://doi.org/10.1039/C9RA00116F>.
- [15] W. Liu, L. Xu, K. Sheng, C. Chen, X. Zhou, B. Dong, X. Bai, S. Zhang, G. Lu, H. Song, APTES-functionalized thin-walled porous WO₃ nanotubes for highly selective sensing of NO₂ in a polluted environment, *J. Mater. Chem. A* 6 (2018) 10976–10989, <https://doi.org/10.1039/C8TA02452A>.
- [16] M. Hijazi, Valérie Stambouli, Mathilde Rieu, Guy Tournier, Christophe Pijolat, J.-P. Viricelle, Sensitive and selective Ammonia gas sensor based on molecularly modified SnO₂, *Euro Sensors* (2017), <https://doi.org/10.3390/proceedings1040399>.
- [17] S. Vallejos, Z. Fohlerová, M. Tomić, I. Gràcia, E. Figueras, C. Cané, Room temperature ethanol microsensors based on silanized tungsten oxide nanowires, *Proceedings* (2018), <https://doi.org/10.3390/proceedings2130790>.
- [18] S.E. Powers, C.S. Hunt, S.E. Heermann, H.X. Corseuil, D. Rice, P.J.J. Alvarez, The transport and fate of ethanol and BTEX in groundwater contaminated by gasoline, *Crit. Rev. Environ. Sci. Technol.* 31 (2001) 79–123, <https://doi.org/10.1080/20016491089181>.
- [19] G. Lu, J. Xu, J. Sun, Y. Yu, Y. Zhang, F. Liu, UV-enhanced room temperature NO₂ sensor using ZnO nanorods modified with SnO₂ nanoparticles, *Sensors Actuators B Chem.* 162 (2012) 82–88, <https://doi.org/10.1016/j.snb.2011.12.039>.
- [20] S. Vallejos, I. Gràcia, N. Pizúrová, E. Figueras, J. Čechal, J. Hubálek, C. Cané, Gas sensitive ZnO structures with reduced humidity-interference, *Sensors Actuators B Chem.* 301 (2019) 127054, <https://doi.org/10.1016/j.snb.2019.12.054>.
- [21] P. Yu, M. Cardona, *Fundamentals of Semiconductors: Physics and Materials Properties*, Springer-Verlag, Berlin, Heidelberg, 2001. <https://link.springer.com/book/10.1007/978-3-642-00710-1>.
- [22] H. Watanabe, K. Fujikata, Y. Oaki, H. Imai, Band-gap expansion of tungsten oxide quantum dots synthesized in sub-nano porous silica, *Chem. Commun. (Camb.)* 49 (2013) 8477–8479, <https://doi.org/10.1039/C3CC44264K>.
- [23] R.G. Acres, A.V. Ellis, J. Alvino, C.E. Lenahan, D.A. Khodakov, G.F. Metha, G. G. Andersson, Molecular structure of 3-Aminopropyltriethoxysilane layers formed on silanol-terminated silicon surfaces, *J. Phys. Chem. C* 116 (2012) 6289–6297, <https://doi.org/10.1021/jp212056s>.
- [24] E.T. Vandenberg, L. Bertilsson, B. Liedberg, K. Uvdal, R. Erlandsson, H. Elwing, I. Lundström, Structure of 3-aminopropyl triethoxy silane on silicon oxide, *J. Colloid Interface Sci.* 147 (1991) 103–118, [https://doi.org/10.1016/0021-9797\(91\)90139-Y](https://doi.org/10.1016/0021-9797(91)90139-Y).
- [25] J.-H. Huang, T.-Y. Huang, H.-Y. Wei, K.-C. Ho, C.-W. Chu, Wet-milled transition metal oxide nanoparticles as buffer layers for bulk heterojunction solar cells, *RSC Adv.* 2 (2012) 7487–7491, <https://doi.org/10.1039/C2RA20543B>.
- [26] H. Kyaw, S.H. Al-Harhi, A. Sellai, J. Dutta, Self-organization of gold nanoparticles on silanated surfaces, *Beilstein J. Nanotechnol.* 6 (2015) 2345–2353, <https://doi.org/10.3762/bjnano.6.242>.
- [27] M. Vasilopoulou, A. Soulati, D.G. Georgiadou, T. Stergiopoulos, L.C. Palilis, S. Kennou, N.A. Stathopoulos, D. Davazoglou, P. Argitis, Hydrogenated under-stoichiometric tungsten anode interlayers for efficient and stable organic photovoltaics, *J. Mater. Chem. A* 2 (2014) 1738–1749, <https://doi.org/10.1039/C3TA13975A>.
- [28] P. Saravanan, K. Jayamoorthy, S. Anandakumar, Fluorescence quenching of APTES by Fe₂O₃ nanoparticles – sensor and antibacterial applications, *J. Lumin.* 178 (2016) 241–248, <https://doi.org/10.1016/j.jlumin.2016.05.031>.
- [29] S. Cui, H. Pu, S.A. Wells, Z. Wen, S. Mao, J. Chang, M.C. Hersam, J. Chen, Ultrahigh sensitivity and layer-dependent sensing performance of phosphorene-based gas sensors, *Nat. Commun.* (2015), <https://doi.org/10.1038/ncomms9632>.
- [30] C. Reichardt, *Solvents and Solvent Effects in Organic Chemistry*, Wiley-VCH, Weinheim/Germany, 2003. <https://www.wiley.com/en-us/Solvents+in+and+Solvent+Effects+in+Organic+Chemistry%2C+3rd%2C+Updated+and+Enlarged+Edition-p-9783527605675>.
- [31] N. Baran, H. Gebavi, L. Mikac, D. Ristić, M. Gotić, K.A. Syed, M. Ivanda, Sensing properties of oxidized nanostructured silicon surface on vaporized molecules, *Sensors* 19 (2019), <https://doi.org/10.3390/s19010119>, 119.
- [32] S. Vallejos, V. Khatko, J. Calderer, I. Gràcia, C. Cané, E. Llobet, X. Correig, Micro-machined WO₃-based sensors selective to oxidizing gases, *Sensors Actuators B Chem.* 132 (2008) 209–215, <https://doi.org/10.1016/j.snb.2008.01.044>.
- [33] Z. Ling, C. Leach, The effect of relative humidity on the NO₂ sensitivity of a SnO₂/WO₃ heterojunction gas sensor, *Sensors Actuators, B Chem.* 102 (2004) 102–106, <https://doi.org/10.1016/j.snb.2004.02.017>.
- [34] C. Guo, Z. Lin, W. Song, X. Wang, Y. Huang, K. Wang, Synthesis, UV response, and room-temperature ethanol sensitivity of undoped and Pd-doped coral-like SnO₂, *J. Nanopart. Res.* 15 (2013) 1998, <https://doi.org/10.1007/s11051-013-1998-2>.
- [35] H. Chen, Y. Liu, C. Xie, J. Wu, D. Zeng, Y. Liao, A comparative study on UV light activated porous TiO₂ and ZnO film sensors for gas sensing at room temperature, *Ceram. Int.* 38 (2012) 503–509, <https://doi.org/10.1016/j.ceramint.2011.07.035>.
- [36] Y. Mun, S. Park, S. An, C. Lee, H.W. Kim, NO₂ gas sensing properties of Au-functionalized porous ZnO nanosheets enhanced by UV irradiation, *Ceram. Int.* 39 (2013) 8615–8622, <https://doi.org/10.1016/j.ceramint.2013.04.035>.
- [37] J. Zhai, L. Wang, D. Wang, Y. Lin, D. He, T. Xie, UV-illumination room-temperature gas sensing activity of carbon-doped ZnO microspheres, *Sensors Actuators B Chem.* 161 (2012) 292–297, <https://doi.org/10.1016/j.snb.2011.10.034>.
- [38] S. Park, H. Ko, S. Lee, H. Kim, C. Lee, Light-activated gas sensing of Bi₂O₃-core/ZnO-shell nanobelt gas sensors, *Thin Solid Films* 570 (2014) 298–302, <https://doi.org/10.1016/j.tsf.2014.02.110>.
- [39] E. Espid, F. Taghipour, Development of highly sensitive ZnO/In₂O₃ composite gas sensor activated by UV-LED, *Sensors Actuators B Chem.* 241 (2017) 828–839, <https://doi.org/10.1016/j.snb.2016.10.129>.
- [40] S. Park, S. An, Y. Mun, C. Lee, UV-enhanced NO₂ gas sensing properties of SnO₂-Core/ZnO-Shell nanowires at room temperature, *ACS Appl. Mater. Interfaces* 5 (2013) 4285–4292, <https://doi.org/10.1021/am400500a>.
- [41] C.-H. Lin, R.-S. Chen, T.-T. Chen, H.-Y. Chen, Y.-F. Chen, R.-S. Chen, L.-C. Chen, High photocurrent gain in SnO₂ nanowires, *Appl. Phys. Lett.* 93 (2008) 112115, <https://doi.org/10.1063/1.2987422>.
- [42] M. Ekrami, G. Magna, Z. Emam-djomeh, M. Saeed Yarmand, R. Paolesse, C. Di Natale, Porphyrin-functionalized zinc oxide nanostructures for sensor applications, *Sensors* 18 (2018) 2279, <https://doi.org/10.3390/s18072279>.

M. Tomić received the B.Sc. and M.Sc. degree in chemical engineering from the University of Belgrade, Serbia, in 2011. She is currently PhD student at the Institute of Microelectronics of Barcelona (IMB-CNM, CSIC) in Spain. Her research interests include synthesis and characterization of the gas sensitive metal oxide materials and development of gas sensors devices.

Z. Fohlerova received her PhD degree from the Technical University in Brno. She is currently researcher at Central European Institute of Technology. Here research interests include surface functionalization and biomedical applications.

I. Gracia received her PhD degree in physics in 1993 from the Autonomous University 18 of Barcelona, Spain, working on chemical sensors. She joined the National Microelectronics Center (CNM) working on photolithography, currently she is full time 20 senior researcher in the Micro-Nano Systems department of the CNM and her work is focused on gas sensing technologies and MEMS reliability.

E. Figueras graduated in Physics in 1983 at Universitat Autònoma de Barcelona and received his Ph.D. Physics in 1988. Since 1989 is Tenured Scientist (Científico Titular) at

the Microelectronic Institute of Barcelona (IMB-CNM, CSIC). He spent ten years as head of the clean room, carrying out the standardization of the new technologies developed at the Institute. Since 2000 his research is in the field of micro/nanostructures for gas sensors.

C. Cané is Telecommunication Engineer since 1985 and he got the PhD in 1989. Since 1990 he is full time senior researcher at the National Microelectronics Centre in Spain IMB-CNM-CSIC and has been working in the development of CMOS technologies and also on mechanical and chemical sensors, MEMs and microsystems. Over the years he has been coordinator of several R&D projects, both at national and international level.

S. Vallejos received her PhD degree in Electronic Engineering from the Universitat Rovira i Virgili, Spain. Currently, she holds a Ramón y Cajal fellowship and her research is focused on gas sensing technologies and nanomaterials. She is interested in exploring scalable synthesis methods to tailor and engineer the sensing properties of nanomaterials, as well as in the development of gas sensing microsystems for applications in safety, medicine, and environment.

Supporting Information

UV-light activated APTES modified WO_{3-x} nanowires sensitive to ethanol and nitrogen dioxide

M. Tomić,^{1,2} Z. Fohlerova,^{3,4} I. Gracia,¹ E. Figueras,¹ C. Cané,¹ and S. Vallejos^{1,3}*

5 ¹ Institute of Microelectronics of Barcelona (IMB-CNM, CSIC), Campus UAB, 08193 Cerdanyola del Vallès (Barcelona), Spain.

² Autonomous University of Barcelona (UAB), Campus UAB, 08193 Cerdanyola del Vallès (Barcelona), Spain.

10 ³ CEITEC - Central European Institute of Technology, Brno University of Technology, 61200 Brno, Czech Republic.

⁴ Department of Microelectronics, Faculty of Electrical Engineering and Communication, Brno University of Technology, Technická 3058/10, 61600 Brno, Czech Republic.

15 **S1. Setting of condition for the modification of WO_{3-x} nanowires with APTES**

Generally, the adsorption of APTES at a MOX surface is complex and predetermined by various experimental parameters such as the APTES concentration, process time, and temperature. Oxygen plasma treatment was used as an initial driving force for APTES adsorption to MOX. This energy-saving and eco-friendly technique that has been already reported in the literature as a simple method for the activation of MOX surface by creating hydroxyl groups [1] is considered the responsible for the APTES adsorption. Hence, the silanization conditions were set by adjusting three parameters, including the duration of plasma treatment, APTES deposition time, and the amount of silane. The concentrations of Si, O, W, N, and C elements at the surface were determined from the XPS spectra recorded for each condition using CasaXPS software. A summary of these results is displayed in **Table S1**, in which the control refers to the reference sample prior plasma treatment and APTES functionalization. Results demonstrated that the APTES adsorption on WO_{3-x} for a deposition time of 10 minutes is more efficient in the 1 minute plasma-treated surface (Si = 8.8 wt.% and N = 5.5 wt.%) than in the 5 minutes plasma-treated surface (Si = 5.7 % and N = 3.7 %) as shown in **Table S1a**. Moreover, increasing the deposition time from 10 minutes to 30 and to 50 minutes indicated no further adsorption of the APTES molecules at the WO_{3-x} with the contents of Si and N reporting only 6.9 wt.% and 4.6 wt.% for 30 minutes of deposition and 7.1 wt.% and 4.9 wt.% for 50 minutes of deposition, respectively (**Table S1b**). These results indicate that best conditions for Si and N adsorption at the WO_{3-x} surface occurs when using larger volumes, e.g., 1000 µl (Si = 11.5 wt. % and N = 7.9 wt.%) (**Table S1c**). Therefore, these conditions were used for the APTES modified samples characterized in this work.

Table S1. Concentration of elements (Si, O, W, N, and C) at the APTES modified WO_{3-x} samples obtained under the different experimental conditions - **a)** plasma treatment time (1 and 5 min), **b)** deposition time (10, 30 and 50 min), and **c)** amount of silane (15, 100 and 1000 μ l).

a)				b)				c)			
wt. %	Control	1 min	5 min	wt. %	10 min	30 min	50 min	wt. %	15 μ l	100 μ l	1000 μ l
Si 2p	-	8.8	5.7	Si 2p	8.8	6.9	7.1	Si 2p	8.8	6.9	11.5
O 1s	61.2	40.1	44.9	O 1s	40.1	45.2	39.2	O 1s	40.1	46.1	33.7
W 4f	22.8	11.9	15.2	W 4f	11.9	14.9	13.1	W 4f	11.9	16.1	8.3
N 1s	1.5	5.5	3.7	N 1s	5.5	4.6	4.9	N 1s	5.5	4.9	7.9
C 1s	14.5	33.8	30.4	C 1s	33.8	28.3	35.8	C 1s	33.8	26.1	38.6

5

S2. Results – material characterization

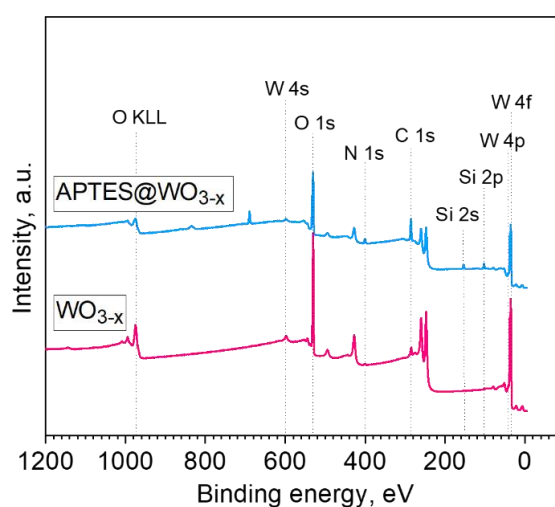
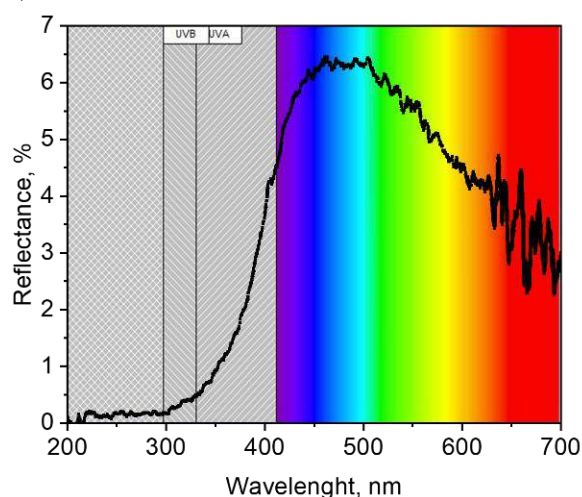


Figure S1. XPS spectra of the APTES modified and non-modified WO_{3-x} nanowires (only the peaks of interest have been marked).



10

Figure S2. Diffuse reflectance spectra of the non-modified WO_{3-x} nanowires. Examination of the films after APTES modification showed similar spectrum.

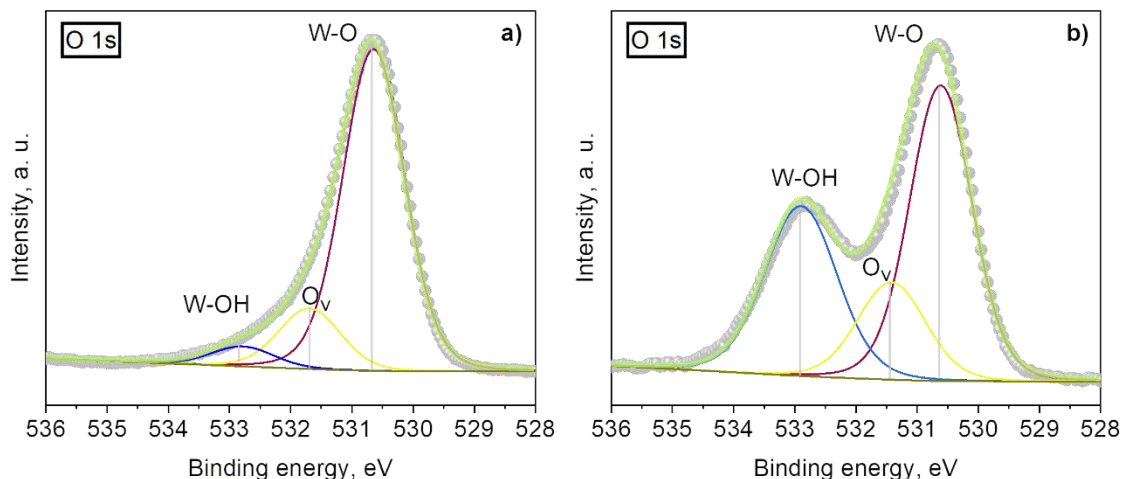


Figure S3. O 1s core level XPS spectra recorded on the WO_{3-x} nanowires **a)** before and **b)** after the plasma treatment. The gray dots show the XPS raw data, colored solid lines correspond to the envelope-fitting curve and the components. O1s peak is fitted to three peaks, at around 530.6 eV, 531.5 eV, and 532.8 eV, that correspond to the W-O bonds, the oxygen defects in the matrix of metal oxides related to oxygen vacancies, and the W-OH bonds, respectively [2]. The spectra after plasma treatment shows remarkably higher intensity for the component associated to the W-OH bonds, which can be assigned to the additional hydroxyl groups incorporated into the lattice.

10 S3. Results – gas sensing tests

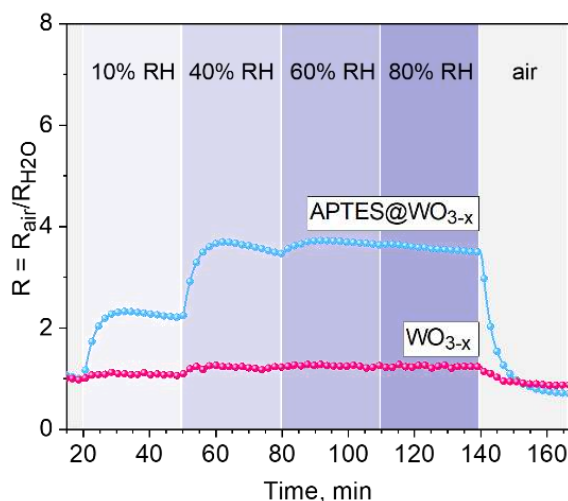


Figure S4. Typical response to various relative humidity percentages registered by the sensors based on WO_{3-x} and APTES modified WO_{3-x} nanowires employing a radiant flux of $1800 \text{ mW} \cdot \text{cm}^{-2}$. The blue bars represent the different relative humidity set at RT ($24 \text{ }^\circ\text{C}$).

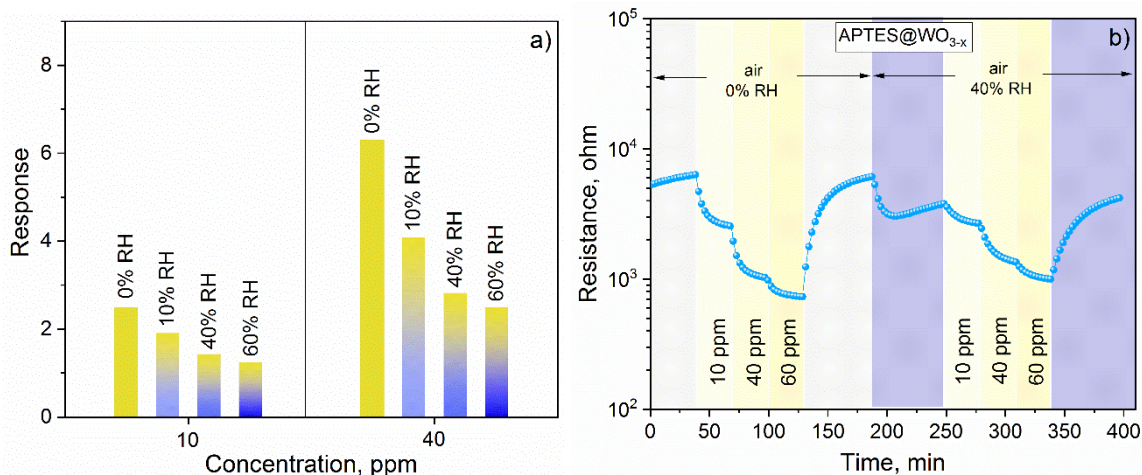


Figure S5. APTES modified WO_{3-x} response to ethanol in dry and humid ambient employing a radiant flux of $1800 \text{ mW}\cdot\text{cm}^{-2}$. **a)** Response comparison to various relative humidity conditions and ethanol concentrations, **b)** typical sensor resistance changes towards 0% RH and 40% RH for various ethanol concentrations (10, 40, 60 ppm).

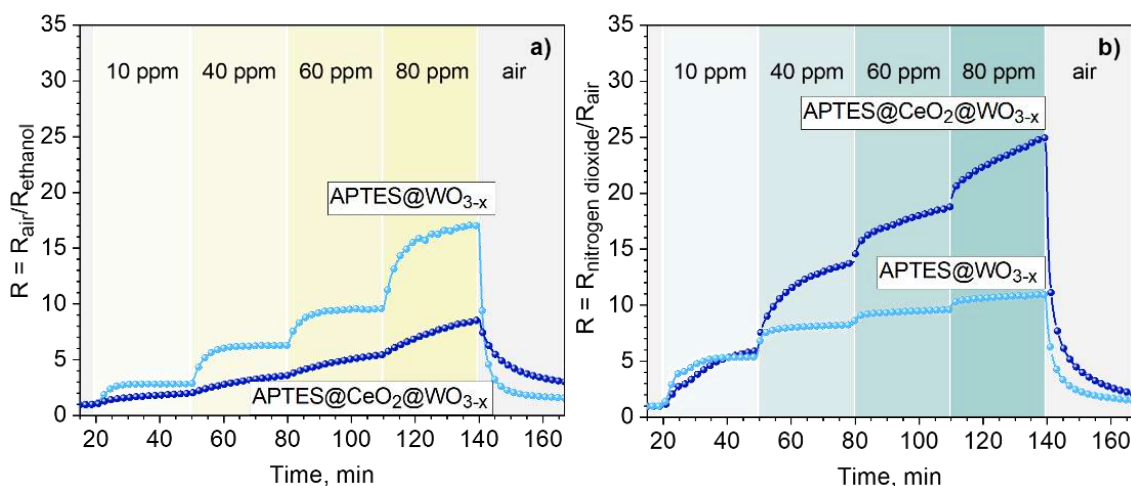


Figure S6. Typical response to various concentrations of **a)** ethanol and **b)** nitrogen dioxide registered by the sensors based on APTES modified WO_{3-x} and APTES modified $CeO_2@WO_{3-x}$ nanowires employing a radiant flux of $1800 \text{ mW}\cdot\text{cm}^{-2}$. The yellow and green bars represent the on-off for the different concentrations of ethanol and nitrogen dioxide, respectively.

S4. References

- [1] A. Merenda, E. des Ligneris, K. Sears, T. Chaffraix, K. Magniez, D. Cornu, J.A. Schütz, L.F. Dumée, Assessing the temporal stability of surface functional groups introduced by plasma treatments on the outer shells of carbon nanotubes, *Sci. Rep.* 6 (2016) 31565. <https://pubmed.ncbi.nlm.nih.gov/27507621>.
- [2] S. Jain, J. Shah, N. Negi, C. Sharma, R.K. Kotnala, Significance of interface barrier at electrode of hematite hydroelectric cell for generating ecopower by water splitting, *Int. J. Energy Res.* 43 (2019) 4743–4755. <https://onlinelibrary.wiley.com/doi/abs/10.1002/er.4613>.

Gas microsensors based on cerium oxide modified tungsten oxide nanowires

Milena Tomić, Isabel Gràcia, Marc Salleras, Eduard Figueras, Carles Cané, Stella Vallejos*

Instituto de Microelectrónica de Barcelona (IMB-CNM, CSIC)

Campus UAB, 08193 Cerdanyola del Vallès (Barcelona), Spain

*Correspondence: stella.vallejos@imb-cnm.csic.es; Tel.: +34 935 94 77 00

Abstract—A gas sensitive material consisting of tungsten oxide nanowires (NWs) modified with cerium oxide nanoparticles (NPs) was developed and integrated into micromachined transducing platforms via aerosol assisted chemical vapor deposition. Results validate the functionality of the sensors and demonstrate the enhancement of the sensing properties of tungsten oxide towards ethanol (EtOH) by its surface modification with cerium oxide. These results are attributed to the formation of heterojunctions which provides an electronic sensitization along the whole gas sensitive film.

Keywords—gas sensors, VOCs, metal oxides, heterojunctions, AACVD

I. INTRODUCTION

Generally the exhaled breath contains oxygen, nitrogen, carbon dioxide, and water vapor, although it may also contain trace concentrations of various volatile organic compounds (VOCs) [1]. Among them, the most significant are ethanol, acetone and toluene, which are generated via the biochemical processes of the body. Monitoring of these vapors in exhaled breath can be used in early detection of several diseases, such as diabetes and cancer. For example, ethanol concentration in exhaled breath of patients with lung or breast cancer and diabetes is higher (~2.1 ppm) in comparison to healthy patients (~0.2 ppm) [2-4].

Because the traditionally used technologies for breath analysis (gas chromatography, ion-mobility or mass spectrometry) are expensive and employ massive equipment [5], the development of miniaturized and low cost system, with excellent performances for VOCs detection is of great importance. In this context, semiconducting metal oxides (SMOX) are attractive as they are inexpensive, easily synthesized and ready-to-use gas sensors. Various SMOX nanostructures in the form of wires, rods, sheets, *etc.*, are used as gas sensitive materials because they have proved to enhance the functionality of the sensors, particularly in terms of sensitivity, due to their higher surface area to volume ratio as opposed to bulk SMOXs. Also, it has been proved that the surface modification of SMOXs with

second-phase constituent (noble metal or another SMOX) has a drastic effect on their sensing properties by improving the sensitivity, selectivity, stability, and reproducibility of both, the host SMOX and the second-phase constituent, especially if the size of these materials is within the Debye length of the surface (typically on the order of 2–100 nm) and the second constituent is introduced in small amount [6]. When the second-phase constituent is a SMOX, the difference in band energy of both oxides enables the formation of nanoscale heterojunctions at the interface of the two SMOXs, which provides an additional electronic sensitization to the modified material as compared to non-modified [6].

Beside commonly used tin oxide and zinc oxide, tungsten oxide have drawn a lot of attention as gas sensitive material due to its inherent electrical conductivity and sensitivity towards nitrogen dioxide [7], ozone [7], and ammonia [8,9]. Furthermore, when modified with noble metal (e.g., gold, platinum) or other SMOX (e.g., copper oxide, iron oxide), tungsten oxide showed strong sensitivity to hydrogen [10], hydrogen sulphide [11] and toluene [12]. Even though less explored than tungsten oxide, cerium oxide have distinctive features that make this oxide a potential candidate for application in gas sensors. The specificity of this oxide lies in a good redox behavior and catalytic activity caused by the formation of defect sites as a result of valence state changes between two cerium species - Ce(III) and Ce(IV), which alter considerably the concentration of oxygen vacancies [13-15].

The synthesis route can significantly affect the morphology and sensing properties of SMOX. Aerosol assisted chemical vapor deposition (AACVD) is a variant of the conventional CVD technique which uses solvent aerosols to transport precursors to a heated reaction zone. This method was previously used for the deposition of non-modified (e.g., tungsten oxide) or modified SMOXs (e.g., iron oxide modified tungsten oxide) [12,16] with enhanced gas sensing properties. AACVD process does not require volatile precursors, as long as they are soluble, which makes this method ideal for the synthesis of various SMOXs, including cerium

oxide. Thus, here we use AACVD to synthesize tungsten oxide NWs modified with cerium oxide NPs and validate its gas sensing properties upon ethanol (EtOH).

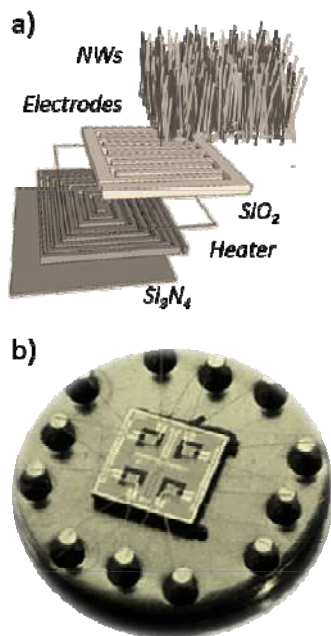


Fig. 1. Schematic view of the layers comprising the microsensors (a) and photograph of the array of 4 micromachined sensors mounted on a standard TO8 package (b).

II. MATERIALS AND METHODS

The nanowire synthesis is carried out in two stages using previously described AACVD method [12]. In first stage non-modified tungsten oxide nanowires (NWs) were grown directly onto micromachined transducing platforms. In the second stage the cerium oxide modified tungsten oxide nanowires were deposited using a cerium (III) acetylacetonate hydrate (28 mg, Ce(acac)₃·xH₂O, Sigma-Aldrich) as a precursor and methanol (2 ml, Sigma-Aldrich) as a solvent at the temperature of 500 °C. Subsequently the sensitive films (non-modified and modified) were annealed at 500 °C. The scheme and photograph of the microsensors are shown in **Fig. 1**.

The samples were analyzed using scanning electron microscopy (SEM – Carl Zeiss, Auriga Series, 3 KV) for examination of morphology of the films and X-ray photoelectron spectroscopy (XPS – Kratos Axis Supra with monochromatic K α radiation with emission current of 15 mA and hybrid lens mode) for investigation of chemical composition of the films.

Gas sensor testing was carried out in a continuous flow test chamber provided with mass flow controllers that allow the mixture of dry/humid air and EtOH to obtain the desired concentration. For relative humidity (RH) control an evaluation kit (EK-H4, Sensirion AG) with a humidity sensor is installed inside the gas test

chamber. The sensor response was defined as R_a/R_g , where R_a and R_g are the resistance in dry/humid air and the resistance after 600 s of ethanol exposure, respectively.

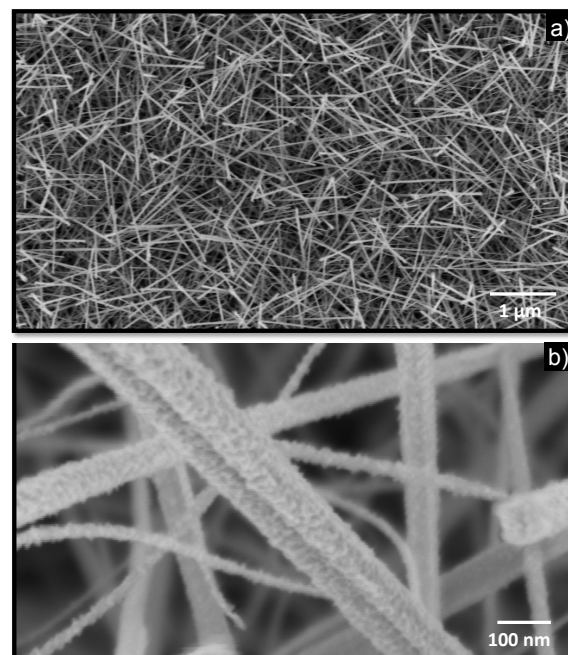


Fig. 2. Low (a) and high (b) magnification SEM of the cerium oxide modified tungsten oxide nanowires

III. RESULTS

SEM imaging of the microsensors demonstrated the integration of tungsten oxide NWs with diameters of less than 100 nm. The non-modified structures displayed bare NWs, similarly to those synthesized previously via AACVD [12], whereas the modified structures showed a thin layer covering the NWs, which corresponds to the cerium oxide NPs (**Fig. 2**). Further analysis on the modified films using XPS proved the incorporation of cerium oxide at the tungsten oxide NWs, displaying typical W 4f and Ce 3d core level peaks.

Gas sensing tests towards different EtOH concentration in dry air showed a direct proportional dependence of the response to the analyte concentration for both materials (**Fig. 3**), indicating enhanced responses for the cerium oxide modified NWs ($R=3.9$ for 80 ppm EtOH) as compared to the non-modified NWs ($R=1.9$ for 80 ppm EtOH). Further tests in humid ambient at 10 and 20% RH (**Fig. 4**) showed similar behavior, with the sensors on exposure to 20 % of RH showing a response of approximately 2.8 and 1.5 for the cerium oxide modified tungsten oxide NWs and tungsten oxide NWs, respectively, although with an attenuation of the response above 20 % with respect to the responses in dry ambient.

The reason for better functionality of cerium oxide modified tungsten oxide nanostructures lies in the difference of the energy bands of the two oxides, which results in the formation of nanoscale heterojunctions between the cerium oxide NPs and the tungsten oxide NWs. This causes electron migration from cerium oxide

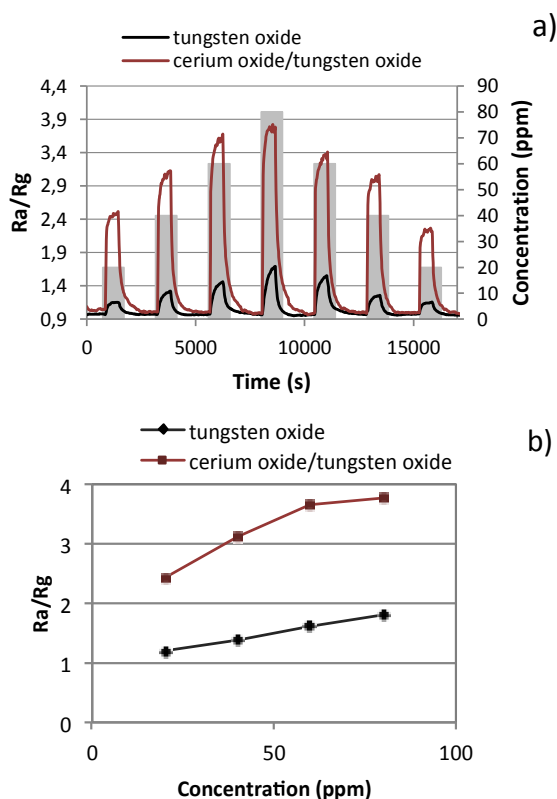


Fig. 3. Sensor response (a) and calibration curves (b) towards various concentrations (from 20 to 80 ppm) of ethanol for the microsensors based on non-modified and cerium oxide modified tungsten oxide nanowires

to tungsten oxide and the formation of an accumulation layer at the tungsten oxide surface, which leads to additional oxygen adsorption at the modified tungsten oxide surface [17,18]. Consequently, there is a compression of the conduction channel along the wire, which results in a decrease of the conductivity along the structure (**Fig. 5a**). On the other hand, when the sensitive film is exposed to a reducing gas (e.g., ethanol), electrons are released back to the conduction band, which narrows the depletion layer and at the same time increases the width of conduction channel and the conductivity along the NW (**Fig. 5b**). Although the same mechanism is present in both, modified and non-modified materials, in the case of modified materials electron migration occurring at the interface of the oxides provides larger electron density to the tungsten oxide (wider accumulation layer), and as a consequence greater changes in the depletion layer during sensor exposure to air/analyte compared to non-modified oxides. This provides higher conductivity changes and in turn higher sensor response of those materials.

Recently, we have also found that a similar mechanism enhances the functionality of the cerium oxide modified tungsten oxide NWs upon other reducing gases such as acetone, toluene, carbon monoxide and hydrogen [19].

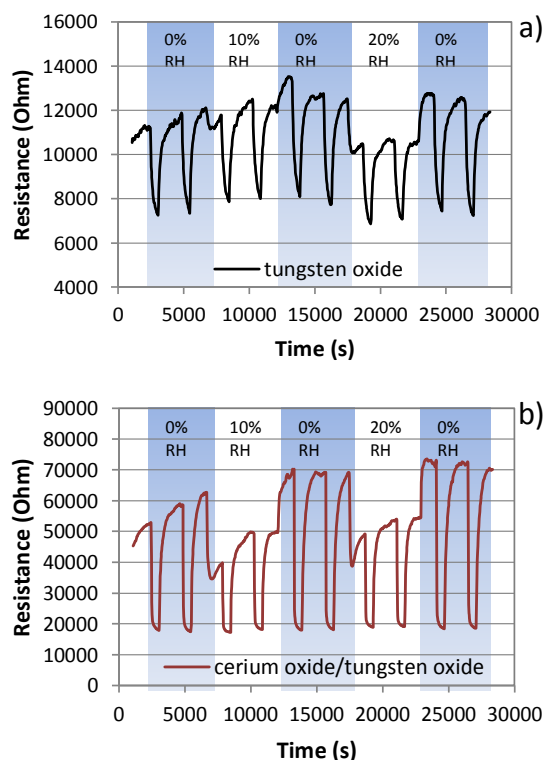


Fig. 4. Response recorded on the microsensors based on non-modified (a) and cerium dioxide modified tungsten oxide nanowires (b) towards 80 ppm of ethanol in dry and humid (10 and 20 % RH) ambient.

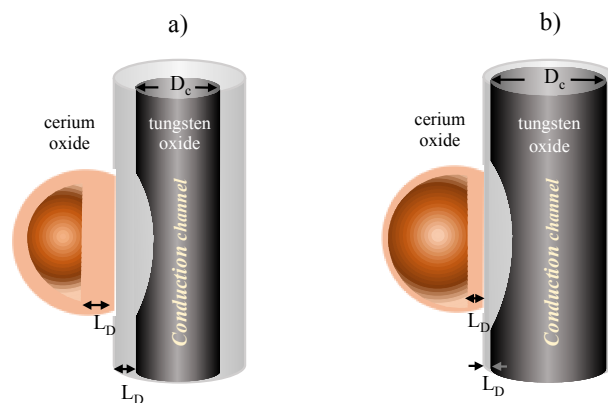


Fig. 5. Schematic view of the heterojunction formed at the surface of the cerium oxide modified tungsten oxide wires and the possible mechanism (a) after exposure to air and (b) reducing gases such as ethanol. L_D is the Debye length or depth of the depletion region from the surface and D_c represents the conduction channel (not at scale)

IV. CONCLUSION

Cerium oxide modified tungsten oxide nanowires were successfully synthesized and integrated into micromachined transducing platforms using AACVD

method. The obtained modified wires based sensor exhibited higher response and sensitivity towards EtOH as compared to pure non-modified wires based sensor. The enhancement in sensor performances is linked to the formation of nanoscale heterojunctions at the interface of the two oxides, which provides an additional electronic sensitization along the film. Humidity tests also revealed higher responses for the cerium oxide modified tungsten oxide structures than for non-modified, although with an attenuation of the response above 20% with respect to the tests in dry ambient.

ACKNOWLEDGMENTS

This work has been supported by the Spanish Ministry of Science and Innovation via Grant TEC2015-74329-JIN-(AEI/FEDER, EU) and TEC2016-79898-C6-(AEI/FEDER, EU). SV acknowledge the support of the Ramón y Cajal programme. This research has used the Spanish ICTS Network MICRONANOFABS (partially funded by MINECO).

REFERENCES

- [1] I. Nardi-Agmon, and N. Peled, "Exhaled breath analysis for the early detection of lung cancer: recent developments and future prospects," *Lung Cancer: Targets and Therapy*, vol. 8, pp. 31–38, 2017.
- [2] S. Das, S. Pal, and M. Mitra, "Significance of Exhaled Breath Test in Clinical Diagnosis: A Special Focus on the Detection of Diabetes Mellitus," *J. Med. Electron. Biol.*, vol. 36, pp. 605-624, 2016.
- [3] A. G. Dent, T. G. Sutedja, and P. V. Zimmerman, "Exhaled breath analysis for lung cancer," *J. Thorac. Dis.*, pp. S540-S550, 2013.
- [4] J. Li, Y. Peng, Y. Liu, W. Li, Y. Jin, Z. Tang, *et al.*, "Investigation of potential breath biomarkers for the early diagnosis of breast cancer using gas chromatography–mass spectrometry," *Clin. Chim. Acta*, vol. 436, pp. 59-67, 2014.
- [5] K. D. van de Kant, L. J. van der Sande, Q. Jöbsis, O. C. van Schayck, and E. Dompeling, "Clinical use of exhaled volatile organic compounds in pulmonary diseases: a systematic review," *Respir. Res.*, vol. 13, pp. 117-140, 2012.
- [6] D. R. Miller, S. A. Akbar, and P. A. Morris, "Nanoscale metal oxide-based heterojunctions for gas sensing: a review," *Sens. Actuator, B*, vol. 204, pp. 250-272, 2014.
- [7] S. Vallejos, V. Khatko, J. Calderer, I. Gracia, C. Canè, E. Llobet, *et al.*, "Micro-machined WO₃-based sensors selective to oxidizing gases," *Sens. Actuators B*, vol. 132, pp. 209-215, 2008.
- [8] D.D. Nguyen, D.V. Dang, and D.C. Nguyen, "Hydrothermal synthesis and NH₃ gas sensing property of WO₃ nanorods at low temperature," *Adv. Nat. Sci.: Nanosci. Nanotechnol.*, vol. 6, pp. 1-6, 2015.
- [9] A. Reghu, D. Deniz, R. Stennett, G. Bernhardt, D. Frankel, R. Lad, and J. Vetelino, "WO₃ sensor for ppb detection of ammonia, in: Metal Oxide-based gas sensors V", The 14th International Meeting on Chemical Sensors, IMCS, Nuremberg, Germany, pp. 457–460, 2012.
- [10] S. Vallejos, P. Umek, T. Stoycheva, F. Annanouch, E. Llobet, X. Correig, *et al.*, "Single-step deposition of Au- and Pt-nanoparticle-functionalized tungsten oxide nanoneedles synthesized via aerosol-assisted CVD, and used for fabrication of selective gas microsensor arrays," *Adv. Funct. Mater.*, vol. 23, pp. 1313-1322, 2013.
- [11] F. E. Annanouch, Z. Haddi, S. Vallejos, P. Umek, P. Guttman, C. Bittencourt, *et al.*, "Aerosol-assisted CVD-grown WO₃ nanoneedles decorated with copper oxide nanoparticles for the selective and humidity-resilient detection of H₂S," *ACS Appl. Mater. Inter.*, vol. 7, pp. 6842-6851, 2015/04/01 2015.
- [12] S. Vallejos, I. Gràcia, E. Figueras, and C. Cané, "Nanoscale heterostructures based on Fe₂O₃@WO_{3-x} nanoneedles and their direct integration into flexible transducing platforms for toluene sensing," *ACS Appl. Mater. Interfaces*, vol. 7, pp. 18638-18649, 2015/08/26 2015.
- [13] R. Ma, M. Jahurul Islam, D. Amaranatha Reddy, and T. K. Kim, "Transformation of CeO₂ into a mixed phase CeO₂/Ce₂O₃ nanohybrid by liquid phase pulsed laser ablation for enhanced photocatalytic activity through Z-scheme pattern," *Ceram. Int.*, vol. 42, pp. 18495-18502, 2016.
- [14] T. Montini, M. Melchionna, M. Monai, and P. Fornasiero, "Fundamentals and Catalytic Applications of CeO₂-Based Materials," *Chem. Rev.*, vol. 116, pp. 5987-6041, 2016.
- [15] G. Magesh, B. Viswanathan, R. P. Viswanath, and T. K. Varadarajan, "Photocatalytic behavior of CeO₂-TiO₂ system for the degradation of methylene blue," *Indian Journal of Chemistry -Section A*, vol. 48A, pp. 480-488, 2009.
- [16] S. Vallejos, I. Gràcia, J. Bravo, E. Figueras, J. Hubálek, and C. Cané, "Detection of volatile organic compounds using flexible gas sensing devices based on tungsten oxide nanostructures functionalized with Au and Pt nanoparticles", *Talanta*, vol. 139, 27–34, 2015.
- [17] S. Wang, Y. Wang, H. Zhang, X. Gao, J. Yang, and Y. Wang, "Fabrication of Porous α -Fe₂O₃ Nanoshuttles and Their Application for Toluene Sensors," *RSC Adv.*, vol. 4, pp. 30840–30849, 2014.
- [18] L. Wang, J. Deng, Z. Lou, and T. Zhang, "Nanoparticles-Assembled Co₃O₄ Nanorods P-Type Nanomaterials: One-Pot Synthesis and Toluene-Sensing Properties," *Sens. Actuators, B*, vol. 201, pp. 1–6, 2014.
- [19] M Tomić, M Šetka, O. Chmela, I. Gràcia, E. Figueras, C. Cané, and S. Vallejos, "Cerium Oxide-Tungsten Oxide Core-Shell Nanowire-Based Microsensors Sensitive to Acetone," *Biosensors*, vol. 8, pp. 116–127, 2018.

3.3 Modification of zinc oxide by nanoscale interfaces

Along with WO_3 , ZnO is one of the most interesting gas-sensitive MOX materials due to its n-type behavior, wide band gap of 3.3 eV, and versatile application in microelectronics [23]. Similar to WO_3 , intrinsic ZnO structures synthesized by AACVD have been a subject of investigation at the *IMB-CNM (CSIC)* in the previous years [139] [142] [181]. This thesis, however, goes a step further by exploring and setting up methods to modify the surface of the AACVD ZnO structures with either noble metals (i.e., Au) or other MOXs (i.e., Cu_2O or Fe_2O_3) particles. This section presents the synthesis methods and thermoactivated gas sensing tests of these materials, which were reported as a research article in the journal *Sensors MDPI*, with the title **“ZnO structures with surface nanoscale interfaces formed by Au, Fe_2O_3 , or Cu_2O modifier nanoparticles: characterization and gas sensing properties”** [154]. The section also shows part of the photoactivated gas sensing tests of these materials, which were published in the *CDE 2021* conference proceeding with the title **“ZnO nanorods and their modification with Au nanoparticles for UV-light activated gas sensing”** [182].

3.3.1. Results

The study on the modification of zinc oxide with Au, Fe_2O_3 , or Cu_2O modifier nanoparticles allowed determining the best synthesis conditions via AACVCD and impregnation for the incorporation of Au, Fe_2O_3 , or Cu_2O nanoparticles onto the zinc oxide structures. The chemical composition of the materials, determined by XPS, revealed the presence of Fe in the form of oxide - Fe_2O_3 , Cu in the form of two oxides - CuO and Cu_2O with the major presence of Cu_2O ; and Au in three oxidation states - Au^{3+} , Au^+ , and Au^0 , with the highest content of metallic Au (2.6 at.%). The validation of sensors based on these materials towards nitrogen dioxide, ethanol, acetone, carbon monoxide, and toluene showed the best response for the Au@ZnO sensors among the others, especially for NO_2 , with about 47 times higher response to 10 ppm of NO_2 compared to the pure ZnO sensors.

As the Au@ZnO sensors showed the best thermoactivated responses, the next step in this thesis was focused on the photoactivated test of these sensors. In this context, the sensors were tested at room temperature using UV-light activation and the results showed enhanced sensitivity and better speed of response for the Au modified ZnO structures compared to the non-modified ZnO structures, providing 3 times higher response to ethanol and acetone. The improvements were also noticed in the sensor's stability and reproducibility, in favor of the decorated sensor. These results suggest that the sensitivity of the material can also be tuned by the activation principle, as the thermoactivated structures suited better to nitrogen dioxide, whereas the photoactivated structures were more sensitive to ethanol and acetone. The possible gas sensing mechanism of these surface nanoscale interfaces formed between ZnO and the other materials (Au, Fe_2O_3 , or Cu_2O) was discussed in detail in the publications listed above.

3.3.2. Conclusions

The study of synthesis conditions for the modification of the ZnO structures demonstrate the best results for the modification of ZnO with Au nanoparticles by using the impregnation method. In contrast, the AACVD method showed more appropriate for the incorporation of

Fe₂O₃ and Cu₂O onto the ZnO structures. The results confirmed the importance of the surface modification of the 'host' MOX in the overall sensing properties of the sensors showing advantages for the structures modified with gold nanoparticles, particularly in front of nitrogen dioxide. This was attributed to a combination of factors in these samples, including the oxygen vacancies, the gas sensing mechanism influenced by the nano-interfaces formed between ZnO and Au, and possible catalytic effects of the Au nanoparticles. The Au modified ZnO structures also show improved photoactivity by showing enhanced responses to ethanol and acetone with respect to the intrinsic structures. Similarly, the formation of heterojunctions provides advantages in the sensing performance of the ZnO structures modified with the n-type Fe₂O₃. This behavior, however, turned to be opposite for the ZnO structures modified with p-type Cu₂O, which buffered the response of ZnO, particularly to oxidizing gases. This is because the ionosorption of oxygen favors further the conduction by holes, contrary to n-type semiconductors, and thus diminishes the resistance changes of ZnO when exposed to an oxidizing gas.

3.3.3. Journal Article 4

ZnO structures with surface nanoscale interfaces formed by Au, Fe₂O₃, or Cu₂O modifier nanoparticles: characterization and gas sensing properties, Tomić, M., Claros, M., Gràcia, I., Figueras, E., Cané, C., Vallejos, S., *Sensors*, 2021, 21, 4509, doi: 10.3390/s21134509.

3.3.4. Conference Paper 2

ZnO nanorods and their modification with Au nanoparticles for UV-light activated gas sensing, Tomić, M., Gràcia, I., Figueras, E., Cané, C., Vallejos, S., *Spanish Conference on Electron Devices (CDE), Sevilla, Spain, 2021*, doi: 0.1109/CDE52135.2021.9455726.

Article

ZnO Structures with Surface Nanoscale Interfaces Formed by Au, Fe₂O₃, or Cu₂O Modifier Nanoparticles: Characterization and Gas Sensing Properties

Milena Tomić^{1,2}, Martha Claros³ , Isabel Gràcia¹ , Eduard Figueras¹ , Carles Cané¹ and Stella Vallejos^{1,3,*}

¹ Institute of Microelectronics of Barcelona (IMB-CNM, CSIC), Campus UAB, Cerdanyola del Vallès, 08193 Barcelona, Spain; milena.tomic@imb-cnm.csic.es (M.T.); isabel.gracia@imb-cnm.csic.es (I.G.); eduard.figueras@imb-cnm.csic.es (E.F.); carles.cane@imb-cnm.csic.es (C.C.)

² Department of Electronic Engineering, Campus UAB, Autonomous University of Barcelona (UAB), Cerdanyola del Vallès, 08193 Barcelona, Spain

³ CEITEC-Central European Institute of Technology, Brno University of Technology, 61200 Brno, Czech Republic; martha.claros@ceitec.vutbr.cz

* Correspondence: stella.vallejos@imb-cnm.csic.es; Tel.: +34-935-947700

Abstract: Zinc oxide rod structures are synthesized and subsequently modified with Au, Fe₂O₃, or Cu₂O to form nanoscale interfaces at the rod surface. X-ray photoelectron spectroscopy corroborates the presence of Fe in the form of oxide—Fe₂O₃; Cu in the form of two oxides—CuO and Cu₂O, with the major presence of Cu₂O; and Au in three oxidation states—Au³⁺, Au⁺, and Au⁰, with the content of metallic Au being the highest among the other states. These structures are tested towards nitrogen dioxide, ethanol, acetone, carbon monoxide, and toluene, finding a remarkable increase in the response and sensitivity of the Au-modified ZnO films, especially towards nitrogen dioxide and ethanol. The results for the Au-modified ZnO films report about 47 times higher response to 10 ppm of nitrogen dioxide as compared to the non-modified structures with a sensitivity of 39.96% ppm⁻¹ and a limit of detection of 26 ppb to this gas. These results are attributed to the cumulative effects of several factors, such as the presence of oxygen vacancies, the gas-sensing mechanism influenced by the nano-interfaces formed between ZnO and Au, and the catalytic nature of the Au nanoparticles.

Keywords: zinc oxide; gold; iron oxide; copper oxide; interfaces; Schottky junctions; heterojunctions; gas sensing; nitrogen dioxide



Citation: Tomić, M.; Claros, M.; Gràcia, I.; Figueras, E.; Cané, C.; Vallejos, S. ZnO Structures with Surface Nanoscale Interfaces Formed by Au, Fe₂O₃, or Cu₂O Modifier Nanoparticles: Characterization and Gas Sensing Properties. *Sensors* **2021**, *21*, 4509. <https://doi.org/10.3390/s21134509>

Academic Editor: Ilaria Fratoddi

Received: 8 June 2021

Accepted: 29 June 2021

Published: 30 June 2021

Publisher's Note: MDPI stays neutral with regard to jurisdictional claims in published maps and institutional affiliations.



Copyright: © 2021 by the authors. Licensee MDPI, Basel, Switzerland. This article is an open access article distributed under the terms and conditions of the Creative Commons Attribution (CC BY) license (<https://creativecommons.org/licenses/by/4.0/>).

1. Introduction

Gas sensors are applied in diverse scenarios, including industry, environmental protection, medicine, food quality, public safety, etc., and their usage is projected to increase further as the Internet of Things (IoT) settles [1]. Amongst a host of available gas sensor technologies based on nanomaterials, metal oxide semiconductors (MOX) based gas sensors are very promising due to their good sensitivity, small dimensions, compatibility with microelectronic fabrication processes, and potentially low cost. These devices have shown sensitivity to various gases (e.g., CO, NO₂, NH₃, H₂S) and vapors (alcohols, ketones, aldehydes, aromatic compounds), although their performance in terms of limits of detection and selectivity is still a subject of improvement [2–4].

Since the gas sensing response and mechanism of MOX are surface-dependent, previous research on gas-sensitive MOXs and their functional properties (e.g., sensitivity, selectivity, stability, speed of response) found it significant to reduce the particle size of these materials to improve their properties [5]. Other studies, moreover, showed that crystalline structures with specific surface morphologies (e.g., rods, wires, plates, etc.) are determinants to achieve better gas sensing properties [6]. The modification of these nanosized crystalline structures with second-phase constituents, either noble metals or other MOXs, demonstrated another via to enhance the functionality of the MOX support

to different gases and vapors. These improvements are generally connected with the increment of adsorption centers at the surface and the band energy structure modification due to the formation of Schottky-barrier-like junctions (metal–MOX) or heterojunctions (MOX–MOX) [7]. Consequently, the interest in finding synthetic methods that allow for crystalline MOXs with tuned second-phase constituents (metals or MOXs) has kept constant in the gas sensing field, as well as the use of methods that provide scalability to these materials and compatibility with state-of-the-art microfabrication processes for possible multi-purpose microelectronic devices [3,7].

Zinc oxide (ZnO) is an n-type semiconductor with a wide band-gap ($E_G = 3.3$ eV), high chemical and thermal stability, and tunable surface morphology due to its stable wurtzite structure [8,9]. This MOX, in its pristine form and modified with noble metals (e.g., Au, Ag, Pt, or Pd) [10–13] or another MOX (e.g., CuO) [14], is one of the most representative gas-sensitive MOXs with proved sensitivity to gases, such as CO, H₂, H₂S, and NO₂, and vapors such as ethanol, methanol, and acetaldehyde [3]. ZnO was synthesized previously by different methods, including wet- and vapor-chemical routes, delivering films and powders with varied forms, e.g., nanoplates, nanospheres, nanowires, nanorods, nanotubes, nanoflowers, nanofibers, nanoneedles, and nanoribbons [3,4]. Recently, we developed a method to deposit ZnO by aerosol-assisted chemical vapor deposition (AACVD), which offers significant advantages over other CVD techniques, including atmospheric pressure and relatively low-temperature process, as well as the possibility of tuning the material morphology and structure [15,16]. This method allowed the formation of crystalline rod-like ZnO structures and their direct integration into microsensors [17]. The surface modification of MOX structures with second-phase constituents can also be achieved by different methods [7]; amongst them, AACVD [18–20] and impregnation [21,22] methods proved effective to modify structures with both metals and MOXs. Recently, for instance, AACVD was employed to modify ZnO with iron and copper [3], although the gas sensing performance of these systems was not evaluated. Similarly, impregnation procedures based on the reduction of a chemical inorganic precursor were used to incorporate Ag and Au particles over ZnO [23,24]. However, these procedures usually do not include gold and silver preformed nanoparticles, as in the present work, and they were not employed for modifying gas-sensitive ZnO structures.

Here, we use these synthetic methods to develop crystalline ZnO structures modified with Au, Cu₂O, and Fe₂O₃ particles and go further by exploring their applicability on gas sensing. The work includes a broad analysis of the properties of these materials with nanoscale interfaces towards several gases, such as nitrogen dioxide, ethanol, acetone, carbon monoxide, and toluene, and a discussion of their influence on the gas sensing mechanism.

2. Materials and Methods

ZnO rod structures were synthesized at 400 °C on Si/SiO₂ tiles (40 mm × 40 mm) and Si-based transducing platforms (40 mm × 40 mm) via the AACVD of ZnCl₂ (50 mg, ≥98.0%, Sigma–Aldrich, St. Louis, MO, USA) dissolved in ethanol (5 mL, ≥99.9%, PanReac, Chicago, IL, USA), as described earlier [17]. The transducing platforms contained 100 pairs of Cr/Au (40/200 nm thick) interdigitated electrodes (5 × 2000 μm) with an electrode gap of 5 μm isolated from the Si substrate by a SiO₂ layer. The ZnO structures were modified with Au, Ag, Fe₂O₃, and Cu₂O in a second step using AACVD or impregnation with preformed colloidal nanoparticles. The AACVD of FeCl₃·6H₂O (3 mg, ≥99.0%, Sigma–Aldrich) at 430 °C and Cu(NO₃)₂·6H₂O (3 mg, ≥99.9%, Sigma–Aldrich) at 450 °C dissolved in acetone (3 mL, ≥99.9%, PanReac) and ethanol (3 mL, ≥99.9%, PanReac), respectively, allowed the incorporation of iron and copper oxides at the ZnO rods, similarly to our previous studies [25]. However, the AACVD at 400 °C of ethanolic solutions (3 mL) of HAuCl₄·3H₂O or AgNO₃ in concentrations up to 19 mM did not show appropriate for the incorporation of Au and Ag at the ZnO rods, despite previous evidence of the AACVD of these solutions on Si and glass tiles and other materials including WO₃ structures [26,27]. Hence, the ZnO

structures were modified with Au and Ag by impregnation method using (preformed) colloidal nanoparticles synthesized by chemical reduction of $\text{HAuCl}_4 \cdot 3\text{H}_2\text{O}$ ($\geq 99.9\%$, Sigma–Aldrich) or AgNO_3 ($\geq 99.0\%$, Sigma–Aldrich) with $\text{Na}_3\text{C}_6\text{H}_5\text{O}_7 \cdot 2\text{H}_2\text{O}$ (Ph Eur, BP, JP, USP, E 331, Sigma–Aldrich) [28] or NaBH_4 (99.0%, Sigma–Aldrich) [29], respectively. The as-synthesized nanoparticles were washed with distilled water by centrifugation (12,000 rpm, 30 min) to eliminate the unreacted chemicals before the impregnation process, which consisted of immersing the ZnO samples (60 s) into the solution with suspended preformed Au or Ag colloids heated at 60 °C.

The samples were annealed in synthetic air at 450 °C for 1 h. An examination of the samples' morphology before and after annealing using SEM (Scanning Electron Microscopy—Zeiss Auriga series, 3 kV) did not show noticeable changes. The samples synthesized on Si tiles were used to perform most of the physical and chemical analysis to avoid possible interferences from the Cr/Au electrodes, whereas the Si-based transducing platforms were used primarily for gas sensing tests after performing SEM and confirm the integration of structures with similar characteristics to those registered on the Si tiles. An analysis of the samples synthesized on Si-tiles involved the examination of morphology by TEM (Transmission Electron Microscopy—FEI Tecnai, 200 kV), including STEM (Scanning Transmission Electron Microscopy) mode with elemental analysis by EDS (Energy Dispersive Spectroscopy) and HRTEM (High-Resolution Transmission Electron Microscopy) mode. The crystalline structure was analyzed by XRD (X-ray Diffraction—Bruker, AXS D8 Advance, Cu $K\alpha$ radiation operated at 40 kV and 40 mA), and the chemical composition by XPS (X-ray Photoelectron Spectroscopy—Kratos Axis Supra spectrometer, with Al/Ag monochromatic X-ray source).

The structures were tested in a continuous flow system with dry air as the reference gas and ethanol, acetone, toluene, carbon monoxide, and nitrogen dioxide either in dry or humid ambient as analyte gases. After the exposure (10 min) to each gas analyte, the structures were recovered in the air for 30 min. Humidity was introduced to the system by bubbling through the water under controlled conditions at 25 °C. The relative humidity (RH) just at the outlet of the test chamber was monitored throughout the whole test using a humidity/temperature sensor (SHT71, operating ranges from 0 to 100% RH, accuracy of $\pm 3\%$ RH and ± 0.4 °C) [25]. The sensor response (R) was defined as $(R_a - R_g)/R_a$ for the reducing gases and $(R_g - R_a)/R_a$ for the oxidizing gases. R_a and R_g represent the electrical resistance in air and after 10 min of gas exposure, respectively. The sensitivity was defined as the ratio of a sensor response change (ΔR) to a given gas concentration change (ΔC). The structures were tested, replicating the tests for each condition (analyte, concentration, and operating temperature) at least three times. Thus, the structures operated about 120 h for 4 weeks in total.

3. Results and Discussion

The aerosol-assisted chemical vapor deposited ZnO films were characterized by a greyish color that uniformly covered the substrates. The morphological, structural, and chemical characteristics of these films were consistent with those observed in our previous work on ZnO [17]. Specifically, SEM images of the films displayed quasi-aligned rods (NRs) with lengths of approximately 1.5 μm and an average diameter of 200 nm. Similarly, TEM showed crystalline structures with a marked planar spacing of 0.26 nm and rod-like morphology. Further analysis of the films using XRD corroborated the presence of diffraction patterns corresponding to a hexagonal ZnO phase (P63mc space group, ICDD card No. 00-005-0664), and XPS confirmed the presence of typical Zn 2p and O 1s spectra characteristic for the ZnO films, as shown in Figure S1, (Supplementary Materials). The films modified with Au, Ag, Fe_2O_3 , and Cu_2O in the second-step process showed morphological, crystalline, and chemical composition that corroborated the incorporation of these materials in the host ZnO structures, except for the Ag NPs modifications, which did not display clear evidence of Ag incorporation, neither by TEM nor by XPS, despite the apparent presence of Ag NPs at the ZnO surface after impregnation and annealing process

(Figure S2, Supplementary Materials). Hence, hereafter, the results and discussion focus on the modification of ZnO with Au, Fe₂O₃, and Cu₂O.

3.1. Gold-Modified Zinc Oxide Films

Figure 1a shows the morphology of the gold-modified zinc oxide films (Au@ZnO) recorded by SEM. The SEM images display the ZnO structured films with uniform rod-like morphology and the presence of equally distributed NPs due to the incorporation of Au NPs. XRD of the Au@ZnO films (Figure 1b) displays diffraction patterns connected with the hexagonal ZnO phase, in agreement with our previous observations [17], and an absence of Au diffraction peaks. This is probably connected with the high dispersion of the Au NPs over the film, their small size, and their low amount in the film.

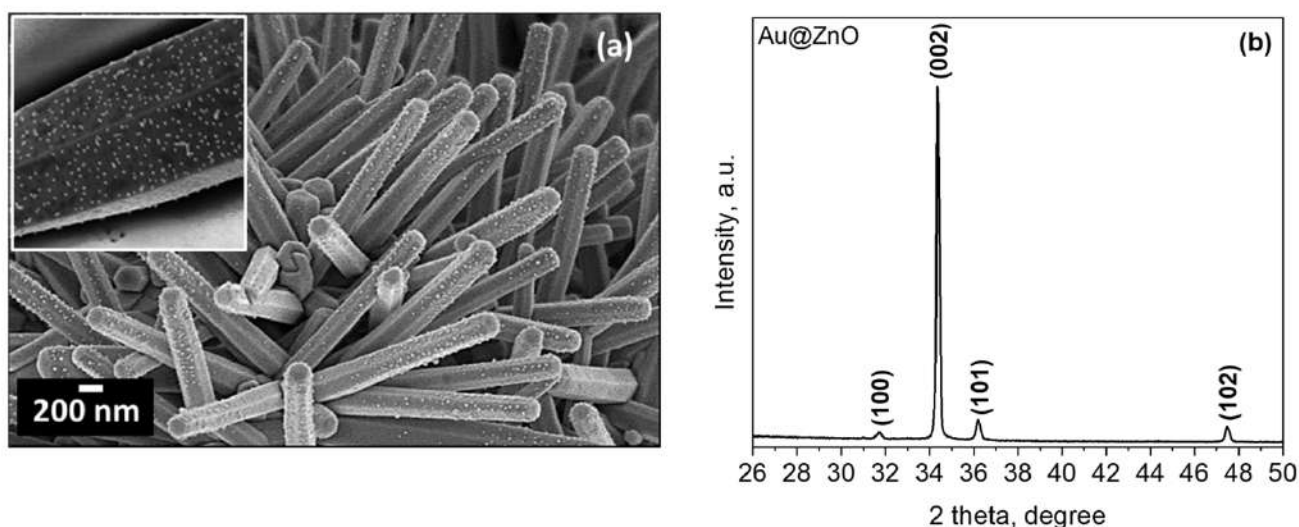


Figure 1. (a) SEM images (the inset shows a magnified image of a single Au decorated ZnO rod). (b) XRD diffraction pattern of the Au@ZnO structured film; all of the diffraction peaks in the data can be indexed to a hexagonal ZnO phase (P63mc space group, ICDD card No. 00-005-0664).

The STEM image of the Au@ZnO structures in Figure 2a confirms the rod-like morphology of ZnO and its decoration with randomly located spherical NPs with diameters between 5 and 40 nm. HRTEM of these particles (Figure 2b) reveals the presence of highly ordered crystalline lattices with interplanar spacings of 0.26 nm and 0.23 nm, consistent with the hexagonal ZnO (002) [17] and cubic Au (111) planes (Fm-3m space group, ICDD card No. 00-004-0784), respectively. Similarly, the energy dispersive spectroscopy (EDS) line-scan profiles in Figure 2c,d show the components recorded on the particle along the red line (Figure 2a) and confirm the relative locations of the elements and the incorporation of Au NPs at the ZnO rod surface.

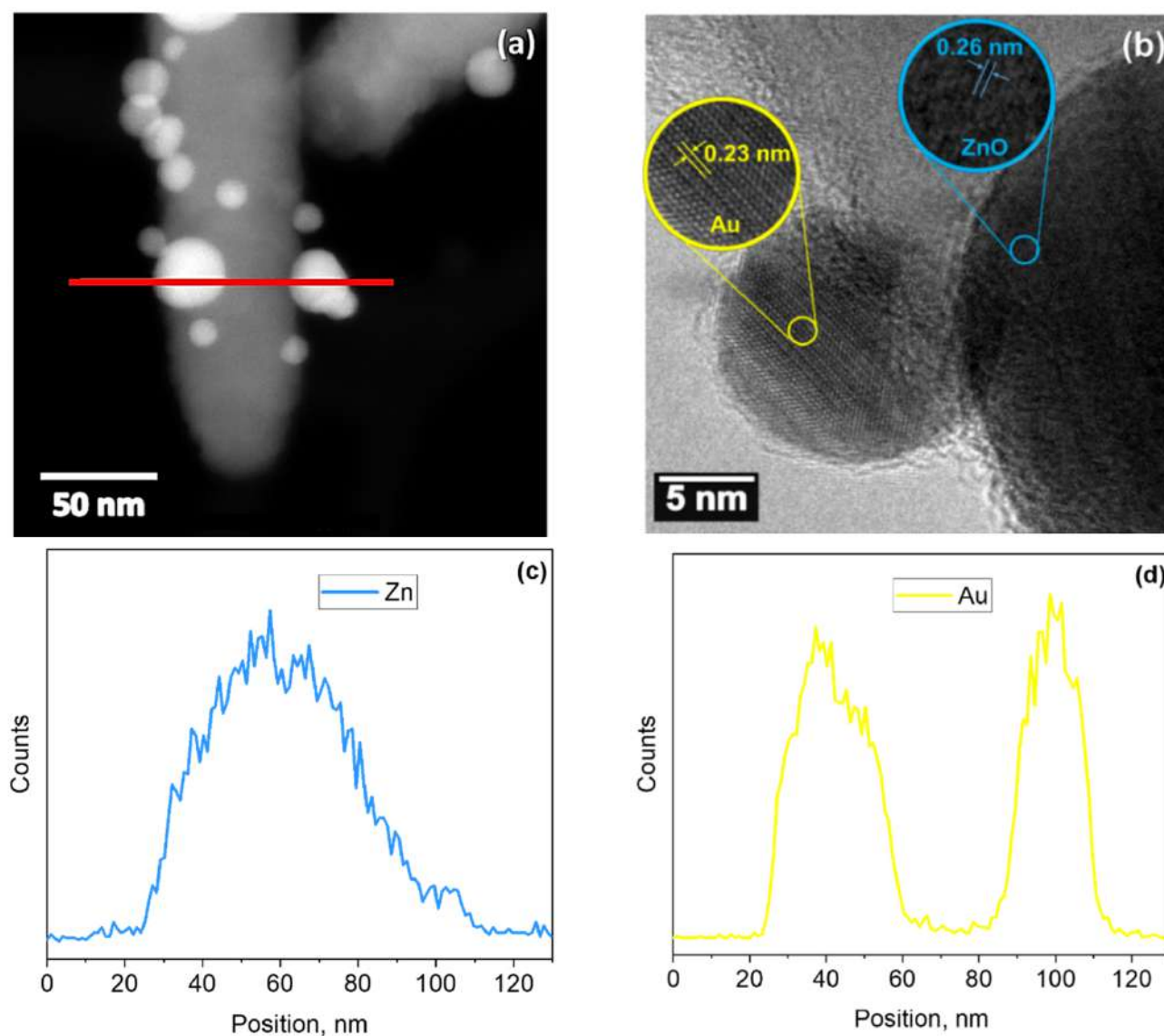


Figure 2. TEM image of an Au-modified ZnO rod. (a) Low-magnification STEM image, (b) high-resolution TEM image, and EDS line-scan profiles corresponding to the (c) ZnO rod and (d) Au nanoparticles recorded along the red line in (a).

XPS was used to analyze further the elemental and chemical composition of the Au-modified ZnO films. The main core-level spectra and their corresponding components are shown in Figure 3. The Zn 2p core-level spectrum recorded on the Au@ZnO film (Figure 3a) shows the typical Zn 2p doublet appearing at characteristic binding energies (1022.3 eV for Zn 2p_{3/2} and 1045.4 eV for Zn 2p_{1/2}), together with a shake-up peak at 1040.7 eV. The binding energy separation ($\Delta BE = 23.1$ eV) of this doublet is in agreement with the literature [30], and the ΔBE registered for the Zn 2p core-level peaks of the non-modified ZnO films (see Figure S1a, Supplementary Materials). However, it is noticed that the Zn 2p peaks of Au@ZnO are located on slightly higher binding energies (~ 0.7 eV) than those of ZnO, probably due to the incorporation of Au NPs into the ZnO film.

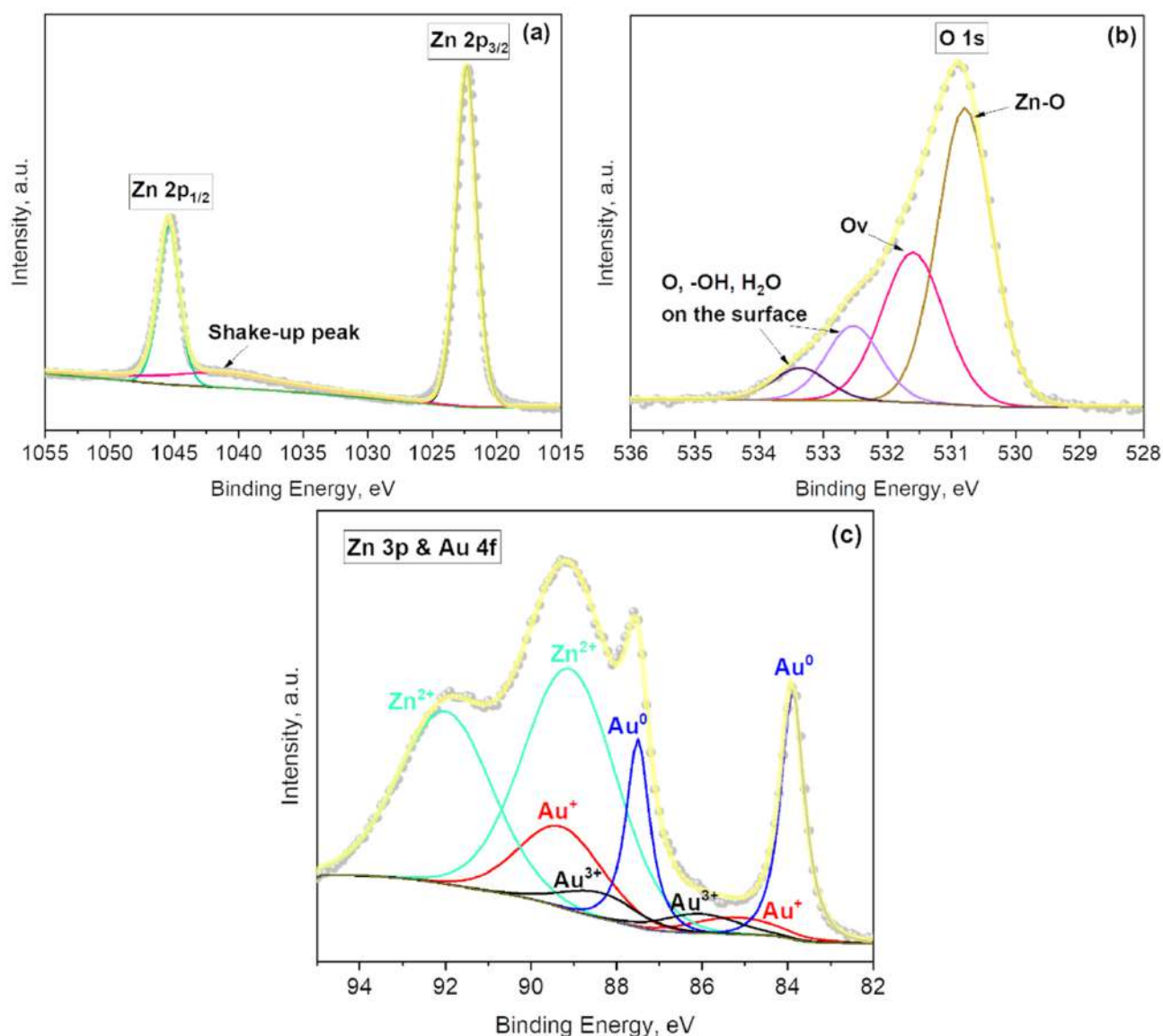


Figure 3. (a) Zn 2p, (b) O 1s, and (c) Au 4f and Zn 3p core-levels XPS spectra recorded on the Au@ZnO films. Grey dots represent the raw data, the solid yellow line corresponds to the envelope/fitting curve, and the other colored curves to the deconvoluted components.

The deconvolution of the O 1s XPS spectrum of the Au@ZnO films indicates the presence of four peaks centered at 530.8 eV, 531.6 eV, 532.5 eV, and 533.4 eV (Figure 3b). The first component corresponds to the Zn–O bonds, the second to oxygen defects in the matrix of metal oxides related to oxygen vacancies, and the third and fourth to the physical or chemical adsorbed oxygen, hydroxides, and H₂O on the surface of Au@ZnO film [31–34]. The number of components is similar to those found on the non-modified ZnO films, although their positions are minimally shifted to higher energy values (Figure S1b, Supplementary Materials).

Figure 3c displays the Au 4f spectrum of the Au@ZnO films. The deconvolution of this spectrum indicate the presence of six components assigned to different states of gold (Figure 3c), Au⁰ (at 83.9 eV and 87.5 eV), Au⁺ (at 85.2 eV and 89.3 eV), and Au³⁺ (at 86.1 eV and 88.4 eV) [35,36]. Moreover, two additional components are located at 89.1 eV and 92.0 eV, which originate from the Zn 3p emission band [37]. The formation of Au oxidized species in gold nanoparticles was reported previously and is plausible, particularly in small well-dispersed clusters [38]. An evaluation of the Au@ZnO films after the aging process at 310 °C in the same atmosphere used for the gas sensing tests (i.e., air and target gases, see

Section 3.4) corroborated the stability of the gold nanoparticles incorporated at the ZnO surface and their chemical state. Quantification of the components related to gold indicate higher amounts of metallic gold (2.6 at.%) compared to Au^+ (1.8 at.%) and Au^{3+} (0.7 at.%); this represents a 51%, 35%, and 14% of Au^0 , Au^+ , and Au^{3+} , respectively, from the total gold content at the Au@ZnO sample.

3.2. Iron-Modified Zinc Oxide Films

The SEM images of the iron-modified zinc oxide films ($\text{Fe}_2\text{O}_3@\text{ZnO}$) are presented in Figure 4a. These images show the modification of the ZnO structures with particles of flake-like morphology particularly concentrated on the top of the rods (inset in Figure 4a). The nanoflakes (NFs) are varied in size and do not exceed 20 nm in thick and 100 nm in diameter. The XRD pattern of these films corroborates the presence of the hexagonal ZnO phase determined earlier [17] and the appearance of new low-intensity diffractions. The first at 33.0° 2θ corresponds to the (222) plane of the cubic Fe_2O_3 (Ia-3 space group, ICSD Card No. 108905) and is consistent with previous Fe_2O_3 structures deposited by AACVD [39]. The second and third at 39.4° 2θ and 44.0° 2θ are connected with the rhombohedral ZnSiO_3 (R-3 space group, ICSD Card No. 340575) and cubic $\text{Fe}_2\text{O}_4\text{Zn}$ (Fd-3m space group, ICSD Card No. 91940), most likely present at the interfaces of $\text{Fe}_2\text{O}_3/\text{ZnO}$ and ZnO/Si (from the substrate), respectively. This is consistent with our previous observation for similarly structured films [25].

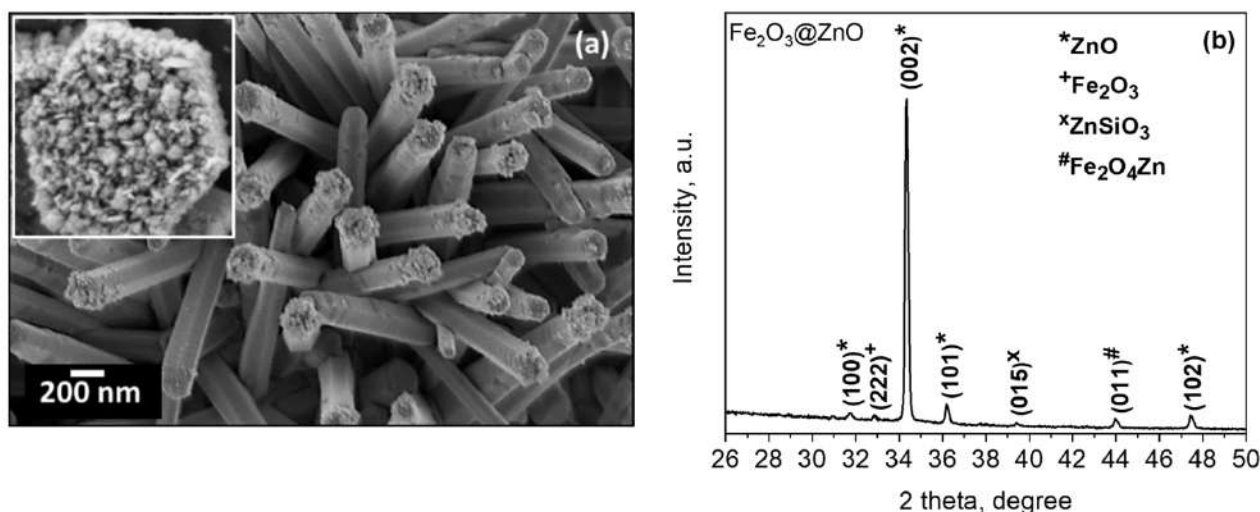


Figure 4. (a) SEM images (the inset shows a magnified image of the top of the Fe decorated ZnO rod) and (b) XRD diffraction pattern of the $\text{Fe}_2\text{O}_3@\text{ZnO}$ structured film.

STEM images of the $\text{Fe}_2\text{O}_3@\text{ZnO}$ structures (Figure 5a) showed a rod-like morphology covered by tiny particles. HRTEM images of these particles (Figure 5b) revealed crystalline structures with lattice spacings of 0.26 nm and 0.28 nm, assigned to the (002) plane of the hexagonal ZnO and the (222) plane of the cubic phase of the Fe_2O_3 identified by XRD, respectively. EDS line-scan profiles (Figure 5c,d) recorded along the red line in Figure 5a confirm the presence of Zn and Fe in the rod area and only Fe in the outer area of the rod.

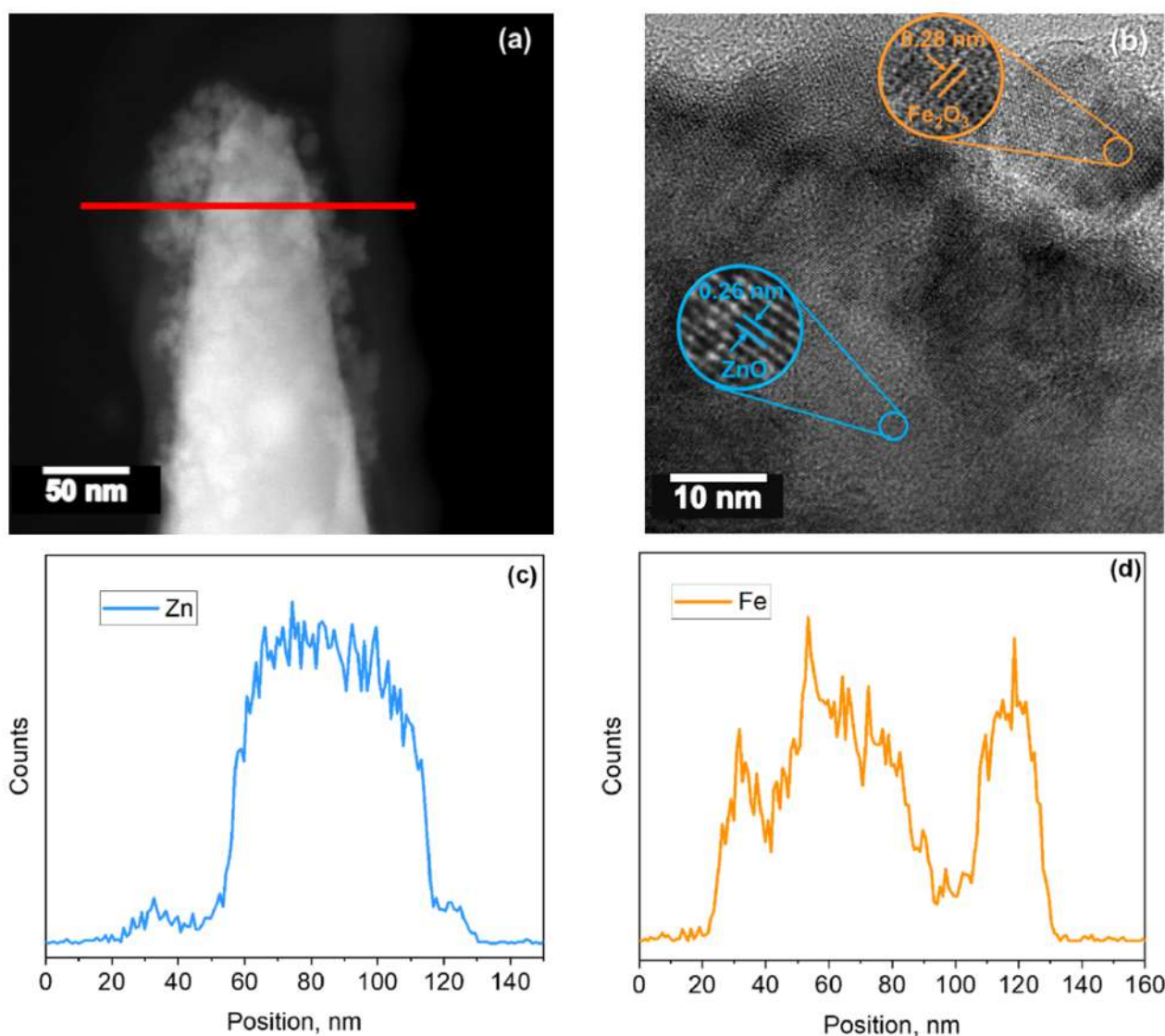


Figure 5. TEM image of a ZnO rod modified with Fe₂O₃. (a) Low-magnification STEM image, (b) high-resolution TEM image, and EDS line-scan profiles corresponding to (c) Zn and (d) Fe recorded along the red line in (a).

The surface chemical state of the Fe₂O₃@ZnO films characterized by XPS is presented in Figure 6. Similar to our previous observations on Au@ZnO films, the Zn 2p core-level spectrum of the Fe₂O₃@ZnO films showed a doublet ($\Delta BE = 23.2$ eV) with the Zn 2p_{3/2} and Zn 2p_{1/2} peaks centered at 1021.8 eV and 1044.9 eV (Figure 6a), respectively, in agreement with the previous literature [25]. The Zn 2p core-level peaks from Fe₂O₃@ZnO show nearly identical positions to those of ZnO films and a slight shift to lower binding energies in relation to those of Au@ZnO films (see Figure S1a, Supplementary Materials, and Figure 3a).

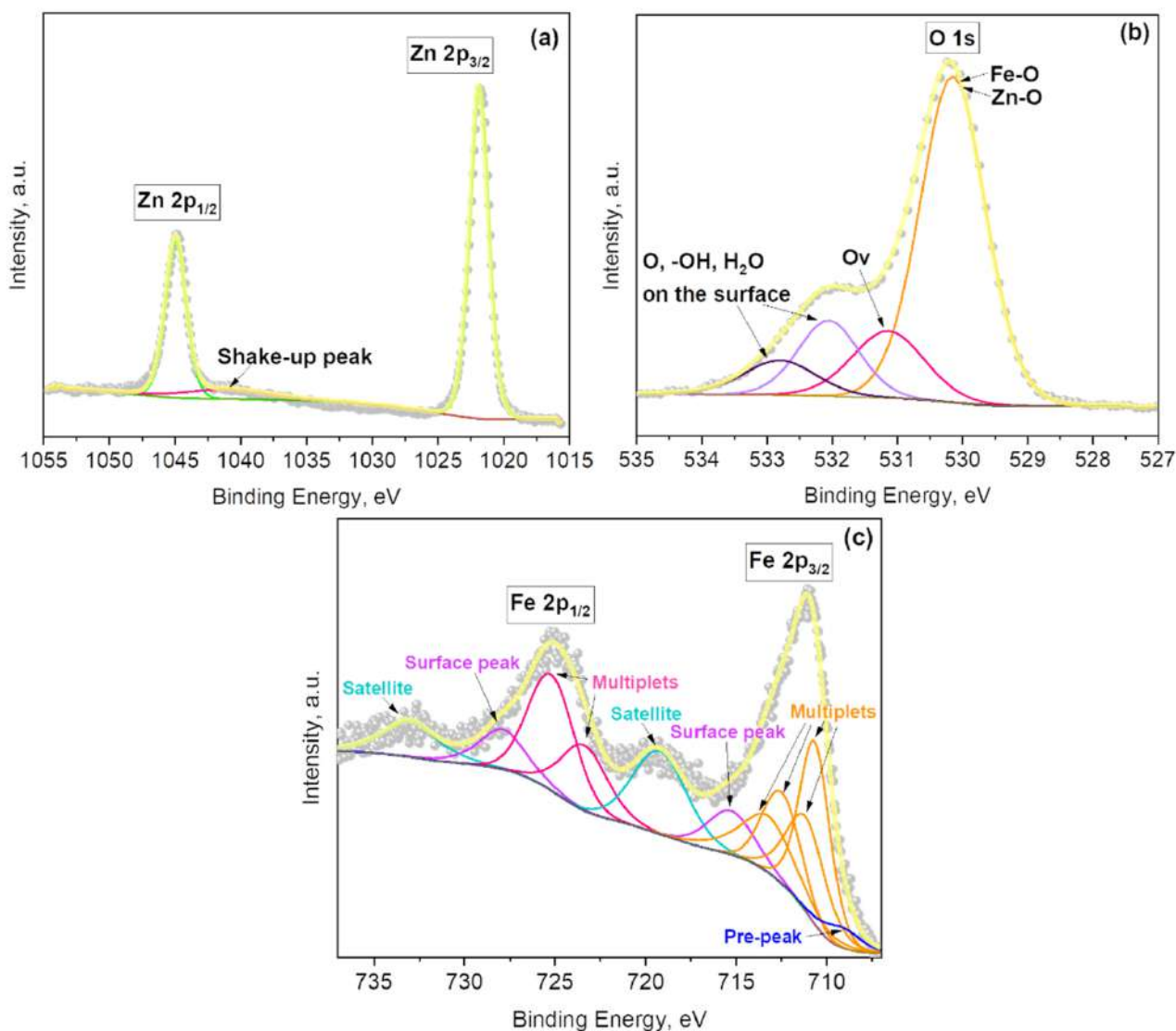


Figure 6. (a) Zn 2p, (b) O 1s, and (c) Fe 2p core levels XPS spectra recorded on the Fe₂O₃@ZnO film. The grey dots represent the raw data, the yellow solid line corresponds to the envelope/fitting curve, and the other colored curves to the deconvoluted components.

The O 1s spectrum of the Fe₂O₃@ZnO films (Figure 6b) reveals the presence of four components. The first of them, with binding energy at 530.1 eV, corresponds to oxygen lattice bonds (Fe–O and Zn–O). The second component at 531.1 eV is assigned to the oxygen defects in the matrix of metal oxides due to oxygen vacancies. The third component, at 532.1 eV, and the fourth component, at 532.8 eV, are associated with the presence of physical or chemical adsorbed oxygen, hydroxides, and H₂O on the surface of the structures, similarly to Au@ZnO film. These results indicate the Fe³⁺ ion incorporation into the ZnO lattice in agreement with the previous O 1s spectrum recorded on Fe₂O₃@ZnO films [25]. This is also consistent with the XRD results, which demonstrated the presence of the Fe₂O₄Zn compound at 44.0° 2θ (Figure 4b). Apart from the presence of one additional O 1s component in the Fe₂O₃@ZnO spectra compared to that of ZnO and Au@ZnO, one can also observe slight differences in the component positions, with the O 1s components of Fe₂O₃@ZnO showing higher binding energies (~0.4 eV) than the O 1s components of ZnO (Figure S1b, Supplementary Materials).

The Fe 2p spectrum displayed in Figure 6c shows two characteristic peaks at 711.1 eV and 725.0 eV, accompanied by two satellite peaks at 719.2 eV and 733.0 eV obtained from the photoelectrons emitted from Fe 2p_{3/2} and Fe 2p_{1/2}, respectively. In total, the Fe 2p

spectrum contains eleven components: four multiplets of Fe 2p_{3/2} peak, two multiplets of Fe 2p_{1/2} peak, two satellite peaks, two surface peaks, and one characteristic pre-peak usually present in the Fe 2p_{3/2} spectrum. The results and the binding energies of the peaks are in good agreement with the literature and suggest a Fe³⁺ oxidation state for iron [25,40,41]. The total content of iron in the sample amounts is 7.5 at. %.

3.3. Copper-Modified Zinc Oxide Films

SEM images of the copper-modified zinc oxide films also showed the presence of NPs distributed at the top and along the rod walls (Figure 7a). The XRD pattern of these films (Figure 7b) showed the intense diffractions that correspond to the hexagonal zinc oxide identified above with additional diffractions at 32.9° 2θ, 39.4° 2θ, and 44.0° 2θ. The first is connected to the (110) plane of the monoclinic copper(II) oxide phase (C12/c1 space group, ICSD Card No. 98-062-8618). The second and third are assigned to the ZnSiO₃ (R-3 space group, ICSD Card No. 340575) and the cubic ZnCuO (0.85/0.15/1) compound (Fm-3m space group, ICSD Card No. 181023), both present most likely at the interface of ZnO with the modifier NPs and the Si substrate, respectively. The presence of diffraction peaks from the copper(I) oxide phase is not evident, probably due to the low amount of particles and their broad distribution. However, their presence is not ruled out as the (101) diffraction of ZnO overlaps the highest intensity diffraction peak of copper(I) oxide phase generally appearing at 36.4 2θ, e.g., for the ICSD Card No. 00-005-0667.

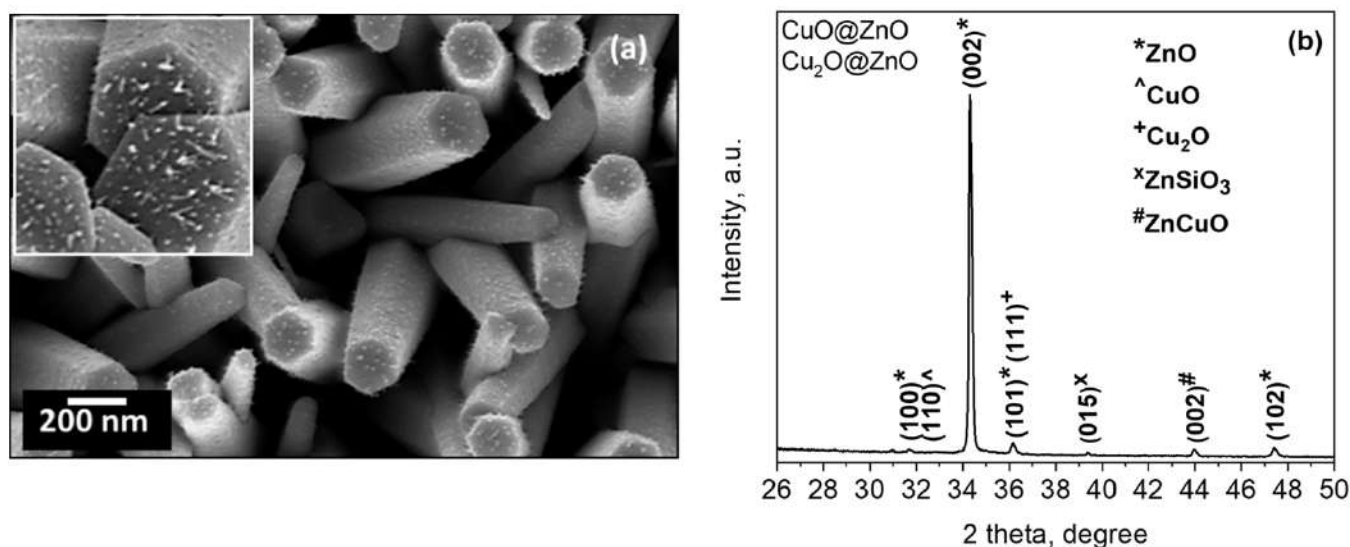


Figure 7. (a) SEM images (the inset shows a magnified image of the Cu decorated ZnO rods) and (b) XRD diffraction pattern of the copper-modified zinc oxide structured films.

The STEM and HRTEM images in Figure 8a,b show the crystalline copper-modified zinc oxide rods covered by spherical NPs. These particles display lattice spacings of 0.26 nm and 0.25 nm, first corresponding to the (002) plane of the hexagonal ZnO phase and second to either the (002) plane of the monoclinic copper(II) oxide or (111) cubic copper(I) oxide phase inferred by XRD. The EDS line-scan profiles of the components recorded along the red line in Figure 8a demonstrate the presence of Zn (Figure 8c) and Cu (Figure 8d) in the particles. These profiles also suggest that the CuO-Cu₂O NPs are between 5 and 25 nm in size.

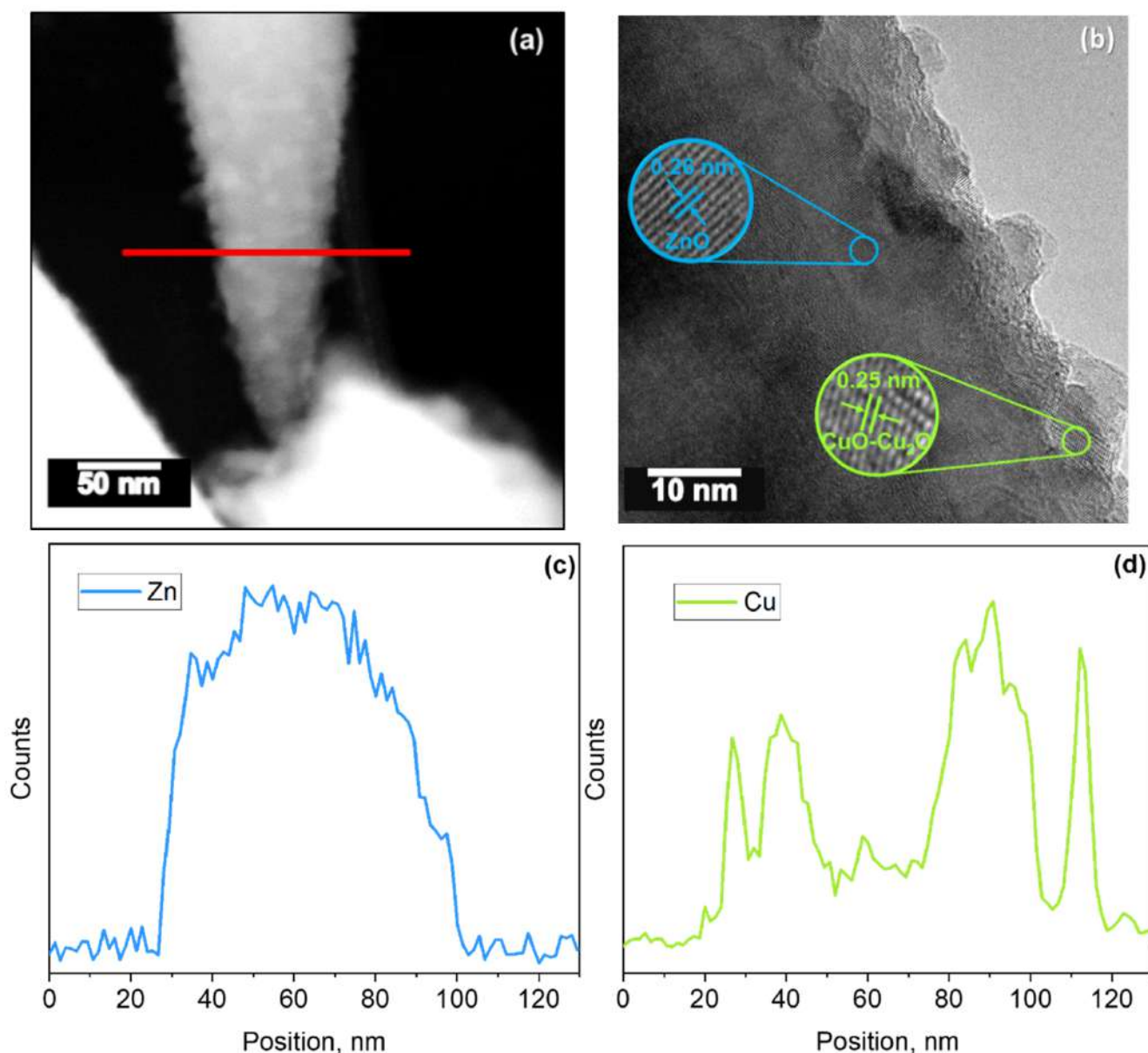


Figure 8. TEM images of a copper-modified ZnO rod. (a) Low-magnification TEM image, (b) high-resolution TEM image, and EDS line-scan profiles of the marked line in (a) corresponding to (c) Zn and (d) Cu.

An XPS analysis of the copper-modified zinc oxide films reported characteristic Zn $2p_{3/2}$ and Zn $2p_{1/2}$ core level peaks at 1021.9 eV and 1045 eV, respectively, separated by 23.1 eV and with a shake-up peak at 1040.3 eV (Figure 9a), similarly to previous studies [25]. These results are comparable to those for $\text{Fe}_2\text{O}_3@\text{ZnO}$ as the Zn 2p doublet is located almost at the same binding energies for the copper-modified zinc oxide and $\text{Fe}_2\text{O}_3@\text{ZnO}$. Consequently, the Zn 2p doublet of the copper-modified zinc oxide films is located at higher and lower binding energies than those registered for the ZnO and Au@ZnO films, respectively (see Figure S1a, Supplementary Materials, and Figure 3a).

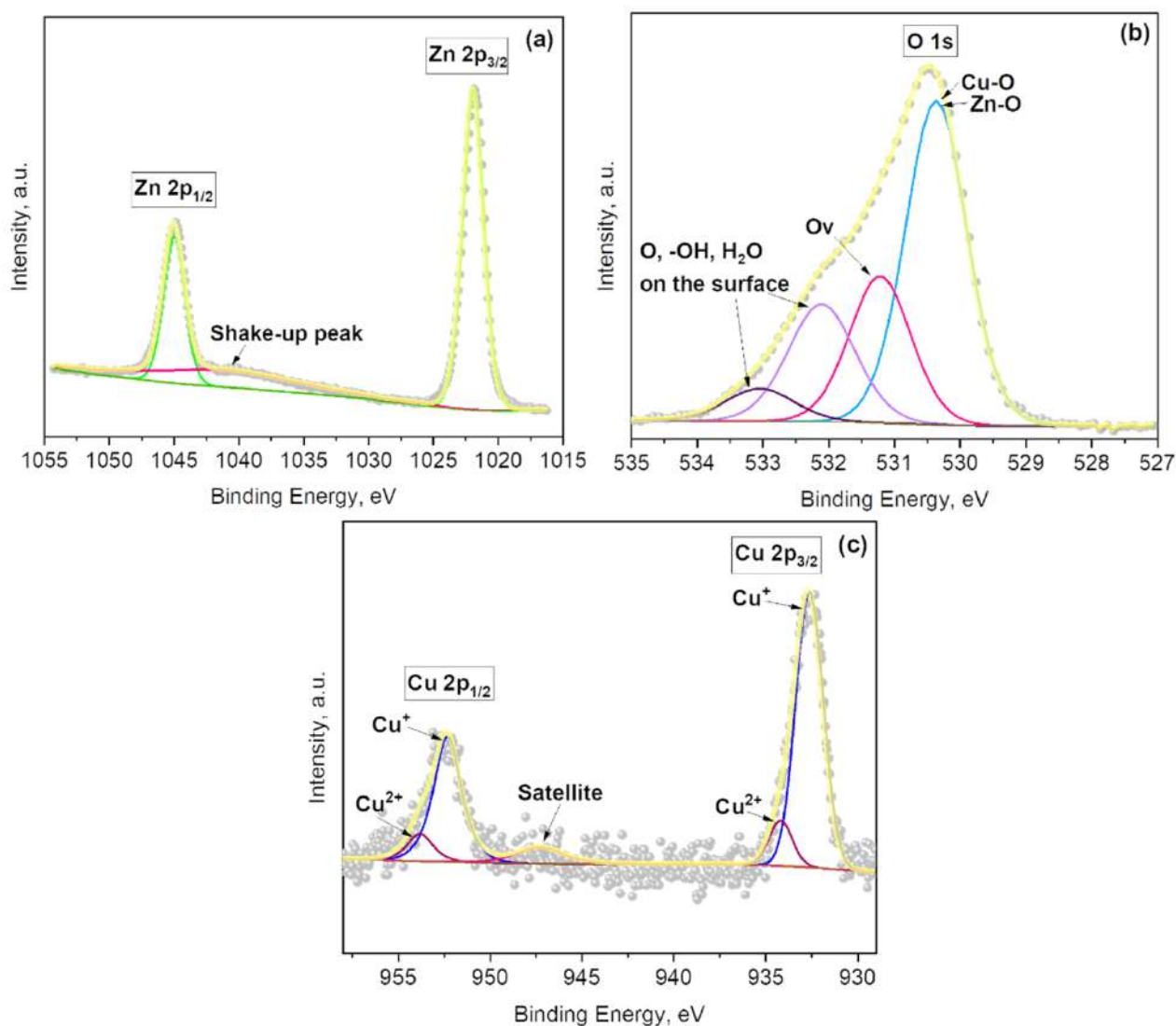


Figure 9. (a) Zn 2p, (b) O 1s, and (c) Cu 2p core levels XPS spectra for $\text{Cu}_2\text{O}@\text{ZnO}$ film. Grey dots represent the raw data, the solid yellow line corresponds to the envelope/fitting curve, and the other colored curves to the deconvoluted components.

The O 1s spectrum (Figure 9b) of the copper-modified zinc oxide films contains four components. These are located at 530.4 eV (from Cu–O and Zn–O bonds), 531.2 eV (from oxygen defects in the matrix of metal oxides related to oxygen vacancies), and 532.1 eV and 533.0 eV (from chemisorbed oxygen, hydroxides, and H_2O on the surface of the copper-modified zinc oxide film). These components are in agreement with the O1s spectra of the previously described materials.

The copper-modified zinc oxide films also displayed two doublets with components in Cu $2p_{3/2}$ at 932.6 eV and 934.2 eV, and Cu $2p_{1/2}$ at 952.3 eV and 953.9 eV (Figure 9c). The doublet with lower intensities (at 932.6 eV and 952.3 eV) indicates the presence of a Cu^+ oxidation state from Cu_2O , while the doublet with higher intensities (at 934.2 eV and 953.9 eV) corresponds to Cu^{2+} oxidation state from CuO [42]. The additional broad peak with low intensity in the area between 940 eV and 950 eV could be assigned to the satellite peak coming from the Cu^{2+} component [43]. This is consistent with the XRD and TEM analysis above, in which both species were also inferred. Quantification of the Cu^+ and Cu^{2+} species at the surface of the samples suggest the presence of a higher amount of Cu_2O (0.93 at.%) than CuO (0.13 at.%) at the surface of the samples; i.e., 87.7% of Cu_2O and 12.3% of CuO from the total content of copper oxides at the copper-modified zinc oxide

sample. Therefore, hereafter the discussion centers on the major copper oxide component (i.e., Cu_2O), and the copper-modified zinc oxide films are abbreviated as $\text{Cu}_2\text{O}@\text{ZnO}$.

3.4. Gas Sensing Tests

Gas sensing tests of the structured films (i.e., ZnO , $\text{Au}@\text{ZnO}$, $\text{Fe}_2\text{O}_3@\text{ZnO}$, and $\text{Cu}_2\text{O}@\text{ZnO}$) were carried out to various gases (nitrogen dioxide, ethanol, acetone, carbon monoxide, and toluene) by using dc resistance measurements. To determine the thermal dependence of the response, the structures were initially tested to 80 ppm of ethanol at various operating temperatures, from 200 to 310 °C. These results showed that the dynamic and magnitude of the response improved as the operating temperature increased, registering the highest and fastest responses at the highest temperature tested. Therefore, the subsequent tests were carried out at 310 °C using four samples of each structure type and performing at least three replicates for each condition.

Figure 10 summarizes the obtained results towards 10 ppm of nitrogen dioxide and 80 ppm of ethanol, acetone, carbon monoxide, and toluene. Overall, results reveal a significant improvement of the ZnO response due to its modification with Au NPs. One can also notice that the ZnO rods modified with Fe_2O_3 nanoflakes show an improvement compared to the non-modified ZnO , although not as high as that reported for the ZnO modified with Au. In contrast, the response observed for the ZnO structures modified with Cu_2O NPs showed a decrement of the response compared to the non-modified ZnO structures.

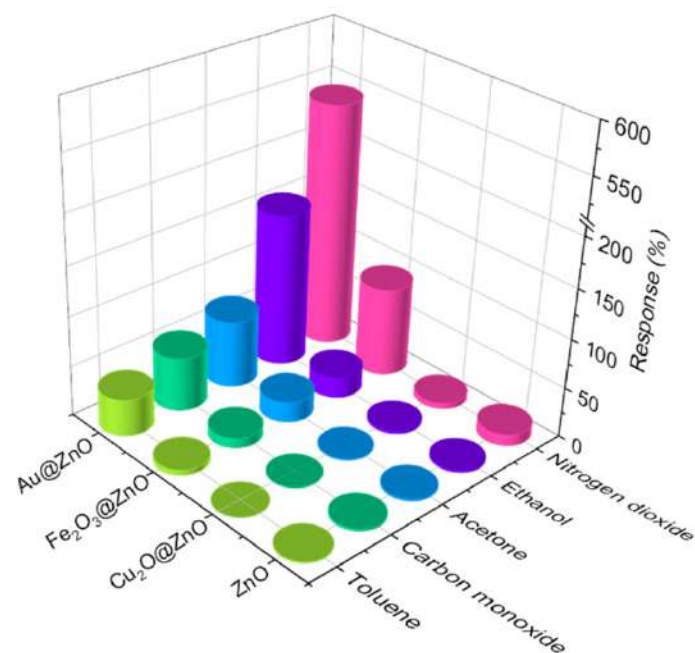


Figure 10. Responses towards 10 ppm of nitrogen dioxide and 80 ppm of ethanol, acetone, carbon monoxide, and toluene for the ZnO , $\text{Au}@\text{ZnO}$, $\text{Fe}_2\text{O}_3@\text{ZnO}$, and $\text{Cu}_2\text{O}@\text{ZnO}$ sensors.

Figure 11 displays the results obtained by testing the sensors to various concentrations of each gas (1 to 10 ppm for nitrogen dioxide and 20 to 80 ppm for ethanol, acetone, carbon monoxide, and toluene). Overall, the four structures demonstrate their highest responses to nitrogen dioxide, despite the lower concentrations of nitrogen dioxide compared to the other gases. The results also show a proportional increase in the response with the gas concentration. The tests corroborated the best response for the $\text{Au}@\text{ZnO}$ structures among the other structures for all tested gases and applied concentrations. For instance, the $\text{Au}@\text{ZnO}$ response to 10 ppm of nitrogen dioxide is about 47 times higher than that of ZnO (see Figure 11a,b). The difference in the response of these two structures to 80 ppm of ethanol is similar, showing around 45 times higher response for $\text{Au}@\text{ZnO}$ compared

to ZnO. For the low concentration, the difference in the responses of Au@ZnO and ZnO is still significant. For example, the responses of Au@ZnO sensors to 1 ppm of nitrogen dioxide and 20 ppm of ethanol are approximately 37 and 25 times higher, respectively, in comparison to the response of ZnO.

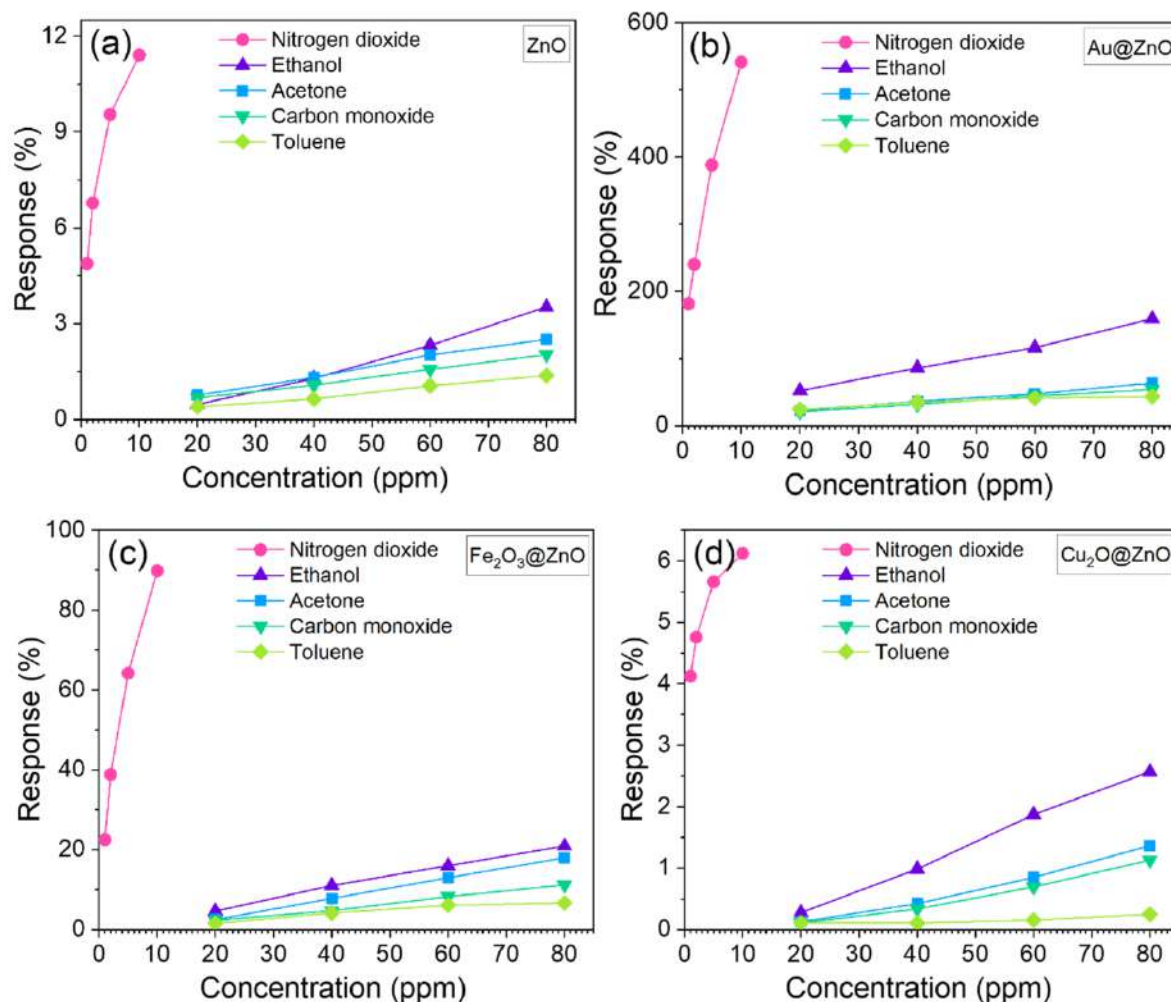


Figure 11. Response of the (a) ZnO (b) Au@ZnO, (c) Fe₂O₃@ZnO, and (d) Cu₂O@ZnO sensors towards various concentrations of each target analyte.

Figure 12 displays the electrical resistance changes recorded on the ZnO, Au@ZnO, Fe₂O₃@ZnO, and Cu₂O@ZnO structures to each gas and concentration. Overall the structures indicate an n-type semiconducting behavior, reporting an increase in the electrical resistance to nitrogen dioxide (oxidizing gas) and a decrease in the resistance in front of reducing gases such as ethanol, acetone, carbon monoxide, and toluene. The responses are reversible for each analyte and concentration, showing a full recovery of the initial baseline resistance after purging the target analytes.

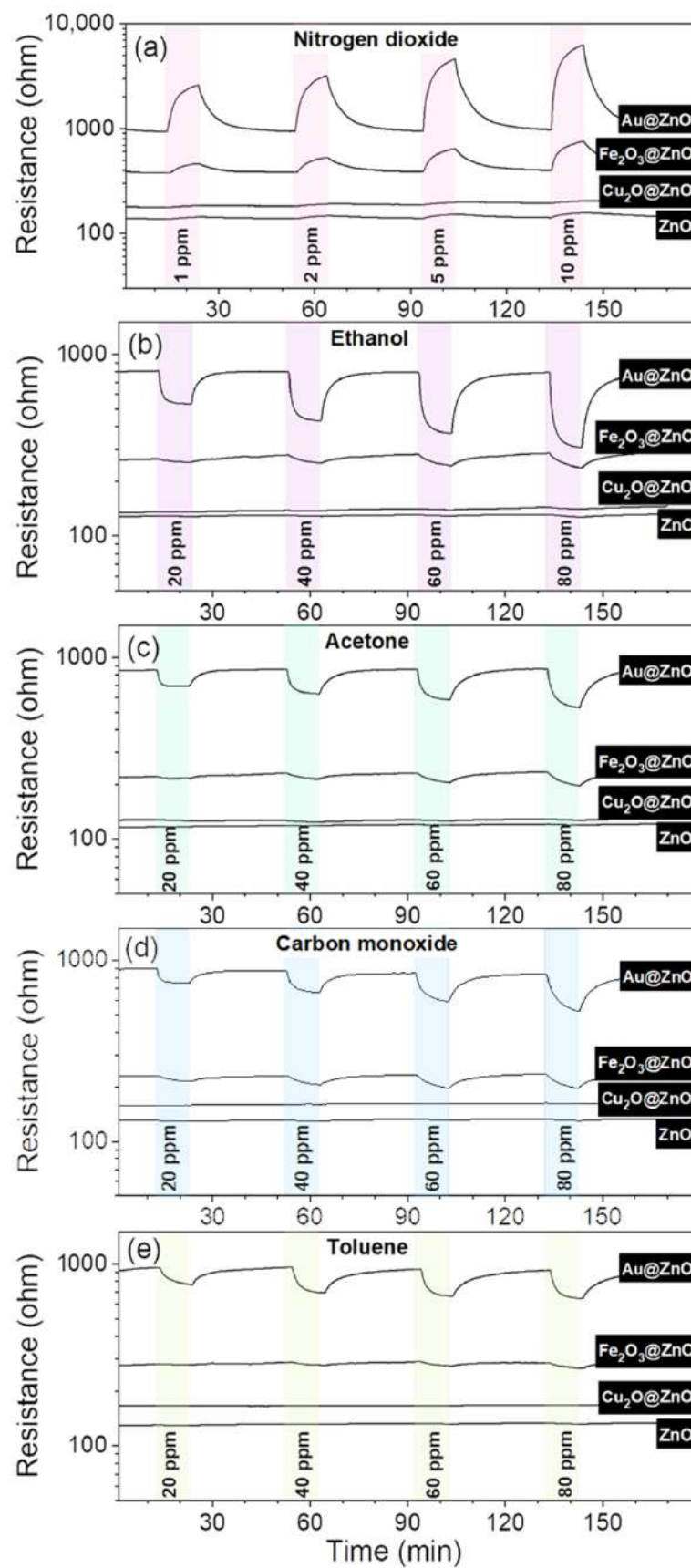


Figure 12. Electrical resistance changes to various concentrations of (a) nitrogen dioxide, (b) ethanol, (c) acetone, (d) carbon monoxide, and (e) toluene.

Figure 13 sums up the response (t_R) and recovery (t_r) time of each structure towards nitrogen dioxide and ethanol. As it can be noticed, the response time to nitrogen dioxide does not show significant changes among the four structures, showing periods between 4 and 6 min. However, this is different for the recovery time, which demonstrates faster recovery for the Au@ZnO (5 min) and Fe₂O₃@ZnO (8 min) structures compared to the ZnO (22 min) and Cu₂O@ZnO (15 min) structures. The results for ethanol, in contrast, reveal the fastest response time for Au@ZnO (1.5 min) and nearly similar recovery time (4 min) for ZnO, Au@ZnO, and Fe₂O₃@ZnO.

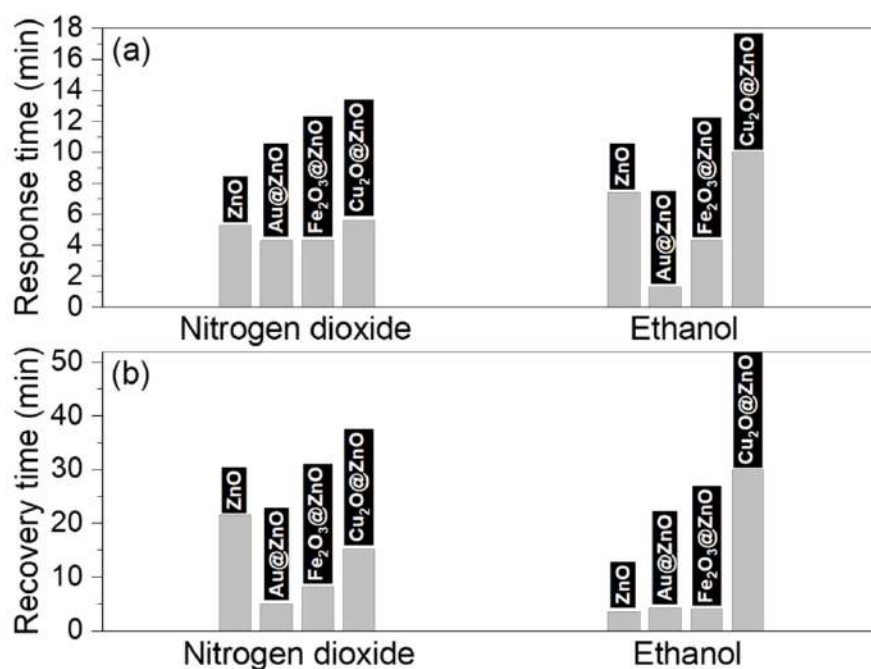


Figure 13. (a) Response and (b) recovery times to 1 ppm of nitrogen dioxide and 20 ppm of ethanol recorded with the non-modified and modified ZnO structures.

A summary of the sensitivity of each structure to the target analytes in the tested concentrations range is presented in Table 1. These results evidence the high sensitivity of Au@ZnO and Fe₂O₃@ZnO structures to nitrogen dioxide with an estimated limit of detection (LOD) for each system of 26 and 114 ppb, respectively. The results also suggest an improvement of the selectivity of ZnO to nitrogen dioxide by its modification with Au or Fe NPs. The partial selectivity of Au@ZnO to ethanol among the other reducing gases is also worth it of mention.

Table 1. Sensitivity ($\Delta R/\Delta C$) in % ppm⁻¹ to ethanol, acetone, carbon monoxide, and toluene for concentrations between 20 and 80 ppm and nitrogen dioxide for concentrations between 1 and 10 ppm.

Analyte	ZnO	Au@ZnO	Fe ₂ O ₃ @ZnO	Cu ₂ O@ZnO
Nitrogen dioxide	0.73	39.96	7.48	0.22
Ethanol	0.05	1.79	0.27	0.04
Acetone	0.03	0.68	0.26	0.02
Carbon Monoxide	0.02	0.55	0.15	0.02
Toluene	0.02	0.31	0.08	0.002

The test of the sensors to reducing gases in humid ambient revealed sensor response losses by increasing the relative humidity (RH). In contrast, the test to nitrogen dioxide

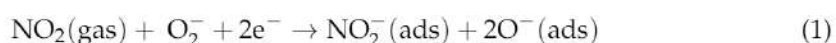
in humid ambient showed responses with a tendency to increase, although with poor stability and high signal noise. The greatest response changes in both cases were registered by increasing the humidity from 0% RH to 20% RH. Above this value, the changes were negligible due to the saturation of the response to relative humidity, as noticed previously for similar AACVD ZnO structures [44]. The loss of the response for ethanol, acetone, and carbon monoxide is displayed in Figure S3, Supplementary Materials. These results show that the Au@ZnO sensors lose 30% of their response to ethanol and acetone and 18% to carbon monoxide, whereas the loss of response for the Fe₂O₃@ZnO sensors is about 20% towards ethanol and acetone and 2% to carbon monoxide. The changes in the response due to humidity for the Cu₂O@ZnO and ZnO sensors were minor, and the highest losses (8% and 2%) were recorded for Cu₂O@ZnO to ethanol and ZnO to carbon monoxide.

3.5. Gas Sensing Mechanism

Chemoresistive gas sensors based on MOXs rely on the changes in the sensitive-material resistance upon exposure to target gases. These changes depend to a great extent on the gas analytes and their adsorption and desorption at the MOX surface. The gas sensing tests in this work demonstrate that the resistance changes of ZnO to nitrogen dioxide are significant compared to the other gases, and so that at first, we focus the discussion on the possible sensing mechanism of ZnO towards nitrogen dioxide.

In the first phase, the sensing mechanism involves the interaction of the ZnO surface with air. Consequently, oxygen is adsorbed at the ZnO surface by trapping electrons from its conduction band and forming chemisorbed species in the form of O₂⁻, O⁻, or O²⁻. However, due to the high operating temperatures employed in the test, O⁻ and O²⁻ species tend to be dominant at the surface [45]. This process leads to the formation of an electron depletion layer at the surface and, accordingly, an increase in the ZnO electrical resistance (Figures 14a and 15a).

In the second phase, when the sensing material is exposed to a target gas, such as nitrogen dioxide, the adsorbed oxygen species react with the gas. As nitrogen dioxide is a strong oxidizing agent with electrophilic properties, it acts as an electron acceptor, pulling out electrons from the conduction band (CB). Consequently, the electron depletion layer width increases (Figures 14a and 15a), leading to an increase in the sensor resistance. According to previous studies [46], the reaction between nitrogen dioxide and the formed oxygen species may be as follows:



The sensing mechanism of the Au, Fe₂O₃, and Cu₂O modified ZnO structures, apart from the described above, involves additional synergistic effects due to the materials modifiers. These effects generally include spill-over of reactive species from the modifiers to ZnO and/or electronic effects due to the formation of extra nano-interfaces that facilitate the charge transfer during the gas–solid interactions at the surface. The modified materials can also have an impact on surface defects and oxygen vacancies (Ov) with respect to the pristine structure. This, in part, also influences the sensing performance of the material, to the extent that the oxygen vacancies act as donors modifying the baseline conductivity of the sensor material and consequentially the sensor response [47,48]. The XPS components associated with the oxygen vacancies in the results above indicate a higher amount of vacancies at the Au@ZnO films (19.1 at.%) compared to Cu₂O@ZnO (15.4 at.%), Fe₂O₃@ZnO (10.6 at.%), and pure ZnO (7.8 at.%) films, which partially explains the better gas sensing performances of the modified Au@ZnO and Fe₂O₃@ZnO. However, this is not consistent with the Cu₂O@ZnO results, which show a different behavior most likely influenced by the type of interface formed between these materials. The band energy of each system also has a role in the sensing response, and therefore below, we focus the discussion on the effect of each modifier material on the band bending and band alignment at the surface and the sensing properties of each ZnO-based system.

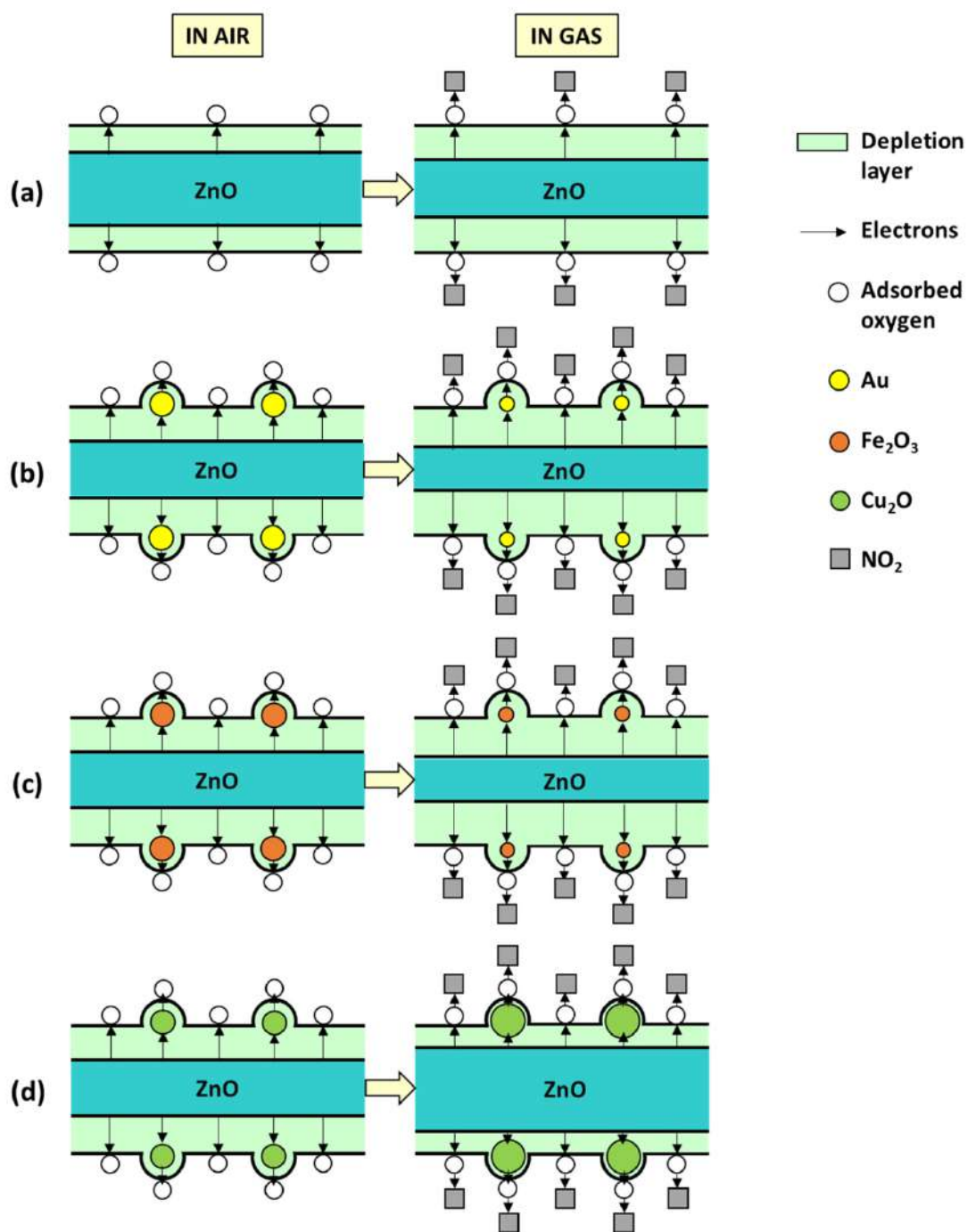


Figure 14. Schematic representation of the possible sensing mechanism of (a) ZnO, (b) Au@ZnO, (c) Fe₂O₃@ZnO, and (d) Cu₂O@ZnO to nitrogen dioxide.

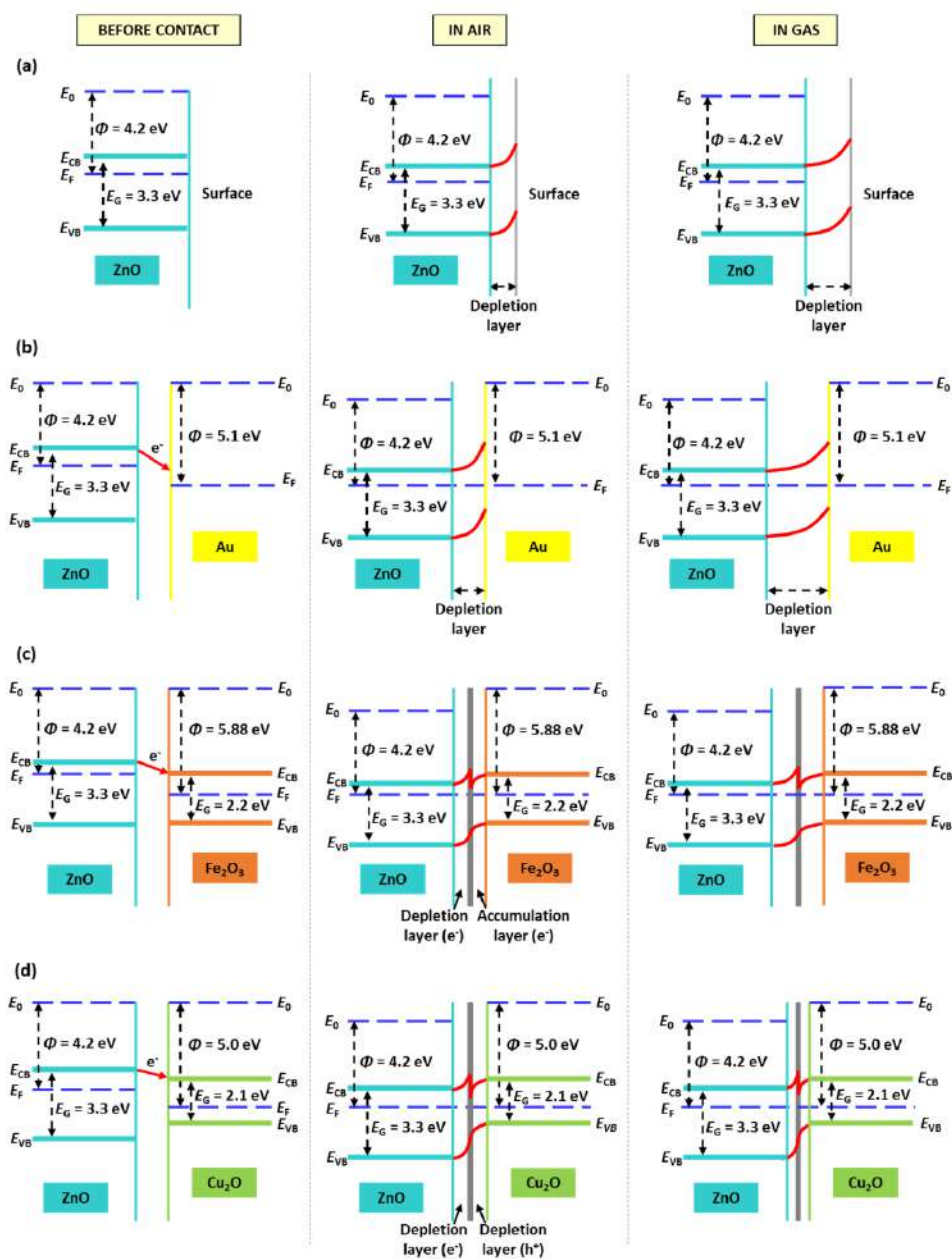


Figure 15. Energy band diagrams of (a) ZnO, (b) Au@ZnO, (c) Fe₂O₃@ZnO, and (d) Cu₂O@ZnO films at room temperature and before contact between ZnO with Au, Fe₂O₃, or Cu₂O (first column), after contact and in air (second column), and in gas (third column).

3.5.1. Gold-Modified Zinc Oxide Films

The results above showed that the decoration of the pristine ZnO structures with Au improves the gas sensing performance of the first, similarly to the previous literature results for noble metal modified ZnO systems [24,49]. The chemical composition of the Au@ZnO films corroborated the incorporation of gold (Au⁰, Au⁺, Au³⁺) at the ZnO surface with a major presence of Au⁰ (2.6 at.%) than Au⁺ (1.8 at.%) or Au³⁺ (0.7 at.%), suggesting the sensing mechanism of Au@ZnO films rely mainly on the metallic Au state. Hence, the performance improvements could be linked particularly to two phenomena—the formation of nano Schottky junctions between Au and ZnO and the catalytic activity of Au NPs. However, the electronic influence of the Au oxidized species is not ruled out, which may enhance the interaction of the gold nanoparticles with ZnO and contribute to better gas sensing performance, as observed previously [26].

Schottky junctions are formed when contacting a noble metal (e.g., Au) and a MOX (e.g., ZnO) with different work functions (WF), 4.2 eV (ZnO) [50] and 5.1 eV (Au) [51], and consequentially different Fermi level energies. Since the WF of Au is higher than that of ZnO, most of the energy required to withdraw an electron from bulk to surface is higher compared to ZnO. Because of that, free electrons from ZnO are more prone to move from ZnO to Au until the Fermi energies become equal (Figure 15b). Therefore, in the first phase of the gas sensing mechanism, when Au@ZnO is exposed to air, the electron transferring from ZnO to Au leads to the adsorption of more oxygen species and, in turn, the formation of a thicker depletion layer compared to the pristine ZnO films for the same conditions. Consequently, the resistance of the Au@ZnO sensors is higher than that of the ZnO sensors. This is consistent with the electrical resistance registered for these sensors (Figure 12).

In the second phase of the mechanism, when Au@ZnO is exposed to nitrogen dioxide, adsorbed oxygen species will react with the gas, and more electrons will be consumed from the conduction band of the modified ZnO films compared to the non-modified one. This leads to a proportional increase in the electron depletion layer width (Figures 14b and 15b) and, eventually, a higher increase in the Au@ZnO resistance compared to the ZnO sensors.

Additionally, the catalytic activity of Au NPs, as reported previously in the literature [52,53], may play a role in accelerating the kinetics of the surface reactions during the sensing mechanism. This is consistent with the better dynamics of the Au@ZnO sensor's response (Figure 12), which shows faster response and recovery times, particularly for the reducing gases (Figure 13) in contrast to the ZnO sensors.

3.5.2. Iron- and Copper-Modified Zinc Oxide Films

Although Fe₂O₃@ZnO and Cu₂O@ZnO rely on similar gas sensing mechanism principles because both systems present the formation of nano-heterojunctions at the interface of the ZnO rods and the decorating MOX (Fe₂O₃ or Cu₂O) particles, the difference between these materials lies in their type of conductivity. Cu₂O reports p-type semiconductor behavior [54], whereas Fe₂O₃ may present either n- or p-type behavior [7]. Our previous studies, however, demonstrated that the Fe₂O₃ films obtained via the AACVD of FeCl₃·6H₂O have an n-type behavior with a typical increase in conductivity when exposed to reducing gases [39]. Therefore, hereafter we discuss the sensing mechanism of Fe₂O₃@ZnO and Cu₂O@ZnO, considering their n- and p-type behavior, respectively.

Due to the different work function (5.88 eV [55]) and band-gap (2.2 eV [56]) of Fe₂O₃ compared to ZnO (4.2 eV and 3.3 eV [57], respectively), and higher position of the CB of ZnO, free electrons from the CB of ZnO migrate to the CB of Fe₂O₃. This is the opposite for the holes, which migrate from the valence band (VB) of Fe₂O₃ to that of ZnO until the Fermi levels of both materials reach equilibrium (Figure 15c). These processes increase the number of electrons near the surface of the system so that when Fe₂O₃@ZnO sensors are exposed to air, more oxygen species can be adsorbed at the surface in comparison to pristine ZnO as displayed in Figure 14c. Consequentially, in the gas stage (e.g., nitrogen dioxide), more gas molecules react with the adsorbed oxygen, and a higher amount of electrons is trapped, enhancing the response of the Fe₂O₃@ZnO sensors compared to Zn.

Similarly, Cu₂O, with a work function of 5.0 eV and a band-gap of 2.1 eV [54], has a CB below that of ZnO, meaning that the transfer of electrons occurs from the ZnO side towards the Cu₂O side as shown in Figure 15d. Analogously to the Fe₂O₃@ZnO sensor, more electrons will provide more adsorbed oxygen on the surface and more active sites for gas molecules to react (Figure 14d). However, in the case of p-type semiconductors, such as Cu₂O, which have as main carriers holes, the ionosorption of oxygen favors the conduction by holes (Figure 15d), contrary to n-type semiconductors. Therefore, when the oxidizing gas NO₂ comes in contact with a p-type semiconductor, NO₂ will trap the electrons, which will increase further the numbers of holes at the interface [58] and decrease the resistance of the whole Cu₂O@ZnO system partially; a similar effect was reported previously for instance for ZnO decorated with p-type Cr₂O₃ [59]. This is most likely the rationale behind

the loss of sensitivity to nitrogen dioxide for the Cu₂O@ZnO sensors compared to the pristine ZnO and the modified ZnO with gold and iron (see Table 1).

The presented mechanism described the sensing behavior of the different ZnO systems towards oxidizing gases (e.g., nitrogen dioxide). Reducing gases, such as ethanol, behave in an opposite way, providing electrons to ZnO and thus decreasing its resistance, as can be noticed in the electrical resistance changes in Figure 12b–e.

As we can conclude from the previous, all three systems are influenced by the incorporation of nano-interfaces, which provide slightly different gas sensing mechanisms that favor especially the sensing performance of the structures modified with Au due to the formation of Schottky junction and catalytic properties of Au. The formation of heterojunctions also shows advantages in the sensing performance of the structures modified with Fe, although it shows an opposite effect for the structures modified with Cu, most likely due to the difference in the conductivity type of Fe₂O₃ (n-type) and Cu₂O (p-type) semiconductors. Generally, Fe₂O₃ and Cu₂O could also act as catalyzers, but in light of the dynamic of response observed, their catalytic activity is not the main parameter that influences the response of these modified structures.

4. Conclusions

Zinc oxide structures were deposited and modified with Au, Fe₂O₃, and Cu₂O nanoparticles. The results showed the formation of ZnO rods (approximately 1.5 μm long with an average diameter of 200 nm) as well as the incorporation of crystalline Au nanoparticles (diameters between 5 and 40 nm), Fe₂O₃ nanoflakes (thickness smaller than 20 nm and diameter of 100 nm), and Cu₂O nanoparticles (diameters between 5 and 25 nm). Chemical composition determination by XPS revealed the presence of Fe in the form of oxide—Fe₂O₃; Cu in the form of two oxides—CuO and Cu₂O, with the major presence of Cu₂O; and Au in three oxidation states—Au³⁺, Au⁺, and Au⁰, with the content of metallic Au (2.6 at.%) being the highest among the other states. Gas sensing results showed the best response for the Au@ZnO sensors among the others, especially for nitrogen dioxide, with about 47 times higher response to 10 ppm of nitrogen dioxide compared to the ZnO sensors. The sensitivity (39.96% ppm⁻¹) and limit of detection (26 ppb) reported for this modified material to nitrogen dioxide were also higher compared to the other sensor structures. This was attributed to a combination of factors, including the oxygen vacancies, the gas sensing mechanism influenced by the nano-interfaces formed between ZnO and Au, and possible catalytic effects of the Au nanoparticles.

Supplementary Materials: The following are available online at <https://www.mdpi.com/article/10.3390/s21134509/s1>. Figure S1: (a) Zn 2p, and (b) O 1s core levels XPS spectra for non-modified ZnO film. Grey dots represent the raw data, the solid yellow line corresponds to the envelope/fitting curve, and the other colored curves to the deconvoluted components. Figure S2: SEM images (the inset shows a magnified image of a single Ag decorated ZnO rod) of the Ag@ZnO structured film. Figure S3: Responses towards 80 ppm of ethanol, acetone, carbon monoxide for the ZnO, Au@ZnO, Fe₂O₃@ZnO, and Cu₂O@ZnO sensors at 0% and 20% RH.

Author Contributions: Conceptualization, M.T. and S.V.; methodology, M.T., M.C., I.G., E.F., C.C.; validation, M.T., I.G.; formal analysis, M.T., M.C., S.V.; writing—original draft preparation, M.T.; writing—review and editing, S.V., M.C.; funding acquisition, S.V., C.C. All authors have read and agreed to the published version of the manuscript.

Funding: This work has been supported by the Spanish Ministry of Science and Innovation via Grant PID2019-107697RB-C42 (AEI/FEDER, EU) and the Ramón y Cajal programme, and the Czech Science Foundation (GAČR) via Grant No 20-20123S.

Institutional Review Board Statement: Not applicable.

Informed Consent Statement: Not applicable.

Data Availability Statement: Not applicable.

Acknowledgments: This research has made use of the infrastructures of the Spanish ICTS Network MICRONANOFABS, partially supported by MINECO, and Czech CEITEC Nano Research Infrastructure, supported by MEYS CR (LM2018110).

Conflicts of Interest: The authors declare no conflict of interest.

References

1. Potyrailo, R.A. Multivariable sensors for ubiquitous monitoring of gases in the era of Internet of Things and industrial internet. *Chem. Rev.* **2016**, *116*, 11877–11923. [[CrossRef](#)]
2. Sun, Y.F.; Liu, S.B.; Meng, F.L.; Liu, J.Y.; Jin, Z.; Kong, L.T.; Liu, J.H. Metal oxide nanostructures and their gas sensing properties: A review. *Sensors* **2012**, *12*, 2610–2631. [[CrossRef](#)]
3. Tomić, M.; Šetka, M.; Vojtkůvka, L.; Vallejos, S. VOCs Sensing by Metal Oxides, Conductive Polymers, and Carbon-Based Materials. *Nanomaterials* **2021**, *11*, 552. [[CrossRef](#)] [[PubMed](#)]
4. Nunes, D.; Pimente, A.; Gonçalves, A.; Pereira, S.; Branquinho, R.; Barquinha, P.; Fortunato, E.; Martins, R. Metal oxide nanostructures for sensor applications. *Semicond. Sci. Technol.* **2019**, *34*, 043001. [[CrossRef](#)]
5. Yamazoe, N.; Sakai, G.; Shimano, K. Oxide semiconductor gas sensors. *Catal. Surv. Asia* **2003**, *7*, 63–75. [[CrossRef](#)]
6. Gurlo, A. Nanosensors: Towards morphological control of gas sensing activity. SnO₂, In₂O₃, ZnO and WO₃ case studies. *Nanoscale* **2011**, *3*, 154–165. [[CrossRef](#)]
7. Miller, D.R.; Akbar, S.A.; Morris, P.A. Nanoscale metal oxide-based heterojunctions for gas sensing: A review. *Sens. Actuators B Chem.* **2014**, *204*, 250–272. [[CrossRef](#)]
8. Djurisic, A.B.; Chen, X.; Leung, Y.H.; Man, A.; Ng, C. ZnO nanostructures: Growth, properties and applications. *J. Mater. Chem.* **2012**, *22*, 6526–6535. [[CrossRef](#)]
9. Zhang, S.; Byun, H.; Lim, J.; Huh, J.; Lee, W. Controlled synthesis of ZnO nanostructures for sub-ppm-level VOC detection. *IEEE Sens. J.* **2012**, *12*, 3149–3155. [[CrossRef](#)]
10. Arunkumar, S.; Hou, T.; Kim, Y.-B.; Choi, B.; Park, S.H.; Jung, S.; Lee, D.-W. Au Decorated ZnO hierarchical architectures: Facile synthesis, tunable morphology and enhanced CO detection at room temperature. *Sens. Actuators B Chem.* **2017**, *243*, 990–1001. [[CrossRef](#)]
11. Li, Z.; Zhang, G.; Gao, W.; Zhao, R.; Wang, Y. Ag decorated ZnO nanocrystallines synthesized by a low-temperature solvothermal method and their application for high response H₂ gas sensor. *J. Mater. Sci. Mater. Electron.* **2019**, *30*, 18959–18969. [[CrossRef](#)]
12. Xuan, J.; Zhao, G.; Gong, Q.; Wang, L.; Ren, J.; Sun, M.; Zhou, T.; Xing, F.; Yin, G.; Liua, B. Fabrication of in-situ grown and Pt-decorated ZnO nanoclusters on new-type FTO electrode for room-temperature detection of low-concentration H₂S. *J. Alloys Compd.* **2021**, *860*, 158499–158510. [[CrossRef](#)]
13. Dilova, T.; Atanasova, G.; Dikovska, A.O.; Avdeev, G.; Machida, M.; Terakawa, M.; Stefanov, P.; Nedyalkov, N.N. Effect of Pd-decoration on the sensing properties of ZnO nanostructures. *Thin Solid Films* **2020**, *693*, 137693. [[CrossRef](#)]
14. Vuong, N.M.; Chinh, N.D.; Huy, B.T.; Lee, Y.I. CuO-decorated ZnO hierarchical nanostructures as efficient and established sensing materials for H₂S Gas Sensors. *Sci. Rep.* **2016**, *6*, 26736. [[CrossRef](#)]
15. Powell, M.J.; Potter, D.B.; Wilson, R.L.; Darr, J.A.; Parkin, I.P.; Carmalt, C.J. Scaling aerosol assisted chemical vapour deposition: Exploring the relationship between growth rate and film properties. *Mater. Des.* **2017**, *129*, 116–124. [[CrossRef](#)]
16. Taylor, M.; Pullar, R.C.; Parkin, I.P.; Piccirillo, C. Nanostructured titanium dioxide coatings prepared by Aerosol Assisted Chemical Vapour Deposition (AACVD). *J. Photochem. Photobiol. A Chem.* **2020**, *400*, 112727. [[CrossRef](#)]
17. Vallejos, S.; Pizúrová, N.; Čechal, J.; Gràcia, I.; Cané, C. Aerosol-assisted Chemical Vapor Deposition of Metal Oxide Structures: Zinc Oxide Rods. *JøVE* **2017**, *127*, e56127. [[CrossRef](#)]
18. Palgrave, R.G.; Parkin, I.P. Aerosol assisted chemical vapor deposition using nanoparticle precursors: A route to nanocomposite thin films. *J. Am. Chem. Soc.* **2006**, *128*, 1587–1597. [[CrossRef](#)] [[PubMed](#)]
19. Vallejos, S.; Stoycheva, T.; Umek, P.; Navio, C.; Snyders, R.; Bittencourt, C.; Llobet, E.; Blackman, C.; Moniz, S.; Correig, X. Au nanoparticle-functionalised WO₃ nanoneedles and their application in high sensitivity gas sensor devices. *Chem. Commun.* **2011**, *47*, 565–567. [[CrossRef](#)] [[PubMed](#)]
20. Tomić, M.; Šetka, M.; Chmela, O.; Gràcia, I.; Figueras, E.; Cané, C.; Vallejos, S. Cerium Oxide-Tungsten Oxide Core-Shell Nanowire-Based Microsensors Sensitive to Acetone. *Biosensors* **2018**, *8*, 116. [[CrossRef](#)]
21. Rodríguez-Martínez, C.; García-Domínguez, Á.E.; Guerrero-Robles, F.; Saavedra-Díaz, R.O.; Torres-Torres, G.; Felipe, C.; Ojeda-López, R.; Silahua-Pavón, A.; Cervantes-Urbe, A. Synthesis of Supported Metal Nanoparticles (Au/TiO₂) by the Suspension Impregnation Method. *J. Compos. Sci.* **2020**, *4*, 89. [[CrossRef](#)]
22. Laugel, G.; Arichi, J.; Bernhardt, P.; Molière, M.; Kiennemann, A.; Garin, F.; Louisa, B. Preparation and characterisation of metal oxides supported on SBA-15 as methane combustion catalysts. *Comptes Rendus Chim.* **2009**, *12*, 731–739. [[CrossRef](#)]
23. Savastenko, N.A.; Filatova, I.I.; Lyushkevich, V.A.; Chubrik, N.I.; Brüser, V.; Shcherbovich, A.A.; Maskevich, S.A. Effect of impregnation by silver nanoparticles on the efficiency of plasma-treated ZnO-based photocatalysts. *High Temp. Mater. Process.* **2020**, *24*, 21–45. [[CrossRef](#)]
24. Ponnuvelu, D.V.; Dhakshinamoorthy, J.; Prasad, A.K.; Dhara, S.; Kamruddin, M.; Pullithadathil, B. Geometrically Controlled Au-Decorated ZnO Heterojunction Nanostructures for NO₂ Detection. *ACS Appl. Nano Mater.* **2020**, *3*, 5898–5909. [[CrossRef](#)]

25. Claros, M.; Setka, M.; Jimenez, Y.P.; Vallejos, S. AACVD Synthesis and Characterization of Iron and Copper Oxides Modified ZnO Structured Films. *Nanomaterials* **2020**, *10*, 471. [[CrossRef](#)] [[PubMed](#)]
26. Vallejos, S.; Umek, P.; Stoycheva, T.; Annanouch, F.; Llobet, E.; Correig, X.; De Marco, P.; Bittencourt, C.; Blackman, C. Single-step deposition of Au- and Pt-nanoparticle-functionalized tungsten oxide nanoneedles synthesized via aerosol-assisted CVD, and used for fabrication of selective gas microsensor arrays. *Adv. Funct. Mater.* **2013**, *23*, 1313–1322. [[CrossRef](#)]
27. Sari, W.P.; Blackman, C.; Zhu, Y.; Covington, J.A. AACVD Grown WO₃ Nanoneedles Decorated with Ag/Ag₂O Nanoparticles for Oxygen Measurement in a Humid Environment. *IEEE Sens. J.* **2019**, *19*, 826–832. [[CrossRef](#)]
28. Turkevich, J.; Stevenson, P.C.; Hillier, J. A study of the nucleation and growth processes in the synthesis of colloidal gold. *Discuss. Faraday Soc.* **1951**, *11*, 55–75. [[CrossRef](#)]
29. Mulfinger, L.; Solomon, S.D.; Bahadory, M.; Jeyarajasingam, A.V.; Rutkowsky, S.A.; Boritz, C. Synthesis and Study of Silver Nanoparticles. *J. Chem. Educ.* **2007**, *84*, 322. [[CrossRef](#)]
30. Feng, J.; Liu, J.; Cheng, X.; Liu, J.; Xu, M.; Zhang, J. Hydrothermal cation exchange enabled gradual evolution of Au@ZnS–AgAuS yolk–shell nanocrystals and their visible light photocatalytic applications. *Adv. Sci.* **2018**, *5*, 1700376. [[CrossRef](#)]
31. Jain, S.; Shah, J.; Negi, N.; Sharma, C.; Kotnala, R.K. Significance of interface barrier at electrode of hematite hydroelectric cell for generating ecopower by water splitting. *Int. J. Energy Res.* **2019**, *43*, 4743–4755. [[CrossRef](#)]
32. Wang, H.; Baek, S.; Song, J.; Lee, J.; Lim, S. Microstructural and optical characteristics of solution-grown Ga-doped ZnO nanorod arrays. *Nanotechnology* **2008**, *19*, 075607. [[CrossRef](#)] [[PubMed](#)]
33. De La Rosa, E.; Sepúlveda-Guzman, S.; Reeja-Jayan, B.; Torres, A.; Salas, P.; Elizondo, N.; Jose Yacaman, M. Controlling the growth and luminescence properties of well-faceted ZnO nanorods. *J. Phys. Chem. C* **2007**, *111*, 8489–8495. [[CrossRef](#)]
34. Meng, L.J.; Moreira de Sá, C.P.; dos Santos, M.P. Study of the structural properties of ZnO thin films by X-ray photoelectron spectroscopy. *Appl. Surf. Sci.* **1994**, *78*, 57–61. [[CrossRef](#)]
35. Song, K.W.; Park, M.H.; Kim, T.H.; Lim, S.H.; Yang, C.W. UV enhanced synthesis of high density Au coated ZnO nanocomposite. *J. Nanosci. Nanotechnol.* **2014**, *14*, 8766–8770. [[CrossRef](#)] [[PubMed](#)]
36. Casaletto, M.P.; Longo, A.; Martorana, A.; Prestianni, A.; Venezia, A.M. XPS study of supported gold catalysts: The role of Au⁰ and Au^{+δ} species as active sites. *Surf. Interface Anal.* **2006**, *38*, 215–218. [[CrossRef](#)]
37. Wang, T.; Jin, B.; Jiao, Z.; Lu, G.; Ye, J.; Bi, Y. Photo-directed growth of Au nanowires on ZnO arrays for enhancing photoelectrochemical performances. *J. Mater. Chem. A* **2014**, *2*, 15553–15559. [[CrossRef](#)]
38. Miller, J.T.; Kropf, A.J.; Zha, Y.; Regalbuto, J.R.; Delannoy, L.; Louis, C.; Bus, E.; van Bokhoven, J.A. The effect of gold particle size on Au–Au bond length and reactivity toward oxygen in supported catalysts. *J. Catal.* **2006**, *240*, 222–234. [[CrossRef](#)]
39. Vallejos, S.; Gràcia, I.; Figueras, E.; Cané, C. Nanoscale Heterostructures Based on Fe₂O₃@WO_{3-x} Nanoneedles and Their Direct Integration into Flexible Transducing Platforms for Toluene Sensing. *ACS Appl. Mater. Interfaces* **2015**, *7*, 18638–18649. [[CrossRef](#)]
40. McIntyre, N.S.; Zetaruk, D.G. X-ray Photoelectron Spectroscopic Studies of Iron Oxides. *Anal. Chem.* **1977**, *49*, 1521–1529. [[CrossRef](#)]
41. Yamashita, T.; Hayes, P. Analysis of XPS spectra of Fe²⁺ and Fe³⁺ ions in oxide materials. *Appl. Surf. Sci.* **2008**, *254*, 2441–2449. [[CrossRef](#)]
42. An, X.; Li, K.; Tang, J. Cu₂O/reduced graphene oxide composites for the photocatalytic conversion of CO₂. *ChemSusChem* **2014**, *7*, 1086–1093. [[CrossRef](#)]
43. Ma, X.; Zhang, J.; Wang, B.; Li, Q.; Chu, S. Hierarchical Cu₂O foam/g-C₃N₄ photocathode for photoelectrochemical hydrogen production. *Appl. Surf. Sci.* **2018**, *427*, 907–916. [[CrossRef](#)]
44. Vallejos, S.; Gràcia, I.; Pizúrová, N.; Figueras, E.; Čechal, J.; Hubálek, J.; Cané, C. Gas sensitive ZnO structures with reduced humidity-interference. *Sens. Actuators B Chem.* **2019**, *301*, 127054. [[CrossRef](#)]
45. Barsan, N.; Weimar, U. Conduction Model of Metal Oxide Gas Sensors. *J. Electroceramics* **2001**, *7*, 143–167. [[CrossRef](#)]
46. Zou, C.W.; Wang, J.; Xie, W. Synthesis and enhanced NO₂ gas sensing properties of ZnO nanorods/TiO₂ nanoparticles hetero-junction composites. *J. Colloid Interface Sci.* **2016**, *478*, 22–28. [[CrossRef](#)] [[PubMed](#)]
47. Ge, Y.; Wei, Z.; Li, Y.; Qu, J.; Zu, B.; Dou, X. Highly sensitive and rapid chemiresistive sensor towards trace nitro-explosive vapors based on oxygen vacancy-rich and defective crystallized In-doped ZnO. *Sens. Actuators B Chem.* **2017**, *244*, 983–991. [[CrossRef](#)]
48. Pati, S.; Majumder, S.B.; Banerji, P. Role of oxygen vacancy in optical and gas sensing characteristics of ZnO thin films. *J. Alloys Compd.* **2012**, *541*, 376–379. [[CrossRef](#)]
49. Tian, H.; Fan, H.; Ma, J.; Liu, Z.; Ma, L.; Lei, S.; Fang, J.; Long, C. Pt-decorated zinc oxide nanorod arrays with graphitic carbon nitride nanosheets for highly efficient dual-functional gas sensing. *J. Hazard. Mater.* **2018**, *341*, 102–111. [[CrossRef](#)]
50. Gutmann, S.; Conrad, M.; Wolak, M.A.; Beerbom, M.M.; Schlaf, R. Work function measurements on nano-crystalline zinc oxide surfaces. *J. Appl. Phys.* **2012**, *111*, 123710. [[CrossRef](#)]
51. Cao, P.J.; Huang, Q.G.; Navale, S.T.; Fang, M.; Liu, X.K.; Zeng, Y.X.; Liu, W.J.; Stadler, F.J.; Lu, Y.M. Integration of mesoporous ZnO and Au@ZnO nanospheres into sensing device for the ultrasensitive CH₃COCH₃ detection down to ppb levels. *Appl. Surf. Sci.* **2020**, *518*, 146223. [[CrossRef](#)]
52. Lopez, N.; Nørskov, J.K. Catalytic CO oxidation by a gold nanoparticle: A density functional study. *J. Am. Chem. Soc.* **2002**, *124*, 11262–11263. [[CrossRef](#)] [[PubMed](#)]
53. Carabineiro, S.A.C. Supported gold nanoparticles as catalysts for the oxidation of alcohols and alkanes. *Front. Chem.* **2019**, *7*, 702. [[CrossRef](#)]

54. Deuermeier, J.; Liu, H.; Rapenne, L.; Calmeiro, T.; Renou, G.; Martins, R.; Muñoz-Rojas, D.; Fortunato, E. Visualization of nanocrystalline CuO in the grain boundaries of Cu₂O thin films and effect on band bending and film resistivity. *APL Mater.* **2018**, *6*, 113704. [[CrossRef](#)]
55. Zhang, J.; Liu, X.; Wang, L.; Yang, T.; Guo, X.; Wu, S.; Wang, S.; Zhang, S. Synthesis and gas sensing properties of α -Fe₂O₃@ZnO core-shell nanospindles. *Nanotechnology* **2011**, *22*, 185501. [[CrossRef](#)] [[PubMed](#)]
56. Qin, Y.X.; Yang, Z.Z.; Wang, J.J.; Xie, Z.Y.; Cui, M.Y.; Tian, C.M.; Du, Y.G.; Zhang, K.H.L. Epitaxial growth and band alignment of p-NiO/n-Fe₂O₃ heterojunction on Al₂O₃ (0 0 0 1). *Appl. Surf. Sci.* **2019**, *464*, 488–493. [[CrossRef](#)]
57. Aghonbad, M.M.; Sedghi, H. Spectroscopic-ellipsometry measurement of the optical properties of zinc oxide thin films prepared by sol-gel method: Coating speed effect. *Micro Nano Lett.* **2018**, *13*, 959–964. [[CrossRef](#)]
58. Abideen, Z.U.; Kim, J.H.; Lee, J.H.; Kim, J.Y.; Mirzaei, A.; Kim, H.W.; Kim, S.S. Electrospun metal oxide composite nanofibers gas sensors: A review. *J. Korean Ceram. Soc.* **2017**, *54*, 366–379. [[CrossRef](#)]
59. Woo, H.S.; Na, C.W.; Kim, I.D.; Lee, J.H. Highly sensitive and selective trimethylamine sensor using one-dimensional ZnO-Cr₂O₃ hetero-nanostructures. *Nanotechnology* **2012**, *23*, 245501. [[CrossRef](#)]

Supplementary Materials

ZnO structures with surface nanoscale interfaces formed by Au, Fe₂O₃, or Cu₂O modifier nanoparticles: characterization and gas sensing properties

Milena Tomić^{1,2}, Martha Claros³, Isabel Gràcia¹, Eduard Figueras¹, Carles Cané¹, and Stella Vallejos^{1,3*}

¹ Institute of Microelectronics of Barcelona (IMB-CNM, CSIC), Campus UAB, 08193 Cerdanyola del Vallès, Barcelona, Spain; milena.tomic@imb-cnm.csic.es (M.T.); isabel.gracia@imb-cnm.csic.es (I.G.); eduard.figueras@imb-cnm.csic.es (E.F.); carles.cane@imb-cnm.csic.es (C.C.)

² Autonomous University of Barcelona (UAB), Department of Electronic Engineering, Campus UAB, 08193 Cerdanyola del Vallès, Barcelona, Spain

³ CEITEC - Central European Institute of Technology, Brno University of Technology, 61200 Brno, Czech Republic; martha.claros@ceitec.vutbr.cz (M.C.)

* Correspondence: stella.vallejos@imb-cnm.csic.es (S.V.); Tel.: +34 935 947700

S1. Results – Material characterization

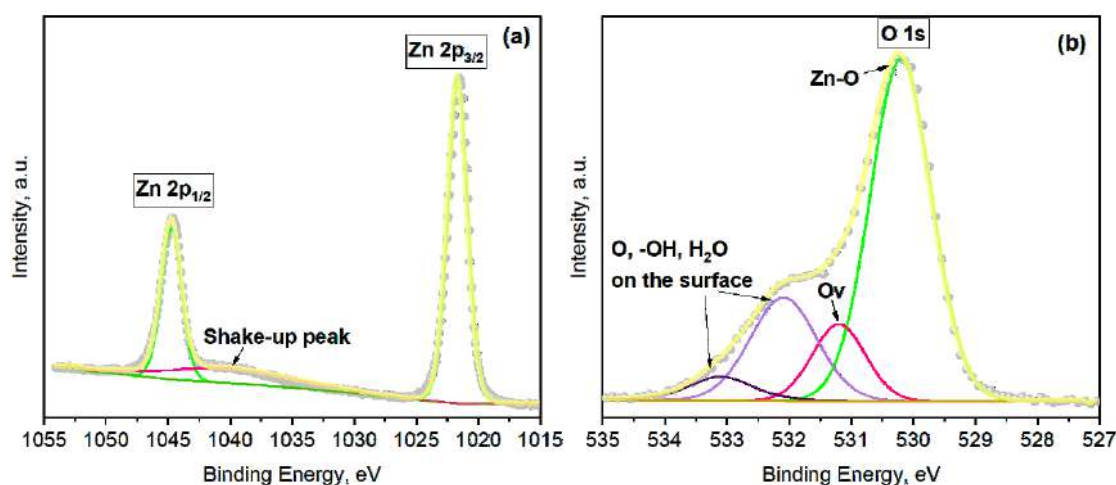


Figure S1. (a) Zn 2p, and (b) O 1s core levels XPS spectra for non-modified ZnO film. Grey dots represent the raw data, the solid yellow line corresponds to the envelope/fitting curve, and the other colored curves to the deconvoluted components.

The Zn 2p core-level spectrum recorded on non-modified ZnO film showed good agreement with the literature [1], proving the presence of Zn²⁺ state of zinc, with two main peaks at 1021.6 eV and 1044.7 eV that corresponds to the Zn 2p_{3/2} and Zn 2p_{1/2} peaks (**Figure S1a**), respectively, with the binding energy separation of 23.1 eV. Additional peak located at 1040.2 eV is related to the shake-up peak.

The O 1s XPS spectrum (**Figure S1b**) presents an asymmetric curve as reported earlier in the literature [2]. After the deconvolution, four different components are determined that indicate the presence of different oxygen species. The component centered at 530.2 eV is attributed to O²⁻ ions in the Zn-O bonding. The component at 531.2 eV is associated to O⁻ and O₂⁻ ions in the oxygen-deficient regions – oxygen vacancies. The components at 532.1 eV and 533.1 eV are connected to the presence of weak bonds from the physical or chemical adsorbed oxygen, hydroxides, and H₂O on the surface of ZnO film [3] [4] [5] [6].

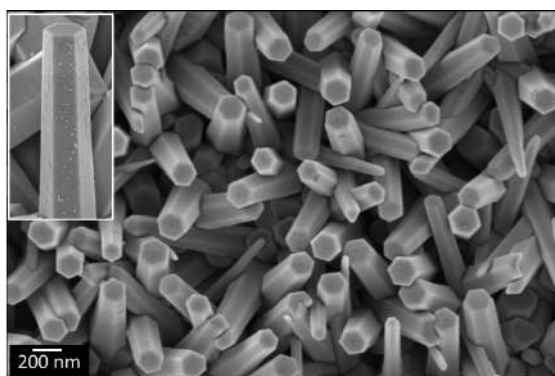


Figure S2. SEM images of the Ag@ZnO structured film (the inset shows a magnified image of a single Ag-modified ZnO rod).

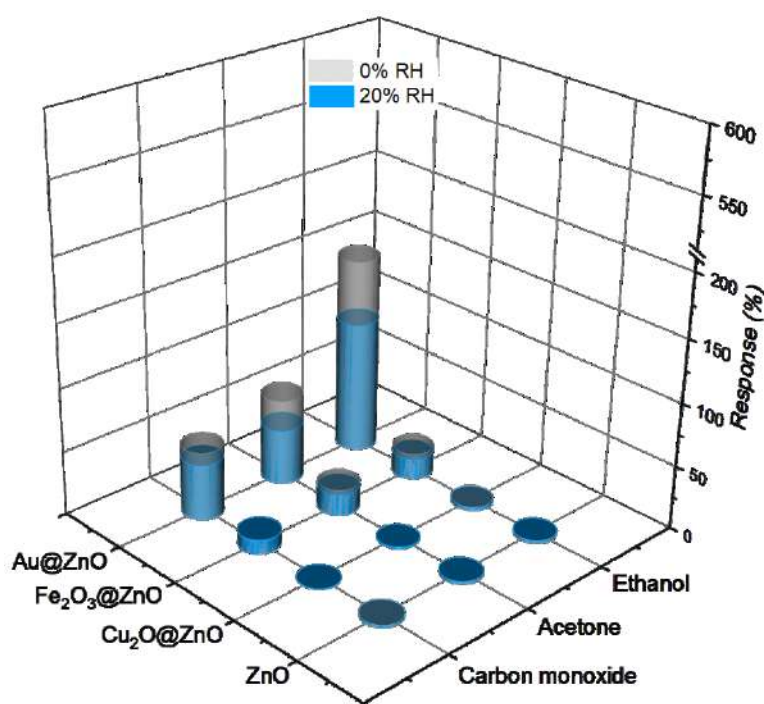


Figure S3. Responses towards 80 ppm of ethanol, acetone, carbon monoxide for the ZnO, Au@ZnO, Fe₂O₃@ZnO, and Cu₂O@ZnO sensors at 0% and 20% RH.

References:

- [1] S. Vallejos *et al.*, "ZnO rods with exposed {100} facets grown via a self-catalyzed vapor-solid mechanism and their photocatalytic and gas sensing properties," *ACS Appl. Mater. Interfaces*, vol. 8, no. 48, pp. 33335–33342, 2016, doi: 10.1021/acsami.6b12992.
- [2] J. H. Zheng, Q. Jiang, and J. S. Lian, "Synthesis and optical properties of flower-like ZnO nanorods by thermal evaporation method," *Appl. Surf. Sci.*, vol. 257, no. 11, pp. 5083–5087, 2011, doi: 10.1016/j.apsusc.2011.01.025.
- [3] S. Jain, J. Shah, N. Negi, C. Sharma, and R. K. Kotnala, "Significance of interface barrier at electrode of hematite hydroelectric cell for generating ecopower by water splitting," *Int. J. Energy Res.*, vol. 43, pp. 4743–4755, 2019, doi: 10.1002/er.4613.
- [4] H. Wang, S. Baek, J. Song, J. Lee, and S. Lim, "Microstructural and optical characteristics of solution-grown Ga-doped ZnO nanorod arrays," *Nanotechnology*, vol. 19, no. 7, p. 075607, Jan. 2008, doi: 10.1088/0957-4484/19/7/075607.
- [5] E. De La Rosa *et al.*, "Controlling the growth and luminescence properties of well-faceted ZnO nanorods," *J. Phys. Chem. C*, vol. 111, no. 24, pp. 8489–8495, Jun. 2007, doi: 10.1021/jp071846t.
- [6] L. J. Meng, C. P. Moreira de Sá, and M. P. dos Santos, "Study of the structural properties of ZnO thin films by x-ray photoelectron spectroscopy," *Appl. Surf. Sci.*, vol. 78, no. 1, pp. 57–61, May 1994, doi: 10.1016/0169-4332(94)90031-0.

ZnO Nanorods and Their Modification with Au Nanoparticles for UV-light Activated Gas Sensing

Milena Tomić^{1,2}

¹ *Institute of Microelectronics of Barcelona (IMB-CNM, CSIC)*

² *Department of Electronic Engineering Autonomous University of Barcelona*
08193 Cerdanyola del Vallès,
Barcelona, Spain
milena.tomic@imb-cnm.csic.es

Isabel Gràcia¹

¹ *Institute of Microelectronics of Barcelona (IMB-CNM, CSIC)*

08193 Cerdanyola del Vallès,
Barcelona, Spain
isabel.gracia@imb-cnm.csic.es

Eduard Figueras¹

¹ *Institute of Microelectronics of Barcelona (IMB-CNM, CSIC)*

08193 Cerdanyola del Vallès,
Barcelona, Spain
eduard.figueras@imb-cnm.csic.es

Carles Cané¹

¹ *Institute of Microelectronics of Barcelona (IMB-CNM, CSIC)*

08193 Cerdanyola del Vallès,
Barcelona, Spain
carles.cane@imb-cnm.csic.es

Stella Vallejos^{1,*}

¹ *Institute of Microelectronics of Barcelona (IMB-CNM, CSIC)*

08193 Cerdanyola del Vallès,
Barcelona, Spain
stella.vallejos@imb-cnm.csic.es

***Corresponding Author**

Tel.: +34-935-947700

Abstract— Aerosol assisted chemical vapour deposited ZnO nanostructured films integrated into Si-based transducing platforms are modified with preformed Au nanoparticles (NPs) via impregnation. The morphological, structural, and chemical characterization of these films using different characterisation techniques shows the incorporation of well-distributed and stable Au nanoparticles (NPs) at the surface of ZnO. Photoactivated gas sensing tests at room temperature (RT) demonstrate enhanced sensitivity and better speed of response for the Au modified ZnO films (AuZn) providing 3 times higher response to ethanol and acetone as compared to the non-modified ZnO films (Zn).

Keywords—gas sensors, ZnO, gold nanoparticles, AACVD, UV-light activation, ethanol

I. INTRODUCTION

Nanostructured metal oxides (MOX) are attractive in gas sensing because of their ability to enhance the performance of these devices, not only due to their higher surface-area-to-volume-ratio, as opposed to bulk materials, but also due to the presence of specific crystal facets that provide a particular electronic structure to the surface. Among various MOX, ZnO has been one of the most investigated materials for gas sensors due to its nontoxicity, stability, and low fabrication cost [1]. Although ZnO based sensors have remarkable performances, it is possible to improve their gas sensing properties even further by decoration with noble metal NPs, such as Au, Ag, Pt, or Pd [2] [3] [4] [5].

MOX based gas sensors usually operate at high temperatures (approximately 200 – 500 °C) [6]. Alternatively, they can operate at room temperature (RT) when the sensing material is activated using light irradiation, usually in the ultraviolet (UV) range [7]. Usage of photoactivation can help to overcome typical disadvantages of thermoactivation, such as frequent calibration and maintenance of heaters, limitation in the detection of flammable and explosive gases, and issues

with stability and poisoning of the sensitive material [8] [9]. Photoactivation can also reduce power consumption during operation with respect to thermoactivated sensors [8].

Therefore, in this paper, we show the fabrication of gas sensors based on non-modified and Au modified ZnO nanostructured films that operate under UV-light at RT. The physical and chemical characteristics of the gas sensitive films are analysed and the assembled sensor devices are tested towards various gases such as ethanol, acetone, toluene, and hydrogen.

II. MATERIALS AND METHODS

ZnO nanorods were directly deposited over Si-based transducing platforms (40 mm × 40 mm) at 400 °C via aerosol assisted chemical vapor deposition (AACVD) of zinc chloride (ZnCl₂, 50 mg, Sigma-Aldrich, ≥98%) dissolved in ethanol (5 ml, PanReac, ≥99.8%). Further details of this method were reported previously [10]. The modification of ZnO structures was achieved in a second step by impregnation with preformed Au NPs synthesized by the Turkevich method [11]. The impregnation process was performed by immersing the ZnO samples for 60 s into the solution with suspended Au NPs heated at 60 °C. Prior to the characterization, the samples were annealed in synthetic air at 450 °C for 1 h.

The morphology of the films was examined using scanning electron microscopy (SEM, Carl Zeiss, Auriga series, 3 kV) and transmission electron microscopy (TEM, FEI Tecnai F20, 200 kV). The optical properties were analyzed using UV-Vis diffuse reflectance spectroscopy (DRS, AvaSpec-UV/VIS/NIR, Avantes, Apeldoorn) and applying Kubelka-Munk transformation. The crystallinity of the films were examined using X-ray powder diffraction technique (XRD, Bruker, AXS D8 Advance, operated at 40 kV and 40 mA, Cu K α radiation), while the chemical composition was determined using X-ray photoelectron spectroscopy (XPS).

AuZn and Zn sensors were tested to ethanol, acetone, toluene, and hydrogen at RT using continuous photoactivation with a light-emitting diode (LED) at a wavelength of 365 nm in a gas flow system with dry air as the reference. The sensor response (R) was defined as $(R_a - R_g)/R_a$, where R_a and R_g represent the electrical resistance of the sensitive film in air and after 10 min of gas exposure, respectively.

III. RESULTS

Analysis of the samples by SEM proved the integration of Au modified ZnO structures over the transducing platforms. The SEM images (Fig. 1) show uniform ZnO rod-like morphology (with estimated average length of $\sim 1.5 \mu\text{m}$ and diameter of 200 nm) covered with well-distributed Au NPs with diameters between 5 and 40 nm.

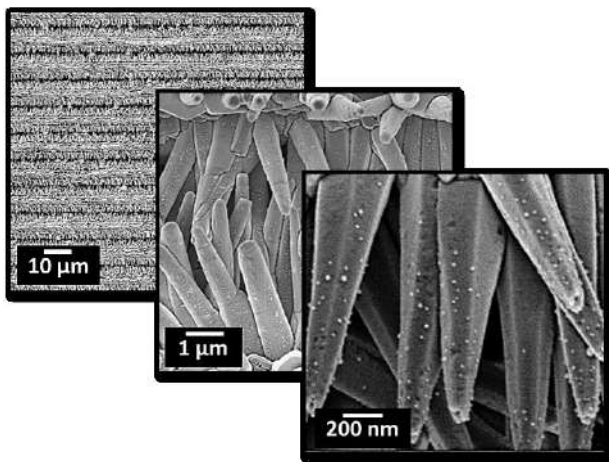


Fig. 1. Low and high magnification SEM images of the AuZn structured films deposited over the transducing platform.

Further analysis of these structures using high-resolution transmission electron microscopy (HRTEM) and scanning transmission electron microscopy (STEM) (Fig. 2) confirmed the formation of rod-like structures covered with spherical Au NPs.

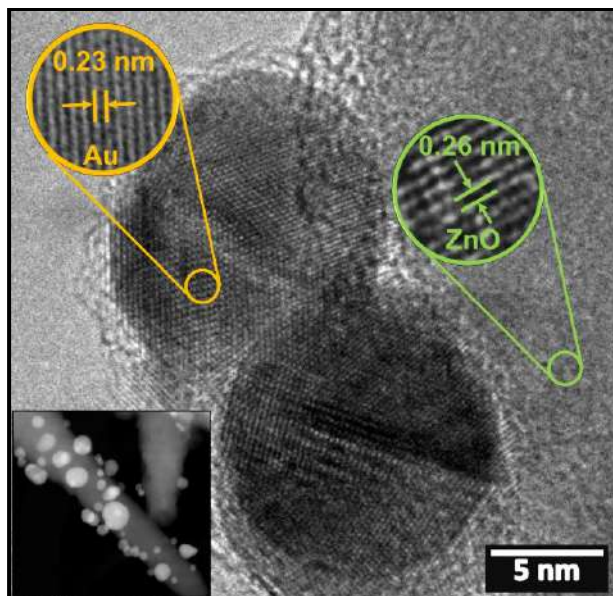


Fig. 2. HRTEM image with the inset showing a STEM image of a ZnO nanorod modified with Au nanoparticles.

High resolution images of these particles also revealed the presence of highly ordered crystalline lattices with the interplanar spacing of 0.26 nm and 0.23 nm, consistent with the hexagonal ZnO (002) [10] and cubic Au (111) planes (Fm3m space group, ICDD card No. 00-004-0784), respectively.

XRD (Fig. 3) corroborates the presence of the hexagonal ZnO phase with the absence of extra diffractions from Au NPs, most likely due to their small size, low amount, and high dispersion over the film.

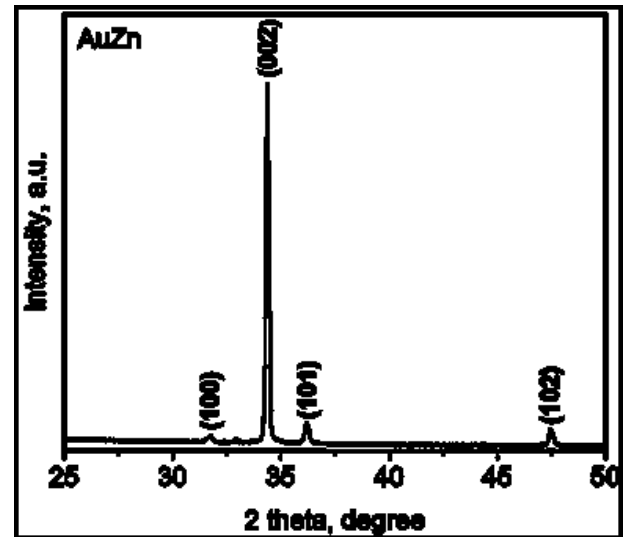


Fig. 3. Typical XRD diffraction pattern of the AuZn films

DRS results (Fig. 4) display the band gap transition of ZnO at $\sim 3.3 \text{ eV}$ (estimated by Kubelka-Munk transformation for the adsorption wavelength of 375 nm) and the surface plasmon resonance band of gold at $\sim 520 \text{ nm}$, which is in agreement with the literature data for ZnO [12] and Au [13].

XPS results (Fig. 5) also confirm the presence of the typical Zn 2p and Zn 3p core level spectrum recorded on both, Zn and AuZn films, and additional Au 4d and Au 4f core level spectrum, recorded only on the AuZn films.

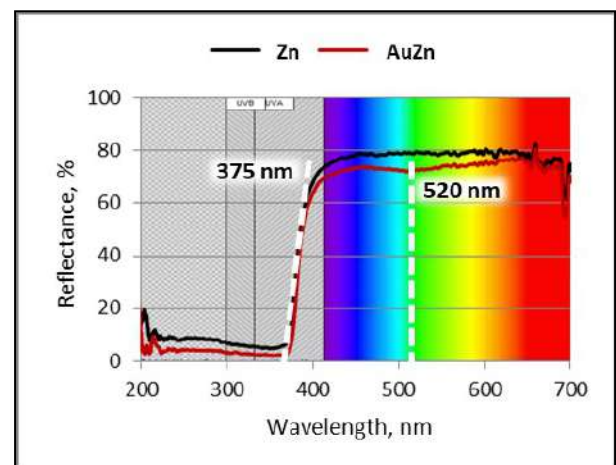


Fig. 4. Diffuse reflectance spectra (DRS) of the Zn and AuZn structured films.

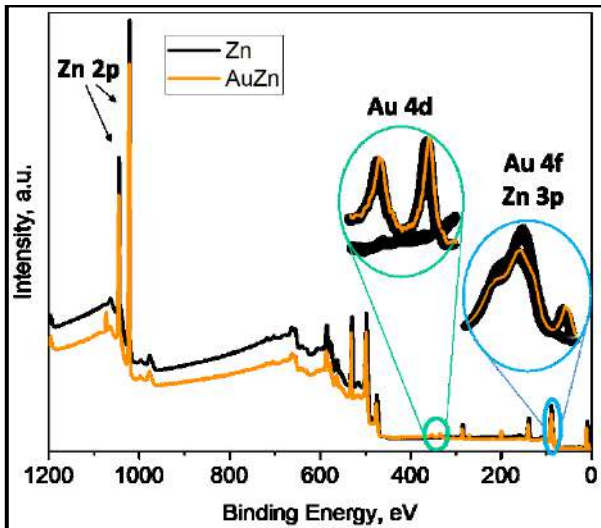


Fig. 5. XPS spectra recorded on the Zn and AuZn films. Only the peaks of interest have been marked.

Photoactivated gas sensing tests towards 80 ppm of ethanol, acetone, toluene, and hydrogen show enhanced responses with better recovery and response times for the AuZn sensors to all gases except hydrogen, which shows no differences in response, as compared to the Zn sensors (Fig. 6). The major improvement in sensor response after Au decoration is noticed for ethanol and acetone detection, with approximately 3 times higher response to both gases compared to non-modified films.

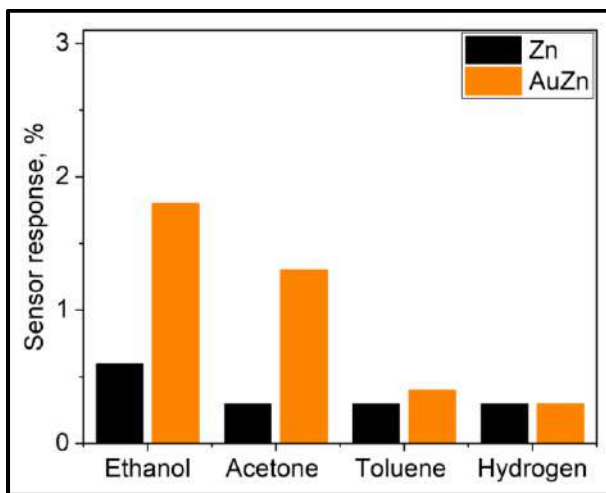


Fig. 6. Photoactivated response of Zn and AuZn sensors towards 80 ppm of ethanol, acetone, toluene, and hydrogen.

Fig. 7 displays the resistance changes for both types of sensors, Zn (Fig. 7a) and AuZn (Fig. 7b) when exposed to 80 ppm of ethanol under UV-light irradiation. The sensors showed a typical n-type MOX semiconductor response, with an increase in electrical resistance when subjected to reducing gases such as ethanol. Additionally, these results demonstrated improved reproducibility and stability of the AuZn sensor as well as better dynamics of the response, unlike the non-modified Zn sensor.

Gas sensing mechanism

A schematic illustration of the gas sensing mechanism of the modified films is depicted in Fig. 8. This figure shows that

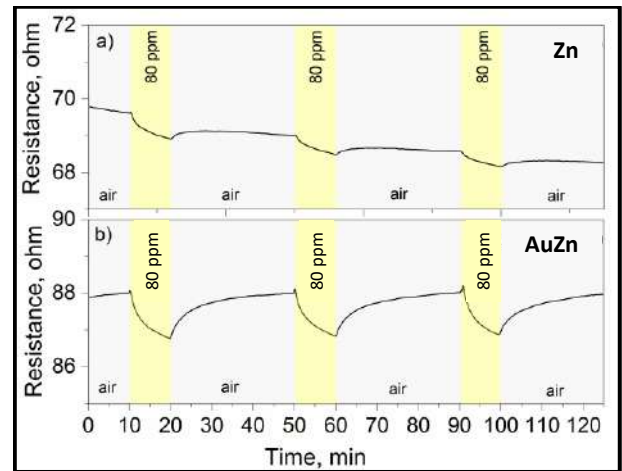
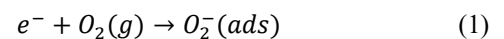


Fig. 7. Typical resistance changes recorded on the Zn and AuZn sensors to 80 ppm of ethanol.

when the sensor is not exposed to UV light source and gas (Fig. 8a), the free electrons from the MOX are extracted and trapped by oxygen molecules from the atmosphere ($O_2(g)$), forming oxygen ions ($O_2(ads)$) which are adsorbed on the sensor's surface, as shown in (1):



This adsorption leads to the formation of a depletion layer at the MOX's surface, with a built-in electric field [14], around the ZnO rod as well as around the Au NPs.

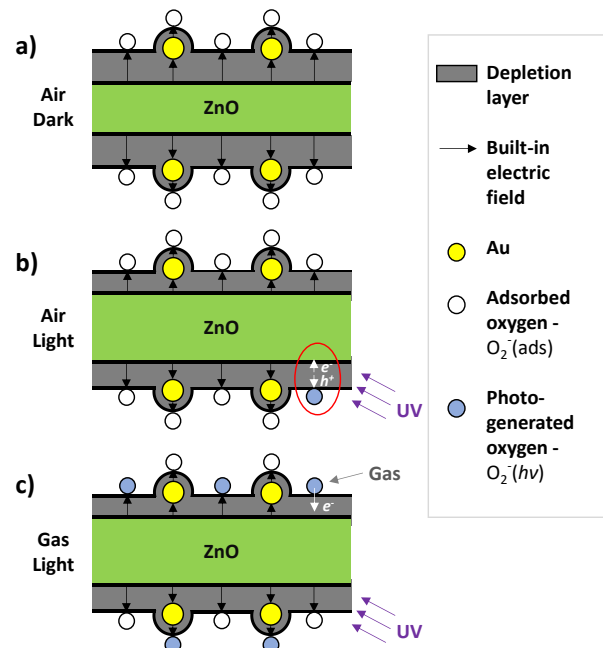
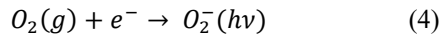
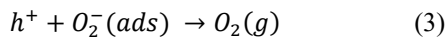


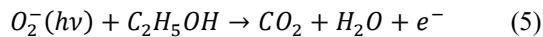
Fig. 8. Schematic representation of the AuZn gas sensing mechanism during UV-light activation. The illustration shows different stages of the sensor: a) exposed to dry air in the dark, b) exposed to dry air under UV-light, and c) exposed to ethanol under UV-light.

Under UV-light exposure (Fig. 8b), electrons and holes are generated in the sensing material and separated due to the built-in electric field. Then, photo-generated holes release the previously adsorbed oxygen ions from the surface (ambient oxygen desorption), while the photo-generated electrons react with the oxygen from the atmosphere and form the new photo-

induced oxygen ions, $O_2^-(hv)$, according to the following reactions:



After reaching the balance in oxygen desorption and adsorption, the sensor is prepared for the reaction with the target gas (**Fig 8c**). The gas reacts with the adsorbed photo-generated oxygen, which results in electrons releasing, as the example for ethanol in equation (5), and therefore it is observed an increase in conductance.



According to the gas sensing results, Au modification made a great impact on the sensor performance, especially for ethanol and acetone sensing. The improved sensing properties on the AuZn based sensors, compared to the Zn sensors, is attributed the catalyst effect of the Au NPs as well as to the additional interface formed between the ZnO rod and the Au NPs, and consequentially, additional electron transfer during the gas-solid interactions [15].

IV. CONCLUSIONS

Non-modified and Au modified ZnO gas sensors were fabricated and tested towards several gases at room temperature, employing UV photoactivation. Analysis of the materials (i.e. Zn and AuZn) by SEM, TEM, XRD, DRS, and XPS confirmed the presence of crystalline ZnO nanorods, as well as the incorporation of Au nanoparticles at the surface of the ZnO modified rods. Gas sensing results demonstrated improved sensing properties for the AuZn sensors, especially for ethanol and acetone, showing 3 times higher response to both gaseous analytes compared to the Zn sensors. The improvement was also noticed in the sensor's stability and reproducibility, in favour of the decorated sensor.

ACKNOWLEDGMENT

This work has been supported by the Spanish Ministry of Science and Innovation, via Grant PID2019-107697RB-C42 (AEI/FEDER, EU) and the Ramón y Cajal programme.

REFERENCES

- [1] S. Zhang, H. Byun, J. Lim, J. Huh, and W. Lee, "Controlled Synthesis of ZnO Nanostructures for Sub-ppm-Level VOC Detection," *IEEE Sens. J.*, vol. 12, no. 11, pp. 3149–3155, 2012, doi: 10.1109/JSEN.2012.2208950.
- [2] S. Arunkumar, T. Hou., Y-B. Kim, B. Choi, S. H. Park, S. Jung, D-W. Lee, "Au Decorated ZnO hierarchical architectures: Facile

- [3] Z. Li, G. Zhang, W. Gao, R. Zhao, and Y. Wang, "Ag decorated ZnO nanocrystallines synthesized by a low-temperature solvothermal method and their application for high response H₂ gas sensor," *J. Mater. Sci. Mater. Electron.*, vol. 30, pp. 18959–18969, 2019, doi: 10.1007/s10854-019-02253-5.
- [4] J. Xuan *et al.*, "Fabrication of in-situ grown and Pt-decorated ZnO nanoclusters on new-type FTO electrode for room-temperature detection of low-concentration H₂S," *J. Alloys Compd.*, vol. 860, pp. 158499–158510, 2021, doi: 10.1016/j.jallcom.2020.158499.
- [5] T. Dilova *et al.*, "Effect of Pd-decoration on the sensing properties of ZnO nanostructures," *Thin Solid Films*, vol. 693, p. 137693, Jan. 2020, doi: 10.1016/j.tsf.2019.137693.
- [6] M. Tomić, M. Šetka, L. Vojkúvka, and S. Vallejos, "VOCs Sensing by Metal Oxides, Conductive Polymers, and Carbon-Based Materials," *Nanomaterials*, vol. 11, no. 2, p. 552, Feb. 2021, doi: 10.3390/nano11020552.
- [7] V. S. Bhati, M. Hojamberdiev, and M. Kumar, "Enhanced sensing performance of ZnO nanostructures-based gas sensors: A review," *Energy Reports*, vol. 6, pp. 46–62, 2020, doi: 10.1016/j.egyr.2019.08.070.
- [8] N. Markiewicz, O. Casals, C. Fabrega, I. Gràcia, C. Cané, H.S. Wasisto, A. Waang, J. D. Prades., "Micro light plates for low-power photoactivated (gas) sensors," *Appl. Phys. Lett.*, vol. 114, no. 5, p. 053508, Feb. 2019, doi: 10.1063/1.5078497.
- [9] E. Espid, B. Adeli, and F. Taghipour, "High Performance UV-LED Activated Sensor Development By Modulating the Morphology and Composition," *ECS Meet. Abstr.*, vol. MA2020-01, no. 30, pp. 2277–2277, May 2020, doi: 10.1149/ma2020-01302277mtgabs.
- [10] S. Vallejos, N. Pizúrová, J. Čechal, I. Gràcia, and C. Cané, "Aerosol-assisted Chemical Vapor Deposition of Metal Oxide Structures: Zinc Oxide Rods," *JoVE*, vol. 127, p. e56127, 2017.
- [11] J. Turkevich, P. C. Stevenson, and J. Hillier, "A study of the nucleation and growth processes in the synthesis of colloidal gold," *Discussions of the Faraday Society*, vol. 11, no. 0. The Royal Society of Chemistry, pp. 55–75, Jan. 1951, doi: 10.1039/DF9511100055.
- [12] A. B. Djurisić, X. Chen, Y. H. Leung, A. Man, and C. Ng, "ZnO nanostructures: growth, properties and applications," *J. Mater. Chem.*, vol. 22, pp. 6526–6535, 2012, doi: 10.1039/c2jm15548f.
- [13] V. Amendola, "Surface plasmon resonance of silver and gold nanoparticles in the proximity of graphene studied using the discrete dipole approximation method," *Phys. Chem. Chem. Phys.*, vol. 18, no. 3, pp. 2230–2241, Jan. 2016, doi: 10.1039/c5cp06121k.
- [14] M. Tomić, Z. Fohlerova, I. Gràcia, E. Figueras, C. Cané, and S. Vallejos, "UV-light activated APTES modified WO_{3-x} nanowires sensitive to ethanol and nitrogen dioxide," *Sensors Actuators, B Chem.*, vol. 328, p. 129046, 2021, doi: 10.1016/j.snb.2020.129046.
- [15] D. V. Ponnuvelu, J. Dhakshinamoorthy, A. K. Prasad, S. Dhara, M. Kamruddin, and B. Pullithadathil, "Geometrically Controlled Au-Decorated ZnO Heterojunction Nanostructures for NO₂ Detection," *ACS Appl. Nano Mater.*, vol. 3, no. 6, pp. 5898–5909, Jun. 2020, doi: 10.1021/acsnm.0c01053.

3.4 Modification of iron oxide by nanoscale interfaces

Comparing to MOXs such as WO_3 and ZnO , iron oxide (Fe_2O_3) is less investigated in gas sensing, despite its high abundance in nature, low cost, high stability, high resistance to corrosion, and nontoxicity, as well as magnetic and catalytic properties [183]–[185]. Fe_2O_3 has a band gap of ~ 2.1 eV and it can have n-type or p-type semiconducting behavior [19], but mostly it shows n-type conductivity [186]. The literature review shows that Fe_2O_3 has been synthesized in the form of particles [34], and structures including wires [187], rods [188], and other hierarchical structures [189] [190] for sensing, magnetic, and energy applications. The literature shows as well that this material achieved good results in the detection of gases, such as ethanol [41], acetone [44], and nitrogen dioxide [48]. Previously, the *Gas Sensors* group at *IMB-CNM (CSIC)* also explored the use of Fe_2O_3 as a ‘guest’ material in WO_3 and ZnO structures [34] [140] [154], finding potential for Fe_2O_3 to act as ‘host’ element rather than only as a modifier. Moreover, it is important to remark that the current literature shows an absence of AACVD methods for Fe_2O_3 structuration. In that context, this thesis investigated further the structuration of Fe_2O_3 via AACVD and its modification with Au nanoparticles by exploring different AACVD conditions including precursor solutions, temperatures, and aerosol fluxes, amongst others. Additionally, the gas sensing properties of these non-modified and Au modified structures were evaluated towards various gases, including acetone, ethanol, toluene, CO, H_2 , and NO_2 . These results belong to the most recent findings of the thesis and soon will be placed into consideration for their publication in a specialized primary journal with the title **“Aerosol assisted chemical vapor deposition of gas-sensitive Fe_2O_3 and Au-modified Fe_2O_3 structures”**.

3.4.1. Results

The research of non-modified and Au modified Fe_2O_3 firstly includes the result of setting the optimal conditions for the AACVD synthesis of four types of Fe_2O_3 structures (named flattened pyramids, pyramids, porous pyramids, and sheets) and search of the conditions for incorporation of Au nanoparticles at the surface of these structures in a second AACVD deposition step. In that aspect, the results show detailed information about the tuned AACVD conditions, including deposition temperatures, solvents, precursors, and their concentrations. The characterization techniques, such as SEM, TEM, XRD, and XPS gave information about the morphology, crystallinity, and chemical composition of the synthesized materials. From the four different structures, porous pyramids exhibited the best sensing performances showing high responses, particularly to acetone and ethanol. Gas sensing tests of the Au modified Fe_2O_3 pyramids also displayed high responses to acetone and ethanol, although with less intensity than the responses observed for the non-modified Fe_2O_3 . However, these results are in part contradictory, as the previous observations in this thesis revealed frequently enhanced gas sensing properties for the surface modified MOXs with respect to non-modified materials. This contradictory behavior suggested being connected with the high loads (9.5 at. %) of gold found at the samples’ surface, which exceed in about 46 % the typical loads employed in previous systems (e.g. for Au@ZnO 5.1 at.%).

3.4.2. Conclusions

A new AACVD method for the synthesis of Fe_2O_3 structures and Au modified Fe_2O_3 structures was developed. Results demonstrated the possibility to tune selectively the morphology of Fe_2O_3 from pyramid-like structures to sheet-like structures mainly by controlling the deposition temperature, precursor concentration, and the location of the substrate in the reactor. Results also proved the incorporation of Au particles over the Fe_2O_3 . Gas sensing tests of these structures demonstrated good sensitivity to acetone and ethanol, showing the highest response for the Fe_2O_3 porous pyramids-based sensors. Overall, the sensors showed good stability and response/recovery times. The modification of the structures with gold led to a loss of Fe_2O_3 gas sensitivity, most likely caused by the blockage of adsorption centers on the Fe_2O_3 surface due to the excessive loading of Au particles. A tuning of the Au loadings to lower amounts (e.g., < 5 at.%) is recommended in light of previous literature reports and the results obtained with other Au modified MOX structures such as the Au@ZnO structures reported in *Section 3.3* of this thesis.

3.4.3. Journal Article 5

Aerosol assisted chemical vapor deposition of gas sensitive Fe_2O_3 and Au-modified Fe_2O_3 structures, Tomić, M., Gràcia, I., Figueras, E., Cané, C., Vallejos, S. – To be submitted

Aerosol Assisted Chemical Vapor Deposition of gas sensitive Fe₂O₃ and Au-modified Fe₂O₃ structures

Abstract

Iron oxide (Fe₂O₃) structures with different morphologies, including flattened pyramids, pyramids, porous pyramids, and sheets are synthesized selectively via AACVD. Among all synthesized structures, porous pyramids show the best sensing properties especially towards acetone and ethanol with comparable characteristics to other works in the literature for Fe₂O₃, and sensitivity of 2.7 and 1.9 % ppm⁻¹, respectively. The incorporation of gold nanoparticles at the pyramid surface proves to diminish the gas sensing response of Fe₂O₃ contrary to previous reports in which gold modifiers led to enhanced responses. This behavior is attributed to the high amount of Au particles (9.5 at%) incorporated over the surface of Fe₂O₃ during the AACVD process; a fact that reduces the adsorption sites at the surface of this gas-sensitive material, diminishing its sensors response.

Keywords: AACVD, gas sensor, hematite, surface modification, metal oxides, Au nanoparticles

Introduction

Metal oxide (MOX) gas sensors draw a lot of attention due to their small size, low cost, short response time and long-lasting life, and simplicity in operation and mass production [1] [2]. Due to that, they found application in gas sensors devices for environmental monitoring [3], health care [4], security [5], artificial olfaction [6] and so on. Amongst the most studied MOXs for gas sensing application are ZnO, SnO₂, TiO₂, and WO₃ [7] due to their wide band gaps and low activation energies. However, other MOXs such as iron oxide (Fe₂O₃) have also shown great potential in gas sensing. Fe₂O₃ is usually known for its catalytic and magnetic properties [8], although it has also shown sensing properties to gases such as ethanol [9] [10], acetone [11] [12], and nitrogen dioxide [13] [14], to cite a few. The most stable iron oxide under ambient conditions is hematite (α -Fe₂O₃), which is an n-type semiconductor with the band gap of ~2.1 eV [15]. This MOX has shown interesting practical advantages due to its high stability, high resistance to corrosion, nontoxicity, and low cost given iron's abundance [16] [10].

It is known that structuration of MOX materials improves their gas sensing properties as compared to bulk material due to their large surface area [17]. Additionally, modification of MOX surface with noble metals adds chemical and electronic sensitization effects that improve further the MOX gas sensing performances [7] [18]. In that context, the set of new scalable chemical synthesis routes for MOX structuration and surface modification are still attractive in the gas-sensing field. Previously, the structuration of Fe₂O₃ structures of different morphologies, such as particles [19], wires [20] [21], fibers [22] [23], rods [24] [25], spindles [26] [27], belts [28] [29], tubes [30] [31], and urchin-like structures [12] were achieved and used mainly in the area of energy and magnetism, but some of them also in gas sensing. Moreover, surface modification of Fe₂O₃ structures with Au [32] or Pt [33] for acetone detection, Au for ethanol detection [34] or Pd for propane [35] and H₂S [36] detection were also reported in the literature. The most common synthesis methods for achieving these structured and modified Fe₂O₃ usually include solvothermal synthesis [37], sol-gel method [38], thermal decomposition method [39], hydrothermal synthesis [40], and sonoelectrochemical anodization method [41]. However, to

the best of our knowledge, Aerosol Assisted Chemical Vapor Deposition (AACVD) route for Fe₂O₃ structuration was reported only in our previous works [19] [42] [43], in which this material was used as a modifier material rather than ‘host’ material for gas sensing.

Therefore, here we report a new synthesis route based on AACVD for the structuration of α -Fe₂O₃ and its modification with Au NPs. This work also evaluates the surface and chemical properties of the synthesized structures and their performance as gas-sensitive materials.

Materials and Methods

Iron oxide structures were grown directly onto an array of 4 silicon micromachined platforms (400 x 400 μ m each) using the AACVD system reported previously [44]. Table 1 lists the obtained morphologies (including flattened pyramids, pyramids, porous pyramids, and sheets) and the main AACVD conditions used for each one. Briefly, the structures were deposited using a precursor solution of iron(III) chloride hexahydrate (80 or 100 mg, \geq 99.0%, Sigma–Aldrich) and either pure acetone (5 mL, \geq 99.9%, PanReac) or acetone – ethanol mixture consisting of 4 ml of acetone and 1 ml of ethanol (\geq 99.9%, PanReac,). The aerosol droplets of the solutions were transported to the heated substrate using nitrogen gas flow (200 sscm). The modification with Au NPs was achieved in a second AACVD step at 370 °C using HAuCl₄·3H₂O, (50 μ g, \geq 99.0%, Sigma–Aldrich) dissolved in methanol (2 mL, \geq 99.9%, PanReac). The deposition times last approximately 25 min for the structuring step and 10 min for the modification step.

Table 1. Experimental conditions for the synthesis of non-modified Fe₂O₃ with flattened pyramids (fPys), pyramids (Pys), porous pyramids (pPys), and sheets (Shs) -like morphologies using AACVD method.

Morphology	Precursor	Solvent	Aerosol capacity, l/h	Deposition temperature, °C	Substrate position in the chamber
fPys	FeCl ₃ *6H ₂ O, 100 mg	Acetone, 5 ml	0.3	370	Outlet
Pys	FeCl ₃ *6H ₂ O, 100 mg	Acetone, 5 ml	0.3	370	Inlet
pPys	FeCl ₃ *6H ₂ O, 80 mg	Acetone, 5 ml	0.3	370	Inlet
Shs	FeCl ₃ *6H ₂ O, 100 mg	Acetone, 4 ml + Ethanol, 1 ml	0.3	340	Outlet

Prior to the material characterization, the samples were annealed in synthetic air for 1 h at 400 °C. The morphology of the structures was examined using scanning electron microscopy (SEM – Auriga Series, 3 KV, Carl Zeiss) and the crystallinity using X-ray Diffraction (XR – Bruker, AXS D8 Advance, Cu K α radiation operated at 40 kV and 40 mA). Further analysis of the samples involved the examination of morphology by TEM (Transmission Electron Microscopy – FEI Tecnai, 200 kV), including STEM (Scanning Transmission Electron Microscopy) mode and HRTEM (High-Resolution Transmission Electron Microscopy) mode. The chemical composition of the material was carried out using X-ray photoelectron spectroscopy (XPS – Kratos Axis Supra spectrometer with Al/Ag monochromatic X-ray source).

The gas microsensors were tested in a continuous flow test chamber [45] provided with mass flow controllers that allow the mixture of dry/humid air and calibrated gaseous analytes (all purchased from Praxair, Danbury, CT, USA) to obtain the desired concentration. The operating temperature of the sensors was 350 °C. The tested gases include acetone (C₃H₆O),

ethanol (C₂H₅OH), toluene (C₇H₈), carbon monoxide (CO), hydrogen (H₂), and nitrogen dioxide (NO₂). After the exposure (10 min) to each gas analyte, the sensors were recovered in the synthetic air until the initial baseline resistance was achieved.

The electrical resistance measurements were performed using a multimeter Keithley 2700 with a switch system for monitoring several sensors simultaneously. The sensor response (R) was defined as R_a/R_g for reducing and R_g/R_a for oxidizing gases, where R_a and R_g represent the electrical resistance of the sensitive film in air and after 600 s in the target gas, respectively. The sensitivity of the sensor (S) expresses the variation of the sensor response as a function of the change in the tested gas concentration. The response time was defined as the time required for a sensor to reach 90 % of the total response upon exposure to the target gas, while the recovery time was defined as the time required for a sensor to return to 90 % of the original baseline signal after the target gas is removed and the sensor is subsequently cleaned with dry air. The sensors were tested for a period of four months during which each sensor accumulated 290 h of operation.

Results and discussion

Material analysis

SEM images of the Fe₂O₃ structures obtained by AACVD using different synthesis conditions (Table 1), showed uniformly deposited structured films with different morphologies – fPys, Pys, pPys, and Shs. The biggest structures (fPys in Figure 1a) were obtained at 370 °C, when the substrate was positioned at the outlet of the chamber. Their width ranges between 200 and 300 nm, while the length is ~1.2 μm. The Pys (Figure 1b) and pPys (Figure 1c), deposited at the same temperature as fPys but at the inlet of the chamber, show similar sizes, with the lateral edge of ~250 nm and base edge of ~370 nm. Contrary to the smooth surface of the Pys structures, the pPys display pores over the surface of irregular shape and size. The thinnest structures (30-40 nm thick) are the Shs (Figure 1d) synthesized with the acetone-ethanol mixture at the lowest temperature of 340 °C.

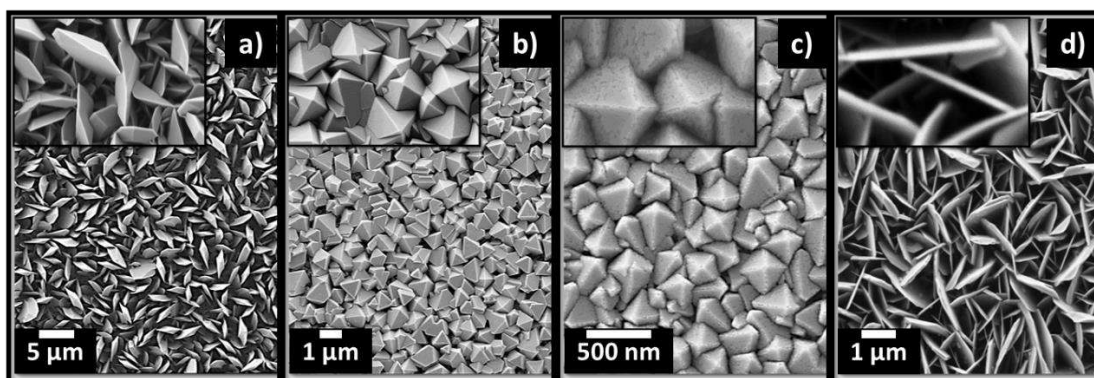


Figure 1. SEM images of the Fe₂O₃ **a)** fPys, **b)** Pys, **c)** pPys, and **d)** Shs deposited by AACVD method using different synthesis conditions.

The STEM images of the Fe₂O₃ structures in the first column of Figure 2 display the structured particles removed from the substrate. These particles suggest similar morphologies to those observed by SEM. The HRTEM images, showed in the second and third column of Figure 2, reveal the presence of highly ordered crystalline lattices with the fringe spacing (d) of 0.27 nm approximately for all four morphologies.

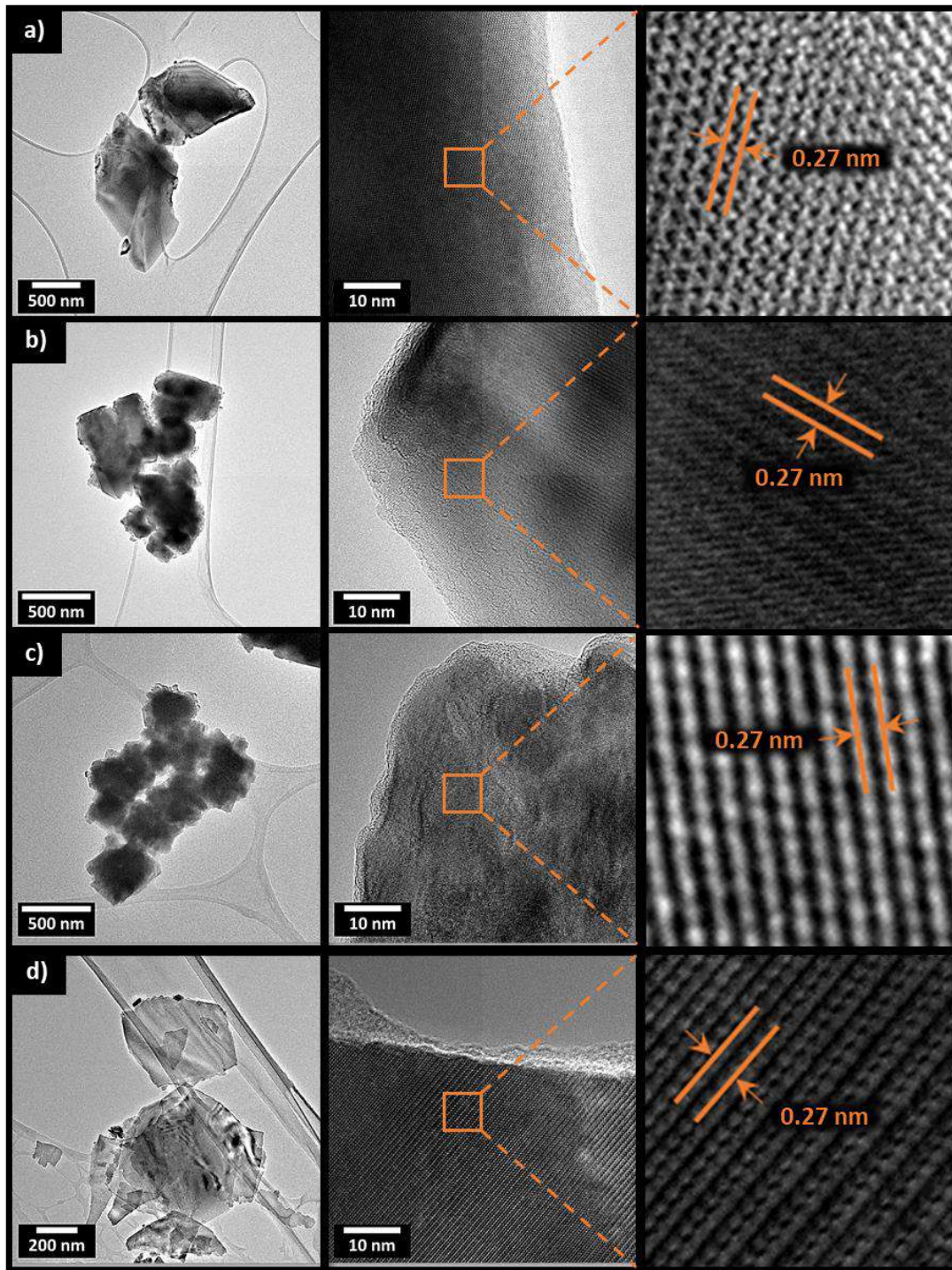


Figure 2. Low-magnification STEM (first column) and corresponding HRTEM images (second and third column) of the Fe_2O_3 **a) fPys, b) Pys, c) pPys, and d) Shs.**

A preliminary test of these sensors to fixed gas concentrations of acetone (80 ppm), ethanol (80 ppm), and NO_2 (5 ppm) revealed the best performance for the pPy [46]. The reason for better response of these structures lays most likely in their porosity. Previously, it was observed [7] that porous structures show remarkable sensing performance not only due to their surface-to-volume-ratio, but also because of the particular surface defects induced by the pores and

their irregular arrangement. Hence, further material analysis, decoration with Au NPs, and gas sensing tests, were focused only on these structures.

The SEM images in Figure 3 display the Fe_2O_3 pPys before and after their decoration with Au NPs. The formation of Fe_2O_3 porous pyramid structures with uniformly dispersed Au NPs of 30-40 nm, over their surface is evidenced in Figure 3b. It is interesting to notice that the surface of pPys after the decoration appears to be smoother, probably as a consequence of the Au NPs filling the Fe_2O_3 pores as the SEM images show a visible brightness difference between the pyramid surface and the particles/pores at the surface, as opposite to the pyramid surface in Figure 3a.

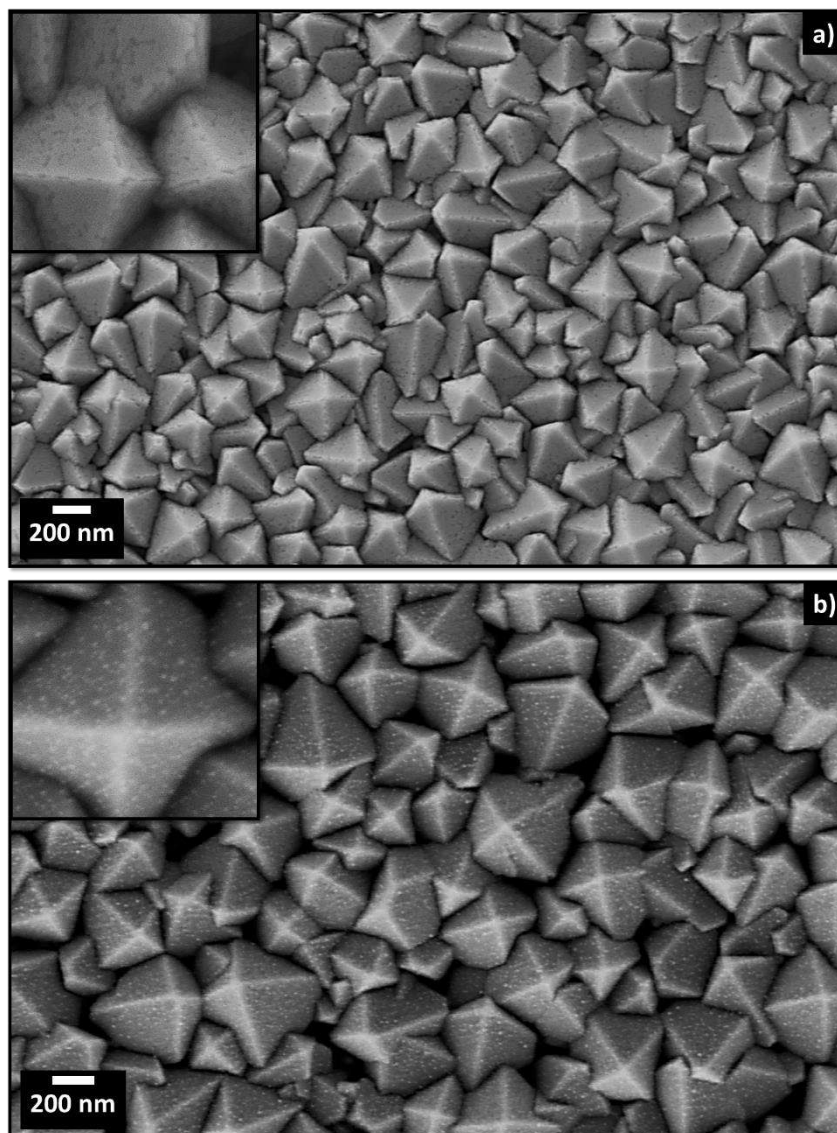


Figure 3. SEM images of the Fe_2O_3 structures **a)** before, and **b)** after their decoration with Au NPs.

XRD analysis of the Fe_2O_3 and $\text{Au@Fe}_2\text{O}_3$ pPys (Figure 4) demonstrated the presence of a rhombohedral (hexagonal) $\alpha\text{-Fe}_2\text{O}_3$ phase (R-3c space group, ICDD card no. 33-0664) recorded on both samples and cubic Au phase (Fm-3m space group, ICDD card No. 00-004-0784) recorded only on the modified samples (Figure 4b). This is consistent with the literature data for rhombohedral (hexagonal) $\alpha\text{-Fe}_2\text{O}_3$ [47] and cubic Au [48]. The intense peak at $33.1^\circ 2\theta$

corresponds to the (104) plane of Fe_2O_3 , while the peak recorded on modified structured film at $38.1^\circ 2\theta$ is attributed to the (111) plane of Au NPs.

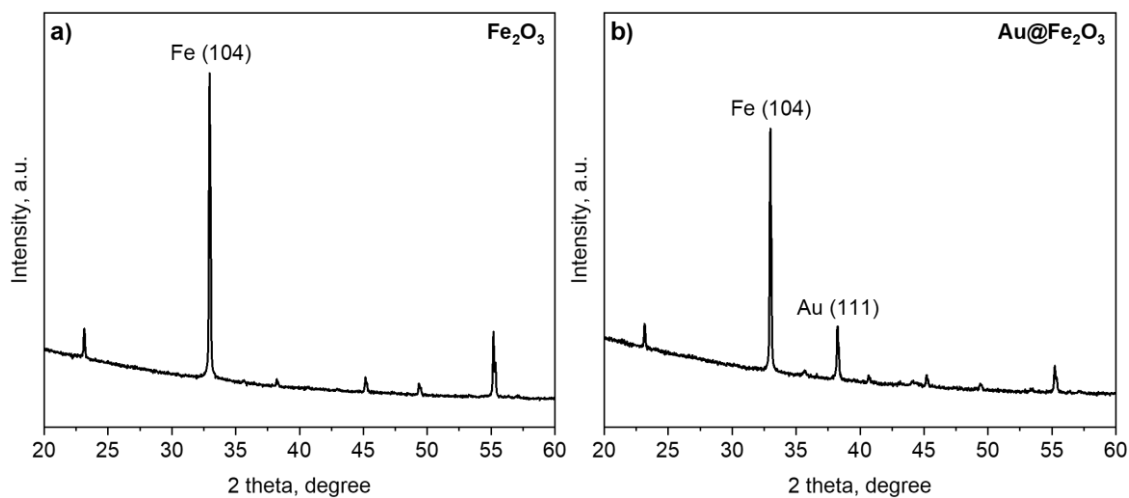


Figure 4. XRD diffraction pattern of the **a)** Fe_2O_3 pPy, and **b)** $\text{Au@Fe}_2\text{O}_3$ pPy. The diffraction peaks in the data can be indexed to a rhombohedral (hexagonal) Fe_2O_3 phase (R-3c space group, ICDD card no. 33-0664) and cubic Au phase (Fm-3m space group, ICDD card No. 00-004-0784). Only the peaks of high intensity have been marked.

The elemental and chemical composition of the Fe_2O_3 and $\text{Au@Fe}_2\text{O}_3$ pPys was analyzed using XPS (Figure 5). The wide and narrow XPS spectra of the samples show that both films display typical Fe 2p core level peaks with similar characteristics to those observed in our previous work [42] [43]. Specifically, the Fe 2p spectrum displayed in Figure 5c shows two characteristic peaks at 711.0 eV and 724.8 eV, and two satellite peaks at 719.3 eV and 732.9 eV originating from the photoelectrons emitted from Fe $2p_{3/2}$ and Fe $2p_{1/2}$, respectively. The Fe 2p spectrum is fitted to eleven components: four multiplets of Fe peak, two multiplets of Fe $2p_{1/2}$ peak, two satellite peaks, two surface peaks, and one characteristic pre-peak usually present in the Fe $2p_{3/2}$ spectrum. According to the binding energies of these peaks, iron is present in the oxidation state Fe^{3+} [43].

Additionally, the modified sample confirms the presence of Au 4d and Au 4f peaks at the characteristic binding energies for this element (i.e. 83.8 eV for $4f_{7/2}$ eV and 87.5 eV for $4f_{5/2}$) in agreement with the literature [49]. Figure 5d displays the Au 4f spectrum of the $\text{Au@Fe}_2\text{O}_3$ pPys. The deconvolution of this spectrum suggests the presence of two components (at 84.1 eV and 87.8 eV) with a binding energy separation of 3.7 eV, consistent with the Au^0 oxidation state [43][50]. The content of Au in the film was estimated to be 9.5 at%.

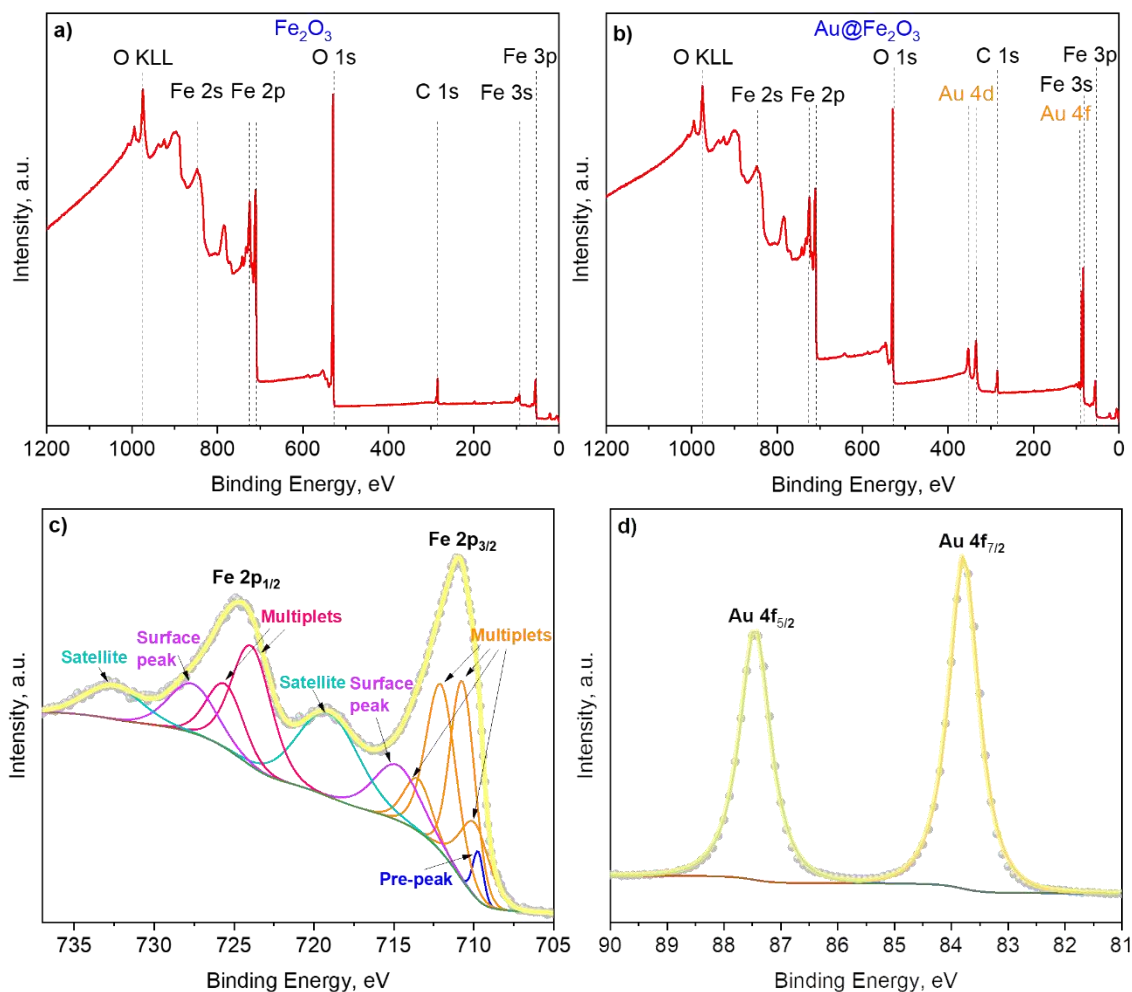


Figure 5. a) XPS spectra recorded on the Fe_2O_3 pPys and b) $\text{Au@Fe}_2\text{O}_3$ pPys. c) Typical Fe 2p core level XPS observed in both samples. d) Au 4f core level XPS spectra recorded on the $\text{Au@Fe}_2\text{O}_3$ pPys.

Gas sensing tests

The responses of the Fe_2O_3 and $\text{Au@Fe}_2\text{O}_3$ gas sensors were tested to various operating temperatures, finding the lowest temperature with maximum response to the target gases at 350 °C. Therefore, the subsequent tests of the sensors were performed using this operating temperature as a reference. Initially, both sensors, Fe_2O_3 and $\text{Au@Fe}_2\text{O}_3$, were tested towards various fix gas concentrations (80 ppm for ethanol, acetone, CO, toluene, and H_2 , and 5 ppm for NO_2). A comparison of the response to each gas analyte is displayed in Figure 6. Overall, the sensors show a better behavior to acetone and ethanol, particularly for the non-modified sensors. The sensors also show significant responses to gaseous analytes such as nitrogen dioxide, considering the lower NO_2 concentration used (compared to the other target gases).

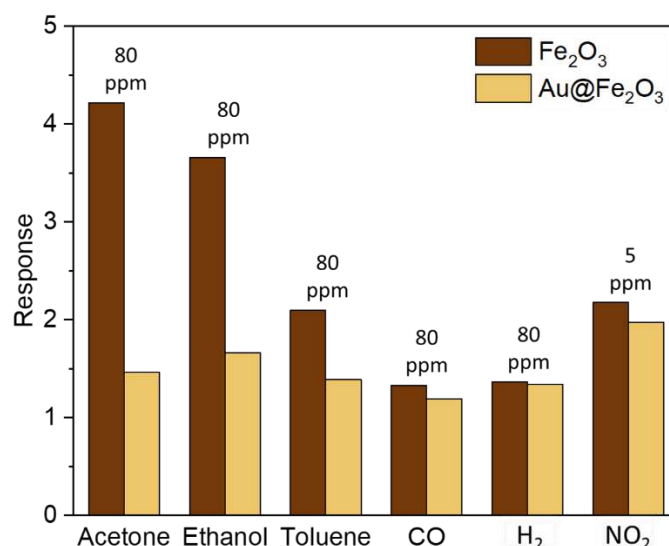


Figure 6. Comparative gas sensing results of the non-modified and Au modified Fe₂O₃ pPy towards fixed gas concentrations of each target analyte at 350 °C.

Further tests of the sensors to different concentrations of ethanol and acetone showed a proportional increase of the sensor response as a function of the gas concentration (Figure 7). These results also revealed the sensitivity (*S*) of the sensors, which turned to be higher for acetone than for ethanol when employing the non-modified Fe₂O₃ sensors, in agreement with the responses obtained for the fixed gas concentrations.

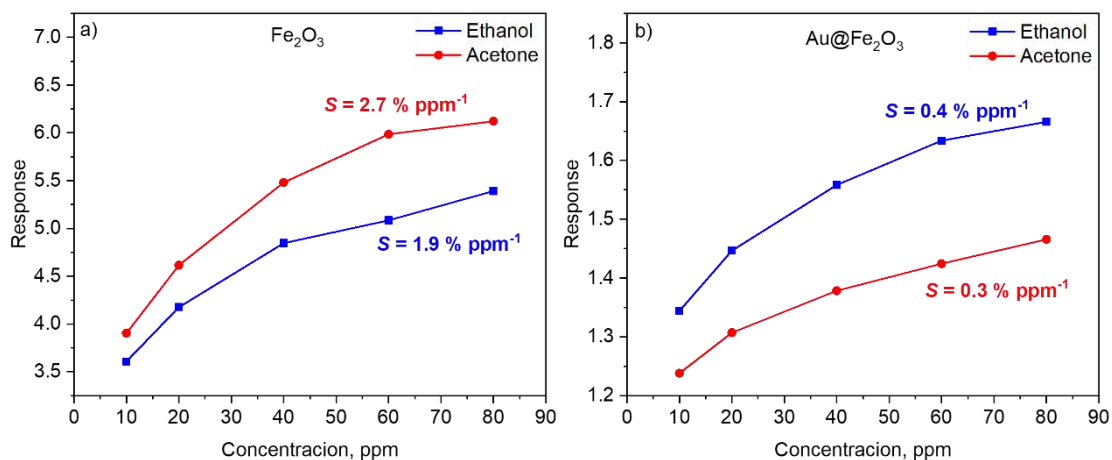


Figure 7. Dependence of the response on ethanol and acetone concentration (10 to 80 ppm) for the a) Fe₂O₃ and b) Au@Fe₂O₃ pPy sensors

Figure 8 depicts a comparison of the dynamic of the responses to various concentrations (10 – 80 ppm) of ethanol and acetone registered by the Fe₂O₃ and Au@Fe₂O₃ sensors. Generally, both sensors show good reproducibility and reversibility, with slightly better stability in the Au@Fe₂O₃ sensor. Both sensors reached full recovery after purging the analyte with the synthetic air. The drop in the Fe₂O₃ sensor response with the lowering of the analyte concentration demonstrated that the response declines approximately 10 % on average for ethanol and 13 % for acetone for each change in the concentration of 20 ppm. Following this trend, it can be concluded that these sensors can be used to detect ethanol and acetone even when their concentration is lower than 10 ppm.

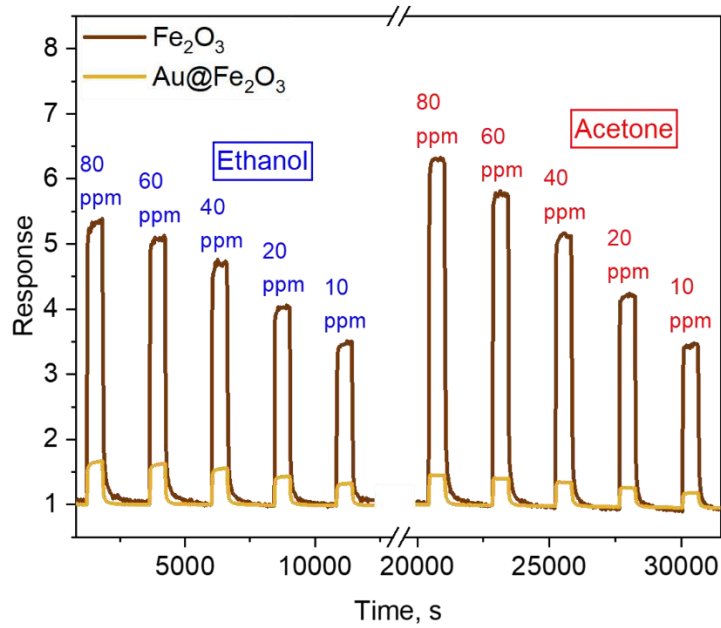


Figure 8. A typical response of the Fe_2O_3 pPy and $\text{Au@Fe}_2\text{O}_3$ pPy to 10 - 80 ppm of ethanol and acetone.

The response and recovery times of the Fe_2O_3 and $\text{Au@Fe}_2\text{O}_3$ sensors towards acetone and ethanol are presented in Table 2. The results demonstrated similar response times for both types of sensors in the case of acetone and a faster response time for the Fe_2O_3 sensors in the case of ethanol detection. On the other hand, faster recovery times are recorded for the $\text{Au@Fe}_2\text{O}_3$ sensors to both tested gases.

Table 2. Response and recovery times of the Fe_2O_3 pPy and $\text{Au@Fe}_2\text{O}_3$ pPy to 80 ppm of acetone and ethanol.

		Fe_2O_3	$\text{Au@Fe}_2\text{O}_3$
$t_{R, \text{min}}$	Acetone	1.0	1.0
	Ethanol	1.5	2.9
t_r, min	Acetone	7.9	4.8
	Ethanol	6.9	4.5

Further tests of the sensors were performed in the humid ambient with 20 % of relative humidity (RH). Both types of sensors demonstrated lower response to acetone and ethanol in the humid ambient in comparison with dry ambient. For instance, the response of the Fe_2O_3 sensors to 80 ppm of acetone and ethanol is decreased by 13 % in both cases, while the response of $\text{Au@Fe}_2\text{O}_3$ to the same gases and concentration is decreased in 9.5 % and 12.5 %, respectively. This decrease in response can be explained by the proportional drop of the baseline resistance to relative humidity, which is commonly present in metal oxides exposed to humidity due to the formation of hydroxyl groups at operating temperatures above 100 °C [51].

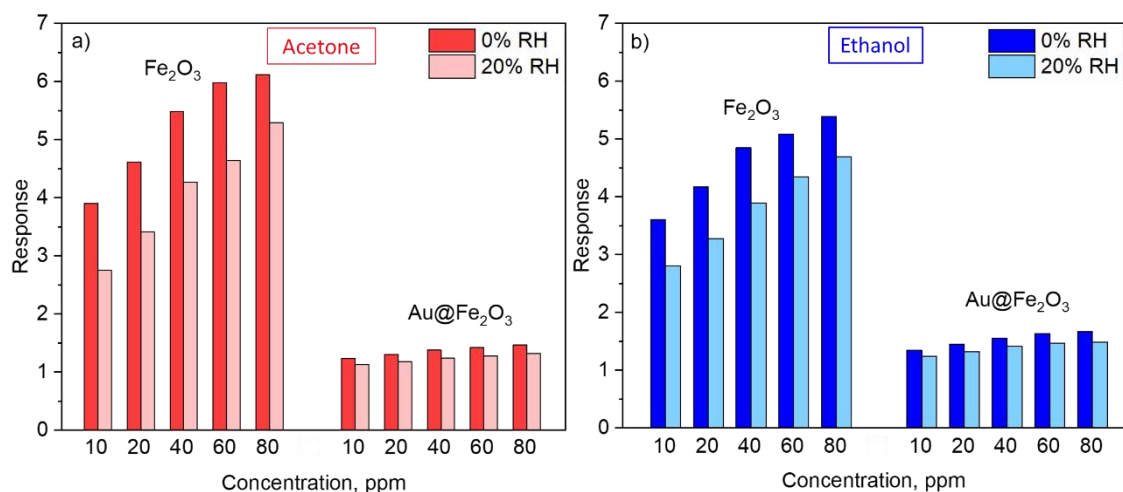


Figure 9. Typical Fe₂O₃ pPy and Au@Fe₂O₃ pPy response towards various concentration of **a)** acetone and **b)** ethanol at 0% RH and 20% RH.

Overall, results show higher response for the Fe₂O₃ pPy sensors compared to the Au@Fe₂O₃ pPy. For instance, the response to acetone and ethanol was 2.8 and 2.2 times higher for the Fe₂O₃ than for the Au@Fe₂O₃, respectively. However, these results are in part contradictory, as our previous observations revealed frequently enhanced gas sensing properties for the surface modified MOXs with respect to non-modified materials. This contradictory behavior is most likely connected with the high loads (9.5 at. %) of the modifier Au NPs found at the samples' surface, which exceeds in about 46 % the typical values employed in our previous systems (e.g. for Au@ZnO 5.1 at.% [43]). Similar observation can also be found in previous literature reports [18], in which it can be noticed that optimal catalyst particle loadings do not exceed 5 at% [52] [53]. The excessive amount of particles apparently lock the active sites on the surface of Fe₂O₃, responsible for the gas adsorption, and thus lower the sensing capability of the sensor. Actually, the SEM images in Figure 3 support this as they show a clear difference in the Fe₂O₃ pyramid surface before and after the gold particle deposition. Note that the Fe₂O₃ pyramids have a porous surface, while the Au@Fe₂O₃ pyramids lose the porosity and became smooth. This suggests a need for further tuning of the AACVD conditions used for modifying the Fe₂O₃ structures with gold.

A comparison of the Fe₂O₃ response with other similar systems in the literature to ethanol and acetone is presented in Table 3. Although the gas testing conditions vary in the listed references, it can be noticed that our Fe₂O₃ sensors show good responses that are in the same order of magnitude or higher considering the concentrations tested in each work. It is also observed that other types of structures have more complex morphology such as columnar structures, which provide improved response compared to the porous pyramid structures developed here for similar concentrations. These results, however, could be further improved by better tuning the loading of modifier particles or using another combination of modifiers such as those explored for WO₃ previously [54] [55]. Therefore, it is of great importance that the process of modification is performed in such a way that the loading of the metal nanoparticles and their distribution over the MOX surface is controlled. In that aspect, the AACVD method used in this paper is considered a convenient method for tuning the process of modification.

Table 3. Comparison of the responses for various α -Fe₂O₃-based sensors reported in the literature towards acetone and ethanol.

Material	Morphology	T, °C	Gas	c, ppm	R	Ref.
α -Fe ₂ O ₃	NPs	250	Acetone	100	9.5	[32]
α -Fe ₂ O ₃	CSs	150	Acetone	100	23.5	[32]
α -Fe ₂ O ₃	3D U-I	275	Acetone	100	10	[12]
α -Fe ₂ O ₃	3D U-I	260	Acetone	100	7	[12]
α -Fe ₂ O ₃	NPs	160	Acetone	1000	10	[36]
α -Fe ₂ O ₃	hMSps	350	Acetone	100	7	[56]
α -Fe ₂ O ₃	NSpds	300	Acetone	50	2.8	[57]
α -Fe ₂ O ₃	pPys	350	Acetone	80	6.1	This work
α -Fe ₂ O ₃	pNSps	260	Ethanol	50	6.7	[10]
α -Fe ₂ O ₃	NPs	160	Ethanol	1000	12	[36]
α -Fe ₂ O ₃	3D U-I	275	Ethanol	100	8	[12]
α -Fe ₂ O ₃	3D U-I	260	Ethanol	100	12	[12]
α -Fe ₂ O ₃	NSpds	300	Ethanol	50	2.2	[57]
α -Fe ₂ O ₃	pPys	350	Ethanol	80	5.4	This work

T – operating temperature, c – analyte concentration, ppm – parts per million, R – response, t_r – response time, t_r – recovery time, NPs – nanoparticles, CSs – columnar superstructures, N/A – not available, pNSps – porous nanospheres, U-I – urchin-like, hMSps – hollow microspheres, NSpds – nanospindles, pPys – porous pyramids.

Conclusion

Results demonstrate a new route for depositing selectively Fe₂O₃ with different morphologies via AACVD. In this work, four different morphologies of iron oxide were analyzed in the aspect of morphology, structure, and chemical composition using characterization techniques such as SEM, XRD, TEM, and XPS. Among these morphologies, porous pyramids showed the best sensing properties and therefore were subjected to further decoration with Au nanoparticles. Gas testing results towards acetone, ethanol, CO, toluene, H₂, and NO₂, showed higher response for the non-modified Fe₂O₃ sensors to all tested gases. The reason for low responses in the gold modified samples seems to be connected with the high amount of Au NPs (9.5 at%) incorporated over the surface of Fe₂O₃. The excess of gold particles apparently locks the pores at the Fe₂O₃ surface and reduces the adsorption sites along the Fe₂O₃ surface. These results indicated the need for further tuning of the contents of gold at the pyramidal structures.

References

- [1] A. Mirzaei, S. G. Leonardi, and G. Neri, "Detection of hazardous volatile organic compounds (VOCs) by metal oxide nanostructures-based gas sensors: A review," *Ceram. Int.*, vol. 42, no. 14, pp. 15119–15141, 2016, doi: 10.1016/j.ceramint.2016.06.145.
- [2] S. Feng *et al.*, "Review on Smart Gas Sensing Technology," *Sensors*, vol. 19, no. 17, 2019, doi: 10.3390/s19173760.
- [3] G. F. Fine, L. M. Cavanagh, A. Afonja, and R. Binions, "Metal Oxide Semiconductor Gas Sensors in Environmental Monitoring," *Sensors*, vol. 10, no. 6, pp. 5469–5502, 2010, doi: 10.3390/s100605469.
- [4] J. B. K. Law and J. T. L. Thong, "Improving the NH₃ gas sensitivity of ZnO nanowire sensors by reducing the carrier concentration," *Nanotechnology*, vol. 19, no. 20, p. 205502, May 2008, doi: 10.1088/0957-4484/19/20/205502.

- [5] A. A. Tomchenko, G. P. Harmer, and B. T. Marquis, "Detection of chemical warfare agents using nanostructured metal oxide sensors," *Sensors Actuators B Chem.*, vol. 108, no. 1, pp. 41–55, 2005, doi: <https://doi.org/10.1016/j.snb.2004.11.059>.
- [6] W. Göpel, "From electronic to bioelectronic olfaction, or: from artificial 'moses' to real noses," *Sensors Actuators B Chem.*, vol. 65, no. 1, pp. 70–72, 2000, doi: [https://doi.org/10.1016/S0925-4005\(99\)00308-1](https://doi.org/10.1016/S0925-4005(99)00308-1).
- [7] M. Tomić, M. Šetka, L. Vojkúvka, and S. Vallejos, "VOCs Sensing by Metal Oxides, Conductive Polymers, and Carbon-Based Materials," *Nanomaterials*, vol. 11, no. 2, p. 552, 2021, doi: 10.3390/nano11020552.
- [8] M. Mohapatra and S. Anand, "Synthesis and applications of nano-structured iron oxides/hydroxides – a review," *Int. J. Eng. Sci. Technol.*, vol. 2, no. 8, pp. 127–146, Feb. 2011, doi: 10.4314/ijest.v2i8.63846.
- [9] L. HOU *et al.*, "Ethanol Gas Sensor Based on γ -Fe₂O₃ Nanoparticles Working at Room Temperature with High Sensitivity," *Chinese J. Anal. Chem.*, vol. 46, no. 7, pp. e1854–e1862, Jul. 2018, doi: 10.1016/S1872-2040(18)61098-9.
- [10] H. Chen *et al.*, "Glycine-assisted hydrothermal synthesis of peculiar porous α -Fe₂O₃ nanospheres with excellent gas-sensing properties," *Anal. Chim. Acta*, vol. 659, no. 1–2, pp. 266–273, Feb. 2010, doi: 10.1016/J.ACA.2009.11.040.
- [11] S. Liang, J. Li, F. Wang, J. Qin, X. Lai, and X. Jiang, "Highly sensitive acetone gas sensor based on ultrafine α -Fe₂O₃ nanoparticles," *Sensors Actuators B Chem.*, vol. 238, pp. 923–927, Jan. 2017, doi: 10.1016/J.SNB.2016.06.144.
- [12] P. Sun, W. Wang, Y. Liu, Y. Sun, J. Ma, and G. Lu, "Hydrothermal synthesis of 3D urchin-like α -Fe₂O₃ nanostructure for gas sensor," *Sensors Actuators B Chem.*, vol. 173, pp. 52–57, 2012, doi: <https://doi.org/10.1016/j.snb.2012.05.057>.
- [13] M. Hjiri, M. S. Aida, and G. Neri, "NO₂ Selective Sensor Based on α -Fe₂O₃ Nanoparticles Synthesized via Hydrothermal Technique," *Sensors (Basel)*, vol. 19, no. 1, Jan. 2019, doi: 10.3390/S19010167.
- [14] S. T. Navale *et al.*, "Synthesis of Fe₂O₃ nanoparticles for nitrogen dioxide gas sensing applications," *Ceram. Int.*, vol. 39, no. 6, pp. 6453–6460, Aug. 2013, doi: 10.1016/J.CERAMINT.2013.01.074.
- [15] V. Balouria *et al.*, "Nano-crystalline Fe₂O₃ thin films for ppm level detection of H₂S," *Sensors Actuators B Chem.*, vol. 181, pp. 471–478, 2013, doi: <https://doi.org/10.1016/j.snb.2013.02.013>.
- [16] B. Sun, J. Horvat, H. S. Kim, W.-S. Kim, J. Ahn, and G. Wang, "Synthesis of Mesoporous α -Fe₂O₃ Nanostructures for Highly Sensitive Gas Sensors and High Capacity Anode Materials in Lithium Ion Batteries," *J. Phys. Chem. C*, vol. 114, no. 44, pp. 18753–18761, Nov. 2010, doi: 10.1021/JP102286E.
- [17] Z. L. Wang, "Splendid One-Dimensional Nanostructures of Zinc Oxide: A New Nanomaterial Family for Nanotechnology," *ACS Nano*, vol. 2, no. 10, pp. 1987–1992, Oct. 2008, doi: 10.1021/nn800631r.
- [18] D. R. Miller, S. A. Akbar, and P. A. Morris, "Nanoscale metal oxide-based heterojunctions for gas sensing: A review," *Sensors and Actuators, B: Chemical*, vol. 204, pp. 250–272, 2014, doi: 10.1016/j.snb.2014.07.074.

- [19] S. Vallejos, I. Gràcia, E. Figueras, and C. Cané, "Nanoscale Heterostructures Based on $\text{Fe}_2\text{O}_3@ \text{WO}_{3-x}$ Nanoneedles and Their Direct Integration into Flexible Transducing Platforms for Toluene Sensing," *ACS Appl. Mater. Interfaces*, vol. 7, no. 33, pp. 18638–18649, Aug. 2015, doi: 10.1021/acsami.5b05081.
- [20] Y.-L. Chueh, M.-W. Lai, J.-Q. Liang, L.-J. Chou, and Z. L. Wang, "Systematic Study of the Growth of Aligned Arrays of $\alpha\text{-Fe}_2\text{O}_3$ and Fe_3O_4 Nanowires by a Vapor–Solid Process," *Adv. Funct. Mater.*, vol. 16, no. 17, pp. 2243–2251, Nov. 2006, doi: 10.1002/ADFM.200600499.
- [21] R. Wang, Y. Chen, Y. Fu, H. Zhang, and Christian Kisielowski, "Bicrystalline Hematite Nanowires," *J. Phys. Chem. B*, vol. 109, no. 25, pp. 12245–12249, Jun. 2005, doi: 10.1021/JP051197Q.
- [22] Y. Zhu, J. C. Zhang, J. Zhai, and L. Jiang, "Preparation of superhydrophilic $\alpha\text{-Fe}_2\text{O}_3$ nanofibers with tunable magnetic properties," *Thin Solid Films*, vol. 510, no. 1–2, pp. 271–274, Jul. 2006, doi: 10.1016/J.TSF.2005.09.004.
- [23] T. Ren, P. He, W. Niu, Y. Wu, L. Ai, and X. Gou, "Synthesis of $\alpha\text{-Fe}_2\text{O}_3$ nanofibers for applications in removal and recovery of Cr(VI) from wastewater," *Environ. Sci. Pollut. Res. 2012 201*, vol. 20, no. 1, pp. 155–162, Mar. 2012, doi: 10.1007/S11356-012-0842-Z.
- [24] K. Woo, H. J. Lee, J.-P. Ahn, and Y. S. Park, "Sol–Gel Mediated Synthesis of Fe_2O_3 Nanorods," *Adv. Mater.*, vol. 15, no. 20, pp. 1761–1764, Oct. 2003, doi: 10.1002/ADMA.200305561.
- [25] Y.-M. Lin, P. R. Abel, A. Heller, and C. B. Mullins, " $\alpha\text{-Fe}_2\text{O}_3$ Nanorods as Anode Material for Lithium Ion Batteries," *J. Phys. Chem. Lett.*, vol. 2, no. 22, pp. 2885–2891, Nov. 2011, doi: 10.1021/JZ201363J.
- [26] S. Zeng *et al.*, "Hematite Hollow Spindles and Microspheres: Selective Synthesis, Growth Mechanisms, and Application in Lithium Ion Battery and Water Treatment," *J. Phys. Chem. C*, vol. 111, no. 28, pp. 10217–10225, Jul. 2007, doi: 10.1021/jp0719661.
- [27] J. S. Chen, T. Zhu, X. H. Yang, H. G. Yang, and X. W. Lou, "Top-Down Fabrication of $\alpha\text{-Fe}_2\text{O}_3$ Single-Crystal Nanodiscs and Microparticles with Tunable Porosity for Largely Improved Lithium Storage Properties," *J. Am. Chem. Soc.*, vol. 132, no. 38, pp. 13162–13164, Sep. 2010, doi: 10.1021/ja1060438.
- [28] H. Wang *et al.*, "Synthesis and Characterization of Single Crystal $\alpha\text{-Fe}_2\text{O}_3$ Nanobelts," *Chem. Lett.*, vol. 34, no. 2, pp. 184–185, Feb. 2005, doi: 10.1246/cl.2005.184.
- [29] X. Wen, S. Wang, Y. Ding, Z. L. Wang, and S. Yang, "Controlled Growth of Large-Area, Uniform, Vertically Aligned Arrays of $\alpha\text{-Fe}_2\text{O}_3$ Nanobelts and Nanowires," *J. Phys. Chem. B*, vol. 109, no. 1, pp. 215–220, Jan. 2005, doi: 10.1021/jp0461448.
- [30] J. Chen, L. Xu, W. Li, and X. Gou, " $\alpha\text{-Fe}_2\text{O}_3$ Nanotubes in Gas Sensor and Lithium-Ion Battery Applications," *Adv. Mater.*, vol. 17, no. 5, pp. 582–586, Mar. 2005, doi: 10.1002/ADMA.200401101.
- [31] S. K. Mohapatra, S. E. John, S. Banerjee, and M. Misra, "Water Photooxidation by Smooth and Ultrathin $\alpha\text{-Fe}_2\text{O}_3$ Nanotube Arrays," *Chem. Mater.*, vol. 21, no. 14, pp. 3048–3055, Jul. 2009, doi: 10.1021/cm8030208.
- [32] J. Li, L. Wang, L. Zhuo, Y. Wang, and W. Shengli, "Au-modified $\alpha\text{-Fe}_2\text{O}_3$ columnar superstructures assembled with nanoplates and their highly improved acetone sensing properties," *J. Alloys Compd.*, vol. 728, pp. 944–951, 2017.

- [33] S. Zhang *et al.*, "An acetone gas sensor based on nanosized Pt-loaded Fe₂O₃ nanocubes," *Sensors Actuators B Chem.*, vol. 290, pp. 59–67, 2019, doi: <https://doi.org/10.1016/j.snb.2019.03.082>.
- [34] X. Liu, J. Zhang, X. Guo, S. Wu, and S. Wang, "Porous α -Fe₂O₃ decorated by Au nanoparticles and their enhanced sensor performance," *Nanotechnology*, vol. 21, no. 9, p. 095501, Jan. 2010, doi: 10.1088/0957-4484/21/9/095501.
- [35] G. Picasso, M. Sun-Kou, L. Lagos, and J. Rojas Barreto, "Preparation and application of sensors based on α -Fe₂O₃ nanoparticles for detection of propane," *Rev. ION*, vol. 25, pp. 35–41, Sep. 2012.
- [36] Y. Wang, F. Kong, B. Zhu, S. Wang, S. Wu, and W. Huang, "Synthesis and characterization of Pd-doped α -Fe₂O₃ H₂S sensor with low power consumption," *Mater. Sci. Eng. B*, vol. 140, no. 1, pp. 98–102, 2007, doi: <https://doi.org/10.1016/j.mseb.2007.04.004>.
- [37] B. Tao, Q. Zhang, Z. Liu, and B. Geng, "Cooperative effect of pH value and anions on single-crystalline hexagonal and circular α -Fe₂O₃ nanorings," *Mater. Chem. Phys.*, vol. 136, no. 2, pp. 604–612, 2012, doi: <https://doi.org/10.1016/j.matchemphys.2012.07.033>.
- [38] S. Mao, G. Lu, and J. Chen, "Nanocarbon-based gas sensors: Progress and challenges," *J. Mater. Chem. A*, vol. 2, no. 16, pp. 5573–5579, Apr. 2014, doi: 10.1039/c3ta13823b.
- [39] E. Darezereshki, F. Bakhtiari, M. Alizadeh, A. Behrad vakylabad, and M. Ranjbar, "Direct thermal decomposition synthesis and characterization of hematite (α -Fe₂O₃) nanoparticles," *Mater. Sci. Semicond. Process.*, vol. 15, no. 1, pp. 91–97, 2012, doi: <https://doi.org/10.1016/j.mssp.2011.09.009>.
- [40] K. He, C.-Y. Xu, L. Zhen, and W.-Z. Shao, "Fractal growth of single-crystal α -Fe₂O₃: From dendritic micro-pines to hexagonal micro-snowflakes," *Mater. Lett.*, vol. 62, no. 4, pp. 739–742, 2008, doi: <https://doi.org/10.1016/j.matlet.2007.06.082>.
- [41] Z. Zhang, M. F. Hossain, and T. Takahashi, "Fabrication of shape-controlled α -Fe₂O₃ nanostructures by sonoelectrochemical anodization for visible light photocatalytic application," *Mater. Lett.*, vol. 64, no. 3, pp. 435–438, 2010, doi: <https://doi.org/10.1016/j.matlet.2009.10.071>.
- [42] M. Claros, M. Setka, Y. P. Jimenez, and S. Vallejos, "AACVD Synthesis and Characterization of Iron and Copper Oxides Modified ZnO Structured Films," *Nanomaterials*, vol. 10, no. 3, pp. 471–487, 2020, doi: 10.3390/nano10030471.
- [43] M. Tomić, M. Claros, I. Gràcia, E. Figueras, C. Cané, and S. Vallejos, "ZnO Structures with Surface Nanoscale Interfaces Formed by Au, Fe₂O₃, or Cu₂O Modifier Nanoparticles: Characterization and Gas Sensing Properties," *Sensors*, vol. 21, no. 13, p. 4509, Jun. 2021, doi: 10.3390/s21134509.
- [44] S. Vallejos, N. Pizúrová, J. Čechal, I. Gràcia, and C. Cané, "Aerosol-assisted Chemical Vapor Deposition of Metal Oxide Structures: Zinc Oxide Rods," *JoVE*, vol. 127, p. e56127, 2017, doi: 10.3791/56127.
- [45] S. Vallejos, I. Gràcia, O. Chmela, E. Figueras, J. Hubálek, and C. Cané, "Chemoresistive micromachined gas sensors based on functionalized metal oxide nanowires: Performance and reliability," *Sensors Actuators B Chem.*, vol. 235, pp. 525–534, Nov. 2016, doi: 10.1016/J.SNB.2016.05.102.

- [46] M. Tomić, I. Gràcia, E. Figueras, C. Cané, and S. Vallejos, "Unpublished work," 2021.
- [47] A. Lassoued, B. Dkhil, A. Gadri, and S. Ammar, "Control of the shape and size of iron oxide (α -Fe₂O₃) nanoparticles synthesized through the chemical precipitation method," *Results Phys.*, vol. 7, pp. 3007–3015, Jan. 2017, doi: 10.1016/J.RINP.2017.07.066.
- [48] S. Krishnamurthy, A. Esterle, N. C. Sharma, and S. V Sahi, "Yucca-derived synthesis of gold nanomaterial and their catalytic potential," *Nanoscale Res. Lett.* 2014 91, vol. 9, no. 1, pp. 1–9, Nov. 2014, doi: 10.1186/1556-276X-9-627.
- [49] J. Liu *et al.*, "Catalytic Application and Mechanism Studies of Argentite Chloride Coupled Ag/Au Hollow Heterostructures: Considering the Interface Between Ag/Au Bimetals," *Nanoscale Res. Lett.*, vol. 14, no. 1, p. 35, 2019, doi: 10.1186/s11671-019-2862-9.
- [50] J.-P. Sylvestre, S. Poulin, A. V Kabashin, E. Sacher, M. Meunier, and J. H. T. Luong, "Surface Chemistry of Gold Nanoparticles Produced by Laser Ablation in Aqueous Media," *J. Phys. Chem. B*, vol. 108, no. 43, pp. 16864–16869, Oct. 2004, doi: 10.1021/jp047134+.
- [51] M. Tomić *et al.*, "Cerium Oxide-Tungsten Oxide Core-Shell Nanowire-Based Microsensors Sensitive to Acetone," *Biosensors*, vol. 8, no. 4, p. 116, 2018, doi: 10.3390/bios8040116.
- [52] X. Han, Y. Sun, Z. Feng, G. Zhang, Z. Chen, and J. Zhan, "Au-deposited porous single-crystalline ZnO nanoplates for gas sensing detection of total volatile organic compounds," *RSC Adv.*, vol. 6, no. 44, pp. 37750–37756, Apr. 2016, doi: 10.1039/C6RA05941D.
- [53] F. Di Maggio, M. Ling, A. Tsang, J. Covington, J. Saffell, and C. Blackman, "Aerosol-assisted CVD synthesis, characterisation and gas-sensing application of gold-functionalised tungsten oxide," *J. Sensors Sens. Syst.*, vol. 3, no. 2, pp. 325–330, 2014, doi: 10.5194/jsss-3-325-2014.
- [54] M. Tomić, Z. Fohlerova, I. Gràcia, E. Figueras, C. Cané, and S. Vallejos, "UV-light activated APTES modified WO_{3-x} nanowires sensitive to ethanol and nitrogen dioxide," *Sensors Actuators, B Chem.*, vol. 328, p. 129046, 2021, doi: 10.1016/j.snb.2020.129046.
- [55] S. Vallejos *et al.*, "Single-step deposition of Au- and Pt-nanoparticle-functionalized tungsten oxide nanoneedles synthesized via aerosol-assisted CVD, and used for fabrication of selective gas microsensor arrays," *Adv. Funct. Mater.*, vol. 23, no. 10, pp. 1313–1322, 2013, doi: 10.1002/adfm.201201871.
- [56] S. Wang *et al.*, "Porous α -Fe₂O₃ hollow microspheres and their application for acetone sensor," *J. Solid State Chem.*, vol. 183, no. 12, pp. 2869–2876, 2010, doi: <https://doi.org/10.1016/j.jssc.2010.09.033>.
- [57] J. Zhang *et al.*, "Au-Functionalized Hematite Hybrid Nanospindles: General Synthesis, Gas Sensing and Catalytic Properties," *J. Phys. Chem. C*, vol. 115, no. 13, pp. 5352–5357, Apr. 2011, doi: 10.1021/jp110421v.

Chapter 4

Conclusions and future work

The main goal of this thesis was to develop and examine the properties of sensors based on surface modified structured MOX materials with formed nanoscale interfaces between the 'host' MOX and the 'guest' material (i.e., another MOX, metal NPs, or organo-functional molecules). In that line, during this thesis, seven types of modified structured MOX based gas sensors and their corresponding non-modified versions were developed and evaluated towards several gases. A summary of the synthesis conditions of these structures and their main properties is given in **Table 4.1**, while a comparison of the best sensors' performances and their operating conditions are summarized in **Table 4.2**.

From **Table 4.1**, the following conclusions are remarked:

- Three types of structured 'host' MOX materials (WO_3 , ZnO, and Fe_2O_3) were deposited by AACVD without using catalyst seeds. Whilst the tuning of the conditions for WO_3 deposition resulted in the growth of 1D structures in the form of wires, many different AACVD conditions (including different precursors, solvents, and concentrations, amongst others) applied for ZnO and Fe_2O_3 synthesis proved to be unsuccessful in the attempt to deposit this type of structure. Instead, ZnO was deposited in the form of rods, whereas Fe_2O_3 was deposited in the form of pyramids or sheets. Hence, the aspect ratio (i.e. length to diameter or length to width ratio) of these structures was higher for the WO_3 wires (100) than for the ZnO rods (7.5) and Fe_2O_3 pyramids (1.5). These structured morphologies and their synthesis routes, particularly for Fe_2O_3 , are novel in the state of the art of AACVD.
- The incorporation of 'guest' materials was achieved in a second step, mainly by AACVD. The morphology of the AACVD incorporated particles (Au, CeO_2 , Fe_2O_3 , and Cu_2O) was characterized by agglomerated particles in the case of CeO_2 and Fe_2O_3 , whereas the modification with Au (using AACVD or impregnation) and Cu_2O lead to highly dispersed nanoparticles over the 'host' structures. The synthesis routes for incorporating these modifier particles on the structured 'host' MOXs represent an advance to the state of the art of AACVD.
- The synthesis routes of these materials used commercial precursors such as $\text{W}(\text{CO})_6$, a metal-organic precursor, that was found appropriate for AACVD growth of structured WO_3 . Chloride-based salts such as ZnCl_2 and $\text{FeCl}_3 \cdot 6\text{H}_2\text{O}$ were more suitable for the structuration of ZnO and Fe_2O_3 . For the particles deposition, nitric-based salt ($\text{Cu}(\text{NO}_3)_2 \cdot 6\text{H}_2\text{O}$) and chloride-based salt ($\text{HAuCl}_4 \cdot 3\text{H}_2\text{O}$) gave the desired particle morphology to Cu_2O and Au, while for CeO_2 better results were obtained by using acetylacetonate (acac) based precursor, $\text{Ce}(\text{acac})_3 \cdot x\text{H}_2\text{O}$. Incorporation of Au particles via impregnation method was successfully achieved using Au colloids formed by reduction of the same chloride-based salt ($\text{HAuCl}_4 \cdot 3\text{H}_2\text{O}$) as the one used for AACVD.

- The deposition temperatures for the AACVD synthesis were in the range of 370 – 500 °C. For the growth of WO₃ wires, the best results were obtained at the deposition temperature of 390 °C, for the ZnO rods at 400 °C, while for the Fe₂O₃ pyramids the deposition temperature was 370 °C. The optimal deposition temperatures for the 'guest' materials were 430 °C for Fe₂O₃ particles, 500 °C for CeO₂, and 450 °C for Cu₂O, whereas for Au particles the deposition temperature was 370 °C. APTES deposition was performed via a CVD silanization process at a lower temperature (120 °C) and lower pressure (5 torr) than AACVD method. Overall, the deposition conditions for all materials synthesized proved compatible with the Si-based platforms, allowing for the direct integration of the structures into both, bulk and micromachined Si-based platforms.

The gas sensing results summarized in **Table 4.2** lead to the following findings:

- Overall, the results demonstrated that the surface modified samples exhibited enhanced gas sensing properties compared to pristine sensors, except in the case of Au@Fe₂O₃, which is explained by the excessive Au loading (9.5 at.%), that locks the active sites on the surface of Fe₂O₃ and lowers the sensing capability of the sensor. The lower amount of Au particles (5.1 at.%), used for decoration of the ZnO sensor, was found to be more appropriate as it enhanced the gas sensitivity of ZnO. Similarly, the loadings of decorating MOXs that provided good sensor performances were 11.5 at.% of Ce in CeO₂@WO₃ sensor and 7.5 at.% of Fe in Fe₂O₃@ZnO sensor. Cu₂O@ZnO sensor with only 1.1 at.% of Cu did not show a significant response to the tested gases and additionally acted opposite to Fe₂O₃ by reducing the response to oxidizing gases as NO₂, instead of increasing it. This opposite behavior was connected with the p-type behavior of Cu₂O.
- The operating temperatures of the sensors were between 300 and 350 °C for thermoactivated sensors and RT for photoactivated sensors, which reported the best results for UV-light irradiance of 1800 mW·cm⁻². The highest response of the thermoactivated WO₃ and ZnO based sensors were recorded at the temperature of 300 and 310 °C, respectively, while for the Fe₂O₃ based sensors the optimal temperature was higher, 350 °C. Additionally, it was demonstrated that photoactivation can successfully replace thermoactivation principle and this is especially noticeable for APTES@WO₃ and APTES@CeO₂@WO₃, which exhibited high sensitivity to ethanol and NO₂ at RT. ZnO based sensors (non-modified ZnO and Au@ZnO) also demonstrated the possibility to detect gases such as ethanol and acetone at RT, with UV light activation. However, the concentration changes were not detected appropriately and its performance is still not as good as the thermoactivated ZnO based sensors or photoactivated APTES@WO₃ based sensors.
- The sensors demonstrated the best results in sensing acetone, ethanol, and NO₂. The highest sensitivity to acetone was recorded for the photoactivated APTES@CeO₂@WO₃ sensors (6.6 % ppm⁻¹), whereas the highest sensitivity to ethanol was recorded for the photoactivated APTES@WO₃ sensors (19.2 % ppm⁻¹), both operating at RT. Photoactivated APTES@CeO₂@WO₃ sensors also exhibited remarkable sensitivity (27.3 % ppm⁻¹) to NO₂. However, the sensitivity of Au@ZnO sensors, thermoactivated at 310 °C, showed higher sensitivity to NO₂ (39.96 % ppm⁻¹), even for lower NO₂ concentration range (1-10 ppm) than those measured with the APTES modified sensors (20-80 ppm), which makes this type of sensor superior to the

others studied here for NO₂ detection. Overall, the sensors demonstrated responses with higher or the same order of magnitude than other MOX sensors in the literature. More details of this comparative analysis can be found in the published articles in sections 3.2, 3.3, and 3.4 of this thesis. The improvement of sensitivity in MOXs at room temperature by silanizing their surface and using photoactivation represent an advance in the state of the art of MOX-based gas sensors that opens a new possibility for circumventing the use of microheaters and potentially reduce the power consumption of the sensor.

- Overall, the response of the sensors was stable and reversible, and the tests demonstrated that the sensors can operate at least four weeks accumulating a minimum of 120 h of operation without significant deviations. Stability tests for longer periods were not evaluated. The response times of the sensors were in the range of 1.5 to 10 minutes, while the recovery times were in the range of 1 to 40 minutes. Generally, thermoactivated sensors detected gases faster and needed less time to recover. The shortest response and recovery times were revealed for thermoactivated Fe₂O₃ based sensors. In contrast, photoactivated sensors showed longer times, especially during the recovery step, which needed approximately 30 minutes on average.

As a continuation of this research, the future work may explore:

- The use of different organic molecules for the surface modification of MOXs that can be activated with or without light excitation and be sensitive to gases at room temperature.
- The integration of other transducing principles (i.e. optical), besides the resistive, in a single sensor device to obtain simultaneous physical changes from the same gas-sensitive material.
- Following the use of other transducing principles, such as optical, another area of interest includes the research on modified gas-sensitive MOXs that show optical changes due to gas adsorption. These gas-sensitive materials could involve, apart from typical modifier elements with plasmonic properties (e.g., Au, Ag), other modifier elements, for instance, rare earth metals (i.e. Er and Eu) that have shown to modulate the optical properties of MOXs when used as dopants. Other studies may also include the formation of heterojunctions with n- and/or p-type MOXs that are photoactive and produce optical changes due to gas adsorption.
- The literature shows that there is still plenty of room for developing further the gas sensors' sensitivity and ability to detect specific gases in sub-ppm concentrations, especially VOCs from the group of aromatic hydrocarbons, carbonyl compounds, and aliphatic hydrocarbons.

Table 4.1. Comparison of the synthesis conditions and material morphologies of the sensors fabricated in this thesis.

	Sensor	Loading	Deposition method	T _D , °C	Precursor	Morphology, nm	
JA2	WO ₃		AACVD	390	W(CO) ₆	WO ₃ : Ws, 100 [∅] , 10000 ^L , 100 ^{AR}	
	CeO ₂ @WO ₃	11.5 at.% Ce	WO ₃ CeO ₂	AACVD AACVD	390 500	W(CO) ₆ Ce(acac) ₃ ·xH ₂ O	CeO ₂ : Ps, <40 [∅]
JA3	WO ₃		AACVD	390	W(CO) ₆	WO ₃ : Ws, 100 [∅] , 10000 ^L , 100 ^{AR}	
	APTES@WO ₃	1000 μl	WO ₃ APTES	AACVD Silanization	390 120		W(CO) ₆ APTES
	APTES@CeO ₂ @WO ₃	11.5 at.% Ce	WO CeO ₂ APTES	AACVD AACVD Silanization	390 500 120	W(CO) ₆ Ce(acac) ₃ ·xH ₂ O APTES	CeO ₂ : Ps, <40 [∅] ,
JA4	ZnO		AACVD	400	ZnCl ₂	ZnO: Rds, 200 [∅] , 1500 ^L , 7.5 ^{AR}	
	Au@ZnO	5.1 at.% Au	ZnO Au	AACVD Impregnation	400 60	ZnCl ₂ Colloidal Au	Au: Ps, 5-40 [∅]
	Fe ₂ O ₃ @ZnO	7.5 at.% Fe	ZnO Fe ₂ O ₃	AACVD AACVD	400 430	ZnCl ₂ FeCl ₃ ·6H ₂ O	Fe ₂ O ₃ : Fls, 20 ^T , <100 [∅] , 5 ^{AR}
	Cu ₂ O@ZnO	1.1 at.% Cu	ZnO Cu ₂ O	AACVD AACVD	400 450	ZnCl ₂ Cu(NO ₃) ₂ ·6H ₂ O	Cu ₂ O: Ps, 5-25 [∅]
JA5	Fe ₂ O ₃		AACVD	370	FeCl ₃ ·6H ₂ O	Fe ₂ O ₃ : pPys, 250 ^{LE} , 370 ^{BE} , 1.5 ^{AR}	
	Au@Fe ₂ O ₃	9.5 at.% Au	Fe ₂ O ₃ Au	AACVD AACVD	370 370	FeCl ₃ ·6H ₂ O HAuCl ₄ ·3H ₂ O	Au: Ps, 10 [∅]
CP2	ZnO		AACVD	400	ZnCl ₂	ZnO: Rds, 200 [∅] , 1500 ^L , 7.5 ^{AR}	
	Au@ZnO	5.1 at.% Au	ZnO Au	AACVD Impregnation	400 60	ZnCl ₂ Colloidal Au	Au: Ps, 5-40 [∅]

JA – journal article, CP – conference paper, APTES – (3-aminopropyl)triethoxysilane, AACVD – aerosol assisted chemical vapor deposition, T_D – deposition temperature, W(CO)₆ – tungsten hexacarbonyl, Ce(acac)₃·xH₂O – cerium(III)acetylacetonate hydrate, Ws – wires, Ps- particles, Rds – rods, Fls- flakes, pPys – porous pyramids, ^{AR} – aspect ratio, [∅] – diameter, ^L – length, ^T – thickness, ^{LE} – lateral edge, ^{BE} – base edge.

Table 4.2. Comparison of the sensing performances and working conditions of the sensors fabricated in this thesis.

Sensor			JA2		JA3			JA4				JA5	
			WO ₃	CeO ₂ @WO ₃	WO ₃	APTES@WO ₃	APTES@CeO ₂ @WO ₃	ZnO	Au@ZnO	Fe ₂ O ₃ @ZnO	Cu ₂ O@ZnO	Fe ₂ O ₃	Au@Fe ₂ O ₃
T_{GS}, °C			300		RT			310				350	
c_R, ppm			20-80		20-80			20-80				20-80	
S, % ppm⁻¹	Acetone		0.8	4.7	0.4	1.1	6.6	0.03	0.68	0.26	0.22	2.7	0.3
	Ethanol		0.8	2.2	1.1	19.2	10.3	0.05	1.79	0.27	0.04	1.9	0.4
	NO ₂		-	-	0.4	7.6	27.3	0.73*	39.96*	7.48*	0.22*	5.4**	5.0**
t_R, min	Acetone	80 ppm	5.5	1.9	9	9.3	8.8	-	-	-	-	1.0	1.0
	Ethanol	80 ppm	7.4	2.5	9	5.4	9.3	8.3	2.9	7.5	8.2	1.5	2.9
	NO ₂	80, 5, or 1 ppm	-	-	10 [†]	7 [†]	8 [†]	5.2 ^{††}	4.3 ^{††}	4.3 ^{††}	5.6 ^{††}	1.5 ^{†††}	5.9 ^{†††}
t_r, min	Acetone	80 ppm	5.0	9.5	22	39	38	-	-	-	-	7.9	4.8
	Ethanol	80 ppm	6.1	17.8	23	35	40	20	10.7	18.3	23.3	6.9	4.5
	NO ₂	80, 5, or 1 ppm	-	-	35 [†]	27 [†]	20 [†]	22 ^{††}	5 ^{††}	8 ^{††}	15 ^{††}	1 ^{†††}	6.9 ^{†††}

JA – journal article, T_{GS} – working temperature of a gas sensor, c_R – concentration range, S – sensitivity, defined as $\Delta R/\Delta c$, ΔR - change in response, Δc - fixed change in analyte concentration, t_R – response time, t_r – recovery time, ppm – parts per million, RT – room temperature.

*Sensitivity is calculated for the concentration range of 1-10 ppm.

** Sensitivity is calculated for the concentration range of 1-5 ppm.

† Response time is measured for the NO₂ concentration of 80 ppm.

†† Response time is measured for the NO₂ concentration of 1 ppm.

††† Response time is measured for the NO₂ concentration of 5 ppm.

References

- [1] M. Hjiri, L. El Mir, S. G. Leonardi, A. Pistone, L. Mavilia, and G. Neri, "Al-doped ZnO for highly sensitive CO gas sensors," *Sensors Actuators B Chem.*, vol. 196, pp. 413–420, Jun. 2014, doi: 10.1016/J.SNB.2014.01.068.
- [2] T. Hübert, L. Boon-Brett, G. Black, and U. Banach, "Hydrogen sensors – A review," *Sensors Actuators B Chem.*, vol. 157, no. 2, pp. 329–352, Oct. 2011, doi: 10.1016/J.SNB.2011.04.070.
- [3] G. Korotcenkov, S. Do Han, and J. R. Stetter, "Review of Electrochemical Hydrogen Sensors," *Chem. Rev.*, vol. 109, no. 3, pp. 1402–1433, Mar. 2009, doi: 10.1021/CR800339K.
- [4] S. Mahajan and S. Jagtap, "Metal-oxide semiconductors for carbon monoxide (CO) gas sensing: A review," *Applied Materials Today*, vol. 18. Elsevier Ltd, p. 100483, Mar. 01, 2020, doi: 10.1016/j.apmt.2019.100483.
- [5] T. Li *et al.*, "Sub-ppm level NO₂ sensing properties of polyethyleneimine-mediated WO₃ nanoparticles synthesized by a one-pot hydrothermal method," *J. Alloys Compd.*, vol. 783, pp. 103–112, Apr. 2019, doi: 10.1016/J.JALLCOM.2018.12.287.
- [6] P. Peterson *et al.*, "Practical Use of Metal Oxide Semiconductor Gas Sensors for Measuring Nitrogen Dioxide and Ozone in Urban Environments," *Sensors*, vol. 17, no. 7, p. 1653, Jul. 2017, doi: 10.3390/s17071653.
- [7] D. Punetha, M. Kar, and S. K. Pandey, "A new type low-cost, flexible and wearable tertiary nanocomposite sensor for room temperature hydrogen gas sensing," *Sci. Rep.*, vol. 10, no. 1, pp. 1–11, Dec. 2020, doi: 10.1038/s41598-020-58965-w.
- [8] W.-C. Shen, P.-J. Shih, Y.-C. Tsai, C.-C. Hsu, and C.-L. Dai, "Low-Concentration Ammonia Gas Sensors Manufactured Using the CMOS–MEMS Technique," *Micromachines*, vol. 11, no. 1, p. 92, Jan. 2020, doi: 10.3390/mi11010092.
- [9] F. Peng *et al.*, "Ultrasensitive ppb-level H₂S gas sensor at room temperature based on WO₃/rGO hybrids," *J. Mater. Sci. Mater. Electron.*, vol. 31, no. 6, pp. 5008–5016, Mar. 2020, doi: 10.1007/s10854-020-03067-6.
- [10] R. Binions and A. J. T. Naik, "Metal oxide semiconductor gas sensors in environmental monitoring," in *Semiconductor Gas Sensors*, Elsevier Ltd, 2013, pp. 433–466.
- [11] E. Llobet, J. Brunet, A. Pauly, A. Ndiaye, and C. Varenne, "Nanomaterials for the selective detection of hydrogen sulfide in air," *Sensors (Switzerland)*, vol. 17, no. 2. 2017, doi: 10.3390/s17020391.
- [12] J. Sun *et al.*, "Volatile organic compounds emissions from traditional and clean domestic heating appliances in Guanzhong Plain, China: Emission factors, source profiles, and effects on regional air quality," *Environ. Int.*, vol. 133, p. 105252, Dec. 2019, doi: 10.1016/J.ENVINT.2019.105252.
- [13] M. Mohd Ali, N. Hashim, S. Abd Aziz, and O. Lasekan, "Principles and recent advances in electronic nose for quality inspection of agricultural and food products," *Trends Food Sci. Technol.*, vol. 99, pp. 1–10, May 2020, doi: 10.1016/J.TIFS.2020.02.028.

- [14] G. B. Hanna, P. R. Boshier, S. R. Markar, and A. Romano, "Accuracy and Methodologic Challenges of Volatile Organic Compound–Based Exhaled Breath Tests for Cancer Diagnosis: A Systematic Review and Meta-analysis," *JAMA Oncol.*, vol. 5, no. 1, pp. e182815–e182815, Jan. 2019, doi: 10.1001/JAMAONCOL.2018.2815.
- [15] P. J. Sabourin, W. E. Bechtold, and R. F. Henderson, "A high pressure liquid chromatographic method for the separation and quantitation of water-soluble radiolabeled benzene metabolites," *Anal. Biochem.*, vol. 170, no. 2, pp. 316–327, May 1988, doi: 10.1016/0003-2697(88)90637-9.
- [16] V. P, L. L, B. G, S. J, and R. D, "Analysis of aldehydes in beer using solid-phase microextraction with on-fiber derivatization and gas chromatography/mass spectrometry," *J. Agric. Food Chem.*, vol. 51, no. 24, pp. 6941–6944, Nov. 2003, doi: 10.1021/JF034410T.
- [17] H. Wang, Y. Qu, H. Chen, Z. Lin, and K. Dai, "Highly selective n-butanol gas sensor based on mesoporous SnO₂ prepared with hydrothermal treatment," *Sensors Actuators B Chem.*, vol. 201, pp. 153–159, Oct. 2014, doi: 10.1016/J.SNB.2014.04.049.
- [18] C. Gu, X. Xu, J. Huang, W. Wang, Y. Sun, and J. Liu, "Porous flower-like SnO₂ nanostructures as sensitive gas sensors for volatile organic compounds detection," *Sensors Actuators B Chem.*, vol. 174, pp. 31–38, Nov. 2012, doi: 10.1016/J.SNB.2012.08.039.
- [19] D. R. Miller, S. A. Akbar, and P. A. Morris, "Nanoscale metal oxide-based heterojunctions for gas sensing: A review," *Sensors and Actuators, B: Chemical*, vol. 204, pp. 250–272, 2014, doi: 10.1016/j.snb.2014.07.074.
- [20] W. Liu *et al.*, "APTES-functionalized thin-walled porous WO₃ nanotubes for highly selective sensing of NO₂ in a polluted environment," *J. Mater. Chem. A*, vol. 6, no. 23, pp. 10976–10989, Jun. 2018, doi: 10.1039/C8TA02452A.
- [21] N. D. Cuong *et al.*, "Facile synthesis of α -Fe₂O₃ nanoparticles for high-performance CO gas sensor," *Mater. Res. Bull.*, vol. 68, pp. 302–307, Aug. 2015, doi: 10.1016/J.MATERRESBULL.2015.03.069.
- [22] R. Malik, V. K. Tomer, Y. K. Mishra, and L. Lin, "Functional gas sensing nanomaterials: A panoramic view," *Applied Physics Reviews*, vol. 7, no. 2, American Institute of Physics Inc., p. 021301, Jun. 01, 2020, doi: 10.1063/1.5123479.
- [23] N. Kamarulzaman, M. F. Kasim, and N. F. Chayed, "Elucidation of the highest valence band and lowest conduction band shifts using XPS for ZnO and Zn_{0.99}Cu_{0.01}O band gap changes," *Results Phys.*, vol. 6, pp. 217–230, Jan. 2016, doi: 10.1016/j.rinp.2016.04.001.
- [24] Y. Kang, F. Yu, L. Zhang, W. Wang, L. Chen, and Y. Li, "Review of ZnO-based nanomaterials in gas sensors," *Solid State Ionics*, vol. 360, p. 115544, Feb. 2021, doi: 10.1016/j.ssi.2020.115544.
- [25] H. Song, H. Yang, and X. Ma, "A comparative study of porous ZnO nanostructures synthesized from different zinc salts as gas sensor materials," *J. Alloys Compd.*, vol. 578, pp. 272–278, Nov. 2013, doi: 10.1016/J.JALLCOM.2013.05.211.
- [26] F. Meng *et al.*, "Flower-like hierarchical structures consisting of porous single-crystalline ZnO nanosheets and their gas sensing properties to volatile organic compounds (VOCs)," *J. Alloys Compd.*, vol. 626, pp. 124–130, Mar. 2015, doi:

- 10.1016/J.JALLCOM.2014.11.175.
- [27] S. L. Zhang, J. O. Lim, J. S. Huh, J. S. Noh, and W. Lee, "Two-step fabrication of ZnO nanosheets for high-performance VOCs gas sensor," *Curr. Appl. Phys.*, vol. 13, no. 4 SUPPL.2, pp. S156–S161, Jul. 2013, doi: 10.1016/J.CAP.2012.12.021.
- [28] S. Zhang, H. Byun, J. Lim, J. Huh, and W. Lee, "Controlled synthesis of ZnO nanostructures for sub-ppm-level VOC detection," *IEEE Sens. J.*, vol. 12, no. 11, pp. 3149–3155, 2012, doi: 10.1109/JSEN.2012.2208950.
- [29] P. R. Godse, A. T. Mane, Y. H. Navale, S. T. Navale, R. N. Mulik, and V. B. Patil, "Hydrothermally grown 1D ZnO nanostructures for rapid detection of NO₂ gas," *SN Appl. Sci.* 2021 33, vol. 3, no. 3, pp. 1–18, Feb. 2021, doi: 10.1007/S42452-021-04357-2.
- [30] S. Ren, G. Fan, S. Qu, and Q. Wang, "Enhanced H₂ sensitivity at room temperature of ZnO nanowires functionalized by Pd nanoparticles," *J. Appl. Phys.*, vol. 110, no. 8, p. 084312, Oct. 2011, doi: 10.1063/1.3647310.
- [31] Vijayakumar, B. W. Shivaraj, C. Manjunatha, B. Abhishek, G. Nagaraju, and P. K. Panda, "Hydrothermal synthesis of ZnO nanotubes for CO gas sensing," *Sensors Int.*, vol. 1, p. 100018, Jan. 2020, doi: 10.1016/J.SINTL.2020.100018.
- [32] D. B. Migas, V. L. Shaposhnikov, V. N. Rodin, and V. E. Borisenko, "Tungsten oxides. I. Effects of oxygen vacancies and doping on electronic and optical properties of different phases of WO₃," *J. Appl. Phys.*, vol. 108, no. 9, p. 093713, Nov. 2010, doi: 10.1063/1.3505688.
- [33] S. Vallejos, I. Gràcia, J. Bravo, E. Figueras, J. Hubálek, and C. Cané, "Detection of volatile organic compounds using flexible gas sensing devices based on tungsten oxide nanostructures functionalized with Au and Pt nanoparticles," *Talanta*, vol. 139, pp. 27–34, Jul. 2015, doi: 10.1016/J.TALANTA.2015.02.034.
- [34] S. Vallejos, I. Gràcia, E. Figueras, and C. Cané, "Nanoscale Heterostructures Based on Fe₂O₃@WO_{3-x} Nanoneedles and Their Direct Integration into Flexible Transducing Platforms for Toluene Sensing," *ACS Appl. Mater. Interfaces*, vol. 7, no. 33, pp. 18638–18649, Aug. 2015, doi: 10.1021/acsami.5b05081.
- [35] Z. Hua, M. Yuasa, T. Kida, N. Yamazoe, and K. Shimano, "H₂ Sensing Mechanism of Pd-Loaded WO₃ Nanoparticle Gas Sensors," *Chem. Lett.*, vol. 43, no. 9, pp. 1435–1437, May 2014, doi: 10.1246/CL.140396.
- [36] M. Hübner, C. E. Simion, A. Haensch, N. Barsan, and U. Weimar, "CO sensing mechanism with WO₃ based gas sensors," *Sensors Actuators B Chem.*, vol. 151, no. 1, pp. 103–106, Nov. 2010, doi: 10.1016/J.SNB.2010.09.040.
- [37] J. Zhao, M. Hu, Y. Liang, Q. Li, X. Zhang, and Z. Wang, "A room temperature sub-ppm NO₂ gas sensor based on WO₃ hollow spheres," *New J. Chem.*, vol. 44, no. 13, pp. 5064–5070, Mar. 2020, doi: 10.1039/C9NJ06384F.
- [38] S. Vallejos *et al.*, "Au nanoparticle-functionalised WO₃ nanoneedles and their application in high sensitivity gas sensor devices," *Chem. Commun.*, vol. 47, no. 1, pp. 565–567, 2011, doi: 10.1039/c0cc02398a.
- [39] A. Mirzaei, B. Hashemi, and K. Janghorban, "α-Fe₂O₃ based nanomaterials as gas sensors," *J. Mater. Sci. Mater. Electron.* 2015 274, vol. 27, no. 4, pp. 3109–3144, Dec. 2015, doi: 10.1007/S10854-015-4200-Z.

- [40] L. Huo, Q. Li, H. Zhao, L. Yu, S. Gao, and J. Zhao, "Sol-gel route to pseudocubic shaped α -Fe₂O₃ alcohol sensor: preparation and characterization," *Sensors Actuators B Chem.*, vol. 107, no. 2, pp. 915–920, Jun. 2005, doi: 10.1016/J.SNB.2004.12.046.
- [41] L. HOU *et al.*, "Ethanol Gas Sensor Based on γ -Fe₂O₃ Nanoparticles Working at Room Temperature with High Sensitivity," *Chinese J. Anal. Chem.*, vol. 46, no. 7, pp. e1854–e1862, Jul. 2018, doi: 10.1016/S1872-2040(18)61098-9.
- [42] J. Chen, L. Xu, W. Li, and X. Gou, " α -Fe₂O₃ Nanotubes in Gas Sensor and Lithium-Ion Battery Applications," *Adv. Mater.*, vol. 17, no. 5, pp. 582–586, Mar. 2005, doi: 10.1002/ADMA.200401101.
- [43] H. Pan, L. Jin, B. Zhang, H. Su, H. Zhang, and W. Yang, "Self-assembly biomimetic fern leaf-like α -Fe₂O₃ for sensing inflammable 1-butanol gas," *Sensors Actuators B Chem.*, vol. 243, pp. 29–35, May 2017, doi: 10.1016/J.SNB.2016.11.080.
- [44] S. Liang, J. Li, F. Wang, J. Qin, X. Lai, and X. Jiang, "Highly sensitive acetone gas sensor based on ultrafine α -Fe₂O₃ nanoparticles," *Sensors Actuators B Chem.*, vol. 238, pp. 923–927, Jan. 2017, doi: 10.1016/J.SNB.2016.06.144.
- [45] R. C. Biswal, "Pure and Pt-loaded gamma iron oxide as sensor for detection of sub ppm level of acetone," *Sensors Actuators B Chem.*, vol. 157, no. 1, pp. 183–188, Sep. 2011, doi: 10.1016/J.SNB.2011.03.047.
- [46] N. Van Hoang *et al.*, "Enhanced H₂S gas-sensing performance of α -Fe₂O₃ nanofibers by optimizing process conditions and loading with reduced graphene oxide," *J. Alloys Compd.*, vol. 826, p. 154169, Jun. 2020, doi: 10.1016/J.JALLCOM.2020.154169.
- [47] Z. Wu *et al.*, "Ultrafast Response/Recovery and High Selectivity of the H₂S Gas Sensor Based on α -Fe₂O₃ Nano-Ellipsoids from One-Step Hydrothermal Synthesis," *ACS Appl. Mater. Interfaces*, vol. 11, no. 13, pp. 12761–12769, Apr. 2019, doi: 10.1021/ACSAMI.8B22517.
- [48] M. Hjiri, M. S. Aida, and G. Neri, "NO₂ Selective Sensor Based on α -Fe₂O₃ Nanoparticles Synthesized via Hydrothermal Technique," *Sensors (Basel)*, vol. 19, no. 1, Jan. 2019, doi: 10.3390/S19010167.
- [49] S. T. Navale *et al.*, "Synthesis of Fe₂O₃ nanoparticles for nitrogen dioxide gas sensing applications," *Ceram. Int.*, vol. 39, no. 6, pp. 6453–6460, Aug. 2013, doi: 10.1016/J.CERAMINT.2013.01.074.
- [50] N. D. Cuong, T. T. Hoa, D. Q. Khieu, T. D. Lam, N. D. Hoa, and N. Van Hieu, "Synthesis, characterization, and comparative gas-sensing properties of Fe₂O₃ prepared from Fe₃O₄ and Fe₃O₄-chitosan," *J. Alloys Compd.*, vol. 523, pp. 120–126, May 2012, doi: 10.1016/J.JALLCOM.2012.01.117.
- [51] X. Han, Y. Sun, Z. Feng, G. Zhang, Z. Chen, and J. Zhan, "Au-deposited porous single-crystalline ZnO nanoplates for gas sensing detection of total volatile organic compounds," *RSC Adv.*, vol. 6, no. 44, pp. 37750–37756, Apr. 2016, doi: 10.1039/C6RA05941D.
- [52] F. Xu, C. Zhou, and H. P. Ho, "A rule for operation temperature selection of a conductometric VOC gas sensor based on ZnO nanotetrapods," *J. Alloys Compd.*, vol. 858, p. 158294, Mar. 2021, doi: 10.1016/j.jallcom.2020.158294.
- [53] Z. Jing and J. Zhan, "Fabrication and Gas-Sensing Properties of Porous ZnO Nanoplates," *Adv. Mater.*, vol. 20, no. 23, pp. 4547–4551, Dec. 2008, doi: 10.1002/ADMA.200800243.

- [54] M. Farbod, M. H. Joula, and M. Vaezi, "Promoting effect of adding carbon nanotubes on sensing characteristics of ZnO hollow sphere-based gas sensors to detect volatile organic compounds," *Mater. Chem. Phys.*, vol. 176, pp. 12–23, Jun. 2016, doi: 10.1016/J.MATCHEMPHYS.2016.03.004.
- [55] J. H. Kim *et al.*, "Toluene- and benzene-selective gas sensors based on Pt- and Pd-functionalized ZnO nanowires in self-heating mode," *Sensors Actuators B Chem.*, vol. 294, pp. 78–88, Sep. 2019, doi: 10.1016/J.SNB.2019.05.032.
- [56] H. Huang, P. Xu, D. Zheng, C. Chen, and X. Li, "Sulfuration–desulfuration reaction sensing effect of intrinsic ZnO nanowires for high-performance H₂S detection," *J. Mater. Chem. A*, vol. 3, no. 12, pp. 6330–6339, Mar. 2015, doi: 10.1039/C4TA05963H.
- [57] K. S. Choi and S. P. Chang, "Effect of structure morphologies on hydrogen gas sensing by ZnO nanotubes," *Mater. Lett.*, vol. 230, pp. 48–52, Nov. 2018, doi: 10.1016/J.MATLET.2018.07.031.
- [58] V. L. Patil, S. A. Vanalakar, P. S. Patil, and J. H. Kim, "Fabrication of nanostructured ZnO thin films based NO₂ gas sensor via SILAR technique," *Sensors Actuators B Chem.*, vol. 239, pp. 1185–1193, Feb. 2017, doi: 10.1016/J.SNB.2016.08.130.
- [59] Y. H. Navale *et al.*, "Zinc oxide hierarchical nanostructures as potential NO₂ sensors," *Sensors Actuators B Chem.*, vol. 251, pp. 551–563, Nov. 2017, doi: 10.1016/J.SNB.2017.05.085.
- [60] M. Hjiri, F. Bahanan, M. S. Aida, L. El Mir, and G. Neri, "High Performance CO Gas Sensor Based on ZnO Nanoparticles," *J. Inorg. Organomet. Polym. Mater. 2020 3010*, vol. 30, no. 10, pp. 4063–4071, Apr. 2020, doi: 10.1007/S10904-020-01553-2.
- [61] C. D *et al.*, "The enhanced alcohol-sensing response of ultrathin WO₃ nanoplates," *Nanotechnology*, vol. 21, no. 3, 2010, doi: 10.1088/0957-4484/21/3/035501.
- [62] D. Meng *et al.*, "Synthesis of WO₃ flower-like hierarchical architectures and their sensing properties," *J. Alloys Compd.*, vol. 649, pp. 731–738, Nov. 2015, doi: 10.1016/J.JALLCOM.2015.07.142.
- [63] X.-X. Zou *et al.*, "A precursor route to single-crystalline WO₃ nanoplates with an uneven surface and enhanced sensing properties," *Dalt. Trans.*, vol. 41, no. 32, pp. 9773–9780, Jul. 2012, doi: 10.1039/C2DT30748K.
- [64] H. Zhang, Z. Liu, J. Yang, W. Guo, L. Zhu, and W. Zheng, "Temperature and acidity effects on WO₃ nanostructures and gas-sensing properties of WO₃ nanoplates," *Mater. Res. Bull.*, vol. 57, pp. 260–267, Sep. 2014, doi: 10.1016/J.MATERRESBULL.2014.06.013.
- [65] J. Huang, X. Xu, C. Gu, M. Yang, M. Yang, and J. Liu, "Large-scale synthesis of hydrated tungsten oxide 3D architectures by a simple chemical solution route and their gas-sensing properties," *J. Mater. Chem.*, vol. 21, no. 35, pp. 13283–13289, Aug. 2011, doi: 10.1039/C1JM11292A.
- [66] S.-J. Choi *et al.*, "Selective Diagnosis of Diabetes Using Pt-Functionalized WO₃ Hemitube Networks As a Sensing Layer of Acetone in Exhaled Breath," *Anal. Chem.*, vol. 85, no. 3, pp. 1792–1796, Feb. 2013, doi: 10.1021/AC303148A.
- [67] C. H. Wu, Z. Zhu, S. Y. Huang, and R. J. Wu, "Preparation of palladium-doped mesoporous WO₃ for hydrogen gas sensors," *J. Alloys Compd.*, vol. 776, pp. 965–973, Mar. 2019, doi: 10.1016/J.JALLCOM.2018.10.372.

- [68] C. Shekhar Prajapati and Navakanta Bhat, "ppb level detection of NO₂ using a WO₃ thin film-based sensor: material optimization, device fabrication and packaging," *RSC Adv.*, vol. 8, no. 12, pp. 6590–6599, Feb. 2018, doi: 10.1039/C7RA13659E.
- [69] S. S. Shendage *et al.*, "Sensitive and selective NO₂ gas sensor based on WO₃ nanoplates," *Sensors Actuators B Chem.*, vol. 240, pp. 426–433, Mar. 2017, doi: 10.1016/J.SNB.2016.08.177.
- [70] S. Wei, L. Han, M. Wang, H. Zhang, W. Du, and M. Zhou, "Hollow cauliflower-like WO₃ nanostructures: Hydrothermal synthesis and their CO sensing properties," *Mater. Lett.*, vol. 186, pp. 259–262, Jan. 2017, doi: 10.1016/J.MATLET.2016.10.016.
- [71] N. Barsan and U. Weimar, "Conduction Model of Metal Oxide Gas Sensors," *J. Electroceramics*, vol. 7, no. 3, pp. 143–167, 2001, doi: 10.1023/A:1014405811371.
- [72] A. Gurlo, "Nanosensors: Towards morphological control of gas sensing activity. SnO₂, In₂O₃, ZnO and WO₃ case studies," *Nanoscale*, vol. 3, no. 1, pp. 154–165, 2011, doi: 10.1039/c0nr00560f.
- [73] S. Thomas, N. Joshi, and V. K. Tomer, Eds., *Functional Nanomaterials*. Singapore: Springer Singapore, 2020.
- [74] Y. Lingmin, F. Xinhui, Q. Lijun, M. Lihe, and Y. Wen, "Dependence of morphologies for SnO₂ nanostructures on their sensing property," *Appl. Surf. Sci.*, vol. 257, no. 7, pp. 3140–3144, Jan. 2011, doi: 10.1016/j.apsusc.2010.11.013.
- [75] M. Batzill and U. Diebold, "The surface and materials science of tin oxide," *Progress in Surface Science*, vol. 79, no. 2–4. Pergamon, pp. 47–154, Jan. 01, 2005, doi: 10.1016/j.progsurf.2005.09.002.
- [76] H. S. Hassan and M. F. Elkady, "Semiconductor Nanomaterials for Gas Sensor Applications," Springer, Cham, 2020, pp. 305–355.
- [77] D. Nunes *et al.*, "Metal oxide nanostructures for sensor applications," *Semiconductor Science and Technology*, vol. 34, no. 4. p. 043001, 2019, doi: 10.1088/1361-6641/ab011e.
- [78] M. V. Nikolic, V. Milovanovic, Z. Z. Vasiljevic, and Z. Stamenkovic, "Semiconductor Gas Sensors: Materials, Technology, Design, and Application," *Sensors*, vol. 20, no. 22, p. 6694, Nov. 2020, doi: 10.3390/s20226694.
- [79] D. Liu, T. Liu, H. Zhang, C. Lv, W. Zeng, and J. Zhang, "Gas sensing mechanism and properties of Ce-doped SnO₂ sensors for volatile organic compounds," *Mater. Sci. Semicond. Process.*, vol. 15, no. 4, pp. 438–444, Aug. 2012, doi: 10.1016/J.MSSP.2012.02.015.
- [80] E. Şennik, O. Alev, and Z. Z. Öztürk, "The effect of Pd on the H₂ and VOC sensing properties of TiO₂ nanorods," *Sensors Actuators B Chem.*, vol. 229, pp. 692–700, Jun. 2016, doi: 10.1016/J.SNB.2016.01.089.
- [81] S. W. Choi, S. H. Jung, and S. S. Kim, "Significant enhancement of the NO₂ sensing capability in networked SnO₂ nanowires by Au nanoparticles synthesized via γ -ray radiolysis," *J. Hazard. Mater.*, vol. 193, pp. 243–248, Oct. 2011, doi: 10.1016/J.JHAZMAT.2011.07.053.
- [82] B. Behera and S. Chandra, "An innovative gas sensor incorporating ZnO–CuO nanoflakes in planar MEMS technology," *Sensors Actuators B Chem.*, vol. 229, pp. 414–424, Jun.

- 2016, doi: 10.1016/J.SNB.2016.01.079.
- [83] F. Ren *et al.*, "Enhanced BTEX gas-sensing performance of CuO/SnO₂ composite," *Sensors Actuators B Chem.*, vol. 223, pp. 914–920, Feb. 2016, doi: 10.1016/J.SNB.2015.09.140.
- [84] W. Sha, S. Ni, and C. Zheng, "Development of cataluminescence sensor system for benzene and toluene determination," *Sensors Actuators B Chem.*, vol. 209, pp. 297–305, Mar. 2015, doi: 10.1016/J.SNB.2014.11.093.
- [85] N. S. Ramgir *et al.*, "Selective H₂S sensing characteristics of CuO modified WO₃ thin films," *Sensors Actuators B Chem.*, vol. 188, pp. 525–532, Nov. 2013, doi: 10.1016/J.SNB.2013.07.052.
- [86] S. K. Hyun, B. Nam, T. K. Ko, C. Lee, S. B. Choi, and W. I. Lee, "Optimal Composition of ZnO/WO₃ Composite Nanoparticle Gas Sensors," *Phys. status solidi*, vol. 217, no. 12, p. 1900874, Jun. 2020, doi: 10.1002/PSSA.201900874.
- [87] M. Hijazi, M. Rieu, V. Stambouli, G. Tournier, J. P. Viricelle, and C. Pijolat, "Ambient temperature selective ammonia gas sensor based on SnO₂-APTES modifications," *Sensors Actuators B Chem.*, vol. 256, pp. 440–447, Mar. 2018, doi: 10.1016/J.SNB.2017.10.036.
- [88] X. Xing, X. Xiao, L. Wang, and Y. Wang, "Highly sensitive formaldehyde gas sensor based on hierarchically porous Ag-loaded ZnO heterojunction nanocomposites," *Sensors Actuators B Chem.*, vol. 247, pp. 797–806, Aug. 2017, doi: 10.1016/J.SNB.2017.03.077.
- [89] N. Luo, B. Zhang, D. Zhang, and J. Xu, "Enhanced CO sensing properties of Pd modified ZnO porous nanosheets," *Chinese Chem. Lett.*, vol. 31, no. 8, pp. 2033–2036, Aug. 2020, doi: 10.1016/J.CCLET.2020.01.002.
- [90] A. Katoch, J.-H. Kim, Y. J. Kwon, H. W. Kim, and S. S. Kim, "Bifunctional Sensing Mechanism of SnO₂-ZnO Composite Nanofibers for Drastically Enhancing the Sensing Behavior in H₂ Gas," *ACS Appl. Mater. Interfaces*, vol. 7, no. 21, pp. 11351–11358, Jun. 2015, doi: 10.1021/ACSAMI.5B01817.
- [91] B. Bendahmane, M. Tomić, N. E. H. Toudjén, I. Gràcia, S. Vallejos, and F. Mansour, "Influence of MG doping levels on the sensing properties of SnO₂ films," *Sensors (Switzerland)*, vol. 20, no. 7, p. 2158, Apr. 2020, doi: 10.3390/s20072158.
- [92] I. Lee *et al.*, "The stability, sensitivity and response transients of ZnO, SnO₂ and WO₃ sensors under acetone, toluene and H₂S environments," *Sensors Actuators B Chem.*, vol. 197, pp. 300–307, Jul. 2014, doi: 10.1016/J.SNB.2014.02.043.
- [93] D. Peeters *et al.*, "Au/ε-Fe₂O₃ Nanocomposites as Selective NO₂ Gas Sensors," *J. Phys. Chem. C*, vol. 118, no. 22, pp. 11813–11819, Jun. 2014, doi: 10.1021/JP5032288.
- [94] M. Yuasa, T. Masaki, T. Kida, K. Shimano, and N. Yamazoe, "Nano-sized PdO loaded SnO₂ nanoparticles by reverse micelle method for highly sensitive CO gas sensor," *Sensors Actuators B Chem.*, vol. 136, no. 1, pp. 99–104, Feb. 2009, doi: 10.1016/J.SNB.2008.11.022.
- [95] R. Kumar, X. Liu, J. Zhang, and M. Kumar, "Room-Temperature Gas Sensors Under Photoactivation: From Metal Oxides to 2D Materials," *Nano-Micro Lett.* 2020 121, vol. 12, no. 1, pp. 1–37, Aug. 2020, doi: 10.1007/S40820-020-00503-4.
- [96] C. Dong, R. Zhao, L. Yao, Y. Ran, X. Zhang, and Y. Wang, "A review on WO₃ based gas

- sensors: Morphology control and enhanced sensing properties," *J. Alloys Compd.*, vol. 820, p. 153194, Apr. 2020, doi: 10.1016/J.JALLCOM.2019.153194.
- [97] N. Markiewicz *et al.*, "Micro light plates for low-power photoactivated (gas) sensors," *Appl. Phys. Lett.*, vol. 114, no. 5, p. 053508, Feb. 2019, doi: 10.1063/1.5078497.
- [98] E. Espid, B. Adeli, and F. Taghipour, "Enhanced Gas Sensing Performance of Photo-Activated, Pt-Decorated, Single-Crystal ZnO Nanowires," *J. Electrochem. Soc.*, vol. 166, no. 5, p. H3223, Feb. 2019, doi: 10.1149/2.0301905JES.
- [99] J. D. Prades *et al.*, "Equivalence between thermal and room temperature UV light-modulated responses of gas sensors based on individual SnO₂ nanowires," *Sensors Actuators B Chem.*, vol. 140, no. 2, pp. 337–341, Jul. 2009, doi: 10.1016/J.SNB.2009.04.070.
- [100] L. Deng, X. Ding, D. Zeng, S. Tian, H. Li, and C. Xie, "Visible-light activate mesoporous WO₃ sensors with enhanced formaldehyde-sensing property at room temperature," *Sensors Actuators B Chem.*, vol. 163, no. 1, pp. 260–266, Mar. 2012, doi: 10.1016/J.SNB.2012.01.049.
- [101] J. Cui, L. Shi, T. Xie, D. Wang, and Y. Lin, "UV-light illumination room temperature HCHO gas-sensing mechanism of ZnO with different nanostructures," *Sensors Actuators B Chem.*, vol. 227, pp. 220–226, May 2016, doi: 10.1016/J.SNB.2015.12.010.
- [102] N. M. Vuong *et al.*, "Gas-sensing properties of ZnO nanorods at room temperature under continuous UV illumination in humid air," *J. Nanosci. Nanotechnol.*, vol. 16, no. 10, pp. 10346–10350, Oct. 2016, doi: 10.1166/JNN.2016.13157.
- [103] J. Gong, Y. Li, X. Chai, Z. Hu, and Y. Deng, "UV-Light-Activated ZnO Fibers for Organic Gas Sensing at Room Temperature," *J. Phys. Chem. C*, vol. 114, no. 2, pp. 1293–1298, Jan. 2009, doi: 10.1021/JP906043K.
- [104] H. Chen, Y. Liu, C. Xie, J. Wu, D. Zeng, and Y. Liao, "A comparative study on UV light activated porous TiO₂ and ZnO film sensors for gas sensing at room temperature," *Ceram. Int.*, vol. 38, no. 1, pp. 503–509, Jan. 2012, doi: 10.1016/J.CERAMINT.2011.07.035.
- [105] J. Saura, "Gas-sensing properties of SnO₂ pyrolytic films subjected to ultraviolet radiation," *Sensors Actuators B Chem.*, vol. 17, no. 3, pp. 211–214, Feb. 1994, doi: 10.1016/0925-4005(93)00874-X.
- [106] T. Xie *et al.*, "UV-assisted room-temperature chemiresistive NO₂ sensor based on TiO₂ thin film," *J. Alloys Compd.*, vol. 653, pp. 255–259, Dec. 2015, doi: 10.1016/J.JALLCOM.2015.09.021.
- [107] S. Trocino *et al.*, "Gas sensing properties under UV radiation of In₂O₃ nanostructures processed by electrospinning," *Mater. Chem. Phys.*, vol. 147, no. 1–2, pp. 35–41, Sep. 2014, doi: 10.1016/J.MATCHEMPHYS.2014.03.057.
- [108] A. Ilin *et al.*, "UV effect on NO₂ sensing properties of nanocrystalline In₂O₃," *Sensors Actuators B Chem.*, vol. 231, pp. 491–496, Aug. 2016, doi: 10.1016/J.SNB.2016.03.051.
- [109] O. Gonzalez, S. Roso, X. Vilanova, and E. Llobet, "Enhanced detection of nitrogen dioxide via combined heating and pulsed UV operation of indium oxide nano-octahedra," *Beilstein J. Nanotechnol.* 7144, vol. 7, no. 1, pp. 1507–1518, Oct. 2016, doi: 10.3762/BJNANO.7.144.

- [110] H. Ma *et al.*, "Room temperature photoelectric NO₂ gas sensor based on direct growth of walnut-like In₂O₃ nanostructures," *J. Alloys Compd.*, vol. 782, pp. 1121–1126, Apr. 2019, doi: 10.1016/J.JALLCOM.2018.12.180.
- [111] Y. Mun, S. Park, S. An, C. Lee, and H. W. Kim, "NO₂ gas sensing properties of Au-functionalized porous ZnO nanosheets enhanced by UV irradiation," *Ceram. Int.*, vol. 39, no. 8, pp. 8615–8622, Dec. 2013, doi: 10.1016/J.CERAMINT.2013.04.035.
- [112] C. Guo, Z. Lin, W. Song, X. Wang, Y. Huang, and K. Wang, "Synthesis, UV response, and room-temperature ethanol sensitivity of undoped and Pd-doped coral-like SnO₂," *J. Nanoparticle Res. 2013 1510*, vol. 15, no. 10, pp. 1–8, Sep. 2013, doi: 10.1007/S11051-013-1998-2.
- [113] J. Wang, C. Hu, Y. Xia, and S. Komarneni, "Highly sensitive, fast and reversible NO₂ sensors at room-temperature utilizing nonplasmonic electrons of ZnO/Pd hybrids," *Ceram. Int.*, vol. 46, no. 6, pp. 8462–8468, Apr. 2020, doi: 10.1016/J.CERAMINT.2019.12.081.
- [114] A. V. Almaev, N. N. Yakovlev, E. V. Chernikov, and O. P. Tolbanov, "Selective Sensors of Nitrogen Dioxide Based on Thin Tungsten Oxide Films under Optical Irradiation," *Tech. Phys. Lett. 2019 4510*, vol. 45, no. 10, pp. 1016–1019, Nov. 2019, doi: 10.1134/S1063785019100171.
- [115] J. Zhai, L. Wang, D. Wang, Y. Lin, D. He, and T. Xie, "UV-illumination room-temperature gas sensing activity of carbon-doped ZnO microspheres," *Sensors Actuators B Chem.*, vol. 161, no. 1, pp. 292–297, Jan. 2012, doi: 10.1016/J.SNB.2011.10.034.
- [116] E. Espid and F. Taghipour, "Development of highly sensitive ZnO/In₂O₃ composite gas sensor activated by UV-LED," *Sensors Actuators B Chem.*, vol. 241, pp. 828–839, Mar. 2017, doi: 10.1016/J.SNB.2016.10.129.
- [117] L. Zhao *et al.*, "Room temperature formaldehyde sensing of hollow SnO₂/ZnO heterojunctions under UV-LED activation," *IEEE Sens. J.*, vol. 19, no. 17, pp. 7207–7214, Sep. 2019, doi: 10.1109/JSEN.2019.2916879.
- [118] S. Park, S. An, Y. Mun, and C. Lee, "UV-Enhanced NO₂ Gas Sensing Properties of SnO₂-Core/ZnO-Shell Nanowires at Room Temperature," *ACS Appl. Mater. Interfaces*, vol. 5, no. 10, pp. 4285–4292, May 2013, doi: 10.1021/AM400500A.
- [119] S. Park, H. Ko, S. Lee, H. Kim, and C. Lee, "Light-activated gas sensing of Bi₂O₃-core/ZnO-shell nanobelt gas sensors," *Thin Solid Films*, vol. 570, no. PB, pp. 298–302, Nov. 2014, doi: 10.1016/J.TSF.2014.02.110.
- [120] A. Nasriddinov *et al.*, "Sub-ppm Formaldehyde Detection by n-n TiO₂@SnO₂ Nanocomposites," *Sensors 2019, Vol. 19, Page 3182*, vol. 19, no. 14, p. 3182, Jul. 2019, doi: 10.3390/S19143182.
- [121] E. Comini, "Integration of Metal Oxide Nanowires in Flexible Gas Sensing Devices," *Sensors*, vol. 13, no. 8, pp. 10659–10673, Aug. 2013, doi: 10.3390/s130810659.
- [122] Y. Li and J.-J. Delaunay, "Progress Toward Nanowire Device Assembly Technology," in *Nanowires*, InTech, 2010.
- [123] M. Jiao *et al.*, "On-chip hydrothermal growth of ZnO nanorods at low temperature for highly selective NO₂ gas sensor," *Mater. Lett.*, vol. 169, pp. 231–235, Apr. 2016, doi: 10.1016/J.MATLET.2016.01.123.

- [124] A. Mirzaei, G. J. Sun, J. K. Lee, C. Lee, S. Choi, and H. W. Kim, "Hydrogen sensing properties and mechanism of NiO-Nb₂O₅ composite nanoparticle-based electrical gas sensors," *Ceram. Int.*, vol. 43, no. 6, pp. 5247–5254, Apr. 2017, doi: 10.1016/J.CERAMINT.2017.01.050.
- [125] H. Dong *et al.*, "Hierarchically rosette-like In₂O₃ microspheres for volatile organic compounds gas sensors," *Sensors Actuators B Chem.*, vol. 178, pp. 302–309, Mar. 2013, doi: 10.1016/J.SNB.2012.12.103.
- [126] B. Bhowmik, V. Manjuladevi, R. K. Gupta, and P. Bhattacharyya, "Highly Selective Low-Temperature Acetone Sensor Based on Hierarchical 3-D TiO₂ Nanoflowers," *IEEE Sens. J.*, vol. 16, no. 10, pp. 3488–3495, May 2016, doi: 10.1109/JSEN.2016.2530827.
- [127] H.-C. C. and C.-S. Yeh*, "Hydrothermal Synthesis of SnO₂ Nanoparticles and Their Gas-Sensing of Alcohol," *J. Phys. Chem. C*, vol. 111, no. 20, pp. 7256–7259, May 2007, doi: 10.1021/JP0688355.
- [128] L. Zhu, Y. Li, and W. Zeng, "Hydrothermal synthesis of hierarchical flower-like ZnO nanostructure and its enhanced ethanol gas-sensing properties," *Appl. Surf. Sci.*, vol. 427, pp. 281–287, Jan. 2018, doi: 10.1016/J.APSUSC.2017.08.229.
- [129] Y. Lü *et al.*, "MOF-Templated Synthesis of Porous Co₃O₄ Concave Nanocubes with High Specific Surface Area and Their Gas Sensing Properties," *ACS Appl. Mater. Interfaces*, vol. 6, no. 6, pp. 4186–4195, Mar. 2014, doi: 10.1021/AM405858V.
- [130] H. J. Park, J. Kim, N.-J. Choi, H. Song, and D.-S. Lee, "Nonstoichiometric Co-rich ZnCo₂O₄ Hollow Nanospheres for High Performance Formaldehyde Detection at ppb Levels," *ACS Appl. Mater. Interfaces*, vol. 8, no. 5, pp. 3233–3240, Feb. 2016, doi: 10.1021/ACSAMI.5B10862.
- [131] H. Deng *et al.*, "A high sensitive and low detection limit of formaldehyde gas sensor based on hierarchical flower-like CuO nanostructure fabricated by sol–gel method," *J. Mater. Sci. Mater. Electron.*, vol. 27, no. 7, pp. 6766–6772, Jul. 2016, doi: 10.1007/S10854-016-4626-Y.
- [132] K. Galatsis *et al.*, "Comparison of single and binary oxide MoO₃, TiO₂ and WO₃ sol–gel gas sensors," *Sensors Actuators B Chem.*, vol. 83, no. 1–3, pp. 276–280, Mar. 2002, doi: 10.1016/S0925-4005(01)01072-3.
- [133] H. W. Ryu *et al.*, "ZnO sol–gel derived porous film for CO gas sensing," *Sensors Actuators B Chem.*, vol. 96, no. 3, pp. 717–722, Dec. 2003, doi: 10.1016/J.SNB.2003.07.010.
- [134] S. Capone, P. Siciliano, F. Quaranta, R. Rella, M. Epifani, and L. Vasanelli, "Analysis of vapours and foods by means of an electronic nose based on a sol–gel metal oxide sensors array," *Sensors Actuators B Chem.*, vol. 69, no. 3, pp. 230–235, Oct. 2000, doi: 10.1016/S0925-4005(00)00496-2.
- [135] C. Yang, X. Su, J. Wang, X. Cao, S. Wang, and L. Zhang, "Facile microwave-assisted hydrothermal synthesis of varied-shaped CuO nanoparticles and their gas sensing properties," *Sensors Actuators B Chem.*, vol. 185, pp. 159–165, Aug. 2013, doi: 10.1016/J.SNB.2013.04.100.
- [136] B. Li *et al.*, "Sensitive and selective system of benzene detection based on a cataluminescence sensor," *Luminescence*, vol. 29, no. 4, pp. 332–337, Jun. 2014, doi: 10.1002/BIO.2548.

- [137] H. S. Al-Salman and M. J. Abdullah, "Preparation of ZnO nanostructures by RF-magnetron sputtering on thermally oxidized porous silicon substrate for VOC sensing application," *Measurement*, vol. 59, pp. 248–257, Jan. 2015, doi: 10.1016/J.MEASUREMENT.2014.08.011.
- [138] S. Öztürk, A. Kösemen, Z. A. Kösemen, N. Kılınc, Z. Z. Öztürk, and M. Penza, "Electrochemically growth of Pd doped ZnO nanorods on QCM for room temperature VOC sensors," *Sensors Actuators B Chem.*, vol. 222, pp. 280–289, 2016, doi: 10.1016/j.snb.2015.08.083.
- [139] S. Vallejos, N. Pizúrová, J. Čechal, I. Gràcia, and C. Cané, "Aerosol-assisted Chemical Vapor Deposition of Metal Oxide Structures: Zinc Oxide Rods," *JoVE*, vol. 127, p. e56127, 2017, doi: 10.3791/56127.
- [140] M. Claros, M. Setka, Y. P. Jimenez, and S. Vallejos, "AACVD Synthesis and Characterization of Iron and Copper Oxides Modified ZnO Structured Films," *Nanomaterials*, vol. 10, no. 3, pp. 471–487, 2020, doi: 10.3390/nano10030471.
- [141] A. Sáenz-Trevizo *et al.*, "Microstructural, chemical and textural characterization of ZnO nanorods synthesized by aerosol assisted chemical vapor deposition," *Mater. Charact.*, vol. 98, pp. 215–221, Dec. 2014, doi: 10.1016/J.MATCHAR.2014.11.005.
- [142] S. Vallejos *et al.*, "ZnO rods with exposed {100} facets grown via a self-catalyzed vapor-solid mechanism and their photocatalytic and gas sensing properties," *ACS Appl. Mater. Interfaces*, vol. 8, no. 48, pp. 33335–33342, 2016, doi: 10.1021/acsami.6b12992.
- [143] A. Hierlemann and H. Baltes, "CMOS-based chemical microsensors," *Analyst*, vol. 128, no. 1, pp. 15–28, Dec. 2003, doi: 10.1039/B208563C.
- [144] A. Mirzaei, K. Janghorban, B. Hashemi, M. Bonyani, S. G. Leonardi, and G. Neri, "A novel gas sensor based on Ag/Fe₂O₃ core-shell nanocomposites," *Ceram. Int.*, vol. 42, no. 16, pp. 18974–18982, Dec. 2016, doi: 10.1016/J.CERAMINT.2016.09.052.
- [145] J. Janata, "Principles of Chemical Sensors," *Princ. Chem. Sensors*, 1989, doi: 10.1007/978-1-4757-6257-0.
- [146] S. M. Majhi, A. Mirzaei, H. W. Kim, S. S. Kim, and T. W. Kim, "Recent advances in energy-saving chemiresistive gas sensors: A review," *Nano Energy*, vol. 79, p. 105369, Jan. 2021, doi: 10.1016/J.NANOEN.2020.105369.
- [147] L. Zhang *et al.*, "Facile synthesis and ultrahigh ethanol response of hierarchically porous ZnO nanosheets," *Sensors Actuators B Chem.*, vol. 161, no. 1, pp. 209–215, Jan. 2012, doi: 10.1016/J.SNB.2011.10.021.
- [148] P. Ivanov, E. Llobet, X. Vilanova, J. Brezmes, J. Hubalek, and X. Correig, "Development of high sensitivity ethanol gas sensors based on Pt-doped SnO₂ surfaces," *Sensors Actuators B Chem.*, vol. 99, no. 2–3, pp. 201–206, May 2004, doi: 10.1016/J.SNB.2003.11.012.
- [149] S. Umesh, T. C. Balachandra, and A. Usha, "Design and Simulation of MEMS Gas Sensor Topologies for Detection of Inert Gases," *Mater. Today Proc.*, vol. 5, no. 10, pp. 21355–21362, Jan. 2018, doi: 10.1016/J.MATPR.2018.06.540.
- [150] C. Hagleitner *et al.*, "Smart single-chip gas sensor microsystem," *Nat. 2001 4146861*, vol. 414, no. 6861, pp. 293–296, Nov. 2001, doi: 10.1038/35104535.
- [151] X. Hou and K.-L. Choy, "Processing and Applications of Aerosol-Assisted Chemical Vapor

- Deposition," *Chem. Vap. Depos.*, vol. 12, no. 10, pp. 583–596, Oct. 2006, doi: 10.1002/CVDE.200600033.
- [152] M. Tomić *et al.*, "Cerium Oxide-Tungsten Oxide Core-Shell Nanowire-Based Microsensors Sensitive to Acetone," *Biosensors*, vol. 8, no. 4, p. 116, 2018, doi: 10.3390/bios8040116.
- [153] M. Tomić, Z. Fohlerova, I. Gràcia, E. Figueras, C. Cané, and S. Vallejos, "UV-light activated APTES modified WO_{3-x} nanowires sensitive to ethanol and nitrogen dioxide," *Sensors Actuators, B Chem.*, vol. 328, p. 129046, 2021, doi: 10.1016/j.snb.2020.129046.
- [154] M. Tomić, M. Claros, I. Gràcia, E. Figueras, C. Cané, and S. Vallejos, "ZnO Structures with Surface Nanoscale Interfaces Formed by Au, Fe_2O_3 , or Cu_2O Modifier Nanoparticles: Characterization and Gas Sensing Properties," *Sensors*, vol. 21, no. 13, p. 4509, Jun. 2021, doi: 10.3390/s21134509.
- [155] M. A *et al.*, "Assessing the temporal stability of surface functional groups introduced by plasma treatments on the outer shells of carbon nanotubes," *Sci. Rep.*, vol. 6, Aug. 2016, doi: 10.1038/SREP31565.
- [156] S. Vallejos *et al.*, "Single-step deposition of Au- and Pt-nanoparticle-functionalized tungsten oxide nanoneedles synthesized via aerosol-assisted CVD, and used for fabrication of selective gas microsensor arrays," *Adv. Funct. Mater.*, vol. 23, no. 10, pp. 1313–1322, 2013, doi: 10.1002/adfm.201201871.
- [157] W. P. Sari, C. Blackman, Y. Zhu, and J. A. Covington, "AACVD Grown WO_3 Nanoneedles Decorated with Ag/ Ag_2O Nanoparticles for Oxygen Measurement in a Humid Environment," *IEEE Sens. J.*, vol. 19, no. 3, pp. 826–832, 2019, doi: 10.1109/JSEN.2018.2878051.
- [158] J. Turkevich, P. C. Stevenson, and J. Hillier, "A study of the nucleation and growth processes in the synthesis of colloidal gold," *Discussions of the Faraday Society*, vol. 11, pp. 55–75, 1951, doi: 10.1039/DF9511100055.
- [159] J. Sanderson, "Introduction to Light Microscopy," *J. Microsc.*, vol. 193, no. 1, pp. 90–91, Jan. 1999, doi: 10.1046/J.1365-2818.1999.0429B.X.
- [160] B.J. Inkson, "Scanning electron microscopy (SEM) and transmission electron microscopy (TEM) for materials characterization," in *Materials Characterization Using Nondestructive Evaluation (NDE) Methods*, G. Hübschen, I. Altpeter, R. Tschuncky, and H.-G. Herrmann, Eds. Woodhead Publishing, 2016, p. 320.
- [161] A. Ul-Hamid, *A Beginners' Guide to Scanning Electron Microscopy | Anwar Ul-Hamid | Springer*. Springer, Cham, 2018.
- [162] D. B. Williams and C. B. Carter, "The Transmission Electron Microscope," *Transm. Electron Microsc.*, pp. 3–22, 2009, doi: 10.1007/978-0-387-76501-3_1.
- [163] M. Abd Mutalib, M. A. Rahman, M. H. D. Othman, A. F. Ismail, and J. Jaafar, "Scanning Electron Microscopy (SEM) and Energy-Dispersive X-Ray (EDX) Spectroscopy," *Membr. Charact.*, pp. 161–179, Jan. 2017, doi: 10.1016/B978-0-444-63776-5.00009-7.
- [164] A. Barron, Ed., *Physical Methods in Chemistry and Nano Science*. Connexions, 2012.
- [165] F. J. Himpsel, "Ultraviolet Photoelectron Spectroscopy," *Charact. Mater.*, pp. 1–13, May 2012, doi: 10.1002/0471266965.COM061.PUB2.
- [166] M. Y. Adam *et al.*, "High resolution X-ray and He II excited inner valence photoelectron

- spectra of HI," *Chem. Phys.*, vol. 164, no. 1, pp. 123–129, Jul. 1992, doi: 10.1016/0301-0104(92)87136-W.
- [167] J. Epp, "X-ray diffraction (XRD) techniques for materials characterization," *Mater. Charact. Using Nondestruct. Eval. Methods*, pp. 81–124, Jan. 2016, doi: 10.1016/B978-0-08-100040-3.00004-3.
- [168] U. Kramar, "X-Ray Fluorescence Spectrometers," *Encycl. Spectrosc. Spectrom.*, pp. 2989–2999, Jan. 1999, doi: 10.1016/B978-0-12-374413-5.00314-6.
- [169] H. G. Hecht, "The Interpretation of Diffuse Reflectance Spectra," *J. Res. Natl. Bur. Stand. Sect. A, Phys. Chem.*, vol. 80A, no. 4, p. 567, 1976, doi: 10.6028/JRES.080A.056.
- [170] I. Gràcia, J. Santander, C. Cané, M. C. Horrillo, I. Sayago, and J. Gutierrez, "Results on the reliability of silicon micromachined structures for semiconductor gas sensors," *Sensors Actuators B Chem.*, vol. 77, no. 1–2, pp. 409–415, Jun. 2001, doi: 10.1016/S0925-4005(01)00706-7.
- [171] C. Cané *et al.*, "Detection of gases with arrays of micromachined tin oxide gas sensors," *Sensors Actuators B Chem.*, vol. 65, no. 1–3, pp. 244–246, Jun. 2000, doi: 10.1016/S0925-4005(99)00314-7.
- [172] S. Vallejos, I. Gràcia, O. Chmela, E. Figueras, J. Hubálek, and C. Cané, "Chemoresistive micromachined gas sensors based on functionalized metal oxide nanowires: Performance and reliability," *Sensors Actuators B Chem.*, vol. 235, pp. 525–534, Nov. 2016, doi: 10.1016/J.SNB.2016.05.102.
- [173] R. Kumar, O. Al-Dossary, G. Kumar, and A. Umar, "Zinc oxide nanostructures for NO₂ gas–sensor applications: A review," *Nano-Micro Letters*, vol. 7, no. 2. SpringerOpen, pp. 97–120, Dec. 16, 2015, doi: 10.1007/s40820-014-0023-3.
- [174] J. García-Beleño and E. R. de S. Miguel, "Integration of Response Surface Methodology (RSM) and Principal Component Analysis (PCA) as an Optimization Tool for Polymer Inclusion Membrane Based-Optodes Designed for Hg(II), Cd(II), and Pb(II)," *Membr. 2021, Vol. 11, Page 288*, vol. 11, no. 4, p. 288, Apr. 2021, doi: 10.3390/MEMBRANES11040288.
- [175] Y. Şahin, S. Öztürk, N. Kiliç, A. Kösemen, M. Erkovan, and Z. Z. Öztürk, "Electrical conduction and NO₂ gas sensing properties of ZnO nanorods," *Appl. Surf. Sci.*, vol. 303, pp. 90–96, Jun. 2014, doi: 10.1016/J.APSUSC.2014.02.083.
- [176] L. A. Currie, "Detection: International update, and some emerging di-lemmas involving calibration, the blank, and multiple detection decisions," *Chemom. Intell. Lab. Syst.*, vol. 37, no. 1, pp. 151–181, May 1997, doi: 10.1016/S0169-7439(97)00009-9.
- [177] G. Indrayanto, "Validation of Chromatographic Methods of Analysis: Application for Drugs That Derived From Herbs," *Profiles Drug Subst. Excipients Relat. Methodol.*, vol. 43, pp. 359–392, Jan. 2018, doi: 10.1016/BS.PODRM.2018.01.003.
- [178] L. Zhu and W. Zeng, "Room-temperature gas sensing of ZnO-based gas sensor: A review," *Sensors Actuators A Phys.*, vol. 267, pp. 242–261, Nov. 2017, doi: 10.1016/J.SNA.2017.10.021.
- [179] M. Tomić, M. Šetka, L. Vojkúvka, and S. Vallejos, "VOCs Sensing by Metal Oxides, Conductive Polymers, and Carbon-Based Materials," *Nanomaterials*, vol. 11, no. 2, p. 552, 2021, doi: 10.3390/nano11020552.

- [180] M. Tomić, I. Gràcia, M. Salleras, E. Figueras, C. Cané, and S. Vallejos, "Gas Microsensors Based on Cerium Oxide Modified Tungsten Oxide Nanowires," *Proc. 2018 12th Spanish Conf. Electron Devices, CDE 2018*, Dec. 2018, doi: 10.1109/CDE.2018.8597067.
- [181] S. Vallejos *et al.*, "Gas sensitive ZnO structures with reduced humidity-interference," *Sensors Actuators, B Chem.*, vol. 301, p. 127054, 2019, doi: 10.1016/j.snb.2019.127054.
- [182] M. Tomic, I. Gracia, E. Figueras, C. Cane, and S. Vallejos, "ZnO Nanorods and Their Modification with Au Nanoparticles for UV-light Activated Gas Sensing," pp. 117–120, Jun. 2021, doi: 10.1109/CDE52135.2021.9455726.
- [183] B. Sun, J. Horvat, H. S. Kim, W.-S. Kim, J. Ahn, and G. Wang, "Synthesis of Mesoporous α -Fe₂O₃ Nanostructures for Highly Sensitive Gas Sensors and High Capacity Anode Materials in Lithium Ion Batteries," *J. Phys. Chem. C*, vol. 114, no. 44, pp. 18753–18761, Nov. 2010, doi: 10.1021/JP102286E.
- [184] H. Chen *et al.*, "Glycine-assisted hydrothermal synthesis of peculiar porous α -Fe₂O₃ nanospheres with excellent gas-sensing properties," *Anal. Chim. Acta*, vol. 659, no. 1–2, pp. 266–273, Feb. 2010, doi: 10.1016/J.ACA.2009.11.040.
- [185] M. Mohapatra and S. Anand, "Synthesis and applications of nano-structured iron oxides/hydroxides – a review," *Int. J. Eng. Sci. Technol.*, vol. 2, no. 8, pp. 127–146, Feb. 2011, doi: 10.4314/ijest.v2i8.63846.
- [186] V. Balouria *et al.*, "Nano-crystalline Fe₂O₃ thin films for ppm level detection of H₂S," *Sensors Actuators B Chem.*, vol. 181, pp. 471–478, 2013, doi: <https://doi.org/10.1016/j.snb.2013.02.013>.
- [187] Y.-L. Chueh, M.-W. Lai, J.-Q. Liang, L.-J. Chou, and Z. L. Wang, "Systematic Study of the Growth of Aligned Arrays of α -Fe₂O₃ and Fe₃O₄ Nanowires by a Vapor–Solid Process," *Adv. Funct. Mater.*, vol. 16, no. 17, pp. 2243–2251, Nov. 2006, doi: 10.1002/ADFM.200600499.
- [188] K. Woo, H. J. Lee, J.-P. Ahn, and Y. S. Park, "Sol–Gel Mediated Synthesis of Fe₂O₃ Nanorods," *Adv. Mater.*, vol. 15, no. 20, pp. 1761–1764, Oct. 2003, doi: 10.1002/ADMA.200305561.
- [189] S. Zeng *et al.*, "Hematite Hollow Spindles and Microspheres: Selective Synthesis, Growth Mechanisms, and Application in Lithium Ion Battery and Water Treatment," *J. Phys. Chem. C*, vol. 111, no. 28, pp. 10217–10225, Jul. 2007, doi: 10.1021/jp0719661.
- [190] P. Sun, W. Wang, Y. Liu, Y. Sun, J. Ma, and G. Lu, "Hydrothermal synthesis of 3D urchin-like α -Fe₂O₃ nanostructure for gas sensor," *Sensors Actuators B Chem.*, vol. 173, pp. 52–57, 2012, doi: <https://doi.org/10.1016/j.snb.2012.05.057>.

Appendix A

Collaborative Journal Article 1

Influence of Mg doping levels on the sensing properties of SnO₂ films, Bendahmane B., Tomić M., Toudjen N. H., Gràcia I., Vallejos S., Mansour F., Sensors, 2020, 20, 2158, doi: 10.3390/s20072158

Article

Influence of Mg Doping Levels on the Sensing Properties of SnO₂ Films

Bouteina Bendahmane ^{1,*}, Milena Tomić ², Nour El Houda Toudjen ¹, Isabel Gràcia ², Stella Vallejos ^{2,3,*} and Farida Mansour ¹

¹ Electronic Materials Study for Medical Applications (LEMEAMED) Laboratory, Electronic Department, Science and Technology Faculty, Frères Mentouri University, 25000 Constantine, Algeria; houdatoudjen@yahoo.fr (N.E.H.T.); farida.mansour@yahoo.fr (F.M.)

² Instituto de Microelectrónica de Barcelona (IMB-CNM, CSIC), Campus UAB, 08193 Bellaterra, Spain; milena.tomic@imb-cnm.csic.es (M.T.); isabel.gracia@imb-cnm.csic.es (I.G.)

³ CEITEC-Central European Institute of Technology, Brno University of Technology, 61200 Brno, Czech Republic

* Correspondence: bendahmane.bouteina92@gmail.com (B.B.); stella.vallejos@imb-cnm.csic.es or vargas@feec.vutbr.cz (S.V.); Tel.: +213-665-385172 (B.B.); +34-935-947700 (S.V.)

Received: 11 March 2020; Accepted: 9 April 2020; Published: 10 April 2020



Abstract: This work presents the effect of magnesium (Mg) doping on the sensing properties of tin dioxide (SnO₂) thin films. Mg-doped SnO₂ films were prepared via a spray pyrolysis method using three doping concentrations (0.8 at.%, 1.2 at.%, and 1.6 at.%) and the sensing responses were obtained at a comparatively low operating temperature (160 °C) compared to other gas sensitive materials in the literature. The morphological, structural and chemical composition analysis of the doped films show local lattice disorders and a proportional decrease in the average crystallite size as the Mg-doping level increases. These results also indicate an excess of Mg (in the samples prepared with 1.6 at.% of magnesium) which causes the formation of a secondary magnesium oxide phase. The films are tested towards three volatile organic compounds (VOCs), including ethanol, acetone, and toluene. The gas sensing tests show an enhancement of the sensing properties to these vapors as the Mg-doping level rises. This improvement is particularly observed for ethanol and, thus, the gas sensing analysis is focused on this analyte. Results to 80 ppm of ethanol, for instance, show that the response of the 1.6 at.% Mg-doped SnO₂ film is four times higher and 90 s faster than that of the 0.8 at.% Mg-doped SnO₂ film. This enhancement is attributed to the Mg-incorporation into the SnO₂ cell and to the formation of MgO within the film. These two factors maximize the electrical resistance change in the gas adsorption stage, and thus, raise ethanol sensitivity.

Keywords: Mg-doped SnO₂; spray pyrolysis; thin films; gas sensing; volatile organic compounds

1. Introduction

The monitoring of volatile organic compounds (VOCs), including ethanol (C₂H₆O), acetone (C₃H₆O), and toluene (C₇H₈), is routinely needed for evaluating environmental quality and industrial safety [1]. Recently, the monitoring of VOCs has also gained importance in clinical applications as a promising tool to identify pathological conditions at early stages (via breath analysis of anomalous concentrations of certain VOCs) [2]. In this context, metal oxides (MOXs)-based gas sensors (chemoresistive sensors) are attractive devices that can be miniaturized and integrated as array systems into compact VOC monitoring equipment at reduced fabrication costs as compared to other technologies (e.g., spectrometers) [1,2]. Previously, MOXs such as ZnO, SnO₂, WO₃, and TiO₂ at the nanoscale have proved promising properties to sense VOCs due to their high surface-to-volume

ratio, which provides better sensitivity and stability compared to bulk MOXs [3–7]. Currently, however, these materials require yet the enhancement of sensitivity to low concentrations of VOCs and, generally, the improvement of selectivity and the minimization of drift effect over time. Thus, various efforts have been focused on this line, pointing out the importance of enhancing both chemical and electronic sensitization by incorporating intentional impurities (e.g., doping) or modifying the surface of traditional gas-sensitive MOXs [6,8].

Tin dioxide (SnO_2) is considered as one of the leading n-type MOXs used in commercial chemoresistive gas sensors, however, the enhancement of its sensing performance remains active to date [9,10]. As mentioned above for other MOXs, a large series of reports has also emphasized the remarkable improvement of SnO_2 sensing characteristics, whether by adding catalysts, introducing functional activators, or doping with impurities [5,10,11]. The latter has proved to be an efficient way to create more oxygen vacancies and to amplify the electrochemical reaction of analytes on the layer's surface [7,12].

In the literature, there are several examples of noble metals (Pd, Pt), rare earth metals (Ce, Pr), and metals (Zn, Al) improving the sensitivity and selectivity of various MOXs including SnO_2 [10,12–16]. Among these materials, magnesium (Mg) is attractive, as it has proved to improve sensitivity to ethanol, H_2 , CO, and ammonia when incorporated into ZnO to form Mg-doped ZnO [17–21]. Similarly, Mg-doped TiO_2 and Mg-doped In_2O_3 have shown to improve sensitivity to CO and ethanol, respectively [3,22]. Mg is also considered a promising candidate to enhance SnO_2 sensing properties, particularly as it presents a close ionic radius (0.67 nm) to that of Sn (0.71 nm), which facilitates Mg^{2+} diffusion into the SnO_2 cell to substitute Sn^{4+} [23]. Despite this, the use of Mg-doped SnO_2 in gas sensing, particularly VOC sensing, is not that common in the state-of-the-art.

In the midst of various techniques used to synthesize doped MOX films, spray pyrolysis proved to be simple, cost effective and allowed a wide variety of substrate coatings [24]. Despite the fact that controlling the size and rate of sprayed droplets remains a challenging factor for films' quality, spray pyrolysis is considered a useful method for the design and development of chemoresistive gas sensors [24,25].

Previously, we proved the spray pyrolysis deposition of SnO_2 films and their potential to detect vapors such as ethanol, methanol and acetone [26]. Herein, we go further into this line and investigate the influence of Mg doping levels on the VOC sensing properties of SnO_2 thin films synthesized via the spray pyrolysis process. This work explores the structural, morphological, and chemical composition properties of the films and their gas sensing properties towards ethanol, acetone and toluene.

2. Materials and Methods

2.1. Thin Film Synthesis and Processing

Magnesium-doped tin dioxide thin films with three doping concentrations (0.8, 1.2, and 1.6 at.%) were synthesized by spray pyrolysis method on cleaned amorphous glass substrate ($70 \times 30 \times 1$ mm) at 400 °C. To obtain a 0.8 at.% Mg-doped SnO_2 film, a mixture of 1088 mg of tin (II) chloride dihydrate ($\text{SnCl}_2 \cdot 2\text{H}_2\text{O}$, Sigma-Aldrich, 98%), 40 mg of magnesium chloride hexahydrate ($\text{MgCl}_2 \cdot 6\text{H}_2\text{O}$, Sigma-Aldrich, 99%), and 100 mL of ethanol (Sigma-Aldrich, 96%) was stirred under heat for 30 min. Afterwards, this solution was sprayed by a nozzle to the heated substrate using airflow (0.5 mL/min) for 30 min. The same process was used to prepare all films, varying the weight ratio of the precursors according to the doping concentrations. The as-prepared Mg-doped SnO_2 thin films were subsequently annealed at 450 °C in dry air for 60 min in order to ensure the stability of the materials during the gas sensing test. The influence of the annealing temperatures on the SnO_2 thin films' properties was reported in our previous work [27]. Finally, the coated samples were cut into parts ($10 \times 15 \times 1$ mm) to be used for characterization and gas tests.

2.2. Characterization Methods

Structural characterization was performed using an X-ray Diffractometer (XRD—Bruker-AXS, LinxEye XE-T detector, KFL Cu 2K (λ (CuK α) = 1.541840 Å) operated at 40 KV and 40 mA) in the 2θ angle from 20° to 80°. X Powder software was employed to refine (peak position, lattice parameters, and crystallites size) the data. The surface morphology was examined by Scanning Electron Microscopy (SEM- Carl Zeiss, Auriga Series) equipped with an EDX spectrometer (Energy Dispersive X-ray Spectroscopy) for elemental composition analysis. The surface properties of the films were analyzed using X-ray Photoelectron Spectroscopy (XPS—Kratos Axis Supra with monochromatic Al K α X-ray radiation, emission current of 15 mA and hybrid lens mode, Manchester, UK) varying the binding energy (BE) range between 0–1350 eV and using CasaXPS for peaks fitting.

2.3. Gas Sensing Measurements

To evaluate the gas sensing properties of Mg-doped SnO₂ thin films towards various gaseous analytes (ethanol, acetone, and toluene), we used the system represented in Figure 1 and reported previously [28]. Briefly, the system consists of a continuous gas supply (dry synthetic air and different calibrated gas analytes) controlled by mass flow controllers (MFC), a test chamber equipped with two probes as the electrical signal collectors, a heating plate with a temperature controller, and a data acquisition system (electronic measurement system, electrometer, and PC). The films were exposed to each analyte for 10 min, and after that, the chamber was purged with synthetic air for 30 min to recover the initial base line resistance. Gas test measurements were recorded fixing the operating temperature (T_{op}) to 160 °C and varying the analyte concentration from 10 to 80 ppm. The gas response is defined as R_a/R_g (reducing gases), where R_a and R_g are the resistances of the film in dry air and after exposure to analyte, respectively, while sensitivity (S), is the report between response and gas concentration ($\Delta R/\Delta C$) [7]. The response and recovery times are defined as the time required for the sensor to reach 90% of the response upon exposure to the target gas, and the time required for a sensor to return to 90% of the original baseline signal upon removal of the target gas, respectively. All samples were alternatively tested towards the target analytes in dry air accumulating a total operating period of 120 h distributed over 30 days. Among these hours, on average, each sample operated for about 20 h. Hereafter, the tested films are labeled as MTO1 (0.8 at.% magnesium-doped tin dioxide), MTO2 (1.2 at.% magnesium-doped tin dioxide), and MTO3 (1.6 at.% magnesium-doped tin dioxide).

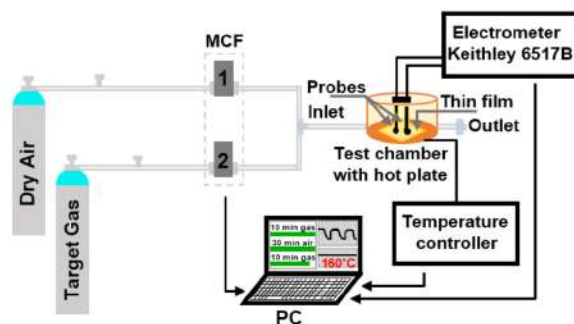


Figure 1. Schematic view of the gas sensing measurement system.

3. Results and Discussion

3.1. Films Analysis and Characterization

X-ray diffraction patterns were evaluated to gain insight into the crystal structure of the Mg-doped SnO₂ thin films. As exhibited in Figure 2, all films are polycrystalline in nature and crystallize in rutile tetragonal tin dioxide (SnO₂) structure (P4₂/mnm space group, ICDD card 72-1147) with a dominant (110) diffraction at 26.53° 2θ approximately. In general, the results show a steady decrease of all SnO₂ diffraction peaks accompanied by a diffraction pattern shift to lower angle values (>0.06° 2θ) as the Mg amount increases in the films. This could be caused in part by the diffusion of Mg²⁺ ions into the SnO₂ lattice and the smaller ionic radii of the guest atom (Mg²⁺: 0.67 Å) compared to the host atom (Sn⁴⁺: 0.71 Å), and also by the lower electronic density of Mg atoms (1.738 g/cm³) compared to Sn atoms (β-Sn = 7.265 g/cm³). The results also indicate a change in the lattice parameters of the Mg-doped SnO₂ thin films (Table 1), which reveal a slight increase in “a” and decrease in “c”, compared to the non-doped SnO₂ film reported in our previous work [27]. In addition, a proportional decrease of the average crystallite size (D) with the increase of the Mg-doping levels can also be observed in Table 1. Overall, these properties suggest the presence of local lattice disorders in the films and, in turn, an increment of surface defects in the Mg-doped samples with respect to the non-doped samples, as noticed earlier in the literature [29].

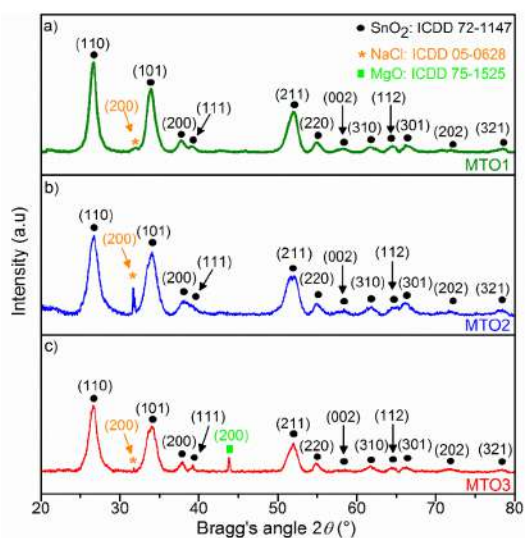


Figure 2. XRD patterns of the Mg-doped SnO₂ thin films, (a) 0.8 at.% magnesium-doped tin dioxide (MTO1); (b) 1.2 at.% magnesium-doped tin dioxide (MTO2); (c) 1.6 at.% magnesium-doped tin dioxide (MTO3).

The ‘extra’ diffraction peak at 43.8° 2θ in the MTO3 pattern is associated with the (200) reflection of MgO in halite structure (ICDD 75-1525). The presence of this diffraction suggests an excess of Mg (over-doping) in MTO3 and the formation of a secondary phase. This is consistent with the unit cell parameters found for MTO3 (Table 1), which show no further change with respect to MTO2, and endorse the fact that the substitution process goes to its saturation. These observations are in agreement with previous reports on Mg-doped SnO₂ by the sol-gel process [30]. Moreover, the Mg-doped SnO₂

patterns also revealed additional diffraction peaks referring to the formation of NaCl crystals (ICDD 05–0628) on the matrix of the films. This could be attributed to the combination of sodium ions (diffused from the glass substrate) and chloride ions (from the metal chloride precursor) to form NaCl crystals [31].

Table 1. Lattice parameters and average crystallite size of the Mg-doped SnO₂ thin films.

Sample	Unit Cell Parameters			Unit Cell Volume	Average Crystallite Size
	$a=b$ (Å)	c (Å)	$\alpha = \beta = \gamma$	$V = a^2c$ (Å ³)	D (nm)
SnO ₂	4.732	3.187	90°	71.39	26 *
MTO1	4.739	3.187	90°	71.58	9.8
MTO2	4.742	3.181	90°	71.51	9.6
MTO3	4.742	3.181	90°	71.51	9.5

* SnO₂ average crystallite size was estimated in our previous work [27].

SEM micrographs of the Mg-doped SnO₂ thin films (Figure 3) display different morphologies with relatively rough topography and irregular particle distribution in all samples. Low magnification SEM images of the films also reveal cracked patterned surfaces after the annealing treatment. Specifically, the SEM images for the MTO1 films (Figure 3a) display the agglomeration of the nanoparticles in cubic shape, whereas the MTO2 films (Figure 3b) show the presence of several hollow microtubes distributed randomly on the surface, and the MTO3 films (Figure 3c) exhibit agglomeration of nanospheres.

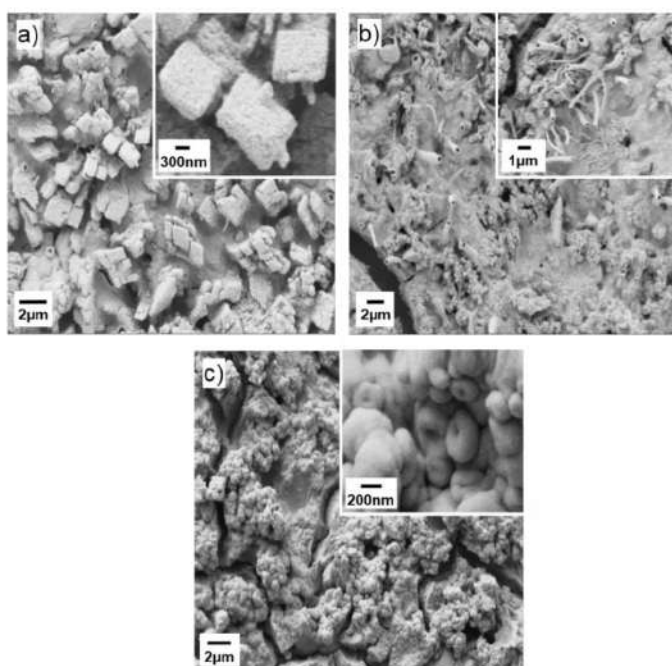


Figure 3. SEM micrographs of the Mg-doped SnO₂ thin films, (a) MTO1; (b) MTO2; (c) MTO3.

EDS analysis corroborated the presence of the three main elements in the films Sn, O, and Mg, with proportional increase of Mg atomic percentage according to the doping level. The presence of other elements, such as Si and Na (associated with the use of glass substrate), and Cl (related to the chloride-based precursors), are also registered and in line with the XRD results. Further properties of the elements at the surface of the films were investigated by XPS.

Figure 4 displays the survey XPS spectrum for each film (i.e., MTO1, MTO2 and MTO3). These spectra show a sharp and intense XPS core level Sn 3d and O 1s peaks around 486.5 eV and 530.3 eV, respectively. The spectra also show minor peaks for Sn 4d_{3/2}, Sn 4p, Sn 4s, C 1s, Mg KLL, Sn 3p_{3/2}, Sn 3p_{1/2}, Sn 3s, O KLL, Sn MNN, and Mg 1s. Na KLL and Cl 2p peaks are also identified in the spectra in concordance with the XRD and EDS results.

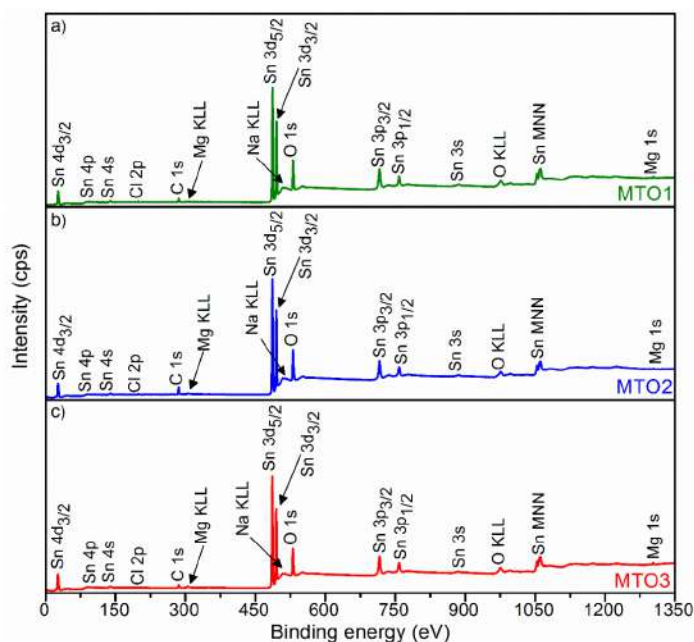


Figure 4. XPS survey spectra of the Mg-doped SnO₂ thin films, (a) MTO1; (b) MTO2; (c) MTO3.

Figure 5 shows the deconvolution of O 1s and Sn 3d XPS core level spectra recorded on the films. The O 1s core level peak exhibits slight asymmetry with a distinct shoulder in all the investigated samples suggesting the presence of three components (Figure 5). The main component centered at ~530.3 eV is assigned to lattice oxygen (O_L) (oxygen directly bounded to a metal atom) [32]. The two other components, found at higher binding energy ~531.6 and ~532.4 eV, are connected with the oxygen vacancies (O_V) mandatory for charge compensation after doping and the chemisorbed oxygen (O_{chem}), respectively, as in the previous literature [33].

The Sn 3d region of the three samples (Figure 5) presents doublets at 486.5 and 494.9 eV for Sn 3d_{5/2} and Sn 3d_{3/2}, respectively. According to the literature [32], the three oxidation states of Sn atoms are defined by three binding energy values as the following Sn⁰ (485.0 eV), Sn²⁺ (485.9 eV), and Sn⁴⁺ (486.6 eV). Our results indicate the absence of Sn⁰ and Sn²⁺ within the films and therefore confirm the Sn⁴⁺ oxidation state and the formation of SnO₂ by spray pyrolysis.

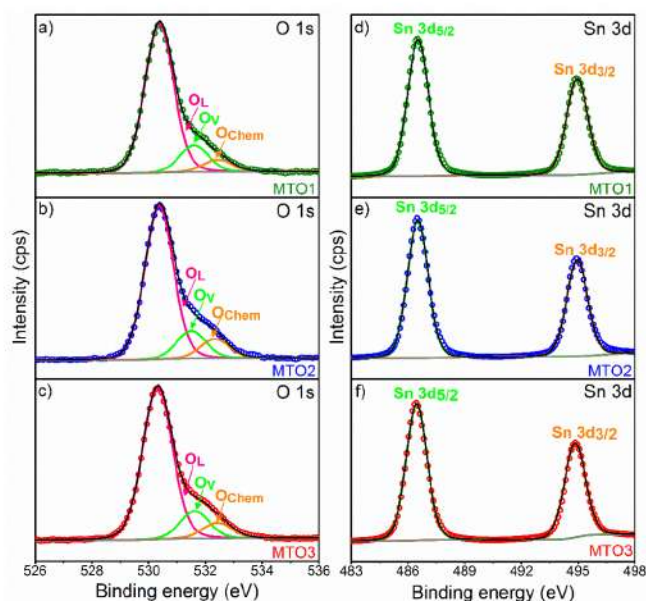


Figure 5. Deconvolution of O 1s (left figure) and Sn 3d (right figure) XPS core level spectra, ((a) and (d)) MTO1; ((b) and (e)) MTO2; ((c) and (f)) MTO3. The circles denote experimental data, colored lines demonstrate the deconvolution of peaks, and the black line corresponds to the sum of peaks fits (envelope).

XPS results also show the Mg 1s core level peak and the Mg KLL Auger emission peak. Estimation of the content of Mg at the samples indicate lower contents for MTO1 and MTO2 (~0.7 at.%) respect to MTO3 (~1 at.%). The results in Figure 6a show the Mg 1s spectrum for the MTO1 and MTO2 films at a lower energy (~1303.6 eV) than that recorded for the MTO3 films, which display a shift to a higher energy (~1303.8 eV) most likely due to the oxidation of Mg [30,34]. The Mg KLL Auger spectrum (Figure 6b–d) supports this fact by showing a component associated to Mg metal in the three samples and a second component (only present in the MTO3 films and shifted 5.2 eV to higher energy) assigned to Mg oxide [35,36]. These results are in line with the MgO diffractions identified by XRD (Figure 2).

Overall, the analysis of the material demonstrates the formation of Mg-doped SnO₂. These results indicate that the morphological differences in the films (i.e., MTO1, MTO2, and MTO3) are attributed to the variation of Mg doping level in the SnO₂ films. The incorporation of the Mg precursor in the spray solution affects the nucleation process and growth conditions of the films. This also slightly deviates the crystalline structure of the doped films (with respect to pristine SnO₂) and, therefore, the film morphology. As the doping reaches a saturation point, the alloy system tends to dissociate and a second phase material emerges (i.e., MgO) causing further change in the growth mechanism and the film morphology. Previously, other authors also observed morphological changes in SnO₂ and ZnO films due to Eu (europium) [37] and Mg doping [38], respectively, and the formation of a MgO second phase material.

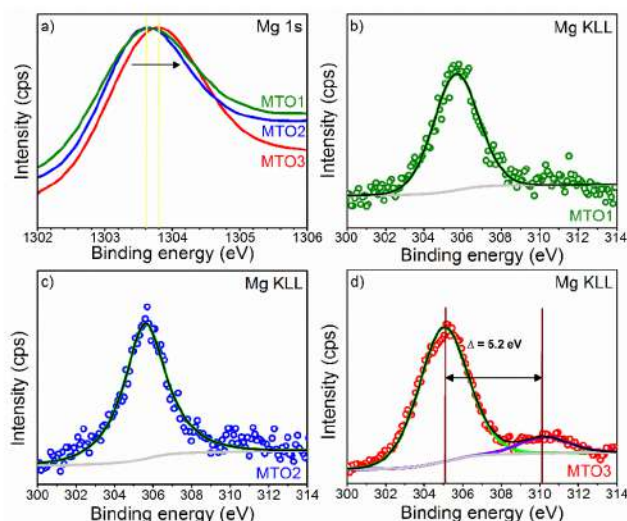


Figure 6. XPS of (a) Mg 1s core level spectra and ((b)–(d)) Mg KLL Auger spectra at MTO1, MTO2, and MTO3. The circles denote experimental data, colored lines demonstrate the deconvolution of peaks, and the black line corresponds to the sum of peaks fits (envelope).

3.2. Gas Sensing Properties

Non-doped and Mg-doped SnO₂ films were exposed consecutively to various reductive gases (ethanol, acetone, and toluene) in a concentration of 80 ppm at an operating temperature (T_{op}) of 160 °C. A summary of the response to each analyte and each sample is presented in Figure 7a. These results reveal low responses for the non-doped SnO₂ film compared to the Mg-doped SnO₂, which show higher responses to the target analytes as the Mg percentage increases in the films (e.g., MTO3 film response to ethanol is almost fourteen times higher than SnO₂ film). In contrast, the response time (Figure 7b) shows a decreasing trend as the Mg percentage increases in the films. Generally, the electrical measurements also revealed an increase of the film electrical resistance by more than five orders of magnitude as the Mg percentage increases from 0 at.% to 1.6 at.%. In addition, the dynamic response to ethanol (Figure 8a) displayed a more reproducible and stable signal for the Mg-doped films compared to the non-doped film, particularly for those doped with a higher Mg concentration (MTO3). Similarly, the dynamic response to acetone and toluene showed reproducible and stable signals as shown in (Figure 8b) for the MTO3 samples. The results in Figures 7 and 8b also show better responses towards ethanol than to acetone and toluene, in proportion to the increase of Mg doping. For instance, the MTO3 film responses were 13.5, 3.1, and 2.3 for a concentration of 80 ppm of ethanol, acetone, and toluene, respectively.

Further testing of the Mg-doped SnO₂ films to various concentrations of ethanol (highest response) and toluene (lowest response) from 10 ppm to 80 ppm displayed a proportional increase of the response with the gas concentration (Figures 9 and 10). We also observe that by increasing the Mg percentage from 0.8 at.% (MTO1) to 1.6 at.% (MTO3), the response to ethanol increases by two times (from 1.6 to 3) for 10 ppm and by four times (from 3.2 to 13.5) for 80 ppm. Coincidentally, we note that the response to ethanol obtained from the MTO1 film to 80 ppm is almost equal to the response obtained from the MTO3 film to 10 ppm. The same behavior, although with lower enhancement than that observed for ethanol, was observed for toluene. Hence, these results demonstrate a major enhancement of the response with the increase of Mg doping in SnO₂ film, especially towards ethanol.

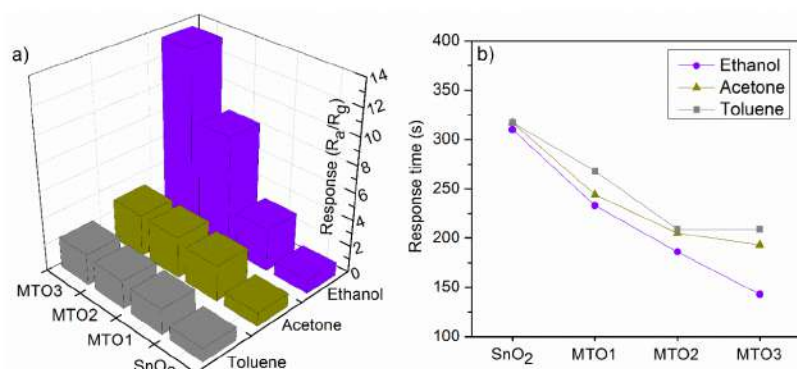


Figure 7. Response (a) and response time (b) towards 80 ppm of ethanol, acetone, and toluene for the non-doped and Mg-doped SnO₂ films.

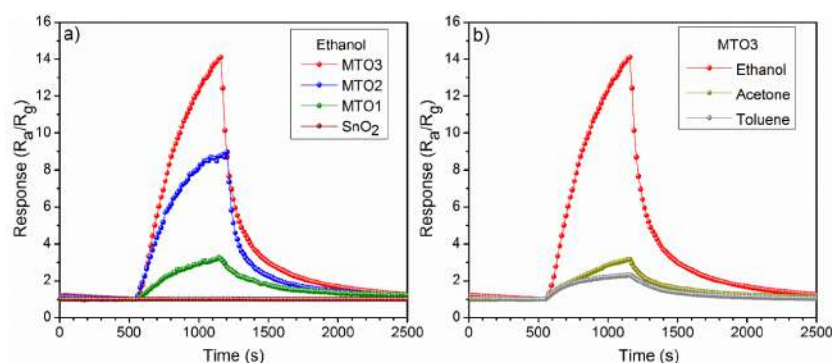


Figure 8. Response of the (a) non-doped and Mg-doped SnO₂ films to 80 ppm of ethanol and (b) MTO3 response to 80 ppm of toluene, acetone, and ethanol recorded at 160 °C.

Similarly, the film doping level also influences the sensitivity of the films (Figure 11), which could be favorable for tuning of the cross-sensitivity (ΔS). Thus, we observed lower cross-sensitivity and in turn, better selectivity between ethanol and toluene for the samples with higher doping levels ($\Delta S = 8.8$ for MTO2 and $\Delta S = 13.9$ for MTO3) as compared to the sample with low doping concentration ($\Delta S = 1.6$ for MTO1). Thus, the results suggest partial selectivity to ethanol, particularly for the MTO3 films.

Further analysis of the dynamic response of the films (Figure 9) shows that the response time (Figure 12) for ethanol and toluene is inversely related to the gas concentration in both cases. For instance, for ethanol at 80 ppm, the response time decreases from 233 s (MTO1) to 143 s (MTO3), which is 90 s faster, by doubling the Mg percentage in the SnO₂ film (from 0.8 at.% to 1.6 at.%). Similar behavior is observed for toluene with a response time decrease of 59 s for MTO3 with respect to MTO1. The results also show a complete recovery of the base line in the three systems, which is accelerated by increasing the Mg percentage in the films (Figure 9).

Overall, the films displayed a low drift of the baseline resistance during each test, most likely connected with the low operating temperature. Despite this, the response magnitudes did not show significant changes. Generally, the MTO3 films showed better medium-term stability displaying 8%

and 6% less deviation in the base line resistance during the whole testing period (see experimental section) compared to the MTO1 and MTO2 films, respectively. Further analysis after the testing period and after having exposed the films to all target analytes showed no significant changes in the main core levels XPS spectrum of tin, magnesium, and oxygen, supporting the stability of the film.

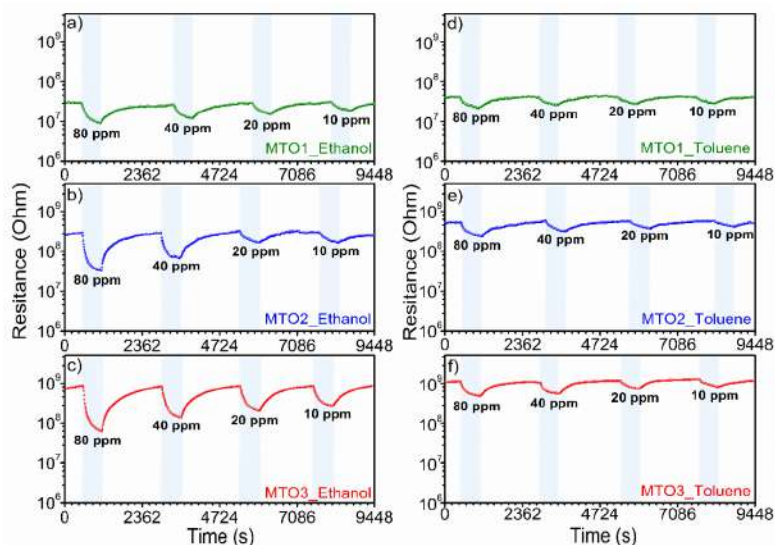


Figure 9. Dynamic response curves of Mg-doped SnO_2 films at different concentrations of ethanol (left figure) and toluene (right figure).

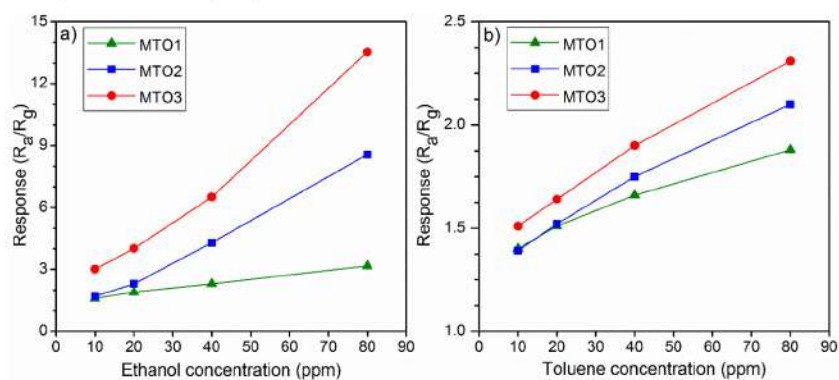


Figure 10. Response of Mg-doped SnO_2 films vs. (a) ethanol and (b) toluene concentration at 160°C .

Table 2 presents a comparison of our results and those for other materials in the literature. The table summarizes the material synthesis method, testing conditions (concentration, operating temperature), and response reported to ethanol and toluene. In this summary, one can notice the use of various materials for sensing both gases, including intrinsic oxides (e.g., SnO_2 , WO_3 , Fe_2O_3) and modified (e.g., SnO_2/ZnO , $\text{SnO}_2/\text{MgAl}_2\text{O}_4$) or doped (Mg-doped ZnO , Pr-doped SnO_2) oxides. Despite the

comparison of the data being complex, as gas sensing results depend on not only the sensing material but also the test conditions, we consider these data still meaningful to offer a general idea of the properties of our samples. Overall, we observe that our results are in agreement with the literature and that the responses recorded to ethanol and toluene with our samples are higher or in the same order at a comparatively lower operating temperature (160 °C) and lower concentration (80 ppm) than other works (which show operating temperatures above 200 °C and typically concentrations of 100 ppm). The response time recorded for the works in the literature is in general in the same order of magnitude (hundreds of seconds) as for our films. Table 2 also includes an example of a similar system (i.e., Mg-doped SnO₂ via spray pyrolysis) although tested towards a different analyte (LPG—liquid petroleum gas). The response (1.4) of this system to 1000 ppm of LPG was registered at 285 °C.

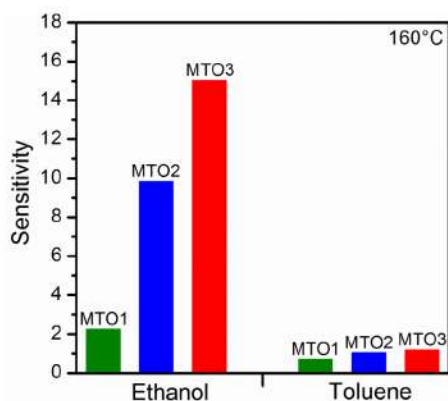


Figure 11. Sensitivity of the Mg-doped SnO₂ films to ethanol and toluene.

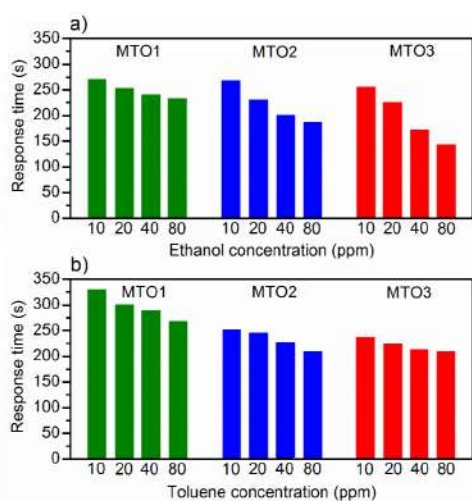


Figure 12. Response time to various concentrations of (a) ethanol, and (b) toluene.

Table 2. Summary of the materials, testing conditions and responses to ethanol and toluene reported in the literature and in our work for MTO3.

Material	Method	Morphology	Concentration (ppm)	T _{op} (°C)	R _a /R _g	t _{res} (s)	Ref
Mg-doped SnO ₂	Spray pyrolysis	Nanospheres	Ethanol 80	160	13.5	143	This work
SnO ₂ /MgAl ₂ O ₄	solid-state and sol-gel	Nanocomposites	Ethanol 100	227	3.33 *	–	[39]
Au/Mg-TiO ₂ /SnO ₂	Hydrothermal	Heterostructure nanosheets	Ethanol 50	260	7	–	[40]
Mg-doped ZnO	RF magnetron sputtering	Rod-like	Ethanol 50	100	2.32 *	–	[19]
Ce-doped SnO ₂	Cosputtering	Nanostructures	Ethanol 100	225	5	4	[14]
Zn-doped SnO ₂	Hydrothermal	Hierarchical architectures	Ethanol 100	213	13.8	–	[16]
SnO ₂ /ZnO	Hydrothermal	Nanostructures	Ethanol 100	400	6.2	–	[41]
Al-doped SnO ₂	Chemical synthesis	powders	Ethanol 100	280	35.25	–	[12]
Pr-doped SnO ₂	Electro-spinning	Hollow nanofibers	Ethanol 100	300	28.62	168	[15]

Table 2. Cont.

Material	Method	Morphology	Concentration (ppm)	T _{op} (°C)	R _a /R _g	t _{res} (s)	Ref
Mg-doped SnO₂	Spray pyrolysis	Nanospheres	Toluene 80	160	2.3	209	This work
SnO ₂	Hydrothermal	Flower microstructures	Toluene 10	250	1	–	[42]
Pt-doped SnO ₂	LPCVD	Island-like structures	Toluene 25	440	6	–	[13]
PdO-decorated ZnO	Hydrothermal	Flower nanostructures	Toluene 100	160	1.9	–	[7]
Fe ₂ O ₃	Hydrothermal	Nanoshuttles	Toluene 100	440	2.3	5	[43]
Co ₃ O ₄	Solvothermal	Nanorods	Toluene 200	120	3	–	[44]
WO ₃	Vapor phase synthesis	Nanoneedles	Toluene 100	250	2.2	398	[6]
Pt@WO ₃	Vapor phase synthesis	NPs@NNs	Toluene 100	250	7	100	[6]
Fe ₂ O ₃ @WO ₃	Vapor phase synthesis	NPs@NNs	Toluene 100	250	8	150	[6]
Mg-doped SnO ₂	Spray pyrolysis	Leaf-like grains	LPG 1000	285	1.4 *	–	[45]

T_{op}: temperature of operation, t_{res}: response time, * R_a/R_g calculated from [19,39,45]

3.3. Gas Sensing Mechanism

Generally, the gas sensing results showed that all films behave as typical n-type semiconductors when exposed to gases, i.e., decreasing the overall electrical resistance in the presence of reducing gases such as ethanol, acetone, and toluene. This is consistent with the most accepted sensing mechanism model proposed in the literature for pristine metal oxides including SnO_2 [46]. According to this model (Figure 13a), when SnO_2 film is exposed to air, oxygen molecules are adsorbed at the surface and form oxygen ions [47,48] (in our case O_2^- is formed because the operating temperature is 160°C [11]), thus extracting electrons from the conduction band. As a result of this electron transfer, a depletion layer is formed and the film electrical resistance is increased. As soon as SnO_2 film is exposed to a desired concentration of a reducing gas, such as ethanol, acetone or toluene, the reductive gas molecules will interact with oxygen negative ions and transfer the electrons back to the SnO_2 conductive band. Therefore, the depletion layer narrows and the film electrical resistance decreases [46].

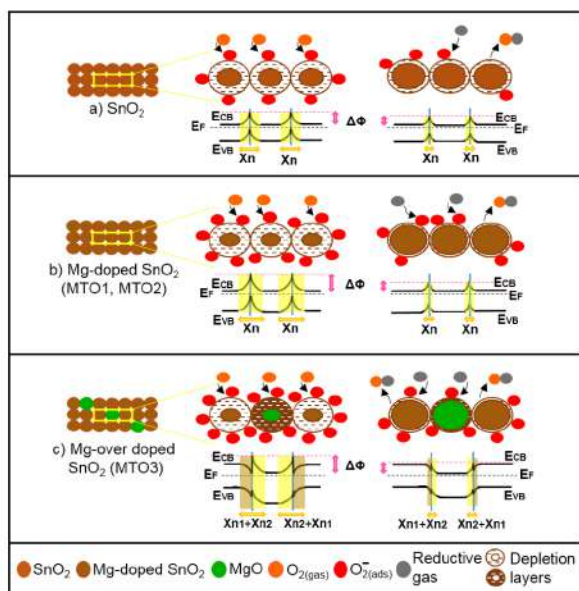


Figure 13. Schematic representation of the gas sensing mechanisms of (a) non-doped and (b and c) Mg-doped SnO_2 films in air (left) and reductive gas (right). E_{CB} is the bottom of conduction band; E_F is the bulk Fermi level; E_{VB} is the top of valence band; $\Delta\Phi$ is the built-in potential barrier; X_n , and X_{n2} are depth of the depletion layer from the surface; X_{n1} is the depth of the accumulation layer from the surface (not to scale).

This mechanism is similar for the Mg-doped films (Figure 13b). However, in this system the incorporation of Mg into the SnO_2 structure enhances the sensing mechanism due to the lattice disorder introduced by the substitution of Sn^{4+} ions by Mg^{2+} ions and the subsequent diminution of the crystallite size by nearly three times with respect to the pristine SnO_2 films (Table 1). Then, more reactive oxygen molecules are adsorbed in the pre-adsorption cycle and available to interact with the reductive gases [16,49].

The mechanism for the over-doped films (Figure 13c), however, includes a new component, introduced by the second phase particles (i.e., MgO) rather than by the change in crystalline size

(notice the crystallite size of MTO1, MTO2, and MTO3 is similar). The presence of second phase particles with low loadings enhances further the sensing mechanism via a 'spillover effect' [50], which can be connected with the faster response and recovery time of MTO3 with respect to MTO2 and MTO1. The second phase particles also introduce an extra potential barrier formed between the MgO and Mg-doped SnO₂ (heterojunction). This extra potential barrier may accumulate or deplete extra-pre-adsorbed oxygen in the boundary grain to grain, thus maximizing the electrical resistance change in the gas (analyte) adsorption stage, as noticed earlier for other gas sensitive materials with nanoscaled heterojunctions [6,51].

On the other hand, the visibly different morphologies in the films, as result of the Mg doping, could also play a role in the sensing performance by providing a different electrical percolation and possible fluctuations (noise) in the grain boundaries. Although the current dc measurements do not give evidence of the level of these fluctuations, we cannot rule out the presence of a parallel mechanism dependent on the grain boundaries, as noticed previously for ethanol and hydrogen by low-frequency noise measurements [52].

4. Conclusions

Mg-doped SnO₂ thin films synthesized via a spray pyrolysis method were investigated for ethanol, acetone, and toluene sensing. Overall, the Mg-doped SnO₂ films proved a more reproducible sensing behavior with complete recovery of the base line resistance compared to the non-doped SnO₂ films. This paper proposes that increasing the Mg-doping level (from 0.8 at.% to 1.6 at.%) is responsible for the improvement of the sensing properties due to the decrease in the crystallites' size and to the increase in defects in the SnO₂ films. The results indicate that this remarkable improvement is also connected with the formation of MgO, which favors the spillover effects at the film and incorporates extra potential barriers formed between the MgO and the Mg-doped SnO₂ grains. Both components (i.e., size reduction and the incorporation of MgO) play an important role in enhancing the ethanol sensing behavior of SnO₂, and thus, the response of the 1.6 at.% Mg-doped SnO₂ films is four times higher and 90 s faster than the response of the 0.8 at.% Mg-doped SnO₂ films.

Author Contributions: All authors (B.B., M.T., N.E.H.T., I.G., S.V. and F.M.) have read and agreed to the published version of the manuscript. B.B. and S.V. wrote the main manuscript text. B.B., N.E.H.T., and F.M. were involved in the synthesis and analysis of the material and B.B., M.T., I.G., and S.V. were involved in the experimental work and/or results analysis of the gas sensing tests. All authors have read and agreed to the published version of the manuscript.

Funding: This work was supported by the Spanish Ministry of Economy and Competitiveness via project TEC2016-79898-C6-1-R (AEI/FEDER, EU) and the 'Ramón y Cajal' Programme. Part of this research used the Czech CEITEC Nano Research Infrastructure, supported by MEYS (2016–2019).

Acknowledgments: We acknowledge the support of MINECO (Spain) via project TEC2016-79898-C6-1-R (AEI/FEDER, EU), and MEYS (Czech Republic) via the Czech CEITEC Nano Research Infrastructure. B.B. thanks the Electronic department of Frères Mentouri University, Constantine, Algeria for granting the excellent doctoral student scholarship. S.V. thanks the support of the 'Ramón y Cajal' Programme. We are grateful to Milena Šetka for acquiring the XPS spectra.

Conflicts of Interest: The authors declare no conflict of interest.

References

1. Schütze, A.; Baur, T.; Leidinger, M.; Reimringer, W.; Jung, R.; Conrad, T.; Sauerwald, T. Highly Sensitive and Selective VOC Sensor Systems Based on Semiconductor Gas Sensors: How to? *Environment* **2017**, *4*, 20. [CrossRef]
2. Yoon, J.-W.; Lee, J.-H. Toward breath analysis on a chip for disease diagnosis using semiconductor-based chemiresistors: Recent progress and future perspectives. *LAB CHIP* **2017**, *17*, 3537–3557. [CrossRef] [PubMed]
3. Kumar, M.; Gupta, A.K.; Kumar, D. Mg-doped TiO₂ thin films deposited by low cost technique for CO gas monitoring. *Ceram. Int.* **2016**, *42*, 405–410. [CrossRef]

4. Vallejos, S.; Gràcia, I.; Lednický, T.; Vojtkuvka, L.; Figueras, E.; Hubálek, J.; Cané, C. Highly hydrogen sensitive micromachined sensors based on aerosol-assisted chemical vapor deposited ZnO rods. *Sens. Actuators B Chem.* **2018**, *268*, 15–21. [CrossRef]
5. Vallejos, S.; Selina, S.; Annanouch, F.E.; Gràcia, I.; Llobet, E.; Blackman, C. Aerosol assisted chemical vapour deposition of gas sensitive SnO₂ and Au-functionalised SnO₂ nanorods via a non-catalysed vapour solid (VS) mechanism. *Sci. Rep.* **2016**, *6*, 28464. [CrossRef] [PubMed]
6. Vallejos, S.; Gràcia, I.; Figueras, E.; Cané, C. Nanoscale heterostructures based on Fe₂O₃@WO_{3-x} nanoneedles and their direct integration into flexible transducing platforms for toluene sensing. *ACS Appl. Mater. Interfaces* **2015**, *7*, 18638–18649. [CrossRef]
7. Lou, Z.; Deng, J.; Wang, L.; Wang, L.; Fei, T.; Zhang, T. Toluene and ethanol sensing performances of pristine and PdO-decorated flower-like ZnO structures. *Sens. Actuators B Chem.* **2013**, *176*, 323–329. [CrossRef]
8. Fu, J.; Zhao, C.; Zhang, J.; Peng, Y.; Xie, E. Enhanced gas sensing performance of electrospun Pt-functionalized NiO nanotubes with chemical and electronic sensitization. *ACS Appl. Mater. Interfaces* **2013**, *5*, 7410–7416. [CrossRef]
9. Tomić, M.; Šetka, M.; Chmela, O.; Gràcia, I.; Figueras, E.; Cané, C.; Vallejos, S. Cerium Oxide-Tungsten Oxide Core-Shell Nanowire-Based Microsensors Sensitive to Acetone. *Biosensors* **2018**, *8*, 116. [CrossRef]
10. Zhang, Q.; Zhou, Q.; Lu, Z.; Wei, Z.; Xu, L.; Gui, Y. Recent advances of SnO₂-based sensors for detecting fault characteristic gases extracted from power transformer oil. *Front. Chem.* **2018**, *6*, 364. [CrossRef]
11. Belmonte, J.C.; Manzano, J.; Arbiol, J.; Cirera, A.; Puigcorbe, J.; Vila, A.; Sabate, N.; Gracia, I.; Cane, C.; Morante, J. Micromachined twin gas sensor for CO and O₂ quantification based on catalytically modified nano-SnO₂. *Sens. Actuators B Chem.* **2006**, *114*, 881–892. [CrossRef]
12. Liu, S.; Sun, Q.; Wang, J.; Hou, H. Charge imbalance induced oxygen-adsorption enhances the gas-sensing properties of Al-doped SnO₂ powders. *J. Phys. Chem. Solids* **2019**, *124*, 163–168. [CrossRef]
13. Kang, J.-g.; Park, J.-S.; Lee, H.-J. Pt-doped SnO₂ thin film based micro gas sensors with high selectivity to toluene and HCHO. *Sens. Actuators B Chem.* **2017**, *248*, 1011–1016. [CrossRef]
14. Liang, Y.-C.; Lee, C.-M.; Lo, Y.-J. Reducing gas-sensing performance of Ce-doped SnO₂ thin films through a cosputtering method. *RSC Adv.* **2017**, *7*, 4724–4734. [CrossRef]
15. Li, W.; Ma, S.; Li, Y.; Li, X.; Wang, C.; Yang, X.; Cheng, L.; Mao, Y.; Luo, J.; Gengzang, D. Preparation of Pr-doped SnO₂ hollow nanofibers by electrospinning method and their gas sensing properties. *J. Alloy. Compd.* **2014**, *605*, 80–88. [CrossRef]
16. Guan, Y.; Wang, D.; Zhou, X.; Sun, P.; Wang, H.; Ma, J.; Lu, G. Hydrothermal preparation and gas sensing properties of Zn-doped SnO₂ hierarchical architectures. *Sens. Actuators B Chem.* **2014**, *191*, 45–52. [CrossRef]
17. Amin, M.; Shah, N.A.; Bhatti, A.S.; Malik, M.A. Effects of Mg doping on optical and CO gas sensing properties of sensitive ZnO nanobelts. *CrystEngComm* **2014**, *16*, 6080–6088. [CrossRef]
18. Goudarzi, S.; Khojier, K. Role of substrate temperature on the ammonia gas sensing performance of Mg-doped ZnO thin films deposited by spray pyrolysis technique: Application in breath analysis devices. *Appl. Phys. A* **2018**, *124*, 601. [CrossRef]
19. Vinoth, E.; Gowrishankar, S.; Gopalakrishnan, N. Effect of Mg doping in the gas-sensing performance of RF-sputtered ZnO thin films. *Appl. Phys. A* **2018**, *124*, 433. [CrossRef]
20. Karthick, K.; Srinivasan, D.; Christopher, J.B. Fabrication of highly c-axis Mg doped ZnO on c-cut sapphire substrate by rf sputtering for hydrogen sensing. *J. Mater. Sci-Mater. Elec.* **2017**, *28*, 11979–11986. [CrossRef]
21. Kwak, C.-H.; Woo, H.-S.; Abdel-Hady, F.; Wazzan, A.; Lee, J.-H. Vapor-phase growth of urchin-like Mg-doped ZnO nanowire networks and their application to highly sensitive and selective detection of ethanol. *Sens. Actuators B Chem.* **2016**, *223*, 527–534. [CrossRef]
22. Jo, Y.-M.; Lee, C.-S.; Wang, R.; Park, J.-S.; Lee, J.-H. Highly sensitive and selective ethanol sensors using magnesium doped indium oxide hollow spheres. *J. Korean Ceram. Soc.* **2017**, *54*, 303–307. [CrossRef]
23. He, H.; Xie, Z.; Li, Q.; Niu, H. On the possibility of p-type doping of SnO₂ with Mg: A first-principles study. *J. Comput. Mater. Sci.* **2015**, *101*, 62–65. [CrossRef]
24. Khatami, S.M.N. Modeling and Spray Pyrolysis Processing of Mixed Metal Oxide Nano-Composite Gas Sensor Films. Ph.D. Thesis, University of Central Florida, Orlando, FL, USA, 2014. Available online: <http://purl.fcla.edu/fcla/etd/CFE0005817> (accessed on 11 March 2020).
25. Falcony, C.; Aguilar-Frutis, M.A.; García-Hipólito, M. Spray pyrolysis technique; high-K dielectric films and luminescent materials: A review. *Micromachines* **2018**, *9*, 414. [CrossRef] [PubMed]

26. Touidjen, N.H.; Bendahmane, B.; Lamri Zeggag, M.; Mansour, F.; Aida, M. SnO₂ thin film synthesis for organic vapors sensing at ambient temperature. *Sens. Biosensing Res.* **2016**, *11*, 52. [CrossRef]
27. Bendahmane, B.; Touidjen, N.H.; Mansour, F. Characterization of SnO₂ Thin Films Fabricated by Chemical Spray Pyrolysis. In Proceedings of the International Conference on Advanced Electrical Engineering (ICAEE), Algiers, Algeria, 19–21 November 2019; IEEE, 2020; pp. 1–6. [CrossRef]
28. Vallejos, S.; Gracia, I.; Chmela, O.; Figueras, E.; Hubálek, J.; Cané, C. Chemoresistive micromachined gas sensors based on functionalized metal oxide nanowires: Performance and reliability. *Sens. Actuators B Chem.* **2016**, *235*, 525–534. [CrossRef]
29. Shajira, P.; Bushiri, M.J.; Nair, B.B.; Prabhu, V.G. Energy band structure investigation of blue and green light emitting Mg doped SnO₂ nanostructures synthesized by combustion method. *J. Lumin.* **2014**, *145*, 425–429. [CrossRef]
30. Mazumder, N.; Bharati, A.; Saha, S.; Sen, D.; Chattopadhyay, K. Effect of Mg doping on the electrical properties of SnO₂ nanoparticles. *Curr. Appl. Phys.* **2012**, *12*, 975–982. [CrossRef]
31. Papadopoulos, N.; Tsakiridis, P.; Hristoforou, E. Structural and electrical properties of undoped SnO₂ films developed by a low cost CVD technique with two different methods: Comparative study. *J. Opt. Adv. Mat.* **2005**, *7*, 2693–2706. Available online: <https://dspace.lib.ntua.gr/xmlui/handle/123456789/16827> (accessed on 11 March 2020).
32. Kwoka, M.; Ottaviano, L.; Passacantando, M.; Santucci, S.; Czempik, G.; Szuber, J. XPS study of the surface chemistry of L-CVD SnO₂ thin films after oxidation. *Thin Solid Films* **2005**, *490*, 36–42. [CrossRef]
33. Aragón, F.H.; Gonzalez, I.; Coaquira, J.A.; Hidalgo, P.; Brito, H.F.; Ardisson, J.D.; Macedo, W.A.; Morais, P.C. Structural and surface study of praseodymium-doped SnO₂ nanoparticles prepared by the polymeric precursor method. *J. Phys. Chem. C* **2015**, *119*, 8711–8717. [CrossRef]
34. Huang, Q.; Li, X.; Liu, T.; Wu, H.; Liu, X.; Feng, Q.; Liu, Y. Enhanced SaOS-2 cell adhesion, proliferation and differentiation on Mg-incorporated micro/nano-topographical TiO₂ coatings. *Appl. Surf. Sci.* **2018**, *447*, 767–776. [CrossRef]
35. Zhou, Y.; Peng, J.; Wang, M.; Mo, J.; Deng, C.; Zhu, M. Tribochemical Behavior of Pure Magnesium During Sliding Friction. *Metals* **2019**, *9*, 311. [CrossRef]
36. Dubecký, F.; Kindl, D.; Hubík, P.; Mičušík, M.; Dubecký, M.; Boháček, P.; Vanko, G.; Gombia, E.; Nečas, V.; Mudroň, J. A comparative study of Mg and Pt contacts on semi-insulating GaAs: Electrical and XPS characterization. *Appl. Surf. Sci.* **2017**, *395*, 131–135. [CrossRef]
37. Kaur, H.; Bhatti, H.S.; Singh, K. Europium doping effect on 3D flower-like SnO₂ nanostructures: Morphological changes, photocatalytic performance and fluorescence detection of heavy metal ion contamination in drinking water. *RSC Adv.* **2019**, *9*, 37450–37466. [CrossRef]
38. Jayanthi, K.; Chawla, S.; Sood, K.; Chhibara, M.; Singh, S. Dopant induced morphology changes in ZnO nanocrystals. *Appl. Surf. Sci.* **2009**, *255*, 5869–5875. [CrossRef]
39. Nithyavathy, N.; Arunmetha, S.; Vinoth, M.; Sriram, G.; Rajendran, V. Fabrication of Nanocomposites of SnO₂ and MgAl₂O₄ for Gas Sensing Applications. *J. Electron. Mater.* **2016**, *45*, 2193–2205. [CrossRef]
40. Xu, H.; Ju, D.; Chen, Z.; Han, R.; Zhai, T.; Yu, H.; Liu, C.; Wu, X.; Wang, J.; Cao, B. A novel hetero-structure sensor based on Au/Mg-doped TiO₂/SnO₂ nanosheets directly grown on Al₂O₃ ceramic tubes. *Sens. Actuators B Chem.* **2018**, *273*, 328–335. [CrossRef]
41. Khoang, N.D.; Van Duy, N.; Hoa, N.D.; Van Hieu, N. Design of SnO₂/ZnO hierarchical nanostructures for enhanced ethanol gas-sensing performance. *Sens. Actuators B Chem.* **2012**, *174*, 594–601. [CrossRef]
42. Tian, J.; Wang, J.; Hao, Y.; Du, H.; Li, X. Toluene sensing properties of porous Pd-loaded flower-like SnO₂ microspheres. *Sens. Actuators B Chem.* **2014**, *202*, 795–802. [CrossRef]
43. Wang, S.; Wang, Y.; Zhang, H.; Gao, X.; Yang, J.; Wang, Y. Fabrication of porous α-Fe₂O₃ nanoshuttles and their application for toluene sensors. *RSC Adv.* **2014**, *4*, 30840–30849. [CrossRef]
44. Wang, L.; Deng, J.; Lou, Z.; Zhang, T. Nanoparticles-assembled Co₃O₄ nanorods p-type nanomaterials: One-pot synthesis and toluene-sensing properties. *Sens. Actuators B Chem.* **2014**, *201*, 1–6. [CrossRef]
45. Thomas, B.; Skariah, B. Spray deposited Mg-doped SnO₂ thin film LPG sensor: XPS and EDX analysis in relation to deposition temperature and doping. *J. Alloy. Compd.* **2015**, *625*, 231–240. [CrossRef]
46. Barsan, N.; Weimar, U. Conduction model of metal oxide gas sensors. *J. Electroceram.* **2001**, *7*, 143–167. [CrossRef]

47. Lenaerts, S.; Roggen, J.; Maes, G. FT-IR characterization of tin dioxide gas sensor materials under working conditions. *Spectrochim. Acta A* **1995**, *51*, 883–894. [[CrossRef](#)]
48. Sinha, M.; Mahapatra, R.; Mondal, B.; Maruyama, T.; Ghosh, R. Ultrafast and reversible gas-sensing properties of ZnO nanowire arrays grown by hydrothermal technique. *J. Phys. Chem. C* **2016**, *120*, 3019–3025. [[CrossRef](#)]
49. Xu, C.; Tamaki, J.; Miura, N.; Yamazoe, N. Grain size effects on gas sensitivity of porous SnO₂-based elements. *Sens. Actuators B Chem.* **1991**, *3*, 147–155. [[CrossRef](#)]
50. Kohl, D. The role of noble metals in the chemistry of solid-state gas sensors. *Sens. Actuators B Chem.* **1990**, *1*, 158–165. [[CrossRef](#)]
51. Miller, D.R.; Akbar, S.A.; Morris, P.A. Nanoscale metal oxide-based heterojunctions for gas sensing: A review. *Sens. Actuators B Chem.* **2014**, *204*, 250–272. [[CrossRef](#)]
52. Ederth, J.; Smulko, J.; Kish, L.B.; Heszler, P.; Granqvist, C.G. Comparison of classical and fluctuation-enhanced gas sensing with Pd₂WO₃ nanoparticle films. *Sens. Actuators B Chem.* **2006**, *113*, 310–315. [[CrossRef](#)]



© 2020 by the authors. Licensee MDPI, Basel, Switzerland. This article is an open access article distributed under the terms and conditions of the Creative Commons Attribution (CC BY) license (<http://creativecommons.org/licenses/by/4.0/>).

Appendix B

Collaborative Journal Article 2

Encapsulation of micro-sized barium ferrate(VI) and its effectiveness in removing clomazone pesticide from water, Nikolić Bujanović, Lj., Čekerevac, M., Simičić, M., Tomić, M., Journal of Materials Science, 2020, 55(17), 7295, doi: 10.1007/s10853-020-04519-4.



Encapsulation of micro-sized barium ferrate(VI) and its effectiveness in removing clomazone pesticide from water

Ljiljana Nikolić Bujanović^{1,*}, Milan Čekerevac¹, Miloš Simičić¹, and Milena Tomić¹

¹ Research and Development Center, IHIS Techno-Experts, Batajnički put 23, Belgrade, Serbia

Received: 7 November 2019

Accepted: 26 February 2020

Published online:

6 March 2020

© Springer Science+Business Media, LLC, part of Springer Nature 2020

ABSTRACT

Synthesis of micro- and nano-sized crystalline BaFeO₄ particles by precipitation from the electrochemically synthesized potassium ferrate(VI) solution by means of barium hydroxide and its encapsulation in paraffin wax were explored using scanning electron microscopy, X-ray diffraction spectroscopy and FTIR spectroscopy. Experimental results showed effective synthesis of the micro-sized and nano-sized BaFeO₄ particles and their coating by the paraffin wax layer. The encapsulated micro- and nano-sized particles of BaFeO₄ were applied in investigating the possibility of degradation of pesticide clomazone in water. The removal of clomazone from water by oxidation using encapsulated BaFeO₄ could be almost 95%.

Introduction

Pesticides are biologically active compounds produced for use in agriculture in order to prevent or limit harmful effects of biological agents, such as insects, rodents, causal agents of plant diseases, undesirable plant species (weeds) and others. However, application of pesticides is often accompanied by the risk of adverse consequences for the environment.

The frequent occurrence of pesticides in wastewater together with other pollutants has led to increased concern for human health, due to their high toxicity, bioaccumulation, carcinogenicity, mutagenicity and endocrine-disrupting effects [1–4].

According to European Union Directive 98/83/EC (1998), the maximum allowable concentration for the pesticide present in drinking water is 0.10 mg/dm³, while the total concentration of pesticides should not be greater than 0.50 g/dm³. The herbicide clomazone (2-[(2-chlorophenyl)methyl]-4,4-dimethyl-3-isoxazolidinone) is particularly widely used against species of annual broadleaf weeds and grass. It is highly effective in weed control in the cultivation of soybeans, cotton, rice, sugar cane, corn, tobacco and a variety of other vegetable crops [5, 6]. However, due to its high water solubility (1100 mg/l) and long half-life dissipation, averaging from 28 to 84 days, it can cause groundwater contamination [6].

Address correspondence to E-mail: mimosa@eunet.rs

The development of oxidative decomposition processes results in new treatment processes in the field of chemical water treatment, known as advanced oxidation processes (AOPs), which include ozonization, electrochemical water oxidation that produces powerful oxidative species, use of peroxy acids and salts and tetraoxo-ferrate(VI) salts [7]. The relative stability of pesticides in the environment, as well as their slow decomposition by photolysis or transformation to toxic products, has led to the need to develop new technologies for purification of water polluted by pesticides. Biodegradation and photodegradation are used as the main techniques in wastewater treatment [8, 9]. However, the above method does not have wide application in industry, mainly because of the long process of purification and low efficiency when the concentration of pollutants is small. Likewise, wastewater containing pesticides cannot be effectively treated by biological methods, due to their toxicity to microorganisms and because their biodegradability is not possible [10].

Application of ferrate(VI) salts in the treatment of water of various origins showed high efficiency and cost-effectiveness compared to conventional methods. It has been shown that ferrate(VI) as environmentally safe compounds could be used as oxidizing agents in various processes of chemical synthesis, strong disinfectants which destroy pathogenic organisms, means for coagulation and flocculation, agents for decontamination of toxins of chemical and biological origins, agents for heavy metal removal from water and wastewater and agents for removal of radioactive elements from radioactive wastewater [11–18].

If kept dry and in a vacuum, solid ferrate(VI) compounds can be stored for years without notable degradation. Hence, there is necessity for its stabilization after synthesis to suppress its decomposition before use [19, 20]. In the neutral and lower pH values of water solutions, ferrate(VI) decompose rapidly, because of water oxidation, as ferrate(VI) redox potential increases with the decrease in solution pH value [21]. Therefore, ferrate(VI) is stabilized by pH adjustment over the value of 10 and by complexation of transition metals cations, which could promote ferrate(VI) decomposition. Also, the partial exchange of iron(VI) (Fe(VI)) in the ferrate(VI) with its isomorphs (Si(VI), S(VI)) can increase its stability [22, 23]. Further, ferrate(VI) salts' stability in water is substantially increased if during the ferrate(VI) salt

synthesis the cations of alkali metals in ferrate(VI) are substituted with the cations of alkaline earth metals, Ba, Ca or Sr [24, 25]. Such ferrate(VI) salts are stable even in moderately acidic aqueous solutions, because of the much slower kinetics of water oxidation by them. Hence, we decided to use barium ferrate(VI) for treatment of clomazone-contaminated water.

Micro-encapsulation modifies properties of a core material, and it is used to control a core material's release characteristics and to improve its stability by protecting it from environmental conditions, which would promote core material decomposition. Paraffin is found to be a good material for encapsulation [26, 27].

Here, we report the results of the experimental coating procedure of micro- and nano-dimensional BaFeO_4 crystallites with paraffin dissolved in cyclohexane and the possibility of using encapsulated BaFeO_4 in the process of removing pesticide clomazone from water.

Materials and methods

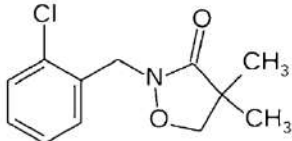
Chemicals

All chemicals were of reagent grade and were used without further purification. Clomazone, 98.8%, pestanal quality, was manufactured by Riedel-de Haën. The chemical structure and main characteristics of pesticide clomazone are presented in Table 1. 35% HCl was obtained from Lachema (Neratovice, Czech Republic), NaOH and KOH from ZorkaPharm (Šabac, Serbia), $\text{Ba}(\text{OH})_2$ from Merck, 96% ethanol paraffin wax (m.p. 58–60 °C, oil content < 0.5%) and cyclohexane from Centrohém (Stara Pazova, Serbia). All solutions were made using doubly distilled water (DDW). The pH of the reaction mixture was adjusted using a diluted aqueous solution of HCl or NaOH.

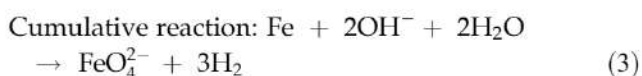
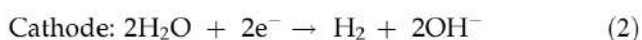
The synthesis process of solid BaFeO_4

BaFeO_4 crystallization was performed by addition of 13 g of $\text{Ba}(\text{OH})_2 \cdot 8 \text{H}_2\text{O}$, as a 10% $\text{Ba}(\text{OH})_2$, in the vigorously agitated 500 ml solution of 0.08 M K_2FeO_4 in 10 M KOH at 30 °C. Applied K_2FeO_4 was synthesized by electrolysis in a solution of 10 M KOH using a two-compartment electrolysis cell, separated with a ceramic anion impermeable membrane according to

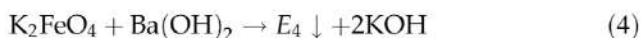
Table 1 Structural formula of clomazone and its properties

Structural formula	2-(2-chlorophenyl)-methyl-4,4-dimethyl-3-isoxazolidinon	
Formula	C ₁₂ H ₁₄ ClNO ₂	
Density	1.19 g/cm ³	
Boiling point	275 °C	
Appearance	White solid	
PubChem	CID: 54778	
Molar mass	239.69806	

the procedure defined in the literature [12, 28] and reactions (1–3).



The concentration of synthesized K₂FeO₄, a purple red anolyte solution, was determined by the chromite method [29]. The resultant anolyte, K₂FeO₄ solution, was removed from the electrolysis chamber and added through a filter to a 10% wt. Ba(OH)₂, using the volume of Ba(OH)₂ solution calculated according to a predetermined Ba/Fe ratio. After 10 min of vigorous stirring, ex situ solid BaFeO₄ can be precipitated due to the low solubility compared to K₂FeO₄, reaction (4):



The resultant suspension was vacuum-filtered through a sintered glass filter B2 and washed with chilly triply distilled water to pH = 7. The washed BaFeO₄ was dried at room temperature for 20 h under 50 mbar to a constant mass and then kept in a desiccator over silica gel under 300 mbar. BaFeO₄ yield and purity were determined by titrimetric chromite analysis [29]. The yield was 90% of theoretical value with purity of 95%.

The encapsulation process of BaFeO₄

Encapsulation of micro- and nano-crystalline barium ferrate(VI) in the paraffin wax was performed by a phase separation method in the organic solvent cyclohexane. The paraffin wax solution was prepared by dissolution of 5 g of paraffin wax in the 100 cm³ cyclohexane. The mixture of paraffin and

cyclohexane was heated to 60 °C and stirred under reflux until the dissolution of paraffin wax. Then, 5 g of the untreated (as-produced) micro-crystalline BaFeO₄ was slowly added in the stirred paraffin wax solution and exposed to reflux for 15 min. Hot suspension in cyclohexane was quickly centrifuged and dried in a vacuum chamber. Encapsulated micro-crystalline BaFeO₄ was stored in a vacuum desiccator prior to further use.

The morphologies of BaFeO₄ particles were examined using a scanning electron microscope (TESCAN, Tescan, Brno, Czech Republic). FTIR spectrum of BaFeO₄ mixed in a conventional KBr pellet was obtained by using a Bomem MB-100, Hartman and Braun spectrophotometer. X-ray diffraction analysis of synthesized BaFeO₄ samples was taken with a PHILIPS PW 1710 X-ray diffractometer, using monochromatized Cu-Kα radiation (λ = 1.5418 Å).

Procedure for clomazone removal from water using the encapsulated BaFeO₄

As oxidative agents for exploration of the possibility of clomazone degradation in double distilled water, the solid-state micro- and nanocrystalline bare and encapsulated BaFeO₄, in solution of 40 mM/l BaFeO₄ versus Fe, were chosen. They were also used as a source of ferric hydroxide, an eco-friendly coagulant and flocculent, which is the product of ferrate(VI) reduction.

The samples of 150 ml of 40 mg/l clomazone solution were treated with 6, 15 and 20 mM/l BaFeO₄ versus Fe at pH = 6.5 and a temperature of 23 °C. The treatment of clomazone samples was carried out using the Jar test equipment with a four-stirrer unit (Velp JLT4, Italy). The mixing rate was at first 300 rpm for 10 min and then 160 rpm for 20 min. The treated samples were then filtered through a ceramic

vacuum filter with a pore size of 0.2 μm . The change in the concentration of clomazone was monitored using a UV–Vis spectrophotometer (UV 1800 Shimadzu, Japan,) at a wavelength of 210 nm and calibration curves.

Results and discussion

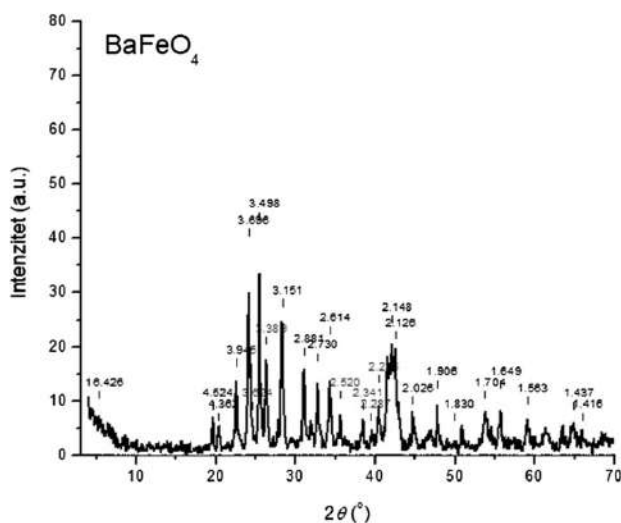
Characterization of the BaFeO₄

Analysis of crystallinity of the synthesized samples by X-ray diffraction spectroscopy showed crystal structure and composition of BaFeO₄, as shown in Fig. 1.

The X-ray diffraction pattern of the synthesized BaFeO₄, seen in Fig. 1, shows diffraction peaks at characteristic wavenumbers which correlate with dimensions of unit cells based on an orthorhombic crystal system which corresponds to literature data [30, 31] for the Pnma space group of the orthorhombic crystal system, same as BaCrO₄ and BaSO₄, the isomorphs with BaFeO₄.

Synthesis of BaFeO₄ is equally confirmed by FTIR spectroscopy. Characteristics of FTIR spectral bands for BaFeO₄ shown in Figs. 2 and 3 correlate well with relevant literature data [20, 32, 33].

The triplet of the absorbance bands at wavenumbers 856, 816 and 777 cm^{-1} , clearly seen on the FTIR spectra in Fig. 2, denotes light absorption of BaFeO₄. Weak band of paraffin wax is seen at wavenumber



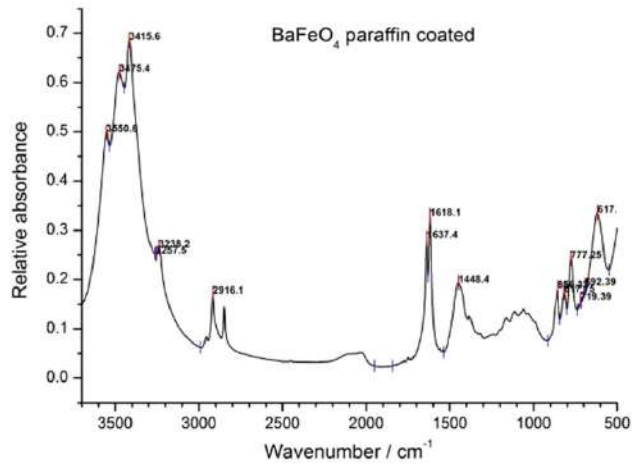


Figure 3 Extended FTIR spectrum of the encapsulated BaFeO₄.

Comparative analysis of treatment of the clomazone-contaminated water by encapsulated and bare solid BaFeO₄

The kinetics of the clomazone concentration decrease in contaminated water after treatment with encapsulated BaFeO₄ was monitored by time-dependent changes in the absorbance of UV–Vis spectra for clomazone in the water, which were recorded for different concentrations of added encapsulated BaFeO₄, as shown in Figs. 6, 7 and 8. The concentration of clomazone during the treatment was determined from the previously obtained calibration dependence of UV–Vis absorbance of the clomazone water solution and clomazone concentration in water.

Figure 4 SEM micrograph of the BaFeO₄ microcrystalline precipitate.

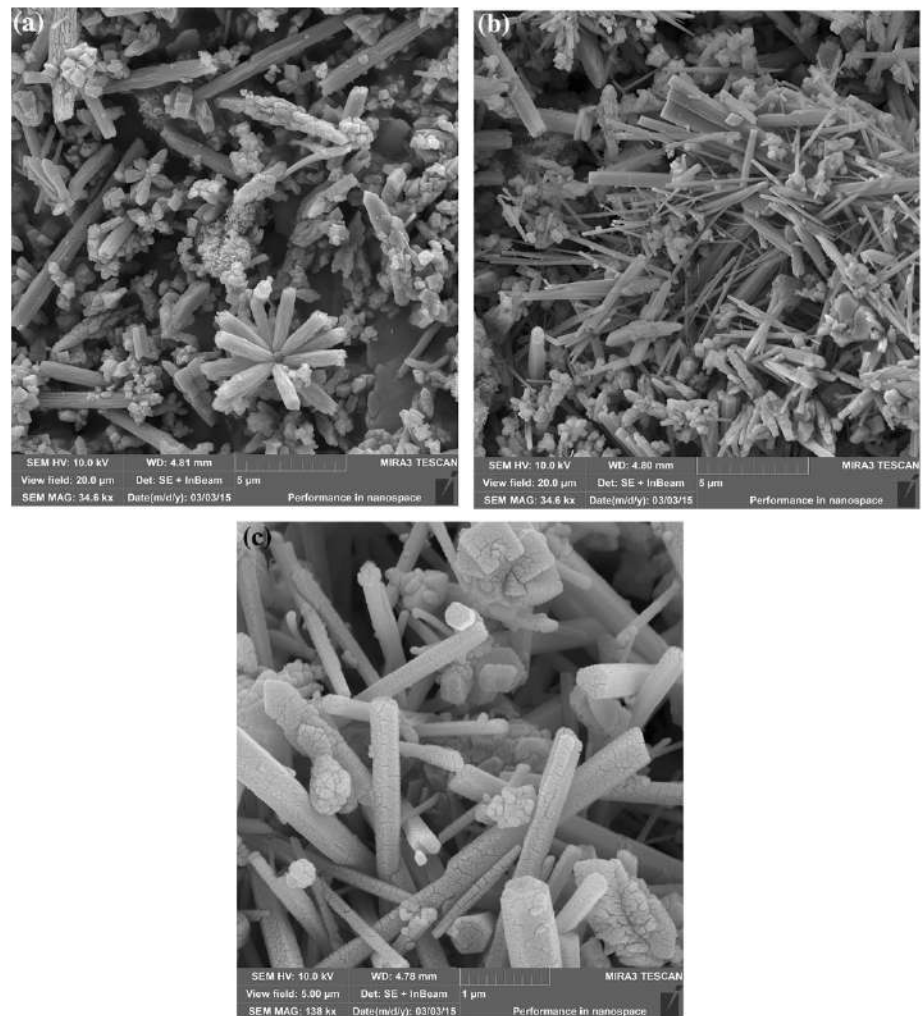
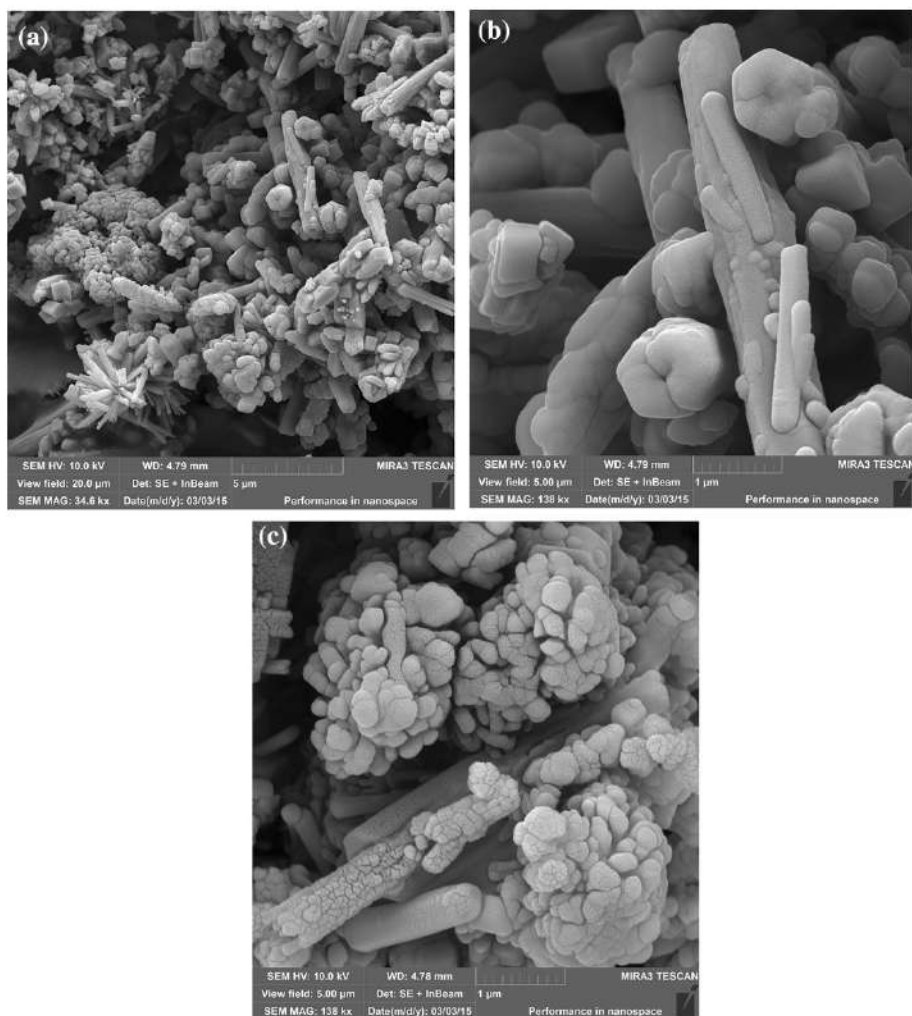


Figure 5 SEM micrograph of the encapsulated BaFeO_4 microcrystalline precipitate.



Kinetic curves that are showing the changes in percentage of clomazone concentration reduction with time presented in Figs. 9 and 10 clearly demonstrate the increase in the clomazone concentration reduction with the increase in the barium ferrate concentration applied in the treatment. Also, the percentage of clomazone concentration reduction after application of the encapsulated BaFeO_4 , as shown in Fig. 9, is notably greater with respect to the case when bare solid BaFeO_4 has been applied, as shown in Fig. 10, in the equal experimental conditions.

The presented results show that for the applied ferrate(VI) concentration of 6 mM/l BaFeO_4 versus Fe, the percentage of clomazone removal is 58% when the bare solid BaFeO_4 is applied and 75% when the encapsulated BaFeO_4 is applied, after a period of 90 min, while for the applied concentration of ferrate(VI) of 15 mM/l and 20 mM/l from bare and encapsulated BaFeO_4 , the removal efficiency is 73%

and 85%, and 87% and 93%, respectively, under the same experimental conditions.

The comparison of the efficacy in reduction in clomazone content in the water after application of non-encapsulated and encapsulated ferrate(VI) salts is shown in Fig. 11, where it can be noticed that the degree of clomazone removal by encapsulated BaFeO_4 is higher than 90%, while the results for non-encapsulated BaFeO_4 are slightly poorer, particularly when lower ferrate(VI) concentration is applied.

It has been shown that the application of 6 mM/l ferrate(VI) from encapsulated BaFeO_4 can remove 76% of clomazone, which is considerably more efficient regarding the application of 6 mM/l ferrate(VI) from freshly synthesized bare BaFeO_4 , which can remove 57% of clomazone.

However, $\text{Fe}(\text{OH})_3$, formed as a product in the reaction of pollutant with ferrate(VI), is a powerful coagulant and flocculent and enhances the efficiency

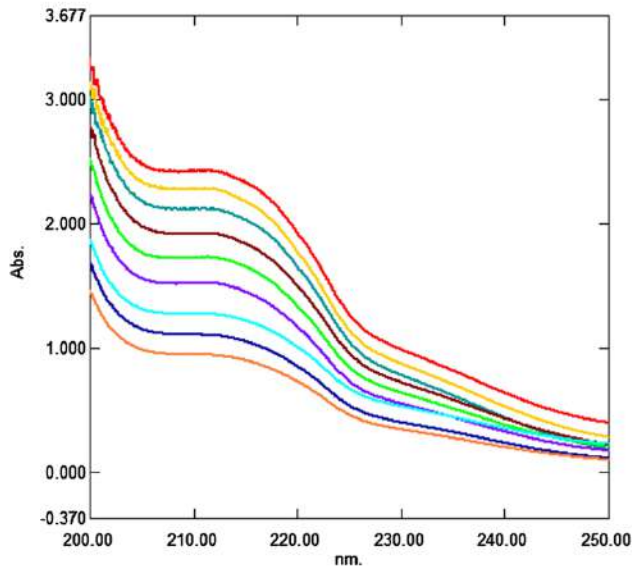


Figure 6 Changes in Abs in UV-Vis spectrum of clomazone (initial $c = 40$ mg/l) with time and after adding of 6 mM/l encapsulated BaFeO₄ versus Fe.

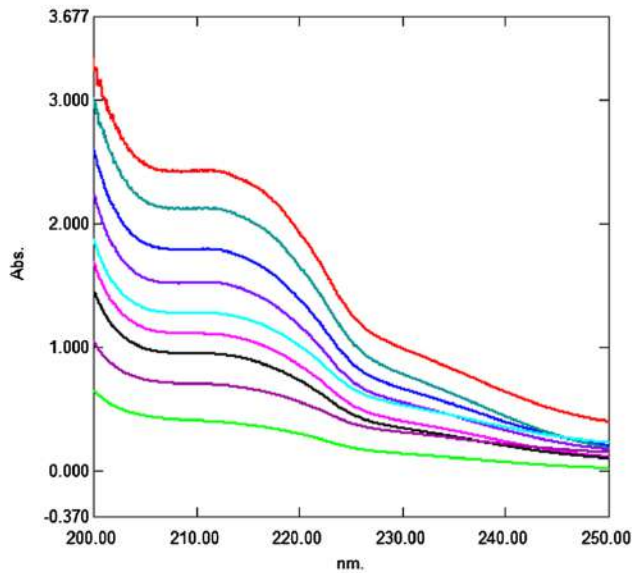


Figure 7 Changes in Abs in UV-Vis spectrum of clomazone (initial $c = 40$ mg/l) with time and after adding of 15 mM/l encapsulated BaFeO₄ versus Fe.

of wastewater depollution, but simultaneously catalyses the reaction of the ferrate(VI) decomposition. So, the positive effect of the ferrate(VI) encapsulation is that it provides slower ferrate(VI) ion release to the extent just necessary for the pollutant oxidation and hence reduces wasting of ferrate(VI) in unwanted reaction. The comparative results of the treatment of water contaminated by clomazone

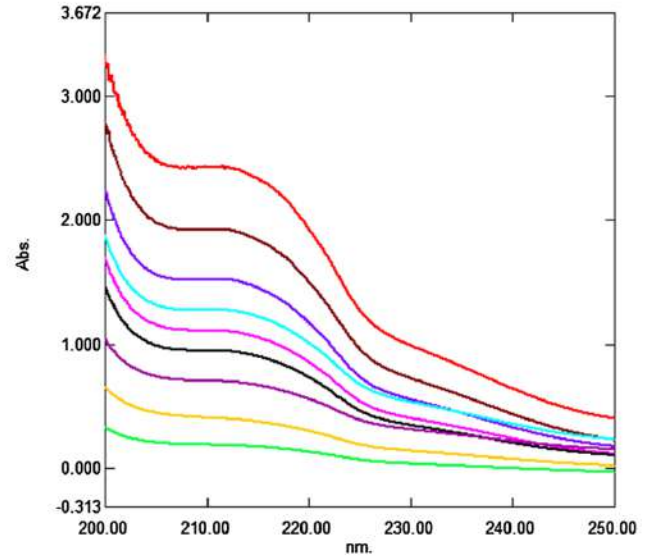


Figure 8 Changes in Abs in UV-Vis spectrum of clomazone (initial $c = 40$ mg/l) with time and after adding of 20 mM/l encapsulated BaFeO₄ versus Fe.

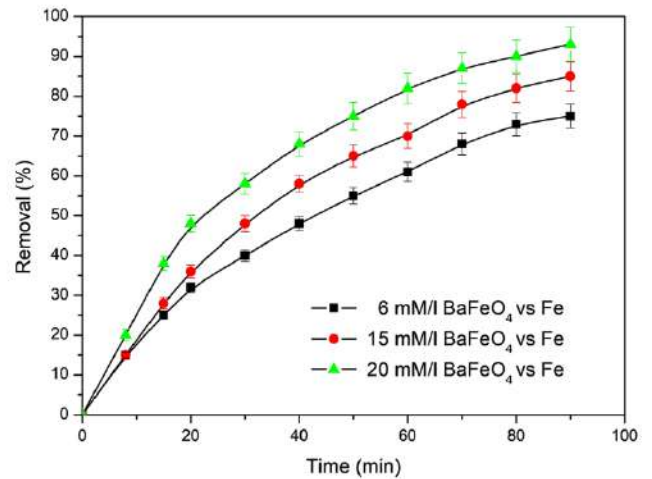


Figure 9 Effect of encapsulated BaFeO₄ on clomazone removal (initial $c = 40$ mg/l) with reaction time at pH = 6.5.

applying bare or encapsulated ferrate(VI), as shown in Figs. 9 and 10, confirm the given explanation.

Conclusion

In this paper, we reported the results from experimental coating procedure of micro- and nano-dimensional BaFeO₄ crystallites with paraffin dissolved in cyclohexane, and we demonstrated the benefits of using encapsulated ferrate(VI) for clomazone pesticide removal.

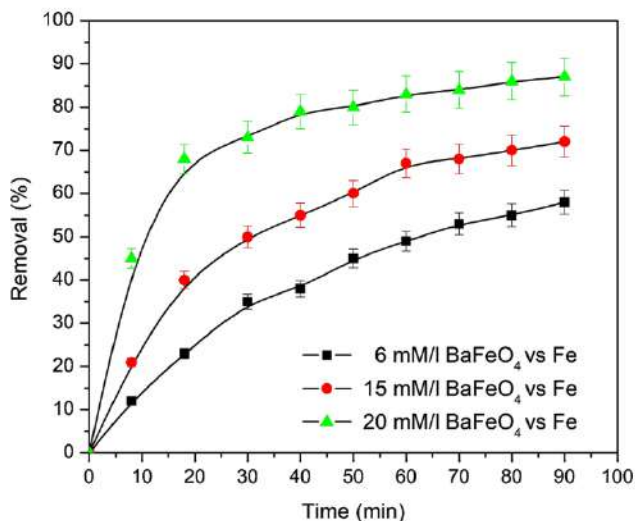


Figure 10 Effect of bare BaFeO₄ on clomazone removal (initial $c = 40$ mg/l) with reaction time at pH = 6.5.

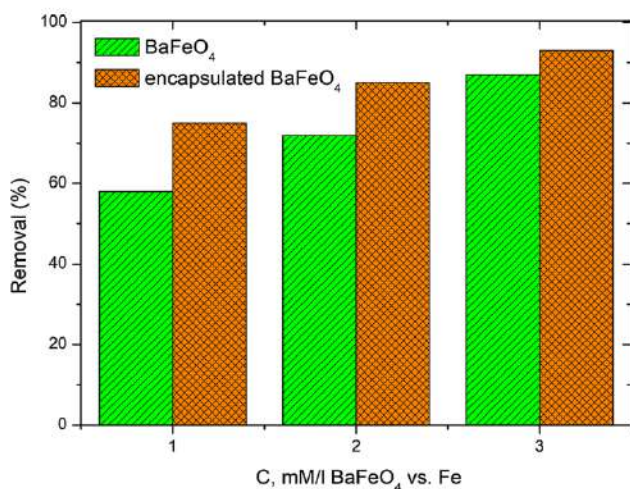


Figure 11 Comparison of the efficiency between bare BaFeO₄ and encapsulated BaFeO₄ in the process of removing different concentrations of pesticide clomazone from contaminated water (numbers 1, 2 and 3 correspond to 6, 15 and 20 mM/l BaFeO₄ vs. Fe).

The results are based on the scanning microscopy, FTIR spectroscopy and X-ray diffractometry of the uncoated and coated BaFeO₄ crystallites. Crystallization of the micro-sized and nano-sized crystallites of barium ferrate(VI), performed by the reaction of barium hydroxide with the potassium ferrate(VI) in the alkaline solution, resulted in the formation of various crystal shapes of the orthorhombic crystal system. Apart from usual forms of this crystal system, pinacoids (parallelohedron), rhombic prisms and rhombic bi-tetragonal pyramids, remarkable

crystal shapes in the form of elongated rhombic prismatic rods, nano-whiskers and nano-tubes have been grown during crystallization. X-ray diffractometry and FTIR spectrometry proved chemical composition and crystallinity of the obtained BaFeO₄. FTIR spectrometry, and scanning electron microscopy showed successful coating of the BaFeO₄ microcrystalline particles with paraffin wax film in the form of microcapsules by a phase separation method from the paraffin wax solution in cyclohexane.

In the case of water treatment with the pesticide clomazone using an encapsulated and non-encapsulated BaFeO₄, the removal with encapsulated BaFeO₄ was improved by about 20%.

Acknowledgements

The work was financially supported by The Ministry of Education, Science and Technological Development, Republic of Serbia, within Projects TRp 34025 and TRp 31080.

Compliance with ethical standards

Conflict of interest The authors declare that they have no conflict of interest.

References

- [1] Wheeler WB (2002) Pesticides in agriculture and the environment. Marcel Dekker, Inc., New York
- [2] Eriksson E, Baun A, Mikkelsen PS (2007) Ledin, A, Risk assessment of xenobiotics in stormwater discharged to Harestrup Å, Denmark. Desalination 215:187–197
- [3] Carter A (2000) How pesticides get into water- and proposed reduction measures. Water 11:149–156
- [4] Moore MT, Lizotte RE Jr, Knight SS, Smith S Jr, Cooper CM (2007) Assessment of pesticide contamination in three Mississippi Delta oxbow lakes using *Hyalella azteca*. Chemosphere 67:2184–2191
- [5] Zanella R, Primel EG, Gonçalves FF, Martins ML, Adaimé MB, Marchesan E, Machado SLO (2008) Study of the degradation of the herbicide clomazone in distilled and in irrigated rice field waters using HPLC_DAD and GC-MS. J Braz Chem Soc 19:987–995
- [6] Mervosh TL, Sims GK, Stollert EW (1995) Clomazone fate in soil as affected by microbial activity, temperature, and soil moisture. J Agric Food Chem 43:537–543

- [7] Oller I, Malato S, Sánchez-Pérez JA (2011) Combination of advanced oxidation processes and biological treatments for wastewater decontamination—a review. *Sci Total Environ* 409:4141–4166
- [8] Jing J, Liu M, Colvin VL, Li W, Yu WW (2011) Photocatalytic degradation of nitrogen-containing organic compounds over TiO₂. *J Mol Catal A Chem* 351:17–28
- [9] Hincapie M, Maldonado MI, Oller I, Gernjak W, Sanchez-Perez JA, Ballesteros MM, Malato S (2005) Solar photocatalytic degradation and detoxification of EU priority substances. *Catal Today* 101:203–210
- [10] Chiron S, Fernandez-Alba A, Rodriguez A, Garcia-Calvo E (2000) Pesticide chemical oxidation: state-of-the-art. *Water Res* 34:366–377
- [11] Čekerevac MI, Nikolić-Bujanović L, Mirković MB, Popović NH (2010) Application of electrochemically synthesized ferrate(VI) in the purification of wastewater from coal separation plant. *Hem Ind* 64:423–430
- [12] Nikolić-Bujanović L, Čekerevac M, Tomić M, Zdravković M (2016) Ibuprofen removal from aqueous solution by in situ electrochemically-generated ferrate(VI): proof-of-principle. *Water Sci Technol* 73(2):389–395
- [13] Jiang JQ (2007) Research progress in the use of ferrate(VI) for the environmental remediation. *J Hazard Mater* 146:617–623
- [14] Jiang JQ, Wang S, Panagouloupoulos A (2006) The exploration of potassium ferrate(VI) as a disinfectant/coagulant in water and wastewater treatment. *Chemosphere* 63:212–219
- [15] Sharma VK (2002) Potassium ferrate(VI): an environmentally friendly oxidant. *Adv Environ Res* 6(2):143–156
- [16] Sharma VK, Kazama F, Jiangyong H, Ray AK (2005) Ferrates iron(VI) and iron(V)—environmentally-friendly oxidants and disinfectant. *J Water Health* 3:45–58
- [17] Potts ME, Churchwell DR (1994) Removal of radionuclides in wastewaters utilizing potassium ferrate(VI). *Water Environ Res* 66:107–109
- [18] Zajícček P, Kolář M, Pucek R, Ranc V, Bednár P, Varma SR, Sharma KV, Zbořil R (2015) Oxidative degradation of triazine- and sulfonyleurea-based herbicides using Fe(VI): the case study of atrazine and iodosulfuron with kinetics and degradation products. *Sep Purif Technol* 156:1041–1046
- [19] Sharma VK, Macova Z, Bouzek K, Millero FJ (2010) Solubility of ferrate(VI) in NaOH–KOH mixtures at different temperatures. *J Chem Eng Data* 55(12):5594–5597
- [20] Licht S, Yu X (2008) Recent advances in Fe(VI) synthesis. In: Sharma V (ed) *Ferrates*. ACS symposium series. Springer, New York, pp 2–51
- [21] Ernst T, Wawrzenczyk M, Cyfert M, Wronska M (1979) Effect of pH on the kinetics of ferrate(VI) decomposition. *Bull Acad Pol Sci Ser Sci Chim* 27:773–778
- [22] Macova Z, Bouzek K (2011) The influence of electrolyte composition on electrochemical ferrate(VI) synthesis. Part II: anodic dissolution kinetics of a steel anode rich in silicon. *J Appl Electrochem* 41:1125–1133
- [23] Čekerevac M, Simičić M, Nikolić Bujanović L, Popović N (2012) The influence of silicate and sulphate anions on the anodic corrosion and the transpassivity of iron and silicon-rich steel in concentrated KOH solution. *Corros Sci* 64:204–212
- [24] Evrard OJ, Gerardin RA, Schmitt N, Evrard J-L (1994) Alkali or alkaline earth metal ferrates, their preparation and their industrial applications. Centre International de l'Eau de Nancy. U.S. Patent No. 5,284,642
- [25] Deininger JP, Dotson RL (1984) Process for the electrochemical production of sodium ferrate Fe(VI), Olin Corporation, New Haven, Conn. US Patent No. 4,435,257
- [26] Chen H, Yang Z, Wen R, Tan Z (2012) Stabilization of potassium ferrate cathodic material coated with tetraphenylporphyrin. *Electrochim Acta* 75:62–70
- [27] Zhang Y, Zhao X, Zhan S, Zhang G, Liu S, Optimized preparation conditions of yttria doped zirconia coatings on potassium ferrate(VI) electrode for alkaline super-iron battery, (2012) *Appl Energy* 99:265–271
- [28] Nikolić-Bujanović L, Čekerevac M, Vojinović-Miloradov M, Jokić A, Simičić M (2012) A comparative study of iron-containing anodes and their influence on electrochemical synthesis of ferrate(VI). *J Ind Eng Chem* 18:1931–1936
- [29] Schreyer JM, Thompson GW, Ockerman LTO (1950) Oxidation of chromium(III) with potassium ferrate(VI). *J Am Chem Soc* 22:1426–1427
- [30] ICSD data base, Hashemite: PDF 35-642, ICSD 62181, space group Pnma, and R 0.053, (ICSD, version 1.8.1, 2011-2)
- [31] ICSD 62181—BaCr_{0.84}S_{0.16}O₄; ICSD 23743—BaSO₄.
- [32] Hauff PL, Foorg EE, Rosenblum S, Hakki W (1983) Hashemite, Ba(Cr,S)O₄, a new mineral from Jordan. *Am Miner* 69:1223–1225
- [33] Coates J (2000) Interpretation of infrared spectra: a practical approach. In: Meyers RA (ed) *Encyclopedia of analytical chemistry*. Wiley, Chichester, pp 10815–10837
- [34] Wang S, Yang Z, Liu D, Yi S, Chi W, Evaluation of potassium ferrate(VI) cathode material coated with 2,3-naphthalocyanine for alkaline super iron battery, (2010) *Electrochem. Commun* 12:367–370
- [35] Coward JL (2010) FTIR spectroscopy of synthesized racemic nonacosan-10-ol: a model compound for plant epicuticular waxes. *J Biol Phys* 36:405–425

Appendix C

Collaborative Conference Papers

Integration of one-dimensional gas-sensitive nanostructures grown via chemical vapour deposition into microdevices, Vallejos S., Tomić M., Gràcia I., Figueras E., Chmela O., Hubalek J., Domènech G., Prades D., Romano-Rodriguez A., Barth S., Cané C., Smart Systems Integration 2018 - International Conference and Exhibition on Integration Issues of Miniaturized Systems, Dresden, Germany, 2018, ISBN: 978-395735082-4.

Room temperature ethanol microsensors based on silanized tungsten oxide nanowires, Vallejos S., Fohlerová Z., Tomić M., Gràcia I., Figueras E., Cané C., International conference Euroensors, Graz, Austria, 2018, doi: 10.3390/proceedings2130790.

Integration of one-dimensional gas sensitive nanostructures grown via chemical vapour deposition into microdevices

S. Vallejos¹, M.Tomic¹, I. Gràcia¹, E. Figueras¹, O. Chmela², J. Hubalek², G. Domènech³, D. Prades³, A. Romano-Rodriguez³, S. Barth⁴, C. Cané¹

¹Centre Nacional Microelectrònica (IMB-CNM, CSIC), Campus UAB, Bellaterra, Spain.

²CEITEC - Central European Institute of Technology, Brno University of Technology, Brno, Czech Republic.

³MIND - Department of Electronics, Universitat de Barcelona (UB), Barcelona, Spain.

⁴Technische Universität Wien, Austria.

Abstract

Nanostructures (NS), e.g., based on metal oxides, are attractive in gas sensors because they proved to enhance their functionality, providing better sensitivity, stability, and selectivity. Further enhancement of the functionality of nanostructures is also known to be achieved by electronic and/or chemical sensitization via the surface modification with second-phase materials (e.g., catalytic nanoparticles with sizes less than 10 nm). [1] The formation of NSs is traditionally achieved via liquid- or vapour-phase routes, with the vapour-phase routes (e.g., CVD) having shown advantages that include greater purity, the ability to generate NSs in continuous rather than batch mode and higher throughputs. This is crucial for developing a low cost manufacturing method of gas sensing devices that may be adequate for high volume Smart System Solutions. Thus, in this work, the use of CVD and aerosol assisted (AA) CVD to synthesize non-modified and modified NSs is proposed.

1. Introduction

As the world population increases there is a need of ensuring a more sustainable development, friendly with the environment and with a circular basis economy for the Better Life challenge, comprising new advanced tools and technologies able to monitor key parameters that allow making prediction and decisions efficiently. In addition, new technologies are also needed, for instance technologies that can be operated with ultra-low power consumption for high autonomy at low cost, fabricated with eco-friendly materials enough robust to have long-term stability and full connectivity to be part of crucial tools such as the internet of things, or smart communications. Currently, these key characteristics are not fully accomplished in commercial devices, and certainly, efficient solutions will not come from single devices, but from Smart Systems based on new micro/nano fabrication concepts with biomimetic properties, nanoscaled functional materials, and optimised sensing modes and control electronics to radically improve the performance of these monitoring systems.

In this context, Biomimetic Systems for Odour Detection (BSOD) aim to develop new and far-reaching systems that accomplish technological breakthroughs to face the above-mentioned challenges. Odour (gases, vapours, aroma) detection systems are

of high interest as they are versatile and non-invasive Key Enabling Technologies, which are relevant both in traditional (e.g., environment, industry) and innovative (e.g., health, agrofood, Internet of Things, smart cities or security) applications [2]. The gas sensor market is forecasted 1,3 B US\$ by 2023 [3], with the environment, transport, and industry being the main market protagonist, and new medical, agro-food and other advanced consumer applications (i.e., wearables) expecting to drive innovation. These applications are certainly part of the Digital agenda paradigm and the SAE concept “Smart anything everywhere”, in which odour sensing devices may be, in a near future, the next family of sensors for Smart Phones.

A lot of research and development has been done in the last decades on different types of gas sensors and sensing systems as there is no unique solution for all scenarios. However, most of the challenges coming from the application field are similar and in general demand from the sensing systems good performances in terms of form factor miniaturization, low cost, with high sensitivity, stability, and selectivity and good connectivity and thus, also showing low-power consumption or self-powered capabilities.

Depending on the final application and sensing scenario the key target gases, aromas or vapours are different, and the limits of detection required also depend on the toxicity of such gases. While in traditional environmental control emissions are monitored by measuring mainly the presence of air pollutants such as CO₂, NO_x and SO_x, in other indoor/outdoor air quality monitoring scenarios other gases such as O₃, CO are also important. In health, food and leisure wearables, volatiles organic compounds (VOCs), particularly, hydrocarbons, ketones and aldehydes, are the main analytes to be monitored.

2. Nanomaterials (MoX) based gas sensors

Compared to most types of gas sensing devices (i.e. optical, electrochemical, gravimetric, acoustic,...) resistive-MoX devices are more prone to accomplish the above mentioned requirements. This is mainly due to the current capability to fabricate gas sensing platforms (transducers), based on “standard” MEMS and CMOS technologies, and bringing the inherent miniaturization performances of such technologies to the gas sensing devices. However, gas sensor are not made only of simple transducers, they also need the sensing materials properly optimized for specific group of analytes determined by the application.

MoX function as gas sensors because adsorbed gaseous species form surface states in the MoX by exchange of electrons with the bulk material. The concentration of the surface states formed is proportional to the partial pressure of the gas impinging on the MoX, and hence the conductivity of the material changes in response to changes in the gas concentration. These chemically induced changes can then be transduced into electrical signals by means of conductivity measurements. When such materials are nanostructured the surface to volume ratio dramatically increases and therefore the sensor response, too. One dimensional

(1D) structures like nanowires, nanorods, nanoneedles,...may also help on the improvement of the stability and, to a certain extent, the selectivity [4].

In this paper, we discuss the use of CVD and aerosol assisted (AA) CVD to synthesize non-modified and modified NSs, demonstrating that the selective synthesis of NSs, their functionalization and their integration into silicon- or polymer-based microsystems can take place in a single processing step. Generally, we take tungsten oxide as model material, although the integration of other chemical vapour deposited NSs (e.g., ZnO, In_2O_3 or SnO_2) with microdevices has proved feasible too. Additionally, we discuss the use of resistive heaters embedded in microdevices to perform CVD of NSs, and the integration of NSs into nanoelectrode arrays systems by dielectrophoresis, as a strategy to achieve a well-defined conduction channel easy to modulate by external stimuli (e.g. gaseous molecules) in chemoresistive sensors. Special focus is also payed to the reduction of the power consumption and to the use of AACVD (which is easily scalable) as a compatible technique for the development of portable Smart Systems solutions.

3. Experimental, results and discussion

One-dimensional NSs were synthesized onto silicon- or polymer-microtransducing platforms *via* AACVD [5]. Briefly, our model material was deposited using a methanolic solution (5 ml) of tungsten hexacarbonyl (20 mg, $\text{W}(\text{CO})_6$, Sigma-Aldrich, $\geq 98\%$). The aerosol of that solution was generated using a piezoelectric ultrasonic atomiser (Liquifog, Johnson Matthey) operating at 1.6 MHz, and subsequently transported to the heated platforms using nitrogen flow (200 sccm). Shadow masks were used during the AACVD process in order to protect the contacts and confine the film deposition to the transducing area (i.e., electrodes). Generally, the AACVD of this solution resulted in the formation of relatively well-adhered uniform films of bluish color as-deposited, showing good coverage of the platforms. By tuning various parameters of the AACVD process, including solutions, concentrations, deposition temperatures, we achieved the selective deposition of polycrystalline films and NSs with different morphologies. Figure 1 displays the Scanning Electron Microscopy (SEM) imaging of selected tungsten oxide films.

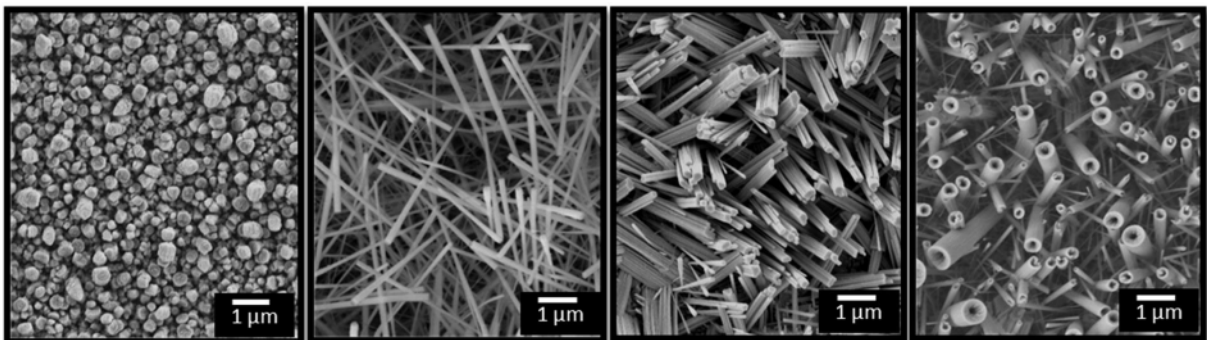


Figure 1: SEM images of tungsten oxide grown via AACVD (from polycrystalline to various nanostructured morphologies).

Further enhancement of the functionality of NSs in sensing applications and catalysis is also known to be achieved by electronic and/or chemical sensitization via the surface modification with second-phase materials (e.g., catalytic nanoparticles with sizes less than 10 nm). In the literature, there are various conceptual routes to modified the surface of MoX NSs with second-phase NPs, based either on liquid-phase or vapour-phase synthesis. These routes normally integrate the sensitive materials into the device using post-transfer (indirect) or direct methods. Synthesizing functionalized materials in the vapour-phase has potential advantages, including the growth of materials with greater purity, continuous mode operation, higher throughput, and the possibility of integrate materials directly into devices. However, its use for synthesis of NSs has demonstrated often the need of pre-catalytic NPs and/or relatively high temperatures (~1000 °C as in conventional CVD), introducing extra fabrication steps and limiting its applicability for their integration with advanced microdevices based either on silicon or non-conventional substrates (e.g. polymers, textiles or paper)[6].

Recently, we have developed a method to modify MoX NSs with second-phase NPs via AACVD, demonstrating that synthesis, functionalization and integration of these structures into the device can take place in a single processing step [7]. This method has demonstrated to be a flexible route to incorporate well-dispersed second-phase NPs including Au, Pt, Cu₂O, and Fe₂O₃ at the surface of the MoX NSs. An example of the results obtained for the modification of tungsten oxide with Au or Pt NPs is depicted in figure 2.

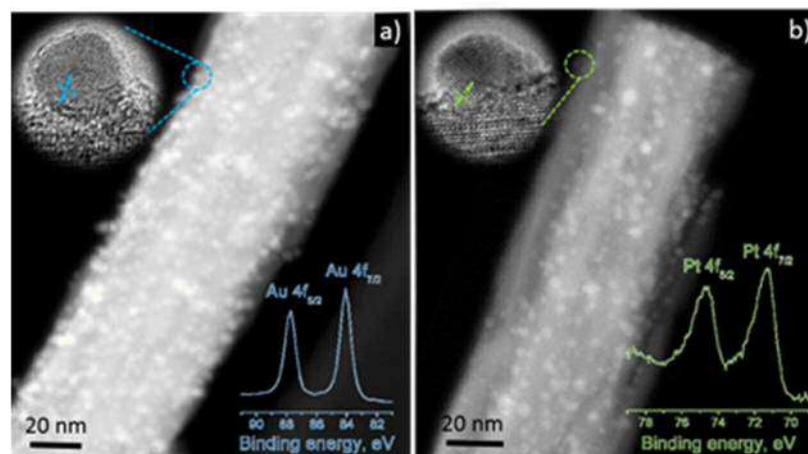


Figure 2: STEM of chemical vapor deposited MoX wires modified with Au (a) or Pt (b) nanoparticles. Insets show the metal NPs with marked planar spacing and the characteristic Au and Pt core-level peaks recorded using XPS.

The low onset temperatures (~350 °C) for the formation of NSs has allowed for the integration of these structures into silicon- and polymer-based microdevices without the assistance of transfer steps, showing the compatibility of AACVD with microelectronics manufacturing processes, as shown in figure 3. The self-heating capability of the CMOS compatible transducing platforms with integrated low power microheaters, that is used to supply the energy to the sensing material for the

effective adsorption-desorption process of gaseous molecules, has also been used to grow locally (into the sensing active area of the device) MoX and modified MoX NSs with similar functionality than those integrated in 'hot-wall' CVD reactors. We used this method previously to integrate NSs of tungsten oxide, and tin oxide via CVD and AACVD. [8,9]

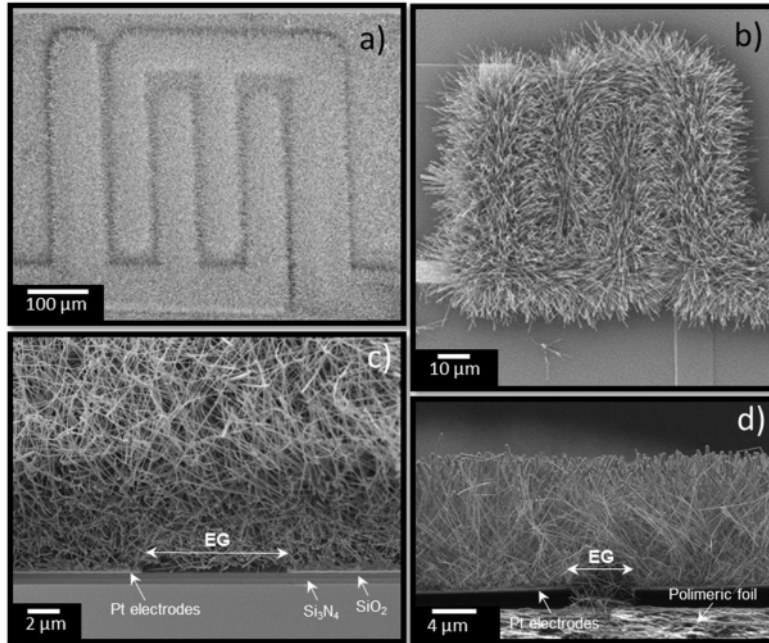


Figure 3: Chemical vapour deposited metal oxide nanostructures grown directly on MEMS-based (a) and polymer-based (b) gas sensing platforms. Section of the MEMS-based device (c) and the polymer-based device (d). EG stands for electrode gap

Recently aerosol assisted chemical vapour deposited NSs have also been integrated into nanoelectrode arrays systems by dielectrophoresis, as a strategy to achieve well-defined conduction channels easy to modulate by external stimuli (e.g, gaseous molecules) in chemoresistive sensors. Figure 4 a) and b) show a view of the devices [10, 11]. Nanostructures are grown on special substrates and transferred to the pre-patterned electrodes of the working devices, see figures c) and d). This technique is a smart alternative to the fabrication of single nanowire devices by depositing solution droplets that contain nanowires onto the microelectrodes and that require the use of focussed ion beam (FIB) technique to write the final connections of the sensing nanowire to the microelectrodes, [12].

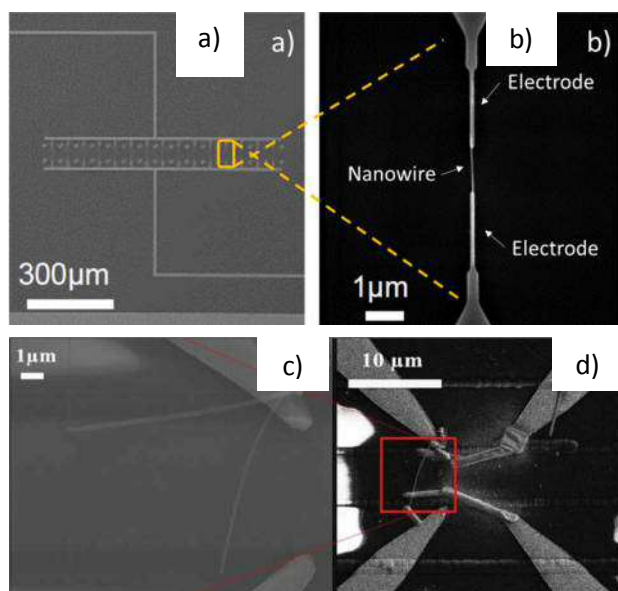


Figure 4: General view of the a) fabricated structure of nanoelectrodes connected in parallel, b) a pair of electrodes with a nanowire integrated across them, c) view of an Indium oxide nanowire over an electrode on top of a suspended microhotplate used to produce a gas sensor, and d) nanowire from image c) already contacted using focused ion beam techniques.

As a generic example for the demonstration of the sensing performances of the materials developed by AACVD, in the next figure the response to 100 ppm of toluene of three types of sensors fabricated on Polymeric foils (Upilex) as shown in figure 5 a) are presented. Tests were carried out at different temperatures in the range of 100–250°C. Sensors were of pure WO_3 and also functionalized with particles of Fe_2O_3 and Pt respectively. Figure 5 b) shows the dependence of the sensor response with the toluene concentration at a working temperature of 220°C.

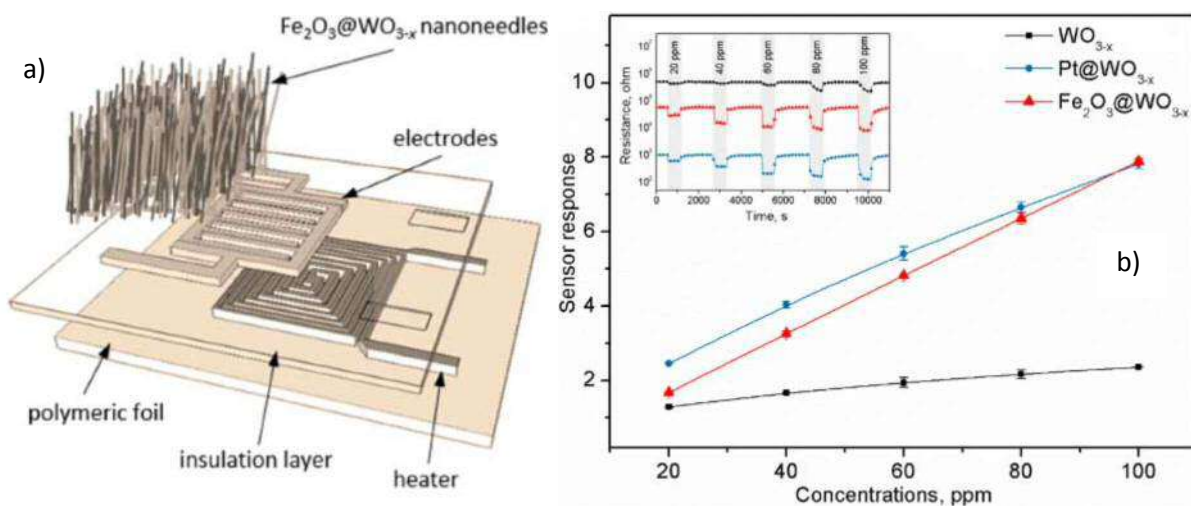


Figure 5: a) Drawing of the structure of the sensors developed on polymeric substrates and b) sensor response to toluene (20-100 ppm) at 220 °C.

Results indicate better performance for the functionalized sensors as opposed to the non functionalized of time response and sensitivity. Similar results were obtained when detecting ethanol or hydrogen and with low cross sensitivity. Other results will be presented at the conference for other concentrations of Toluene and other gases, and with other implementations of materials, with the aim of evaluating the most appropriate materials and devices according to the target applications and to their simple integrability to Smart Systems.

Conclusions

A method for synthesis of MOX-NSs via aerosol assisted CVD (AACVD) achieving deposition at relatively low temperatures was developed with potential to be integrated in microelectronic fabrication due to its flexibility, high deposition rate, easy implementation and good prospects for scaling-up and low cost industrialization. The maximum temperature of operation of the AACVD system allows depositing nanomaterials on top of silicon micromachined structures and also on low cost and flexible polymeric substrates.

Semiconductor oxide sensors based on nanowires of functionalized and non functionalized WO_3 have shown good sensitivity, and time response to a variety of gases (i.e. toluene, ethanol, hydrogen,...) concentrations and test conditions. Complete characterisation of different types of sensors for different gases will be presented in the conference.

This method well complements other approaches formerly studied for the development of gas sensors based on the one-step localized CVD growth of matrixes of nanowires on CMOS compatible substrates or on the two-step post-growth deposition/transfer of single nanowires to substrates patterned with nanoelectrode arrays. The aim was to have a set of techniques that may allow fabricating low cost gas sensors that may accomplish the challenging requirements of Smart Systems Integration.

Acknowledgments

This work has been supported in part by the Spanish Ministry of Science and Innovation via Grant TEC2015-74329-JIN-(AEI/FEDER, EU), TEC-2013-48147 (AEI/FEDER, EU), and TEC2016-79898-C6-1-R (AEI/FEDER, EU). This research has made use of the infrastructures of the SIX Research Centre and of the Spanish ICTS Network MICRONANOFABS, partially supported by MINECO.

References

- [1] S. Vallejos, I. Gràcia, O. Chmela, E. Figueras, J. Hubálek, and C. Cané, "Chemoresistive micromachined gas sensors based on functionalized metal oxide nanowires: Performance and reliability," *Sensors and Actuators B: Chemical*, vol. 235, pp. 525-534, 2016.
- [2] E. Comini, "Metal oxide nanowire chemical sensors: innovation and quality of life," *Materials Today*, vol. 19, pp. 559-567, 2016.
- [3] "Gas Sensors Market by Gas Type, Technology, End-Use Application, Geography - Global Forecast 2023", report from MarketsandMarkets.
- [4] S. Vallejos, P. Umek, T. Stoycheva, F. Annanouch, E. Llobet, X. Correig, P. De Marco, C. Bittencourt and C. Blackman. "Single-Step Deposition of Au- and Pt-Nanoparticle-Functionalized Tungsten Oxide Nanoneedles Synthesized Via Aerosol-Assisted CVD, and Used for Fabrication of Selective Gas Microsensor Arrays". *Advanced Functional Materials*, 2013, **23**, 1313-1322.
- [5] S. Vallejos, N. Pizúrová, J. Čechal, I. Gràcia and C. Cané. "Aerosol-assisted chemical vapor deposition of metal oxide structures: Zinc oxide rods" *J. Visualized Exp.*, 2017, **127**, e56127.
- [6] E. Comini, "Integration of Metal Oxide Nanowires in Flexible Gas Sensing Devices". *Sensors*, 2013, **13**, 10659-10673.
- [7] S. Vallejos, P. Umek, T. Stoycheva, F. Annanouch, E. Llobet, X. Correig, "Single-step deposition of Au- and Pt-nanoparticle-functionalized tungsten oxide nanoneedles synthesized via aerosol-assisted CVD, and used for fabrication of selective gas microsensor arrays". *Advanced Functional Materials*, 2013, **23**, 1313-1322
- [8] S. Barth, R. Jiménez-Díaz, J. Sama, J. Daniel Prades, I. Gràcia, J. Santander, C. Cane and A. Romano-Rodríguez. "Localized growth and in situ integration of nanowires for device applications". *Chem. Commun.*, 2012, **48**, 4734-4736.
- [9] F. E. Annanouch, I. Gràcia, E. Figueras, E. Llobet, C. Cané and S. Vallejos. "Localized aerosol-assisted CVD of nanomaterials for the fabrication of monolithic gas sensor microarrays. *Sensors and Actuators, B*, 2015, **216**, 374-383.
- [10] J. Guilera, C. Fàbrega, O. Casals, F. Hernández-Ramírez, S. Wang, S. Mathur, F. Udrea, A. De Luca, S. Z. Ali, A. Romano-Rodríguez, J. D. Prades and J. R. Morante. "Facile integration of ordered nanowires in functional devices" *Sensors and Actuators B: Chemical*, 2015, 221, 104-112
- [11] O. Chmela, J. Sadílek, J. Samà, A. Romano-Rodríguez, J. Hubálek and S. Vallejos. in SPIE Proc. 102480F-102480F-102487.
- [12] G. Domènech-Gil, S. Barth, J. Samà, P. Pellegrino, I. Gràcia, C. Cané, A. Romano-Rodríguez. Gas sensors based on individual indium oxide nanowire. *Sensors and Actuators B* 238 (2017) 447-454

Room Temperature Ethanol Microsensors Based on Silanized Tungsten Oxide Nanowires [†]

Stella Vallejos ^{1,2*}, Zdenka Fohlerová ¹, Milena Tomić ², Isabel Gràcia ², Eduard Figueras ² and Carles Cané ²

¹ CEITEC—Central European Institute of Technology, Brno University of Technology, 61200 Brno, Czech Republic; zdenka.fohlerova@ceitec.vutbr.cz

² Instituto de Microelectrónica de Barcelona (IMB-CNM, CSIC), Campus UAB, 08193 Bellaterra, Spain; milena.tomic@imb-cnm.csic.es (M.T.); isabel.gracia@imb-cnm.csic.es (I.G.); Eduard.Figueras@imb-cnm.csic.es (E.F.); carles.cane@imb-cnm.csic.es (C.C.)

* Correspondence: vargas@feec.vutbr.cz or stella.vallejos@imb-cnm.csic.es; Tel.: +420-5-4114-6153

[†] Presented at the Eurosensors 2018 Conference, Graz, Austria, 9–12 September 2018.

Published: 22 November 2018

Abstract: Gas microsensors based on tungsten oxide (WO_{3-x}) nanowires (NWs) silanized with APTES (3-aminopropyltriethoxysilane) are developed in this work. These surface modified microsensors are highly sensitive to ethanol at room temperature (RT) via photoactivation and show enhanced selectivity towards other volatile organic compounds (VOCs) including acetone and toluene.

Keywords: gas sensors; tungsten oxide; silanization

1. Introduction

Metal oxide (MOX) NWs are attractive in gas sensors because they have proved to enhance the functionality of these devices, particularly in terms of sensitivity, due to their higher surface area to volume ratio as opposed to bulk MOXs. These materials can be synthesized with tuned surface morphologies via scalable and industrially relevant bottom-up techniques. For instance, previously, we have demonstrated the synthesis of various MOX (e.g., WO_{3-x} , ZnO, and SnO_2) structures using a vapor-phase method enabled via aerosol-assisted (AA) chemical vapor deposition (CVD), and their enhanced sensitivity, stability and reproducibility to various gaseous analytes [1]. However, the lack of selectivity and need of relatively high temperatures, above 200 °C, for proper operation of these materials were also evidenced, as for other MOX in the literature [2]. In this context, a next generation of gas sensor devices operating at low temperatures, ideally RT, and providing good selectivity to key target analytes, such as VOCs (ketones, hydrocarbons and aldehydes) is highly desirable to reduce the operational power consumption and achieve the demand of specific applications in terms of selectivity.

Photoactivation of gas sensitive materials can be used as an alternative to thermoactivation to circumvent high power consuming resistive heaters allowing gas sensing at RT [3]. Furthermore, the modification of the surface chemistry of inorganic semiconducting supports with organo functional molecules can also be used to enhance the selectivity and influence the electrical properties of the support. Previous studies in the field of modified surfaces for gas sensing have focused particularly on the surface modification of Si NWs and the determination of the characteristics of the molecular modifying layers to achieve better functionality [4]. However, the modification of gas sensitive MOX with organo functional molecules in the literature is still less common. Therefore, here we present our recent results on the fabrication of microsensors based on silanized WO_{3-x} NWs. Silanization is a widely used method to modify MOX surfaces and encourage the formation of bonds across the

interface between the MOX and organic compounds (e.g., VOCs). Hence, in this work we also study the sensing properties of the silanized microsensors towards VOCs such as ethanol, acetone and toluene using UV photoactivation at RT.

2. Materials and Methods

The microsensors consist of a membrane of $\text{Si}_3\text{N}_4/\text{SiO}_2$ (300 nm/500 nm thick) with Ti/Pt interdigitated electrodes (25 nm/250 nm thick) on the top. WO_{3-x} NWs were grown directly onto the interdigitated electrodes using the AACVD method described previously [3]. Subsequently, the gas sensitive NWs underwent a cleaning process, which included rinsing in deionized water, drying in desiccator, and finally removing the adsorbed species and generating active hydroxyl groups on the surface by plasma treatment. The silanization was carried out at 120 °C via CVD. An aminosilane (APTES; 3-aminopropyltriethoxysilane, Sigma) solution was used to modify the sensitive films. The whole process spanned 10 min. A photograph of the sensor device is displayed in Figure 1a.

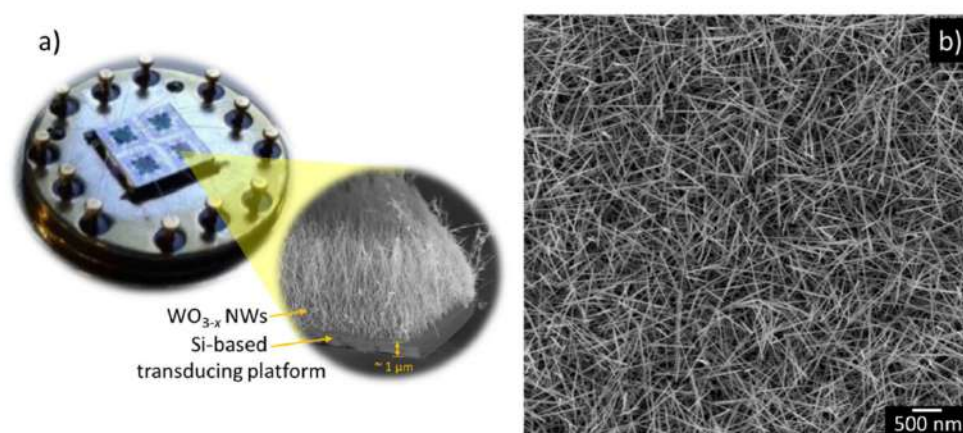


Figure 1. Photograph of the sensor device mounted on a TO-8 package and its cross-section after integration of the WO_{3-x} NWs (a). SEM imaging (top-view) of the WO_{3-x} NWs (b).

The morphology of the films was examined using Scanning Electron Microscopy (SEM— Carl Zeiss, Auriga Series) and the chemical composition using X-ray photoelectron spectroscopy (AXIS SupraTM Kratos Analytical, with Al/Ag monochromatic X-ray source). Further analysis of the films were carried out using X-ray Diffraction (XRD—Rigaku SmartLab 3 kW, Cu $K\alpha$ radiation) and transmission electron microscopy (HRTEM—FEI Tecnai F20, 200 kV).

Microsensors were tested in a continuous flow (200 sccm) test chamber provided of mass flow controllers and continuous illumination from a LED (light-emitting diode) with wavelength of 365 nm. Sensors were exposed to various calibrated concentrations of ethanol, acetone and toluene and subsequently the gaseous analytes were purged with air (3X, Praxair) until the initial baseline resistance in air was recovered. The sensor response was defined as R_a/R_g , where R_a and R_g are the resistance in air and in gas, respectively.

3. Results

SEM imaging of the films displayed NWs with diameters of ~100 nm and lengths of ~8 μm, corresponding to an aspect ratio of 80 (Figure 1). XRD analysis of the NWs showed crystalline structures with intense diffraction peaks at $23.1^\circ 2\theta$ ($d = 3.85 \text{ \AA}$) and $47.2^\circ 2\theta$ ($d = 1.92 \text{ \AA}$) that correspond the (002) and (004) reflections of the monoclinic phase WO_3 (P21/n; ICCD card no. 72-0677). Similarly, HRTEM also revealed highly ordered crystalline NW structures with marked planar spacing of 3.6 \AA along the NW, consistent with the unit cell observed by XRD and with previous results [2].

Figure 2 displays the XPS spectra for the APTES modified and non-modified WO_{3-x} NWs. Both samples display W 4f core level peaks with similar characteristics to those observed in our previous

works. Additionally, the spectrum recorded for the modified films shows the presence of Si 2p, Si 2s and N 1s core-level peaks, thus demonstrating the silanization of the WO_{3-x} NWs surface.

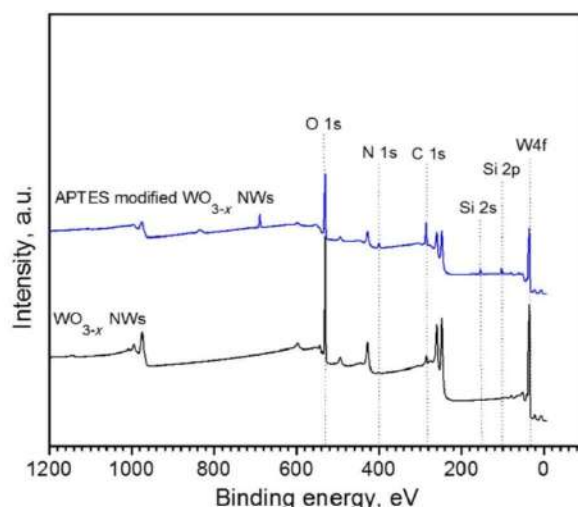


Figure 2. Survey XPS spectra for the APTES modified and non-modified WO_{3-x} NWs (only the peaks of interested have been marked).

Photoactivated gas sensing tests performed at RT towards various concentrations of acetone, ethanol and toluene demonstrated noticeable selectivity towards ethanol for the APTES modified WO_{3-x} NWs as opposed to the non-modified WO_{3-x} NWs, which displayed negligible response to the gases tested (Figure 3a). The response of the APTES modified microsensors to ethanol reached nine-fold the response of the non-modified microsensors for a concentration of 80 ppm (Figure 3). The higher sensitivity of the APTES modified sensors to ethanol is attributed to the higher polarity of this molecule as compared to acetone and toluene [5].

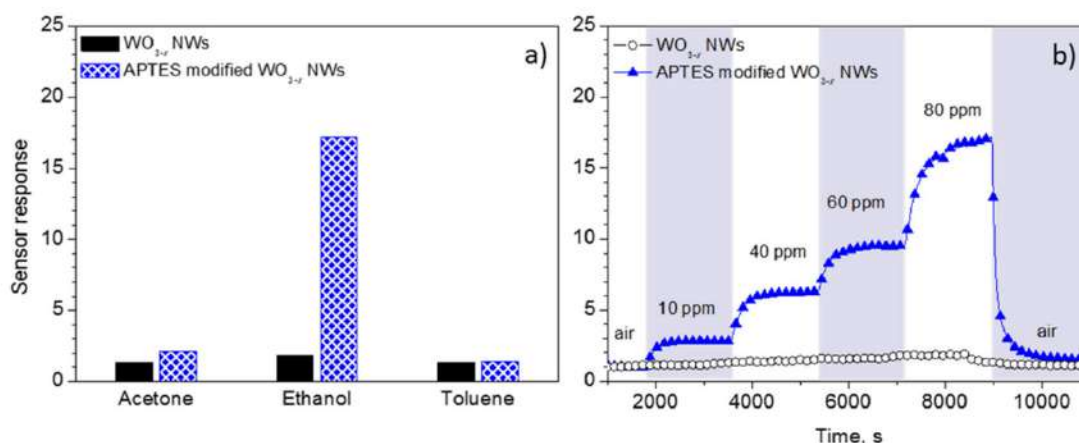


Figure 3. Sensor response to 80 ppm of acetone, ethanol and toluene (a), and sensor response towards various concentrations of ethanol (b) for the APTES modified and non-modified WO_{3-x} NWs.

4. Conclusions

Gas microsensors based on silanized WO_{3-x} NWs have been developed in this work. Both, the synthesis of WO_{3-x} NWs and the silanization of their surface (using aminosilane) were performed directly on microtransducing platforms via CVD. XPS analysis of the modified WO_{3-x} NWs confirmed the silanization of their surface. Photoactivated gas sensing test at RT demonstrated that the silanized structures (as opposed to non-silanized structures) are highly sensitive and selective to ethanol towards other volatile organic compounds including acetone and toluene.

Author Contributions: All authors conceived and designed the experiments; S.V., Z.F., M.T., and I.G. fabricated the sensor device and analyzed the gas sensitive material. S.V., I.G., E.F., and C.C. perform and analyzed the gas sensing test; S.V. wrote the paper.

Acknowledgments: This work has been supported by the Czech Science Foundation (GAČR) via Grant no. 17-16531S. The support of the Spanish Ministry of Economy and Competitiveness via the Ramón y Cajal programme and projects TEC2015-74329-JIN-(AEI/FEDER, EU) and TEC2016-79898-C6-1-R (AEI/FEDER, EU) are also acknowledged. This research has made use of the infrastructures of the Spanish ICTS Network MICRONANOFABS partially supported by MINECO. CEITEC Nano Research Infrastructure (IDL2015041, MEYS CR, 2016–2019) is also acknowledged.

Conflicts of Interest: The authors declare no conflict of interest. The founding sponsors had no role in the design of the study; in the collection, analyses, or interpretation of data; in the writing of the manuscript, and in the decision to publish the results.

References

1. Vallejos, S.; Umek, P.; Blackman, C. AACVD Control parameters for selective deposition of tungsten oxide nanostructures. *J. Nanosci. Nanotechnol.* **2011**, *11*, 8214–8220, doi:10.1166/jnn.2011.5027.
2. Vallejos, S.; Gracia, I.; Chmela, O.; Figueras, E.; Hubálek, J.; Cané, C. Chemoresistive micromachined gas sensors based on functionalized metal oxide nanowires: Performance and reliability. *Sens. Actuator B* **2016**, *235*, 525–534, doi:10.1016/j.snb.2016.05.102.
3. Prades, J.D.; Jimenez-Diaz, R.; Hernandez-Ramirez, F.; Barth, S.; Cirera, A.; Romano-Rodriguez, A.; Mathur, S.; Morante, J.R. Equivalence between thermal and room temperature UV light-modulated responses of gas sensors based on individual SnO₂ nanowires. *Sens. Actuator B* **2009**, *140*, 337–341, doi:10.1016/j.snb.2009.04.070.
4. Wang, B.; Haick, H. Effect of Functional Groups on the Sensing Properties of Silicon Nanowires toward Volatile Compounds. *ACS Appl. Mater. Interfaces* **2013**, *5*, 2289–2299, doi:10.1021/am4004649.
5. Reichardt, C.; Welton, T. *Solvents and Solvent Effects in Organic Chemistry: Third, Updated and Enlarged Edition*; John Wiley & Sons, Inc.: Hoboken, NJ, USA, 2003.



© 2018 by the authors. Licensee MDPI, Basel, Switzerland. This article is an open access article distributed under the terms and conditions of the Creative Commons Attribution (CC BY) license (<http://creativecommons.org/licenses/by/4.0/>).